Properties and Sensing Applications of Long-Period Gratings

by

Vikram Bhatia

Dissertation submitted to the Faculty of the

Virginia Polytechnic Institute and State University

in partial fulfillment of the requirements for the degree of

DOCTOR OF PHILOSOPHY

IN

ELECTRICAL ENGINEERING

APPROVED:

Kent A. Murphy, Chairman

Ioannis M. Besieris

Richard O. Claus

Guy J. Indebetouw

Ira Jacobs

November, 1996

Blacksburg, Virginia

Keywords: Optical fibers sensors, Long-period gratings, Temperature sensor, Strain sensor, Index of refraction sensor, Multi-parameter measurements

PROPERTIES AND SENSING APPLICATIONS OF LONG-PERIOD GRATINGS

by
Vikram Bhatia
Dr. Kent A. Murphy, Chairman
Electrical Engineering

(ABSTRACT)

A long-period grating is obtained by introducing a periodic refractive index modulation in the core of a hydrogen-sensitized germanosilicate fiber. The phase-matching condition causes light from the fundamental guided mode to couple to discrete, forward-propagating cladding modes. These cladding modes attenuate rapidly on propagation and result in loss bands at distinct wavelengths in the grating transmission spectrum. We present a comprehensive analysis of the spectral modulation provided by long-period gratings. An analytical model is developed to predict the location of the resonance bands as functions of the grating period and the parameters of the host fiber. These gratings with small insertion loss and negligible back-reflection are shown to possess two different regions of operation, namely, normal and anomalous. The fabrication and high-temperature annealing of these devices is detailed, and a novel method to obtain these gratings without employing ultra-violet radiation is presented.

Long-period gratings are proposed as simple yet versatile optical fiber sensors. It is demonstrated that external temperature and axial strain introduce large spectral shifts in the resonance bands. A theoretical evaluation of the sensitivity reveals a strong dependence on the properties of the optical fiber, the grating periodicity, the order of the cladding mode, the writing and annealing conditions, and the index of refraction of the surrounding medium. Temperature-insensitive and strain-insensitive long-period gratings written in standard optical fibers are studied for their sensing characteristics. Long-period grating-based refractive index sensors are obtained without etching the cladding of the fiber. It is demonstrated that long-period grating sensors can be implemented with simple demodulation schemes. Applications of these devices to structural health monitoring and biochemical sensing are presented. Finally, long-period gratings are demonstrated as effective sensors that can be used to separate temperature and axial strain acting simultaneously on the fiber. Strain-insensitive gratings are used to extend the dynamic range of the system in the presence of non-linearities and cross-sensitivities.

Acknowledgments

I wish to extend my sincerest thanks to Dr. Kent A. Murphy for agreeing to serve as my technical advisor and for his constant support and encouragement over the past four years. Thanks also being a friend and helping me mature professionally, really. I would like to acknowledge Dr. Ashish M. Vengsarkar at Bell Laboratories for his innovative insight and for providing me with the opportunity to work on long-period gratings. Words are not enough to express his contribution to my personal growth.

I also would like to thank Dr. Richard O. Claus for financial and moral support throughout my graduate studies and his enthusiasm to encourage novel ideas. I wish to thank Dr. Ira Jacobs for his genuine concern for students and for several suggestions that helped in improving the quality of the work presented here. Additionally, acknowledgments to Dr. Ioannis M. Besieris and Dr. Guy J. Indebetouw for their exemplary teaching skills and for consenting to be members of my advisory committee.

Thanks also to all the students and staff at the Fiber and Electro-Optics Research Center for their help and encouragement during my stay in Blacksburg. The contributions of Dave Campbell, Dan Sherr, Noel Zabaronick, Tiffanie D' Alberto, Mary Kay Burford and Greg Ten Eyck deserve a special mention. I would also like to express my gratitude to Jonathan Greene and Tuan Tran at Fiber and Sensor Technologies, Inc. for their friendship and support during good and bad times. I wish to thank Mike Gunther, Russ May, Dr. Marten deVries, Mallika Sen, Vivek Arya, Jen Elster and Linda Jones for working with me and helping me expand my horizons. Thanks to Dr. Paul Lemaire, Dr. Justin Judkins and Renee Pedrazzani at Bell Laboratories for helping me comprehend the subtleties of long-period gratings.

Most importantly, I would like to acknowledge the support of my parents, Aruna and Mohan Bhatia, and my brother, Pankaj. Their love and affection has helped me overcome numerous hurdles on the road of life. Finally, I am thankful to Sumit Joshi, Sanjeev Raj and Varun Ratta for being friends and for their helpful advice and inspiration.

Table of Contents

Chapter 1 - Introduction 1
1.1 Optical Fiber Sensing Technology 1
1.2 Significance of the Problem 2
1.3 Technical Objectives 5
1.4 Outline 7

Chapter 2 - Photosensitivity and Mode Coupling in Optical Fibers 9
2.1 Photosensitivity in Optical Fibers 9
2.2 Hydrogen-Loading and Thermal-Induced Refractive Index Modulation 12
2.2.1 Hydrogen-Loading of Germanosilicate Fibers 12
2.2.2 Thermal-Sensitivity of Hydrogen-Loaded Germanosilicate Fibers 14
2.3 Mode-Coupling in Optical Fibers 15
2.3.1 Guided and Radiation Modes 16
2.3.2 Coupled Mode Theory 18
2.3.2.1 Co-directional Coupling 19
2.3.2.2 Contra-directional Coupling 24
2.4 Fiber Bragg Gratings 27
2.4.1 Principle of Operation 28
2.4.2 Optical and Physical Properties 30
2.4.3 Fabrication 37
2.4.4 Applications 39
2.4.4.1 Temperature Sensor 41
2.4.4.2 Strain Sensor 42
2.4.4.3 Advantages and Limitations 43
2.5 Guided Mode Coupling Using Long-Period Gratings 45

Chapter 3 - Properties of Long-Period Gratings 49
3.1 Principle of Operation 50
3.2 Analytical Modeling of Long-Period Gratings 60
3.2.1 Fundamental Concepts 60

3.2.2 Waveguide Analysis 65
3.2.2.1 Fundamental Guided Mode Analysis 66
3.2.2.2 Analysis of Cladding Modes 73
3.2.3 Characteristic Curves of Long-Period Gratings 81
3.2.3.1 Differential Propagation Constant 82
3.2.3.2 Characteristic Curves 87
3.2.3.3 Sensitivity Analysis of Characteristic Curves 93
3.2.4 Important Grating Parameters 95
3.2.4.1 Coupling Coefficient 96
3.2.4.2 Resonance Band Separation, Transmission and Bandwidth 99
3.3 Fabrication and Annealing of Long-Period Gratings 105
3.3.1 Fabrication of Long-Period Gratings 105
3.3.1.1 Excimer Laser Method 106
3.3.1.2 Continuous-Wave Laser Method 109
3.3.1.3 CO_2 Laser Method 114
3.3.2 Annealing of Long-Period Gratings 117
3.4 Optical and Physical Properties of Long-Period Gratings 122
3.4.1 Optical Properties 122
3.4.2 Physical Properties 127
3.4.2.1 Bending and Recoating of Long-Period Gratings 127
3.4.2.2 Etching of Long-Period Gratings 129
3.5 Applications of Long-Period Gratings to Communication Systems 131
3.5.1 Applications to Erbium-Doped Fiber Amplifier Systems 131
3.5.2 Other Applications to Communication Systems 138

Chapter 4 - Single-Parameter Long-Period Grating Sensors 143
4.1 Principle of Operation 144
4.2 Temperature Sensor 148
4.2.1 Theoretical Analysis 148
4.2.2 Experimental Results 161
4.2.3 Temperature-Insensitive Gratings 168
4.3 Axial Strain Sensor 173
4.3.1 Theoretical Analysis 173
4.3.2 Experimental Results 183
4.3.3 Temperature-Insensitive Gratings 187

4.3.4 Strain-Insensitive Gratings 192
4.4 Index of Refraction Sensor 196
4.4.1 Theoretical Analysis 197
4.4.2 Experimental Results 205
4.4.3 Temperature-Insensitive Gratings 213
4.5 Demodulation and Multiplexing 217
4.5.1 Demodulation 218
4.5.2 Multiplexing 223
4.6 Applications of Long-Period Grating Sensors 225
4.6.1 Strain Sensor 226
4.6.2 Refractive Index Sensor 227
4.6.3 Other Applications 229
4.7 Comparison of Long-Period Gratings with Other Fiber Optic Sensors 230

Chapter 5 - Simultaneous Strain and Temperature Measurement Systems 235
5.1 Multi-Parameter Measurement 236
5.2 Principle of Operation 239
5.3 Non-Linearities and Cross-Sensitivities 242
5.4 Experimental Results 253
5.4.1 Conventional Grating System 254
5.4.2 Strain-Insensitive Grating System 259
5.4.3 Dual-Grating System 263
5.5 Sensor Stability Analysis 267
5.5.1 Analytical Approach 267
5.5.2 Graphical Approach 270
5.6 System Performance 276

Chapter 6 - Conclusions 280

References 286

Vita 301

List of Figures

Figure 2.1. Phenomenon of photosensitivity in a material exposed to a non-uniform, sinusoidal spatial light distribution [22] 11

Figure 2.2. Thermal reaction at the Si-O-Ge bonds leading to the formation of GODC sites and Si-OH bonds [49] 13

Figure 2.3. Typical variation of the normalized propagation constant (b) with the normalized frequency (V) for a step-index fiber calculated using Gloge's weakly-guiding approximations [54] 16

Figure 2.4. Propagation constants of the forward and reverse-propagating guided modes in an optical fiber. β_{01} and β_{11} are the propagation constants of the two lowest order forward-propagating guided modes. Also represented are the propagation constants of radiation modes [1] 17

Figure 2.5. Propagation constant distribution of cladding modes in an optical fiber. The hatched region represents the cladding modes. $\beta^{(01)}$ and $\beta^{(11)}$ are the propagation constants of the two lowest order forward-propagating cladding modes. The β-space between the two hatched region is occupied by radiation modes 18

Figure 2.6. Illustration of an optical fiber under perturbation. The perturbation exists form z=0 to z=L 19

Figure 2.7. Variation of the power of the two co-propagating eigenmodes a_1 and a_2 involved in coupling for (a) phase-mismatched ($\delta/\kappa=2$), and (b) phase-matched ($\delta/\kappa=0$) case. The values are normalized to the incident power in mode a_2 ($P_2(0)=P_0$) 23

Figure 2.8. Variation of the power of the two counter-propagating eigenmodes a_1 and a_2 involved in coupling for the phase-matched ($\delta=0$) case. This figure should be compared

with Figure 2.7(b) which illustrates the power variation for the phase-matched co-propagating modes 26

Figure 2.9. Mode coupling mechanism in fiber Bragg gratings. The large value of $\Delta\beta$ requires a small periodicity Λ, to satisfy the phase-matching condition 28

Figure 2.10. Interrogation of a Bragg grating of period Λ by a broadband source (I is the intensity and λ is the wavelength) results in reflection at the phase-matching wavelength λ_B. The transmission spectrum consists of the incident spectrum modulated by the loss at the Bragg wavelength. The dark regions in the fiber core represent areas where the refractive index has been modulated by the UV pattern 30

Figure 2.11. Variation of the Bragg wavelength as a function of the grating period for the 1060 nm Corning Flexcor fiber. The wavelength versus period curve may be approximated by a straight line ($d\lambda_B/d\Lambda=2n_{eff}$) 31

Figure 2.12. Variation of the normalized reflected and transmitted powers at the phase-matched Bragg wavelength 33

Figure 2.13. Variation of reflectivity as a function of wavelength for a grating of L=1 cm centered at 1310 nm in Corning SMF-28 fiber. Note the small spectral width of the grating 36

Figure 2.14. Fabrication of Bragg gratings using the interferometric scheme [9] 38

Figure 2.15. Bragg grating fabrication using the prism method [67] 38

Figure 2.16. Phase mask method of fabricating Bragg gratings [13] 39

Figure 2.17. Setup to write Bragg gratings in germanosilicate fibers 39

Figure 2.18. Set up to realize a fiber grating laser using erbium-doped fiber [69] 40

Figure 2.19. Mode coupling between two forward-propagating guided modes. The small value of $\Delta\beta$ results in a large value of the grating periodicity Λ 46

Figure 2.20. Typical variation of the differential propagation constant ($\Delta\beta$) between two forward-propagating guided modes as a function of the operating wavelength. $\Delta\beta$ attains its maximum value $(\Delta\beta)_{max}$ at the equalization wavelength λ_0 [81] 47

Figure 3.1. Coupling of the fundamental guided mode to cladding modes in a long-period grating. Λ is the periodicity of the refractive index modulation in the core.....50

Figure 3.2. Coupling to reverse-propagating cladding modes in a strong fiber Bragg grating [86]. (a) In transmission, the pronounced structure at wavelengths smaller than the Bragg wavelength can be attributed to cladding mode coupling. (b) The reflection spectrum lacks the spiky spectrum at wavelengths shorter than the Bragg peak, confirming the loss to cladding modes 51

Figure 3.3. Mode coupling mechanism in a long-period grating [1]. β_{01} is the propagation constant of the fundamental guided mode and $\beta^{(m)}$ are the propagation constants of the circularly-symmetric cladding modes involved in coupling. The hatched region represents a continuum of forward-propagating radiation modes 52

Figure 3.4. Transmission spectrum of a long-period grating written in Corning 1060 Flexcor fiber with period, Λ=198 μm [1]. The discrete, spiky loss bands correspond to the coupling of the fundamental guided mode to discrete cladding modes 54

Figure 3.5. Spectral modulation provided by a typical long-period grating. λ_1, λ_2 and λ_3 are coupling wavelengths corresponding to three different cladding modes.....55

Figure 3.6. Coupling of LP_{01} guided mode to discrete, forward-propagating cladding modes, (a) coupling to $LP^{(2)}$ cladding mode, (b) stretching of ω-axis for coupling to $LP^{(1)}$ cladding mode, and (c) compressing of ω-axis for coupling to $LP^{(3)}$ cladding mode 56

Figure 3.7. Depiction of the spectral location of λ_{cut} relative to wavelength $\lambda^{(2)}$ in a long-period grating ($\lambda_{cut}<\lambda^{(2)}$) 57

Figure 3.8. Effect of change in the propagation constants of the core and cladding modes. (a) Coupling of the fundamental guided mode (propagation constant β_{01}) to a cladding mode (propagation constant $\beta^{(m)}$), (b) increase in β_{01} and (c) increase in $\beta^{(m)}$ .59

Figure 3.9. Variation of the refractive indices (n_A, n_B and n_C) and the group indices (n_{gA}, n_{gB} and n_{gC}) in bulk samples of three different materials as functions of wavelength. A is quenched SiO_2, B is 13.5% GeO_2:86.5 SiO_2 and C is 6.75% GeO_2:93.25% SiO_2 ..64

Figure 3.10. Fiber geometry used in the analysis of the fundamental guided mode. The core has a radius a, while the cladding is assumed to extend to infinity 67

Figure 3.11. Variation of the effective index n_{eff} and group index n_g of the fundamental LP_{01} guided mode with wavelength for Corning SMF-28 fiber. The effective index is calculated by solving the characteristic equation for N_p=51 and then using a third order polynomial curve fit to obtain a continuous variation. Also shown are the spectral dependence of the core (n_1) and the cladding (n_2) refractive indices 69

Figure 3.12. Variation of the effective index n_{eff} and group index n_g of the fundamental LP_{01} guided mode with wavelength for Corning Flexcore 1060 fiber for N_p=51 and N_o=3. Note the difference in the x and y axes from those in Figure 3.11 70

Figure 3.13. Variation of the effective index n_{eff} of the fundamental guided mode with wavelength for Corning SMF-28 fiber using typical parameters in Table I (middle), with core radius reduced to a=4.11 μm (bottom) and with Δ=0.3636% (top) 71

Figure 3.14. Variation of the normalized power of the fundamental guided mode as a function of radial distance from the fiber axis (r=0) at 1310 nm (inner curve) and 1550 nm (outer curve) for SMF-28 fiber. The broken vertical lines represent the core-cladding interface (r=4.15 μm). The power decays rapidly in the cladding and has negligible magnitude at the outer cladding boundary (r=62.5 μm) 72

Figure 3.15. Spectral variation of the effective index $n_{cl}^{(m)}$ of $LP_{0,m}$ cladding modes (m=2 through 16 in steps of 2) in optical fibers with quenched silica cladding and b=62.5 μm. The ambient medium is assumed to be air (n_3=1). The dashed line represents the refractive index of the cladding 74

Figure 3.16. Variation of the group indices of a few $LP_{0,m}$ cladding modes and the fundamental guided mode (dashed line) for an unperturbed SMF-28 fiber with n_3=1 75

Figure 3.17. Spectral variation of the effective indices of a few $LP_{0,m}$ cladding modes for b=62.5 μm (solid lines) and for b=61.5 μm (dashed lines). For m=1 the change in effective index due to the reduction in cladding radius is hardly discernible 77

Figure 3.18. Spectral variation of the effective indices of a few $LP_{0,m}$ cladding modes for n_3=1.0 (solid lines) and for n_3=1.33 (dashed lines). The change in effective indices becomes larger as the order of the corresponding cladding mode is increased 78

Figure 3.19. Radial variation of the modal power in (a) $LP_{0,1}$ and (b) $LP_{0,6}$ cladding modes at 1310 nm and n_3=1.0. The dashed lines represent the core (r=4.15 μm for SMF-28 fiber) and the cladding (r=62.5 μm) outer surfaces 80

Figure 3.20. Variation of the differential propagation constant with wavelength for the $LP_{0,12}$ cladding mode. Curve A is for an unperturbed SMF-28 fiber while the curve B is for a SMF-28 fiber with core index increased by 10^{-4} 83

Figure 3.21. Characteristic curves for m=12 in Corning SMF-28 fiber. Curve A is for an unperturbed fiber while curve B is for a fiber with core index increased by 10^{-4} 84

Figure 3.22. Variation of the equalization period as a function of the order of the cladding mode for unperturbed SMF-28 fiber. Only modes with equalization wavelengths in the range 1100 nm to 1600 nm are considered 86

Figure 3.23. Characteristic curves for the first ten circularly-symmetric cladding modes in SMF-28 fiber. The ambient material is air (n_3=1) and the peak index change (Δn) is assumed to be 5×10^{-4}. The dashed curve corresponds to λ_{cut} for different periods. The order of the cladding modes increases from right to left 88

Figure 3.24. Characteristic curves for the first ten circularly-symmetric cladding modes in Flexcor 1060 fiber. The dashed curve corresponds to λ_{cut} for different periods 89

Figure 3.25. Characteristic curves for the first ten circularly-symmetric cladding modes in Flexcor 780 fiber 90

Figure 3.26. Characteristic curves for the cladding modes $LP_{0,11}$ through $LP_{0,20}$ in Flexcor 1060 fiber. The order of the cladding modes increases from right to left 91

Figure 3.27. Characteristic curves for the cladding modes $LP_{0,21}$ through $LP_{0,30}$ for Flexcor 1060 fiber. The order of the cladding modes increases from top right to bottom left 92

Figure 3.28. Characteristic curves for typical parameters of SMF-28 fiber (solid lines). The dashed curves are for a SMF-28 fiber with core radius a=4.11 μm while the dotted ones are for the cladding radius b=62 μm 94

Figure 3.29. Characteristic curves for SMF-28 fiber with $\Delta n=5\times10^{-4}$ (solid lines). The dashed curves are for $\Delta n=10^{-4}$ while the dotted curves are for $\Delta n=10^{-3}$. Only modes with m=5 to 10 are considered to keep the representation simple 95

Figure 3.30. Theoretically obtained evolution of a long-period grating in SMF-28 fiber with Λ=360 μm (normal region of operation). The curves A through E represent the transmission spectrum at intervals of one minute each from the time exposure is initiated. The shift to longer wavelengths and the increase in maximum loss can be attributed to the index change during the writing process 103

Figure 3.31. Theoretically obtained transmission spectra of two long-period gratings in SMF-28 fiber with Λ=360 μm. The inner spectrum is for a grating with L=2 cm while that on the outside is for a grating with L=1 cm. The actual resonant wavelength of the 1 cm long grating is about 1565 nm 104

Figure 3.32. Setup to fabricate long-period gratings using an excimer laser [1] 107

Figure 3.33. Evolution of a typical long-period grating on UV exposure [1]. Curves A through E represent the transmission spectrum in one minute intervals after the exposure is initiated. The grating is written in AT&T dispersion-shifted fiber with Λ=488 μm.. 108

Figure 3.34. Procedure to fabricate multiple long-period gratings using the broad dimensions of an excimer laser beam. The number of gratings that can be written is limited only by the excimer beam or amplitude mask dimension orthogonal to the fiber axes [1] 109

Figure 3.35. Setup to fabricate long-period gratings using FRED-CW laser. The lens and the mirror are translated simultaneously to scan the UV beam across the stationary amplitude mask and fiber 110

Figure 3.36. Transmission spectrum of a long-period grating written in SMF-28 fiber using the CW writing method. The periodicity of 320 μm implies that all the resonance bands operate in the normal region 111

Figure 3.37. Growth of a long-period grating band in the anomalous region. The grating was fabricated in Flexcor 1060 fiber with Λ=40 μm using CW exposure. Curves A through D represent the transmission spectrum at 10 minute intervals 112

Figure 3.38. Setup to fabricate long-period gratings using CO_2 laser. The fiber holders are mounted on a translation stage to enable longitudinal movement of the fiber 114

Figure 3.39. Transmission spectrum of a long-period grating written in Flexcore 1060 fiber using the CO_2 laser fabrication method 115

Figure 3.40. Fabrication of multiple long-period gratings using thermal treatment from a CO_2 laser. The arrows depict the direction of the beam traversal 116

Figure 3.41. Variation in the spectral position of a resonance band with time for a long-period grating. The grating was left at room temperature following fabrication (t=0). The discontinuity results form the intermittent collection of data 118

Figure 3.42. Effect of annealing (at 150 °C) on three resonance bands of a grating written in DSF [1]. Time t=0 corresponds to the initiation of the annealing process.... 119

Figure 3.43. Transmission spectra of a long-period grating before and after annealing at 150° C for 10 hours. Note the reduction in the coupling wavelength and isolation 121

Figure 3.44. Transmission spectrum of a strong grating written in AT&T DSF with Λ=402 μm and L=2.54 cm using the excimer laser method [1] 123

Figure 3.45. Transmission spectrum of a long-period grating written in Corning SMF-28 fiber with Λ=320 μm and L=8 cm using CW exposure. The rounding of the peak at the phase-matching wavelength can be attributed to the limited resolution (0.1 nm) of the optical spectrum analyzer. Note the narrow wavelength span of 8 nm 125

Figure 3.46. OCDR back-reflection measurement in a grating written in AT&T dispersion-shifted fiber [1]. The horizontal scale represents the distance from the input end of the fiber 126

Figure 3.47. Effect of different magnitudes of tensioning and compressive bends on a resonance band of a long-period grating fabricated in DSF [99] 128

Figure 3.48. Transmission spectra of a long-period grating written in AT&T DSF before and after etching 130

Figure 3.49. Inverted EDFA gain spectrum (symbols) and the concatenated transmission spectrum (lines) of two distinct long-period gratings. The gratings were fabricated in AT&T DSF with period Λ=474 μm 136

Figure 4.1. Spectral shift (per 100 °C temperature change) as a function of period for SMF-28 fiber (m=7 and $\Delta n=5\times10^{-4}$). The waveguide and material contributions are shown separately 151

Figure 4.2. Wavelength shift (per 100 °C temperature change) as a function of period for SMF-28 fiber for (a) m=1,2 and 3, and (b) m=6,7 and 8 ($\Delta n=5\times10^{-4}$) 152

Figure 4.3. Wavelength shift (per 100 °C temperature change) as a function of grating period for SMF-28 fiber (m=7). The three curves correspond to different index changes during fabrication, $\Delta n=3\times10^{-4}$ (bottom), $\Delta n=5\times10^{-4}$ (middle) and $\Delta n=7\times10^{-4}$ (top)..... 154

Figure 4.4. Dependence of the temperature sensitivity of long-period gratings of different periods (m=7 in SMF-28 fiber with $\Delta n=5\times10^{-4}$) as a function of ambient index. Curve A is the temperature-induced shift (per 100 °C) with air as the surrounding medium ($n_3=1.0$). Curves B and C are the shifts with water as the ambient medium ($n_3=1.33$) by ignoring and including the thermo-optic coefficient of water ($dn/dT=-1.34\times10^{-4}$/°C [123]), respectively. Curve D is the shift for an index oil with $n_3=1.42$ and $dn/dT=-3.98\times10^{-4}$/°C [124] 155

Figure 4.5. Theoretically determined temperature-induced shifts in the four resonance bands of a long-period grating written in SMF-28 fiber with $\Lambda=280$ μm. The locations of the bands A, B, C and D are 1627.8 nm, 1315.9 nm, 1197.8 nm and 1128.3 nm, respectively, for $\Delta n=4\times10^{-4}$ and temperature 30 °C 157

Figure 4.6. Temperature sensitivity of three bands corresponding to m=28 (A), m=29 (B) and m=30 (C) for Flexcor 1060 nm fiber with $n_3=1.0$ and $\Delta n=5\times10^{-4}$. Curve D is the temperature-induced shift for to m=30 with water as the ambient medium ($n_3=1.33$) assuming the thermo-optic coefficient of water $dn/dT=-1.34\times10^{-4}$/°C [123] 159

Figure 4.7. Experimental set up employed to determine the thermal-induced spectral shift in the resonance bands of a long-period grating. The thermocouple is placed adjacent to the grating in the temperature chamber 161

Figure 4.8. Effect of employing a least-squared curve fit on the transmission spectrum of a long-period grating. The offset between the raw data and the corresponding curve fit has been deliberately introduced to prevent overlapping 163

Figure 4.9. Transmission spectrum of a long-period grating used for the temperature test. The grating is fabricated in Corning SMF-28 fiber employing continuous-wave UV radiation ($\Lambda=280$ μm). The wavelength span is limited to 500 nm here but resonance bands are present at wavelengths shorter than 1200 nm also 164

Figure 4.10. Shift in band A with temperature for the grating shown in Figure 4.9. The spectra correspond to temperatures of 22.7 °C, 49.1 °C, 74.0 °C, 100.9 °C, 127.3 °C and 149.7 °C from left to right. The resonant wavelength shifts from 1607.8 nm at 22.7 °C to 1619.6 nm at 149.7 °C 166

Figure 4.11. Shift in the peak loss wavelengths (with respect to that at 31.2 °C) with temperature for various resonance bands of the grating shown in Figure 4.9. The location of the bands A, B, C and D are 1608.6 nm, 1332.9 nm, 1219.7 nm and 1159.6 nm, respectively at 31.2 °C. The experimental data (symbols) are and approximated by linear curve fits. The dashed line (E) is the shift for a Bragg grating at 1550 nm with a temperature coefficient 1.3 nm/°C 167

Figure 4.12. Spectral shift in the resonance band for a grating (Λ=166 μm) written in the fiber with multilayer refractive index profile. The line is a curve-fit to the experimental data (circular symbols). The resonant wavelength shifts from 1522.17 nm at 25 °C (solid curve) to 1521.93 nm at 125 °C (dashed curve) as shown in the inset 169

Figure 4.13. Location of a resonance band as a function of temperature for a grating with Λ=40 μm in Flexcor 1060 fiber. The straight line fit has a slope of -0.16 nm/°C 171

Figure 4.14. Transmission spectra of a long-period grating written in Flexcor 1060 nm fiber with Λ=40 μm at 25 °C (solid curve) and 125 °C (dashed curve). The resonance band shifts by a mere -0.18 nm for 100 °C increase in temperature 172

Figure 4.15. Wavelength shift (for 1%ε) as a function of period for SMF-28 fiber. The waveguide and material contributions are also shown for the mode with m=7 and peak index change $\Delta n=5\times10^{-4}$ 175

Figure 4.16. Wavelength shift (for 1%ε) as a function of period for SMF-28 fiber with (a) m=1,2 and 3, and (b) m=6,7 and 8 ($\Delta n=5\times10^{-4}$) 178

Figure 4.17. Wavelength shift (for 1%ε) as a function of grating period for SMF-28 fiber (m=7). The three curves correspond to different peak index changes in the core during the writing process - $\Delta n=3\times10^{-4}$ (bottom), $\Delta n=5\times10^{-4}$ (middle) and $\Delta n=7\times10^{-4}$ (top)... 179

Figure 4.18. Dependence of the strain sensitivity (for 1%ε) of gratings of different periods (m=7 in SMF-28 fiber with $\Delta n=5\times10^{-4}$) as a function of ambient index. Curves A,B and C are the strain-induced shifts with n_3=1.0, 1.33 and 1.44, respectively 180

Figure 4.19. Theoretically calculated strain-induced shifts in the four resonance bands of a long-period grating written in SMF-28 fiber with Λ=280 μm. The locations of the bands A, B, C and D are 1627.8 nm, 1315.9 nm, 1197.8 nm and 1128.3 nm, respectively, for $\Delta n=4\times10^{-4}$. The shift in band is slightly non-linear 181

Figure 4.20. Strain sensitivity of three bands corresponding to m=28 (A), m=29 (B) and m=30 (C) for Flexcor 1060 nm fiber with n_3=1.0 and $\Delta n=5\times10^{-4}$ 182

Figure 4.21. Experimental set up employed to determine the strain-induced spectral shift in the resonance bands of a grating. L' is termed the gage length of the sensor 184

Figure 4.22. Shift in band A with strain at 22.7 °C for the grating shown in Figure 4.10. The spectra correspond to strain from 0 to 3000 με in steps of 500 με (left to right) 185

Figure 4.23. Shift in the peak loss wavelengths with strain for various resonance bands of the grating shown in Figure 4.9. The location of the bands A, B, C and D are 1607.8 nm, 1332.4 nm, 1219.3 nm and 1159.3 nm, respectively for an unstrained grating. The dashed line (E) is the shift for a Bragg grating with coefficient 11.55 nm/%ε..... 186

Figure 4.24. Shift in the highest wavelength band of the grating in SMF-28 fiber (Λ=280 μm) with strain at four different temperatures. Curve P,Q,R and S correspond to strain tests at temperatures 21.7 °C, 34.0 °C, 44.2 °C and 55.7 °C, respectively..... 187

Figure 4.25. Wavelength shift as a function of axial strain for a grating with Λ=166 μm in temperature-insensitive fiber. The unperturbed band is located at 1522.17 nm at 25 °C. Inset shows the grating spectra at in steps of 488 με from right to left 188

Figure 4.26. Transmission spectrum of a grating in the specially designed fiber [34] at 25 °C (solid curve) and 125 °C (dashed curve) for an unstrained grating (A), and for strain of 500 με (B) and 1000 με (C) [126] 189

Figure 4.27. Spectral shift in the resonance band of a grating in Flexcor fiber (Λ=40 μm) with axial strain (at T=25 °C). The straight line curve fit has a slope of -21.44 nm/%ε [35]. Inset shows the transmission spectrum of the unperturbed grating (solid curve) and that at 2146 με (dashed curve) 190

Figure 4.28. Location of the resonance band of the grating in Flexcor fiber (Λ=40 μm) as a function of strain at three distinct temperatures. The overlapping of the points predicts minimal thermal cross-sensitivity of the strain sensor 191

Figure 4.29. Transmission spectrum of a grating in Flexcor 1060 fiber (Λ=340 μm) with resonance bands at 1638.3 nm, 1362.3 nm and 1257.9 nm. The band at 1257.9 nm is found to have a small strain coefficient of -0.4 nm/%ε 193

Figure 4.30. Experimental results from the temperature measurement on a grating in Flexcor 1060 fiber (Λ=340 μm) perturbed simultaneously by strain and temperature. The strain-insensitive band at 1257.9 nm is used to obtain temperature. The two plots show (a) the actual (line) and calculated (symbols) temperature and (b) applied strain 195

Figure 4.31. Wavelength shift as a function of period for SMF-28 fiber for three different values of ambient index n_3. The calculations are for the mode with m=7 and peak index change $\Delta n=5\times10^{-4}$. The shift for each index value is measured with respect to the wavelength location at n_3=1.0 199

Figure 4.32. Shift in the coupling wavelength (for a change in n_3 from 1.0 to 1.43) as a function of period for SMF-28 fiber with (a) m=1,2 and 3, and (b) m=6,7 and 8 200

Figure 4.33. Shift in the coupling wavelength (for a change in n_3 from 1.0 to 1.43) as a function of grating period for SMF-28 fiber (m=7). The three curves correspond to different peak index changes in the core during the writing process - $\Delta n=3\times10^{-4}$ (top), $\Delta n=5\times10^{-4}$ (middle) and $\Delta n=7\times10^{-4}$ (bottom) 202

Figure 4.34. Shift in the coupling wavelength (for a change in n_3 from 1.0 to 1.43) as a function of grating period for SMF-28 fiber (m=5). The three curves correspond to cladding diameters of 125 μm (A), 120 μm (B) and 115 μm (C) 203

Figure 4.35. Theoretically determined shifts in the four resonance bands of a long-period grating in SMF-28 fiber (Λ=300 μm). The resonance bands A,B,C and D are located at 1525.5.1 nm, 1323.5 nm, 1225.1 nm and 1165.4 nm, respectively (n_3=1.0). The shift for each band is measured with respect to the location at n_3=1.0 204

Figure 4.36. Experimental set up to determine the shift in the resonance bands of a long-period grating due to changes in the refractive index of the medium surrounding the cladding. The laboratory jack level is adjusted such that the glass slide placed on it is just below the bare fiber 205

Figure 4.37. Transmission spectrum of a grating written in SMF-28 fiber with Λ=320 μm. The bands at 1496.6 nm (A), 1329.3 nm (B), 1243.8 nm (C) and 1192.1 nm (D) were used for refractive index experiments. The grating was annealed at 300 °C 206

Figure 4.38. Experimental shift in the four resonance bands of the grating depicted in Figure 4.37 as a function of the index of the ambient medium. The shifts are measured with respect to the locations at n_3=1.0. The indices of the oils are calculated at the corresponding resonant wavelengths of the bands 207

Figure 4.39. Transmission spectrum of a long-period grating written in SMF-28 fiber with Λ=320 μm at different values of ambient refractive index (n_3). The resonance band shifts to shorter wavelengths as n_3 approaches the effective index of the cladding mode. The indices of the oils are specified at 589.3 nm and should be reduced by approximately 0.01 to obtain their values at 1550 nm [124] 209

Figure 4.40. Spectral shift in a resonance band of a grating (Λ=434 μm) as a function of the ambient index for three different cladding diameters. Curves A,B and C correspond to claddings with diameters 125 μm, 109.7 μm and 99.5 μm, respectively 212

Figure 4.41. Shift in the resonance band of a long-period grating written in the fiber with special refractive index profile [126]. The unperturbed band is located at 1520.6 for the grating with period Λ=166 μm. The inset depicts the resonance spectra for different ambient indices. The indices of the oils are specified at 589.3 nm 214

Figure 4.42. Shift in a resonance band of a grating written in Flexcor 1060 fiber with Λ=40 μm [126]. Inset depicts the transmission spectra with n_3=1.0 (solid curve) and n_3=1.428 (dashed curve). The indices of the oils are specified at 589.3 nm 215

Figure 4.43. Shift in the spectral position of a grating in Flexcor 1060 nm fiber (Λ=40 μm) immersed in a water bath (n_3=1.33). The wavelength shift is measured with respect to the position of the band at 25.7 °C and n_3=1.33 (λ=1145.6 nm) 216

Figure 4.44. Simple demodulation scheme for long-period grating sensors 218

Figure 4.45. Shift in the spectral position of the resonance band (centered at λ_1) to a higher wavelength under external perturbation. The transmission spectrum of the optical filter, with pass-band centered at λ_f, is also shown 219

Figure 4.46. Demodulation of a long-period grating by employing a fiber Bragg grating. The reflection spectrum of the Bragg grating overlaps the resonance band in a manner similar to the optical filter in Figure 4.45 220

Figure 4.47. Change in transmission through a grating for increasing (circles) and decreasing (squares) temperature. The resonance band under test is centered at 1294 nm (50 °C) while the laser diode is located at 1312 nm. The transmission is normalized to 0 dB at 50 °C. Inset shows the grating transmission spectra in steps of 50 °C 221

Figure 4.48. Change in transmission of a laser diode (λ=1317 nm) through a grating as a function of strain for three independent trials [21]. The transmission is normalized to 0 dB for an unperturbed grating. Inset shows the grating transmission spectra at 0, 2878 and 5036 $\mu\varepsilon$ (from left to right) 222

Figure 4.49. Multiplexing of spectrally offset long-period gratings using an LED and an optical spectrum analyzer (OSA) 223

Figure 4.50. Multiplexing of two long-period gratings (denoted by L1 and L2) using a pair of Bragg gratings (B1 and B2). The center wavelengths of the two bandpass filters are matched to the resonant wavelengths of the Bragg gratings (λ_1 and λ_2) 224

Figure 4.51. Time-division multiplexing of two long-period gratings (denoted by L1 and L2) using a single laser diode and photodetector 225

Figure 4.52. Strain measurement on a loaded reinforcing-bar using a long-period grating written in SMF-28 fiber (Λ=240 μm) [33]. Inset shows the grating transmission spectrum for an unperturbed grating (left curve) and at 1000 $\mu\varepsilon$ 226

Figure 4.53. Effect of sucrose solutions on the spectral position (left axis) of a resonance band of a long-period grating in AT&T dispersion-shifted fiber. The right axis represents the index of refraction of solutions with different sucrose concentrations 228

Figure 5.1. Transmission spectrum of the grating shown in Figure 4.9 for an unstrained case (solid curve) and for a strain of 3000 $\mu\varepsilon$ (dashed curve) at 21.85 °C. The grating is fabricated in Corning SMF-28 fiber employing continuous-wave UV radiation (Λ=280 μm). The wavelength shifts $\Delta\lambda_1$, $\Delta\lambda_2$ and $\Delta\lambda_3$ correspond to the unperturbed bands located at λ_1=1607.9 nm, λ_2=1332.9 nm and λ_3=1219.4 nm, respectively 240

Figure 5.2. Shift in the resonance bands located at 1607.9 nm (circles) and 1332.9 nm (squares) as functions of temperature change ΔT with T_0=21.85 °C. The data for the band at the higher wavelength is fitted with a second order polynomial while that at the shorter wavelength is fitted with a straight line 243

Figure 5.3. Shift in the resonance bands located at 1607.9 nm (circles) and 1332.9 nm (squares) as functions of axial strain at 21.85 °C. Polynomials of order two and one are used to obtain curve fits for the data of the higher and lower wavelength bands, respectively 245

Figure 5.4. Variation of the linear strain coefficient of the higher order peak as a function of temperature. The cross-sensitivity between strain and temperature makes the coefficient B (Equation 5.1) a function of temperature 246

Figure 5.5. Variation of the first ($B_{0\varepsilon}$) and second ($B_{1\varepsilon}$) order cross-sensitivity coefficients of the higher wavelength band as functions of ΔT (T_0=21.85 °C). The linear curve fits to the data points yield values of the coefficients B_0, B_1, B_2 and B_3 247

Figure 5.6. Variation in wavelength of the strain-insensitive band (Figure 4.29) with ambient temperature. The wavelength is represented on the x-axis to obtain values of the coefficients c_0, c_1, c_2 and c_3 (Equation (5.16)) using a third order curve fit 251

Figure 5.7. Variation in wavelength of the higher order band (Figure 4.29) with ambient temperature. The third order curve fit yields values of the coefficients a_0, a_1, a_2 and a_3 in Equation (5.17) 253

Figure 5.8. Experimental set up for simultaneous measurement of strain and temperature using a single long-period grating. The coupler combines the spectrum of the two LEDs centered at distinct wavelengths 255

Figure 5.9. Comparison between actual (unfilled symbols) and calculated (filled symbols) values for simultaneous measurement of strain and temperature using a long-period grating written in SMF-28 fiber with Λ=280 μm. Results are from a static test where the grating was stabilized at different temperatures and then strained..... 257

Figure 5.10. Comparison between measured (symbols) and actual (lines) values of (a) temperature (b) strain using the long-period grating shown in Figure 5.1. The average rate of temperature change was -0.64 °C/min 258

Figure 5.11. Comparison between actual (unfilled symbols) and calculated (filled symbols) values for simultaneous measurement of strain and temperature using a long-period grating written in SMF-28 fiber with Λ=340 μm (Figure 4.29). Results are from a static test where the grating was stabilized at different temperatures and then strained. 260

Figure 5.12. Comparison between measured (symbols) and actual (lines) values of (a) temperature (b) strain using the long-period grating shown in Figure 4.29. The average rate of temperature change was -1.08 °C/min 262

Figure 5.13. Comparison between actual (unfilled symbols) and calculated (filled symbols) values for simultaneous measurement of strain and temperature using two long-period gratings. Results are from a static test where the gratings were stabilized at different temperatures and then strained 264

Figure 5.14. Comparison between measured (symbols) and actual (lines) values of (a) temperature (b) strain using two long-period gratings. The temperature rate of change was as large as 2 °C/min 266

Figure 5.15. Equiwave plots for the two resonance bands in the T-ε plane. The degree of linearity of the curves predicts the non-linearity and cross-sensitivity while the difference in their slopes gives a measure of the stability of the dual-parameter measurement system 270

Figure 5.16. Equiwave plots for the simultaneous temperature and strain sensing scheme using the long-period grating shown in Figure 5.1 ($\Delta\lambda$=0.1 nm, T_0=21.85 °C). The calculated data for the higher (circles) and lower (squares) wavelength resonance bands are fitted to straight lines 272

Figure 5.17. Depiction of equiwave plots for well-conditioned sensitivity matrices in the T-ε plane. (a) Equiwave plots along the T and ε axes since the higher order resonance band is affected only by strain and the other resonance band is influenced only by temperature. (b) Equiwave plots in different quadrants. The temperature and strain coefficients of the higher order resonance bands are positive. For the second resonance band the temperature coefficient is positive while the strain coefficient is negative..... 274

List of Tables

Table I. Sellmeier parameters for bulk glass samples of different compositions [62]....63

Table II. Typical parameters for fibers used in long-period grating model [65,61].....66

Table III. Linear temperature and strain coefficients for the two bands in each of the three configurations proposed in Section 5.4. Also shown is the corresponding reciprocal of the sensitivity matrix condition number, rcond (S) 269

Chapter 1 - Introduction

The rapid progress in optical fiber communication and sensing systems has hastened the quest of researchers and scientists to develop devices that serve to overcome the existing limitations and perform the task of precursors for future advancements in photonics technology. Long-period gratings, first proposed by Vengsarkar *et al.* [1,2,3] over a year ago, are fast gaining popularity as simple yet versatile components for a multitude of applications in optical engineering. Long-period gratings are formed by inducing a spatial refractive index modulation in the core of germanosilicate fibers with periodicities typically ranging in hundreds of micrometers [1]. The phase-matching condition between the guided and cladding modes causes the propagating light to couple out of the core at discrete wavelengths. This dissertation focuses on providing a comprehensive analysis of the state-of the-art long-period grating technology and related applications as optical fiber single- and multi-parameter sensors. The properties of these periodic structures are investigated and the spectral modulation available in the transmission spectra is used to implement novel temperature, strain and index of refraction sensors.

The following section reviews the principal characteristics and recent developments in fiber optic sensing systems. This is done to obtain a better understanding of the problems that are commonly encountered in conventional optical fiber sensors.

1.1 Optical Fiber Sensing Technology

A generic fiber optic sensing system consists of one or more optical fibers carrying light from a source to a detector. An applied perturbation modulates the properties of the transmitted light and produces a change at the detection end. Fiber optic sensors, have in recent years shown tremendous potential as feasible commercial measurement systems due to their inherent small size and immunity to electromagnetic interference [4]. The desired characteristics of an ideal sensor include high resolving power, low insertion loss, wide dynamic range, ease of fabrication, simple signal processing, multiplexing features and multi-measurand capabilities [5]. Fiber optic sensors have been proposed for measurement of strain, temperature, pressure, magnetic and electric fields, liquid level,

rotation rate, acceleration, acoustic waves and index of refraction [6]. The current research and development thrust is towards developing robust strain, temperature, pressure and refractive index sensors for the commercial market.

Fiber optic sensors may broadly be classified as phase-based or intensity-based depending on the parameter of the propagating light that is modulated by the external perturbation. Phase-based or interferometric sensors [7] are highly sensitive and have been demonstrated as excellent short gage-length strain and temperature transducers. Intensity-based sensors have simple signal processing techniques and provide absolute, real-time information about the measurand [5]. Recently, fiber Bragg gratings have been proposed as effective and efficient in-line fiber optic sensors [8]. A Bragg grating is formed by impinging a periodic ultra-violet radiation pattern on the fiber core that causes light at the phase-matching wavelength to be reflected towards the source [9]. The grating-based sensors transform the applied perturbation, such as strain or temperature, into a wavelength shift in the reflected spectrum of a broadband optical source. Bragg grating sensors are all-fiber components that possess a large dynamic range and can be easily multiplexed for distributed measurements [10].

Fiber optics sensors are still in their infancy and a lot of work needs to be done to promote and develop their use in advanced applications. Novel optical fiber sensors that offer excellent performance characteristics would ease the transition of laboratory research to commercial products that offer a viable alternative to electronic and mechanical transducers.

1.2 Significance of the Problem

This section lists the common limitations encountered while dealing with optical fiber sensing systems. This would make the reader realize the importance of these drawbacks and elucidate the reasons for attempts to arrive at solutions to these problems.

As stated in the previous section, optical fiber sensors should ideally possess a number of desired characteristics. Most intensity-based and interferometric sensors satisfy a majority of these features but are ultimately limited by one or more drawbacks. For example, interferometric sensors offer a very high degree of sensitivity but suffer from the requirement of expensive demodulation schemes, such as fringe counters.

Additionally, the basic forms of such sensors suffer from directional ambiguity at certain points of the transfer function curve [7]. Phase-based sensors that operate over the linear region of the sinusoidal output curve are highly susceptible to drifts in the source central wavelengths and to minute ambient temperature fluctuations. Intensity-based sensors offer unambiguous, absolute output but require calibration that might be a function of the optical source characteristics and physical deformities along the fiber length. Moreover, such sensors provide limited sensitivities and might be difficult to multiplex.

Even the elegant Bragg grating-based sensors have a few limitations that have prevented their utilization in certain specific applications. Bragg grating sensors suffer from a number of frailties that include the requirement of a highly stable fabrication system [9], and until recently the inability to perform temperature-independent strain measurements [11]. Moreover, Bragg grating sensors have limited temperature and strain-induced wavelength shifts [8] and in order to implement sensors with higher sensitivities, uneconomical interferometric demodulation techniques have to be employed [12]. Since Bragg gratings are based on coupling of light to the reverse-propagating guided mode, optical isolators might be required to prevent back-reflection-induced source oscillations. Hence the expensive grating fabrication technique [13] and requirement of uneconomical demodulation methods have limited the potential of short-period Bragg gratings.

Additionally, existing fiber optic index of refraction sensors are either too complex for feasible implementation or have limited sensitivities. For example Bragg grating-based refractive index sensors require that the fiber cladding be etched to within a few micrometers of the core to gain access to the evanescent field of the guided mode [14]. The etching process reduces the strength and integrity of the sensor and degrades the sensor performance under harsh environmental conditions. Optical fiber-based surface-plasmon sensors have recently been proposed as attractive refractive index sensors. Surface-plasmon sensors also require polishing the cladding of the fiber for interaction of the induced plasmon with the evanescent filed of the propagating mode [15]. Though such sensors are highly sensitive to small changes in the ambient index of refraction, they suffer from polarization sensitivity and are difficult to fabricate [16].

Fiber optic sensors are inherently prone to ambient temperature fluctuations. For example, the cross-sensitivity to thermal changes can result in erroneous measurements in a sensor that has been calibrated to measure a perturbation other than temperature [11].

The temperature sensitivity of fiber optic sensors becomes critical in applications where a high degree of accuracy is required. Although temperature compensation and stabilization methods can be employed to overcome the thermal cross-sensitivity, such schemes either complicate the signal processing or result in increased system cost. Thus temperature-insensitive strain and refractive index sensors are highly attractive for applications where large thermal fluctuations are expected. Additionally, most applications of fiber optic temperature sensors require that the sensing region be either bonded to the surface of the substrate or embedded inside the structure. The finite thermal expansion coefficient of the host combined with the strain sensitivity of the sensor can result in errors in the temperature measurements. In such cases temperature sensors that are immune to axial strain effects would be highly useful.

An area that has recently undergone much research and development is that of multi-parameter measurement using fiber optic sensors [17]. In some applications it is often necessary to simultaneously monitor two or more perturbations acting on the fiber. The most common pair of measurands that has been investigated is the one consisting of strain and temperature. The separation of the effects of strain and temperature has been proposed in the past using various combinations of interferometric sensors [17,18]. For example, the modal interference in a dual-mode fiber can be used in conjunction with the polarimetric interference in the single mode domain to obtain two simultaneous equations with strain and temperature as unknowns [18]. In Bragg grating systems, the most common method to perform simultaneous measurements is to use two superimposed gratings and separate the strain and temperature effects using the spectral shifts [19]. As stated earlier, interferometric sensors provide differential outputs that can be cumbersome to demodulate. Hence, cost and complexity are again the limiting factors in the design of interferometric-based multi-parameter measurement systems. Also in some of these schemes, the polarization control of the propagating signal becomes a critical issue [18]. A majority of these systems also suffer from non-linearities in temperature or strain response of the sensor [20] and this adds to the complexity of the signal processing at the detection end, and in some cases makes the systems prohibitively uneconomical. The cross-sensitivity between strain and temperature is another driving factor in the search for the ideal multi-parameter sensor. This cross-sensitivity reduces the dynamic range of the sensor and might also provide measured values that differ significantly from the actual strain and temperature that perturb the fiber. All the above issues need to be addressed to implement a simple and economical strain and temperature measurement system.

The large-scale commercialization of optical fiber sensors has to a certain sense been restricted by one or more limitations discussed above. One of the most significant issues is the cost of the sensor and the signal processing equipment. Interferometric sensors can prove to be uneconomical for applications that require low-cost transducers. Bragg grating-based sensors, though easily multiplexed, need either spectrum analyzers or complex interferometric schemes to detect a shift in the reflected spectrum. Thus, the optical fiber sensor market would benefit tremendously from a sensing scheme that is simple to implement and demodulate, provides absolute and real-time outputs, and can be easily configured for multi-parameter measurements.

The next section presents an outline of the major objectives of this dissertation. We briefly analyze the manner in which long-period gratings can be employed to overcome the current limitations of fiber optic sensing systems. It will be shown that long-period gratings are attractive in-line sensing elements that can be implemented with simple demodulation techniques [21].

1.3 Technical Objectives

This dissertation aims to investigate the major properties of long-period gratings and explore their novel applications as high-performance sensing devices. This section outlines the technical goals of this research effort and discusses the utilization of long-period gratings for overcoming the problems discussed in the preceding section.

The origins of the phenomena of photosensitivity [22] and mode-coupling [23,24] in optical fibers are traced and their applications to implementation of versatile devices are evaluated [25]. The transfer of power between co- and counter-propagating modes is studied by employing coupled mode theory [23]. The fabrication and properties of short-period fiber Bragg gratings [9] are analyzed in detail. This would provide a stepping stone to understand the operation and characteristics of long-period gratings. Long-period gratings that couple power from one guided mode to another are also reviewed [26,27]. Recent developments such as hydrogen-loading [28] to enhance fiber photosensitivity and thermal-treatment [28,29] to induce refractive index changes are discussed.

Long-period gratings are introduced as periodic structures that couple light from the fundamental guided mode to discrete cladding modes [1]. Their principle of operation is studied using a simple pictorial representation of the propagation constants of the different spatial modes. An analytical model is proposed to explain the functioning mechanism of long-period gratings. It is demonstrated that the response of these devices is a strong function of the parameters of the host fiber, the grating period and the writing conditions. Long-period gratings are economical to batch-produce and offer simple alternatives as spectrally-selective devices. The methods of fabrication of these gratings by using pulsed [1] as well as continuous-wave ultra-violet sources are outlined and compared. A novel process for large-scale production of long-period gratings is proposed. This scheme uses the thermally-induced refractive index changes in the core of hydrogen-loaded germanosilicate fibers to fabricate long-period gratings [28,29]. An assessment of the effects of molecular hydrogen-loading and its diffusion from the fiber core is carried out to determine the stability of the grating. It is shown that high temperature annealing serves to provide short- and long-term stability to the grating spectrum [1]. Long-period gratings are compared to their short-period counterparts and other photoinduced devices. Significant properties such as the effect of etching the cladding, recoating and packaging of gratings [1], and their bend sensitivity are also addressed. Finally, the applications of long-period gratings to communication devices are briefly investigated. The use of these devices in equalizing the gain spectrum [30] and suppressing the amplified spontaneous emission [31] in erbium-doped fiber amplifiers are reviewed and applications as potential in-fiber polarizers and modulators are proposed.

Long-period gratings are demonstrated as effective and versatile temperature, strain and index of refraction sensors [21]. We show that these transducers possess high sensitivity and due to their large spectral width, may be implemented with simple demodulation schemes. It is demonstrated that the spectral shift of the gratings can be converted to an intensity modulation by using a laser diode at specific wavelengths or by employing optical filters. We present analytical models for the strain, temperature and refractive index sensitivities and show that the induced wavelength shifts are strong function of the grating period, the order of the cladding mode and the writing conditions. Strain and temperature long-period grating sensors are demonstrated to possess larger spectral shifts than conventional Bragg grating sensing elements. The long-period grating refractive index sensor does not require etching the cladding and is shown to have wide-ranging applications in chemical and biomedical engineering [32]. Long-period grating strain

sensors are demonstrated for measurements on a loaded reinforcing-bar commonly used in advanced civil structures [33]. The cross-sensitivity to temperature fluctuations during the measurements of strain and refractive index can be overcome by employing gratings written in fibers with special power profiles [34]. It is demonstrated that temperature-insensitive gratings can also be fabricated in standard telecommunication grade fibers by using specific grating periodicities [35]. Strain-insensitive gratings are shown as effective temperature measurement devices in the presence of axial strain. We hence confirm that single-parameter long-period gratings are economical to mass-produce, simple to demodulate and can be suitably modified to overcome the problem of cross-sensitivity to temperature. Long-period grating-based sensors overcome a number of limitations (outlined in Section 1.1) faced by conventional fiber optic sensors.

Long-period grating sensors are proposed for simultaneous measurement of strain and temperature by utilizing the differential modulation of the multiple resonance bands [36,37]. We analyze the principle of operation of these multi-parameter sensors assuming negligible cross-sensitivity and linear system response. The influence of cross-sensitivity between strain and temperature is evaluated and the problems of non-linearities are addressed. We show that by using strain- or temperature-insensitive resonance bands, the limitations imposed by cross-sensitivities and non-linearities can be easily overcome. Experimental results from three distinct simultaneous strain and temperature measurement configurations are presented. Linear system theory is employed to determine the stability of the systems to measurement inaccuracies and the concept of the conditioning of the sensitivity matrix is used to evaluate the performance of different configurations [18]. Long-period grating simultaneous strain and temperature sensing systems are compared to conventional fiber optic techniques.

In the final analysis, long-period gratings are demonstrated as versatile devices that can be used as single- or multi-parameter sensors. Future directions in long-period grating research and development are discussed and it is shown that these devices possess tremendous potential for integration into fiber optic sensing systems.

1.4 Outline

The outline of this dissertation is as follows. Chapter 2 is an introduction to the phenomena of photosensitivity and mode coupling in optical fibers and also reviews

photoinduced devices such as fiber Bragg gratings. Chapter 3 discusses the principle of operation, fabrication and basic properties of long-period gratings. Experimental results and analytical models for temperature, strain and refractive index sensors are presented in Chapter 4. Chapter 5 is devoted to the analysis of the long-period grating-based simultaneous strain and temperature sensing techniques. Chapter 6 presents a summary of the work and outlines future research efforts that might be undertaken in the field of long-period grating sensors.

Chapter 2 - Photosensitivity and Mode Coupling in Optical Fibers

This chapter presents an overview of the phenomenon of photosensitivity [22,25] and mode coupling [38] in optical fibers. Presence of molecular hydrogen [28] in the fiber cores is shown to enhance the photosensitivity of germanosilicate fibers. The process of hydrogen loading in optical fibers is discussed and it is demonstrated that large refractive index modulation can be obtained in such fibers by simple thermal treatment [28,29]. Coupled mode theory is used to analyze the transfer of power between two modes in a perturbed system [23,24]. A comprehensive analysis of both co-directional and counter-directional mode coupling is carried out for the case of a periodic perturbation. The principle of operation, fabrication techniques and applications of short-period fiber Bragg gratings [9,25] are examined and their limitations are analyzed. Long-period gratings that couple light from one guided mode to another are studied and their properties and applications are reviewed [30,31]. This chapter intends to provide the reader with an appreciation of the fundamental concept of mode-coupling in optical fibers in the presence of a perturbation such as a refractive index grating. The understanding of the basic photosensitive devices such as fiber Bragg gratings will enable a much easier visualization of the mechanism of long-period gratings that are introduced in Chapter 3.

2.1 Photosensitivity in Optical Fibers

Photosensitivity is defined as the property of a photo-conductive and electro-optic material to exhibit and retain differential modulation in its index of refraction owing to exposure to spatial distributions of intense electromagnetic radiation [22]. A photo-conductive material absorbs photons and this results in increased conductivity due to generation of electron-hole pairs that act as free charge carriers. The electro-optic or Pockels effect, on the contrary, is the variation in refractive index due to the influence of an electric field. The phenomenon of photosensitivity is depicted in Figure 2.1 [22] and can be explained as follows. Incident light generates free charge carriers (electrons or

holes) by excitation of impurity energy levels at a rate proportional to optical power [22]. These charge carriers diffuse to locations of low electromagnetic radiation intensity, leaving behind fixed charges of opposite polarity. The free carriers are then trapped by impurity ions leading to recombination and deposition of charge [22]. The overall effect is the creation of an inhomogeneous space-charge distribution that can exist permanently until stronger radiation or high temperature destroys it. The spatial charge distribution results in an internal electric field that causes the refractive index of the material to change owing to Pockels electro-optic effect [22].

Photosensitivity (or photorefractivity) is commonly used to spatially modulate the refractive index of materials and fabricate devices such as gratings. A refractive index grating is simply an optical device that serves to periodically modulate the amplitude or phase of an incident wave [22]. Bulk-optics diffraction gratings have been demonstrated for filtering and spectrum analysis. Some of the important photosensitive materials are lithium niobate, gallium arsenide and barium titanate [22].

Photosensitivity in optical fibers was first discovered by Hill *et al.* [25] in 1978 and is increasingly being used to fabricate high-performance communication and sensing devices. Hill *et al.* [25] used the interference pattern of two counter-propagating beams of blue-green light (488 or 514 nm) inside a germanium-doped single mode fiber to form a refractive index grating internal to the fiber core. Such gratings couple light from the forward-propagating LP_{01} fundamental mode to the reverse-propagating LP_{01} mode at a wavelength for which the phase-matching condition for mode coupling is satisfied [25]. For the grating fabricated by Hill *et al.*, the reflection wavelength, also referred to as Bragg wavelength, was equal to the writing UV wavelength since the grating was written by launching light in the fiber core. Thus, these gratings in the visible spectrum were not useful for communication applications at 1.31 μm. Telecommunication devices hence had limited applications of fiber Bragg gratings till late 1980s when the transverse holographic method for grating fabrication was proposed by Meltz, *et al.* [8]. The side-writing technique enabled simple mass production of in-line fiber gratings at the desired wavelength using the interference pattern between two spatially and temporally coherent UV beams. Thus photosensitivity in optical fibers has been employed to obtain Bragg gratings by side-writing as well as by using two counter-propagating waves in the fiber core. Bragg gratings will be discussed in detail in Section 2.4. Photosensitivity has also

been used to modify the mode field diameter of the fundamental guided mode to assist in mode conversion [39].

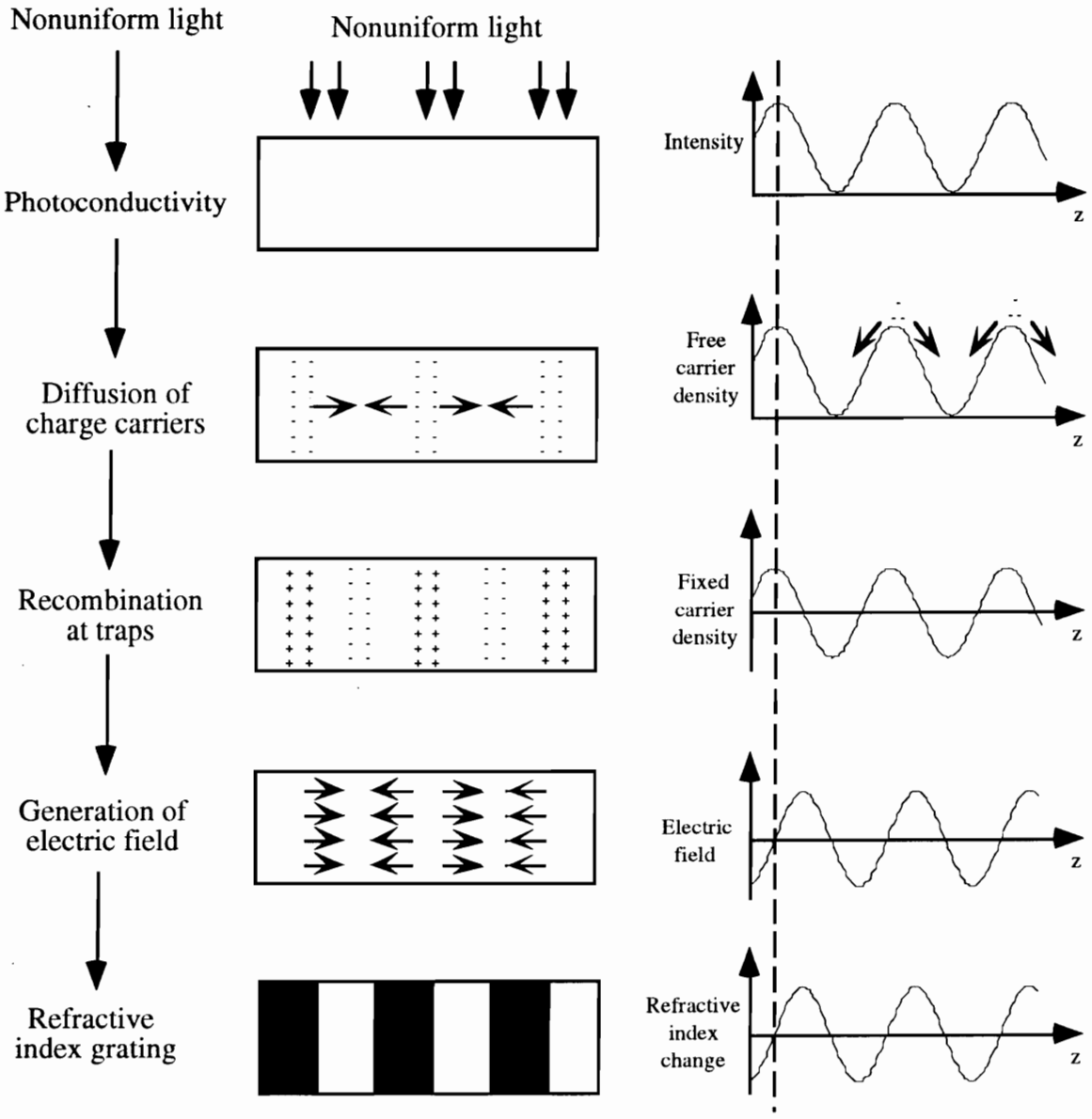

Figure 2.1. Phenomenon of photosensitivity in a material exposed to a non-uniform, sinusoidal spatial light distribution [22].

A number of theories have been proposed to explain the photosensitivity of germanium-doped fibers. These include the use of absorption changes in the Kramers-Kronig relationship to analyze the refractive index variation [40]. It has also been observed that

the maximum refractive index change in Ge-doped glass, and hence a stronger grating formation occurs when the wavelength of the incident UV radiation coincides with the absorption wavelength of the germanium-oxygen deficiency center (GODC) [9]. The bleaching of this absorption band and also formation of defects within glass that have a strong absorption in the deep UV (wavelengths less than 200 nm) leads to intensity dependent refractive index modulation along the length of the exposed region [41]. Although photosensitivity has been reported in fibers doped with cerium [42] and europium [43], germanosilicate fibers have been demonstrated to undergo maximum refractive index change. Typically, the magnitude of the observed photosensitivity is proportional to the Ge content in the fiber core (which also implies a greater concentration of GODC defects) and refractive index changes around 3×10^{-5} can be obtained for standard single mode fibers with 3% germania [44].

2.2 Hydrogen-Loading and Thermal-Induced Refractive Index Modulation

This section discusses the techniques to enhance the index changes in fibers by about two orders of magnitude owing to sensitization of the germanium-doped fiber with molecular hydrogen or deuterium. It is observed that apart from exposure to UV radiation, another method to obtain refractive index variations in such fibers is by simple thermal treatment.

2.2.1 Hydrogen-Loading of Germanosilicate Fibers

In 1985, Tomita and Lemaire [45] were the first show that hydrogen results in defect formation in germanosilicate glass. Later Ouellete *et al.* [46] suggested that optical fibers treated with hot hydrogen show increased photosensitivity in applications involving second harmonic generation. It was also shown that this phenomenon can be used for grating formation in fibers and for achieving permanent index changes in germania-silica planar waveguides [47]. The chemical bonding of hot hydrogen enables permanent increase in the photosensitivity of germanium-doped fibers.

Recently, the high-pressure loading of germanosilicate optical fibers with molecular hydrogen has also been demonstrated to increase the photoinduced refractive index changes due to ultraviolet radiation [28,29]. The addition of hydrogen to Ge-doped glass leads to the breakdown of the Si-O-Ge bonds, resulting in the formation of Si-OH bonds and germanium-oxygen deficiency centers (GODCs), both of which lead to increase in

the index of refraction (Figure 2.2) [49]. The absence of any refractive index modulation in hydrogen-loaded, non-germanosilicate fibers lends credence to the belief that hydrogen attacks the germanium sites to produce index changes [29].

The Si-OH band has an absorption band centered at 1390 nm, and can hence be detrimental to the performance of communication and sensing systems operating in that spectral region. This limitation can be overcome by substituting molecular hydrogen with deuterium which results in the formation of corresponding Ge-OD bonds with absorption peaks outside the telecommunication spectral window [28]. With hydrogen or deuterium loading, refractive index changes as large as 10^{-2} have been reported by Lemaire *et al.* [29] and this figure is at least two orders of magnitude larger than the index modulation previously achieved in fibers not loaded with hydrogen [44]. In hydrogen-loaded fibers, the loss at 1390 nm can also be measured to estimate the OH concentration in the fiber. It has been found experimentally that the OH concentration in a photo-exposed fiber is slightly lower than the GeO_2 content of the fiber [28] which reveals that hydrogen loading forces a majority of the germania sites in the glass network to participate in the photosensitivity process.

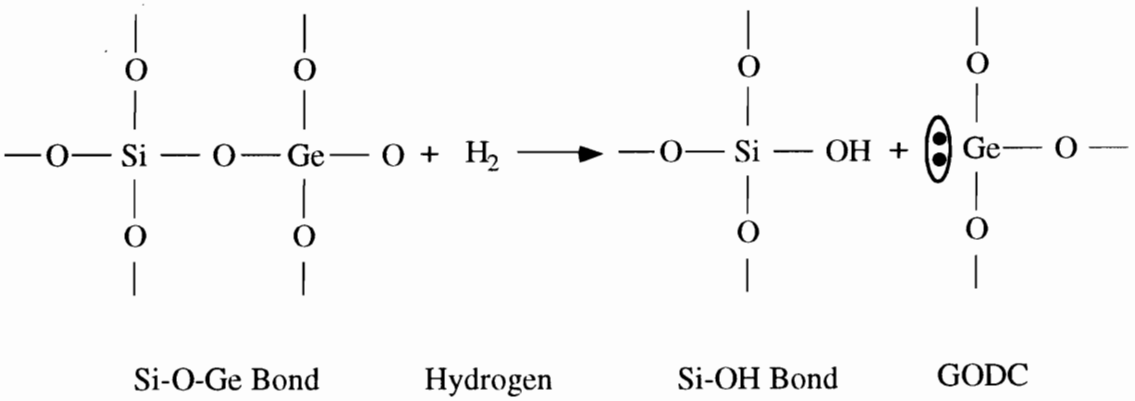

Figure 2.2. Thermal reaction at the Si-O-Ge bonds leading to the formation of GODC sites and Si-OH bonds [49].

The process of hydrogen loading involves exposure of the fiber to gaseous hydrogen at high pressure (100-700 atm) and temperatures ranging from 20 to 100 °C [28]. The fiber coating for this process need not be removed since acrylate provides negligible resistance to hydrogen diffusion. The addition of hydrogen to optical fibers produces a first overtone absorption at 1240 nm and this loss may hence be related to the magnitude of

hydrogen present in the fibers [28]. For standard fibers, hydrogen loading at room temperature requires one to two weeks to obtain a concentration of 1-2% (1% is defined as 1 mole of H_2 per 100 moles of SiO_2). The out-diffusion of the hydrogen-sensitized fiber is prevented by storing the fiber at high pressure or low temperature. To ensure that all germania sites participate in the formation of defects, the hydrogen content in the fiber is made higher than the GeO_2 doping level. Thus at the completion of UV irradiation process there is typically some excess hydrogen remaining in the fiber. Since the depletion of hydrogen occurs only in the regions that undergo refractive index modulation, this results in a differential hydrogen concentration along and across the fiber. The presence of hydrogen itself enhances the index of refraction locally and its diffusion to maintain equilibrium causes short-term instability in the characteristics of the photoinduced fiber. It hence becomes necessary to remove this excess hydrogen from the fiber prior to the use of the device in a particular application. A simple way to do this is to anneal the fiber at high temperature for a short period of time. The annealing process also serves to remove the unstable germanium defects (at the expense of reduction in refractive index) and provides long-term stability at lower operating temperatures [49,50]. The annealing of long-period gratings will be discussed in detail in Section 3.3.2.

2.2.2 Thermal-Sensitivity of Hydrogen-Loaded Germanosilicate Fibers

This section reviews the process of inducing large refractive index changes in the cores of hydrogen loaded fibers by exposure to high temperatures. It is demonstrated that the thermal treatment offers a simple method to obtain index modulation without resorting to the conventional method of irradiating the fiber with ultra-violet radiation.

In 1993 Lemaire *et al.* [28] showed that it is possible to obtain refractive index changes in the cores of germanium doped fibers sensitized with hydrogen. A fiber with 3% germania and 4.3% hydrogen was heated rapidly using a gas-oxygen torch over a length of a few centimeters. The increase in the loss at 1390 nm was recorded and the OH content was calculated as 2.9%, indicating that the presence of hydrogen causes almost all the germania sites to participate in the index transformation [28]. This was further confirmed by the formation of a number of germanium oxygen deficiency centers (GODCs) owing to the increase in the 242 nm band in the deep UV. The thermal-induced index change was found to be 0.006 in the core of fiber with 9% GeO_2 content and 1.8% hydrogen. Lemaire *et al.* [28] also reported index modulations of 0.002 and

0.003 in hydrogen-loaded phosphosilicate and alumino-phosphosilicate fibers, respectively. Moreover, it has been shown that no index modulation is obtained in hydrogen-loaded fibers with undoped silica cores [29]. These results indicate that although the presence of GeO_2 is not essential to achieve thermal-induced index changes, some specific form is doping is necessary to observe index variations by this method.

Greene *et al.* [51] have made an attempt to explain the thermal-initiated reactions in hydrogen loaded germanosilicate fibers by comparing the Raman spectra of a heated fiber with those of a test fiber. AT&T Accutether fiber was heated to about 1000 °C and two major peaks in the Raman spectrum, corresponding to GeH and SiOH, were observed [51]. This experiment suggests that the reaction responsible for index change is the one where molecular hydrogen adds across the Ge-O bond at high temperatures (Figure 2.2).

The process of thermal treatment provides a simple method to obtain significant refractive index modulation in germanium-doped hydrogen-loaded fiber. Index changes over a large fiber length may be achieved by flame heating, or by simply using a heat gun. The basic limitation of the high temperature treatment method is that it may be difficult to exactly control the heated region due to the diffusion of heat in all directions. The index variation can be localized by exposing the fiber to output from a CO_2 laser or by using the heat produced during electric arcing between two electrodes of a fusion splicer. The temperature treatment precludes the requirement of expensive ultra-violet radiation emitting lasers, and provides the user with options to obtain index changes over varying lengths of the fiber. The thermal-induced index modulation will be utilized to demonstrate a novel method to produce long-period gratings in Section 3.3.1.3.

2.3 Mode-Coupling in Optical Fibers

This section introduces the concept of exchange of power between one or more modes in a perturbed optical fiber system. Coupled mode theory is utilized to elucidate the interaction between various modes and the phase-matching condition for a periodic perturbation is derived [38]. The transfer of power between co-directional- and contra-directional-propagating modes is analyzed using a pair of coupled mode equations. We first discuss the various types of modes in a fiber and then employ β-plots [52] to obtain a representation of their propagation constants.

2.3.1 Guided and Radiation Modes

A mode in an optical fiber is a set of electromagnetic waves that participates in the propagation of energy in the fiber [53]. A finite number guided modes travel in the fiber with discrete propagation constants (β) that are functions of the optical source wavelength and fiber parameters, and can be determined using Maxwell's equations and the electric and magnetic field boundary conditions at the core-cladding interface [53]. The typical variation of the normalized propagation constant with the normalized frequency for the first few guided modes in a weakly guiding step-index fiber is shown in Figure 2.3. These simplified linearly-polarized (LP) modes are obtained using the approximations listed by Gloge [54].

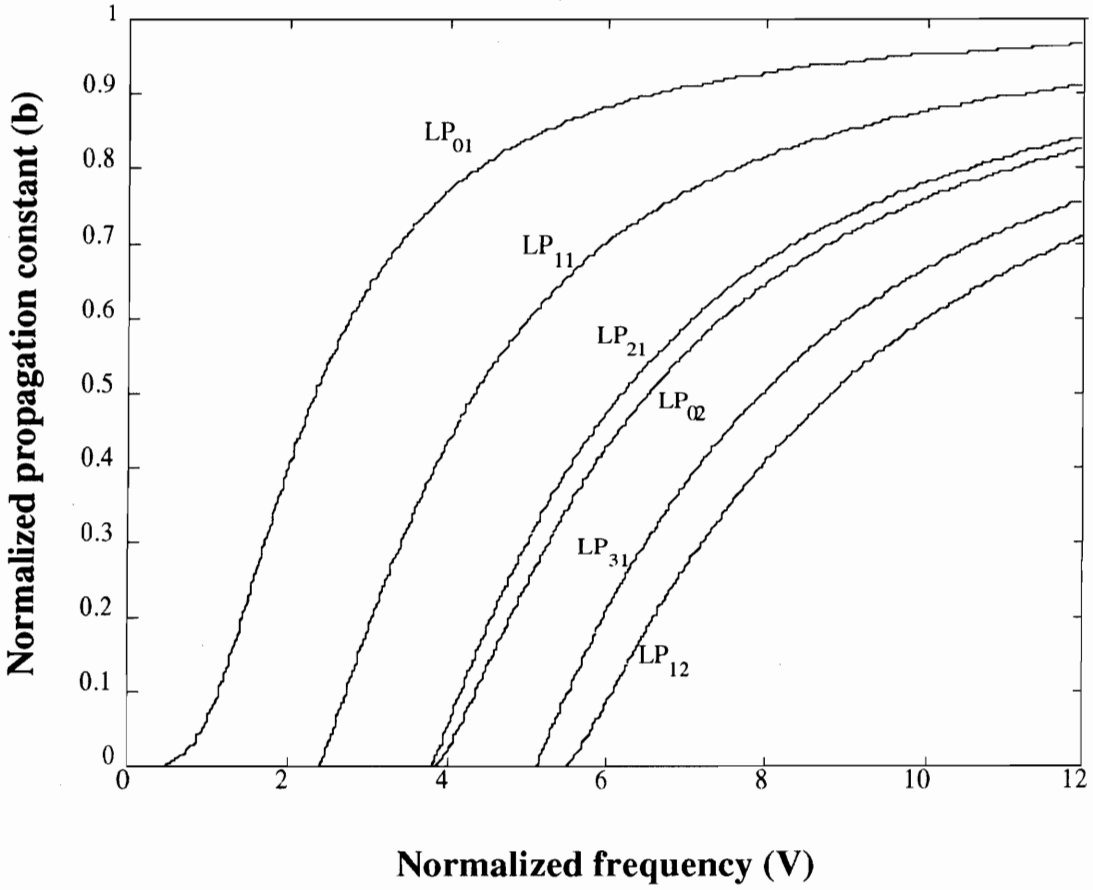

Figure 2.3. Typical variation of the normalized propagation constant (b) with the normalized frequency (V) for a step-index fiber calculated using Gloge's weakly-guiding approximations [54].

It can be shown that the discrete values of propagation constants for the guided modes are confined to $n_2k<|\beta|<n_1k$, where n_1 and n_2 are respectively the core and cladding refractive indices, and k is the free space propagation constant at wavelength λ ($k=2\pi/\lambda$). Figure 2.4 depicts the propagation constants of the forward ($\beta>0$) and reverse-propagating ($\beta<0$) guided modes as functions of the optical frequency. The propagation constant is also given by the expression $\beta=\omega n/c$, where ω is the angular frequency, n is the effective index of refraction ($n_2<|n|<n_1$), and c is the speed of light in vacuum. This simple pictorial representation of the modal propagation constants in terms of the angular frequency is termed the β-plot [1].

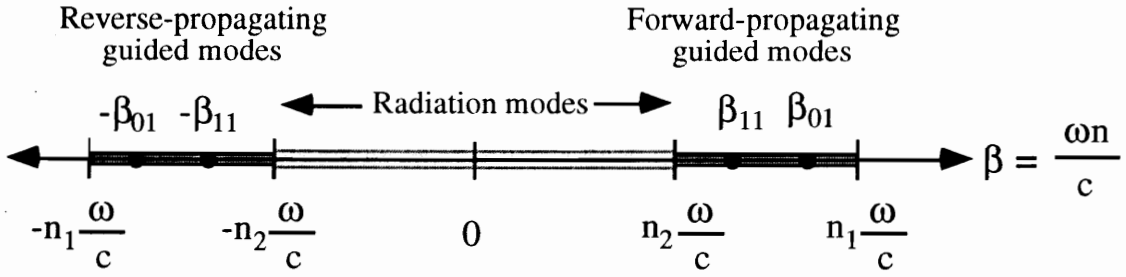

Figure 2.4. Propagation constants of the forward and reverse-propagating guided modes in an optical fiber. β_{01} and β_{11} are the propagation constants of the two lowest order forward-propagating guided modes. Also represented are the propagation constants of radiation modes [1].

Analysis reveals that apart from the guided modes, another set of modes also satisfies the electromagnetic Maxwell's equations and the boundary values [55]. These modes are commonly termed radiation modes and owing to the presence of waveguide imperfections, result in continuous loss of power from the guided modes. In simpler terms, the radiation modes are not guided by the fiber and in most applications proper precautions have to be taken to prevent this power loss. The infinite number of radiation modes present in an optical fiber possess a continuum of complex propagation constants in the range, $0<|\beta|<n_2k$, as depicted in Figure 2.4.

For simplified analysis of guided modes, the fiber cladding is assumed to extend to infinity [53]. This approximation is justified since the guided modes have a rapidly decaying field outside the core and retain insignificant values of these field at the outer

boundary of the cladding. But when radiation modes are analyzed this assumption can be shown to be dubious. The ambiguity results from the knowledge that radiation modes extend to infinity and are influenced strongly by the outer cladding boundary. In fact some of this radiation is trapped by the cladding due to the reflection at the cladding outer boundary. The subset of modes that arise from the radiation modes reflections at the outer surface of the finite cladding are termed cladding modes [55]. Here n_3 is the index of the medium surrounding the cladding (with air as the ambient index, $n_3=1$) and the cladding mode propagation constants are bounded by $n_3k<|\beta|<n_2k$.

The cladding modes, similar to the guided modes, may travel in either forward or reverse direction and possess discrete propagation constants (Figure 2.5), but due to their higher density almost form a continuum [55]. The cladding modes attenuate rapidly due to bends in the fiber, scattering losses and absorption by the fiber jacket. The coupling or transfer of energy from guided modes to discrete cladding modes forms the basic operating mechanism of long-period gratings.

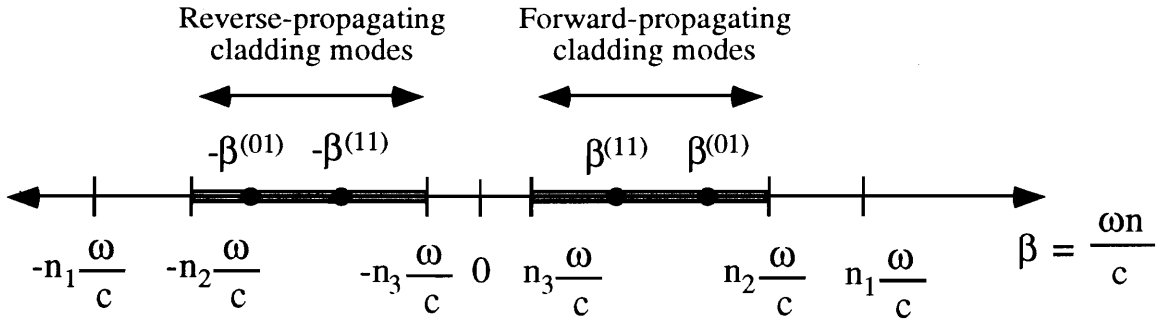

Figure 2.5. Propagation constant distribution of cladding modes in an optical fiber. The hatched region represents the cladding modes. $\beta^{(01)}$ and $\beta^{(11)}$ are the propagation constants of the two lowest order forward-propagating cladding modes. The β-space between the two hatched region is occupied by radiation modes.

2.3.2 Coupled Mode Theory

The transfer of power between two propagating modes was first analyzed by Pierce [56] in 1953. He studied mode coupling, encountered in common devices such as wave filters and traveling wave tubes, assuming linearity and conservation of energy. In optical fibers, the power is transferred in the form of modes. In a lossless unperturbed system,

each mode propagates without losing or gaining power along the fiber length. But in reality, any small disturbance or irregularity in the system can cause power to couple between two or more modes. An optical fiber can be perturbed by either bending the fiber, modifying the refractive index or diameter of the core or of the cladding, or by simply moving the fiber to the vicinity of another waveguiding structure [55]. In long-haul communication systems, coupling of light from guided to radiation modes due to microbends can lead to significant attenuation in the transmitted intensity [57,58] and hence special precautions are taken during fiber fabrication and installation. On the contrary, interesting and useful devices can be fabricated by utilizing the mode coupling in one or more fibers. These components include directional couplers [55], mode couplers [26, 38] and refractive index gratings [25] that are finding increased applications in fiber optic systems. Hence for one perform a comprehensive analysis of these devices it becomes necessary to understand the subtleties of mode coupling in optical fibers.

2.3.2.1 Co-directional Coupling

In this section we follow the approach used by Pierce [56] and by Taylor and Yariv [23] to arrive at solutions to coupled mode equations for two modes propagating in the same direction, under the influence of a periodic perturbation. We also use coupled mode equations to depict the importance of phase-matching condition between the two modes for significant exchange of power.

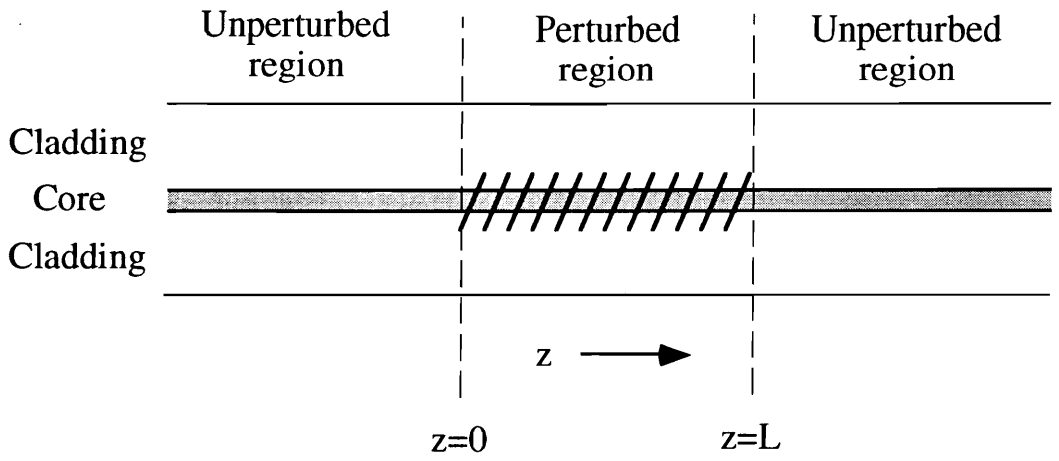

Figure 2.6. Illustration of an optical fiber under perturbation. The perturbation exists form z=0 to z=L.

Consider an optical fiber of Figure 2.6 that is disturbed by a perturbation of period Λ along the fiber axis, originating at z=0 and terminating at z=L. The perturbation can be caused by a periodic variation in the core index such as a refractive index grating, or simply by external bends in the fiber. Consider two modes denoted by a_1 and a_2 traveling in the positive z direction with discrete propagation constants β_1 and β_2, respectively, such that [23],

$$a_1(z,t) = A_1(z)\, e^{j(\omega t - \beta_1 z)}, \tag{2.1a}$$

$$a_2(z,t) = A_2(z)\, e^{j(\omega t - \beta_2 z)}, \tag{2.1b}$$

where ω is the angular frequency and $A_1(z)$ and $A_2(z)$ are complex normalized amplitudes that are independent of z in a lossless unperturbed fiber. The presence of a disturbance or irregularity causes the two modes to exchange energy such that A_1 and A_2 become functions of the propagating distance [23]. The objective of coupled mode theory is to find the variation in A_1 and A_2 as a function of z. Without resorting to detailed mathematical analysis we merely outline the procedure to obtain the basic coupled mode equations. The electric field of the perturbed fiber is expressed as a linear combination of the two eigenmodes in Equation (2.1) and substituted in the scalar wave equation for the perturbed system [24]. For an unperturbed fiber, the driving polarization produced by the disturbance is nonexistent and hence we simply get the standard scalar wave equation. For a perturbed fiber, we use the slowly-varying approximation (SVA) to neglect the effect of second order derivatives of the complex amplitudes and integrate over the fiber cross-section to obtain two coupled, first order differential equations of the following form [23],

$$\frac{dA_1(z)}{dz} = \kappa_{12}\, A_2(z)\, e^{-j\Delta z}, \tag{2.2a}$$

$$\frac{dA_2(z)}{dz} = \kappa_{21}\, A_1(z)\, e^{+j\Delta z}, \tag{2.2b}$$

where κ_{12} and κ_{21} are termed the cross-coupling coefficients and dictate the magnitude of coupling between the two modes. The characteristics of the coupling coefficient for interaction between two co-propagating modes will be investigated in Chapter 3. In Equation (2.2), Δ is the phase mismatch between the propagating modes [23] and is typically the difference in their propagation constants and is modified to,

$$\Delta = \beta_1 - \beta_2 - \frac{2\pi}{\Lambda}, \tag{2.3}$$

in the presence of a perturbation of period Λ. Since β_1 and β_2 are functions of the optical wavelength the phase-mismatch, Δ has a strong spectral dependence. An analysis of the coupled mode equations reveals that for synchronous transfer of power between the two modes, the value of Δ should ideally be zero. Using Equation (2.3), we obtain what is commonly termed the phase-matching condition between the two modes,

$$\Delta\beta = \beta_1 - \beta_2 = \frac{2\pi}{\Lambda}, \tag{2.4}$$

where $\Delta\beta$ is their differential propagation constant.

The mode coupling phenomenon can also be interpreted in the following manner. The perturbation simply interacts with the mode a_1 to generate a propagating polarization wave that finally results in mode a_2 [23]. This mode further interacts with the perturbation to alter the energy in mode a_1. This sustained exchange of power between the two eigenmodes is hence dependent on the differential propagation constant ($\Delta\beta=\beta_1-\beta_2$) and the periodicity of the perturbation. For the phase-matched case, the mode coupling is optimized and the power transfer between the two modes is a function of the coupling coefficients. The magnitude of interaction between the modes is expected to be negligible far away from the phase-matching condition.

The total power carried by modes a_1 and a_2 is given by $|A_1(z)|^2$ and $|A_2(z)|^2$, respectively. Since in a lossless system, there is no variation of the total power in the z direction, we can manipulate Equation (2.2) to obtain [23],

$$\kappa_{12} = -\kappa_{21}^{*}. \tag{2.5}$$

where, * denotes the complex conjugate. If we assume that only mode a_2 carries power at z=0, we get the following boundary conditions,

$$a_1(0) = 0, \tag{2.6a}$$
$$a_2(0) = A, \tag{2.6b}$$

which can be used to solve the coupled mode equations. Thus the complex modal amplitudes can be written as [27],

$$A_1(z) = A\frac{2\kappa_{12}}{\sqrt{4\kappa^2+\Delta^2}}e^{-j\left(\frac{\Delta z}{2}\right)}\sin\left[\frac{1}{2}\left(\sqrt{4\kappa^2+\Delta^2}\right)z\right], \tag{2.7}$$

and,

$$A_2(z) = A\,e^{j\left(\frac{\Delta z}{2}\right)}\left\{\cos\left[\frac{1}{2}\sqrt{4\kappa^2+\Delta^2}\;z\right] - j\frac{\Delta}{\sqrt{4\kappa^2+\Delta^2}}\sin\left[\frac{1}{2}\left(\sqrt{4\kappa^2+\Delta^2}\right)z\right]\right\}, \tag{2.8}$$

where,

$$\kappa^2 = |\kappa_{12}|^2 . \tag{2.9}$$

The eigenmodes can now be obtained by substituting the values of the complex amplitudes $A_1(z)$ and $A_2(z)$ in Equation (2.1). The power in the two modes is given by,

$$P_1(z) = |A_1(z)|^2 = P_0\frac{\sin^2\left[\kappa z\sqrt{1+\left(\frac{\delta}{\kappa}\right)^2}\right]}{1+\left(\frac{\delta}{\kappa}\right)^2}, \tag{2.10}$$

and,

$$P_2(z) = |A_2(z)|^2 = P_0\left\{\frac{\cos^2\left[\kappa z\sqrt{1+\left(\frac{\delta}{\kappa}\right)^2}\right]+\left(\frac{\delta}{\kappa}\right)^2}{1+\left(\frac{\delta}{\kappa}\right)^2}\right\}, \tag{2.11}$$

where $\delta=\Delta/2$ is termed the detuning parameter and P_0 is the incident power in eigenmode a_2 ($P_0=P_2(0)=|A|^2$). We hence see that the two modes have sinusoidal variations in the propagating power. The frequency and magnitude of power coupling is a function of the detuning ratio δ/κ. Figure 2.7 depicts the variation in the incident power normalized values of $P_1(z)$ and $P_2(z)$ as functions of κz for two different values of detuning ratio. We observe from Figure 2.7(a) that under the condition of phase-mismatch ($\delta\neq0$), the mode coupling is small and becomes negligible for $\delta/\kappa>>1$. On the other hand, for the phase matching condition ($\delta=0$), Equations (2.10) and (2.11) can be modified to yield,

$$P_1(z) = P_0\sin^2(\kappa z), \tag{2.12}$$

and,

$$P_2(z) = P_0\cos^2(\kappa z), \tag{2.13}$$

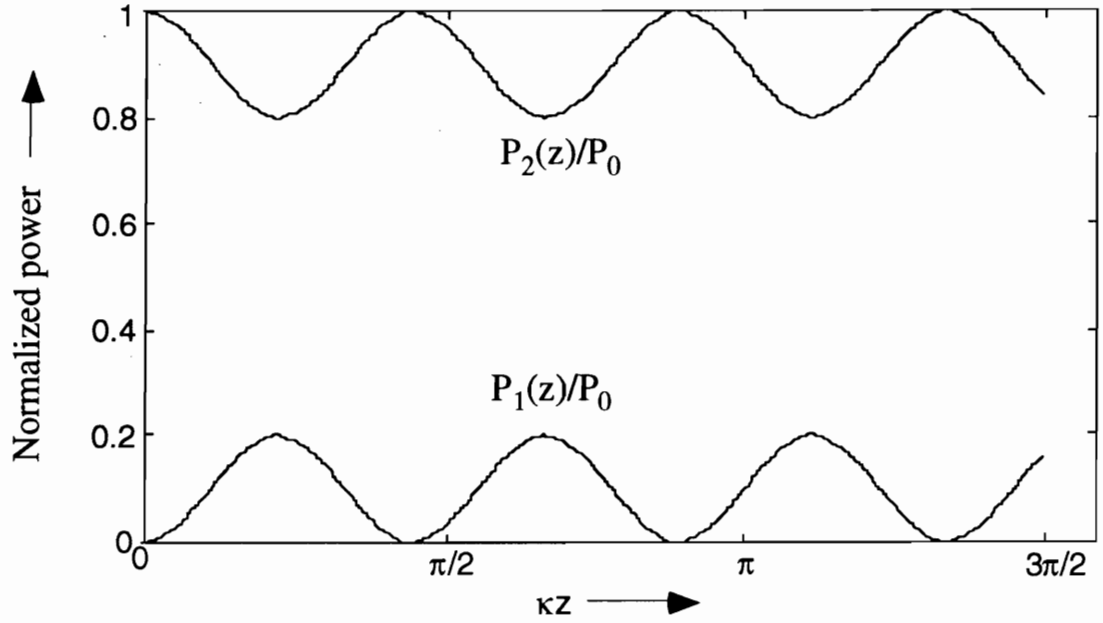

(a)

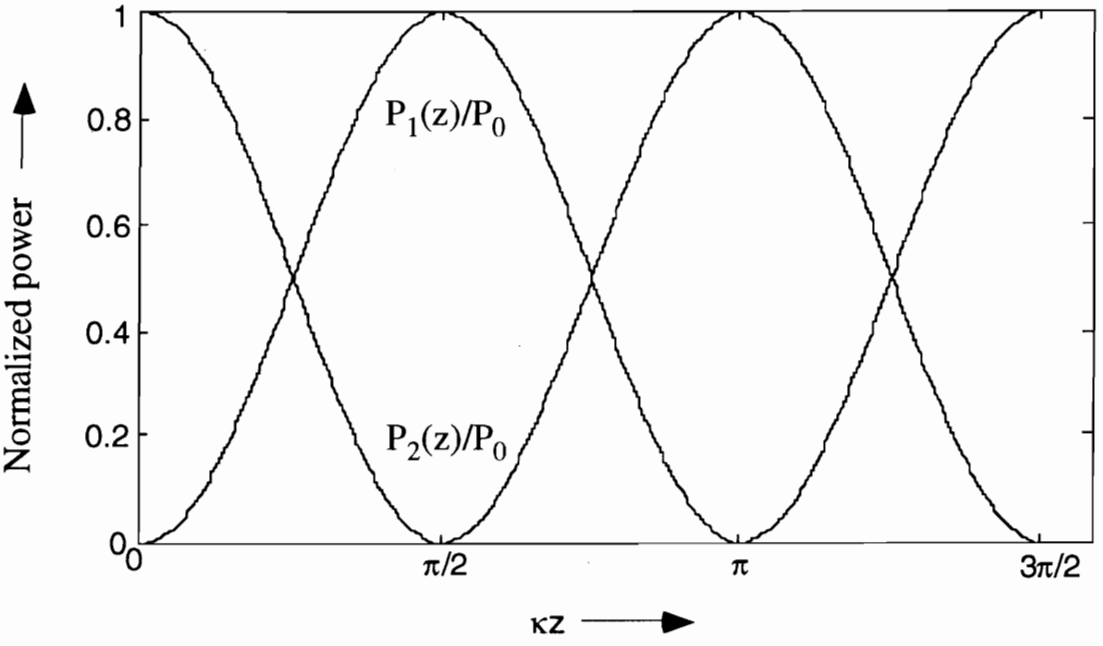

(b)

Figure 2.7. Variation of the power of the two co-propagating eigenmodes a_1 and a_2 involved in coupling for (a) phase-mismatched ($\delta/\kappa=2$), and (b) phase-matched ($\delta/\kappa=0$) case. The values are normalized to the incident power in mode a_2 ($P_2(0)=P_0$).

which predict a large degree of interaction between the two modes depending on the value of the coupling coefficient. This observation is confirmed in Figure 2.7(b) which shows that the modes continuously exchange power in the region of perturbation with a spatial period given by π/κ. The modal interaction terminates at z=L, where the perturbation ceases to exist. At that point, the ratio C (C≤1) of the power in mode a_1 to that originally in a_2 can be determined from Equations (2.10) and (2.11) as [59],

$$C = \frac{P_1(L)}{P_2(0)} = \frac{\sin^2\left[\kappa L \sqrt{1 + \left(\frac{\delta}{\kappa}\right)^2}\right]}{1 + \left(\frac{\delta}{\kappa}\right)^2}. \tag{2.14}$$

At z=L, the normalized power remaining T in mode a_2 is simply given by T=1-C. For most applications the length L of the perturbation region is constant while the coupling coefficient κ is varied to achieve complete power transfer from mode a_2 to a_1 [1]. Although the maximum power transfer occurs when $\kappa L = m\pi/2$, where m is an integer, the device operation is typically optimized for m=1, which yields $\kappa = \pi/2L$.

In this section we analyzed the coupling between the two co-propagating modes in the presence of a perturbation. The power transfer was found to be dependent on the degree of phase-matching between the modes. It was shown that the power variation along the propagating direction is sinusoidal for the two modes. The following section discusses the coupling between two counter-propagating modes in the presence of a periodic perturbation.

2.3.2.2 Contra-directional Coupling

We adopt an analysis similar to the one used in Section 2.3.2.1 to predict the coupling characteristics of two modes propagating in opposite directions. Consider the propagation of eigenmode a_1 towards left (-z) and that of eigenmode a_2 towards right (+z). Equation (2.1) may then be rewritten as [23],

$$a_1(z,t) = A_1(z)\, e^{j(\omega t + \beta_1 z)}, \tag{2.15a}$$

$$a_2(z,t) = A_2(z)\, e^{j(\omega t - \beta_2 z)}, \tag{2.15b}$$

where β_1 and β_2 are the respective propagation constants of the two modes. Using the mathematical manipulation described in the previous section it can be shown that the coupled mode equations for the contra-directional case are the same as those in co-directional propagation (Equation (2.2)) though the relationship between the cross-coupling coefficients is modified to [23],

$$\kappa_{12} = \kappa_{21}^{*} . \tag{2.16}$$

The characteristics of the coupling coefficient for fiber Bragg gratings that involve contra-directional mode coupling, will be investigated in Section 2.4.2. Again, mode a_2 is assumed to have an amplitude A at z=0 ($a_2(0)$=A) while $a_1(L)$=0. Solving the coupled mode equations for these boundary conditions yields [23],

$$A_1(z) = A\frac{2j\kappa_{ab}}{-\Delta\sinh\left(\frac{SL}{2}\right)+jS\cosh\left(\frac{SL}{2}\right)}e^{-j\left(\frac{\Delta z}{2}\right)}\sinh\left[\frac{S}{2}(z-L)\right], \tag{2.17}$$

and,

$$A_2(z) = A\frac{1}{-\Delta\sinh\left(\frac{SL}{2}\right)+jS\cosh\left(\frac{SL}{2}\right)}e^{j\left(\frac{\Delta z}{2}\right)}\left\{\Delta\sinh\left[\frac{S}{2}(z-L)\right]+jS\cosh\left[\frac{S}{2}(z-L)\right]\right\}, \tag{2.18}$$

where $S=\sqrt{4\kappa^2-\Delta^2}$, and $\kappa=|\kappa_{12}|$. The power carried by the two modes is given by,

$$P_1(z) = P_0\frac{\sinh^2\left[\kappa(z-L)\sqrt{1-\left(\frac{\delta}{\kappa}\right)^2}\right]}{\cosh^2\left[\kappa L\sqrt{1-\left(\frac{\delta}{\kappa}\right)^2}\right]-\left(\frac{\delta}{\kappa}\right)^2}, \tag{2.19}$$

and,

$$P_2(z) = P_0\frac{\cosh^2\left[\kappa(z-L)\sqrt{1-\left(\frac{\delta}{\kappa}\right)^2}\right]-\left(\frac{\delta}{\kappa}\right)^2}{\cosh^2\left[\kappa L\sqrt{1-\left(\frac{\delta}{\kappa}\right)^2}\right]-\left(\frac{\delta}{\kappa}\right)^2}, \tag{2.20}$$

where $\delta=\Delta/2$ is again the detuning parameter and P_0 is the incident power in eigenmode a_2. For the phase-matched condition (δ=0), Equations (2.19) and (2.20) can be reduced to,

$$P_1(z) = P_0 \frac{\sinh^2[\kappa(z - L)]}{\cosh^2(\kappa L)}, \tag{2.21}$$

and,

$$P_2(z) = P_0 \frac{\cosh^2[\kappa(z - L)]}{\cosh^2(\kappa L)}. \tag{2.22}$$

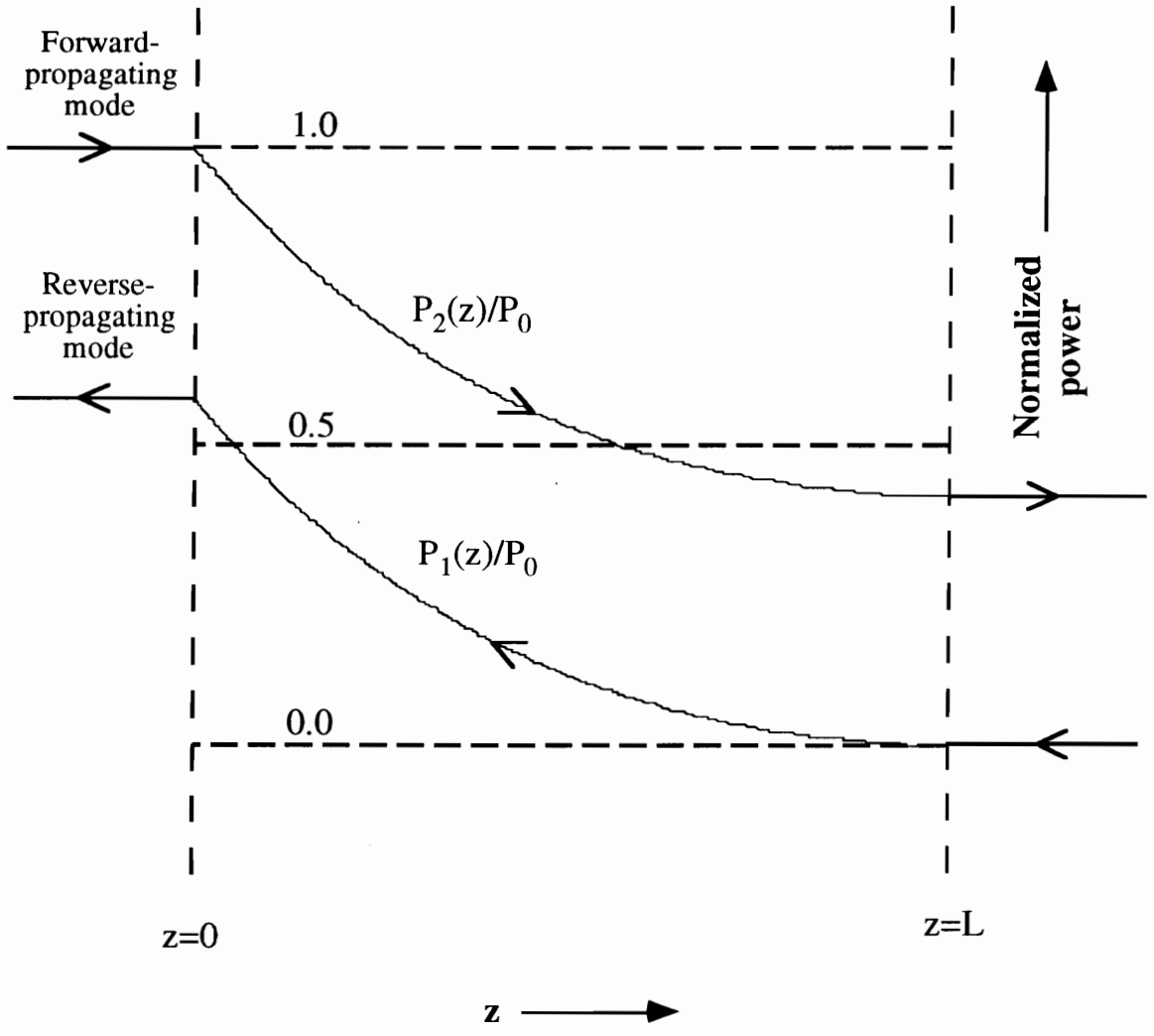

Figure 2.8. Variation of the power of the two counter-propagating eigenmodes a_1 and a_2 involved in coupling for the phase-matched (δ=0) case. This figure should be compared with Figure 2.7(b) which illustrates the power variation for the phase-matched co-propagating modes.

Figure 2.8 shows the typical variation in the incident power normalized values of $P_1(z)$ and $P_2(z)$ with z for the phase-matched case. We observe that while the power in the forward-propagating mode a_2 decays exponentially for large arguments of the hyperbolic sine and cosine functions, the reverse-propagating mode increases in power from zero (at z=L) to its maximum value (at z=0) [52]. The normalized reflected power R in eigenmode a_1 is given by,

$$R = \frac{P_1(0)}{P_2(0)} = \frac{\sinh^2\left[\kappa L \sqrt{1 - \left(\frac{\delta}{\kappa}\right)^2}\right]}{\cosh^2\left[\kappa L \sqrt{1 - \left(\frac{\delta}{\kappa}\right)^2}\right] - \left(\frac{\delta}{\kappa}\right)^2}, \tag{2.23}$$

which for the phase-matched case reduces to, $R=\tanh^2(\kappa L)$. The normalized residual power T in the mode a_2 at z=L is, T=1-R.

In this section we discussed the transfer of power between two counter-propagating modes in a perturbed optical fiber. Coupled mode equations were used to predict the exchange of power between the two eigenmodes. We use the next section to provide a comprehensive analysis of fiber Bragg gratings that use mode coupling between the fundamental guided modes propagating in opposite directions.

2.4 Fiber Bragg Gratings

Fiber Bragg gratings were described briefly in Section 2.1 during the discussion of the phenomenon of photosensitivity. Bragg gratings were first proposed by a group of researchers from the Communications Research Center in Canada [25]. Hill *et al.* [25] demonstrated that by spatially modulating the index of refraction along the fiber core it is possible to couple power from the forward-propagating fundamental guided mode to its reverse-propagating counterpart. These photoinduced devices have been an area of intense research and development over the past decade and have found a multitude of applications in fiber optic systems. This section discusses the properties, fabrication and applications of fiber Bragg gratings in single mode fibers. The β-plot will be used to illustrate the coupling between the two counter-propagating guided modes and the phase-matching condition will be employed to derive an expression for the coupling

wavelength. The side-writing technique [9] for Bragg grating fabrication is discussed and applications of these devices to communication and sensing systems are analyzed.

2.4.1 Principle of Operation

Fiber Bragg gratings are based on the phase-matching between the forward- and backward-propagating LP_{01} guided modes in an optical fiber [25]. These gratings are typically formed by exposing the core of a hydrogen-loaded germanosilicate fiber to ultra-violet radiation of suitable frequency. The refractive index modulation of the fiber core has a spatial periodicity Λ that is dependent on the impinging pattern. The phase-matching condition, also given in Equation (2.4), is simply expressed as,

$$\Delta\beta = \beta_1 - \beta_2 = \frac{2\pi}{\Lambda}, \tag{2.24}$$

where $\Delta\beta$ is the difference in the propagation constants of the two modes involved in mode coupling. The propagation constants, β_1 and β_2, are positive for the forward-propagating modes and negative for the reverse-propagating modes. Since the propagation constants are functions of wavelength, the phase-matching is highly wavelength selective. For a fiber Bragg grating, $\beta_1>0$ while $\beta_2<0$.

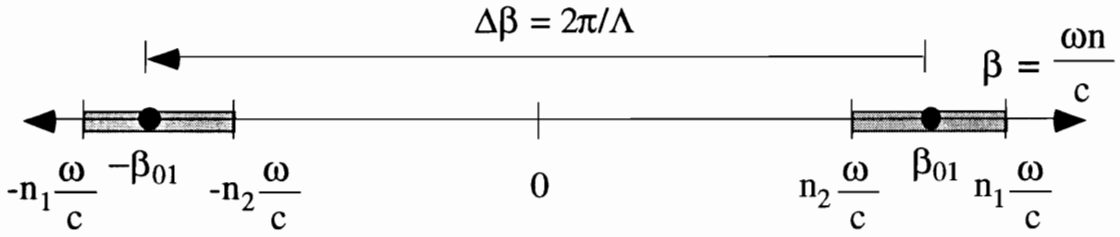

Figure 2.9. Mode coupling mechanism in fiber Bragg gratings. The large value of $\Delta\beta$ requires a small periodicity Λ, to satisfy the phase-matching condition.

Figure 2.9 depicts the mode coupling mechanism in fiber Bragg gratings using the β-plot discussed in Section 2.3.1. The forward-propagating fundamental guided mode has a propagation constant β_{01}, where $\beta_{01}=2\pi n_{eff}/\lambda$, at wavelength λ. As discussed in Section 2.3.1, the effective index of the guided mode n_{eff} lies in the range $n_2<|n_{eff}|<n_1$, where n_1 and n_2 are the indices of refraction of the fiber core and the cladding, respectively. The

reverse-propagating guided mode has a propagation constant with the same magnitude as its counterpart but with opposite polarity ($\beta_{-01}=-\beta_{01}=-2\pi n_{eff}/\lambda$). The phase-matching condition for these modes then reduces to [60],

$$\lambda_B = \frac{2\, n_{eff}\, \Lambda}{N}, \tag{2.25}$$

where λ_B is termed the Bragg wavelength and N is the order of interaction between the two modes (typically N=1). Bragg wavelength is the wavelength at which the forward-propagating LP_{01} mode couples to the reverse-propagating LP_{01} mode. Hence, if a fiber Bragg grating is interrogated by a broadband optical source, the phase-matching wavelength λ_B is reflected back. The operation of a fiber Bragg grating is illustrated in Figure 2.10. The coupling wavelength is a function of the grating periodicity (Λ) and the effective index (n_{eff}) of the fundamental mode. Since strain and temperature effects can modulate both these parameters, the Bragg wavelength undergoes a shift with these external perturbations. This spectral shift is utilized to fabricate Bragg gratings for sensing applications [8] and this phenomenon will be discussed in detail in Section 2.4.4. A grating can be designed to reflect different wavelengths along its length by making the period or effective index a function of z. Such chirped gratings have found useful applications as dispersion-compensating devices in fiber optic communication systems and will also be discussed in Section 2.4.4.

In Figure 2.9, the length of the arrow represents the magnitude of the differential propagation constant between the two modes. This phase-matching vector predicts the degree of modal mismatch that needs to be overcome using a perturbation introduced by the refractive index modulation. Since the difference in propagation constants ($\Delta\beta$) between the modes involved in coupling is large, we note from the phase-matching condition (Equation (2.24)) that a small value of periodicity Λ is needed to induce this mode coupling. For telecommunication applications, the typical value of λ_B is around 1.55 μm. From Equation (2.25), Λ is determined to be 0.53 μm (for $n_{eff}=1.45$). Due to their small periodicities (less than 1 μm), Bragg gratings are often classified as short-period gratings. The period of the refractive index modulation hence has the same order of magnitude as the wavelength of light. During the fabrication of these devices, the tolerance on the period is small and thus special precautions might need to be observed.

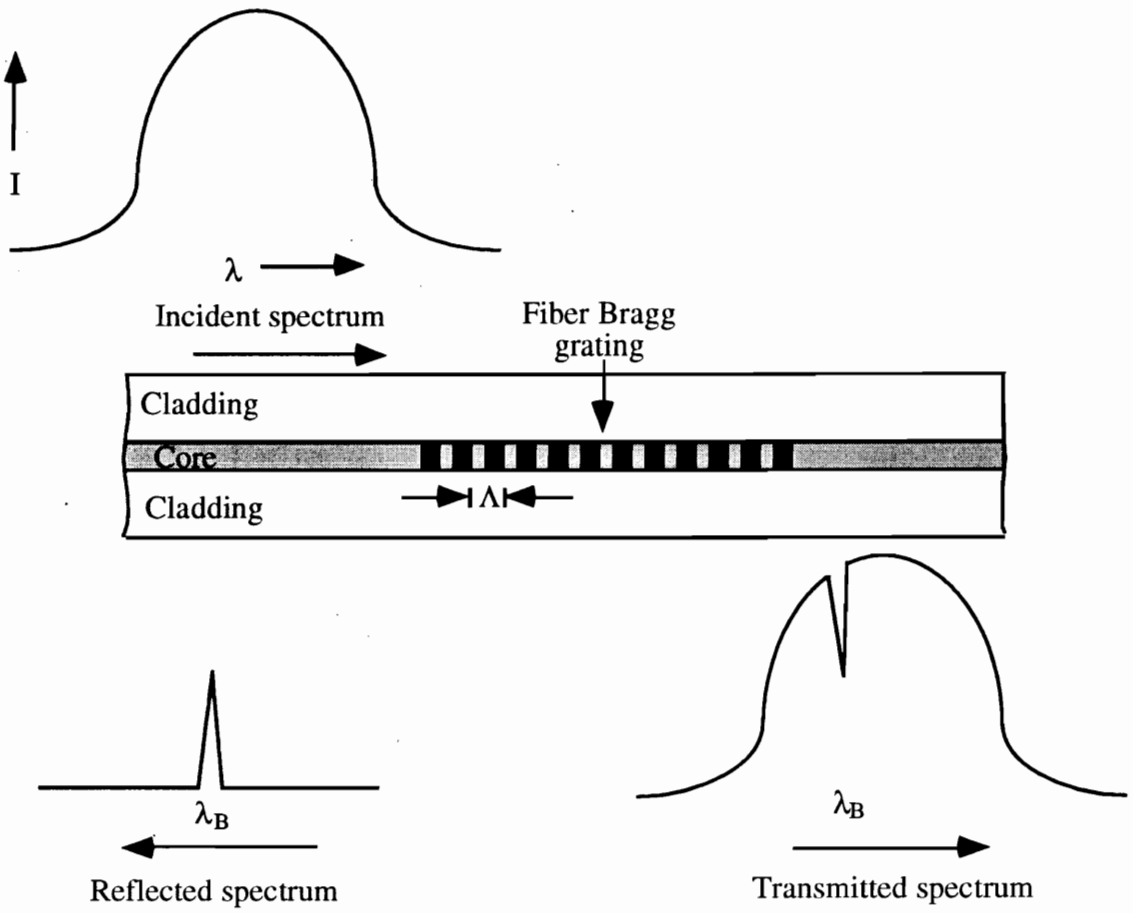

Figure 2.10. Interrogation of a Bragg grating of period Λ by a broadband source (I is the intensity and λ is the wavelength) results in reflection at the phase-matching wavelength λ_B. The transmission spectrum consists of the incident spectrum modulated by the loss at the Bragg wavelength. The dark regions in the fiber core represent areas where the refractive index has been modulated by the UV pattern.

2.4.2 Optical and Physical Properties

This section describes some of the important optical and physical characteristics of fiber Bragg gratings. We obtain expressions for the coupling coefficient in terms of the overlap integral of the two modes. The spectral response of a Bragg grating is analyzed and parameters such as bandwidth and peak reflectivity are studied. The effects of physically deforming the fiber by bending and etching are also discussed.

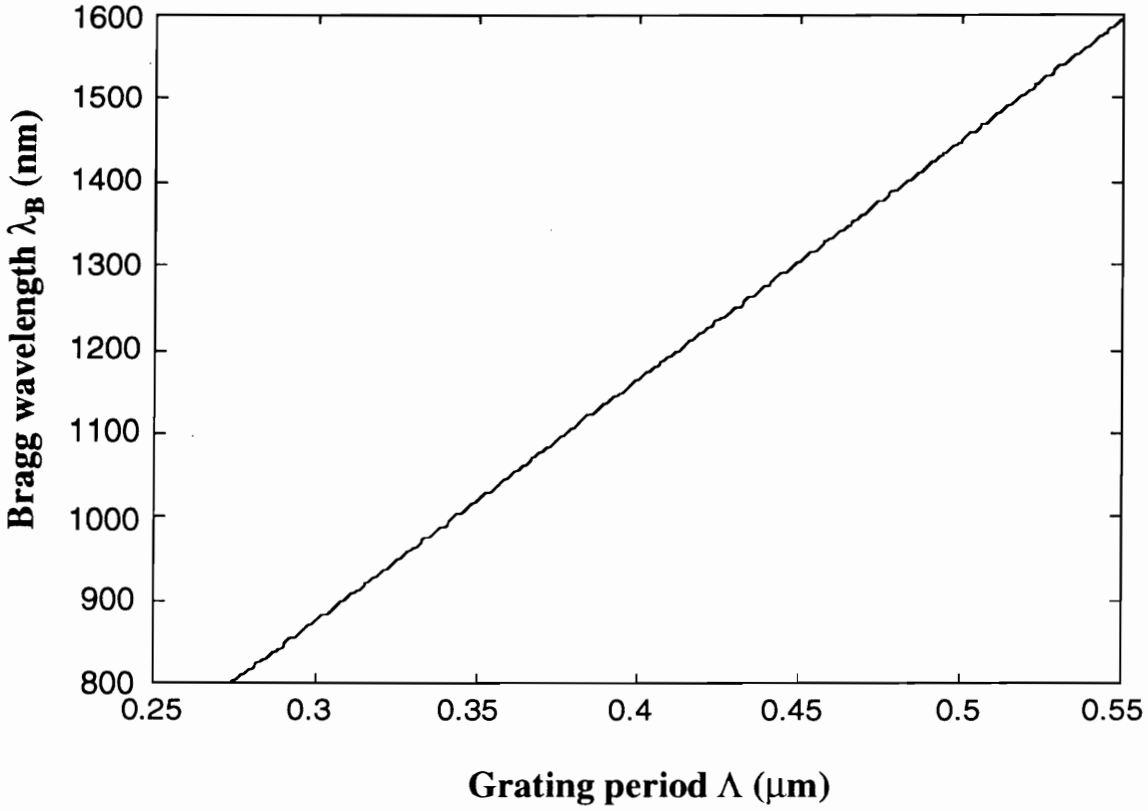

Figure 2.11. Variation of the Bragg wavelength as a function of the grating period for the 1060 nm Corning Flexcor fiber. The wavelength versus period curve may be approximated by a straight line ($d\lambda_B/d\Lambda=2n_{eff}$).

As stated in the previous section, the Bragg wavelength is a function of the grating period and the effective index of the guided mode. Figure 2.11 shows the expected variation in the coupling wavelength as a function of the periodicity for gratings fabricated in 1060 nm Corning Flexcor fiber. The Flexcor fiber is a step-index fiber with core radius a=2.5 μm and the index difference Δ=0.36% [61]. Weakly-guiding analysis [54] was used to solve for the fundamental guided mode propagation constant and the spectral variation of the core and the cladding indices was included by using the Sellmeier coefficients [62]. The process to arrive at solutions to the guided mode characteristic equations will be detailed in Section 3.2.2.1. Figure 2.11 reveals that the coupling wavelength increases almost linearly with the grating period which implies that an incremental change in the period produces approximately the same variation in the Bragg wavelength at all values of the grating period. We also interpret that the spectral dependence of the modal effective index can be neglected for Bragg grating analysis. This assumption greatly

simplifies the investigation of the spectral characteristics of Bragg gratings. It was also observed that small variations in the values of the core radius or the index difference do not significantly alter the curve in Figure 2.11.

Section 2.3.2.2 described the coupling between two counter-propagating modes in the presence of a periodic perturbation. We now use that analysis to investigate the spectral properties of a Bragg grating. Equation (2.23) for the normalized reflection produced by a Bragg grating is reproduced here,

$$R = \frac{\sinh^2\left[\kappa L \sqrt{1 - \left(\frac{\delta}{\kappa}\right)^2}\right]}{\cosh^2\left[\kappa L \sqrt{1 - \left(\frac{\delta}{\kappa}\right)^2}\right] - \left(\frac{\delta}{\kappa}\right)^2}, \tag{2.26}$$

where δ/κ is the detuning ratio. In Equation (2.26), L is the length of the grating, δ is the detuning parameter and κ is the coupling coefficient. The detuning parameter for a Bragg grating of period Λ is given by,

$$\delta = \beta_{01} - \frac{\pi}{\Lambda}, \tag{2.27}$$

where $\beta_{01}=2\pi n_{eff}/\lambda$, λ is the wavelength and n_{eff} is the effective modal index. For the phase-matched case ($\delta=0$), Equation (2.27) reduces to Equation (2.25).

The peak reflectivity R_0 can be derived from Equation (2.26) as,

$$R_0 = \tanh^2(\kappa L). \tag{2.28}$$

At the phase-matching condition, the normalized transmission T_0 of the forward-propagating guided mode can be obtained from Equation (2.20) as,

$$T_0 = \operatorname{sech}^2(\kappa L). \tag{2.29}$$

Figure 2.12 depicts the variation of the peak reflectivity R_0 and minimum transmission T_0 as functions of κL. The peak reflectivity increases with κL and for large values of κL undergoes saturation. During a typical grating fabrication process, a fixed length L of the

fiber is exposed to the UV radiation. The irradiation is stopped when the peak reflectivity reaches a desired value.

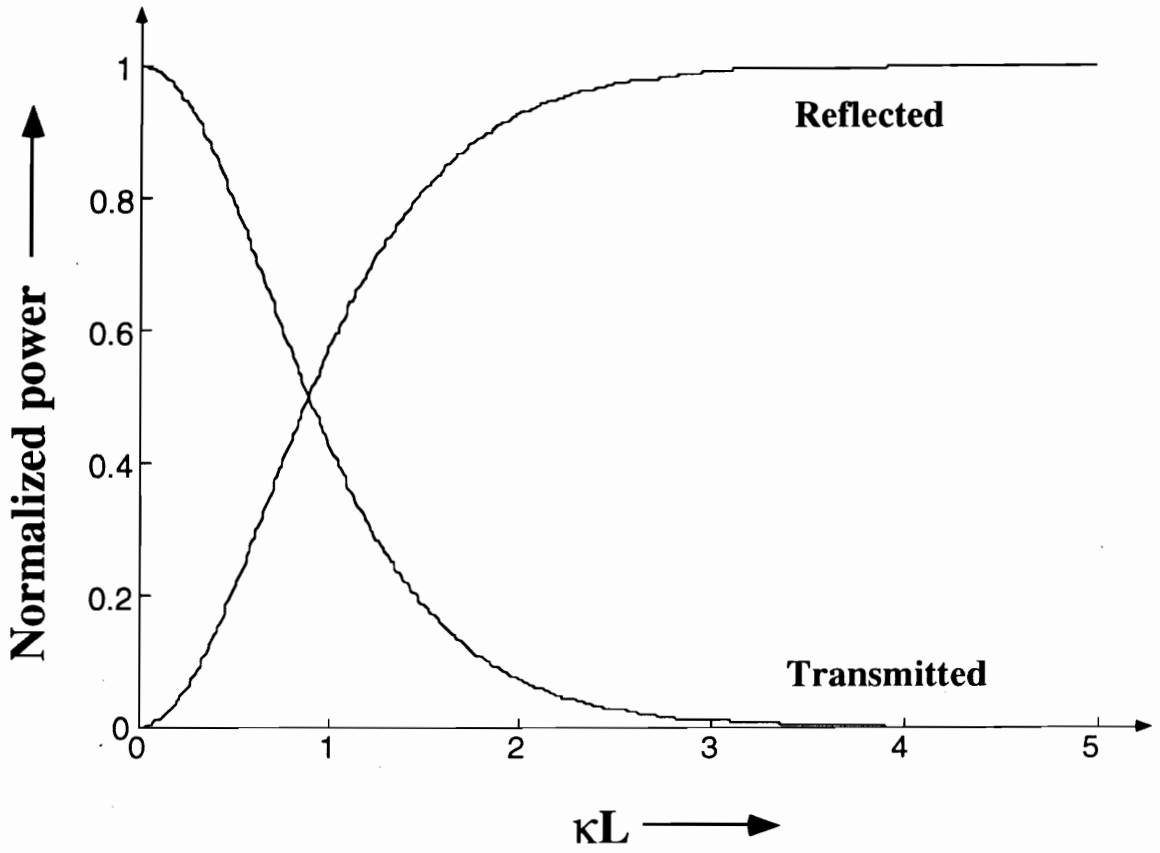

Figure 2.12. Variation of the normalized reflected and transmitted powers at the phase-matched Bragg wavelength.

We now consider the properties of the coupling coefficient κ and the factors influencing its magnitude. Consider a Bragg grating with a periodic spatial refractive index modulation δn that can be expressed as the following function of the propagating direction z [60],

$$\delta n = \frac{\Delta n}{2} \sum_{N=-\infty}^{\infty} A_N e^{-j\frac{2\pi N}{\Lambda} z}, \tag{2.30}$$

where Λ is the grating periodicity and Δn is the UV-induced peak index change. Here N is the order of interaction between the two modes that allows for the phase-matching condition of Equation (2.25) to be satisfied and A_N is the corresponding Fourier coefficient. For a first order interaction (N=1) and assuming a purely sinusoidal index modulation ($\delta n=\Delta n\cos(2\pi z/\Lambda)$), $A_1=A_{-1}=1$. The perturbed modified index profile n_p of the fiber core after UV exposure is then given by, $n_p=n_1+\delta n$.

The coupling coefficient κ for a Bragg grating at λ_B may simply be expressed as [9,60],

$$\kappa = \frac{\pi A_N}{\lambda_B} \eta \,, \tag{2.31}$$

where, η is the overlap integral between the forward- and reverse-propagating guided modes and is calculated over the area where the perturbation exists (the fiber core in case of a Bragg grating). The electric field distribution $E_{01}(r)$ of the fundamental guided mode is given by [53],

$$E_{01}(r) = A\, J_0(ur) \qquad \text{for } r<a \,, \tag{2.32a}$$

$$E_{01}(r) = B\, K_0(wr) \qquad \text{for } r>a, \tag{2.32b}$$

where r is the radial direction and we have ignored the phase factor $e^{j(\omega t-\beta z)}$. In Equation (2.32) A and B are arbitrary constants, J_0 and K_0 are the zeroth order Bessel and modified Bessel functions of the first kind, and u and w are the usual waveguide parameters defined as [53],

$$u = \sqrt{k_1^2 - \beta_{01}^2} \,, \tag{2.33}$$

and,

$$w = \sqrt{\beta_{01}^2 - k_2^2} \,, \tag{2.34}$$

where $k_1=2\pi n_1/\lambda$ and $k_2=2\pi n_2/\lambda$.

The overlap integral is expressed in terms of the modal power overlap of the two modes involved in coupling and for a Bragg grating reduces to [60],

$$\eta = \frac{\int_0^a (\Delta n)\, E_{01}^2(r)\, r\, dr}{\int_0^\infty E_{01}^2(r)\, r\, dr}, \tag{2.35}$$

where the modal overlap is considered only over the area that undergoes index modulation. Since the refractive index modulation in the core has no transverse variation, the modes involved in coupling have no azimuthal dependence [57]. The coupling to non-circularly symmetric modes can be achieved by giving the index modulation a spatial variation in the transverse direction. We will consider the applications of such blazed gratings [63] for coupling to radiation modes in Section 2.4.4.

We observe from Equation (2.31) that the coupling coefficient is directly proportional to the value of the overlap integral. Hence to obtain good power coupling between two modes we need two main conditions to be fulfilled - one that of phase-matching, and the other of sufficient modal overlap over the region of perturbation. The magnitude of the detuning ratio (δ/κ) in Equation (2.26) has a strong dependence on these conditions and for significant power transfer this ratio should be close to zero.

The coupling coefficient can be calculated as a function of wavelength if the spectral variation of the modal fields are known. For an unblazed grating, η is simply the product of Δn and the fraction of the modal power in the core F ($\eta = \Delta n F$), where [64],

$$F \cong 1 - \frac{1}{V^2}. \tag{2.36}$$

In Equation (2.37), V is the normalized frequency of operation and is defined as [53],

$$V = \frac{2\pi a}{\lambda}\sqrt{n_1^2 - n_2^2}\,. \tag{2.37}$$

We hence observe that for a given Δn, the value of the overlap integral increases as we move to lower wavelengths (or higher V-numbers). This is because the guided mode has a smaller modal confinement within the core at higher wavelengths.

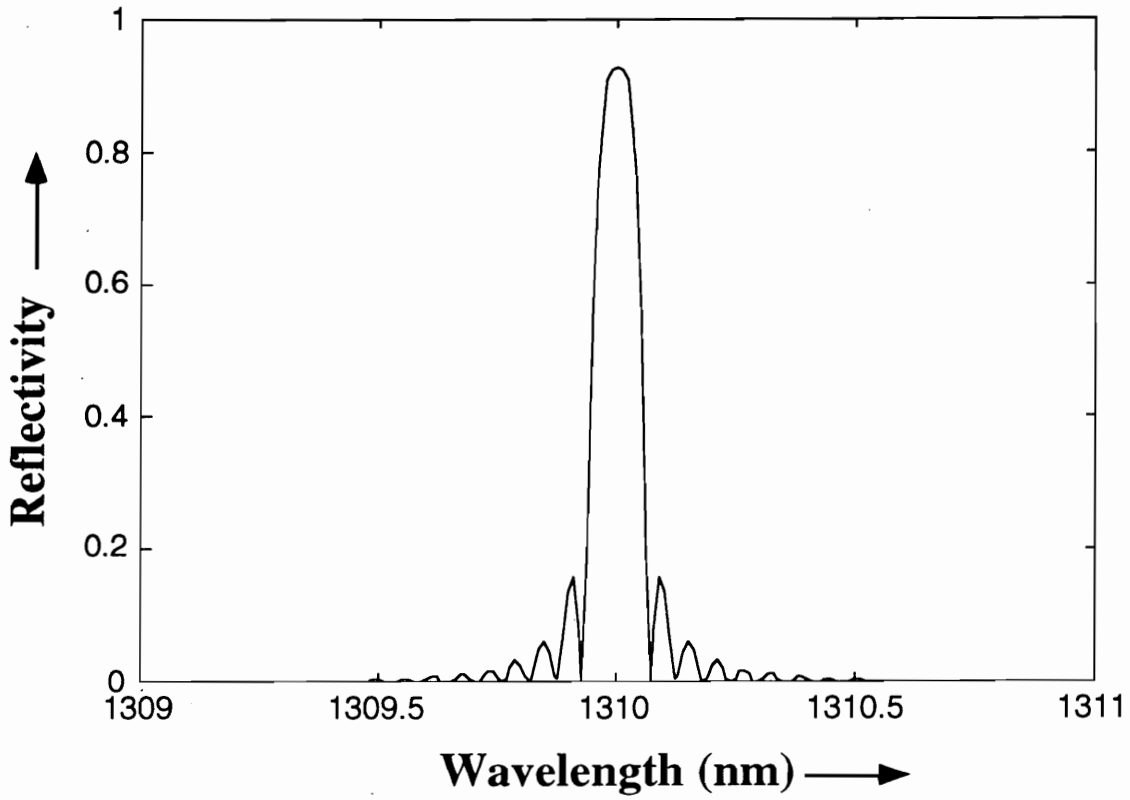

Figure 2.13. Variation of reflectivity as a function of wavelength for a grating of L=1 cm centered at 1310 nm in Corning SMF-28 fiber. Note the small spectral width of the grating.

We now determine the variation of the normalized reflectivity of Bragg grating as a function of wavelength. Consider a Bragg grating written in Corning SMF-28 fiber (a=4.5 μm, Δ=0.36% [65]) at 1310 nm and length L=1 cm with a sinusoidal index modulation ($\Delta n=1\times10^{-4}$). The coupling coefficient κ for this grating is calculated to be about 2 cm^{-1} at the Bragg wavelength and assumed to be constant over the grating bandwidth. This approximation is justified since the spectral width of Bragg gratings is very small compared with the wavelength range over which κ shows significant variation. Using Equations (2.26) and (2.27) and neglecting the spectral dependence of the effective index of the guided mode, we plot the reflectivity of the grating in Figure 2.13. The peak reflectivity of this grating is $R_0=0.93$ which is in agreement Equation (2.28). The presence of sidelobes (Figure 2.13) in a Bragg grating might not be desirable in certain applications. It has been shown that sidelobe suppression can be achieved by making the coupling coefficient a function of the distance along the grating [66].

The spectrum in Figure 2.13 is a strong function of the values of the coupling coefficient κ and the grating length L. Increasing the value of either or both these parameters results in enhanced peak reflectivity. On the other hand, if both κ and L are changed while keeping their product constant, interesting variations in the grating width can be obtained for the same peak reflectivity. For example, increase in value of κ makes the grating wider since it reduces the phase-mismatch ratio (δ/κ) over a larger spectral range. Hydrogen-loading the fiber enhances the UV-induced index change (Δn) and hence provides a means to increase the coupling ratio and grating width. It has been shown that the full bandwidth $\Delta\lambda$ (wavelength separation between the first zeros of the reflection spectrum) of a Bragg grating is given by [60],

$$\Delta\lambda = \frac{\lambda_B^2}{2n_{eff}L}\sqrt{\pi^2 + (\kappa L)^2}\,. \tag{2.38}$$

It can be deduced from Equation (2.38) that the increase in the length of the grating results in reduced full bandwidth. This feature can be used to determine the minimum device length for applications that require gratings with small bandwidth.

Since the Bragg grating mechanism involves transfer of power between two guided modes, the energy remains well confined to the fiber core. Thus large bend radii do not notably alter the grating characteristics. If the bend radius is reduced significantly, the grating spectrum may be altered, especially if the Bragg wavelength is far from cutoff in the single mode operating region. Similarly, etching small amounts of the fiber cladding around the grating region does not significantly alter the grating features. To see variations in the grating spectrum it is hence necessary to etch the cladding till the evanescent field in the fundamental mode can be accessed. Etched-cladding Bragg gratings have been used to implement refractive index sensors in the past [14].

2.4.3 Fabrication

Fiber Bragg gratings have commonly been manufactured using two side-exposure techniques, namely, interferometric method [9] and phase mask method [13]. The interferometric method, depicted in Figure 2.14, comprises of a UV beam at 244 or 248 nm spilt in two equal parts by a beam-splitter [9]. The two beams are then focused on a

portion of Ge-doped fiber (whose protective coating has been removed) using appropriate optical components. The periodicity of the resulting interference pattern and hence that of the Bragg grating is varied by altering the mutual angle θ [60]. The limitation of this method is that any relative vibration of the pairs of mirrors and lenses may lead to the degradation of the quality of the final grating, and hence the entire system has a stringent stability requirement. To overcome this drawback, Kashyap *et al.* have proposed a novel interferometric technique where the path difference between the interfering UV beams is obtained by propagation through a right-angled prism (Figure 2.15) [67]. The technique is inherently stable because any prism vibration perturbs both the beams in the same manner.

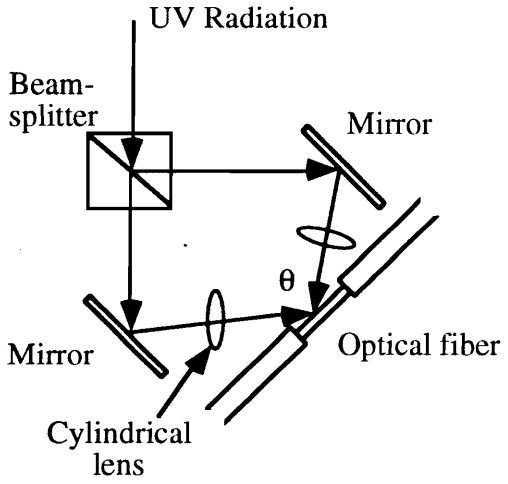

Figure 2.14. Fabrication of Bragg gratings using the interferometric scheme [9].

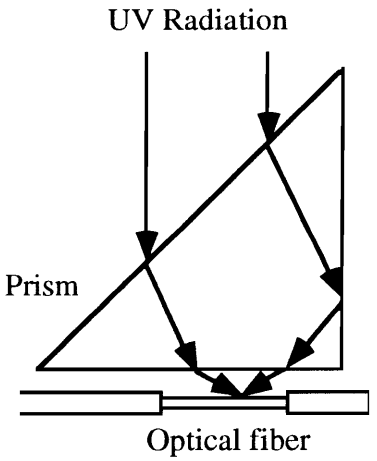

Figure 2.15. Bragg grating fabrication using the prism method [67].

The phase mask technique has recently gained popularity as an efficient holographic side-writing procedure for grating fabrication [13]. In this method (Figure 2.16), an incident UV beam is diffracted into -1, 0 and +1 orders by a relief grating generated on a silica plate by e-beam exposure and plasma etching. The two first diffraction orders undergo total internal reflection at the glass/air interface of a rectangular prism and interfere on the bare fiber surface placed directly behind the mask. The phase mask technique is wavelength-specific since the periodicity of the resulting two-beam interference pattern is uniquely determined by the diffraction angle of -1 and +1 orders and thus, the properties of the phase mask [13]. Obviously, different phase masks are required for fabrication of gratings at distinct Bragg wavelengths. The setup for actively monitoring the growth of

the grating in transmission during fabrication is shown in Figure 2.17. A given length of the fiber is UV irradiated till the transmission (or reflection) spectrum meets the desired specifications. The fiber is typically hydrogen- or deuterium-loaded for all fabrication methods.

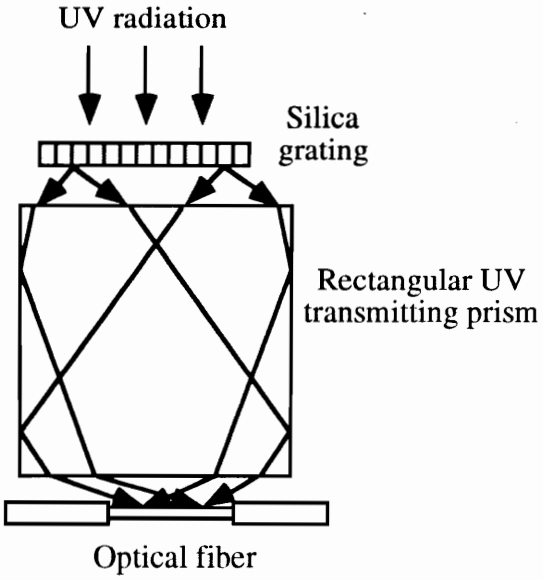

Figure 2.16. Phase mask method of fabricating Bragg gratings [13].

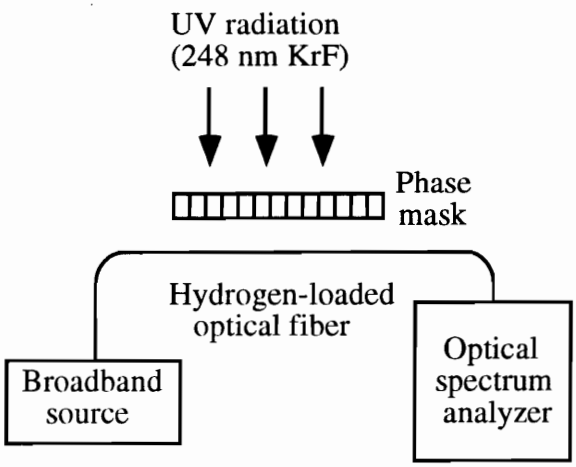

Figure 2.17. Setup to write Bragg gratings in germanosilicate fibers.

2.4.4 Applications

This section describes the some of the important devices that be fabricated by employing fiber Bragg gratings. As discussed earlier, a Bragg grating couples power from the forward-propagating fundamental mode to the reverse-propagating LP_{01} mode at a wavelength that satisfies the phase-matching condition (Equation (2.25)). The reflected wavelength spectrum has been used to make reflection filters, fiber lasers, dispersion compensation devices and sensing systems [60].

Fiber Bragg gratings can be used to fabricate either narrowband or broadband filters by using either one or more multiplexed gratings. The narrowband filters can be employed to separate different channels in wavelength-division multiplexed (WDM) systems by using couplers or circulators [68]. Such gratings can have bandwidths between 0.05 and 20 nm [29] depending on the index modulation that can be achieved. The larger

bandwidths are attained by loading the fiber with sufficient hydrogen so that a higher UV-induced peak index change is obtained.

Fiber Bragg gratings have been used in the past to obtain fiber grating lasers [69]. The simplest configuration of this laser is shown in Figure 2.18. A given length of an erbium-doped fiber is spliced to a reflection grating with a specific Bragg wavelength. On being optically pumped by a 980 or 1480 nm laser source, the transmission from the grating end is observed to be a single longitudinal mode with a narrow linewidth (of the order of 1 GHz) [69]. Excellent system performance has been reported in literature using fiber grating lasers [70]. A laser with a smaller cavity loss has been achieved by fabricating the fiber Bragg grating in the core of a high germanium, erbium-doped fiber [71].

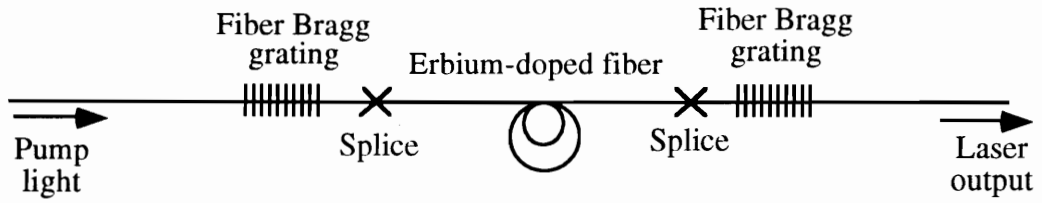

Figure 2.18. Set up to realize a fiber grating laser using erbium-doped fiber [69].

With the introduction of fiber amplifiers, modern communication systems are being increasingly designed to operate at 1550 nm [48,53,72]. Links installed in the past decade were optimized for 1310 nm operation and hence introduce a finite dispersion if 1550 nm optical sources are employed. This presence of dispersion has forced researchers to investigate techniques [73] for restoration of the broadened pulse. Fiber Bragg gratings provide a fiber-compatible and economical alternative to some of the other schemes proposed for dispersion compensation. For this application Bragg gratings are chirped, in either their periodicity or the refractive index, along the axis of the fiber [74]. The chirp introduces a position-dependent wavelength reflection which provides a time delay per unit wavelength that is opposite in sign to the one introduced by the fiber link. One of the major limitations of this technique has been its limited bandwidth. The advent of hydrogen loading has enabled fabrication of gratings with not only large bandwidths but also high reflectivities, permitting broadband dispersion compensation.

Coupling to radiation modes in blazed fiber Bragg gratings has been used to fabricate side-taps filters. Radiation modes are not guided by the core and lose power continuously

which prevents a reflection from the Bragg grating and can be used to flatten the spectrum of erbium gain profile in fiber amplifiers [63]. Eight radiation mode taps with peak spectral loss at different wavelengths have been multiplexed to obtain the inverse of the erbium spectrum [75].

As outlined earlier, fiber Bragg gratings can be used as strain and temperature sensors due to the dependence of the periodicity and the effective modal index on these external perturbations [8]. It has also been shown recently that a large number of gratings can be fabricated in the same fiber during the fiber drawing process [76] which has enabled multiplexing of a large number of such gratings for distributed measurements. The next three sections discuss the temperature and strain Bragg grating sensors and their major advantages and limitations.

2.4.4.1 Temperature Sensor

Bragg grating-based fiber optic temperature sensors have been a topic of extensive research and development in recent years [8,10]. For a first order interaction (N=1), Equation (2.25) for the Bragg wavelength λ_B reduces to,

$$\lambda_B = 2\, n_{eff}\, \Lambda\,, \tag{2.39}$$

where n_{eff} is the guided mode effective index and Λ is the grating period.

If a temperature change ΔT is applied to a Bragg grating, the wavelength shift per unit temperature change $d\lambda_B/dT$ can be obtained using the chain rule of derivatives,

$$\frac{d\lambda_B}{dT} = \frac{d\lambda_B}{dn_{eff}} \frac{dn_{eff}}{dT} + \frac{d\lambda_B}{d\Lambda} \frac{d\Lambda}{dT}\,. \tag{2.40}$$

Equation (2.40) predicts that the thermal-induced change in the Bragg wavelength is due to two major contributions - the first due to the change in effective index of the fiber, and the second owing to the change in the grating period. We will denote the first term on the right-hand side of Equation (2.40) as the material effect since it results in a spectral shift due to a change in the material property of refractive index. The second term is called the waveguide effect because it causes a change in the waveguide length due to thermal

expansion. From Figure 2.11 we observe that the slope ($d\lambda_B/d\Lambda$) of the coupling wavelength versus grating period is constant with value $2n_{eff}$. Moreover, the spectral variation of the effective index can be neglected and this thus Equation (2.40) yields,

$$\frac{d\lambda_B}{dT} = 2\Lambda\left(\frac{dn_{eff}}{dT} + n_{eff}\frac{1}{\Lambda}\frac{d\Lambda}{dT}\right). \tag{2.41}$$

Approximating the effective index with the index of refraction of pure silica n_{si}, Equations (2.39) and (2.41) can be combined to produce,

$$\frac{d\lambda_B}{dT} = \lambda_B\left(\frac{1}{n_{si}}\frac{dn_{si}}{dT} + \frac{1}{L}\frac{dL}{dT}\right), \tag{2.42}$$

where L is the length of the grating ($d\Lambda/\Lambda dT = dL/LdT$). The first term in the parenthesis is the material contribution to wavelength shift and can be obtained from the thermo-optic coefficient dn_{si}/dT of silica. The waveguide contribution (second term) is termed the coefficient of thermal expansion dL/LdT for silica. Using $n_{si}=1.458$, $dn_{si}/dT=7.8\times10^{-6}$ /°C and $dL/LdT=4.1\times10^{-7}$ /°C [77], Equation (2.42) can be rewritten as,

$$\Delta\lambda_B = 5.76\times10^{-6}\,\lambda_B\,\Delta T\,, \tag{2.43}$$

where $\Delta\lambda_B$ is the Bragg wavelength shift for ΔT change in temperature. Thus Bragg gratings at 1310 nm and 1550 nm are expected to have temperature coefficients of 0.008 nm/°C and 0.009 nm/°C, respectively. Experimentally determined values of coefficients at these wavelengths are 0.011 nm/°C and 0.013 nm/°C, respectively [6]. It is important to note here that both material and waveguide contributions (Equation (2.42)) are positive. The material effect is more than an order of magnitude larger than the waveguide effect. Hence conventional Bragg gratings have a positive temperature coefficient dominated by the material contribution that arises from the change in the refractive index of the host glass.

2.4.4.2 Strain Sensor

Bragg grating sensors have been used as effective strain gages in commercial applications in both embedded and surface-mounted configurations [66]. Wavelength-division

multiplexed sensors in a single fiber can be used for distributed strain measurement in high-performance materials and structures.

To obtain an expression for the strain sensitivity we employ a procedure similar to that used in previous section. Any axial strain $\Delta\varepsilon$ applied to the grating changes the periodicity and the effective index and results in a shift in the Bragg wavelength that is given by,

$$\frac{d\lambda_B}{d\varepsilon} = \lambda_B \left(\frac{1}{n_{si}} \frac{dn_{si}}{d\varepsilon} + \frac{1}{L} \frac{dL}{d\varepsilon} \right), \tag{2.44}$$

where the first term in the parenthesis is again the material contribution to the strain-induced shift due to the change in the index of refraction of silica. The second term is the waveguide contribution and equals unity ($\Delta\varepsilon=\Delta L/L$). Using the photoelastic coefficient of silica, $(1/n_{si})dn_{si}/d\varepsilon=-0.22$ [78], we get,

$$\Delta\lambda_B = 0.78\, \lambda_B\, \Delta\varepsilon\,, \tag{2.45}$$

where, $\Delta\lambda_B$ is the Bragg wavelength shift for $\Delta\varepsilon$ applied strain. Thus Bragg gratings at 1310 nm and 1550 nm are expected to have strain coefficients of 10.2 nm/%ε and 12.1 nm/%ε, respectively, which are very close to the experimental values. We observe that unlike the temperature sensor, material and waveguide contributions have opposite polarities for the strain sensor. The reduction in the refractive index due to strain causes a spectral shift to lower wavelengths while the increase in period results in a positive wavelength shift. The waveguide contribution dominates and hence produces an overall positive strain-induced shift.

2.4.4.3 Advantages and Limitations

Bragg grating strain and temperature sensors are finding numerous applications in various engineering disciplines. In this section we analyze the major advantages and limitations of Bragg grating sensors over other fiber optic sensors.

The most significant advantage of Bragg gratings sensors is that a number of these can be multiplexed for distributed measurements [10]. A single optical spectrum analyzer can

be used to detect the spectral shift in wavelength multiplexed strain or temperature sensors. The small bandwidth of these gratings enables the use of a single broadband optical source to interrogate the multiplexed sensors. On the contrary, interferometric- and intensity-based sensors are difficult to multiplex due to the potentially complex nature of signal processing required at the receiver end. The wavelength-encoded signal in Bragg gratings is independent of source intensity fluctuations and bends in the lead-in/lead-out fiber. Intensity-based sensors are limited by factors that alter the power in the lead-in/lead-out fibers. Bragg grating sensors can be operated in the reflection configuration to obtain single-ended operation which enables easier and quicker installation of such gratings in difficult to access locations in comparison with sensors that operate in transmission mode. The spectrum of Bragg gratings remains practically unchanged for large bend radii at the sensor head. A major limitation of Bragg grating sensors is the requirement of expensive phase masks to obtain different Bragg wavelengths. Moreover, in the interferometric technique [9], stability of the set up is a critical factor to obtain high quality gratings.

The second major drawback of Bragg grating sensors is the limited strain- and temperature-induced wavelength shifts. The temperature shift is a mere 1.3 nm for 100 °C change in temperature while the spectral shift due to 1% strain is about 11 nm. These limited wavelength shifts require high-resolution spectrum analyzers to monitor the grating spectrum in the presence of minute perturbations. Kersey and Berkoff have proposed an unbalanced Mach-Zender interferometer to detect the perturbation-induced wavelength shift [12]. Two unequal arms of the Mach-Zender interferometer are excited by the backreflection from a Bragg grating sensor element. Any change in the input optical wavelength modulates the phase difference between the two arms and results in a time-varying sinusoidal intensity at the output. The interference signal can be related to the shift in the Bragg peak and hence the magnitude of the perturbation can be deduced. The unbalanced interferometers are themselves susceptible to external perturbations and thus need to be isolated from the parameter under investigation. Moreover, the non-linear output might require fringe counting equipment which can be complex and expensive.

Fiber Bragg gratings have also been proposed as refractive index sensors in chemical analysis. Etching of the fiber cladding around the grating has been employed to gain access to the evanescent field of the guided mode [14]. A refractive index change around the etched grating serves to change the effective index of the guided mode, resulting in a

shift in the Bragg resonance wavelength. A major limitation of these sensors is that the etching process reduces the strength and integrity of the grating. Thus these refractive index sensors may not feasible for operation under harsh environmental conditions. Additionally, these gratings have limited ambient refractive index-induced shifts [14].

Lastly, Bragg gratings used in the reflection configuration can cause fluctuations in the source intensity due to optical feedback. Gratings for highly sensitive measurements might hence require the use of expensive isolators to prevent such back-reflections. The feedback to the source may also be eliminated by using optical circulators.

In summary, Bragg grating-based sensors are highly attractive due to their multiplexing and absolute measurement capabilities. These sensors are expensive to fabricate although batch-production can significantly lower the cost of individual transducers. Strain and temperature sensors have limited wavelength shifts and require expensive spectrum analyzers or unbalanced interferometers for demodulation.

2.5 Guided Mode Coupling Using Long-Period Gratings

Fiber Bragg gratings discussed in the previous section assist in coupling between the fundamental guided modes propagating in opposite directions. In certain applications, it is essential to couple light from the LP_{01} mode to other forward-propagating guided modes. This section outlines the operation, fabrication, properties and applications of gratings that implement the transformation of one guided mode to another.

The β-plot in Figure 2.19 depicts the mode-coupling mechanism between two forward-propagating guided modes. Since the differential propagation constant ($\Delta\beta$) is small in this case, large values of the grating periodicity are required to satisfy the phase-matching condition (Equation (2.24)). The periodicity of the resultant devices are typically hundreds of micrometers (compared to less than one micrometer for fiber Bragg gratings) and such gratings are termed long-period gratings. It is important to reiterate here that these long-period gratings couple light between two guided modes. Hill *et al.* [26] were the first to propose the use of such gratings for guided mode coupling. They used a point-by-point external writing technique to couple the LP_{01} mode to LP_{11} mode employing a periodicity of 590 μm which resulted in mode-conversion at 820 nm for a fiber that had a cutoff wavelength of 1100 nm [26]. Since coupling in this case occurs

from a circularly-symmetric to asymmetric mode, the grating needs to be blazed to attain optimum mode coupling [57]. The coupling wavelength can be varied by changing both the periodicity and the blaze angle of the grating. The authors have demonstrated 96% conversion efficiency for this particular grating [26].

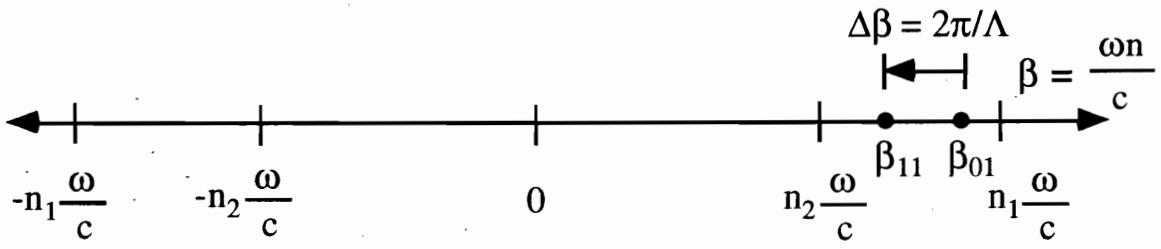

Figure 2.19. Mode coupling between two forward-propagating guided modes. The small value of $\Delta\beta$ results in a large value of the grating periodicity Λ.

In 1991, Bilodeau *et al.* [27] proposed a grating that coupled the fundamental guided mode to the circularly-symmetric LP_{02} mode using an internal writing technique in two-mode fibers. The grating did not require blazing because both LP_{01} and LP_{02} modes possess circular symmetry. A grating periodicity of 209 μm resulted in a coupling wavelength of 619 nm [27]. In the same year, Vengsarkar *et al.* demonstrated internally written gratings for coupling to the LP_{11} mode in dual-mode, elliptical-core fibers [79]. The disadvantage of using internal fabrication techniques is that the coupling wavelength is equal to the writing wavelength (usually 514 nm or 488 nm). External writing techniques are preferred since the mode-couplers can be fabricated at any desired wavelength.

In 1992, Johnson *et al.* [80] proposed long-period gratings that couple light from one polarization component of the fundamental mode to the other in standard telecommunication fibers. The differential propagation constant between the two orthogonal polarizations is very small, resulting in a large period (Λ=64 cm). The length of the fiber corresponding to half the beat-length was first exposed to UV radiation from an excimer laser. The fiber was then moved by another beat-length in the direction perpendicular to the incident UV beam and again photo-exposed. The alternating exposure caused the core refractive index to be modulated with a period equal to the beat-length between the two polarization modes. The filter was 10.89 m long with 17 periods

and possessed a bandwidth of 58 nm at 1540 nm [80]. This rocking filter coupled light from one polarization to another with a 99% efficiency.

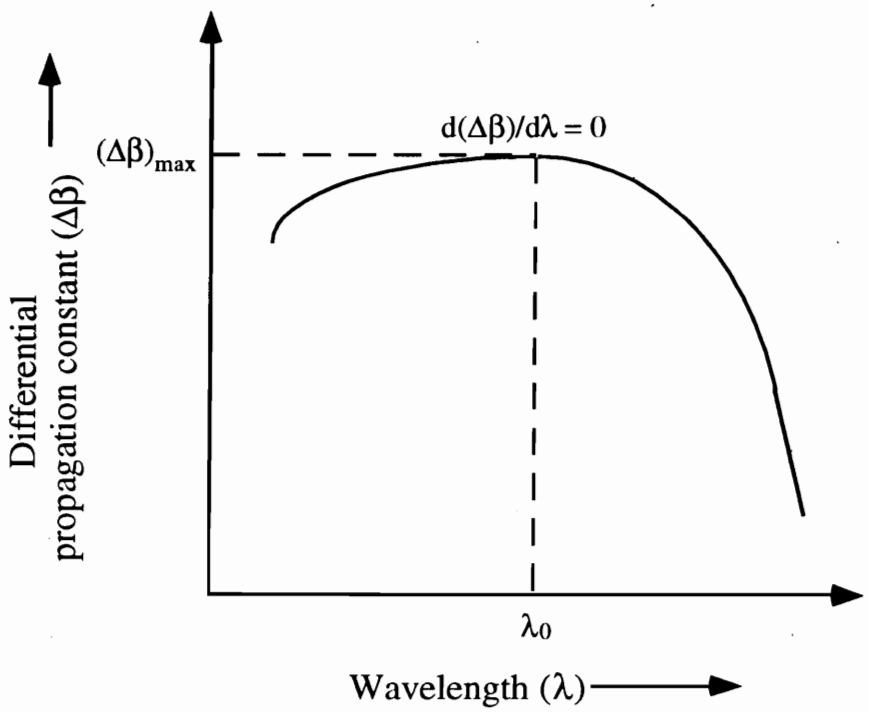

Figure 2.20. Typical variation of the differential propagation constant ($\Delta\beta$) between two forward-propagating guided modes as a function of the operating wavelength. $\Delta\beta$ attains its maximum value $(\Delta\beta)_{max}$ at the equalization wavelength λ_0 [81].

A typical variation of the differential propagation constant ($\Delta\beta$) between two forward-propagating guided modes is shown in Figure 2.20 [81]. It can be seen that the value of $\Delta\beta$ can be the same at two different operating wavelengths. Thus the same grating period might result in modal coupling at two values of wavelength ($\Delta\beta=2\pi/\Lambda$). The spectral dependence of the coupling coefficient might cause a difference in the coupling magnitude at the two wavelengths. The wavelength λ_0, at which the slope of the $\Delta\beta$ versus λ curve is zero, is termed the equalization wavelength between the two modes [82]. It is expected that the polarity of the slope of the λ versus Λ curve will depend on the relative location of the operating wavelength with respect to λ_0. It will be shown in Chapter 3 that at the equalization wavelength, the group indices of the two modes are equal. The availability of both positive and negative slopes for the λ versus Λ curves between two forward-propagating modes offers a lot of versatility in the grating

properties. For example, we will show in Chapter 4 that long-period gratings that couple a guided mode to cladding modes have interesting properties if the coupling wavelengths lie in the region with $d\lambda/d\Lambda<0$.

The modal couplers discussed above can be used for a large number of communication and sensing applications. Effective in-line spectral filters can be fabricated using these gratings. Recently, Poole *et al.* proposed a novel dispersion-compensation technique in which the large negative dispersion of higher order spatial modes near their cutoff wavelength was utilized to equalize the positive dispersion of the fiber link at 1.55 μm [83]. This scheme requires the efficient conversion of the fundamental mode to a higher order guided mode and long-period gratings are ideal for this purpose. Vengsarkar *et al.* have proposed the use of these gratings for sensing strain and vibration modes in high-performance civil structures [84,85]. The rocking filter used for coupling between the polarization components of the fundamental mode can be used as an optical switch for picosecond pulses. Johnson *et al.* have shown that these filters can be used to self-switch a soliton pulse of width 193 fs and a peak power of 1177 W [80].

This chapter reviewed the concept of photosensitivity and its applications to optical fiber technology. Coupling between co- and counter-propagating modes was analyzed and important devices like fiber Bragg gratings and guided mode couplers were investigated. We conclude that photosensitivity offers a simple method to perturb an optical fiber. This external perturbation causes coupling of power between different spatial modes depending on the phase-matching condition, the modal overlap and the blaze angle. The resulting devices have a number of interesting applications to optical fiber communication and sensing systems. Chapter 3 introduces photoinduced long-period gratings that couple the guided mode to cladding modes. The principle of operation, theoretical background, fabrication and properties of long-period gratings are investigated.

Chapter 3 - Properties of Long-Period Gratings

The previous chapter discussed the phenomenon of photosensitivity and its application to mode coupling in optical fibers. This chapter introduces long-period gratings that couple light from the guided mode to various cladding modes in the presence of a periodic perturbation in the fiber core [1]. The objective will be to provide a comprehensive analysis of the fundamental properties and characteristics of long-period gratings. This study forms the background for examining the applications of these periodic structures as optical fiber single-parameter sensing systems in Chapter 4.

The outline of Chapter 3 is as follows. We first discuss the principle of operation of long-period gratings by using the concept of β-plots. Section 3.2 is devoted to the analytical modeling of these devices by employing the techniques of waveguide analysis. The model is applied to characterize the behavior of gratings written in three different telecommunications grade optical fibers using the parameters provided by the manufacturer. The effect of small variations in the fiber parameters on the location of the resonance bands is also analyzed. In Section 3.3 we study important grating characteristics such as the coupling coefficient, the wavelength separation between resonance bands and the grating bandwidth. The process of fabricating long-period gratings using pulsed and continuous UV irradiation is discussed, and a novel and economical method for grating production is outlined. The technique is based on the fact that refractive index changes can be introduced in the core of hydrogen-loaded germanosilicate fibers under thermal exposure [28]. The post-fabrication process of grating stabilization by annealing is also investigated [1]. In Section 3.4 we discuss some important optical and physical properties, such as back-reflection, and the effects of etching and recoating the cladding surrounding the grating [1]. Finally, the applications of long-period gratings to advanced optical fiber communication systems are briefly reviewed [1,2,85].

3.1 Principle of Operation

Long-period gratings that couple power between guided and cladding modes were first proposed by Vengsarkar *et al.* [1,2] in 1995. These devices are typically formed by exposing the core of a germanium-doped fiber to a periodic UV pattern. The periodicity of the refractive index modulation ranges in hundreds of micrometers and this causes light to couple from the fundamental guided mode to discrete forward-propagating cladding modes. The periods for Bragg gratings (Section 2.4), in comparison, are around one-half a micrometer [25]. Although these two types of gratings are similar in terms of introduction of an index modulation in the fiber core through the process of photosensitivity [22], a few fundamental differences exist between the pair in terms of the operating principle and spectral response. This section attempts to outline the unique characteristics and the mechanism of mode coupling in long-period gratings.

The long-period gratings discussed in Section 2.5 couple light from the fundamental LP_{01} mode to other forward-propagating guided modes in few-moded fibers [26,27,80]. These gratings, though useful as modal couplers, find a limited number of applications in fiber optic systems. In these gratings, the mode coupling occurs at wavelengths where the phase matching condition ($\Delta\beta = 2\pi/\Lambda$) is satisfied, and the power is coupled from one guided mode another [26]. Although this power can be completely removed from the fiber by filtering the mode to which coupling is occurring, the modal filter adds to the cost and complexity of the system.

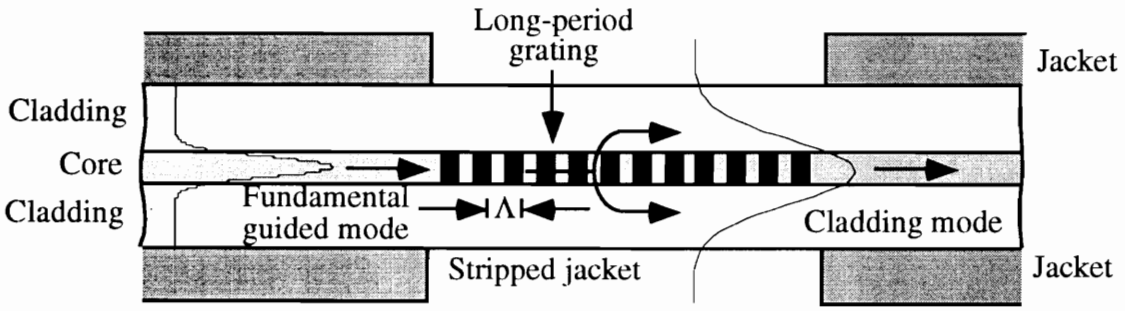

Figure 3.1. Coupling of the fundamental guided mode to cladding modes in a long-period grating. Λ is the periodicity of the refractive index modulation in the core.

The short-period fiber Bragg gratings, on the other hand, can be configured to couple light from the fundamental mode to infinite number of radiation modes [63]. The Bragg

grating is blazed such that the light at the phase matching wavelength is coupled to the lossy radiation modes instead of the backward-propagating LP_{01} mode. This property is useful in applications such as gain flattening of erbium-doped fiber amplifiers (Section 2.4.4) [63], where back-reflections from devices can degrade the system performance.

The principle of operation of long-period gratings proposed by Vengsarkar *et al.* [1] is illustrated in Figure 3.1. Light in the fundamental LP_{01} guided mode is perturbed by the presence of the grating in the fiber core. The difference between the propagation constant of the guided mode and the phase-matching vector of the grating equals the propagation constant of one or more cladding modes at appropriate wavelengths. Cladding modes result from the radiation modes that are trapped by cladding outer surface and were discussed in detail in Section 2.3.1. These modes attenuate rapidly on propagation due to bends in the fiber and absorption due to the cladding, and hence light at the phase-matched wavelengths is lost from the fiber. The attractive feature of these periodic elements is that since the loss mechanism is built-in due to coupling to the cladding modes, mode filtering is not required to obtain spectral modulation.

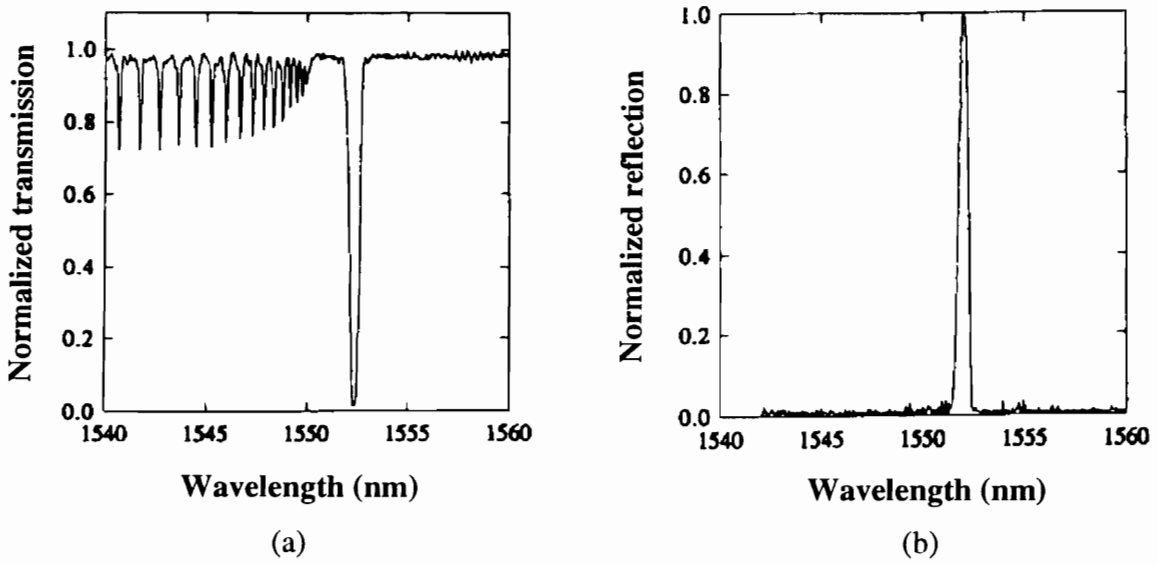

Figure 3.2. Coupling to reverse-propagating cladding modes in a strong fiber Bragg grating [86]. (a) In transmission, the pronounced structure at wavelengths smaller than the Bragg wavelength can be attributed to cladding mode coupling. (b) The reflection spectrum lacks the spiky spectrum at wavelengths shorter than the Bragg peak, confirming the loss to cladding modes.

It should be noted that the concept of coupling the guided modes to cladding modes has been around for a number of years. Weak coupling to several cladding modes was first observed by Bilodeau *et al.* [27] on the long wavelength side of the LP_{01}/LP_{02} resonance as four or five dominant peaks with increasing separation. A classic case that represents the phenomenon of coupling the fundamental guided mode to cladding modes was demonstrated by Mizrahi and Sipe [86]. They observed coupling to cladding modes in a fiber Bragg grating written in hydrogen-loaded, germanosilicate fiber. Figure 3.2 depicts the transmission and reflection spectra of the grating. Multiple peaks at the short wavelength side of the Bragg wavelength (Figure 3.2 (a)) are caused by the coupling to lossy modes. The light coupled out of the fiber can be attributed to cladding modes since the reflection spectrum (Figure 3.2(b)) contains the reflection due to the Bragg peak only. On immersing the grating in index-matching fluid, the cladding modes were found to disappear and radiation mode losses were observed due to elimination of the cladding outer surface.

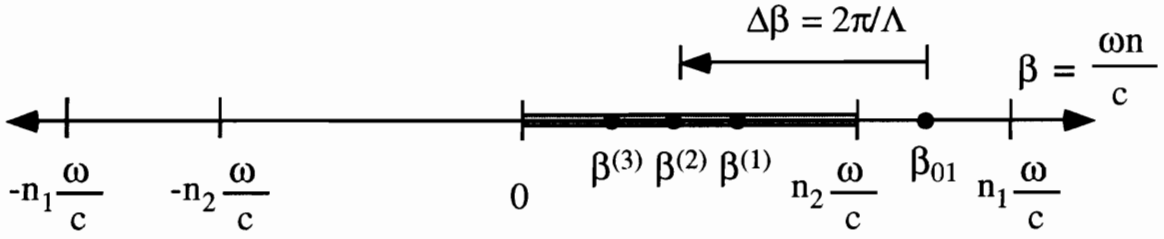

Figure 3.3. Mode coupling mechanism in a long-period grating [1]. β_{01} is the propagation constant of the fundamental guided mode and $\beta^{(m)}$ are the propagation constants of the circularly-symmetric cladding modes involved in coupling. The hatched region represents a continuum of forward-propagating radiation modes.

For the remaining portion of this work, unless otherwise stated, long-period gratings specifically refer to the gratings that couple the guided mode to cladding modes. For most applications, long-period gratings are not blazed, and hence the refractive index perturbation is independent of azimuthal variation. The overlap integral is thus non-zero for only the pair of modes that have the same azimuthal symmetry [57] and this causes the fundamental guided mode to couple to the cladding modes that are circularly-symmetric. These forward-propagating $LP_{0,m}$ cladding modes of order m possess propagation constants that are denoted by $\beta^{(m)}$. The basic operating principle of long-

period gratings can be explained using the β-plot introduced in Section 2.1.1. Figure 3.3 shows the simplified mode coupling mechanism in long-period gratings [1]. In order to keep the representation simple, the index of refraction n_3 of the medium ambient to the cladding is not depicted in the β-plot of Figure 3.3. The forward-traveling cladding mode propagation constants actually fall in the range $\omega n_3/c<\beta^{(m)}<\omega n_2/c$ ($n_2>n_3$) and for the remaining analysis in this chapter ωn_3 will not be represented on the β-plots. The forward-propagating guided mode with propagation constant β_{01} couples light to the azimuthally-symmetric cladding modes traveling in the same direction ($\beta^{(m)}>0$). Rewriting the phase-matching condition, first introduced in Section 2.3.2.1, we get,

$$\Delta\beta^{(m)} = \beta_{01} - \beta^{(m)} = \frac{2\pi}{\Lambda}, \tag{3.1}$$

where $\Delta\beta^{(m)}$ is the differential propagation constant and Λ is the grating periodicity. The small value of $\Delta\beta^{(m)}$ requires that the grating period be much larger than that for Bragg gratings. For a typical long-period grating, more than one cladding mode may satisfy the phase-matching condition and hence the guided mode may be coupled to all these lossy modes. The spectral dependence of the propagation constants of the core and cladding modes results in a highly wavelength-selective response of long-period gratings. Figure 3.4 depicts the transmission spectrum of a typical long-period grating [1]. The coupling of the fundamental guided mode to discrete cladding modes results in distinct resonance bands in the transmission spectrum. The bands have different values of peak loss and bandwidth due to dissimilar coupling coefficients that are functions of the modal overlap. The concept of coupling coefficients will be explored further in Section 3.2.4.1.

The phase-matching condition can be expressed in terms of the effective indices of the guided (n_{eff}) and cladding ($n_{cl}^{(m)}$) modes to predict the coupling wavelength $\lambda^{(m)}$ for the m^{th} order cladding mode,

$$\lambda^{(m)} = \left(\delta n_{eff}^{(m)}\right)\Lambda, \tag{3.2}$$

where $\beta_{01}=2\pi n_{eff}/\lambda^{(m)}$, and $\beta^{(m)}=2\pi n_{cl}^{(m)}/\lambda^{(m)}$, and the differential effective index $\delta n_{eff}^{(m)}$ between the guided mode and the cladding mode of order m is defined as,

$$\delta n_{eff}^{(m)} = n_{eff} - n_{cl}^{(m)}. \tag{3.3}$$

For standard optical fibers the differential effective index between the guided and cladding modes is typically between 10^{-3} and 10^{-2}. Thus for coupling to occur at wavelengths in the communication window (1200-1600 nm), the periods of these gratings are in hundreds of micrometers. It is interesting to note that Equation (3.2) reduces to Equation (2.39) for a Bragg grating if we substitute $-n_{eff}$ for $n_{cl}^{(m)}$. Since the differential effective index between the forward- and backward-propagating guided modes is $2n_{eff}$, Equation (3.3) predicts that in a long-period grating the coupling between such modes (and other forward and reverse-propagating modes) will typically occur at wavelengths outside the optical communication spectrum.

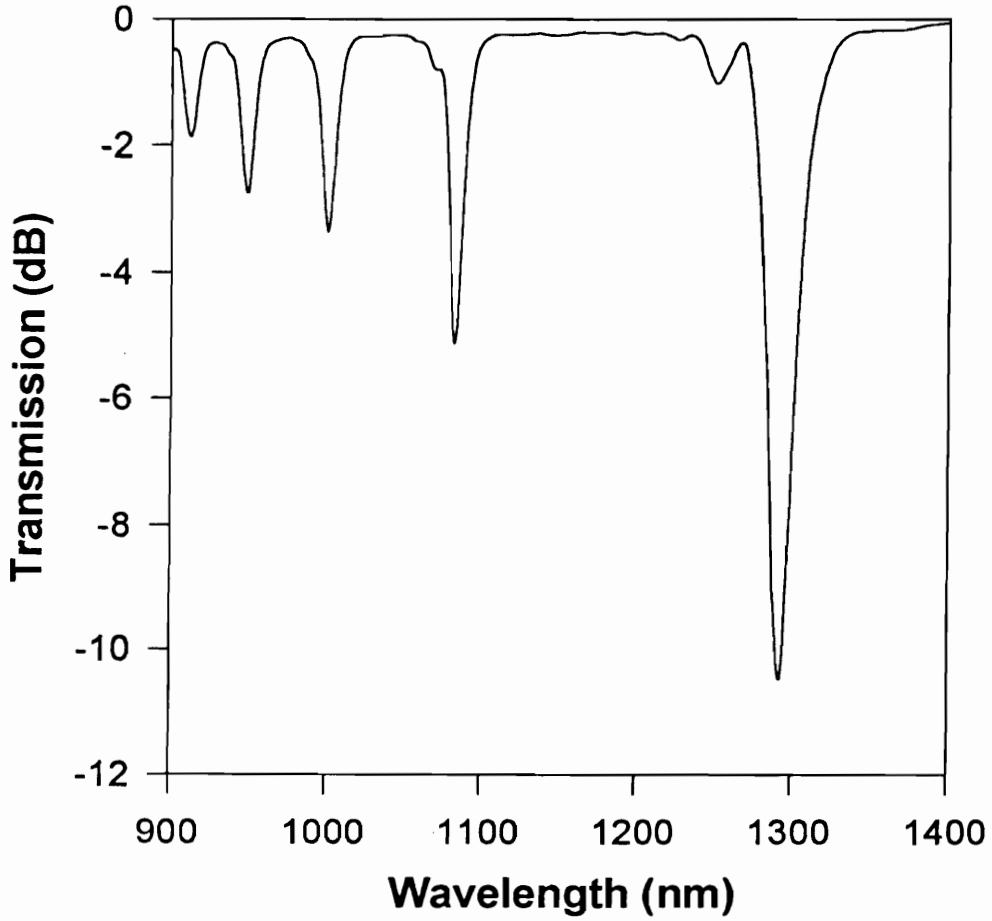

Figure 3.4. Transmission spectrum of a long-period grating written in Corning 1060 Flexcor fiber with period, Λ=198 μm [1]. The discrete, spiky loss bands correspond to the coupling of the fundamental guided mode to discrete cladding modes.

We now compare the spectral modulation provided by long-period gratings to that obtained from conventional short-period Bragg gratings. Figure 3.5 depicts the transmission and reflection spectra of a broadband source used to interrogate a long-period grating. The transmission spectrum consists of loss bands at a number of discrete wavelengths. The light lost at these wavelengths is not reflected back towards the source but is instead lost to the cladding modes. Hence, unlike its short period counterpart, the reflection spectrum of a long-period grating does not contain reflected light at the resonant wavelengths. Small Fresnel reflectors due to index discontinuities in the core may be measured using highly sensitive instruments [1]. The feature of reduced optical feedback in long-period gratings has been used to fabricate versatile devices in optical fiber communication systems [30].

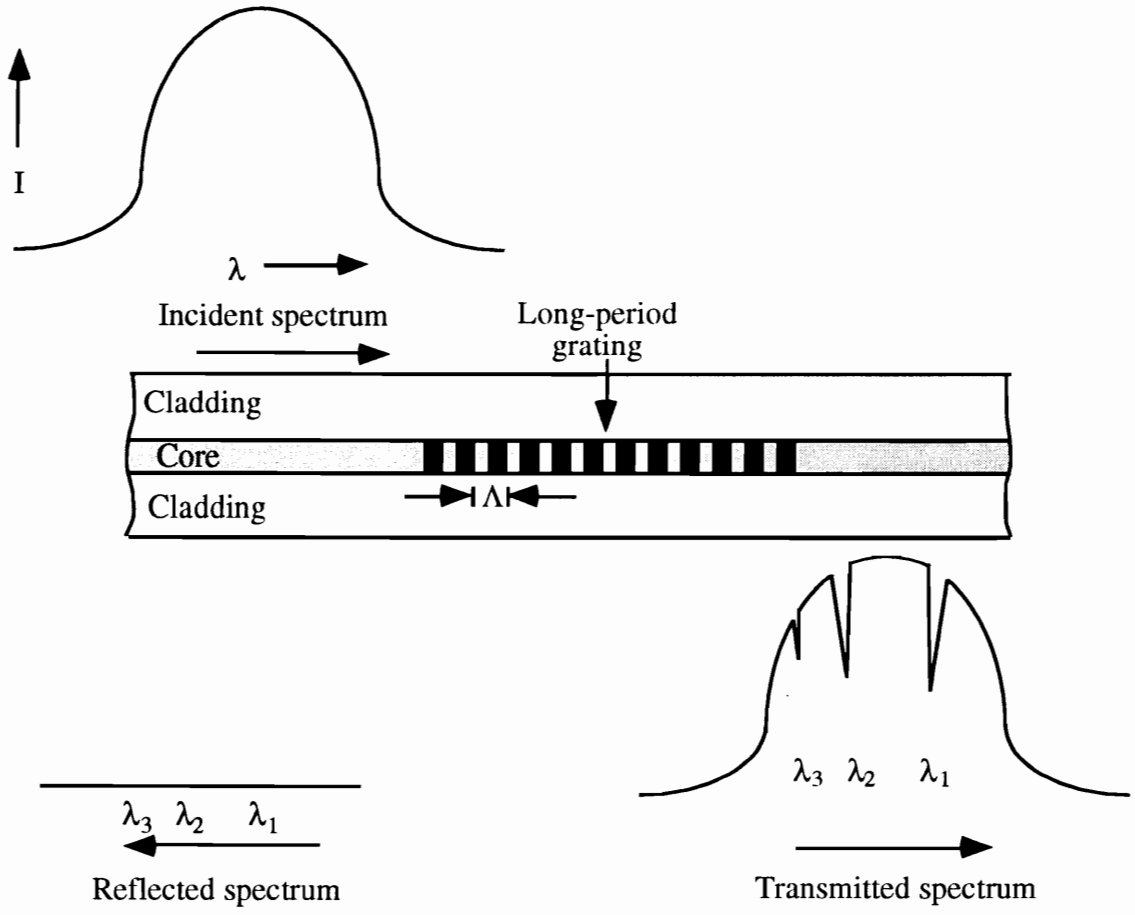

Figure 3.5. Spectral modulation provided by a typical long-period grating. λ_1, λ_2 and λ_3 are coupling wavelengths corresponding to three different cladding modes.

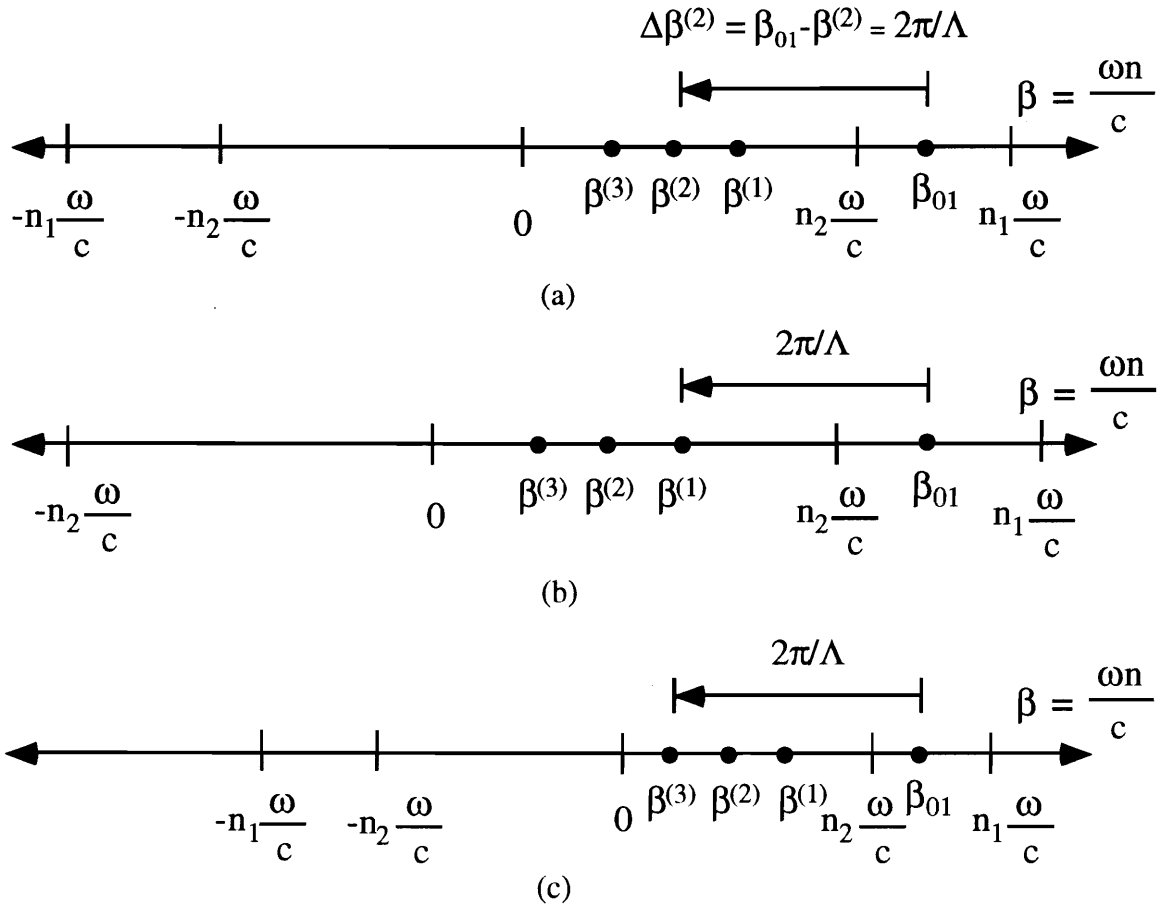

Figure 3.6. Coupling of LP_{01} guided mode to discrete, forward-propagating cladding modes, (a) coupling to $LP^{(2)}$ cladding mode, (b) stretching of ω-axis for coupling to $LP^{(1)}$ cladding mode, and (c) compressing of ω-axis for coupling to $LP^{(3)}$ cladding mode.

The relative location of the attenuation bands in a grating can be estimated using the β-plot of Figure 3.6 [1]. Consider a grating with periodicity Λ such that at a given wavelength (fixed ω), the coupling occurs to the cladding mode denoted by $LP^{(2)}$ (that is, $\beta_{01}-\beta^{(2)}=2\pi/\Lambda$), as shown in Figure 3.5 (a). For coupling to take place to the fundamental cladding mode ($LP^{(1)}$) at the same periodicity, we need to stretch or expand the ω-axis, so that the phase-matching vector now extends from β_{01} to $\beta^{(1)}$ (Figure 3.6 (b)). The increase in ω corresponds to a decrease in wavelength. We thus expect the $LP^{(1)}$ coupling resonance to occur at a wavelength lower than that for coupling to $LP^{(2)}$ cladding mode. The length of the phase-matching vector ($2\pi/\Lambda$) remains unchanged since the grating period is the same for coupling to various cladding modes. Similarly, for power coupling from the guided mode to $LP^{(3)}$ cladding mode, the ω-axis needs to be

compressed or contracted (Figure 3.6 (c)), and this results in coupling wavelength for this mode to occur at wavelengths longer than that for the $LP^{(2)}$ mode. Hence for the grating with the transmission spectrum in Figure 3.4, the phase-matching wavelength increases with the order of the resonance band. It is important to note here that the above analysis assumes that the differential propagation constant $\Delta\beta^{(m)}$ is a decreasing function of wavelength for all m. As will be shown in Section 2.2.1, the opposite is true for certain values of the grating periodicity. In such cases, the higher order cladding modes possess a shorter coupling wavelength than lower order cladding modes.

In Figure 3.3, the cladding modes have propagation constants that lie in the range, $\omega n_3/c<\beta^{(m)}<\omega n_2/c$, where n_3 is the refractive index of the ambient material ($n_2>n_3$). Using these two extreme values of $\beta^{(m)}$ one can calculate the range of coupling wavelength $\lambda^{(m)}$ for the cladding modes. For most applications the cladding around the grating is bare and hence $n_3=1$. The upper limit of the coupling wavelength that is found using $n_{cl}^{(m)}=1$ lies far off from the spectrum of optical sources and detectors and is hence not significant. On the other hand, the maximum value of the cladding mode propagation constant $\beta^{(m)}=\omega n_2/c$ yields a wavelength parameter termed λ_{cut} [1], that will be used to study the grating characteristics in Section 3.2.4.2. Figure 3.7 depicts the relative location of λ_{cut} with respect to the coupling wavelength $\lambda^{(2)}$ for the second order cladding mode. As expected, λ_{cut} is less than the coupling wavelength for all the cladding modes and can be shown to be an increasing function of the grating period Λ by using the β-plot of Figure 3.7.

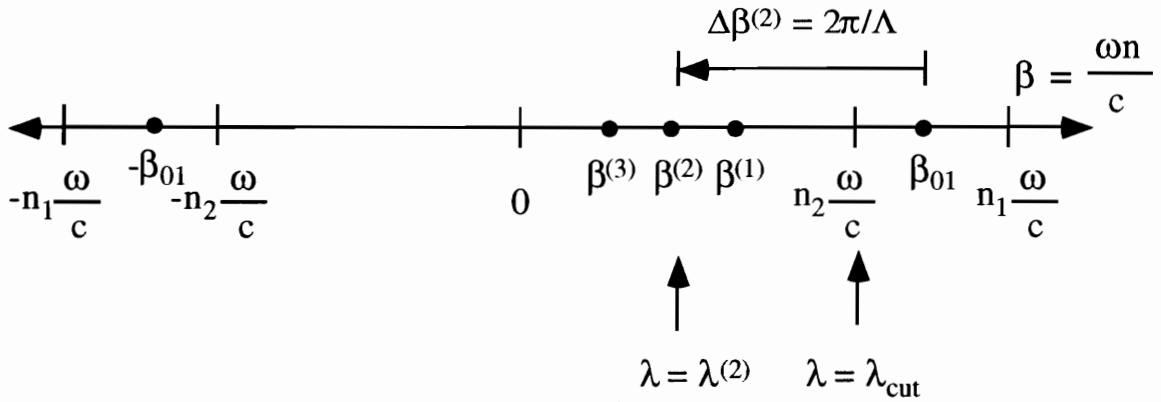

Figure 3.7. Depiction of the spectral location of λ_{cut} relative to wavelength $\lambda^{(2)}$ in a long-period grating ($\lambda_{cut}<\lambda^{(2)}$).

Using a similar β-plot for Bragg gratings it can be shown that the coupling to reverse-propagating cladding modes in those gratings occurs towards the lower wavelength side of the primary Bragg peak, as observed by Mizrahi and Sipe (Figure 3.2(a)) [86]. It can also be demonstrated that while coupling to forward-propagating guided modes (Section 2.5), the resonance bands due to transfer of power to cladding modes will be located at wavelengths larger than the primary guided mode phase-matching wavelength. Due to this fact Bilodeau *et al.* [27] detected coupling to cladding modes on the higher wavelength side of the LP_{01}/LP_{02} resonance band.

Another use of the β-plot is in determining the shift in the spectral location of the resonance bands in long-period gratings with variation in the core and cladding propagation constants. Figure 3.8 (a) illustrates the coupling of the fundamental guided mode to a cladding mode of order m, with propagation constant $\beta^{(m)}$. Keeping the value of the periodicity (Λ) constant, if the value of β_{01} is increased (Figure 3.8 (b)), the ω-axis has to be compressed to maintain the coupling between the LP_{01} guided mode and the $LP^{(m)}$ cladding modes. The compression of the ω-axis implies that an increase in the resonant wavelengths occurs when the value of β_{01} increases. As will be described in Section 3.2, the resonant wavelengths due to all these cladding modes are observed to shift to higher values during the fabrication of long-period gratings. This is because the increase in the refractive index of the core due to photosensitivity enhances the value of β_{01}. Increasing the value of the cladding mode propagation constant $\beta^{(m)}$ (Figure 3.8(c)), on the other hand, requires the stretching of the ω-axis and results in lowering of the resonant wavelengths. Thus the increase in the guided and cladding mode propagation constants results in shifts of opposite polarities in the phase-matching wavelengths which can be attributed to the minus sign between the effective indices of the two modes that appears in the phase-matching condition of Equation (3.2).

The effect of the change in the periodicity Λ of the refractive index modulation is also simple to predict using the β-plot. It can be shown that when the period is increased, the ω-axis has to be compressed to maintain coupling to the same cladding mode. Thus the coupling wavelength for a particular cladding mode is an increasing function of the grating period.

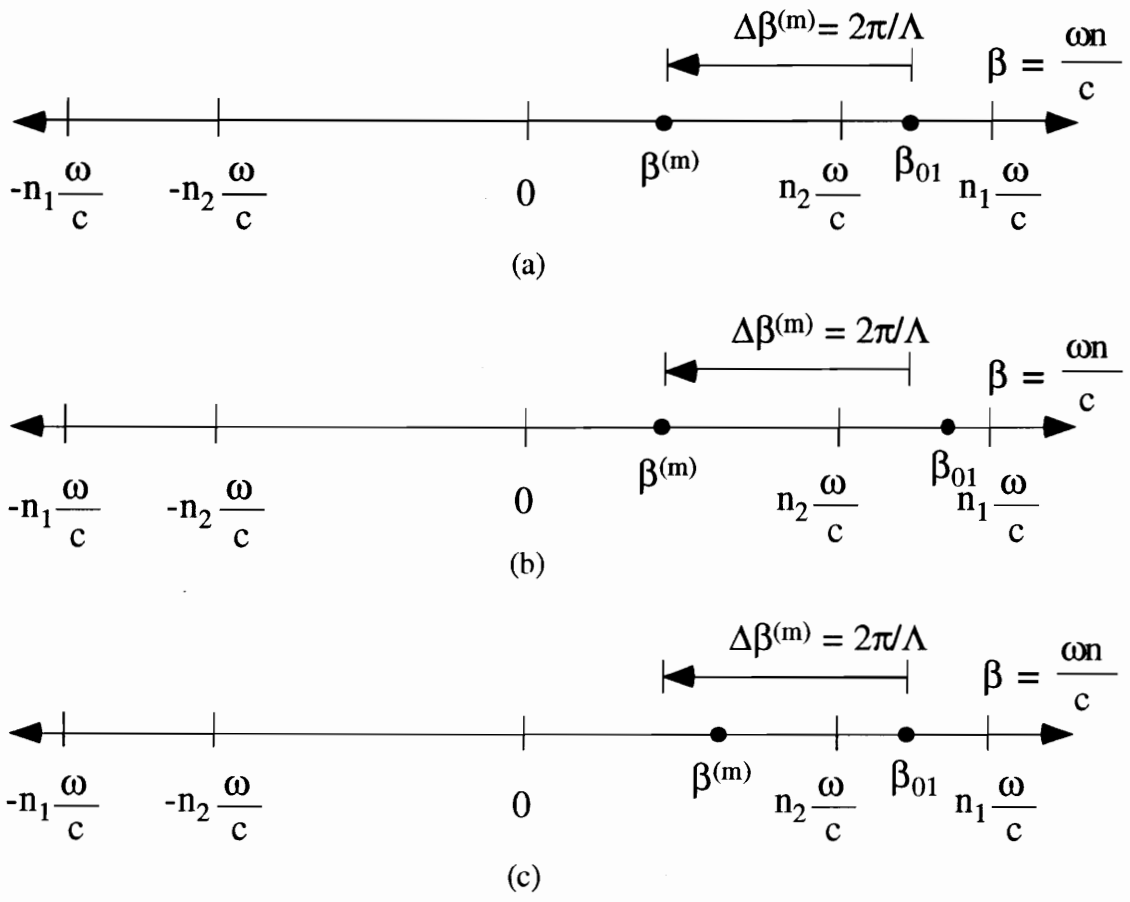

Figure 3.8. Effect of change in the propagation constants of the core and cladding modes. (a) Coupling of the fundamental guided mode (propagation constant β_{01}) to a cladding mode (propagation constant $\beta^{(m)}$), (b) increase in β_{01} and (c) increase in $\beta^{(m)}$.

It is important to reiterate here that the present analysis using β-plots assumes that the differential propagation constant $\Delta\beta^{(m)}$ decreases as the wavelength λ is increased. The assumption is not entirely true for all cladding modes and hence the effects of changing the effective indices or grating period are reversed when $\Delta\beta^{(m)}$ is an increasing function of the wavelength. The interesting dependence of grating properties on the slope of the $\Delta\beta^{(m)}$ versus λ will be explored further in Section 3.2.

In this section we discussed the principle of operation of long-period gratings that couple the fundamental guided mode to circularly-symmetric cladding modes. These gratings were shown to have a different spectral response as compared to their short-period counterparts. Using β-plots we determined the direction of spectral shift when the grating

period or the propagation constants are varied. It was assumed that the fiber is operating in the single-mode regime and hence only the fundamental guided mode was included in the analysis. Although a similar study can be done for other guided modes in few-mode or multi-mode fibers, we will restrict ourselves to long-period gratings operating in the single-mode region.

3.2 Analytical Modeling of Long-Period Gratings

In this section we carry out a comprehensive theoretical analysis of long-period gratings. We use the phase matching condition and waveguide analysis to predict the coupling wavelengths as functions of the grating period. The influence of small variations in the fiber parameters is investigated and expressions are obtained for grating parameters such as the coupling coefficient, the resonant wavelength separation and the grating bandwidth.

3.2.1 Fundamental Concepts

This sub-section introduces the reader to a few principal terms that will be used extensively during the modeling of long-period gratings. We use the basic concept of group index to explain the polarity of the slope of the coupling wavelength versus grating period curve. Equalization wavelength of two modes, first introduced in Section 2.5, is employed to characterize the coupling between the guided mode and a specific cladding mode. It is shown that the refractive index of a material is a function of the operating wavelength and Sellmeier coefficients are employed to calculate the spectral variation of the index of refraction for different germania doping concentrations in a fiber.

We start by rewriting the phase-matching condition of Equation (3.2) as,

$$\Lambda = \frac{\lambda}{\delta n_{eff}}, \tag{3.4}$$

where,

$$\delta n_{eff} = n_{eff} - n_{cl}, \tag{3.5}$$

and δn_{eff} is differential effective index at wavelength λ. To simplify the analysis we have dropped the ordinal m used previously to represent the order of the cladding mode. Since

the δn_{eff} is itself a function of the operating wavelength, differentiating both sides of Equation (3.4) with respect to wavelength yields,

$$\frac{d\Lambda}{d\lambda} = \frac{\delta n_{eff} - \lambda \left(\frac{d(\delta n_{eff})}{d\lambda} \right)}{(\delta n_{eff})^2} . \tag{3.6}$$

We now define the group index of the guided (n_g) and cladding ($n_{g,cl}$) modes as [87],

$$n_g = n_{eff} - \lambda \frac{dn_{eff}}{d\lambda} , \tag{3.7}$$

and,

$$n_{g,cl} = n_{cl} - \lambda \frac{dn_{cl}}{d\lambda} , \tag{3.8}$$

respectively. Using Equations (3.5), (3.7) and (3.8) in Equation (3.6), we obtain an expression for the slope of the coupling wavelength versus grating period curve [34],

$$\frac{d\lambda}{d\Lambda} = \frac{(\delta n_{eff})^2}{\delta n_g} , \tag{3.9}$$

where,

$$\delta n_g = n_g - n_{g,cl} . \tag{3.10}$$

Equation (3.9) reveals that the slope of the coupling wavelength versus period curve is dependent not only on the differential effective index δn_{eff}, but also on the differential group index δn_g between the guided and cladding modes. We term the wavelength versus period curve as the characteristic curve of the grating, since its shape determines the fundamental behavior of the grating. Since δn_{eff} and δn_g are strong functions of the parameters of the optical fiber in which the grating is fabricated, the characteristic curves can be expected to be dependent on the properties of the host fiber. The characteristic curves for different optical fibers will be obtained in Section 3.2.3. It is important to point out here that the polarity of the slope of the characteristic curve at a particular coupling wavelength is the same as the polarity of the differential group index δn_g at that wavelength. For most grating applications, the period is so chosen that the group index of the guided mode is larger than that of the cladding mode at the phase-matching

wavelength ($\delta n_g > 0$). Thus the local slope of the characteristic equation is typically positive. It will be shown in Section 3.2.2.2 that the differential group index between the guided mode and certain cladding modes can in fact be less than zero and this causes the polarity of the slope of the characteristic curves for the corresponding cladding modes to be negative. The operation of the grating at the negative slope region of the characteristic curve will be shown to have interesting applications to optical fiber sensing systems in Chapter 4.

The differential group index is a strong function of the wavelength, and as stated earlier, may be positive or negative depending on the order of the cladding mode and the operating wavelength. Since $\delta n_g(\lambda)$ is continuous with wavelength we deduce that there might exist a wavelength λ_0 in the optical spectrum where $\delta n_g(\lambda_0) = 0$. The wavelength at which the group indices of the guided and cladding modes are identical ($n_g = n_{g,cl} = n_0$) is termed the equalization wavelength of the modes [82]. At this value of wavelength, the two modes travel with the same group velocity $v_g = c/n_0$, where c is the velocity of light in vacuum. We can also represent the equalization wavelength λ_0 in terms of the differential propagation constant $\Delta\beta$, as was done in Section 2.5, where we showed that at the wavelength λ_0, the slope of the $\Delta\beta$ versus λ curve is zero. The differential propagation constant is related to the grating period through the phase-matching condition and it can be shown that,

$$\frac{d(\Delta\beta)}{d\lambda} = -\frac{2\pi}{\Lambda^2}\frac{d\Lambda}{d\lambda}. \tag{3.11}$$

Hence at the equalization wavelength, the slope ($d\lambda/d\Lambda$) of the characteristic curve is expected to be infinite, which follows from Equation (3.9) also (with $\delta n_g = 0$). We hence conclude that the characteristic curves of long-period gratings may possess slopes of both polarities depending on the location of the coupling wavelength with respect to equalization wavelength of the two modes involved in coupling.

We observe from Figure 2.11 that for a short-period Bragg grating the slope of the characteristic curve is positive and constant for all values of the coupling wavelength λ_B. For a long period grating, the magnitude and polarity of the slope is a function of the phase-matching wavelength and hence depends on the grating periodicity. This is a very

important distinguishing feature between the two types of gratings and results in significant differences in their characteristics.

In the next section we will carry out detailed waveguide analysis to determine the spectral dependence of the effective indices of the guided and cladding modes. Since these parameters are functions of the core and cladding refractive indices, it becomes important to include the material variation of the fiber indices in the analysis. We develop a simple technique to predict the change in the core and cladding indices of refraction with wavelength if the germania concentration in the core is known.

Table I. Sellmeier parameters for bulk glass samples of different compositions [62].

Composition	A_1	A_2	A_3	λ_1 (μm)	λ_2 (μm)	λ_3 (μm)
Quenched SiO_2	0.696750	0.408218	0.890815	0.069066	0.115662	9.900559
13.5% GeO_2:86.5 SiO_2	0.711040	0.451885	0.704048	0.064270	0.129408	9.425478

It is a well known fact that the material dispersion in optical fibers is caused by the variation in the refractive index of the host glass over the spectrum of the optical source [62]. Many researchers have carried out extensive analysis of this effect in order to come up with suitable materials that would provide zero total dispersion at desired wavelengths [88,89]. The most common method of approximating the index $n(\lambda)$ as a function of wavelength λ for a particular material uses the Sellmeier equation [62],

$$n^2(\lambda) = 1 + \sum_{i=1}^{M} \frac{A_i \lambda^2}{\lambda^2 - \lambda_i^2}, \tag{3.12}$$

where A_i and λ_i are material dependent parameters that are tabulated in technical literature [62]. For most practical applications only the first three terms (M=3) are necessary to obtain an accuracy of about 10^{-5} in refractive index calculations [62]. Table I lists the first three Sellmeier parameters for a quenched sample of silica with 13.5% GeO_2 and 86.5 SiO_2 [62]. The cladding in a majority of standard optical fibers is made of quenched silica while the core typically consists of quenched silica with an appropriate

doping of GeO_2 [62]. Our discussion will be limited to fibers with germanosilicate cores and silica cladding, although it is simple to modify the analysis for other materials.

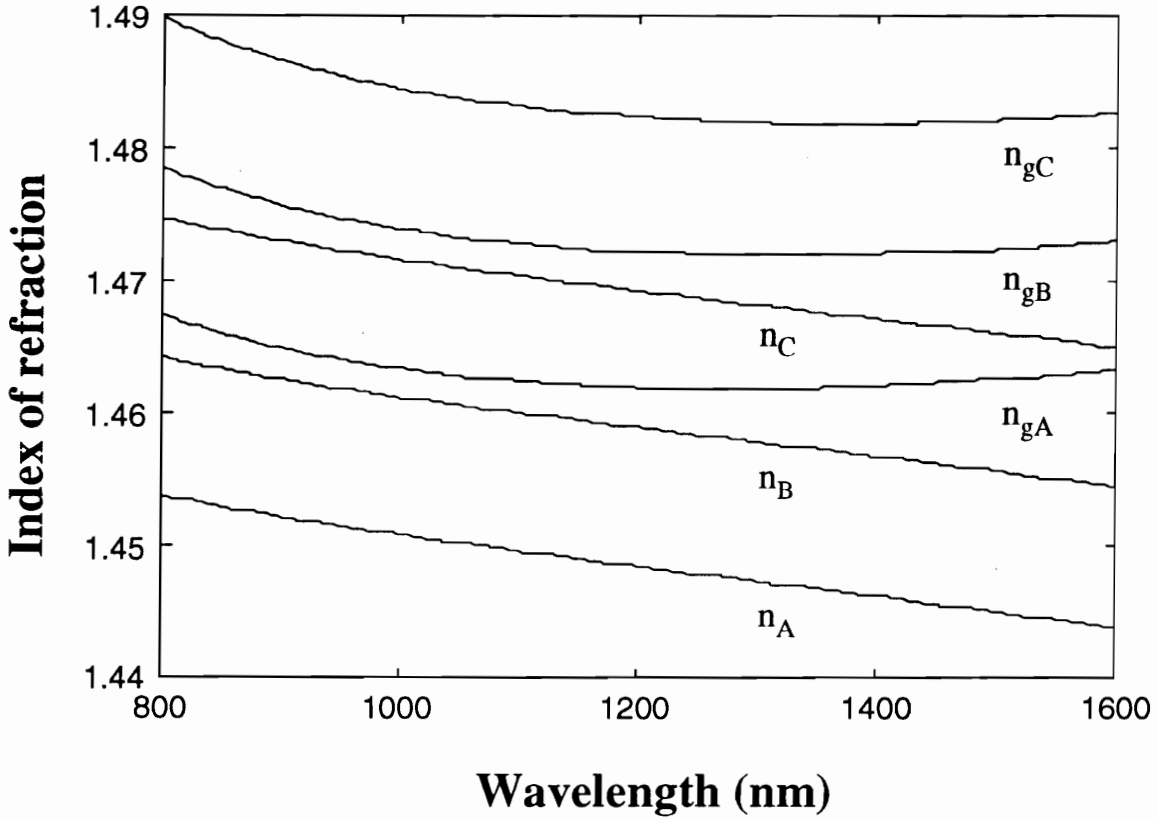

Figure 3.9. Variation of the refractive indices (n_A, n_B and n_C) and the group indices (n_{gA}, n_{gB} and n_{gC}) in bulk samples of three different materials as functions of wavelength. A is quenched SiO_2, B is 13.5% GeO_2:86.5 SiO_2 and C is 6.75% GeO_2:93.25% SiO_2.

The values of the Sellmeier parameters have been measured for only a few specific GeO_2 concentrations and hence the index variation for intermediate doping concentrations can be calculated by interpolation of the given parameters [90]. For example the Sellmeier parameters for a quenched sample of 6.75% GeO_2 and 93.25% SiO_2 can be approximated by averaging the values given in Table I. Figure 3.9 depicts the variation in the index of refraction $n(\lambda)$ of three different types of materials. The group index $n_g(\lambda)$ of the material can then be obtained from Equation (3.12) using [87],

$$n_g(\lambda) = n(\lambda) - \lambda \frac{dn(\lambda)}{d\lambda}, \tag{3.13}$$

and is also shown in Figure 3.9 for the three materials. The group indices are found to initially decrease with wavelength, attain a minimum value and then increase towards higher wavelength. The wavelength at which the slope of the group index versus the wavelength curve $dn_g(\lambda)/d\lambda$ is zero, is termed the zero material dispersion wavelength for the bulk material [53,72]. It can be seen in Figure 3.9 that this value of wavelength increases with the GeO_2 concentration in glass. In an actual fiber, the presence of the cladding causes the waveguide effect to alter the wavelength at which the total dispersion is zero [53,72]. In the following subsection we will use the interpolation method to calculate the index variation with wavelength for fibers with different GeO_2 concentrations.

3.2.2 Waveguide Analysis

In this section we develop techniques to determine the effective indices of the fundamental guided mode and the circularly-symmetric cladding modes for different fibers. This is the first step to the actual analytical modeling of long-period gratings. The second step involves using the phase-matching condition to obtain the characteristic curves and will be implemented in Section 3.2.3.

Although long-period gratings were fabricated in many different optical fibers, we will limit our discussion to only three types of fibers due to the availability of the important fiber parameters [61,65] from the manufacturer (Corning Incorporated). The three fibers that will be used in the analysis have step-index, matched clad profiles with a pure silica cladding and germania-doped core. All the fibers are manufactured using Corning's outside vapor deposition (OVD) technique and possess mechanically strippable dual-layer acrylate coating of appropriate thickness. The parameters of the three fibers, termed SMF-28 [65], Flexcor 1060 nm [61] and Flexcor 780 nm [61] are listed in Table II. The values tabulated are typical values listed in the manufacturer's product information sheet for the respective optical fibers.

During the analysis of cladding modes (Section 3.2.2.2), the refractive index of the ambient medium will be shown to have a significant impact on their effective indices. Typically the bare cladding in the region containing the grating is surrounded by air. Although the refractive index of air is also a function of the operating wavelength [91], its

variation in the region 700 nm to 1700 nm can be considered to have a negligible influence on the grating properties. Thus the analysis of long-period gratings will ignore the spectral variation of index of refraction of air.

Table II. Typical parameters for fibers used in long-period grating model [65,61].

Type of fiber	Optimum wavelength λ_{op} (μm)	Core radius a (μm)	Core delta Δ (%)	Numerical aperture NA	Cutoff wavelength λ_{cutoff} (nm)
SMF-28	1310	4.15	0.36	0.13	<1260
Flexcor 1060	1060	2.5	0.45	0.14	920 (±50)
Flexcor 780	780	2.0	0.45	0.14	720 (±50)

Type of fiber	Mode field diameter at λ_{op} (μm)	Attenuation at λ_{op} α (dB/km)	Cladding diameter 2b (μm)	Coating diameter 2c (μm)	Tensile proof stress F (kpsi)
SMF-28	9.3 (±0.5)	≤0.4	125 (±1)	245 (±10)	100
Flexcor 1060	6.2 (±0.5)	≤1.5	125 (±2)	250 (±15)	100
Flexcor 780	4.6 (±0.5)	≤3.0	125 (±2)	250 (±15)	100

3.2.2.1 Fundamental Guided Mode Analysis

It was stated earlier that the behavior of long-period gratings will only be characterized for fibers operating in the single-mode region. In this section we obtain the variations of the effective index n_{eff} and group index n_g of the fundamental LP_{01} guided mode as functions of wavelength. Since all three fibers have step-index refractive index profiles, we will consider the fiber geometry shown in Figure 3.10. The amplitude of the guided mode decays rapidly as a function of increasing penetration into the cladding and causes it to possess negligible value at the outer cladding boundary. Thus for fibers that have a significantly thick claddings, the analysis becomes simpler if the cladding is assumed to be infinite. In Figure 3.10, a is the core radius, n_1 is the core index and n_2 is the cladding

index. As discussed in the previous section, both n_1 and n_2 are functions of the operating wavelength λ. The normalized frequency or the V-number of the fiber is given by [53],

$$V = \frac{2\pi a}{\lambda}\sqrt{n_1^2 - n_2^2}\ . \tag{3.14}$$

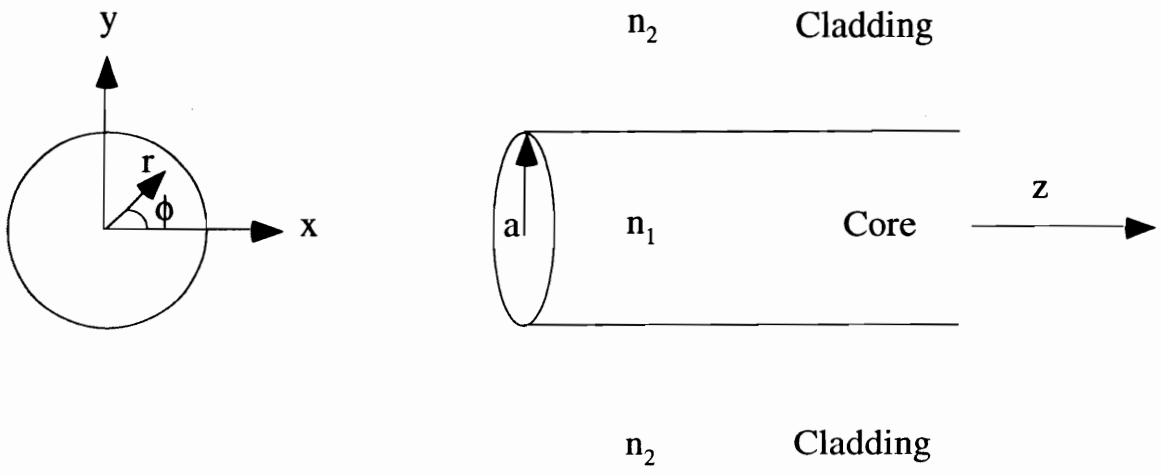

Figure 3.10. Fiber geometry used in the analysis of the fundamental guided mode. The core has a radius a, while the cladding is assumed to extend to infinity.

The normalized index difference Δ between the core and cladding is defined as [53],

$$\Delta = \frac{n_1 - n_2}{n_1}, \tag{3.15}$$

and depends on the germania concentration in the core. Since the cladding in the three fibers under investigation is made from quenched silica, we can calculate the material dispersion for both the core and the cladding if the normalized index difference Δ for the fiber is known. For this process, the interpolation of the Sellmeier parameters [62,90], outlined in the preceding section, is employed. The commonly used waveguide parameters u and w are given by [9],

$$u = \sqrt{k_1^2 - \beta_{01}^2}\ , \tag{3.16}$$

and,

$$w = \sqrt{\beta_{01}^2 - k_2^2}\ , \tag{3.17}$$

where $k_1=2\pi n_1/\lambda$, $k_2=2\pi n_2/\lambda$, and $\beta_{01}=2\pi n_{eff}/\lambda$ is the wavelength-dependent propagation constant of the guided mode.

The characteristic equation for a LP_{0m} guided mode propagating in a weakly-guiding fiber ($n_1 \approx n_2$) with the profile shown in Figure 3.10 is given by [53],

$$\frac{1}{u}\frac{J_1(ua)}{J_0(ua)} = \frac{1}{w}\frac{K_1(wa)}{K_0(wa)}\ , \tag{3.18}$$

where m is the radial order of the mode. In Equation (3.18), J_p and K_p are Bessel and modified Bessel functions of order p, respectively. The characteristic equation was solved numerically in MATLAB for its first root (m=1) using the Newton-Raphson method [92]. The solution was sought till the effective index n_{eff} converged to six decimal places to reduce errors in the final characterization curves.

The complete process of calculating the effective index as a function of the operating wavelength can be outlined as follows. Given the normalized index difference Δ of the fiber, the germania concentration in the core was approximated. Using linear interpolation of the Sellmeier coefficients [62] in Table I, the spectral variation of n_1 and n_2 was obtained at a number N_p of discrete wavelengths. The characteristic equation was then solved at these N_p points to determine the effective index at each wavelength value. A polynomial curve fit of order N_o was used to obtain a continuous variation of the effective index of the guided mode in the wavelength range of interest. The characteristic equation was solved for only a discrete number of wavelengths to reduce the time of computation. As will be shown later in this section, the curve-fitting method was found to yield results with a high degree of accuracy. Typical values of N_p used for the above analysis varied from 20 to 50 over a 500 nm wavelength range, while the polynomial curve fit was of order 2 or 3.

We now present numerical solutions to the characteristic equations for the Corning SMF-28 and Flexcor 1060 fibers. Figure 3.11 shows the spectral variation in the effective index n_{eff} and the group index n_g for the SMF-28 fiber using the typical values of parameters listed in Table II. Also shown are the core and the cladding material indices

as functions of wavelength. The results in Figure 3.11 are for an unperturbed fiber, that is, one with no refractive index modulation of the core. The group indices at 1310 nm and 1550 nm were found to be 1.4676 and 1.4682, respectively. The corresponding values specified in the Corning product literature for SMF-28 fiber are 1.4675 and 1.4681 [65]. The close match between the calculated and actual values of group indices reveals the accuracy of polynomial curve fitting method used for the analysis. Figure 3.12 shows the spectral variation of the same parameters as in Figure 3.11 but for Flexcor 1060 fiber.

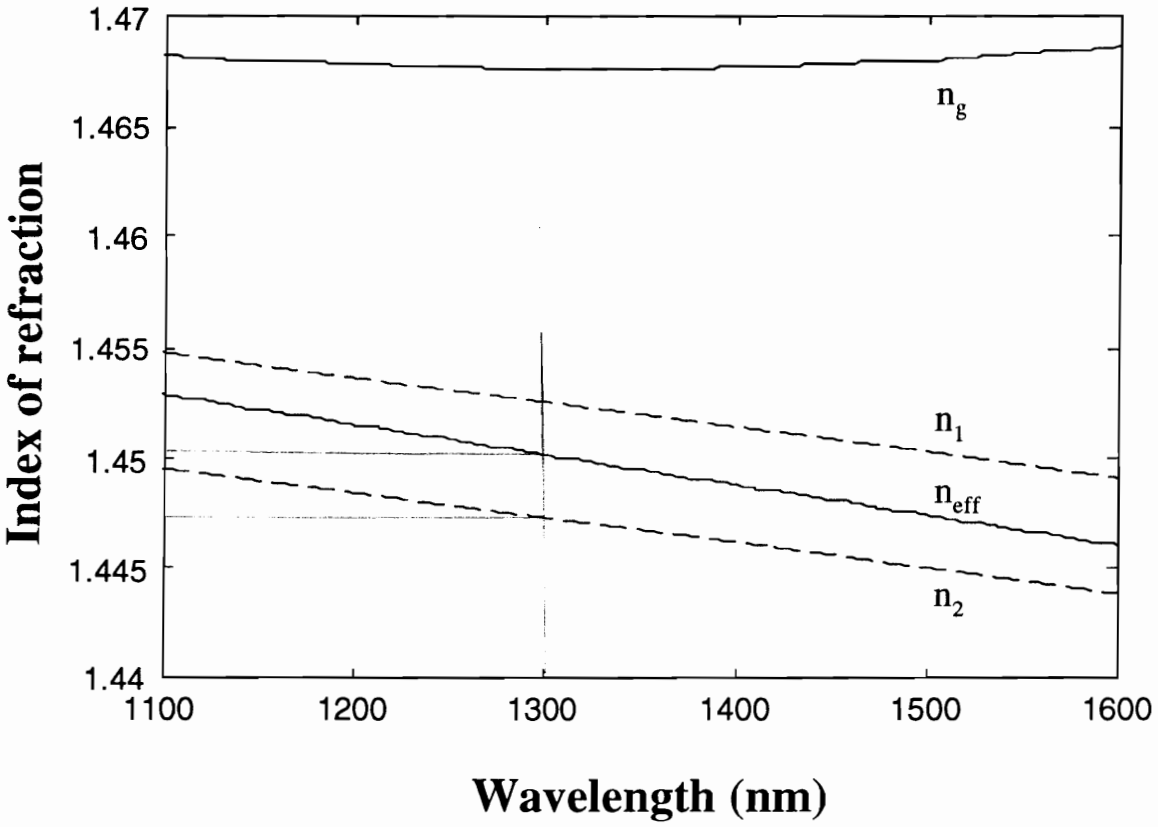

Figure 3.11. Variation of the effective index n_{eff} and group index n_g of the fundamental LP_{01} guided mode with wavelength for Corning SMF-28 fiber. The effective index is calculated by solving the characteristic equation for N_p=51 and then using a third order polynomial curve fit to obtain a continuous variation. Also shown are the spectral dependence of the core (n_1) and the cladding (n_2) refractive indices.

We now discuss the effect of small deviations in the fiber parameters from the typical values specified by the manufacturer [61,65]. These variations may be caused during fiber fabrication due to different mechanical, chemical or thermal conditions and may

result in the parameters departing from their standard values in different spools of fibers, or even as functions of the fiber length along the same spool. It is critical to see how these minute variations alter the modal effective index and the characterization curves of long-period gratings. Figure 3.13 shows the effect of reducing the core radius by 1% from the typical value of 4.15 μm. The effective index is found to decrease by about 3×10^{-5} over the wavelength range of interest. Also shown is the influence of increasing the normalized index difference Δ by 1% of its standard value to 0.3636%. The effective index increases by approximately 4×10^{-5} indicating that n_{eff} is an increasing function of the core diameter and the index difference. The process of writing a grating in the fiber core increases the index difference and causes the effective index of the guided mode to have a higher value than that for an unperturbed fiber. Although the change in effective index appears to be small, the resulting variations in the spectral response of long-period gratings will be shown to be significant.

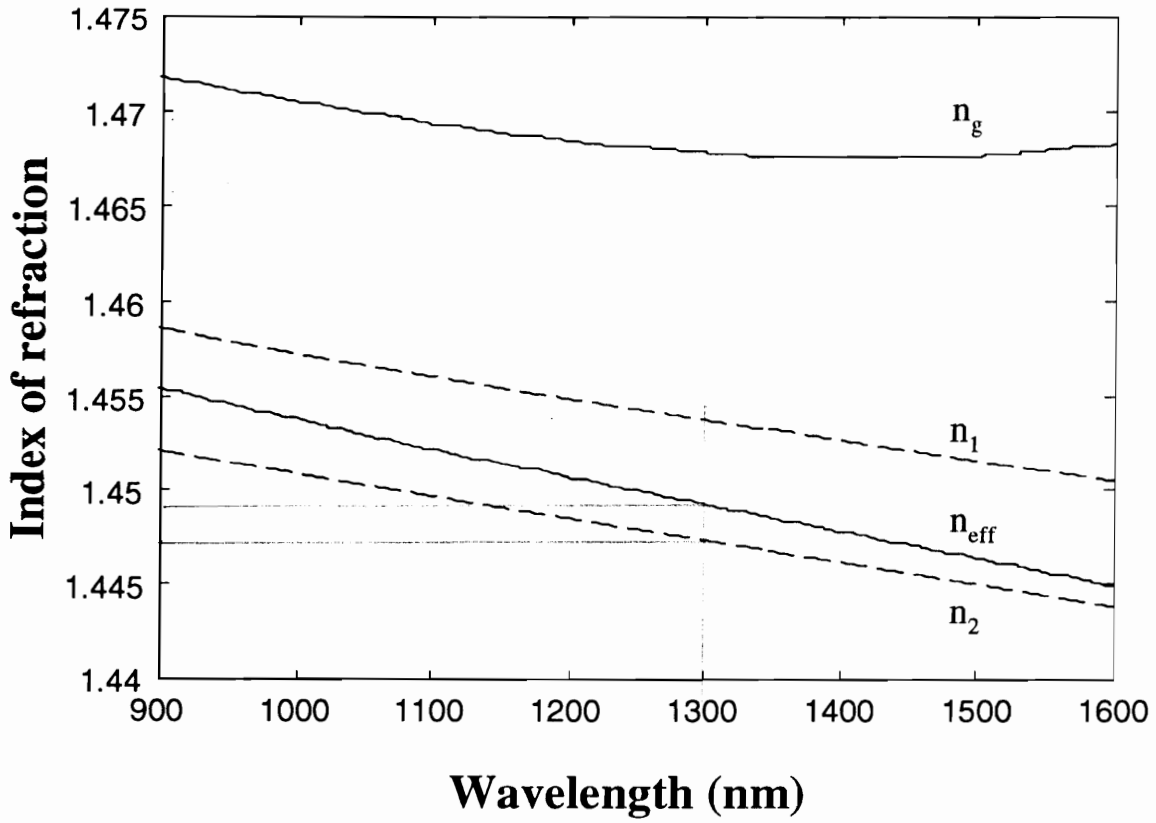

Figure 3.12. Variation of the effective index n_{eff} and group index n_g of the fundamental LP_{01} guided mode with wavelength for Corning Flexcor 1060 fiber for N_p=51 and N_o=3. Note the difference in the x and y axes from those in Figure 3.11.

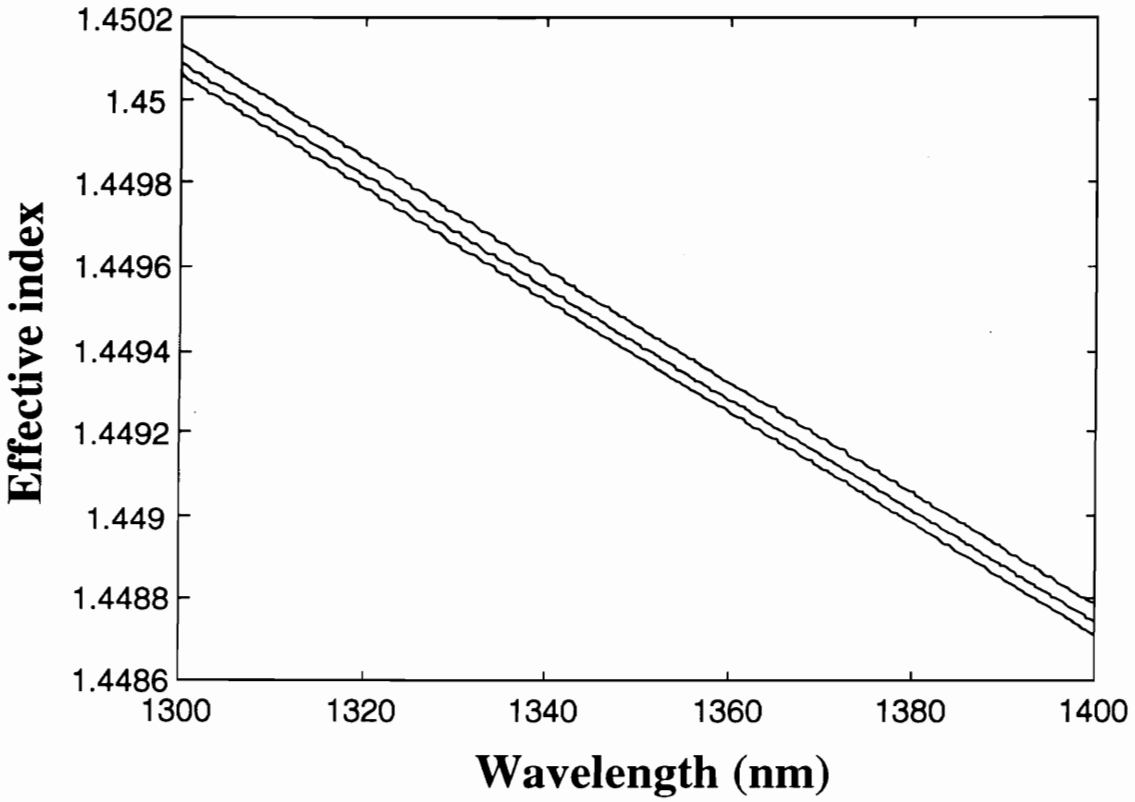

Figure 3.13. Variation of the effective index n_{eff} of the fundamental guided mode with wavelength for Corning SMF-28 fiber using typical parameters in Table I (middle), with core radius reduced to a=4.11 μm (bottom) and with Δ=0.3636% (top).

The electric field of the fundamental guided mode $E_{01}(r)$ is given by the expression [53],

$$E_{01}(r) = A\, J_0(ur)\, e^{j(\omega t - \beta_{01} z)} \qquad \text{for } r<a, \tag{3.19a}$$

$$E_{01}(r) = B\, K_0(wr)\, e^{j(\omega t - \beta_{01} z)} \qquad \text{for } r>a, \tag{3.19b}$$

where u and w are defined in Equations (3.16) and (3.17) and J_0 and K_0 are the zeroth order Bessel and modified Bessel functions of the first kind. The modal spread is hence a function of the operating wavelength and the power variation ($|E_{01}(r)|^2$) is illustrated in Figure 3.14 at λ=1310 nm and at λ=1550 nm for Corning SMF-28 fiber. As expected, the mode confinement within the core reduces as the wavelength is increased. Also the modal amplitude is almost negligible at the outer cladding boundary, lending credibility to the approximation of infinite cladding for the guided mode analysis. The modal field

will be employed in evaluating an expression for the coupling coefficient of long-period gratings in Section 3.2.4.

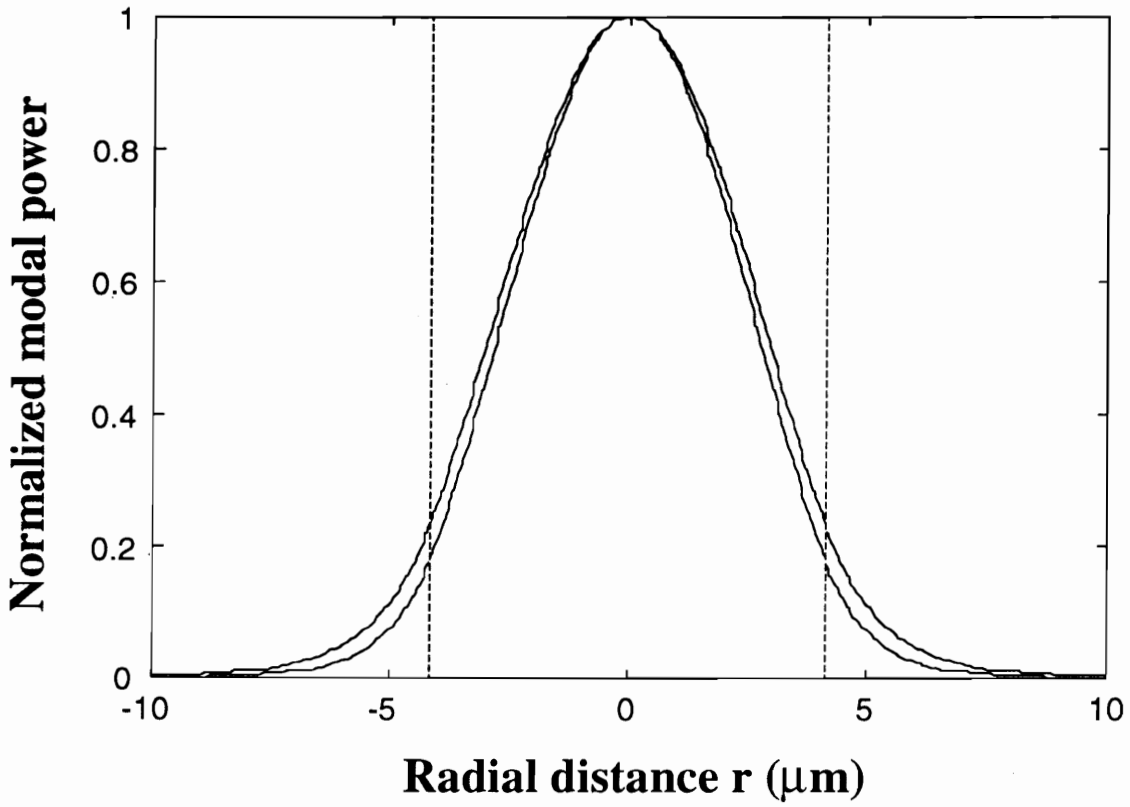

Figure 3.14. Variation of the normalized power of the fundamental guided mode as a function of radial distance from the fiber axis (r=0) at 1310 nm (inner curve) and 1550 nm (outer curve) for SMF-28 fiber. The broken vertical lines represent the core-cladding interface (r=4.15 μm). The power decays rapidly in the cladding and has negligible magnitude at the outer cladding boundary (r=62.5 μm).

In this section we have discussed the analysis of the fundamental guided mode in optical fibers assuming the cladding extends to infinity. The variation of the effective and group index with wavelength was obtained for different types of fibers. It was observed that deviations of about 1% in the typical core radius and normalized index values specified by the manufacturer result in average changes of the order of 10^{-5} in the calculated effective index.

3.2.2.2 Analysis of Cladding Modes

The major step in the theoretical investigation of long-period gratings is the calculation of the effective indices of the circularly-symmetric, forward-propagating cladding modes. In this section the spectral variations of the effective indices, group indices and modal fields are obtained for cladding modes of different orders.

The evaluation of cladding modes uses the approximation that the fiber can be considered as a multi-mode step-index structure ignoring the presence of core, an approach that has commonly been used by researchers such as Marcuse [57] and Vengsarkar *et al.* [1] to simplify cladding mode analysis. For a weakly-guiding fiber with closely matched values of the core and the cladding indices, this assumption is shown to yield fair approximations of the cladding mode propagation constants. Thus the fiber geometry to be analyzed reduces to that for the guided mode in Figure 3.10, except that the core radius a is replaced by the cladding radius b, and the cladding index n_2 substitutes the core index n_1. Also, if n_3 is the index of the medium surrounding the fiber cladding, n_2 in Figure 3.10 is replaced with n_3. The eigenvalue equation for the $LP_{0,m}$ cladding mode can then be approximated by that of a uniform dielectric cylinder surrounded by an infinite medium [53],

$$\left(\frac{J_1'\left(u_{cl}^{(m)}b\right)}{u_{cl}^{(m)}\,J_1\left(u_{cl}^{(m)}b\right)}+\frac{K_1'\left(w_{cl}^{(m)}b\right)}{w_{cl}^{(m)}\,K_1\left(w_{cl}^{(m)}b\right)}\right)\left(k_1^2\frac{J_1'\left(u_{cl}^{(m)}b\right)}{u_{cl}^{(m)}\,J_1\left(u_{cl}^{(m)}b\right)}+k_2^2\frac{K_1'\left(w_{cl}^{(m)}b\right)}{w_{cl}^{(m)}\,K_1\left(w_{cl}^{(m)}b\right)}\right) = \left(\frac{\beta_{cl}^{(m)}}{b}\right)^2\left(\frac{1}{\left[\left(u_{cl}^{(m)}\right)^2+\left(w_{cl}^{(m)}\right)^2\right]}\right)^2, \tag{3.20}$$

where primes denote differentiation with respect to the argument and $u_{cl}^{(m)}$ and $w_{cl}^{(m)}$ are the waveguide parameters for the cladding [53],

$$u_{cl}^{(m)} = \sqrt{k_2^2 - \left(\beta^{(m)}\right)^2}\,, \tag{3.21}$$

and,

$$w_{cl}^{(m)} = \sqrt{\left(\beta^{(m)}\right)^2 - k_3^2}\,. \tag{3.22}$$

In Equations (3.20), (3.21) and (3.22), $\beta^{(m)}=2\pi n_{cl}^{(m)}/\lambda$ is the propagation constant of the $LP_{0,m}$ cladding mode with effective index $n_{cl}^{(m)}$, $k_2=2\pi n_2/\lambda$ and $k_3=2\pi n_3/\lambda$. For most applications, the region containing the long-period grating is unjacketed ($n_3=1$).

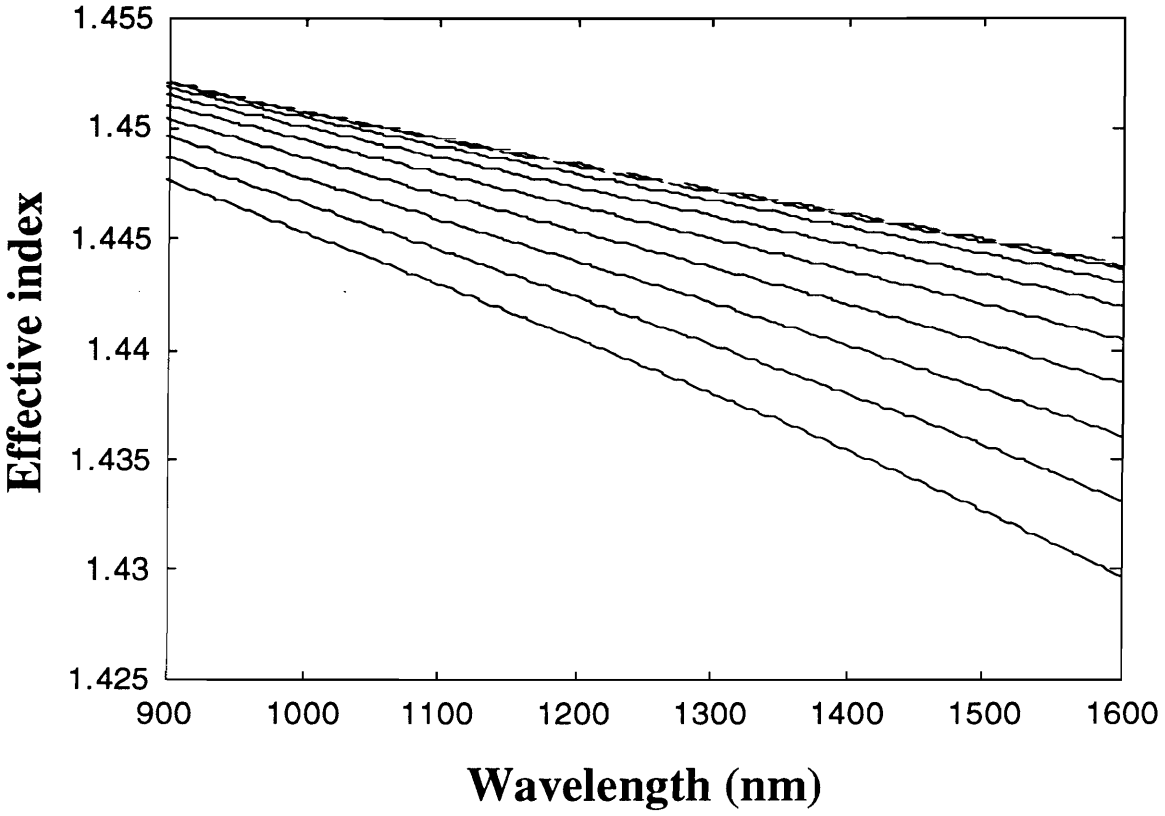

Figure 3.15. Spectral variation of the effective index $n_{cl}^{(m)}$ of $LP_{0,m}$ cladding modes (m=2 through 16 in steps of 2) in optical fibers with quenched silica cladding and b=62.5 μm. The ambient medium is assumed to be air ($n_3=1$). The dashed line represents the refractive index of the cladding.

Equation (3.20) was written as a quadratic equation in $J_1'(ua)/uJ_1(ua)$ and the m^{th} solution corresponding to the negative sign was sought for the $LP_{0,m}$ cladding mode. The equation was solved for n_{cl} at a finite number of wavelengths using the Newton-Raphson method [92] for a convergence till the sixth place of decimal. The spectral dependence of the cladding refractive index n_2 was included in the analysis. The computation time was reduced by assuming an initial value of the effective index given by Marcuse [57],

$$n_{cl}^{(m)} = \sqrt{n_2^2 - \left(\frac{\lambda}{2\pi}\right)^2 \left(\frac{j_m}{b}\right)^2}\ , \tag{3.23}$$

where j_m are the roots of the Bessel function of order zero ($J_0(j_m)=0$) [67]. Comparing Equation (3.23) with Equation (3.21), we can approximate the transverse component of the propagation constant, $u_{cl}^{(m)} \equiv j_m/b$. This approximation will be used to calculate the separation between the resonance bands in Section 3.2.4.2. A polynomial curve fit was used to determine the continuous variation of $n_{cl}^{(m)}$ with wavelength and the results are plotted in Figure 3.15 for even order modes from m=2 to m=16 (top to bottom) with n_3=1. Since the three fibers considered for the analysis have a pure silica cladding and radius b=62.5 μm, the spectral variation of the effective indices of the cladding modes is the same for these fibers. An exact analysis will reveal variations due to the distinct core radii and indices in different fibers. As expected, for a fixed wavelength, the effective index is a decreasing function of the order of the cladding mode m.

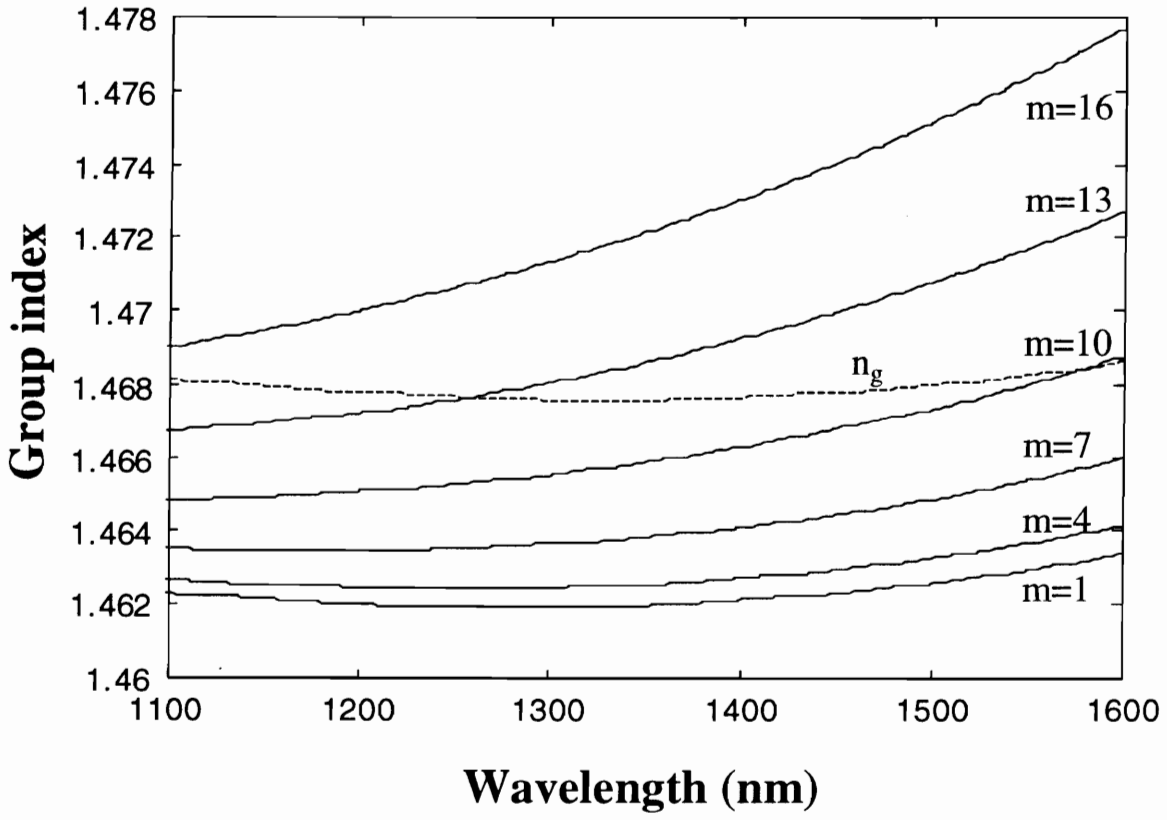

Figure 3.16. Variation of the group indices of a few $LP_{0,m}$ cladding modes and the fundamental guided mode (dashed line) for an unperturbed SMF-28 fiber with n_3=1.

In order to understand the basic mechanism of long-period gratings it is important to obtain the relative values of the group indices of various cladding modes (Equation (3.8)) with respect to the group index of the guided mode (Equation (3.7)) of the host fiber. Figure 3.16 show the spectral variation in $n_{g,cl}^{(m)}$ for cladding modes of order m=1,4,7,10,13 and 16. Only a few cladding modes are depicted to keep the representation simple. The dashed curve is the group index n_g of the fundamental guided mode for the SMF-28 fiber and is calculated using the procedure outlined in the previous section. The group index of the cladding modes is observed to increase with the modal order for a fixed wavelength and can be attributed to the increased slope of the effective index versus wavelength curve for higher order modes (Figure 3.15). In the wavelength region of interest (1100-1600 nm), the group index of the guided mode is greater than that of the cladding modes with m less than 10, or $n_g > n_{g,cl}^{(m)}$ for m<10. On the other hand, $n_g < n_{g,cl}^{(m)}$ for m>15 at all the wavelengths. But for cladding modes $LP_{0,10}$ through $LP_{0,15}$ there exists one wavelength value at which the guided mode group index is equal to that of a cladding mode, or $n_g = n_{g,cl}^{(m)}$.

From the discussion in Section 3.2.1 we had concluded that the slope of the characteristic curves in a long-period grating is the same as the polarity of the differential group index, $\delta n_g = n_g - n_{g,cl}^{(m)}$, between the guided and cladding modes. At the equalization wavelength, where $\delta n_g = 0$, the slope of the characteristic curve for the corresponding cladding mode becomes infinite (Equation (3.9)). At other wavelengths, the slope can be positive or negative depending on the polarity of the differential group index between the guided and cladding modes. For example, the characteristic curve for the $LP_{0,13}$ mode will have a positive slope for wavelengths greater than 1259.8 nm and a negative slope for wavelengths less than this value (Figure (3.16)). On the contrary, modes with m<10 will always have positive slopes and the those with m>15 will have negative slopes in the region 1100-1600 nm. It is important to note that the curves in Figure 3.16 are for an unperturbed fiber. An increase in the refractive index of the core during grating formation enhances the effective index of the guided mode. This process modulates the guided mode group index and changes the nature of the characteristic curves. Moreover, variations in the cladding mode effective indices, such as those induced by changing the index of the ambient material and the cladding diameter also serve to alter the characteristic curves of the corresponding resonance bands.

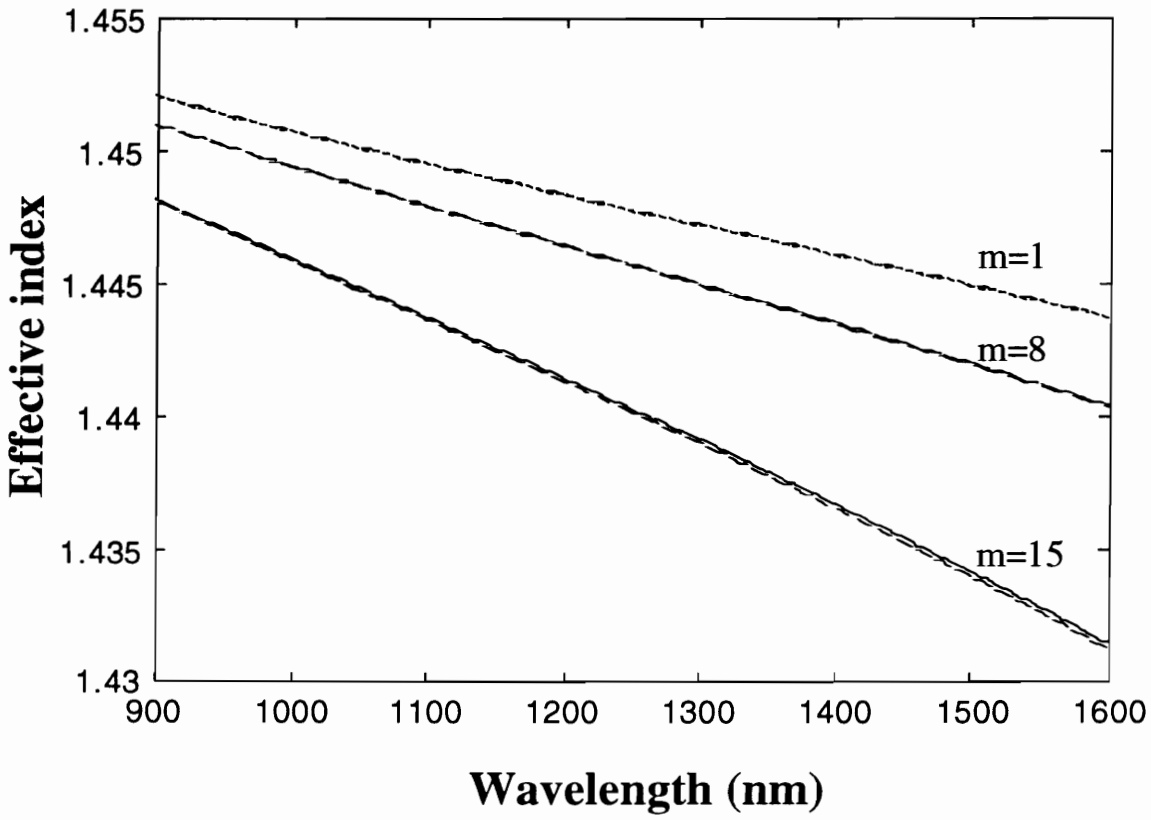

Figure 3.17. Spectral variation of the effective indices of a few $LP_{0,m}$ cladding modes for b=62.5 μm (solid lines) and for b=61.5 μm (dashed lines). For m=1 the change in effective index due to the reduction in cladding radius is hardly discernible.

As for the case of guided mode, we now discuss the effect of deviations in the typical values of fiber parameters on the cladding mode effective indices. We first consider the effect of reducing the cladding diameter by 2 μm from the standard value of 125 μm in Corning SMF-28 fiber. Figure 3.17 shows the variation in the effective indices of modes of order 1, 8 and 15 when the cladding diameter is reduced to 123 μm. The modal effective indices are found to reduce and this is consistent with the observations in the previous section where the guided mode effective index was found to be a decreasing function of the core diameter. The higher order cladding modes are observed to undergo a larger change in their effective indices and this can be attributed to their larger spread in the cladding as compared to the lower order modes. For example, the average change in effective index is about 10^{-6} for m=1 and around 10^{-4} for m=15 for the wavelength range under investigation. Figure 3.18 depicts the variation in the effective indices of the

modes with m=1,8 and 15 when the ambient index is changed from air (n_3=1.0) to water (n_3=1.33). The effective indices of the cladding modes are observed to increase, with the higher order modes undergoing larger changes. Also, in Figures 3.17 and 3.18, the change in the effective indices of the modes is an increasing function of the operating wavelength and this may be explained on the basis of the spectral dependence of the cladding mode confinement.

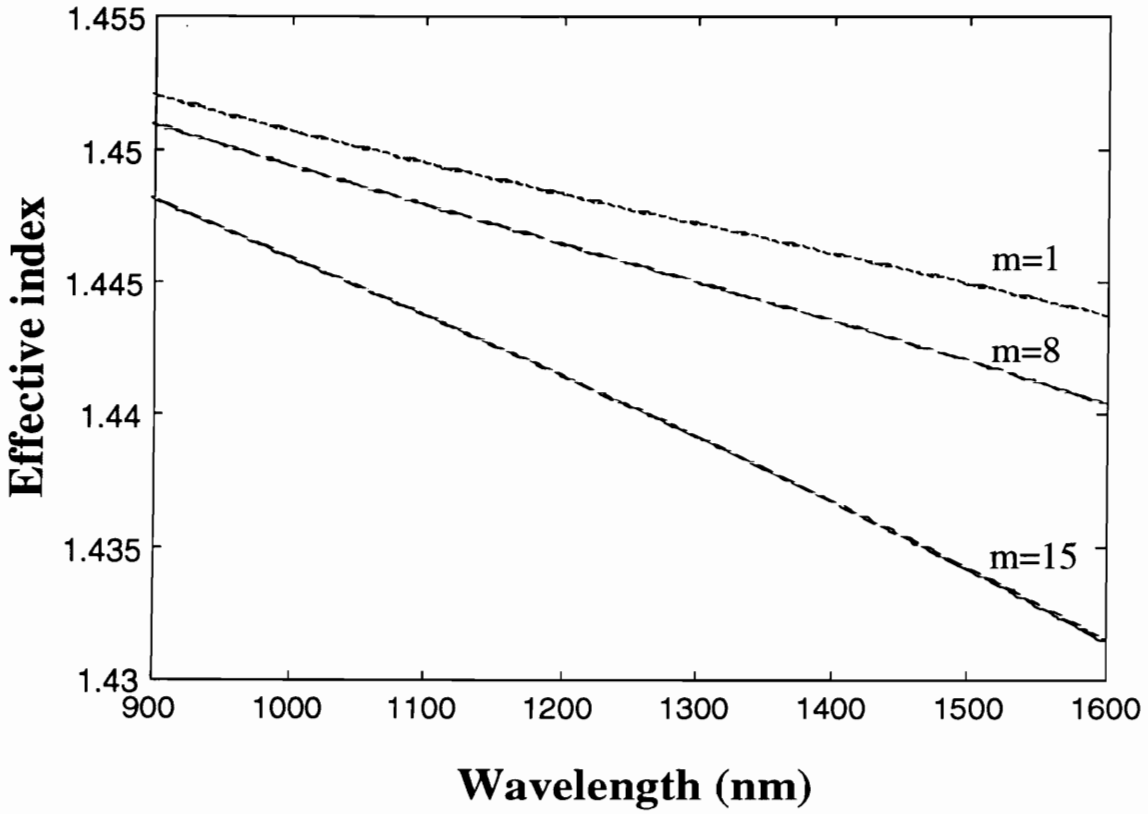

Figure 3.18. Spectral variation of the effective indices of a few $LP_{0,m}$ cladding modes for n_3=1.0 (solid lines) and for n_3=1.33 (dashed lines). The change in effective indices becomes larger as the order of the corresponding cladding mode is increased.

Employing the β-plot of Figure 3.8 (c) we can deduce that the coupling wavelength $\lambda^{(m)}$ for a long-period grating will increase when the cladding of the fiber is etched. We will confirm this observation experimentally in section 2.4. We can also observe from the β-plot that the coupling wavelength should shift to smaller values when the ambient air is substituted by water. This will be verified through experiments in Section 4.4.2 when we discuss long-period grating-based refractive index sensors. Since the effective indices of

the higher order modes are influenced more by variations in the above parameters, it is expected that the resonance bands corresponding to these modes will undergo larger spectral shifts. The previous statement is valid only if a given change in the effective index produces the same wavelength shift in all bands.

Ignoring the presence of the core, the modal fields $E_{cl}^{(m)}(r)$ of the circularly-symmetric cladding modes can be approximated by [53],

$$E_{cl}^{(m)}(r) = A_{cl}^{(m)} J_0(u_{cl}^{(m)} r)\, e^{j(\omega t - \beta_{cl}^{(m)} z)} \qquad \text{for } r<b, \tag{3.24a}$$

$$E_{cl}^{(m)}(r) = B_{cl}^{(m)} K_0(w_{cl}^{(m)} r)\, e^{j(\omega t - \beta_{cl}^{(m)} z)} \qquad \text{for } r>b, \tag{3.24b}$$

where $u_{cl}^{(m)}$ and $w_{cl}^{(m)}$ are the cladding waveguide parameters defined in Equations (3.21) and (3.22), respectively, and $A_{cl}^{(m)}$ and $B_{cl}^{(m)}$ are arbitrary constants. Figure 3.19 shows the modal power distribution in the fundamental cladding mode (m=1) and in a higher order mode with m=6 (λ=1310 nm and n_3=1.0). The fundamental mode has one intensity peak centered at r=0 while the mode with m=6 has 5 smaller peaks around the one along the axis.

As for the guided mode, the spectral dependence of $u_{cl}^{(m)}$ causes the cladding modes to possess a modal spread that is a function of the operating wavelength. The spread for cladding modes is a function of the ambient index and increases as the value of n_3 approaches the effective index of the cladding modes. This is the reason for the non-linear shift in the spectral positions of the band under the influence of ambient index changes (Section 4.4).

In this section we analyzed the important characteristics of forward-propagating circularly-symmetric cladding modes of different orders. The spectral variation of the effective index was obtained and it was shown that certain higher order cladding modes have group indices that are equal or even larger than that of the fundamental guided mode. The influence of variations in the cladding diameter and the ambient index on the effective indices was investigated. We finally discussed the modal power distribution in cladding modes of different orders.

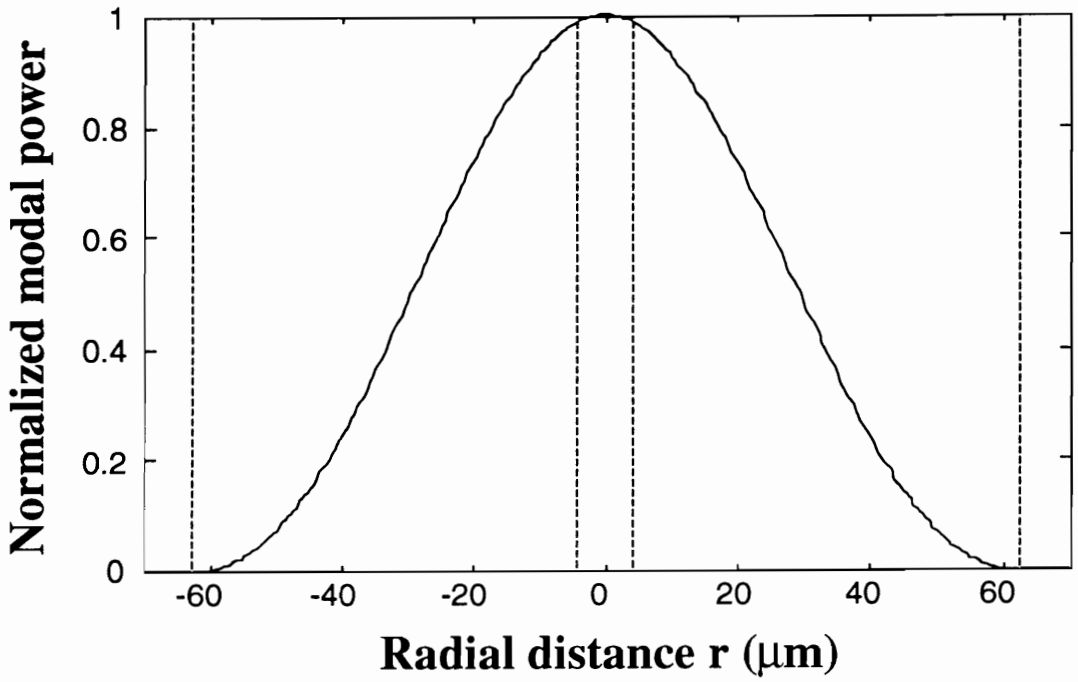

(a)

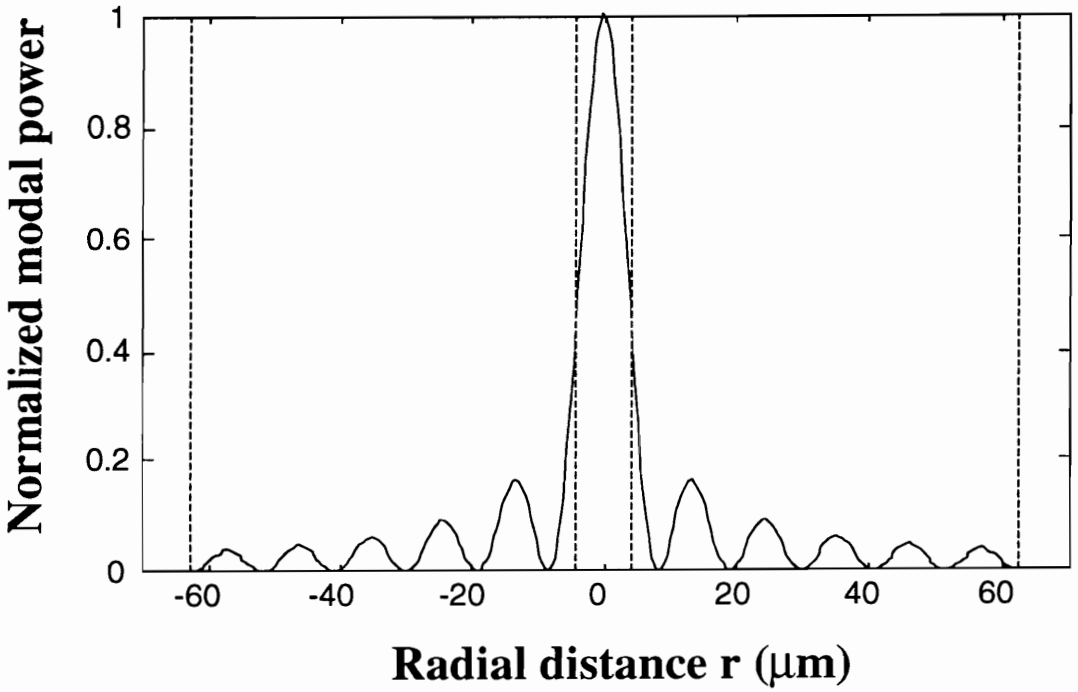

(b)

Figure 3.19. Radial variation of the modal power in (a) $LP_{0,1}$ and (b) $LP_{0,6}$ cladding modes at 1310 nm and n_3=1.0. The dashed lines represent the core (r=4.15 μm for SMF-28 fiber) and the cladding (r=62.5 μm) outer surfaces.

3.2.3 Characteristic Curves of Long-Period Gratings

In the previous section we determined the spectral dependence of the effective index of the fundamental guided mode and those of the circularly-symmetric cladding modes. The next step in the complete characterization of long-period gratings is the evaluation of the set of periods that would induce coupling between the guided mode and cladding modes of different orders at a particular wavelength. We can rewrite the phase-matching condition of Equation (3.2) to determine the grating period Λ required to produce coupling between the guided mode and a cladding mode of order m,

$$\Lambda = \frac{\lambda^{(m)}}{\left(\delta n_{eff}^{(m)}\right)}, \tag{3.25}$$

where $\lambda^{(m)}$ is the coupling wavelength and the differential effective index $\delta n_{eff}^{(m)}$ is given in Equation (3.3). In order to realize the nature of accuracy required in the analysis of long-period gratings, we consider a small error $\Delta(\delta n_{eff}^{(m)})$ in the calculation of the differential effective index $\delta n_{eff}^{(m)}$. If the period Λ can be determined accurately, the overall error in the coupling wavelength $\Delta\lambda^{(m)}$ is then given by,

$$\Delta(\lambda^{(m)}) = \Delta(\delta n_{eff}^{(m)})\, \Lambda\,. \tag{3.26}$$

The above expression implies that for a grating with Λ=100 μm the differential effective index needs to be measured with an accuracy of 10^{-5} to achieve an error less than 1 nm in the calculation of the coupling wavelength. Hence it is expected that small deviations in the fiber parameters that serve to produce changes in the effective indices of the guided and cladding modes (Sections 3.2.2.1 and 3.2.2.2) may severely alter the values of the resonance wavelengths and this effect would be analyzed in detail Section 3.2.4.2. The high sensitivity to slight variations in the differential effective index can be attributed to the coupling mechanism in long-period gratings. Since the coupling occurs between two forward-propagating modes with very close values of effective indices, minute errors in their analysis can result in large discrepancies between the actual and calculated values of coupling wavelengths.

3.2.3.1 Differential Propagation Constant

In this section we determine the differential propagation constant $\Delta\beta^{(m)}$ ($=2\pi\delta n_{eff}^{(m)}/\lambda$) as a function of wavelength for a cladding mode of order m. Figure 3.20 depicts the spectral variation of the differential propagation constant between the fundamental guided mode and the $LP_{0,12}$ cladding mode for an unperturbed SMF-28 fiber (curve A). The propagation constant difference initially decreases with wavelength, reaches a minimum and then starts increasing with wavelength [82]. The equalization wavelength λ_0 (Section 3.1) is defined as the wavelength at which the differential propagation constant does not vary with the operating wavelength. For the $LP_{0,12}$ cladding mode this value is calculated to be 1354.2 nm. Since the equalization wavelength is a function of the order m of the cladding mode, we will denote it by $\lambda_0^{(m)}$. From Equation (3.11) we observe that the slope of the characteristic curve (coupling wavelength versus grating period) is of opposite polarity as the slope of the curve in Figure 3.20. Hence for wavelengths less than the equalization wavelength, the characteristic curve for the $LP_{0,12}$ cladding mode is expected to have a positive slope and vice-versa. Curve A should be compared with the spectral variation of the differential propagation constant between two forward-propagating guided modes (Figure 2.20). The opposite nature of the curves is due to the difference in the spectral variation of the propagation constants of the cladding modes and those of the higher order guided modes. Curve B in Figure 3.20 represents the differential propagation constant between the same modes when the core refractive index is increased by 10^{-4}. The increase in $\Delta\beta^{(m)}$ can be attributed to the increase in effective index of the guided mode at all wavelengths. The equalization wavelength for the perturbed fiber is found to shift to a value of 1367 nm. Hence during the grating writing process when the core index is enhanced, the characteristic curves for the resonance bands are expected to shift.

The curves in Figure 3.20 also reveal the effect of changing the differential propagation constant between the guided and cladding modes. If the coupling wavelength is less than the equalization wavelength ($\lambda^{(m)}<\lambda_0^{(m)}$), an increase in the value of $\Delta\beta^{(m)}$ causes the phase-matching wavelength to shift to a higher value. This is because the period of the grating is unchanged and hence we need to draw a horizontal line from the y-axis to intersect the two curves. The above is equivalent to compressing the ω-axis in the β-plot of Figure 3.8(b) that results in a wavelength shift to higher values. On the other hand, operation at wavelengths longer than the equalization wavelength ($\lambda^{(m)}>\lambda_0^{(m)}$) causes the

phase-matching wavelength to shift to smaller values. Thus in order to use the β-plots (Section 3.1) one has to know the relative location of the coupling wavelength with respect to the equalization wavelength. The wavelength shifts predicted by the β-plots are only valid if the coupling wavelength is smaller than the equalization wavelength. Also since the equalization wavelength depends on the order of the cladding mode for a particular fiber, the value of m needs to be specified to make appropriate use of the β-plots.

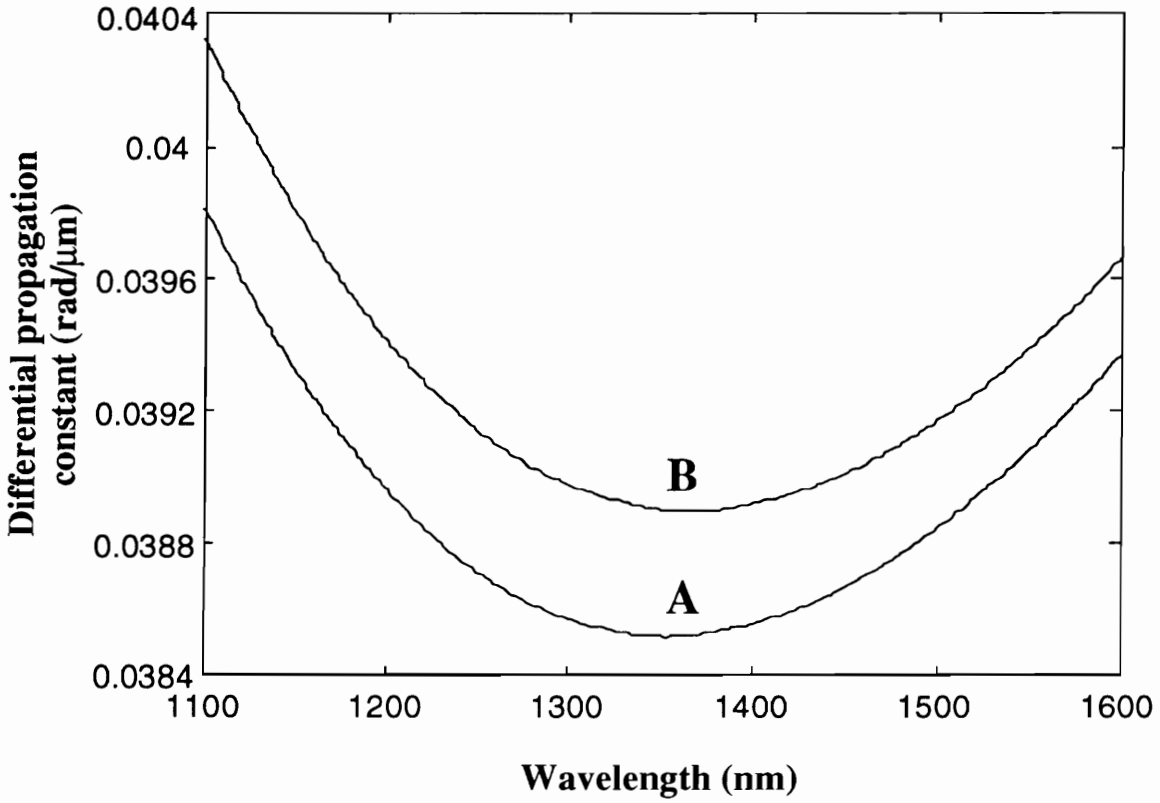

Figure 3.20. Variation of the differential propagation constant with wavelength for the $LP_{0,12}$ cladding mode. Curve A is for an unperturbed SMF-28 fiber while the curve B is for a SMF-28 fiber with core index increased by 10^{-4}.

The above discussion will be much clearer if we consider the coupling wavelength versus the grating period curves shown in Figure 3.21. Here again curve A represents an unperturbed fiber while curve B is for a fiber with 10^{-4} larger core refractive index (m=12). The curves in Figure 3.21 are obtained from those in Figure 3.20 by using the phase-matching condition ($\Lambda=2\pi/\Delta\beta^{(m)}$) and then flipping the x and y axes. To obtain the

coupling wavelengths for a given grating period we draw vertical lines from the x-axis to intersect the curves. As expected the characteristic curve has a positive slope for $\lambda^{(m)}<\lambda_0^{(m)}$ and negative slope for $\lambda^{(m)}<\lambda_0^{(m)}$. We term the range of wavelengths at which the slope of the characteristic curve is positive as the "normal" region of operation while the other part of the spectrum is denoted as the "anomalous" region. The notation has been derived from the two regions of operation of the group velocity dispersion. For long period gratings, the region with $d\lambda/d\Lambda>0$ is termed "normal" since conventional long-period gratings with periods of the order of hundreds of micrometers operate in this part of the spectrum. For cladding modes that have an equalization wavelength within the optical source spectrum proper choice of grating period can result in two resonance bands - one in the normal region and the other in the anomalous region. The curves in Figure 3.21 indicate that for a fixed grating period, as the effective index of the guided mode is enhanced, the coupling wavelengths undergo a shift. The polarity of the shift depends on whether the coupling wavelength is in the normal or anomalous region of operation.

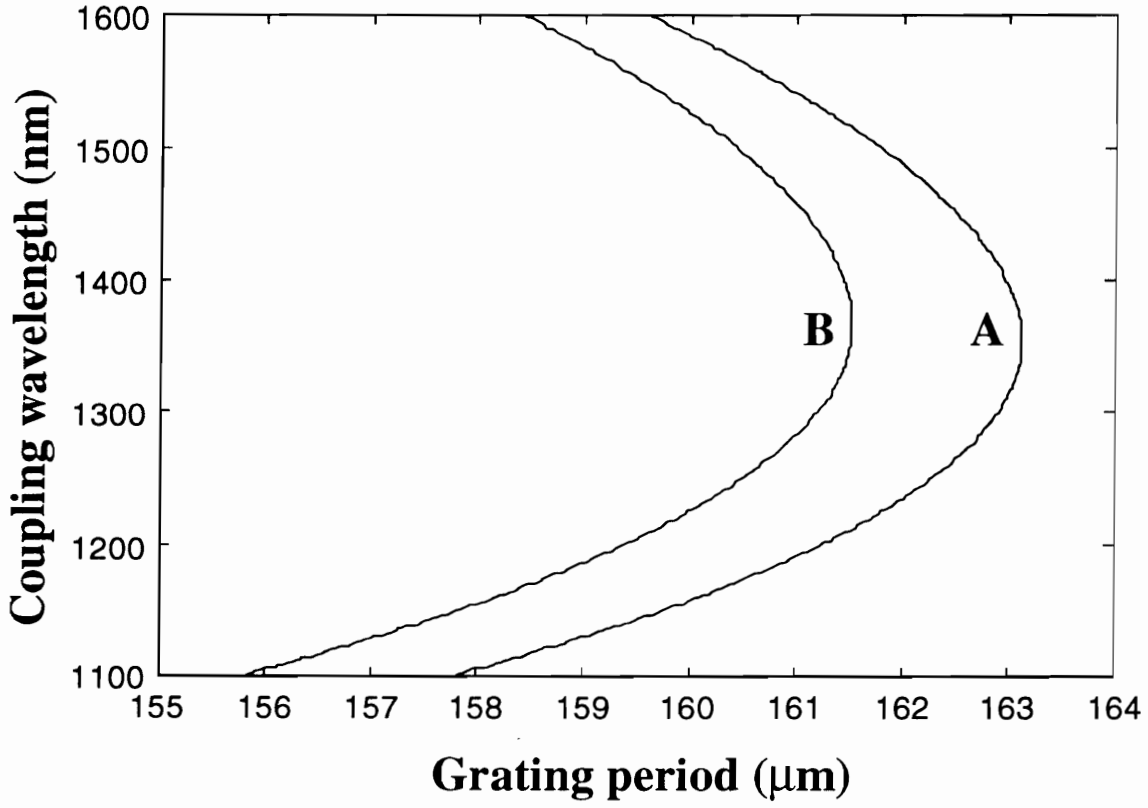

Figure 3.21. Characteristic curves for m=12 in Corning SMF-28 fiber. Curve A is for an unperturbed fiber while curve B is for a fiber with core index increased by 10^{-4}.

Typical long-period gratings possess periods that induce coupling to cladding modes in the normal region. In such cases, we can expect the coupling wavelength to shift to higher values as the core index is increased during the grating fabrication process. We will confirm this observation in Section 3.3 when we discuss different grating manufacturing methods. On the contrary, we deduce from Figure 3.21 that the phase-matching wavelength will shift to lower values if the operation is in the anomalous region. For a given fiber the magnitude of shift during the writing process depends on the UV power, the grating period and the order of the resonance band. For example, if the grating period is such that the coupling to a particular cladding mode occurs near the equalization wavelength, the spectral shift during grating fabrication can be significant (Figure 3.21). The shift is expected to reduce as the coupling wavelength moves away from the equalization wavelength. The dependence on the order of the cladding mode also arises from the fact that the change in the differential effective index with UV exposure is distinct for each mode.

An interesting case is when the grating period is chosen such that there are two phase-matching wavelengths for coupling to a particular cladding mode. During the writing process the resonance band in the normal region of operation will move to higher wavelengths while that in the anomalous region will move to lower wavelengths. These two bands will approach the equalization wavelength of the perturbed fiber and if the exposure to UV is continued, it is expected that the two bands would overlap and then suddenly disappear. The disappearance of the bands can be attributed to the increase of the differential propagation beyond the minimum value required to induce mode coupling (Figure 3.20). The wavelength at which the two bands overlap and disappear is the equalization wavelength of the perturbed fiber. Hence by using an appropriate grating period it is possible to experimentally determine the equalization wavelength for a certain subset of higher order cladding modes in perturbed fibers.

Figure 3.21 reveals that there is a maximum grating period that can induce coupling from the guided mode to a given cladding mode in an unperturbed fiber (Curve A). We will call this maximum period $\Lambda_0^{(m)}$ the equalization period for the mode of order m since it corresponds to the equalization wavelength for an unperturbed fiber. For the $LP_{0,12}$ cladding mode this period is $\Lambda_0^{(12)}$=163.1 μm. Figure 3.22 depicts the variation of the equalization period for cladding modes m=10 through 15 in SMF-28 fiber. The reduction

in the equalization period with the order of the cladding mode can be attributed to the larger value of the minimum differential propagation constant as the modal order is increased.

The plots in Figure 3.20 and 3.21 are for typical SMF-28 fiber parameters from Table I. We have seen in Section 2.2 that small variations in these standard values can alter the differential propagation constants between the guided mode and the cladding modes. Also a variation in the ambient index will cause these plots to change shape which implies that the evolution of a resonance band during the writing process is a function of the medium surrounding the cladding. Moreover, the equalization periods for different cladding modes will also deviate from those in Figure 3.22 if the fiber parameters or the ambient index are changed.

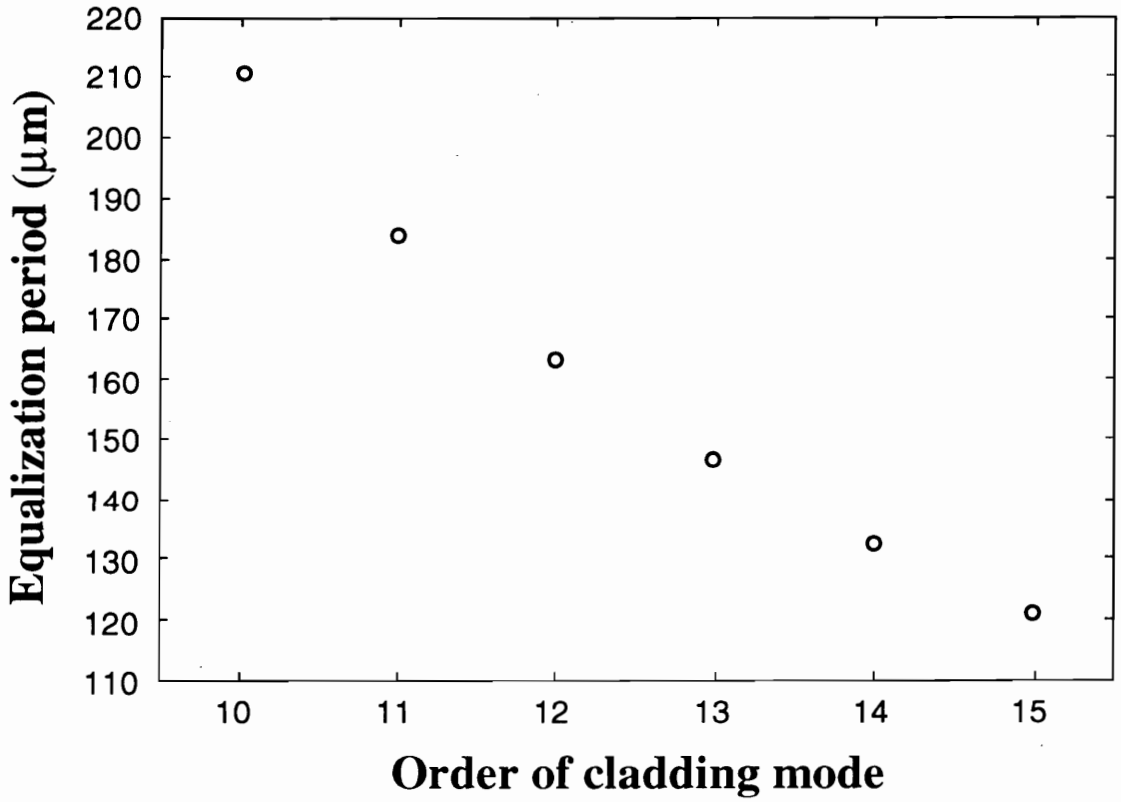

Figure 3.22. Variation of the equalization period as a function of the order of the cladding mode for unperturbed SMF-28 fiber. Only modes with equalization wavelengths in the range 1100 nm to 1600 nm are considered.

We now present the characteristic curves for three different fibers listed in Table I. The range of grating periodicities that result in operation in the anomalous region in Flexcor 1060 fiber are studied. We also analyze effects of small deviations in the typical fiber parameters on the nature of the characteristic curves.

3.2.3.2 Characteristic Curves

Long-period gratings are typically formed by using a periodic rectangular refractive index modulation along the fiber axis. The refractive index change $\delta n(z)$ along the z direction may hence be expressed as,

$$\delta n(z) = \Delta n \, \mathrm{rect}\left(\frac{z}{\Lambda}\right), \tag{3.27}$$

where Λ is the grating period and for a 50% duty cycle the rect(z/Λ) function is given by [93],

$$\mathrm{rect}\left(\frac{z}{\Lambda}\right) = 1 \qquad \text{for } k\Lambda < z < \left(k + \frac{1}{2}\right)\Lambda, \tag{3.28a}$$

$$\mathrm{rect}\left(\frac{z}{\Lambda}\right) = 0 \qquad \text{for } \left(k + \frac{1}{2}\right)\Lambda < z < (k + 1)\Lambda, \tag{3.28b}$$

where k is an integer. In Equation (3.27), Δn is the peak index change produced during the grating fabrication process and for a rectangular index modulation with 50% duty cycle the average increase in the core refractive index in the perturbed region can be approximated by $\Delta n/2$. This factor can change depending on the duty cycle and the refractive index modulation during the writing process. Although the UV-induced index change is expected to be a function of wavelength [94], for the analysis to follow we will assume that the index modulation of the fiber core does not have a spectral dependence. The factor $\Delta n/2$ is added to the core refractive index calculated from the Sellmeier coefficients in Table II and the modified guided mode effective index is calculated using the characteristic equation. Typical values of Δn range from 10^{-4} to 10^{-3} in long-period gratings and depend on the writing conditions and the germania and molecular hydrogen concentrations in the core. Unless otherwise stated we will use $\Delta n = 5\times10^{-4}$ [1] to obtain characteristic curves for various fibers.

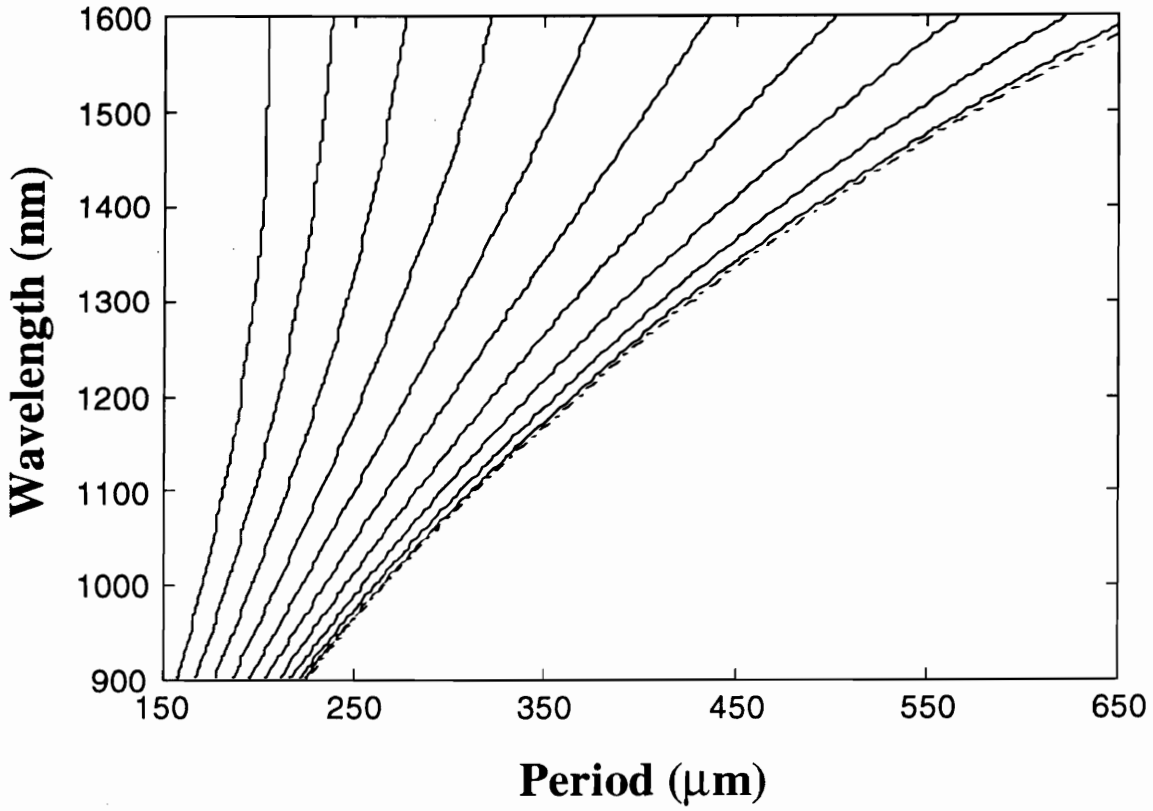

Figure 3.23. Characteristic curves for the first ten circularly-symmetric cladding modes in SMF-28 fiber. The ambient material is air (n_3=1) and the peak index change (Δn) is assumed to be 5×10^{-4}. The dashed curve corresponds to λ_{cut} for different periods. The order of the cladding modes increases from right to left.

Figure 3.23 depicts the characteristic curves for m=1 through 10 in Corning SMF-28 fiber using the typical fiber parameters from Table I. The dashed curve represents λ_{cut} (Section 3.1), the minimum wavelength at which coupling can occur to a cladding mode for a given period [1]. λ_{cut} is calculated at each value of the grating period by using the phase-matching condition (Equation (3.25)) and assuming $n_{cl}=n_2$. λ_{cut} increases with Λ and this implies that resonance bands are located at values larger than this minimum wavelength. The above observation is consistent with the β-plot of Figure 3.7. It can be seen from Figure 3.23 that the slope of all the characteristic curves are positive. For higher order modes (m=9,10) the slopes of the corresponding curves approach infinity at wavelengths higher than 1500 nm. These observations can be explained on the basis of the differential group index between the guided and cladding modes (Section 3.2.4.1). We limit ourselves to discussion of modes that operate in the normal region of spectrum.

The operation in the anomalous region will be analyzed later in this section. The magnitude of the slopes is a function of the differential effective and group indices between the guided and corresponding cladding modes (Equation (3.9)).

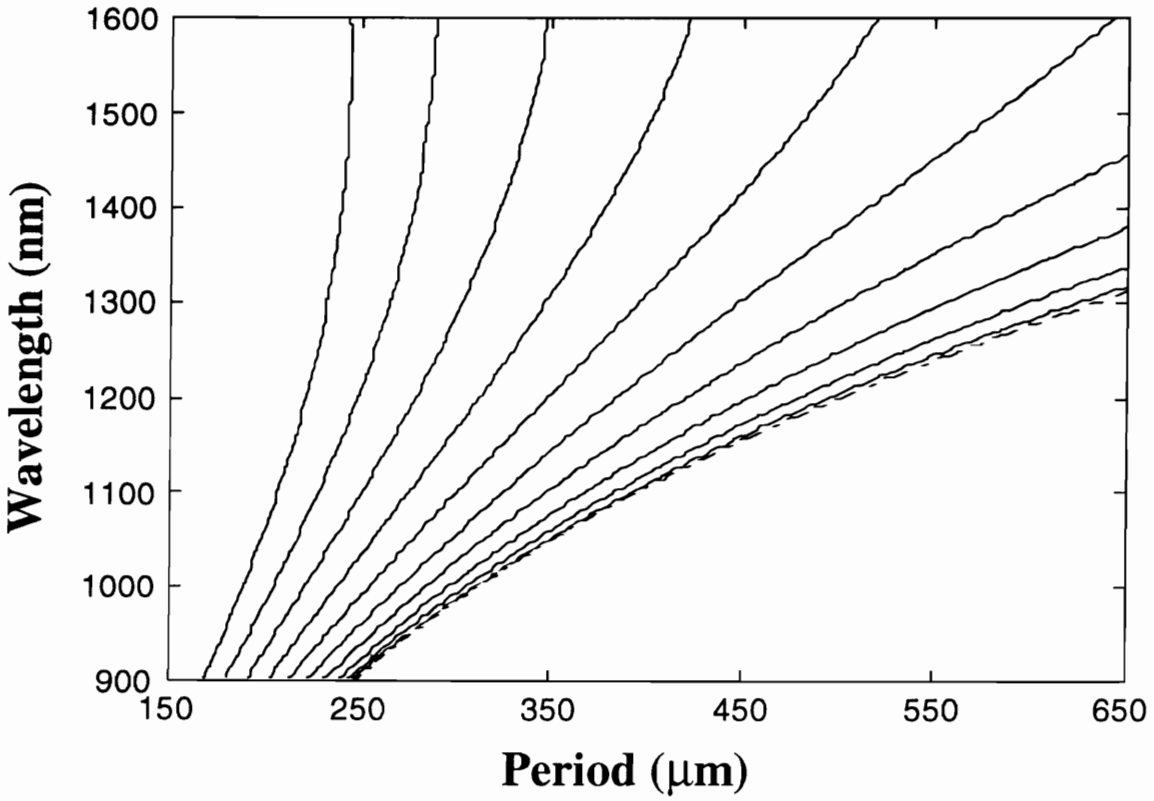

Figure 3.24. Characteristic curves for the first ten circularly-symmetric cladding modes in Flexcor 1060 fiber. The dashed curve corresponds to λ_{cut} for different periods.

Figure 3.23 for a long-period grating should be compared to the characteristic curve for a short-period grating (Figure 2.11). We had seen in Sections 2.4.4.1 and 2.4.4.2 that the waveguide contributions to the strain- and temperature-induced spectral shifts in a Bragg grating are functions of the slope of the characteristic curve. Since this slope is constant for all periods in a Bragg grating the waveguide contribution is the same at all wavelengths. On the other hand, the waveguide contributions to strain and temperature sensitivities are expected to be functions of the grating period for coupling to the same cladding mode. The concept of period-dependent sensitivity of long-period gratings will be discussed in detail in Chapter 4. It should also be noted that in the normal region of operation, the coupling wavelength is an increasing function of the order of the cladding

mode which is consistent with the β-plots of Figure 3.3. Moreover, Figure 3.23 predicts that for a given grating period the wavelength separation between the resonance bands increases with the order of the corresponding cladding modes.

In Figure 3.24 we plot the characteristic curves of the first ten cladding modes for Flexcor 1060 fiber. The differences between Figures 3.23 and 3.24 are due to the distinct parameters of the SMF-28 and Flexcor 1060 fibers that result in non-similar guided mode effective indices. An exact cladding mode analysis, that includes the presence of fiber core, would reveal more subtle differences also. We thus observe that the spectral response of long-period gratings is a strong function of the properties of the host fiber.

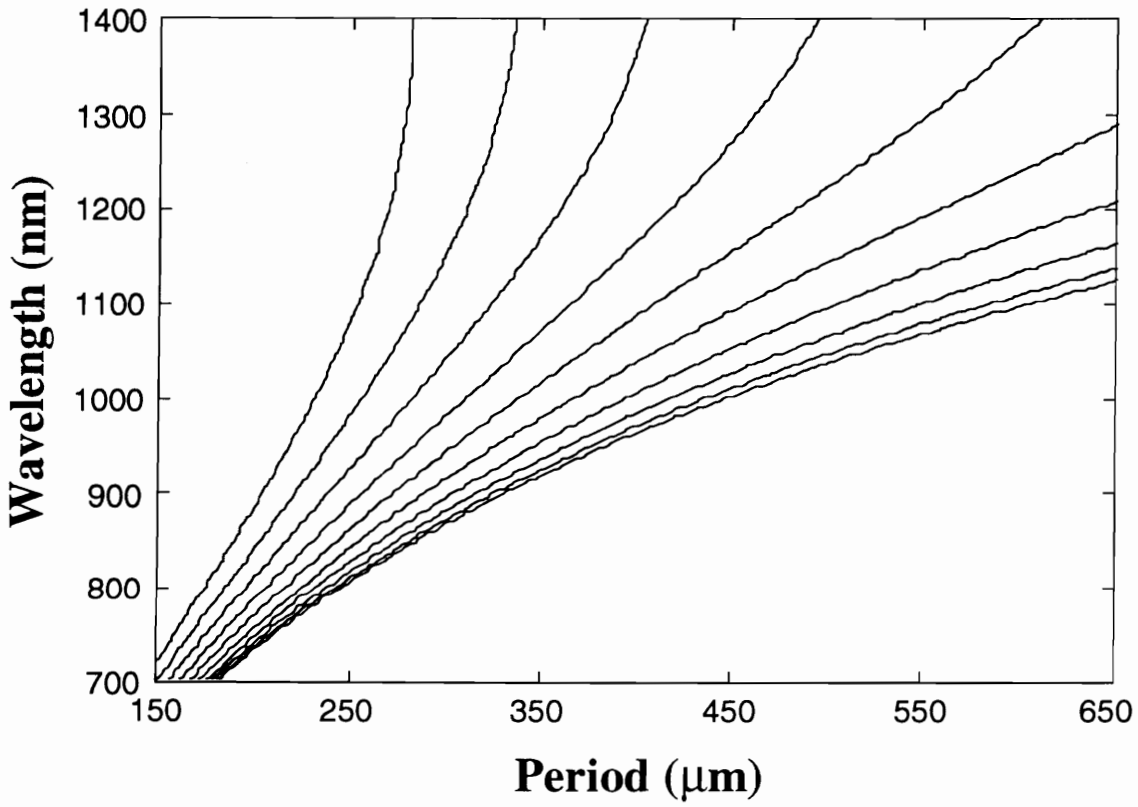

Figure 3.25. Characteristic curves for the first ten circularly-symmetric cladding modes in Flexcor 780 fiber.

Figure 3.25 shows the characteristic curves for Flexcor 780 fiber. The only difference between Flexcor 1060 and 780 fibers is the core radius (Table I). The different characteristic curves for the three fibers investigated here reveal that the same grating

period will result in resonance bands occurring at distinct wavelengths for the same order of cladding mode. Also since the slope of the characteristic curves depends on the grating period for a given fiber, we can expect the waveguide contributions to strain- and temperature-induced shifts to be strong functions of the fiber parameters and grating period. We thus see that the characteristic curves provide a useful tool to analyze the properties of gratings. For a given period, the location of the resonance bands can be easily determined. Moreover, if a band is desired at a certain wavelength, the appropriate period can be selected to obtain a particular spectral separation between any two bands [1]. Thus to completely characterize the behavior of long-period gratings, it is convenient to first obtain the characteristic curves for the host fiber.

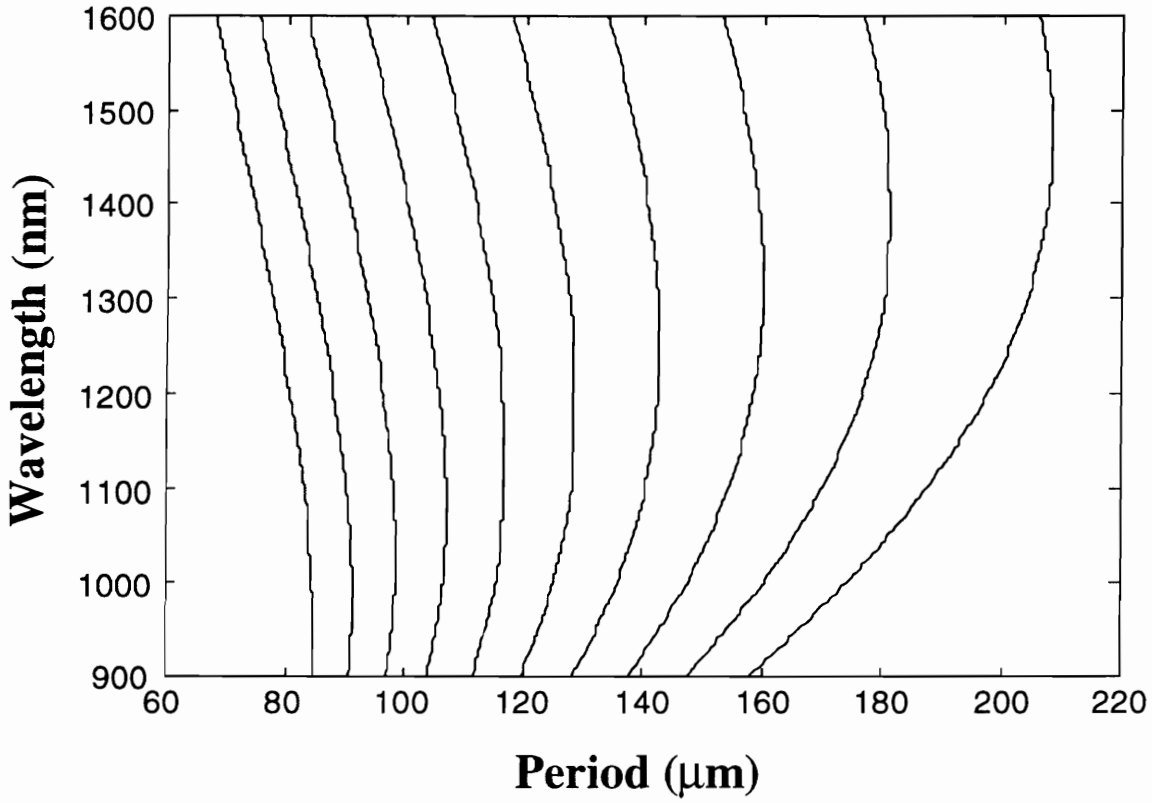

Figure 3.26. Characteristic curves for the cladding modes $LP_{0,11}$ through $LP_{0,20}$ in Flexcor 1060 fiber. The order of the cladding modes increases from right to left.

We now analyze the characteristic curves for Flexcor fibers for cladding modes that operate in the anomalous region of the spectrum. Figure 3.26 depicts the characteristic curves for cladding modes with order m=11 to 20. The slopes of the characteristic curves

are very large due to operation near the equalization wavelength. It is important to point out here that for a given fiber we need smaller periods to operate in the anomalous region than those required to function in the normal spectral range. Additionally, certain periods might result in coupling to a cladding mode that operates in both normal and anomalous region. For example, a grating with Λ=140 μm is expected to have two resonance bands corresponding to the same cladding mode. On the other hand, a grating with Λ=120 μm should result in only one resonance band between 1000 nm and 1600 nm, at about 1560 nm. Thus the number of resonance bands for a long-period grating is a strong function of the periodicity.

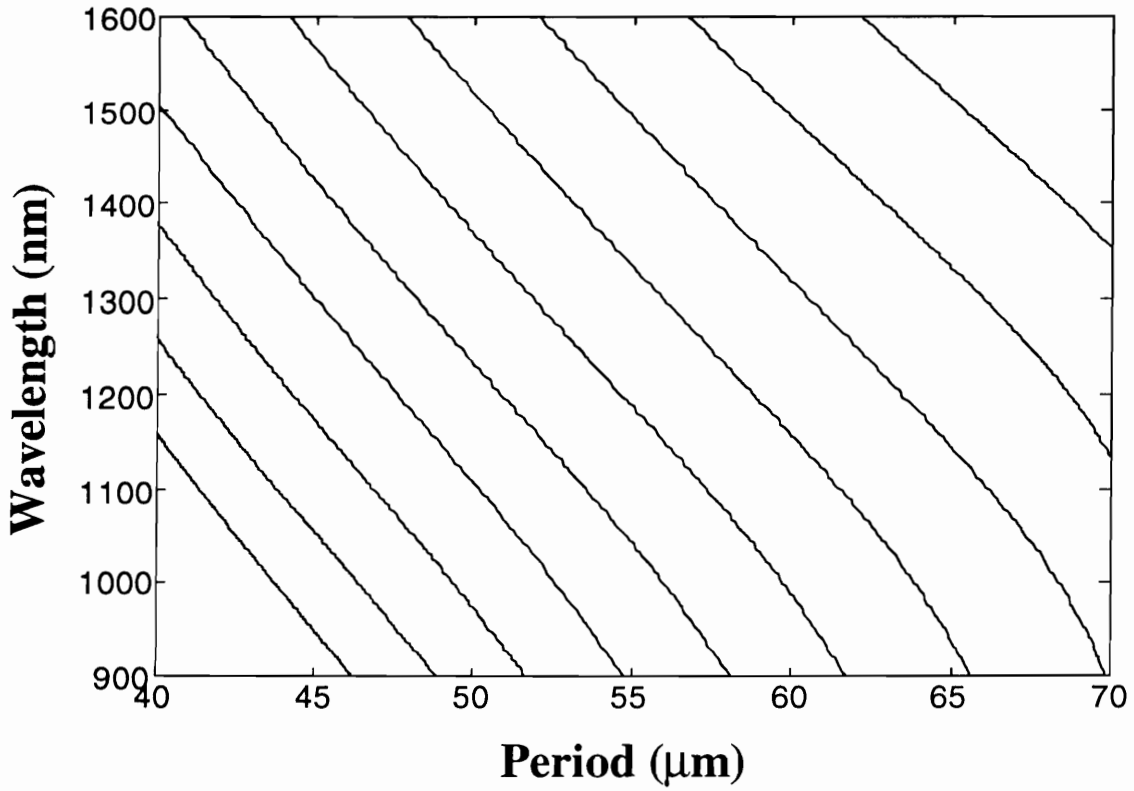

Figure 3.27. Characteristic curves for the cladding modes $LP_{0,21}$ through $LP_{0,30}$ for Flexcor 1060 fiber. The order of the cladding modes increases from top right to bottom left.

Figure 3.27 shows the characteristic curves for Flexcor fiber for cladding modes with m=21 to 30. All the curves have negative slope in the wavelength region of interest. For operation in the anomalous region the wavelength location of the resonance bands is a decreasing function of the order of the cladding modes. Also the curves are almost

parallel to one another and the wavelength separation between the resonant bands for a given period decreases as we move to higher order modes.

We thus observe that for periods (typically less than 160 μm in Flexcor 1060 fiber) smaller those used in conventional gratings, we can obtain coupling to cladding modes that operate in the anomalous region. The operation in the anomalous region will be shown to have interesting applications to long-period grating sensing systems in Chapter 4. It is important to note here that the characteristic curves obtained in this section are merely approximations to the exact curves. The analysis of the cladding modes by neglecting the presence of the core can have significant impact on the effective indices of these modes. Hence the characteristic curves presented here should merely be used as guidelines for obtaining coupling wavelengths at different grating periods [1].

3.2.3.3 Sensitivity Analysis of Characteristic Curves

In this section we analyze the sensitivity of the characteristic curves of SMF-28 fiber to small deviations in the fiber parameters from the typical values specified by the manufacturer. Since typical grating periods (150 to 600 μm [1]) result in operation in the normal region, we use characteristic curves with positive slopes only, but the discussion of the sensitivity will be extended to the anomalous region also.

Figure 3.28 depicts the effects of reducing the core and cladding radii from the standard values (a=4.15 μm, b=62.5 μm) specified in Table I. The solid curves are the same as those in Figure 3.23 for m=1 to 10 while the dashed curves on the lower wavelength sides represent a fiber with a core radius 1% less than the typical value (a=4.11 μm). The reduction in the core radius decreases the guided mode effective index (Figure 3.13) and using the β-plots one can show that the coupling wavelengths should reduce for operation in the normal region. As expected the deviation from the standard curves increases with wavelength for all cladding modes in the normal region. Hence for a given grating period the higher order resonance bands (at higher wavelengths) are expected to undergo a larger shift when the core radius is changed.

The dotted curves in Figure 3.28 represent a SMF-28 fiber with cladding radius reduced to 62 μm. The reduction in the cladding effective index causes the resonance wavelengths to shift to higher values in the normal region. The change increases with the

modal order since the higher order modes undergo larger variations in their effective indices (Figure 3.17). For operation in the anomalous region the decrease in the core radius is expected to shift the resonance bands to higher wavelengths while the opposite effect is anticipated for reduction in the cladding radius. The deviation in the normalized refractive index difference (Δ) between the core and the cladding can also be similarly analyzed. For example, an increase from the typical value of 0.36% will cause the resonance bands in the normal region to move to longer wavelengths.

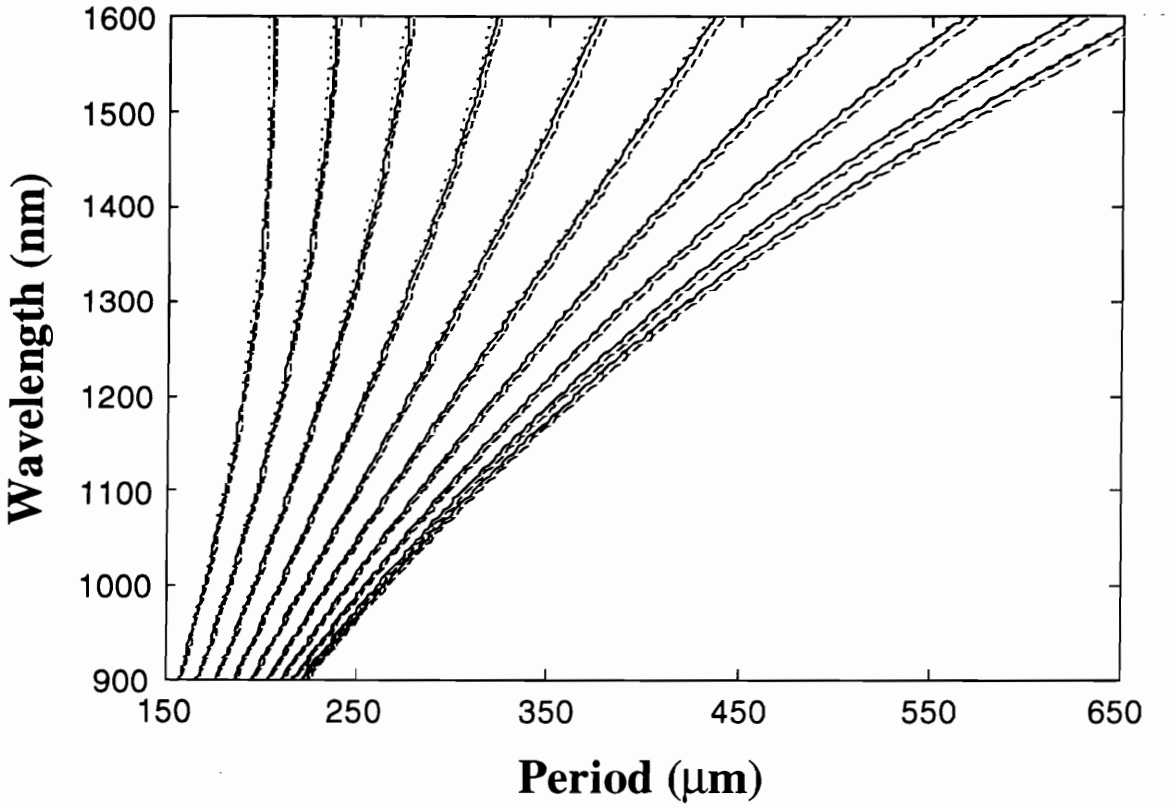

Figure 3.28. Characteristic curves for typical parameters of SMF-28 fiber (solid lines). The dashed curves are for a SMF-28 fiber with core radius a=4.11 μm while the dotted ones are for the cladding radius b=62 μm.

One grating parameter that needs to be thoroughly investigated for its influence on the characteristic curves is the peak refractive index change (Δn) in the fiber core during the writing process. Figure 3.29 depicts the deviation in the characteristic curves for $\Delta n=10^{-4}$ and 10^{-3} for modes m=5 to 10. As expected, a decrease in Δn from a value of 5×10^{-4} causes the bands to shift to lower wavelengths and vice-versa. The curves reveal that

even if the exact analysis is used to determine the guided and cladding mode effective indices and the fibers parameters are precise, variations can still be obtained due to uncertainty in the value of Δn. Hence the determination of the peak index change is important to correctly characterize the behavior of the gratings.

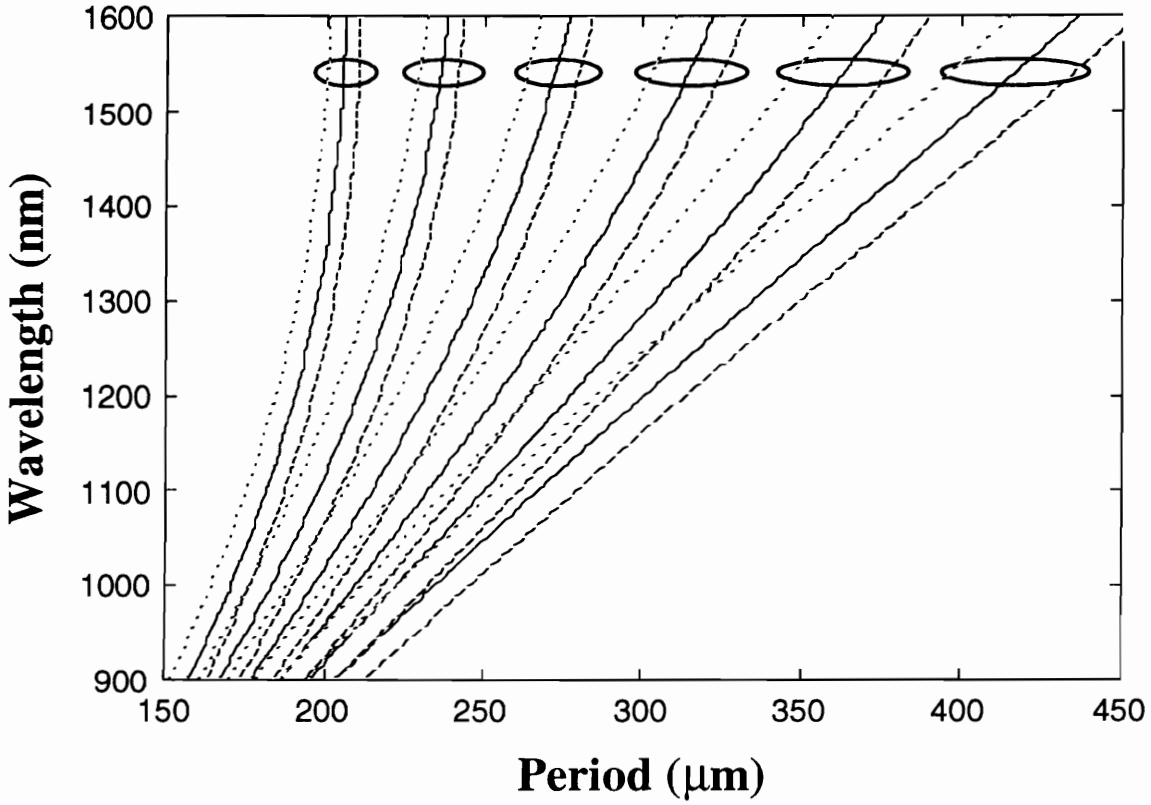

Figure 3.29. Characteristic curves for SMF-28 fiber with $\Delta n=5\times10^{-4}$ (solid lines). The dashed curves are for $\Delta n=10^{-4}$ while the dotted curves are for $\Delta n=10^{-3}$. Only modes with m=5 to 10 are considered to keep the representation simple.

3.2.4 Important Grating Parameters

In this sub-section we analyze some important grating parameters such as the coupling coefficient, the bandwidth and the separation between the resonance bands. The variations in values of the grating length and the coupling coefficient are investigated for influence on the transmission spectrum.

3.2.4.1 Coupling Coefficient

In Section 2.3.2.1 we observed that the coupling between two modes propagating in the same direction is a strong function of the detuning ratio δ/κ, where δ is the detuning parameter and κ is the coupling coefficient of the grating. The detuning parameter is dependent on the proximity of the operating wavelength to the phase-matching wavelength for the grating. The coupling coefficient, on the other hand, is a function of the index change and the modal overlap between the guided and cladding modes over the region of perturbation. It is typically desired that the value of the detuning ratio be as small as possible for maximum power transfer to occur (Figure 2.7) which implies that the coupling coefficient should be optimized to improve the grating performance. We investigate the dependence of the coupling coefficient on the order of the cladding mode, the operating wavelength and the peak index change Δn.

To derive an expression for the coupling coefficient we will adopt the approach used by Snyder and Love [64]. We use a function $\delta n(z)$ to describe the periodic refractive index modulation in the fiber core such that the modified profile $n(z)$ is given by,

$$n(z) = n_1 + \delta n(z) \tag{3.29}$$

where n_1 is the unperturbed core index of refraction. For a rectangular index modulation the function $\delta n(z)$ is given by Equation (3.27). The periodic variation in the index can be expressed in terms of its Fourier series [93],

$$\delta n(z) = \Delta n \left[A_0 + \sum_{N=1}^{\infty} A_N \cos\left(\frac{2\pi N}{\Lambda} z\right) \right], \tag{3.30}$$

where Λ is the grating periodicity, Δn is the peak index change and A_N are the Fourier coefficients. We will limit ourselves to first order interactions (N=1) for coupling to all cladding modes. The coupling coefficient κ is given by the square root of the product of the two cross-coupling coefficients κ_{12} and κ_{21} [64],

$$\kappa = \sqrt{\kappa_{12}\,\kappa_{21}}\ , \tag{3.31}$$

where 1 and 2 denote the guided and the cladding mode, respectively. The cross-coupling coefficients are functions of the order of the mode m and yield [64],

$$\kappa^{(m)} = \frac{k|A_N|}{2} \frac{\left| \int_0^a \Delta n \, E_{01}(r) \, E_{cl}^{(m)}(r) \, r \, dr \right|}{\sqrt{\int_0^\infty (E_{01}(r))^2 \, r \, dr \int_0^\infty \left(E_{cl}^{(m)}(r)\right)^2 \, r \, dr}}, \tag{3.32}$$

where $E_{01}(r)$ and $E_{cl}^{(m)}(r)$ are the electric field distributions of the fundamental guided mode (Equation (3.19)) and the circularly-symmetric cladding mode of order m (Equation (3.24)), respectively. Note that the factor of 2 is missing in the denominator of the right-hand side in Equation (3.32) from that in [95] due to a difference in the definition of the coupling coefficient. The integration in the numerator is over the core only since the refractive index perturbation for the grating is confined to the fiber core. We have assumed that the index modulation is small compared with the unperturbed core index and hence from Equation (3.29), $n^2(z)-n_1^2 = 2n_1\delta n(z)$. Defining the overlap integral $\eta^{(m)}$ as,

$$\eta^{(m)} = \frac{\left| \int_0^a \Delta n \, E_{01}(r) \, E_{cl}^{(m)}(r) \, r \, dr \right|}{\sqrt{\int_0^\infty (E_{01}(r))^2 \, r \, dr \int_0^\infty \left(E_{cl}^{(m)}(r)\right)^2 \, r \, dr}}, \tag{3.33}$$

we can rewrite the coupling coefficient as,

$$\kappa^{(m)} = \frac{\pi |A_N|}{\lambda^{(m)}} \eta^{(m)}, \tag{3.34}$$

where we have assumed that the coupling coefficient is constant across the spectral width of a resonance band of order m and centered at $\lambda^{(m)}$. The coupling coefficient for a long-period grating hence has the same form as that for a Bragg grating in Equation (2.31) [60]. Since the coupling coefficient is directly proportional to the overlap integral, the modal distribution of the cladding mode will have a strong influence on its magnitude. Also since the index modulation has no azimuthal variation, the coupling of the guided

mode can occur to only circularly-symmetric cladding modes, and for all other cladding modes, the overlap integral is zero. Blazing the grating will give the index modulation an azimuthal dependence ($\Delta n=\Delta n(\phi)$) and result in coupling to cladding modes that have the same ϕ variation as $\Delta n(\phi)$ [57]. Additionally, we observe that an enhancement in the magnitude of the peak index change Δn results in an increase in the coupling coefficient.

The amplitude mask used to write long-period gratings is typically rectangular with 50% duty cycle and yields the index modulation given in Equation (3.27). The Fourier series of the rectangular index modulation with a period Λ may be expressed as [93],

$$\delta n(z) = \Delta n\left[\frac{1}{2} + \frac{2}{\pi}\sum_{N=1}^{\infty}\frac{1}{N}\sin\left(\frac{N\pi}{2}\right)\cos\left(\frac{2\pi N}{\Lambda}z\right)\right]. \tag{3.35}$$

Comparing Equations (3.30) and (3.35) we deduce that the Fourier coefficients (N>1) are,

$$A_N = \frac{2}{\pi N}\sin\left(\frac{N\pi}{2}\right). \tag{3.36}$$

For N=1, the Fourier coefficient is, $A_1=2/\pi$. We note that $A_2=0$, and hence for a grating with a perfectly rectangular modulation (50% duty cycle) the second order interaction between the guided and cladding modes does not exist. Moreover, the coupling coefficient scales inversely with the order N and hence other higher order interactions may also be neglected for a simplified analysis. Thus the coupling coefficient for the first order interaction in a long-period grating with rectangular index modulation is given by,

$$\kappa^{(m)} = \frac{2}{\lambda^{(m)}}\eta^{(m)}. \tag{3.37}$$

Since the overlap integral is a dimensionless quantity, the coupling coefficient is expressed in the units of per unit length (typically cm^{-1}). Due to the reasons stated above, we will limit our attention to only first order interactions. For coupling between the guided and cladding modes, Probst *et al.* [58] have shown that the coupling coefficient is a strong function of the order of the cladding mode, the operating wavelength, and the fiber parameters and power profile. For long-period gratings, the index modulation during the writing process makes the coupling coefficient a function of the transmittance function of the amplitude mask (through the dependence on the magnitude of the Fourier

coefficient) and the peak index change. It is important to note that to obtain the exact values of the coupling coefficient it is necessary to include the presence of the core while analyzing the cladding modes. This is because the coupling coefficient includes the overlap between the guided and cladding modes in the fiber core and neglecting the presence of the core during cladding mode analysis can result in large discrepancies between the calculated and actual values [58].

In this section we discussed the dependence of the coupling coefficient in a long-period grating on the order of the cladding mode and peak index change during the writing process. It was determined that the field overlap between the guided and cladding modes has a significant impact on the magnitude of the coupling coefficient.

In Section 3.2.3.3 we had analyzed the sensitivity of the characteristic curves to the index change obtained during the writing process. It was found that the magnitude of the index modulation has to be determined accurately to obtain precise values of the spectral location of the resonance bands. The index change can be back-calculated if the loss of a particular resonance band is known. We will relate the maximum loss or peak isolation in transmission for a resonance band to the coupling coefficient for the corresponding mode in the next section.

3.2.4.2 Resonance Band Separation, Transmission and Bandwidth

We now obtain approximate expressions for the spectral separation between the resonance bands, the grating transmission and loss, and the bandwidth of resonance bands. To calculate the resonance band separation, it is first necessary to calculate the wavelength difference between the band of order m at $\lambda^{(m)}$ and λ_{cut}, the coupling wavelength corresponding to a mode with effective index equal to the index of refraction of the cladding n_2 [1]. In Section 3.2.2.2 we noted that the product of the transverse component $u_{cl}^{(m)}$ of the propagation constant of the cladding mode and the cladding radius b can be approximated by the roots of the Bessel function of order zero ($u_{cl}^{(m)} \cong j_m/b$, where $J_0(j_m)=0$). Thus combining the expressions for $u_{cl}^{(m)}$ (Equation (3.21)) and the phase-matching condition (Equation (3.1)), one can show that [1,95],

$$\lambda^{(m)} - \lambda_{cut} \approx \frac{\lambda_{cut}^2 \Lambda}{8 n_2} \frac{m^2}{b^2}, \tag{3.38}$$

where the effective index of the guided mode (n_{eff}) is assumed to be equal at $\lambda^{(m)}$ and λ_{cut} [1]. Equation (3.38) reveals that the wavelength separation between $\lambda^{(m)}$ and λ_{cut} is an increasing function of the order m and the grating period Λ. Thus for a given period, the wavelength difference will increase as we move to higher order cladding modes. Both these observations are confirmed by the characteristic curves (Figures 3.23 to 3.25) in Section 3.2.3.2.

If m is small $\lambda^{(m)}$ and λ_{cut} can be assumed to be very close and the wavelength separation $\delta\lambda^{(m,m+1)}$ between the resonance bands of orders m and m+1 can be obtained from Equation (3.38) [1],

$$\delta\lambda^{(m,m+1)} = \lambda^{(m+1)} - \lambda^{(m)} \approx \frac{\lambda_{cut}^2 \Lambda}{8 n_2} \frac{2m + 1}{b^2}. \tag{3.39}$$

It can be seen that the wavelength separation between the resonance bands increases as the value of m is increased which is consistent with the transmission spectrum of a typical long-period grating operating in the normal region (Figure 3.4). Also the wavelength separation between any two loss bands increases as the cladding radius b is reduced. This observation will be confirmed experimentally when we discuss etched long-period gratings in Section 3.4.2.1. It is important to stress here that Equation (3.39) is approximate and is only valid for small values of m.

We now use the coupled mode analysis of Chapter 2 to determine the power transmitted through a grating. In Section 2.3.2.1 we derived an expression (Equation (2.14)) for the power coupled from one forward-propagating mode to another in the presence of a perturbation. The ratio C of the power coupled to a cladding mode of order m to the initial power in the fundamental guided mode is hence approximated by [59],

$$C = \frac{P^{(m)}(L)}{P_{01}(0)} = \frac{\sin^2\left[\kappa^{(m)} L \sqrt{1 + \left(\frac{\delta^{(m)}}{\kappa^{(m)}}\right)^2}\right]}{1 + \left(\frac{\delta^{(m)}}{\kappa^{(m)}}\right)^2}, \tag{3.40}$$

where L is the length of the grating and $\kappa^{(m)}$ and $\delta^{(m)}$ are the coupling coefficient and the detuning parameter for the corresponding cladding mode, respectively. The detuning parameter at a wavelength λ is defined as,

$$\delta^{(m)} = \frac{1}{2}\left(\beta_{01} - \beta^{(m)} - \frac{2\pi}{\Lambda}\right) \approx \frac{\pi}{\Lambda}\frac{\left(\lambda^{(m)} - \lambda\right)}{\lambda^{(m)}}, \tag{3.41}$$

and is zero at the phase-matching wavelength $\lambda^{(m)}$. The detuning ratio for the cladding mode of order m is given by $\delta^{(m)}/\kappa^{(m)}$ and its magnitude should be minimized for sufficient transfer of power from the guided to the cladding mode. The normalized power T transmitted by the fundamental guided mode through the grating is then given by,

$$T = \frac{P_{01}(L)}{P_{01}(0)} = \frac{\cos^2\left[\kappa^{(m)}L\sqrt{1 + \left(\frac{\delta^{(m)}}{\kappa^{(m)}}\right)^2}\right] + \left(\frac{\delta^{(m)}}{\kappa^{(m)}}\right)^2}{1 + \left(\frac{\delta^{(m)}}{\kappa^{(m)}}\right)^2}, \tag{3.42}$$

which at the phase-matching wavelength reduces to expression for the peak isolation T_0 of the grating,

$$T_0 = \cos^2\left(\kappa^{(m)}L\right). \tag{3.43}$$

The grating normalized transmission is expressed in decibels (dB) and typically ranges from 5 dB (68.3% coupling) to 35 dB (99.97% coupling). Equation (3.43) reveals that the minimum power in the guided mode is transmitted at the phase-matched wavelength and depends on the coupling coefficient and the length of the grating. Thus if the length of the grating is known, the coupling coefficient and hence the peak index change can be calculated by combining Equations (3.33), (3.37) and (3.43). During the grating writing process the exposure to UV-radiation is continued till the power transmission at the coupling wavelength reduces to almost zero. This is called the condition of complete power transfer to the cladding mode and corresponds to [1],

$$\kappa^{(m)}L = \frac{\pi}{2}. \tag{3.44}$$

At the phase-matched wavelength, the complete power transfer yields C=1 and T=0. If a fixed length of the fiber is UV irradiated, total power transfer is obtained by increasing the peak index change and hence the coupling coefficient. The exposure is stopped as soon as the maximum loss starts receding. For $\kappa^{(m)}L>\pi/2$, the power in the cladding mode starts to couple back into the fundamental guided mode, leading to an increase in the guided mode transmitted power. The oscillation of power is consistent with the mode coupling mechanism between two co-propagating modes (Figure 2.7). It is important to note here that for a fixed Δn, the complete power transfer occurs for a particular cladding mode and all other cladding modes are either under- or over-coupled. Hence it is expected that all the resonance bands will have different peak losses in the transmission spectrum (Figure 3.4). For most applications the band at the highest wavelength (within the optical source spectrum) is monitored during the writing process until the complete power transfer condition is met.

For gratings with the same period that are written for either complete power transfer or the same isolation, for a given order m, the coupling wavelengths will be functions of the grating length. This is because we need to maintain the product $\kappa^{(m)}L$ constant to satisfy the above condition which implies that if the wavelength dependence of the coupling coefficient is ignored, different values of L will require distinct peak index changes Δn (Equation (3.32)). We have already seen in Section 3.2.3.3 that the characteristic curves are functions of Δn (Figure 3.29) and hence the length-dependence of the spectral position follows from that.

Since the effective index of the guided mode changes during the UV exposure, a shift in the spectral position of the resonance band is also expected (Figure 3.29) during the grating writing process. Figure 3.30 depicts the calculated evolution of a resonance band in a grating of length 2 cm and period 360 μm in SMF-28 fiber. It is assumed that the time rate of index change is uniform and grating is written for 5 minutes when the peak loss reaches 20 dB (T=0.01). The excess loss introduced by the grating is neglected in Figure 3.30 but is about 0.2 dB for a typical grating [1]. In Section 3.3 we will analyze different techniques to fabricate long-period gratings and the evolution seen in Figure 3.30 will be confirmed experimentally. The magnitude of shift during the fabrication process is a function of the grating period, the writing conditions and the fiber parameters.

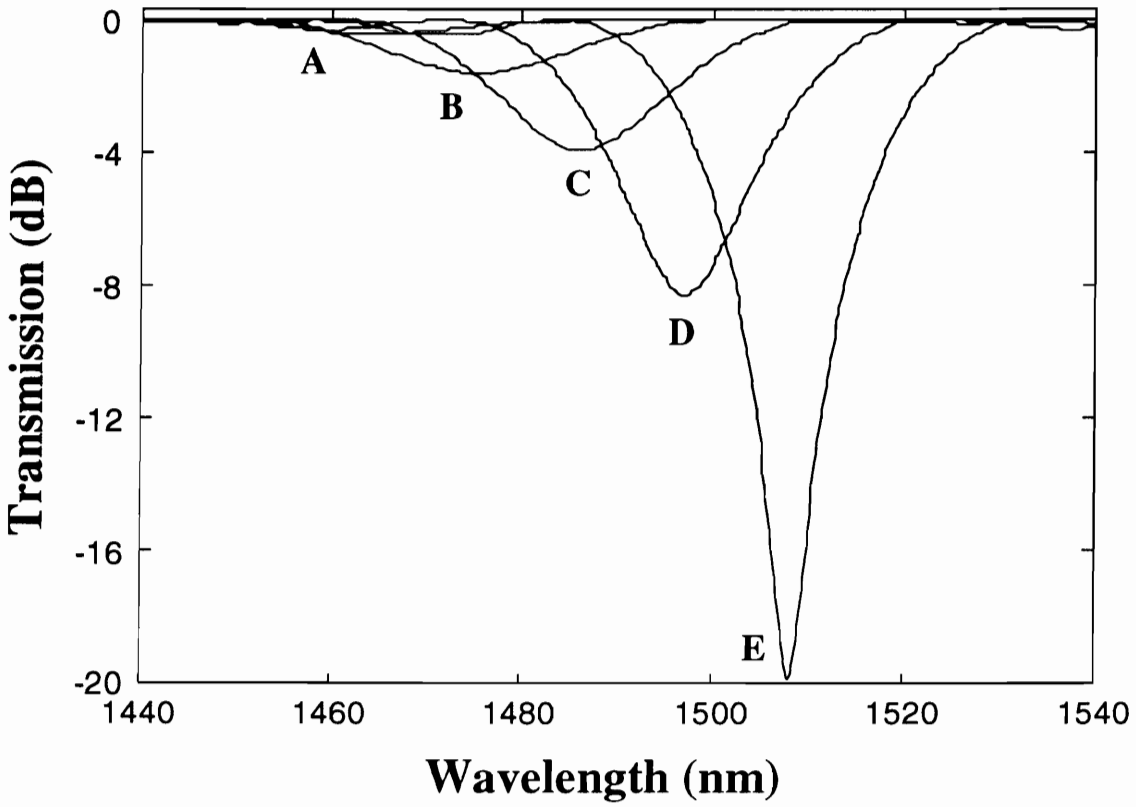

Figure 3.30. Theoretically obtained evolution of a long-period grating in SMF-28 fiber with Λ=360 μm (normal region of operation). The curves A through E represent the transmission spectrum at intervals of one minute each from the time exposure is initiated. The shift to longer wavelengths and the increase in maximum loss can be attributed to the index change during the writing process.

We now determine an approximate expression for the full-width at half maximum (FWHM) for a resonance band of a long-period grating assuming complete power transfer. Putting C=1/2 in Equation (3.40) and using Equation (3.44) we obtain,

$$x^2 - 2\sin^2(\pi x/2) = 0\,, \tag{3.45}$$

where Equation (3.41) provides,

$$x = \sqrt{1 + 4L^2\left(\frac{\lambda^{(m)}}{\Lambda}\right)^2\left(\frac{1}{\lambda_s} - \frac{1}{\lambda^{(m)}}\right)^2}\,. \tag{3.46}$$

In the above equation we have used the phase-matching condition and assumed that the cladding mode effective indices at the 3-dB loss wavelength λ_s and the coupling wavelength $\lambda^{(m)}$ can be approximated by the index of refraction of the cladding n_2. We have also assumed that the coupling coefficient has a negligible variation over the grating bandwidth. The solution of Equation (3.45) is obtained graphically as x=1.2798 and substituted in Equation (3,46) to yield the FWHM $\Delta\lambda^{(m)}$ [1],

$$\Delta\lambda = 2\left|\lambda^{(m)} - \lambda_s\right| \approx \frac{0.8\,\lambda^{(m)}\,\Lambda}{L}, \tag{3.47}$$

where we have assumed that $\lambda_s \approx \lambda^{(m)}$.

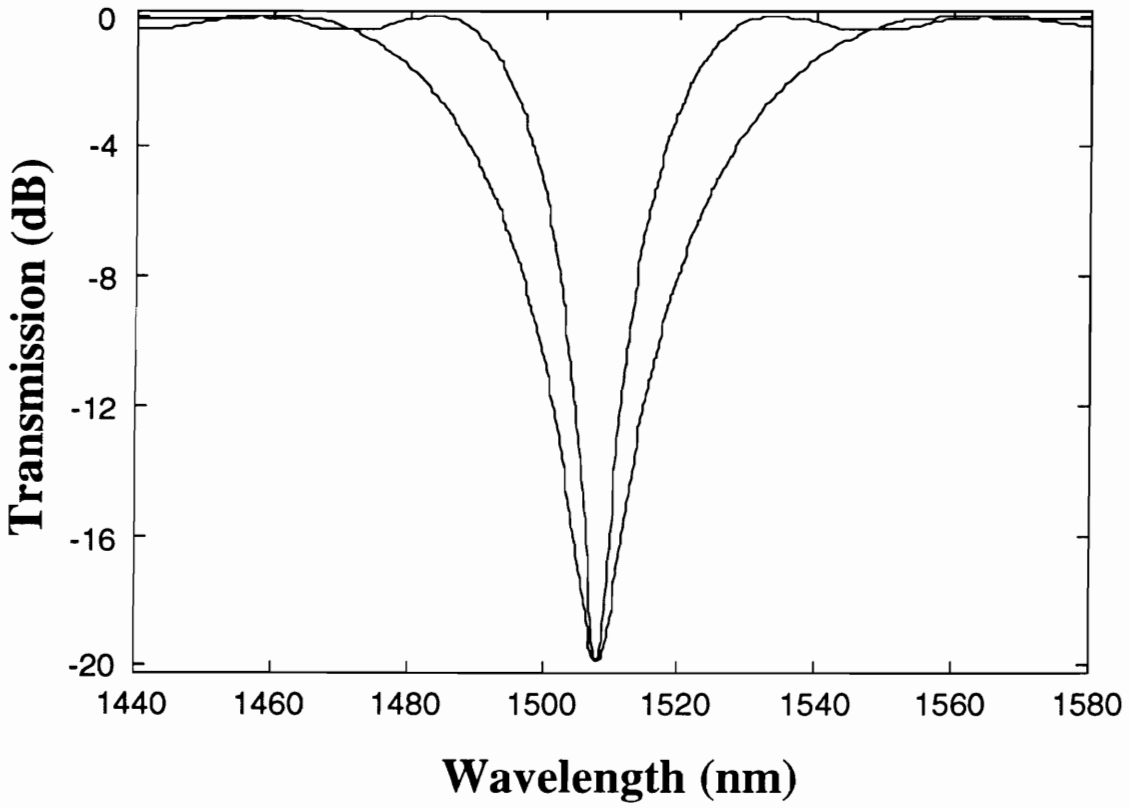

Figure 3.31. Theoretically obtained transmission spectra of two long-period gratings in SMF-28 fiber with Λ=360 μm. The inner spectrum is for a grating with L=2 cm while that on the outside is for a grating with L=1 cm. The actual resonant wavelength of the 1 cm long grating is about 1565 nm.

Equation (3.47) reveals that the FWHM or bandwidth of a resonance band is inversely proportional to the length of the grating L. Thus the resonance band can be made narrower if the length of the grating is increased which is illustrated in Figure 3.31 where we consider the transmission spectra of long-period gratings of lengths 1 cm and 2 cm, respectively. The product $\kappa^{(m)}L$ is maintained the same for both the gratings and hence the peak loss is the same (20 dB). To keep the representation simple, the two gratings are assumed to have the same resonant wavelength. In reality, the spectra in Figure 3.31 will be offset due to different coupling coefficients and hence distinct Δn. The reduction in the spectral width of the resonance band due to increase in the grating length is clearly visible. The FWHM of the two gratings are 46 nm and 23 nm for L=1 cm and L=2 cm, respectively. Equation (3.47) yields the values 43.4 nm and 21.7 nm for the corresponding gratings. The differences can be attributed to the assumptions made while deriving Equation (3.47). The sidebands in the grating spectra are due to the cosine-squared dependence of the transmission spectrum (Equation (3.42)).

In this section we investigated some important parameters of long-period gratings. We derived approximate expressions for the spectral separation of resonance bands and the full-width at half maximum (FWHM). The effect of the grating length on the width of the resonance bands was also examined. In the next section we study the various methods to fabricate long-period gratings. The fabrication set up is detailed and the influence of high temperature annealing is analyzed.

3.3 Fabrication and Annealing of Long-Period Gratings

In this section we discuss the different methods to fabricate long-period gratings by side-exposing hydrogen-loaded germanosilicate fibers. The effect of hydrogen diffusion from the grating after fabrication is analyzed and it is shown the grating spectrum can be stabilized by annealing at high temperatures [1].

3.3.1 Fabrication of Long-Period Gratings

We discuss three different methods of fabricating long-period. The first two schemes involve the use of ultra-violet radiation while the third process employs a CO_2 laser for grating production. The fabrication set ups are illustrated and the relative advantages and limitations of the three methods are investigated.

The germanium-doped fibers used for grating fabrication are hydrogen-loaded [28,29] to enhance the index change during the photosensitivity process (Section 2.2.1). Typically hydrogen is replaced with deuterium to prevent the hydroxyl loss at 1390 nm [28]. In the remainder of this discussion hydrogen will be used to denote hydrogen/deuterium in a sensitized fiber. Hydrogen-loaded fibers can be identified by the loss due to the fundamental overtone at 1240 nm. The loaded fibers are stored at either low temperature or high pressure to prevent out-diffusion of hydrogen. While the latter is cumbersome to implement, the former requires expensive freezers to maintain the fibers at around -80 °C. For this study the fibers were first hydrogen-sensitized in a high pressure chamber and then stored in a low temperature freezer. Corning SMF-28 and Flexcor 1060 fibers were the two fibers commonly employed for grating fabrication.

3.3.1.1 Excimer Laser Method

The most popular used method to fabricate long-period gratings is by employing a pulsed excimer laser and is illustrated in Figure 3.32 [1]. Amplitude masks with rectangular transmittance function were imprinted on chrome-plated glass and have a 100 mJ/cm^2/pulse optical threshold damage level [1]. Several masks with different periods were produced on the surface of a glass plate resulting in economical mask fabrication and providing easier access to different periodicities. The duty cycle of the rectangular function was 50% and the length of the mask varied from 1 to 3 cm. The KrF excimer laser (manufactured by Lumonics Corporation) produced a pulsed beam of area 2.6×1.1 cm^2, energy 250-300 mJ/pulse, repetition frequency 20 pulses/s, and pulse duration 10 ns at a wavelength of 248 nm [1]. The acrylate jacket was removed from about 3 to 4 cm length in the middle of hydrogen-loaded fiber and the fiber was aligned behind the amplitude mask of appropriate period. The fiber was supported on both sides of the bare region to prevent bends from influencing the coupling to cladding modes. Light from a broadband source such as an LED was launched from one end of the fiber while the normalized transmission spectrum was obtained on the optical spectrum analyzer (OSA) display [1]. To avoid blazing the grating, it was ensured that the fiber was exactly parallel to the axis of the mask. A blazed grating couples the fundamental guided mode to cladding modes that lack azimuthal symmetry [57], as discussed in Section 3.2.4.1.

The grating transmission spectrum was monitored real-time as the bare fiber was exposed to UV radiation and resonance bands corresponding to coupling to different cladding modes were observed. Figure 3.33 shows the evolution of the resonance band at the highest wavelength in the optical source spectrum for a standard AT&T dispersion-shifted fiber (DSF) [1]. The resonance band shifts to longer wavelengths and the peak loss increases as the UV irradiation is continued. The spectral shift can be attributed to the increase in the guided mode effective index while the isolation grows due to enhancement in the coupling coefficient. This is in agreement with the theoretical evolution of a long-period grating in Figure 3.30. As discussed earlier, the shift in a resonance band during the writing process is a function of the order of the corresponding cladding mode. The band at the highest wavelength typically shifts from 40 to 100 nm during the fabrication process. The wavelength shift can be related to the magnitude of index modulation during the writing process and hence used to predict the rate of index change in the fiber core [96].

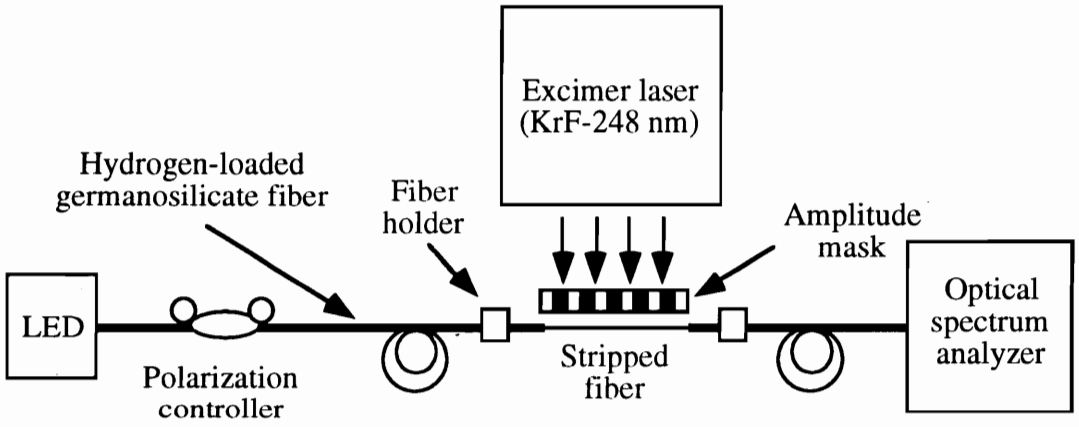

Figure 3.32. Setup to fabricate long-period gratings using an excimer laser [1].

The exposure to UV is stopped when the complete power transfer condition (Equation (3.44)) is satisfied for the resonance band with the longest coupling wavelength in the optical source spectrum. Time required to produce a grating for this condition varies from 5 to 15 minutes for fibers with 3-10% GeO_2 and 2-3% hydrogen [1]. The coupling to different cladding modes is clearly evident in the grating transmission spectrum of Figure 3.4. Each resonance band has a different peak loss or isolation due to the distinct coupling coefficients for the corresponding cladding modes. We note from Figure 3.33 that terminating the UV exposure before complete power transfer is achieved will result

in smaller isolations and coupling wavelengths. This concept can be used to obtain gratings with different spectral characteristics [30]. The presence of sidebands at only wavelengths smaller than the coupling wavelength will be explained in Section 3.4.

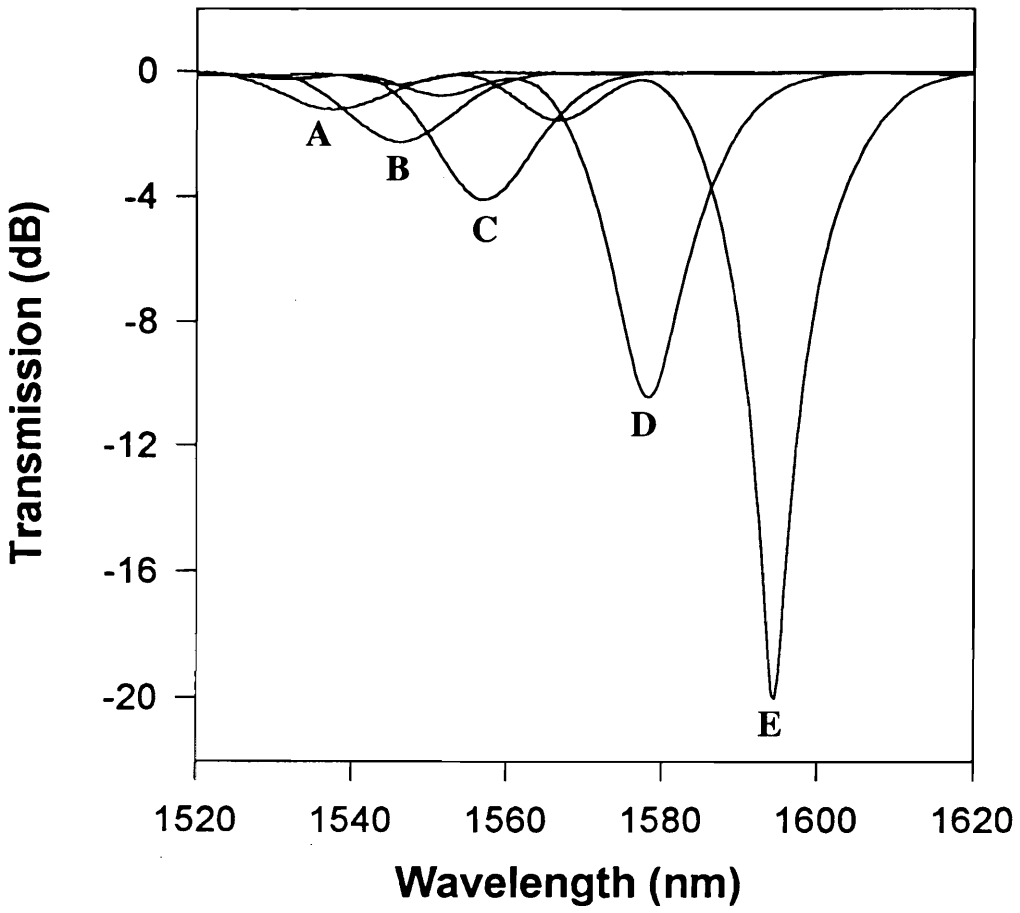

Figure 3.33. Evolution of a typical long-period grating on UV exposure [1]. Curves A through E represent the transmission spectrum in one minute intervals after the exposure is initiated. The grating is written in AT&T dispersion-shifted fiber with Λ=488 μm.

The major advantage of using the excimer laser-based fabrication method is that a number of gratings with the same period may be easily batch-produced [1]. The mass production is done by placing more than a single fiber behind the amplitude mask as shown in Figure 3.34. Although only one grating is monitored during the writing process, if the transverse profile of the UV radiation is assumed invariant, all the gratings in the batch are expected to have similar transmission spectra.

In the above method the amplitude mask can be replaced with a variable size slit that can be translated across the UV beam and the fiber. The width of the aperture is set to half the desired periodicity and the fiber is irradiated for a fixed interval of time. The aperture is then translated a distance equal to the grating period and the fiber is again exposed. The process of exposing alternate half-periods is continued till the desired isolation or coupling wavelength is achieved. The aperture method is advantageous because the same slit can be used to obtain gratings with different periods and/or duty cycle in index modulation by selecting appropriate aperture widths and translation distances. Moreover the grating can also be easily chirped in period or in index change along the fiber axis by making the aperture size and the exposure duration a function of the grating length. The above method can also be implemented by translating the fiber while keeping the aperture stationary.

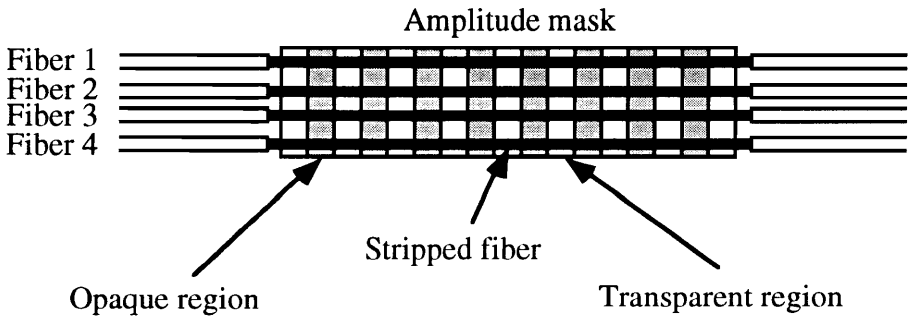

Figure 3.34. Procedure to fabricate multiple long-period gratings using the broad dimensions of an excimer laser beam. The number of gratings that can be written is limited only by the excimer beam or amplitude mask dimension orthogonal to the fiber axes [1].

3.3.1.2 Continuous-Wave Laser Method

In this section we outline the process to manufacture long-period gratings using radiation from a continuous-wave (CW) UV source. The dimensions of the CW beam in a frequency-doubled (FRED) argon-ion laser typically range in hundreds of micrometers. By placing the fiber behind an amplitude mask of rectangular transmittance function, refractive index modulation of the core can only be obtained over the length equal to the beam dimension of the UV source along the fiber axis. Thus the small beam size can severely limit the grating length and result in location of the resonance bands at undesired

wavelengths and/or provide inadequate loss at the resonant wavelengths. The limitation imposed by FRED laser on the grating length can be overcome by scanning the UV beam along the axis of the amplitude mask and the fiber.

The set up for fabricating long-period gratings using UV radiation from a Coherent Incorporated argon-ion FRED laser is shown in Figure 3.35. Blue light at 488 nm was frequency-doubled using a BBO crystal causing the cavity to lase at 244 nm. The UV power obtained in a 500 μm×900 μm output beam was typically limited to a maximum of 160 mW during grating fabrication. The beam was directed to the surface of a UV-reflecting mirror and focused to approximately 500 μm×10 μm size using a cylindrical lens. The mirror and the lens were mounted together on a motorized translation stage offering movement parallel to the radiation incident on the mirror. The speed of translation was controlled using the output from a DC power supply. The output voltage V of the supply could be ramped to change the scan rate of the beam.

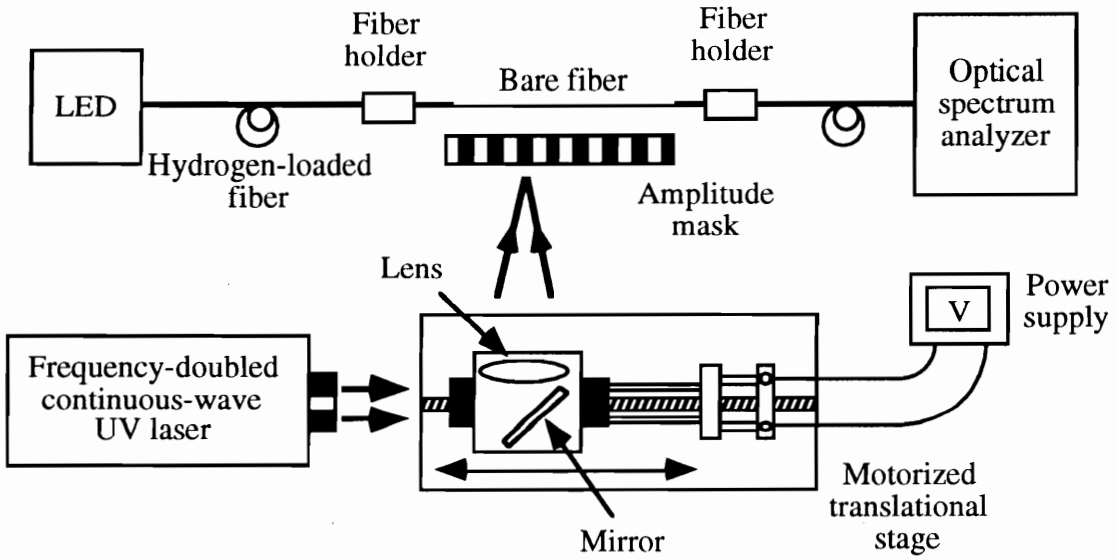

Figure 3.35. Setup to fabricate long-period gratings using FRED-CW laser. The lens and the mirror are translated simultaneously to scan the UV beam across the stationary amplitude mask and fiber.

The combination of the amplitude mask and the bare hydrogen-loaded germanosilicate fiber was placed at the focal point of the cylindrical lens. The height of the fiber from the base was adjusted until a suitable pattern was obtained on a UV fluorescent card located

behind the fiber. The growth of the grating was monitored real-time as the beam was scanned along the fiber axis. Due to beam scanning, any non-uniformity in its profile along the fiber axis was averaged out over the grating length. The exposure was stopped once the desired resonance band reached a particular wavelength or isolation. Typical grating fabrication times vary from 10 to 20 minutes for standard germanosilicate fibers with 2-3% hydrogen and periods in the normal region. Figure 3.36 shows the post-annealed spectrum of a long-period grating written in SMF-28 with period Λ=320 μm and length L=1.4 cm. Annealing is required to stabilize the grating spectrum following the fabrication process and will be discussed in detail in Section 3.3.2.

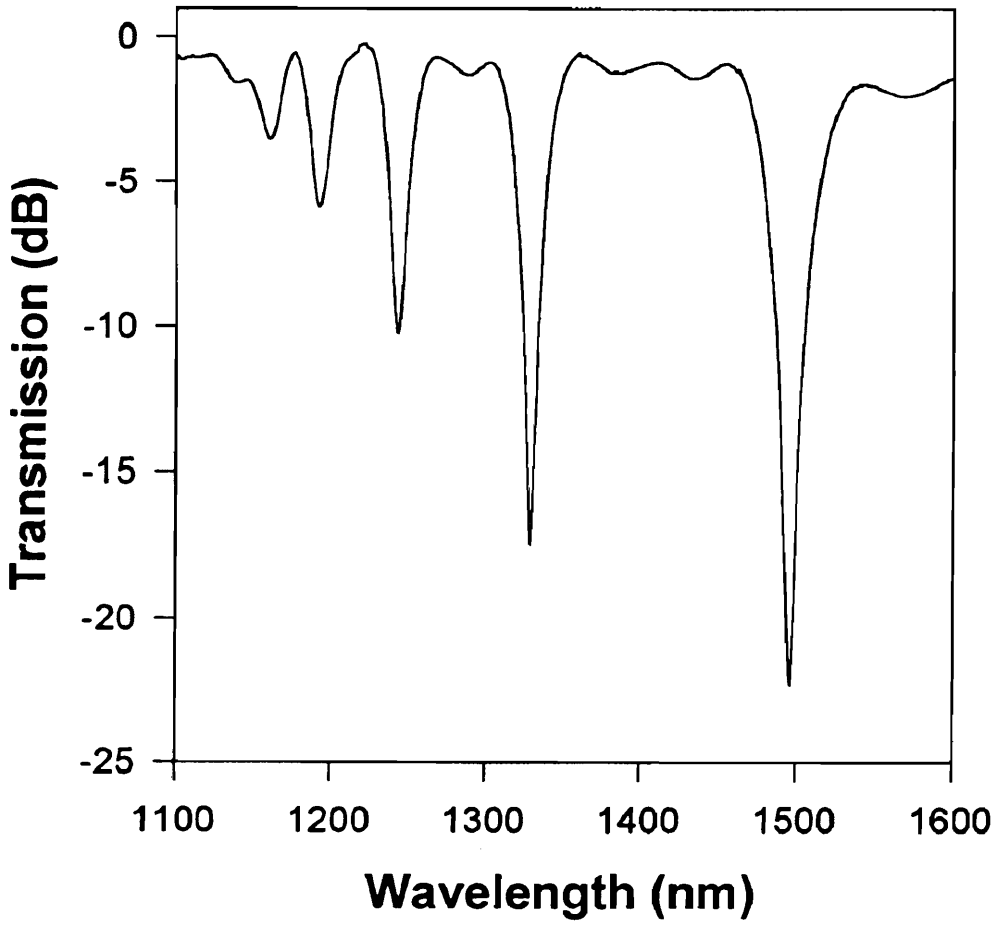

Figure 3.36. Transmission spectrum of a long-period grating written in SMF-28 fiber using the CW writing method. The periodicity of 320 μm implies that all the resonance bands operate in the normal region.

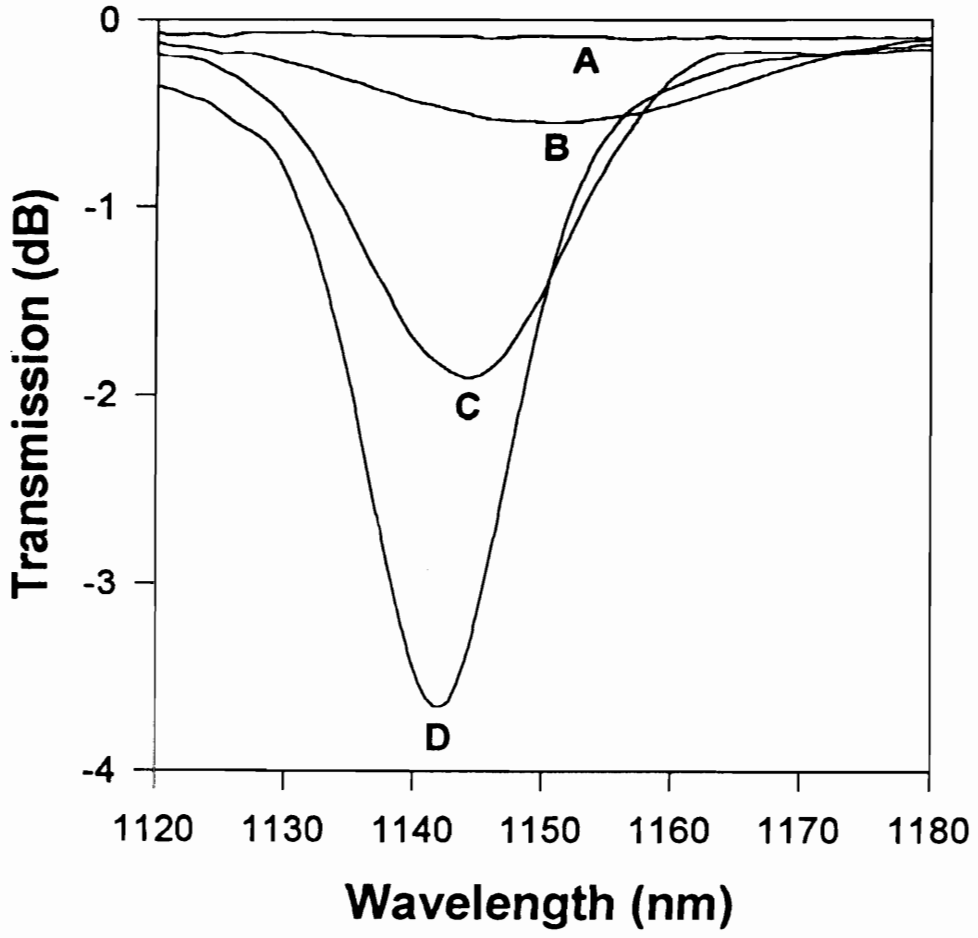

Figure 3.37. Growth of a long-period grating band in the anomalous region. The grating was fabricated in Flexcor 1060 fiber with Λ=40 μm using CW exposure. Curves A through D represent the transmission spectrum at 10 minute intervals.

Figure 3.37 depicts the growth of a resonance band in a grating with Λ=40 μm in Corning 1060 Flexcor fiber using the CW writing technique. Since this period corresponds to the anomalous region of operation for this fiber (Figure 3.27), the resonance band moved to shorter wavelengths with increased exposure to UV radiation. The increase in the peak loss can again be attributed to the enhancement of the coupling coefficient between the guided and cladding modes. Figure 3.37 should be compared to Figure 3.33 which illustrates the evolution of a band in the normal region. For a period of 40 μm, the coupling of the guided mode occurs to cladding modes with very large order m. It can be shown that for such higher order modes fractional changes in the core effective index during the writing process do not significantly alter the phase-matching wavelength.

Hence spectral shifts of typically less than 10 nm are obtained during the grating fabrication. The small value of the peak loss for a grating written for complete power transfer (Figure 3.37) can be attributed to the poor modal overlap between the guided mode and the higher order cladding mode involved in coupling. Thus for a fixed UV power, gratings operating in the anomalous region require increased exposure duration than those in the normal region. It is important to note here that the shift for a band in the anomalous region will be to shorter wavelengths only if the differential effective index between the guided and cladding modes increases during exposure.

During the CW writing process, the grating length as well as the index of refraction of the core are changing. Hence the change in the transmission spectrum of the grating becomes more complicated than in the case when an excimer laser is used. Since the overall rate of change in effective index over the grating length is smaller, the duration required for CW grating fabrication is longer than that for an excimer laser. For a given fiber, the length and the coupling coefficient are functions of the laser power and the scanning speed. Enhancing the voltage V of the power supply increases the length of the grating for the same exposure duration. If the UV power is kept constant, a higher value of V reduces the peak index change along the grating length and hence results in a smaller coupling coefficient for a given resonance band. Thus the final grating spectrum is a function of the laser UV power and the beam scanning speed, and optimization of these parameters is required to write a grating with a particular period in the minimum time possible.

The main disadvantage of using the CW exposure is the limited beam dimension in the direction transverse to the fiber axis. The small beam size of the focused beam prevents the fabrication of more than one grating during one complete scanning cycle. Although the beam can be expanded in the transverse direction, this might introduce distortion and also reduce the average power, resulting in requirement of increased exposure duration. The CW exposure though, offers the advantage of chirping the grating during the translation process. By ramping the voltage V, the index modulation can be made a linear function of the grating length. Quadratic and cubic chirping functions can be obtained by similarly manipulating the voltage of the power supply. The variable slit method can also be employed with the CW exposure to obtain desired duty cycles and grating periods. We have successfully used amplitude masks and slits to fabricate long-period gratings using CW irradiation.

3.3.1.3 CO_2 Laser Method

In this section we introduce a novel method to fabricate long-period gratings without using expensive UV pulsed or CW lasers. The technique uses the concept that refractive index changes can be introduced in hydrogen-loaded germanosilicate fibers by simple thermal treatment (Section 2.2) [28,29].

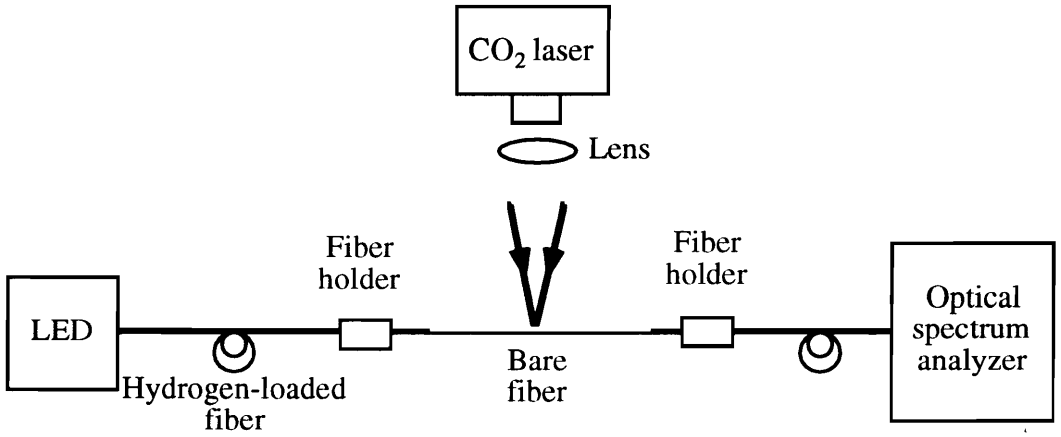

Figure 3.38. Setup to fabricate long-period gratings using CO_2 laser. The fiber holders are mounted on a translation stage to enable longitudinal movement of the fiber.

The set up to fabricate long-period gratings using thermal exposure is shown in Figure 3.38. The beam from a low power CO_2 laser was focused on a plane containing an optical fiber held taut between two fiber holders mounted on a translation stage. Since the CO_2 beam (λ=10.6 μm) is invisible to the human eye, its location on the fiber was traced using a He-Ne laser pointer (λ=633 nm). The CO_2 output simply serves to increase the temperature of the fiber and hence index changes are produced due to thermal effects [28,29]. The beam was first translated in a direction orthogonal to the fiber axis to induce index change across the core cross-section. The speed of translation determines the magnitude of peak refractive index change with smaller speeds producing larger index changes. Very low translation speeds were found to induce permanent damage in the fiber and hence proper precautions need to be taken during this process. The fiber was then translated along its axis by a distance that was equal to the desired grating period. The duty cycle was determined by the size of the CO_2 beam and was varied by moving the fiber away from the focal plane. To avoid blazing the grating it was necessary to have the fiber perpendicular to the direction of propagation of the beam.

With each exposure the isolation of the monitored resonance band increases rapidly and hence the power of the laser has to be carefully selected to prevent overcoupling. Figure 3.39 depicts the transmission spectrum of a grating written in Corning 1060 Flexcor fiber. The number of half-periods needed for almost complete power transfer was just 7. A detailed analysis of the effect of the laser power, beam size and transverse scanning speed will reveal the effectiveness of this method in terms of fabrication time and repeatability.

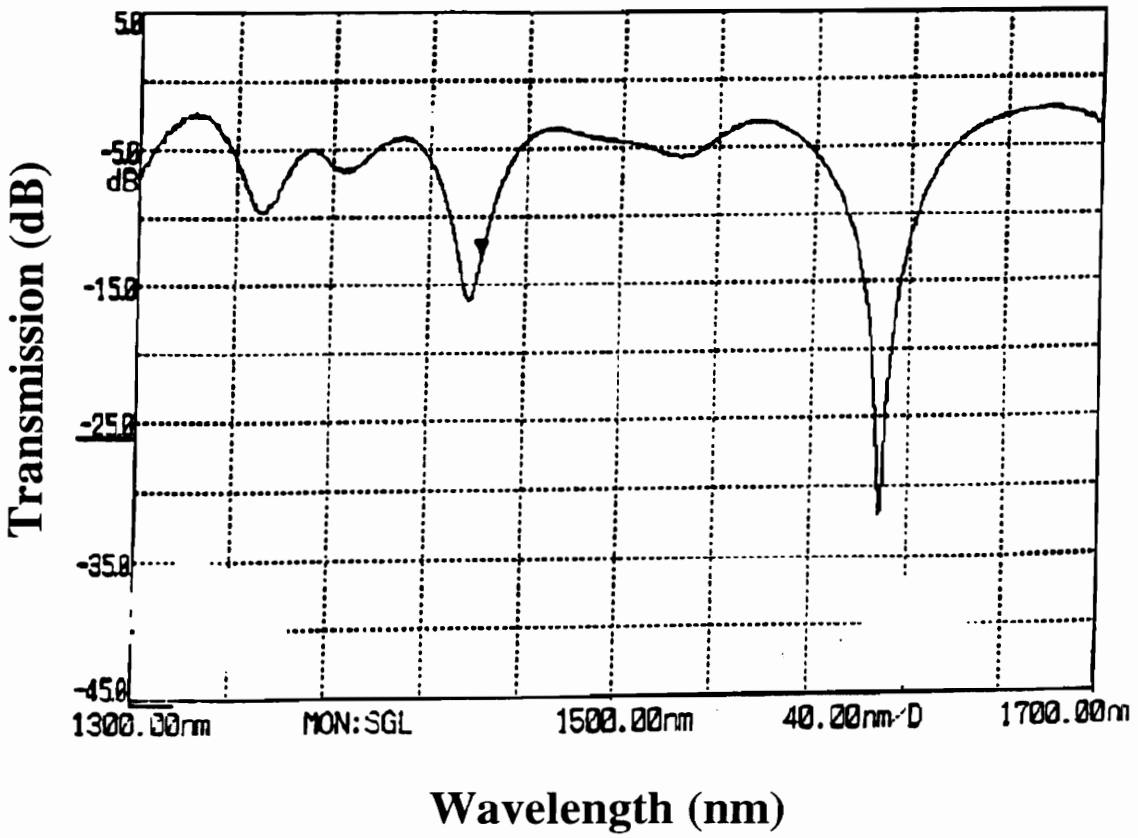

Figure 3.39. Transmission spectrum of a long-period grating written in Flexcor 1060 fiber using the CO_2 laser fabrication method.

Although in its early stage of development, the grating fabrication technique using CO_2 lasers has a lot of potential. The use of cheap CO_2 lasers without resorting to UV-based lasers and amplitude masks is expected to drastically reduce the cost of manufacturing gratings. The process can also be used to manufacture a multitude of gratings simultaneously using the schematic shown in Figure 3.40. A number of fibers are arranged parallel to one another and the CO_2 beam is translated across the fibers in a

manner shown in Figure 3.40. The translation can be done using a motor interfaced to a computer to eliminate human involvement. Another way to implement this scheme is by keeping the beam stationary and translating the fibers in a manner similar to that shown in Figure 3.40. The minimum period that can be obtained using the CO_2 laser is diffraction-limited by the beam. The limitation of the CO_2 method might be the inability to precisely control the grating period due to the diffusion of thermal energy and the effect is expected to be more pronounced for smaller grating periods. Amplitude masks that can withstand the heat generated by CO_2 lasers can be used to regulate the beam size and hence produce gratings of desired periods.

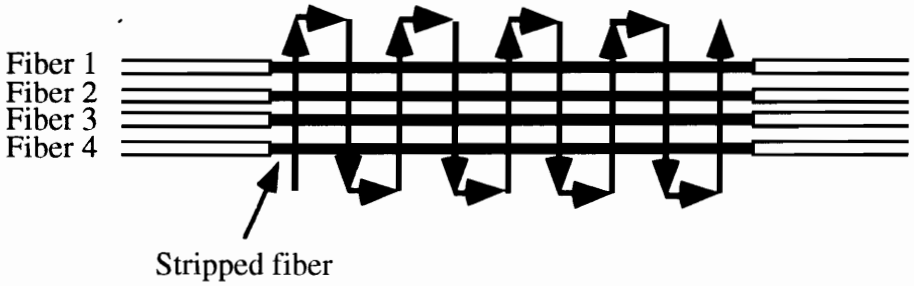

Figure 3.40. Fabrication of multiple long-period gratings using thermal treatment from a CO_2 laser. The arrows depict the direction of the beam traversal.

Another method to produce long-period gratings was recently proposed by Narayanan *et al.* [97]. The two-step technique first requires a pulsed CO_2 laser to create periodic ablations in the outer cladding surface. The separation between the resulting V-grooves determines the period Λ of the grating. The second step is to anneal the fiber with an electric arc which causes the core to deform in the regions of the grooves. The periodic microbending of the core causes the light to couple to forward-propagating cladding modes that are not circularly-symmetric. Using only 10 grooves and Λ=610 μm, a grating with 23 dB peak isolation has been demonstrated in dispersion-shifted fiber at a coupling wavelength of 1536 nm [99]. The increased index change obtained during this method results in a large value of coupling coefficient which causes these gratings to have increased bandwidths and hence be useful for only broadband applications [97].

We thus see that long-period gratings can be fabricated by a number of methods. Pulsed and continuous-wave exposure from UV sources can be used to write gratings using inexpensive amplitude masks or slits of variable sizes. A method employing the thermal

sensitivity of hydrogen-sensitized germanosilicate fibers was also used to demonstrate grating fabrication.

3.3.2 Annealing of Long-Period Gratings

Typically the magnitude of hydrogen present in an optical fiber for grating fabrication is far in excess of that required to achieve a given refractive index change. Thus at the culmination of the writing process there is a finite amount of unused hydrogen remaining in the cladding that can significantly influence the grating transmission spectrum. In this section we analyze the effect of residual hydrogen and show that the grating spectrum can be stabilized by annealing at high temperatures [1].

Prior to modulating the index of the fiber core, the hydrogen concentration in the fiber can be assumed to be uniform. The process of index modulation uses hydrogen in only the regions of the core that are exposed to UV radiation or thermal energy. The cladding and the unexposed parts of the core hence possess a higher concentration of hydrogen once the writing process is terminated. To maintain equilibrium hydrogen starts to diffuse from the high concentration regions to the exposed areas of the core and also out to the surroundings. The diffusion process raises the average index of the core and results in an increase in the value of effective index of the guided mode. This implies that for operation in the normal region the initial diffusion of hydrogen will cause the resonance bands to move to longer wavelengths. Figure 3.41 depicts the shift in the spectral location of a resonance band after the fabrication process. The movement to higher wavelengths is clearly evident during the first few hours after fabrication. The diffusion into the exposed part of the core lasts a few hours at room temperature until equilibrium is attained. The shift in the resonance bands is initially large but eventually tapers off close to the equilibrium condition. The resonance bands can shift by as much as a few hundred nanometers to longer wavelengths depending on the residual hydrogen concentration and the order of the cladding mode involved in coupling.

At equilibrium, hydrogen concentration is uniform throughout the fiber but still larger than that in the surroundings. The concentration imbalance causes hydrogen to diffuse from the fiber into the atmosphere. The diffusion from the fiber reduces the average index of both the core and the cladding and forces the resonance bands to move back to lower wavelengths as shown in Figure 3.41. The process of out-diffusion is very slow at

room temperature and usually takes hundreds of hours to be completed. The resonance bands typically move to wavelengths 50-100 nm lower than the corresponding positions after fabrication and this is presumably because the out-diffusion process removes all the index-raising hydrogen remaining in the fiber after the fabrication is completed.

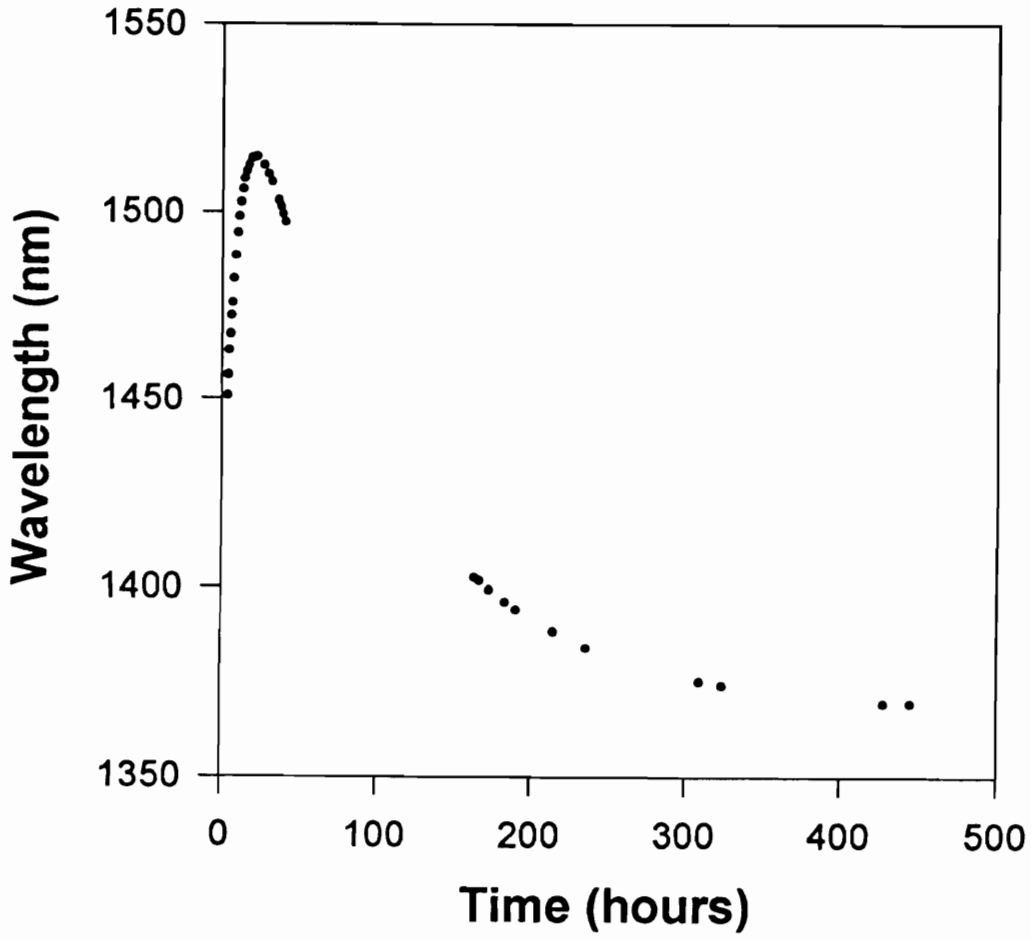

Figure 3.41. Variation in the spectral position of a resonance band with time for a long-period grating. The grating was left at room temperature following fabrication (t=0). The discontinuity results form the intermittent collection of data.

The diffusion process in which hydrogen initially reaches equilibrium in the fiber and then moves to the outer atmosphere introduces a time delay of a few weeks between the fabrication process and the instant when the grating spectrum stabilizes. The prolonged waiting period might not feasible during the commercial production of these gratings. To overcome this limitation, hydrogen can be removed from the fiber in a matter of few

hours by high temperature annealing [1]. The annealing serves to diffuse hydrogen from the grating into the atmosphere more than two orders of magnitude faster than that at room temperature and hence, provides short-term stability to the grating spectrum. Figure 3.42 shows the effect of high temperature (150 °C) annealing on the three resonance bands of a grating [1]. As can be seen, the resonance bands stabilize to their final values in just a few hours after the annealing process is initiated. Thus annealing of long-period gratings following the writing process is an integral part of the complete manufacturing process.

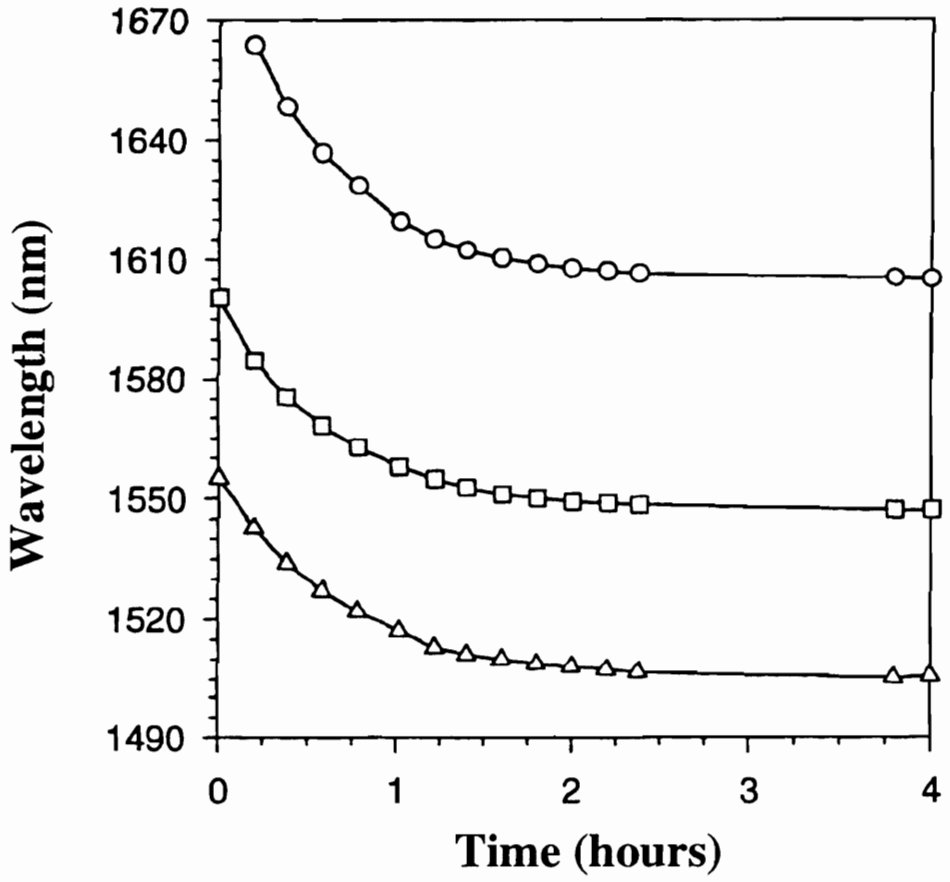

Figure 3.42. Effect of annealing (at 150 °C) on three resonance bands of a grating written in DSF [1]. Time t=0 corresponds to the initiation of the annealing process.

Most long-period gratings are used as components in systems that might need to operate at temperatures higher than room temperature. Ergodan *et al.* [98] have shown that in fiber Bragg gratings written in germanium-doped fibers, a portion of the UV-induced

index change is unstable and decays over time depending on the operating temperature. The instability arises from the subtle reduction in the concentration of the index-raising defect sites. In long-period gratings, the decay of a part of the induced index modulation causes the resonance bands operating in the normal region to shift to lower wavelengths. Moreover, for a grating satisfying the complete power transfer condition, an accompanying reduction in the coupling coefficient will reduce the peak isolation. Hence it is critical that these unstable defects are removed from the grating prior to its use. Additionally, for certain applications, such as high temperature sensing, a majority of these unstable defects have to be removed. This is again achieved by annealing the grating at high temperatures following the writing process. The pre-annealing causes a rapid decay of the unstable portion of the index change and provides long-term stability to the grating spectrum.

Thus annealing the grating serves two major purposes - removal of residual hydrogen and decay of unstable UV sites in the grating [1]. The annealing process involves heating the gratings to an elevated temperature for a period dependent on the expected lifetime of the device. The annealing temperature varies from 150 °C to 200 °C while the duration of this thermal treatment is 10 to 20 hours. Since the removal of hydrogen and UV-sites causes the effective index of the guided mode to reduce, the resonance bands move to lower wavelengths in the normal operating region. The reduction in the coupling coefficient results in the degradation of isolation at the phase-matching wavelength. These two effects are illustrated in Figure 3.43 where the grating spectrum before and after annealing is presented. The coupling wavelength and isolation drop by 39 nm and 11 dB, respectively. Thus care has to be taken while writing a grating for specific applications and one has to account for the reduction in the values of these two parameters. A decay model for these parameters needs to be developed using the annealing temperature and duration, similar to the one for Bragg gratings [98]. Once this change in the peak index is determined, allowance has to be made for its variation during the annealing process. For example, writing a grating to a point where the desired band is overcoupled can provide the excess index change that may selectively be removed by annealing at higher temperatures. The overall shift during the annealing process is a function of the annealing temperature and duration, the order of the resonance bands and the original and residual concentrations of molecular hydrogen (hence the exposure conditions). Thus a grating can be selectively annealed at a given temperature for a duration that provides the desired coupling wavelength or isolation.

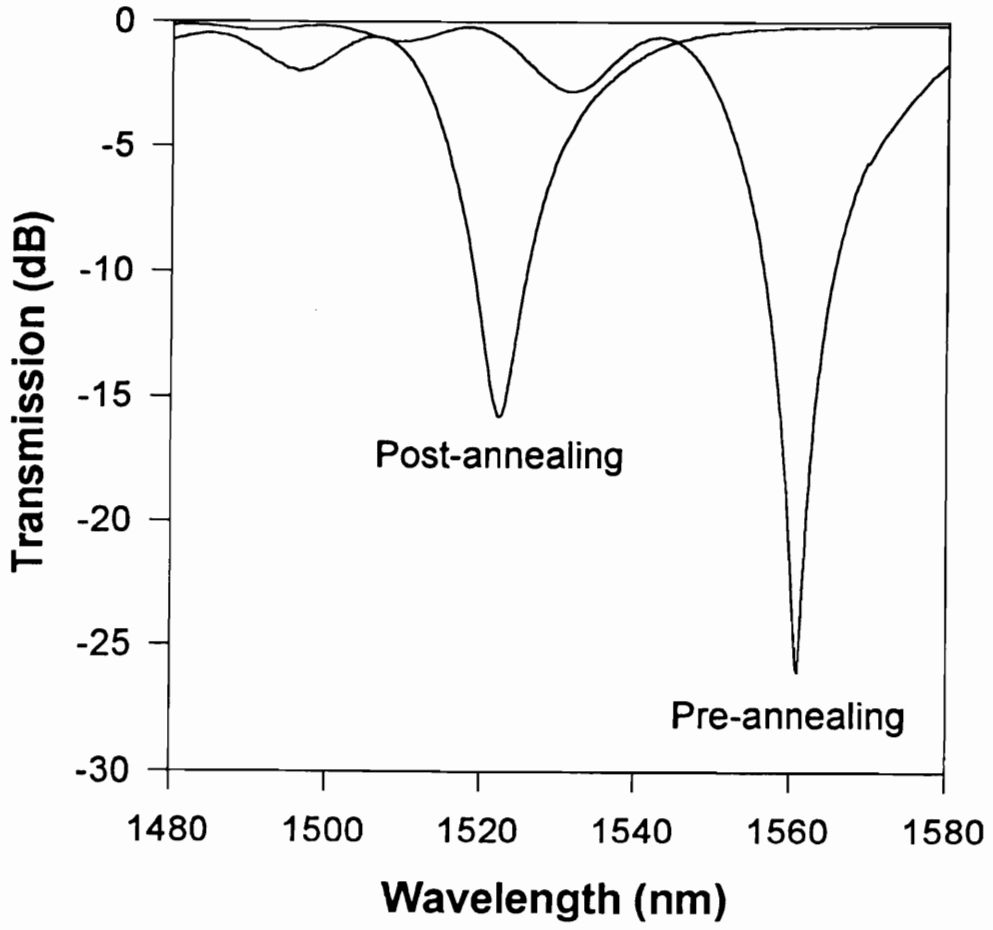

Figure 3.43. Transmission spectra of a long-period grating before and after annealing at 150° C for 10 hours. Note the reduction in the coupling wavelength and isolation.

Once the grating has been annealed, the coupling wavelength of a particular band might need to be tuned for a particular application. Small shifts to lower wavelengths can be obtained by heating the grating region to temperatures higher than the annealing region and inducing a rapid decay of additional index-raising UV sites. Exposing the grating uniformly to UV radiation will increase the overall effective index of the cladding mode and result in spectral shifts to longer wavelengths. Although the annealed core is devoid of hydrogen, small index modulations can still be attained with sufficient UV power. These wavelength displacements will obviously be reversed if the grating is operating in the anomalous region. We will demonstrate in Section 3.4.2.1 that the etching of the bare

cladding surrounding the grating can also be employed to shift the position of the resonance bands.

In this section we discussed the fabrication of long-period gratings. Three different methods to produce these gratings were outlined and their limitations and advantages were analyzed. It was shown that high temperature annealing stabilizes the grating spectrum by removing the residual hydrogen and certain UV-induced defects with small activation energies [1].

3.4 Optical and Physical Properties of Long-Period Gratings

In this section we discuss certain important optical properties of long-period gratings including insertion loss, back-reflection and polarization sensitivity [1]. The effects of some physical processes such as recoating [1] and etching the cladding surrounding the grating region are also investigated.

3.4.1 Optical Properties

Figure 3.44 shows the transmission spectrum of a long-period grating written in standard AT&T dispersion-shifted fiber (DSF) with period Λ=402 μm and length L=2.54 cm [1]. The peak isolation is 32.1 dB at a wavelength of 1517 nm. The high loss achieved at the resonant wavelength makes long-period gratings attractive for applications requiring notch filters. Also, the bandwidth with losses greater than 20 dB and 3 dB are 4 nm and 22 nm, respectively [1]. The full width at half maximum (FWHM) or 3-dB width for this grating is calculated as 19.2 nm (Equation (3.47)). The large value of the FWHM gives long-period gratings an advantage over other filters such as fiber Bragg gratings in broadband applications. For a grating written for complete power transfer, the resonance band typically has an isolation varying from 15 to 35 dB and FWHM between 20 and 30 nm. The out of band losses for wavelengths far off from the phase-matching wavelength are 0.2 dB [1]. The small insertion loss enables concatenation of two or more such devices with similar resonant wavelengths for applications that require large isolation.

The polarization-mode dispersion and polarization-dependent loss of a typical grating are 0.01 ps and 0.02 dB, respectively [1]. The polarization-mode dispersion gives an estimate of the time difference for grating traversal between two signals launched along

the orthogonal axes of the fiber. The polarization-dependent loss is a measure of the difference in the losses of the two orthogonal signals. The negligible polarization sensitivity of long-period gratings makes them attractive for several different applications in optical fiber communication and sensing systems.

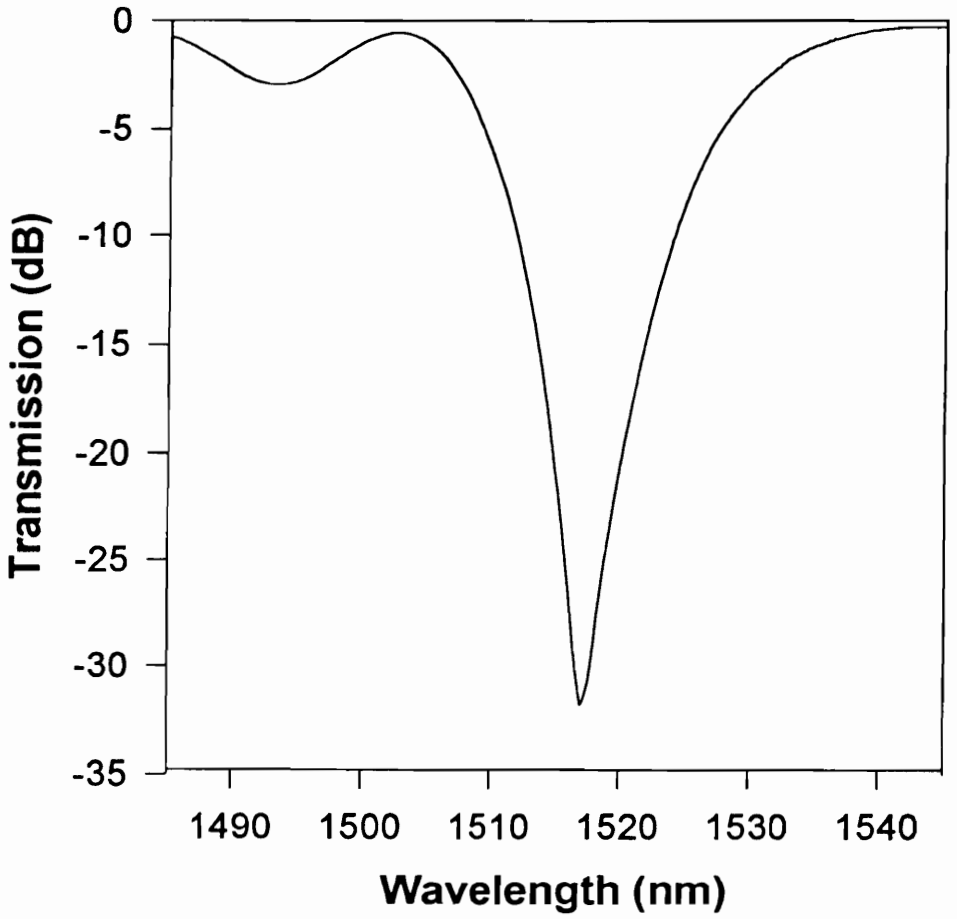

Figure 3.44. Transmission spectrum of a strong grating written in AT&T DSF with Λ=402 μm and L=2.54 cm using the excimer laser method [1].

The spectrum of the grating in Figure 3.44 possesses a sideband on the lower wavelength side of the resonance peak. Typically, a long-period grating can have two to three sidebands on the short wavelength side with peak loss ranging from 0.5 dB to 4 dB. These gratings with sidebands on only one side of the phase-matching wavelength are termed apodized gratings [66]. Apodization typically results from the variation of the peak refractive index modulation (Δn) and/or the effective index (n_{eff}) of the guided mode along the length of the grating. For gratings, such as the one in Figure 3.44,

manufactured using an excimer laser, strong non-uniformities are expected in Δn due to the inherent Gaussian envelope of the UV output [66]. This results in an self-induced chirp that causes n_{eff} to also assume a Gaussian variation along the grating length. The Gaussian profile of both Δn and n_{eff} in Bragg gratings has been previously shown to produce sidebands at only wavelengths shorter than the coupling wavelength [66]. A similar effect of non-uniformities is expected in long-period gratings also.

Maintaining a uniform beam profile across the grating length results in a constant distribution of n_{eff} and Δn, and produces symmetrical resonance bands with sidebands on both sides. The use of the scanning technique during continuous-wave (CW) exposure ensures that the non-uniformities are averaged out over the grating length and this introduces greater symmetry in the spectra of gratings compared to those fabricated without scanning the beam across the fiber. The presence of sidebands may not be desirable for certain applications such as broadband equalization of the erbium-doped fiber spectrum [30]. In Bragg gratings, the elimination of sidebands is achieved by keeping n_{eff} uniform along the grating while maintaining a Gaussian distribution for Δn [66]. This implies that by controlling the effective index and peak index change along the grating length, the sideband characteristics may be manipulated.

The effect of the grating length on the transmission was investigated in Section 3.2.4.2. It was shown that increasing the grating length serves to reduce the spectral width of the resonance bands of a grating (Figure 3.31). Figure 3.45 depicts the transmission spectrum of a grating fabricated in SMF-28 fiber using CW exposure with 110 mW of UV power. The period of the grating was 320 μm while its length was 8 cm. A special amplitude mask, longer than conventional masks, was used to fabricate this grating. The 3-dB width of the resonance band centered at 1241.2 nm was 4.1 nm. The grating in Figure 3.45 should be compared to the one in Figure 3.44 that has a length of 2.54 cm. Although the gratings are written in different fibers with distinct periods and writing conditions, the differences in the spectral widths are clearly evident. Thus long-period gratings with reduced 3-dB widths can easily be fabricated for narrowband applications. In Chapter 4 we will investigate the applications of long-period gratings as fiber optic sensors. Typically an optical spectrum analyzer is used to determine the perturbation-induced shift in the resonance bands. The broad resonance bands in a long-period grating often make it difficult to determine the exact location of the resonance band. The resulting degradation in resolution can be overcome by using gratings with longer

lengths. The accompanying reduction in the spectral width of gratings also helps to multiplex a larger number of these devices in the spectrum of an optical source.

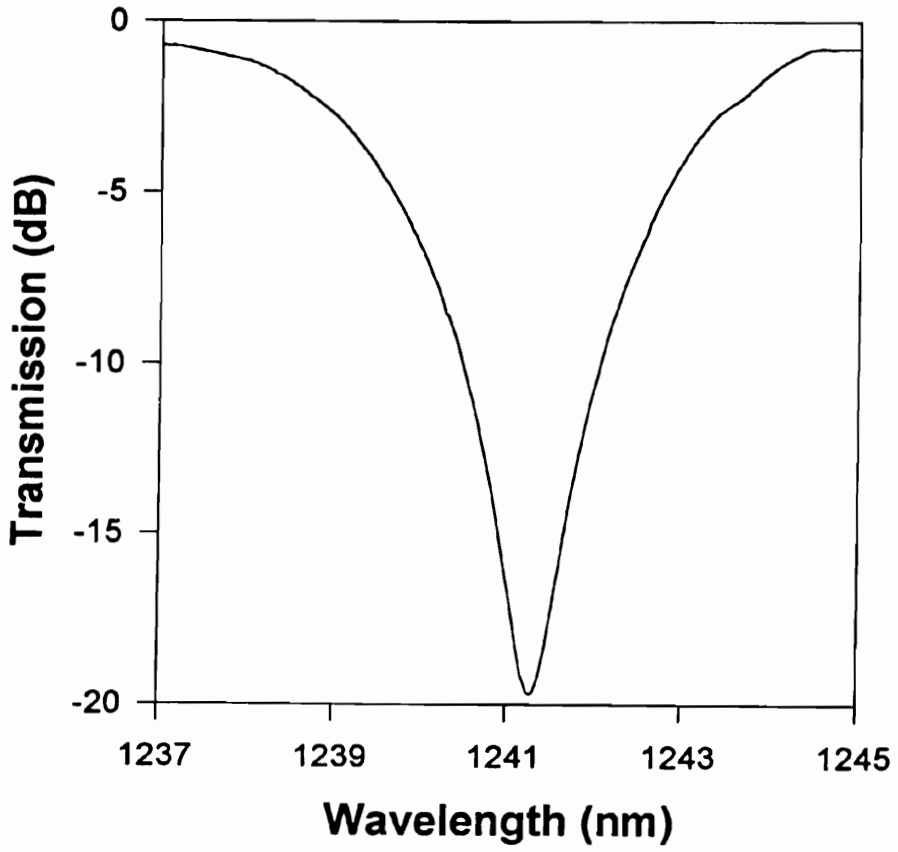

Figure 3.45. Transmission spectrum of a long-period grating written in Corning SMF-28 fiber with Λ=320 μm and L=8 cm using CW exposure. The rounding of the peak at the phase-matching wavelength can be attributed to the limited resolution (0.1 nm) of the optical spectrum analyzer. Note the narrow wavelength span of 8 nm.

Figure 3.46 shows the back-reflection recorded from a long-period grating written in AT&T dispersion-shifted fiber [1]. The measurement was made using a high-sensitivity optical coherence-domain reflectometer (OCDR) provided by Photonetics Incorporated. The optical feedback of less than -80 dB may be attributed to the small Fresnel reflections in the grating region and the resulting value of the peak index change (Δn) is calculated to be 5×10^{-4} [1]. The small back-reflection of these devices is an attractive feature for a multitude of sensing and communication systems where optical feedback is a limiting factor. For example, in a Bragg grating sensing system, the back-reflections to the optical

source can reduce the system signal-to-noise ratio and result in degradation of the sensor sensitivity. Also for gain-flattening of the erbium spectrum in optical amplifiers, feedback is not desirable and hence blazed Bragg gratings are used for this purpose to couple light to radiation modes [63]. Additionally, in communication systems, optical feedback larger than -30 dB can lead to broadening of linewidth of semiconductor lasers and increase the noise and dispersion in the fiber link [72]. Thus in most applications, expensive optical isolators have to be used to suppress the backreflection. The use of long-period gratings as in-fiber devices minimizes the back-reflection and eliminates the requirement of optical isolators. The coupling to lossy forward-propagating cladding modes ensures that only a small amount of incident power is reflected back due to the index discontinuity at the grating.

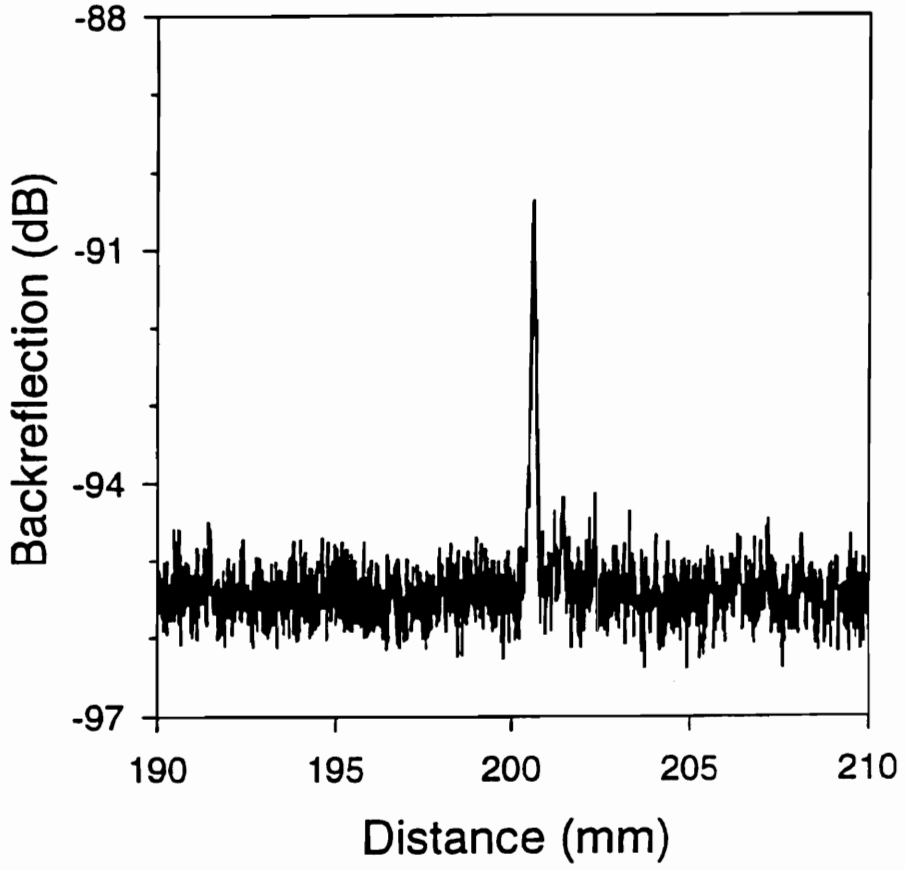

Figure 3.46. OCDR back-reflection measurement in a grating written in AT&T dispersion-shifted fiber [1]. The horizontal scale represents the distance from the input end of the fiber.

In this section we analyzed a few important optical properties of long-period gratings. It was shown that these photoinduced structures have small insertion losses, and negligible back-reflections and polarization sensitivities. The length of the grating and the peak index change in the core can be manipulated to tailor the spectral width of the desired resonance band.

3.4.2 Physical Properties

We now discuss some physical properties of long-period gratings. The effects of etching, bending and recoating the cladding surrounding the grating region are investigated.

3.4.2.1 Bending and Recoating of Long-Period Gratings

Long-period gratings have previously been demonstrated as extremely sensitive to even small bends [99]. Since the guided mode can be assumed to be well confined to the fiber core, the bend sensitivity of long-period gratings arises from the modification of the cladding modes. As the region of the fiber containing the grating is bent, the cladding modes are forced out of the fiber and the coupling between the guided modes and cladding modes is disturbed [1]. The bend-induced perturbation of the cladding mode depends on bend radius of curvature, wavelength, order of the mode, fiber refractive index profile and diameter, and the index of refraction of the medium surrounding the cladding [53].

To experimentally verify its bend sensitivity, a long-period grating fabricated in dispersion-shifted fiber (DSF) was bonded to a flexible cantilever beam supported on one end [99]. The other end of the beam could be displaced from its unperturbed position in either direction. Apart from imparting strain or compression on the grating, the cantilever beam also bends the fiber. To obtain pure bending effects, the grating should be placed on the neutral axis of the beam. Figure 3.47 shows the effect of both compressive and tensioning bends on the transmission spectrum of the grating [99]. With tensioning bends the resonance band moves to the longer wavelengths and reduces in isolation. This can be attributed to the change in the effective index of the corresponding cladding modes, and to the modulation of the overlap integral and hence the variation in the coupling coefficient between the guided and cladding modes. Compressing and bending the grating induce shifts in the resonance wavelengths to higher values with accompanying

reductions in peak loss. The radii of curvature of the bends applied to these fibers were too large for practical measurement but were expected to be of the order of hundreds of centimeters. Thus even small bends (large radii of curvature) produce a distinct change in the transmission spectrum of long-period gratings. The bend-sensitivity of long-period gratings, although a drawback for most applications, can be used favorably to implement sensors for detecting the change in shape or form of a structure. Long-period gratings can be embedded inside or surface-mounted on structures whose shape needs to be monitored. For example, these sensors could be embedded in wings of military or commercial aircraft. A minute undesired distortion in the shape of the wing during flight will change the spectral response of the sensor and a closed-loop feedback system can be employed to correct the deformation.

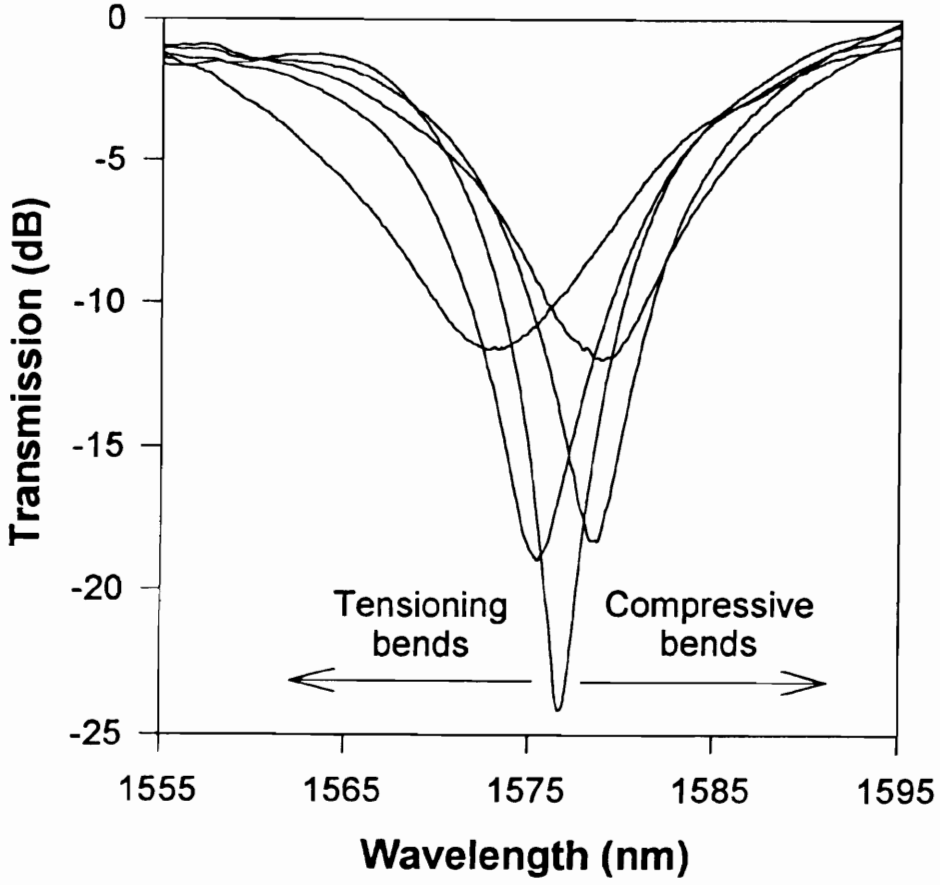

Figure 3.47. Effect of different magnitudes of tensioning and compressive bends on a resonance band of a long-period grating fabricated in DSF [99].

The packaging and recoating of gratings after the fabrication process become critical due to their large bend sensitivity. For a grating written in DSF the isolation of a resonance band has been observed to reduce by about 10 dB on recoating the grating with standard polymer coating [1]. The spectrum of a long-period grating was recorded before and after recoating with a polymer of refractive index 1.38. The shift in the three resonance bands was found to be 2.4 nm, 1.2 nm and 0.4 nm towards shorter wavelengths, with the higher order band undergoing a larger spectral displacement [1]. The spectral shift to smaller values is consistent with the β-plot of Figure 3.8(c) since the values of the effective indices of the cladding modes increase following the recoating process. The larger shift in higher order bands can be attributed to the poorer confinement of the fields corresponding to these cladding modes [1]. The reduction of the isolation of various bands might be due to the absorption of the cladding modes by the coating. Commonly available coatings are designed to absorb any radiation from the guided mode and hence prevent reflection back into the core. The loss in isolation in long-period gratings may be reduced by using coatings made from specific materials [6]. Before long-period gratings are employed for any specific application, one has to ensure that the grating region is free of any bends. The packaging of the gratings should be implemented in a manner that the grating is held taut without changing its optical characteristics. For this purpose, standard techniques used to package short-period Bragg gratings can be employed. The packaging also serves to protect the grating from external vibrations and ambient perturbations.

3.4.2.2 Etching of Long-Period Gratings

In Section 3.2.2.2 we observed that the effective index of the cladding modes is a strong function of the cladding diameter (Figure 3.17). Thus chemically etching the cladding in the region around the grating is expected to alter its transmission spectrum by reducing the effective indices of the cladding modes.

To investigate the effect of reducing the cladding radius on the transmission spectrum, a dispersion-shifted fiber (DSF) grating operating in the normal region was etched for about 90 seconds using a strong solution of hydrofluoric acid (HF). Figure 3.48 depicts the transmission spectrum of the grating before and after etching. Resonance bands corresponding to distinct cladding modes are observed to shift to higher wavelengths, with the band at 1532 nm shifting by 69 nm. The resonance bands at 1389 nm and 1315 nm shift by 16 nm and 7 nm, respectively and this is consistent with Figure 3.17 where

the effective indices of the higher order cladding modes were found to undergo a larger modulation with change in the cladding diameter. The magnitude of the shift is hence a function of the fiber parameters, the etching depth and the order of the resonance bands. Also the wavelength separation between two successive resonance bands increases as the cladding diameter is reduced, in agreement with Equation (3.39). For a grating operating in the anomalous region, the resonance bands are expected to shift to shorter wavelengths with increasing etching depth.

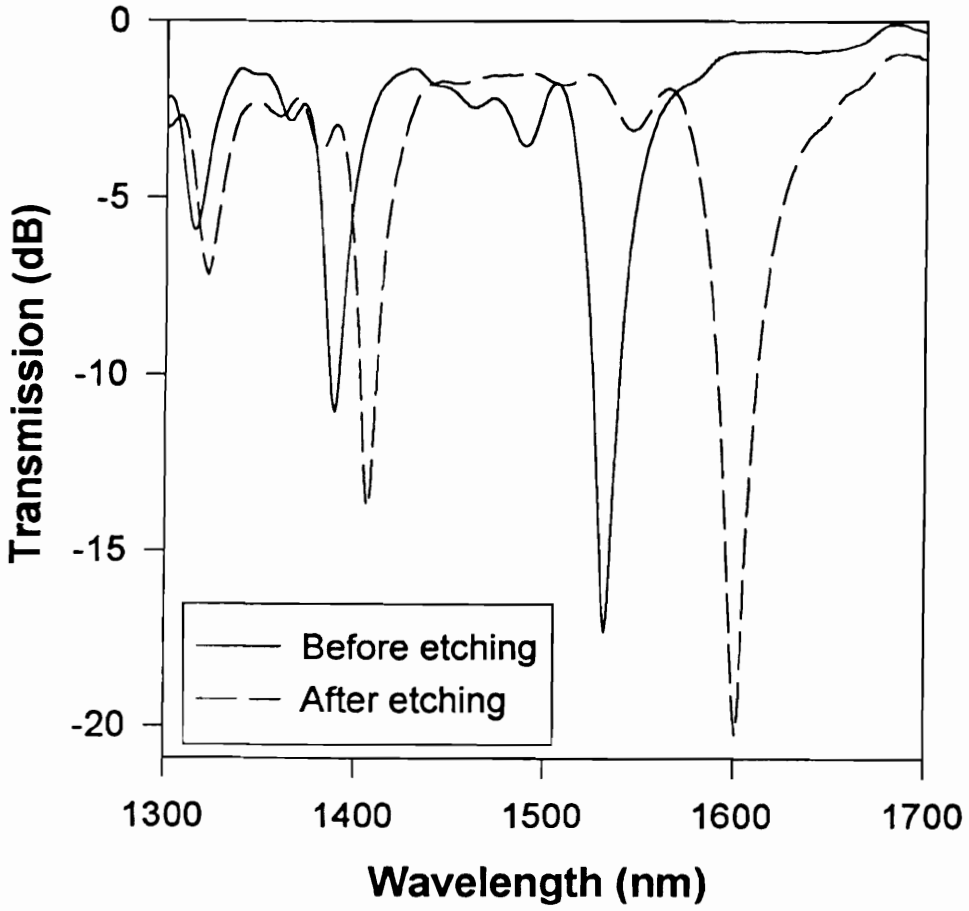

Figure 3.48. Transmission spectra of a long-period grating written in AT&T DSF before and after etching.

If the cladding diameter is reduced significantly during the etching process, the effective index of the guided mode can also be made to vary. In such cases the overall spectral shift will depend on the relative change in the modal effective indices. Etching a grating

will be shown to enhance the refractive index sensitivity of long-period gratings in Section 4.4.2.

3.5 Applications of Long-Period Gratings to Communication Systems

In the previous sections we investigated the fundamental properties of long-period gratings. It was shown that these devices are simple to fabricate and possess small insertion loss, low back-reflection and negligible polarization sensitivity. Chapter 4 and 5 discuss the use of long-period gratings as optical fiber sensors. In this section we review a number of applications of these versatile components to optical fiber communication systems. It has been demonstrated by Vengsarkar *et al.* that long-period gratings can be used for equalization of the gain spectrum [30] and for suppression of amplified spontaneous emission [2] in erbium-doped fiber amplifiers. We analyze these, and few other applications, and propose the use of these gratings as polarizers and modulators in high-performance communication systems.

3.5.1 Applications to Erbium-Doped Fiber Amplifier Systems

The emergence of erbium-doped fiber amplifiers (EDFAs) has revolutionized the optical fiber communication industry [100]. But like other technologies, fiber amplifiers suffer from a few drawbacks which have limited the complete utilization of all their features [100]. For example, although erbium-doped fiber amplifiers offer optical gain over a range of wavelengths in the 1550 nm wavelength window, this amplification is a very strong function of the operating wavelength. The wavelength-dependence of the EDFA gain spectrum can be attributed to the spectral nature of the absorption and emission of the ions [101]. The non-uniformity of the absorption and emission cross-section spectra is the major cause for the double-peaked gain structure. The spectral-dependence is a function of the host and other dopants in the fiber. The second reason for the gain non-uniformity is the variation of the gain coefficient along the length of the erbium-doped fiber [100]. Due to several reasons, such as amplified spontaneous emission (ASE) propagation, the medium inversion is not the same at all points along the fiber. The resultant variation in the gain coefficient further increases the non-uniformity of the EDFA gain spectrum.

The wavelength-dependence of the EDFA gain spectrum can degrade the performance of digital wavelength-division multiplexed (WDM) systems, especially in long amplifier chains. WDM channels that are separated by more than 1 nm can have gain differences that build up on propagation through a large number of amplifiers [100]. Thus the gain tilt causes each channel to have a different signal-to-noise ratio at the detection end, resulting in unacceptably large discrepancies in the receiver bit error rates. In analog systems, the gain tilt of the EDFAs, in presence of chirping can cause composite second order (CSO) distortions [100]. In practice if a semiconductor diode is directly modulated, the instantaneous value of the carrier frequency becomes varies with time [53]. This phenomenon is called chirping and has been used previously to achieve pulse compression in fiber optic links [72]. If μ is the modulation index and $\Delta\lambda_{max}$ is the maximum wavelength chirp for μ=100%, the overall CSO distortion for M carrier components is given by the expression [102,103],

$$CSO(\lambda_s) = M \frac{\mu \Delta\lambda_{max}}{G(\lambda_s)} \left(\frac{dG}{d\lambda}\right)_{\lambda=\lambda_s}, \tag{3.48}$$

where $G(\lambda_s)$ and $(dG/d\lambda)_{\lambda=\lambda_s}$ are the gain and the gain slope at the mean carrier wavelength λ_s, respectively. The typical values of CSO distortion can lie between -60 dBc and -40 dBc (c indicates that the CSO is measured with reference to the carrier power) while the typical standard for CATV (common antenna television) distribution are -65 dBc [104]. Thus gain nonuniformity-induced CSO can significantly alter the picture quality in CATV applications [102,103]. Equation (3.48) predicts that this CSO is zero if chirping is absent ($\Delta\lambda_{max}$=0), or if the gain spectrum is uniform ($(dG/d\lambda)_{\lambda=\lambda_s}$=0). Since chirping is inherent to directly modulated systems [53], CSO effects may be reduced by operating at a gain peak or valley where the gain tilt is zero. By locating the carrier at these wavelengths, the versatility of the EDFA is sacrificed and moreover, minute temperature-induced spectral shifts would again cause CSO distortion to appear. If the gain of the EDFA is uniform over a range of wavelengths around the carrier location, the effects of CSO on the CATV picture quality can be assumed to be negligible. This can enable simultaneous transmission of around 100 optical carriers in a 25 nm bandwidth, each carrier capable of supporting several frequency multiplexed channels [105]. Thus gain uniformity is of prime importance in both analog and digital links employing erbium-doped fiber amplifiers. We now review various conventional techniques that have been commonly employed to achieve gain flattening or gain equalization in EDFAs.

Gain equalization for two channels can simply be obtained by varying either the pump power or the length of the EDFA or both [100] and results in discrete pairs of wavelengths that possess equal gains. The disadvantage of this method is that the gain compression under varying degrees of saturation is a function of the operating wavelength. Hence, when the EDFA is operating under saturation, the gain equalization present for small-signal regime is no longer available. More than two channels can be equalized by operating under maximum pumping, as described by Desurvire [100]. But again, gain saturation causes the number of equalized channels to reduce. Moreover, this gain equalization system makes inefficient use of the large EDFA bandwidth that is otherwise available for amplification.

Many techniques are available for gain flattening of the EDFA gain spectrum. One of the most interesting schemes for obtaining flat spectral gain has been proposed by da Silva *et al.* [106]. This method uses the fact that an inhomogeneously broadened amplifier provides a uniform gain spectrum under saturation. But since a typical EDFA is dominated by homogeneous broadening at room temperature, gain flattening is difficult to implement. On the other hand, if the fiber is cooled to temperatures as low as 77K, the resulting saturation is inhomogeneous in nature and the gain is uniform over a larger bandwidth. The 3-dB gain bandwidth was observed to improve from 25 nm at room temperature to 35 nm at 77K using this technique [106]. The advantage of this technique is that the gain of the EDFA remains practically uniform at any degree of saturation. Eskildsen *et al.* [107] have extended this technique to gain flattening in an amplifier cascade with five multiplexed channels. A six-stage fiber amplifier was used with every third stage being cooled by liquid-nitrogen. The input channels were launched with equal power (-15 dBm) and the power spread at the output was found to reduce by 11 dB after implementing the gain flattening scheme. Laming *et al.* [108] have proposed a method that converts homogeneous saturation to inhomogeneous saturation by decoupling the spatial hole burning for two signal wavelengths using twin-core fibers.

A technique proposed by Giles and DiGiovanni [109,110] for gain equalization at two wavelengths employs a two-stage amplifier with complimentary gain spectra. Two EDFAs were fabricated in germano-aluminosilicate and aluminosilicate hosts and pumped separately at 1480 nm. The pump powers were independently adjusted to obtain equal gains at the two signal wavelengths differing by 2.5 nm. The attractive feature of

this system is that small temporal gain variations in one channel can be equalized real-time, providing a system that is independent of random gain fluctuations. Kashiwada *et al.* [111] have used serially cascaded amplifiers made from different host glasses to obtain gain flattening. Four channels were equalized using two EDFAs whose gain slopes were equal and opposite in the region of operation.

Kashyap and co-workers [63] have proposed the use of blazed short-period Bragg gratings as spectral-shaping elements. As discussed in Section 2.4.4, blazed gratings that couple the fundamental guided mode to lossy radiation modes provide a continuous loss spectrum that can be tuned by changing the periodicity or the blaze angle. The gain peak at 1531 nm was equalized by using a blaze angle of 8° normal to the fiber axis. The grating with an isolation of about 4 dB flattened the gain spectrum to within ±0.1 dB over a bandwidth of 25 nm [63]. Wilkinson *et al.* [112] have also used an external blazed grating etched on the flat surface of the cladding to induce coupling to reverse-propagating cladding and radiation modes. Tachibana *et al.* [113] have used a mechanical grating induced by microbends to introduce an optical notch filter within the fiber. An external grating of periodicity 780 μm serves to couple light from the core to the cladding modes. The peak loss wavelength and the maximum isolation can be easily varied by changing the operating angle and pressure, respectively. The grating suppressed the gain peak of the EDFA at 1532 nm and yielded a 3-dB gain bandwidth of 33 nm [113]. The authors demonstrated that the filter performed better when placed within the EDFA than following the amplifier. Twin-core fibers have also been proposed as passive filters for gain flattening. A twin-core fiber was used to couple the amplified spontaneous emission from the central core to an auxiliary off-axis core of smaller radius [114]. Although a gain-uniformity of ±1.5 dB over 30 nm was demonstrated, this device does not seem practical since the parameters of the twin-core fiber have to be changed each time an EDFA with a different spectrum needs to be flattened.

Su *et al.* [115] have proposed the use of integrated acousto-optic tunable filters (AOTF) for active optical filtering of individual channels. The limitations of this method are the requirement of large input RF power (about 1 W for 10 channels) and a high insertion loss of around 9 dB [115]. Inoue *et al.* [116] have used integrated electro-optic Mach-Zender interferometers for gain flattening. The interferometers provided a wavelength-modulated transmission spectrum that was a function of the path-difference between the sensing and reference arms. The excess loss measured during this demonstration was 1.4

dB per filter which might be unacceptable in a few applications [116]. Betts *et al.* have used a single-stage split-beam Fourier filter to obtain a gain variation of less than ±0.1 dB over an 18 nm bandwidth [117].

Most of the techniques discussed above suffer from a number of limitations that have prevented their widespread application. For example, the use of low temperature cooling [106] to obtain inhomogeneous broadening might be impractical in long distance links. Some of the devices for gain flattening are incompatible with optical fibers and hence possess large insertion losses. The use of external microbends [113] or etching [112] introduces an uncertainty in repeatability and stability of the related devices. The introduction of special fibers, such as those with twin cores might require special launching conditions and hence adds to the complexity of the system. The splicing of additional fibers also serves to introduce discontinuities in the link which might produce optical feedback that can be harmful to the performance of the EDFA. Additionally, a number of gain flattening devices discussed here are difficult to fabricate, especially in large numbers. The polarization-sensitivity and back-reflection might be other limitations of such techniques.

We now show that long-period gratings proposed by Vengsarkar *et al.* [1] overcome a number of drawbacks of conventional gain flattening schemes and are hence attractive choices for networks containing fiber amplifiers that may be installed in the near future. An example of the gain uniformity produced by using long-period gratings is presented, and a system experiment to verify their effectiveness is reviewed.

Long-period gratings are photoinduced structures that provide broadband spectral losses. The location of the loss bands depends on the type of host fiber, the grating period, and the writing conditions. The versatility in filter design is the most attractive feature for gain flattening of EDFAs. The principle of operation is to closely match the inverted EDFA gain spectrum by using the transmission spectra of one or more long-period gratings. Figure 3.49 depicts the gain flattening capability of these devices, as proposed by Vengsarkar *et al.* [30]. The gain spectrum (symbols) was first decomposed into the sum of two Gaussian profiles with distinct center wavelengths and isolations. Two gratings were fabricated in AT&T dispersion-shifted fiber (DSF), each with period Λ=474 μm, using slightly different exposure duration [30]. The fibers containing the two gratings were spliced together and the concatenated filter spectrum (line) is also shown in

Figure 3.49. The choice of periods depends on the center wavelengths and isolations of the two Gaussian spectra and are typically found from previously obtained characteristic curves for the host fiber. Moreover the index change and grating length can be manipulated to obtain the optimum spectral width for each band. The complexity of the gain spectrum determines the number of gratings that need to be serially multiplexed for gain flattening. For example, the gain peak at 1532 nm can be equalized by using a third grating at that wavelength [30]. For most broadband applications, two to three gratings should be sufficient to flatten the gain over the desired bandwidth. The 3-dB bandwidth of the flattened EDFA in Figure 3.49 improved to 50 nm from 19 nm for an unequalized spectrum. The improvement in the device performance by a factor of two to three is promising for long-haul applications.

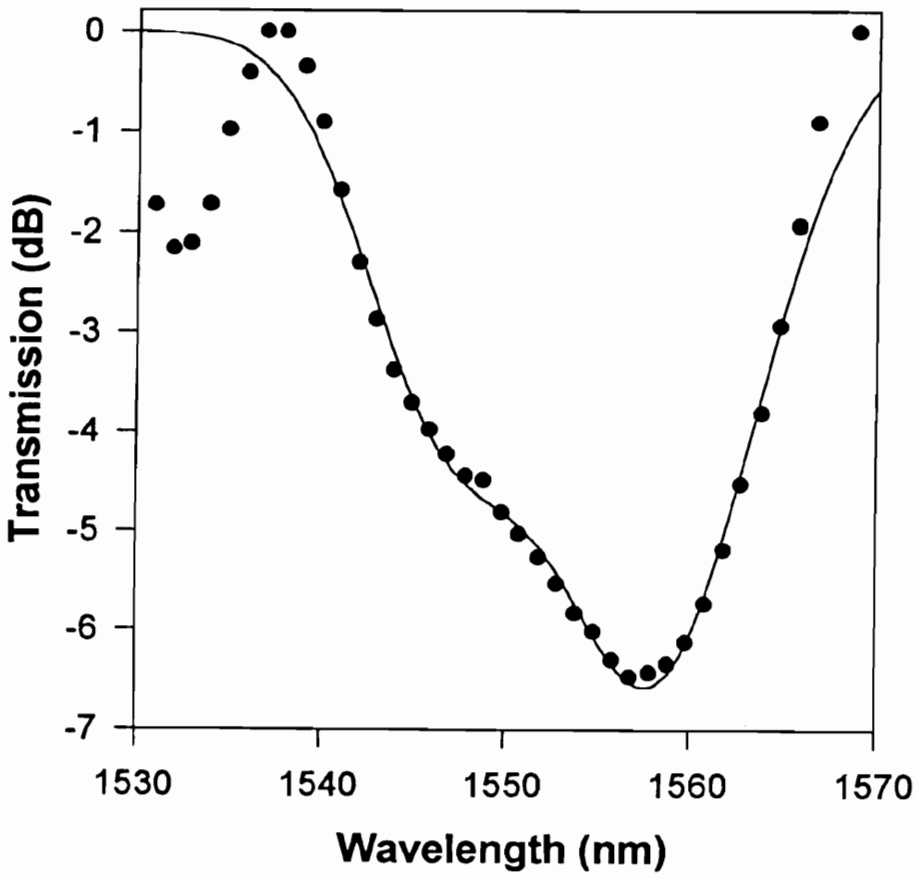

Figure 3.49. Inverted EDFA gain spectrum (symbols) and the concatenated transmission spectrum (lines) of two distinct long-period gratings [30]. The gratings were fabricated in AT&T DSF with period Λ=474 μm.

Vengsarkar *et al.* [30] have demonstrated the applications of long-period gratings for gain flattening in system experiments. Using long-period gratings, 20 multiplexed channels (at 5 Gbits/s each) with 0.6 nm separation were transmitted over a distance of 6300 km. The input signals were placed at wavelengths around 1555 nm and excellent gain uniformity was obtained over 12 nm of amplifier bandwidth. This experiment demonstrates the gain equalization provided by long-period gratings is an effective technique to utilize the immense information capacity offered by optical fiber communication systems.

Although long-period gratings have previously been used as spectral filters following the EDFA, a performance improvement might be achieved by fabricating these devices in the erbium fiber itself. Tachibana *et al.* [113] have shown that placing the microbend filters within the erbium fiber can not only flatten the peak at 1532 nm but also result in gain at higher wavelengths. This can be explained on the basis of the competition for population inversion between the amplified spontaneous emission (ASE) at the peak gain wavelength and at other spectral components within the amplifier bandwidth.

Thus long-period gratings offer a number of advantages over other gain flattening techniques. Long-period gratings are simple and economical to batch produce. These devices have small insertion loss and negligible polarization sensitivity. The most attractive feature of these gratings is their small back-reflection [1] as compared to other techniques. The grating spectrum is a strong function of the host fiber, period, writing and annealing conditions, order of the cladding mode and grating length. One or more of these parameters can be manipulated to obtain the desired wavelength selectivity offered by these components. The limitation of these devices is that the performance is limited by the cross-sensitivity to bends and ambient temperature changes. The former can be overcome by using appropriate packaging techniques while the latter can be surmounted by employing fibers with special refractive index profiles [34] or by using specific grating periods in standard fibers [35]. Additionally, long-period gratings offer only passive gain stabilization and hence in systems where the signal or pump power are expected to vary, the effectiveness of these devices may be limited.

The other major application of long-period gratings to EDFAs is the suppression of the amplified spontaneous emission (ASE) [2]. In a cascaded chain of EDFAs, the buildup

of ASE at the peak gain wavelength undermines the performance of the amplifiers [100]. ASE travels in both forward and backward directions with a power that is proportional to the amplifier gain during complete population inversion and high gain. For increasing gain, the stimulated emission by ASE grows to a value where it starts competing with the pumping rate [100] which causes the excited erbium ions to return to the ground state, specially at either end of the amplifier where the ASE power is maximum. Due to reduction in medium inversion, the amplifier gain saturates even in the absence of the any input signal. Thus while the ASE increases, the signal level drops along the fiber chain, degrading the signal-to-noise ratio at the receiver [100]. Self-saturation can be prevented by periodically filtering the forward ASE noise power along the fiber link. For this purpose in-line long-period gratings with low insertion loss at signal wavelengths are ideal filter elements. Care has to be taken to prevent attenuation of the 1480 nm pump and also that of the signal wavelengths in the 1550 nm region. This may easily be achieved by selecting proper grating periods to tailor the wavelength separation between the resonance bands [1].

Long-period gratings have also been shown as effective in regulating the emission wavelength of dual configuration 980 nm pump diodes stabilized using fiber Bragg gratings [118]. Such diodes tend to split the lasing spectrum due to the band gap filling effect and result in reduction in pump conversion efficiency [119]. It has been shown that this limitation can be surmounted by using a long-period grating with a resonance band centered at 1005 nm [3].

We thus observe that long-period gratings can be used to overcome a number of problems in erbium-doped fiber amplifiers. Their successful application to gain flattening, ASE removal and pump wavelength stabilization promises a large commercial market for these devices in the future.

3.5.2 Other Applications to Communication Systems

This section discusses the applications of long-period gratings to overcome some other limitations of conventional telecommunication systems. Their uses in suppression of residual power in WDM channels [1] and undesired Stokes orders in Raman lasers [120] are reviewed and novel applications as in-line modulators and polarizers are proposed.

Vengsarkar *et al.* have proposed the use of long-period gratings in wavelength division multiplexed systems to filter out the residual power in a channel [1]. For example, if two channels at 1310 nm and 1550 nm are multiplexed at the transmitter and sent along the same fiber, even after demultiplexing the higher wavelength signal, the 1310 nm channel might have traces of 1550 nm signal. Thus a notch filter made from a long-period grating can be used to suppress the 1550 nm component after the demultiplexer. The fiber compatibility and large isolation offered by such devices are advantages over other traditional filters.

Grubb *et al.* [120] have demonstrated the application of long-period gratings in suppressing undesired Stokes order in a cascaded configuration of Raman laser. Such a laser consists of a series short-period Bragg grating resonating cavities that successively convert one Stokes order to the next. An input at 1117 nm from a ytterbium-doped fiber can be shown to result in output at 1480 nm after going through a series of intermediate Stokes orders at distinct wavelengths [120]. The 1175 nm Bragg grating reflector for conversion to the first Stokes order forms an undesired cavity with the ytterbium-doped fiber input and hence degrades the laser efficiency. The insertion of a long-period grating with a loss band centered at 1175 nm has been demonstrated to result in improved performance of the laser [120].

It has been shown previously that simple, in-line polarizers can be fabricated by using the phenomenon of microbends in elliptical-core fibers [121]. Microbends are periodic external perturbations that serve to couple light from the guided mode to non-circularly-symmetric cladding modes. In an elliptical-core fiber the two orthogonal polarizations of the guided mode possess different propagation constants. Hence the location of the loss bands for the incident light will be a function of the input polarization. Light at a particular wavelength is completely transmitted along one polarization but lost to cladding modes at the other. Such polarizers with low back-reflections are highly useful for systems using erbium-doped fiber amplifiers. Long-period gratings, fabricated in elliptical-core fibers can also similarly result in efficient polarizers with large extinction ratios.

In Section 3.2.2.2, we demonstrated that the effective indices of the cladding modes in long-period gratings are strong functions of the refractive index of the ambient material

(Figure 3.18). In Section 4.4 we will demonstrate the application of long-period gratings to refractive index sensing. It will be shown that such devices undergo wavelength shifts in resonance bands when the refractive index of the medium surrounding the bare cladding is changed. This suggests that if the external refractive index can be controlled using a suitable technique, light at a given wavelength can be transmitted or attenuated. For example, modulators that use lithium-niobate ($LiNbO_3$) to control refractive indices are commonly used in transmitters. $LiNbO_3$ is an electro-optic material whose refractive index can be varied by application of an external electric field [122]. By coating a part of the bare fiber around the grating with $LiNbO_3$ and using optically transparent indium tin-oxide electrodes, it might be possible to obtain in-line modulators using long-period gratings. The resonant wavelength of the grating can be made to overlap with the input wavelength for an applied voltage and hence result in complete attenuation. The extinction ratio for this on-off modulator will be a function of a number of parameters including the applied voltage and the induced shift in the resonance band. Thus by using an appropriate host fiber, grating period and length, writing conditions and order of resonance band, it might be possible to optimize the system performance. A device with small insertion loss will be an attractive substitute for external waveguide modulators being used presently.

We thus see that long-period gratings have a number of applications to communication systems. The use of these gratings as versatile components for gain flattening and ASE suppression in EDFAs was reviewed and applications as fiber-compatible polarizers and modulators were proposed.

In this chapter we analyzed the principle of operation, fabrication and properties of long-period gratings that couple the fundamental guided mode to discrete forward-propagating cladding modes [1]. The concept of β-plots was used to elucidate the operating mechanism of these gratings and to distinguish them from other photoinduced devices. An analytical model was developed to obtain the characteristic curves for different fibers. It was shown that the long-period gratings can be operated in two different spectral regions - normal and anomalous. For most applications, the grating period is selected such that the coupling wavelength grows on increasing the periodicity. In this, the normal region of operation, the group index of the guided mode is larger than that of the corresponding cladding mode involved in coupling. For the anomalous region, the cladding mode has a higher group index and thus the slope of the coupling wavelength

versus grating period curve is negative. The response of the grating to changes in the fiber parameters was found to be a function of the differential group index between the guided and cladding modes. Small deviations in the values of the fiber parameters specified by the manufacturer were analyzed for their influence on the characteristic curves. Expressions for important grating parameter such as the coupling coefficient, separation between adjacent resonance bands and the full width at half-maximum were obtained and it was shown that the length of grating and the peak index change determine the grating width for a given period and order of cladding mode.

Three methods to fabricate long-period gratings were outlined. The first two use radiation from pulsed or continuous-wave UV lasers and require either amplitude masks or slits to obtain the rectangular index modulation in the fiber core. The third technique uses the thermal sensitivity of hydrogen-loaded fiber to obtain long-period gratings and employs inexpensive CO_2 lasers for batch-production of gratings. The affect of residual hydrogen on the grating spectrum was investigated and it was shown that high temperature annealing stabilizes the grating by hastening the hydrogen out-diffusion and decay of unstable UV-induced sites [1]. It was proposed that the grating spectrum may be selectively varied by employing appropriate annealing temperatures and duration. We finally discussed the basic optical and physical properties of long-period gratings. These devices have low insertion loss, small back-reflection and negligible polarization dependence [1]. Although sensitive to bends and recoating, long-period gratings can be used in commercial systems by employing suitable packaging techniques.

We finally reviewed some of the common applications of long-period gratings to communication systems. The low insertion loss and negligible back-reflection of these photoinduced devices makes them attractive for gain equalization [30] and ASE filtering [2] in erbium-doped fiber amplifiers. Applications such as removal of unnecessary Stokes orders in Raman lasers [120] and stabilization of 980 nm Bragg grating-based pump diodes [118], were also discussed. The use of long-period gratings as in-line polarizers and modulators was proposed.

In summary, long-period gratings are versatile components that offer a number of advantages over other photoinduced devices. Their spectral response is a strong function of the fiber parameters and hence such gratings offer a lot of flexibility to the system designers. These in-fiber devices produce minimal optical feedback and are hence

attractive to many different sensing and telecommunication applications. Chapter 4 investigates the use of long-period gratings as strain, temperature and index of refraction sensors.

Chapter 4 - Single-Parameter Long-Period Grating Sensors

In Chapter 3 we analyzed the basic properties of long-period gratings [1] that couple light from the guided mode to discrete cladding modes and result in attenuation bands whose spectral locations are functions of the grating period and the differential effective index. Thus any variation in the effective indices of these modes or in the grating period serves to modulate the phase-matching wavelengths. In this chapter we introduce long-period grating temperature, strain and index of refraction sensors based on the above principle [21]. These sensors are shown to possess large perturbation-induced shifts and simple signal processing techniques [21].

The outline of Chapter 4 is as follows. We first discuss the basic operating principle of long-period grating sensors. The mechanism behind the spectral shifts in the resonance bands is explored and it is shown that for a given fiber these wavelength shifts are strong functions of the grating period, the order of the corresponding cladding mode and the writing conditions. Long-period grating temperature sensors are shown to possess an order of magnitude larger spectral shifts than their Bragg grating counterparts [21]. The dependence of the temperature sensitivity on the grating period and the order of the cladding mode is investigated. Temperature-insensitive long-period gratings fabricated in special [34] and standard fibers [35] are studied. Long-period gratings are also demonstrated as highly versatile strain measuring devices [21]. The strain sensitivity is analyzed for its dependence on the period and the order of the resonance band. Strain-insensitive long-period gratings are proposed to overcome the limitations imposed by the finite coefficient of thermal expansion of the host material in embedded or surface-mounted temperature sensors. The temperature cross-sensitivity of strain sensors is also discussed and it is demonstrated that temperature-insensitive gratings can be used to solve this problem. Long-period gratings are shown to be highly sensitive to index changes of the medium surrounding the bare cladding [21]. Experimental results are presented and the thermal cross-sensitivity is analyzed in conventional and temperature-insensitive long-period gratings. We also demonstrate that the spectral shift induced by ambient index variations can be enhanced by etching the cladding surrounding the long-

period grating. Typically, an optical spectrum analyzer is required at the output end to determine the wavelength shift and hence the magnitude of applied perturbation. We present simple demodulation schemes for long-period gratings sensors that employ the conversion of the spectral shift to an intensity modulation [21]. Some schemes to multiplex long-period gratings are proposed to enable distributed measurements using a single optical fiber. Experimental results from practical applications of long-period gratings are presented. The strain sensor is used for measurements during the loading process of a reinforcing-bar, commonly employed in civil structures [33]. The index of refraction sensor is used for determining the concentration of sucrose solutions. We finally compare long-period grating sensors with other fiber optic sensors and discuss their advantages and limitations.

4.1 Principle of Operation

In this section we analyze the principle of operation of long-period grating based sensors. The functioning mechanism is compared to that of short-period Bragg gratings [8] to elucidate the differences in the response of the two sensing systems.

An unblazed long-period grating is based on the coupling between the fundamental guided mode and several circularly-symmetric, forward-propagating cladding modes [1]. As explained in Chapter 3, for a grating with a given period Λ, the magnitude of power transfer is a function of the phase-matching between these modes and the corresponding coupling coefficient. For the present analysis we will assume that all the involved cladding modes possess sufficient overlap with the guided mode and hence the coupling coefficient is not a contributing factor. The value of this coefficient merely changes the magnitude of loss and the width of a particular band and hence is not significant for a majority of sensing applications. The sensing mechanism can be explained on the basis of the phase-matching condition which results in a coupling wavelength λ,

$$\lambda = \left(\delta n_{eff}\right) \Lambda \,, \tag{4.1}$$

where Λ is the grating periodicity and δn_{eff} is the differential effective index between the guided and a cladding mode. To keep the representation simple, we have neglected the ordinal m that was used to represent the order of the cladding mode in Chapter 3. The dependence of the coupling wavelength and the differential effective index on m should

be assumed during the ensuing analysis. The difference between the effective indices of the guided and cladding modes may simply be expressed as,

$$\delta n_{eff} = n_{eff} - n_{cl} . \tag{4.2}$$

where n_{eff} and n_{cl} are the effective indices of the forward-propagating guided and cladding modes, respectively. For a fiber with n_1, n_2 and n_3 ($n_1 > n_2 > n_3$) as the core, cladding and ambient indices, $n_2 < n_{eff} < n_1$ and $n_3 < n_{cl} < n_2$. Equation (4.1) reveals that the coupling wavelength is a function of the effective indices of the guided and cladding modes, and the grating period. The effective indices, on the other hand, are dependent on the fiber parameters such as the core and cladding refractive indices and radii, as discussed in Section 3.2.2. External perturbations such as strain and temperature modulate various optical fiber parameters and the grating period, and hence induce displacements in the coupling wavelengths. Since the spectral variation of the effective indices of the cladding modes involved in coupling are unique, the corresponding resonance bands are expected to possess distinct wavelength shifts. The differential shift can also be attributed to the dissimilar spectral dependence of the guided mode effective index at the discrete coupling wavelengths. Additionally, since the locations of the resonance bands are functions of the grating period (Section 3.2.3.2) and the writing conditions (Section 3.2.3.3), these parameters are also expected to contribute to the distinct magnitudes of spectral shifts. During the discussion in Section 3.2.2.2 we noted that the effective index of a cladding mode is a function of the index of refraction of the medium surrounding the cladding. Hence ambient index changes are also expected to shift the phase-matching wavelengths of different resonance bands. Since each cladding mode has a unique change in the value of its effective index, the spectral shift of a band will depend on the order of the corresponding mode. Thus the principle operating mechanism of long-period grating sensors is based on the modulation of the effective indices of the core and the cladding modes and/or the grating periodicity by the external perturbation. The shift in the resonance bands is typically detected using an optical spectrum analyzer and related to the magnitude of the measurand using a calibration curve.

Consider a perturbation ξ that acts on the region of a fiber that contains a grating with period Λ. The objective is to find the wavelength shift per unit perturbation change $d\lambda/d\xi$ for the given grating. Using the chain rule of derivatives in Equation (4.1), we obtain,

$$\frac{d\lambda}{d\xi} = \frac{d\lambda}{d(\delta n_{eff})} \frac{d(\delta n_{eff})}{d\xi} + \frac{d\lambda}{d\Lambda} \frac{d\Lambda}{d\xi}. \tag{4.3}$$

As expected, the wavelength shift is a function of the change in the differential effective index per unit perturbation $d(\delta n_{eff})/d\xi$, and also of the change in the grating period per unit perturbation $d\Lambda/d\xi$. The factor $d\lambda/d\Lambda$ is a function of the fiber parameters, the grating period, the order of the resonance band, and the writing and annealing conditions. The dependence on the writing conditions arises from the fact that for a given modal order, the coupling wavelength is a function of the peak UV- or thermal-induced index change Δn, which in itself is dependent on the laser power, the exposure period, and the annealing temperature and duration. In fact, as explained in Section 3.2.4.2, for gratings fabricated for a fixed isolation or maximum power transfer, the coupling to the same cladding mode will occur at wavelengths that depend on the length L of the grating. Our analysis, unless otherwise stated, will consider only gratings with the same Δn for all values of periods and lengths, and hence the focus will be on analyzing the differential response based on grating periodicity and other factors such as ambient index of refraction.

In Section 3.2.3 we had shown that the characteristic curves of gratings written in different optical fibers are dependent on fiber parameters such as the core and cladding indices and radii. Hence the slope of a characteristic curve $d\lambda/d\Lambda$ is a function of the various fiber parameters and can be expressed as [34],

$$\frac{d\lambda}{d\Lambda} = \frac{(\delta n_{eff})^2}{\delta n_g}, \tag{4.4}$$

where δn_g is the differential group index between the guided and cladding modes and is given by Equation (3.10). Thus if the effective indices of the guided and cladding modes and their spectral variation are known, the parameters $d\lambda/d(\delta n_{eff})$ and $d\lambda/d\Lambda$ in Equation (4.3) can be determined. Assuming then that the effect of the perturbation on the differential effective index $d(\delta n_{eff})/d\xi$, and on the grating period $d\lambda/d\Lambda$ are known, the induced wavelength shift can be determined. This will be the main principle behind analytical modeling of long-period grating sensors. For a grating with a given period, the variables $d\lambda/d(\delta n_{eff})$ and $d\lambda/d\Lambda$ are functions of the order of the cladding mode and hence

the multiple resonance bands are expected to have distinct spectral displacements under the same perturbation. The differential modulation of the bands will be employed for simultaneous measurement of strain and temperature in Chapter 5.

The differential group index δn_g between the guided mode and a particular cladding mode can be positive or negative depending on the fiber parameters and the coupling wavelength (Section 3.2.3.1). The part of the spectrum where the value of δn_g is positive is called the normal region of operation while the spectral range with negative δn_g is termed the anomalous operating region. Using Equation (4.4), we observe that if $d\Lambda/d\xi$ maintains its sign, the second term on the right-hand side of Equation (4.3) will have opposite polarity for these two different regions. Moreover, for operation around the equalization wavelength, this term will be larger for the same change in period since the slope of the corresponding characteristic curve approaches infinity.

We now revert our attention to Equation (4.3) and divide the spectral shift into two categories as we had done for Bragg grating sensors in Sections 2.4.4.1 and 2.4.4.2. The first term on the right-hand side of the equation is termed as the material contribution [34] since the change in the differential effective index typically arises from the modulation of the material properties of the fiber such as the core and the cladding refractive indices. The second term is called the waveguide contribution [34] since it affects the guiding properties of the fiber by introducing a change in the grating periodicity. The overall shift per unit perturbation $d\lambda/d\xi$ depends on the relative magnitudes and polarities of the material and waveguide contributions. For a fiber with a given period, these two effects might counter-balance to result in gratings that are independent of a certain perturbation. In Section 2.4.4.1 we had observed that conventional fiber Bragg gratings have positive material and waveguide contributions for the temperature-induced shift, and hence such devices have a finite thermal coefficient. On the other hand, strain sensors obtained from such gratings (Section 2.4.4.2) have opposite polarity of material and waveguide contributions and diminish each-other's effects. We will demonstrate that for a given fiber, long-period grating sensors can have positive or negative strain-induced shifts depending on the order of the resonance band and the grating periodicity.

We start the analysis of long-period grating transducers by evaluating the temperature sensor. An analytical model for temperature sensitivity is introduced and experimental

results are presented. Temperature-insensitive gratings are investigated in fibers with special [34] and standard [35] refractive index power profiles.

4.2 Temperature Sensor

Temperature sensors have found a number of applications in commercial and industrial applications [4,6]. Fiber optic sensors have been demonstrated as versatile temperature measurement devices over broad dynamic ranges and with high sensitivities [4,6]. In this section we introduce novel temperature sensors based on long-period gratings that possess large spectral shifts and are economical to mass-produce and demodulate [21].

4.2.1 Theoretical Analysis

Consider a long-period grating with period Λ under the influence of a temperature change ΔT. In the limit $\Delta T \to 0$, Equation (4.3) can be modified with $\xi=T$ to yield [34],

$$\frac{d\lambda}{dT} = \frac{d\lambda}{d(\delta n_{eff})} \frac{d(\delta n_{eff})}{dT} + \frac{d\lambda}{d\Lambda} \frac{d\Lambda}{dT}. \tag{4.5}$$

Thus the material contribution to the thermal-induced shift is a function of the change in the differential effective index with temperature $d(\delta n_{eff})/dT$ while the waveguide effect is dependent on the variation in the grating period with temperature. Using Equation (4.2),

$$\frac{d\lambda}{dT} = \frac{d\lambda}{d(\delta n_{eff})} \left(\frac{dn_{eff}}{dT} - \frac{dn_{cl}}{dT} \right) + \Lambda \frac{d\lambda}{d\Lambda} \frac{1}{L} \frac{dL}{dT}, \tag{4.6}$$

where L is the length of the grating ($d\Lambda/\Lambda dT = dL/LdT$). The sensitivity of a grating to temperature strongly depends on the change in the effective indices of the guided and cladding modes. The material contribution also depends on the δn_{eff} versus λ curve for the corresponding cladding mode. As stated earlier, the effective indices are functions of the core and the cladding indices and radii. It can be shown that the effect of variation in the core and cladding radii has a very small contribution to the temperature sensitivity in comparison to the change in the core index n_1 the cladding index n_2. Thus for the remainder of the temperature sensitivity analysis we will neglect the influence of variations in the core and cladding dimensions. Thus the problem reduces to finding the change in the effective indices due to the temperature-induced deviations in core and

cladding indices. The material contribution is then algebraically added to the waveguide contribution to determine the overall temperature sensitivity from Equation (4.6). Although the solution seems trivial at first sight, numerical techniques have to be used due to the presence of wavelength-dependent terms on either side in Equation (4.6). For fiber Bragg gratings, the spectral dependence of the effective index of the guided mode and that of the slope of the characteristic curve may be neglected to produce a simple expression (Equation (2.43)) for temperature sensitivity. Hence the analysis of long-period grating sensors is much more complicated than that of Bragg grating sensors.

To calculate the waveguide contribution, the value of dL/LdT for the fiber core is required. Although the core is doped with germania we will assume that its coefficient of thermal expansion can be approximated by that of silica and hence $dL/LdT=4.1\times10^{-7}$ /°C [77]. This assumption is justified since the silica cores in standard fibers used in our analysis contain just a few tenths of a percent of germania. Moreover, we will show later that the waveguide contribution to the overall temperature sensitivity is typically very small compared to the material effects, and hence small variations in the second term in the right-hand side of Equation (4.6) are insignificant.

The material contribution was found to be a very strong function of the difference between the thermo-optic coefficients of the core dn_1/dT and cladding dn_2/dT. Since for the standard fiber under analysis, the cladding is fabricated from pure silica, we will approximate the cladding thermo-optic coefficient with that of silica, $dn_2/dT=7.8\times10^{-6}$ /°C [34]. The core of the fiber contains germania and the presence of external dopants modifies its thermal properties [77]. A literature search revealed that the values of the thermo-optic coefficients for germanium-doped fiber cores were not easily available. Hence the following experimental approach was adopted to calculate dn_1/dT for particular fibers. A few gratings were fabricated in SMF-28 fiber and their temperature sensitivities were measured experimentally for different resonance bands. The analytical model proposed in Chapter 3 was used to evaluate the temperature sensitivity of long-period gratings. The values of $dL/LdT=4.1\times10^{-7}$ /°C and $dn_2/dT=7.8\times10^{-6}$ /°C were used for the analysis. Several values of dn_1/dT were tried and those that matched the experimental results closely were recorded for each grating. The average value of thermo-optic coefficient for the core of the SMF-28 fiber [65] was hence calculated to be $dn_1/dT=7.97\times10^{-6}$ /°C. The value is slightly larger than that of the cladding indicating that external doping process alters the thermal properties of the fiber core. The change in

thermo-optic coefficient is expected to be a function of the type and concentration of the dopant [77]. Hence it might be possible to manipulate the temperature sensitivity of long-period gratings by adding various dopants of known concentrations. The spectral dependence of the core and cladding thermo-optic coefficients is neglected in the present analysis. Additionally, the thermo-optic coefficients used here are for homogeneous media and thus any inhomogeneity in the core and the cladding during the fiber fabrication process can result in deviations from these values. It should also be noted that although the grating writing process changes the refractive index of the fiber core, we will assume that the thermal properties of the core are not altered during the fabrication process. Moreover , the core and the cladding thermo-optic coefficients are assumed to be independent of temperature. An exact analysis will include the wavelength and temperature dependence of dn_1/dT and dn_2/dT, and also the change in dn_1/dT as a function of the peak index change Δn. The model proposed in Chapter 3 neglects the presence of core while evaluating the cladding modes. Hence the thermal-induced changes in the effective indices of the cladding modes are assumed to be independent of the core thermo-optic coefficient and this approximation might also result in errors in the present analysis. Although we have separated the waveguide and material contributions to the temperature sensitivity, it can be shown that this two effects have a weak interdependence due to the coupling between δn_{eff} versus Λ through the phase-matching condition (Equation 4.1). This is similar to the relationship between material and waveguide dispersion while evaluating group velocity dispersion in optical fibers [53,72]. It can be shown that the material and waveguide effects can be considered independent while calculating the temperature sensitivity of gratings without introducing large errors in the results.

The objective of the following discussion is to provide a basic understanding of the temperature sensitivity of long-period gratings. It will be shown that the wavelength shift in a long-period grating is a function of the order of the resonance band and the grating period. The effect of different writing conditions and ambient refractive indices will also be discussed. A major part of the analysis is devoted to SMF-28 fiber [64] but can easily be extended to the two types of Flexcor fibers [61]. Once again, MATLAB was employed to obtain the modeling results presented here. Unless otherwise stated, all grating periods result in operation in the normal region.

Figure 4.1 depicts the spectral shift of the resonance band corresponding to m=7 as a function of the grating period for SMF-28 with $\Delta n=5\times10^{-4}$. The wavelength shift on the y-axis is for a temperature change of 100 °C. The material and waveguide contributions are also shown separately. The waveguide contribution is evaluated by assuming that the refractive indices of the core and the cladding do not change under ambient temperature variations. The waveguide-induced shift is small and is an increasing function of the period. The non-linearity in the waveguide contribution can be attributed to the dependence of the slope of the characteristic curves on the period (Figure 3.23). For gratings operating in the normal region, the waveguide contribution to the cumulative temperature-induced wavelength shift is typically 1 to 5%. For a given period each resonance band will have a distinct waveguide-induced shift due to the different slopes of the corresponding characteristic curves.

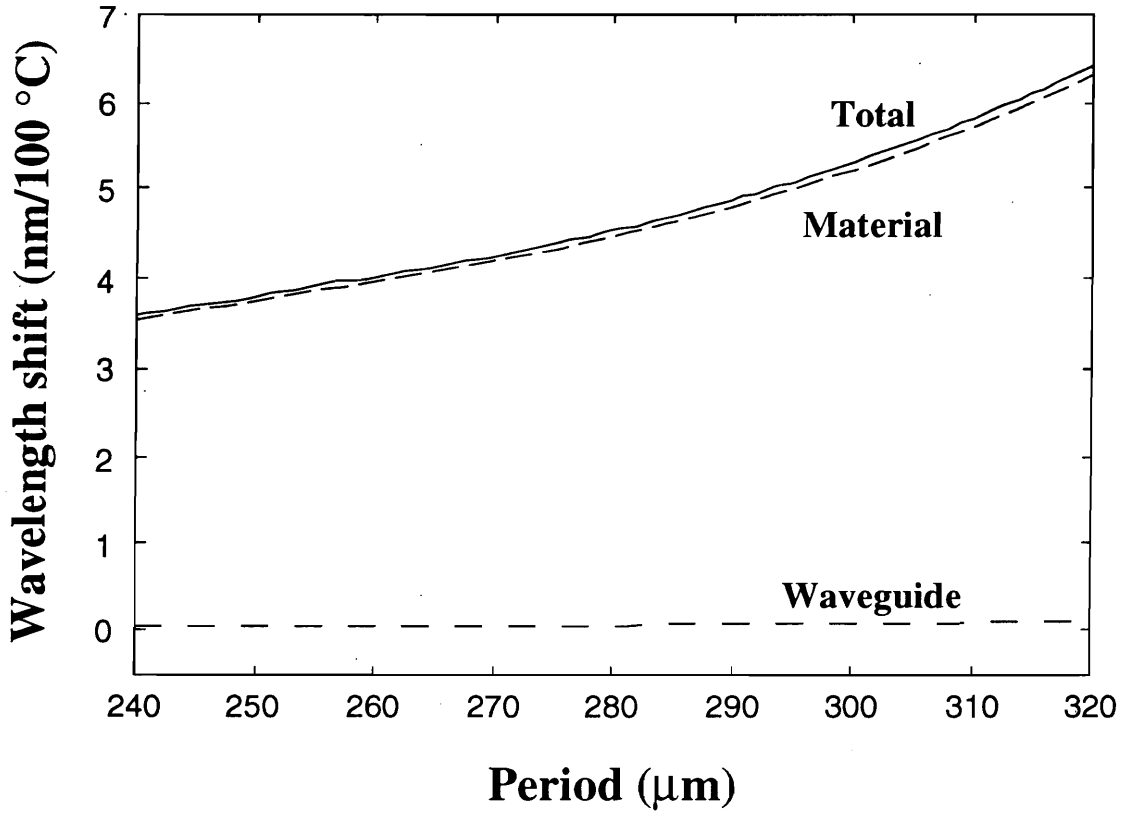

Figure 4.1. Spectral shift (per 100 °C temperature change) as a function of period for SMF-28 fiber (m=7 and $\Delta n=5\times10^{-4}$). The waveguide and material contributions are shown separately.

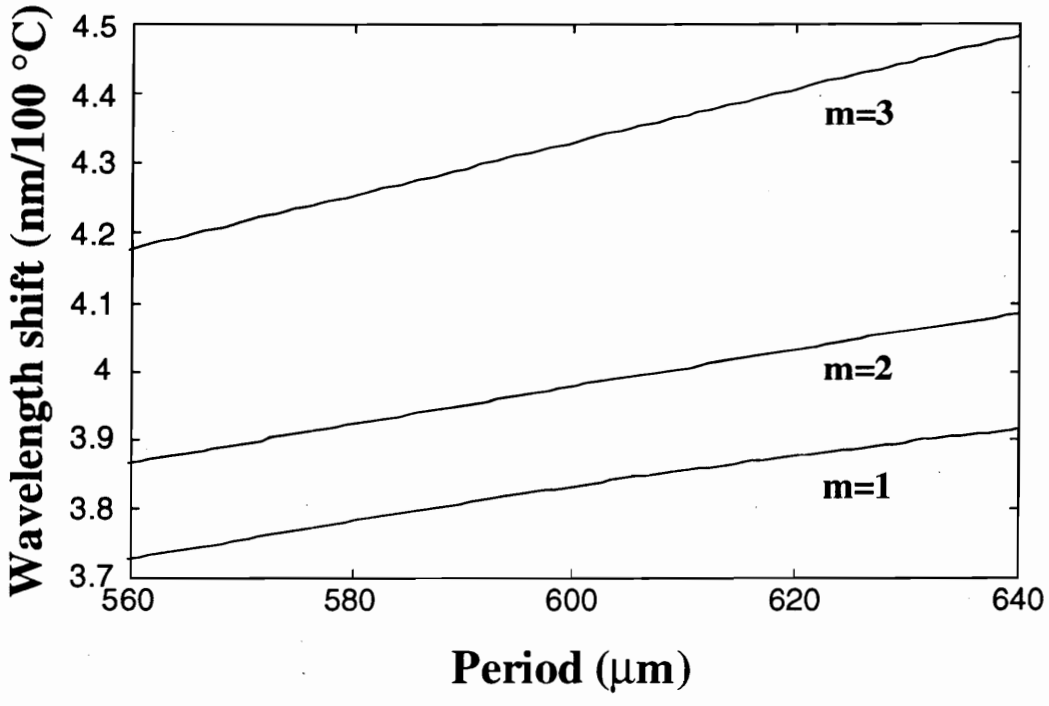

(a)

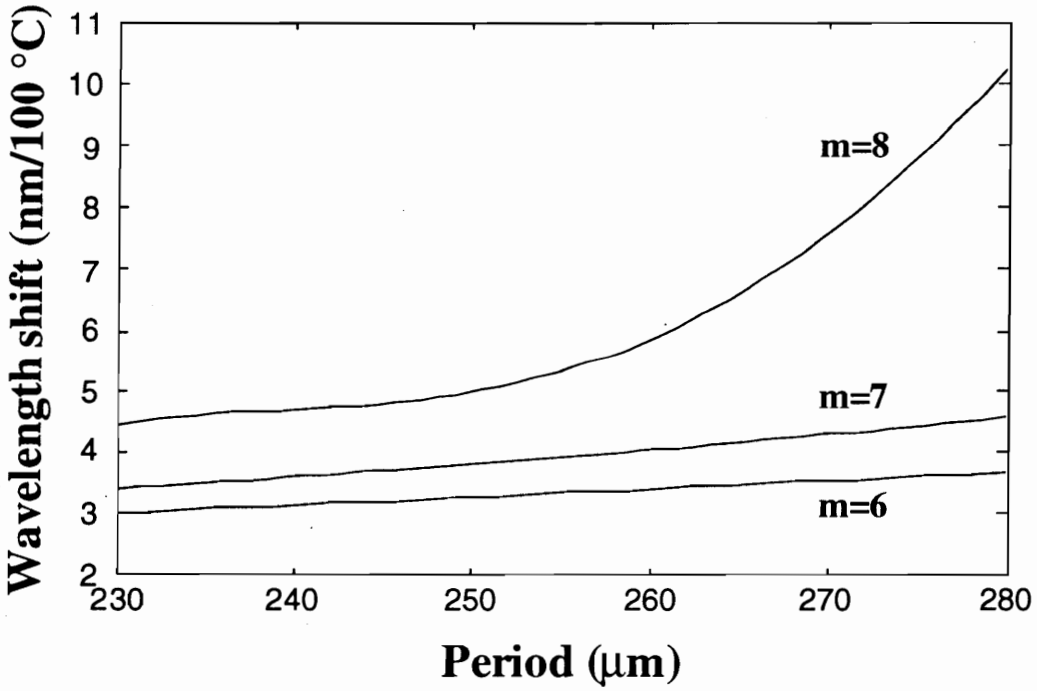

(b)

Figure 4.2. Wavelength shift (per 100 °C temperature change) as a function of period for SMF-28 fiber for (a) m=1,2 and 3, and (b) m=6,7 and 8 ($\Delta n=5\times10^{-4}$).

The material effect is analyzed by assuming that the grating period remains unchanged under temperature variations. It is seen that the material contribution also increases with the grating period and can be explained on the basis of the non-linearity of the differential effective index δn_{eff} versus wavelength λ curve for the corresponding mode. In order to keep the period Λ constant, the phase-matching condition (Equation (4.1)) dictates that the ratio $\lambda/\delta n_{eff}$ remain unchanged. Since δn_{eff} is itself a function of λ, the magnitude and polarity of the material contribution becomes a function of the thermal-induced change in δn_{eff} and also the resultant change in wavelength required to keep $\lambda/\delta n_{eff}$ constant (first term on the right-hand side of Equation (4.6)). It can be shown that for the cladding mode (m=7) in Figure 4.1, a larger change in λ is required at higher periods to keep the ratio $\lambda/\delta n_{eff}$ constant. The discussion implies that in order to obtain the maximum temperature-induced shift for a band of given order, one should choose the largest possible grating periodicity that provides coupling to the corresponding cladding mode. A larger period also results in coupling at longer wavelength and so an appropriate optical source has to be employed. Equation (4.6) reveals that the material effect is a function of the change in the differential effective index with temperature. This variation in the value of δn_{eff} with temperature depends ($d(\delta n_{eff})/dT$) on the order of the cladding mode and the operating wavelength. Its magnitude is expected to reduce as the cladding mode order increases since the higher order modes undergo larger changes in their effective indices. On the other hand, the value of $d\lambda/d(\delta n_{eff})$ is a function of the proximity of the coupling wavelength to the equalization wavelength of the corresponding cladding mode.

Figure 4.2 shows the wavelength shift as a function of grating period for different sets of cladding modes of SMF-28 fiber. The shift shown is cumulative and includes both material and waveguide contributions ($\Delta n=5\times10^{-4}$). For a fixed period the higher order modes are found to have a larger temperature-induced shifts and this can again be attributed to the distinct changes in δn_{eff} at the respective resonant wavelengths and the resultant wavelength shifts to maintain $\lambda/\delta n_{eff}$ uniform (assuming the change in period is negligible). In Figure 4.2(b), the increase in the shift for m=8 is more pronounced than for the other two modes. This is due to the fact that over the same range of periods (230 to 280 μm) the coupling to the cladding mode with m=8 occurs over a wider wavelength span as compared to the other two modes (Figure 3.23). The larger wavelength range permits a greater variation of the δn_{eff} versus λ curve as compared to the smaller change

in the corresponding curves for the lower order modes. This effect is more evident in Figure 4.2(a) where we observe an almost linear change in the wavelength shifts of the bands corresponding to the three lowest order modes.

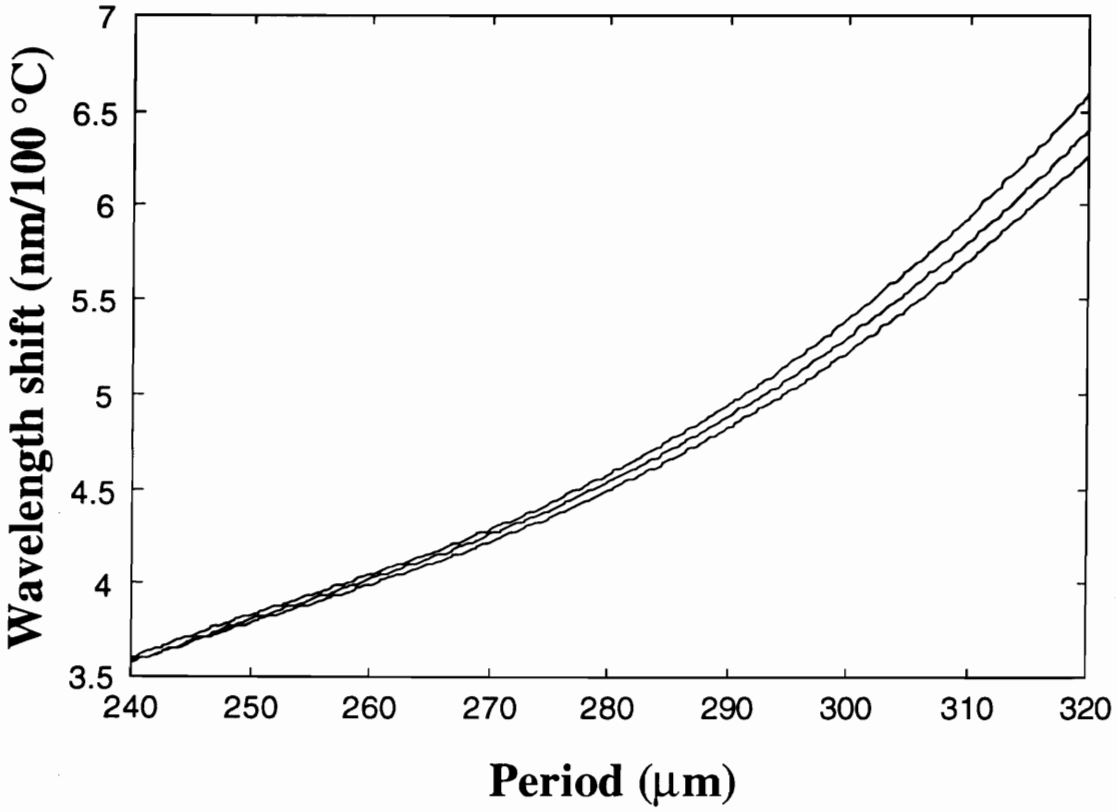

Figure 4.3. Wavelength shift (per 100 °C temperature change) as a function of grating period for SMF-28 fiber (m=7). The three curves correspond to different index changes during fabrication, $\Delta n=3\times10^{-4}$ (bottom), $\Delta n=5\times10^{-4}$ (middle) and $\Delta n=7\times10^{-4}$ (top).

Figure 4.3 shows the variation in the temperature-induced shift for a band corresponding to the cladding mode with m=7 in SMF-28 fiber as a function of the grating period. The variable in this case is the peak UV- or thermal-induced index change (Δn) during the writing process. The temperature sensitivity of the resonance band is found to increase with enhancement in Δn. This can be attributed to the resultant increase in the effective index of the guided mode that serves to shift the coupling wavelength to higher wavelengths where the material and waveguide contributions are larger. The increase in temperature sensitivity is larger for higher periods since the peak index-induced wavelength shift grows with grating period.

The above results imply that the temperature sensitivity is a function of the writing conditions. By increasing the duration of UV or thermal exposure, one can vary the temperature-induced shift. Although this might result in overcoupling the power from cladding to guided mode, this feature can be used to selectively tune the temperature sensitivity of a grating. Another method to vary the grating thermal sensitivity following fabrication is to use a suitable annealing temperature and duration. The annealing conditions would cause the band of interest to shift to a particular wavelength location and result in the desired temperature-induced shift.

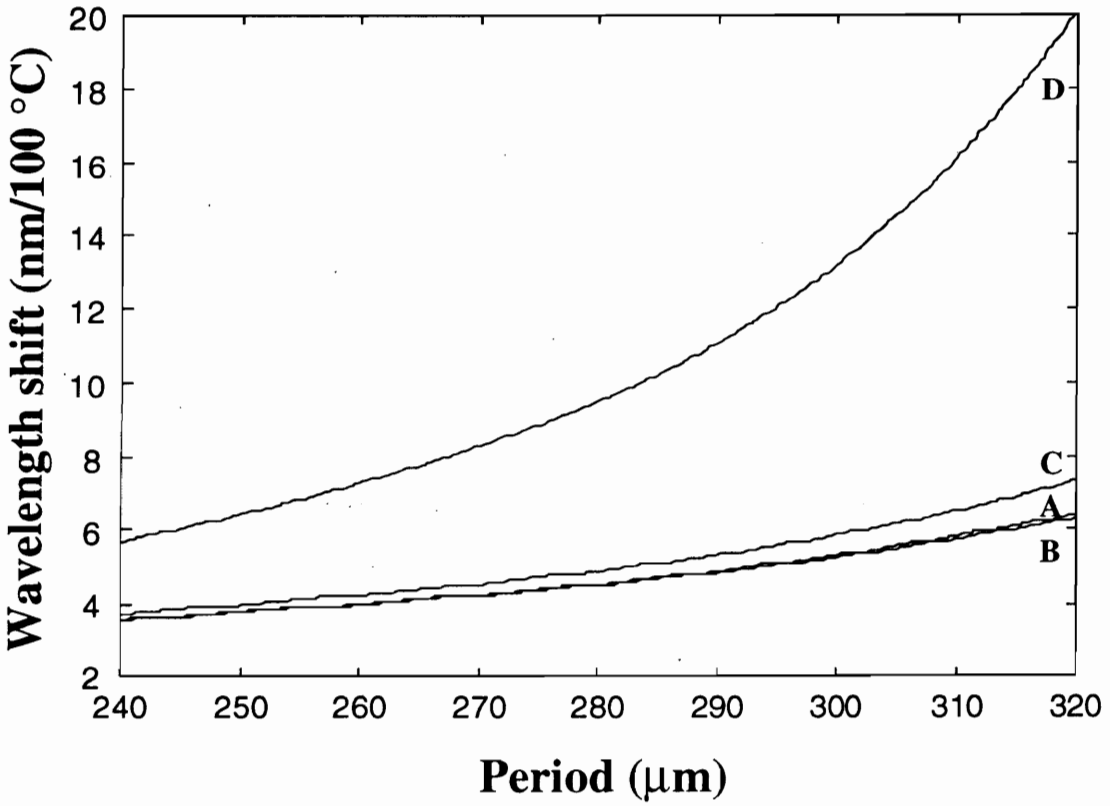

Figure 4.4. Dependence of the temperature sensitivity of long-period gratings of different periods (m=7 in SMF-28 fiber with $\Delta n=5\times10^{-4}$) as a function of ambient index. Curve A is the temperature-induced shift (per 100 °C) with air as the surrounding medium ($n_3=1.0$). Curves B and C are the shifts with water as the ambient medium ($n_3=1.33$) by ignoring and including the thermo-optic coefficient of water ($dn/dT=-1.34\times10^{-4}$/°C [123]), respectively. Curve D is the shift for an index oil with $n_3=1.42$ and $dn/dT=-3.98\times10^{-4}$/°C [124].

We now analyze the effect of ambient index on the temperature sensitivity of long-period gratings. As stated earlier, the material contribution to the temperature-induced shift is dependent on the δn_{eff} versus λ curve and the change in δn_{eff} with temperature. Numerical analysis shows that for a given period, the term $d(\delta n_{eff})/dT$ in Equation (4.6) is an increasing function of the ambient index n_3. On the other hand, the phase-matching condition for a few values of n_3 actually results in reduced temperature-induced shift. For example, Figure 4.4 shows the change in temperature sensitivity with air (n_3=1.0) and water (n_3=1.33) as ambient media. It can be seen that temperature sensitivity reduces when water is the ambient medium. The increase in n_3 enhances the effective index of the cladding mode and hence shifts the coupling wavelength to a lower wavelength. At this lower wavelength the shape of the δn_{eff} versus λ curve results in reduced temperature-induced displacement. In the above analysis we have neglected the finite thermo-optic coefficient of the ambient medium. In practical applications, the index of refraction of most fluids reduces with increase in temperature. For example, the thermo-optic coefficient of water is $dn/dT=-1.34\times10^{-4}$/°C [123], and hence a wavelength shift due to the thermal-induced refractive index will add to the temperature sensitivity of the grating. Curve C in Figure 4.4 includes the influence of the thermo-optic coefficient of water and an increase in the temperature sensitivity over the case n_3=1.0 is clearly evident. Curve D is the plot for n_3=1.42 assuming a thermo-optic coefficient of $dn/dT=-3.98\times10^{-4}$/°C (for index oils supplied by Cargille Laboratories, Inc. [124]). The large temperature sensitivity can again be attributed to the large wavelength shift due to the change in the refractive index of the fluid with n_3=1.42. The non-linearity in Curve D is due to the increase in the refractive index sensitivity for gratings with larger periods. Hence for the resonance band under consideration, the temperature sensitivity can be selectively increased by using appropriate index oils around the bare cladding. For example, using n_3=1.42, the temperature sensitivity can be increased by 50% to 300% for the range of periods shown in Figure 4.4. Although for the two cases discussed here (n_3=1.33 and n_3=1.42), a significant increase in wavelength shift can be ascribed to the thermal-induced refractive index change of the ambient fluid, for higher indices the inherent temperature sensitivity of the grating can be shown to have a large contribution. This is because for such ambient indices the δn_{eff} versus λ curve results in large positive contribution to the overall temperature sensitivity. Thus we observe that the temperature-induced shift in a long-period grating is a strong function of the ambient index. The change in temperature sensitivity with index of refraction of the surrounding medium is

dependent on the grating period and the order of the corresponding cladding modes. The experimental confirmation for these predictions will be provided in Section 4.4.2.

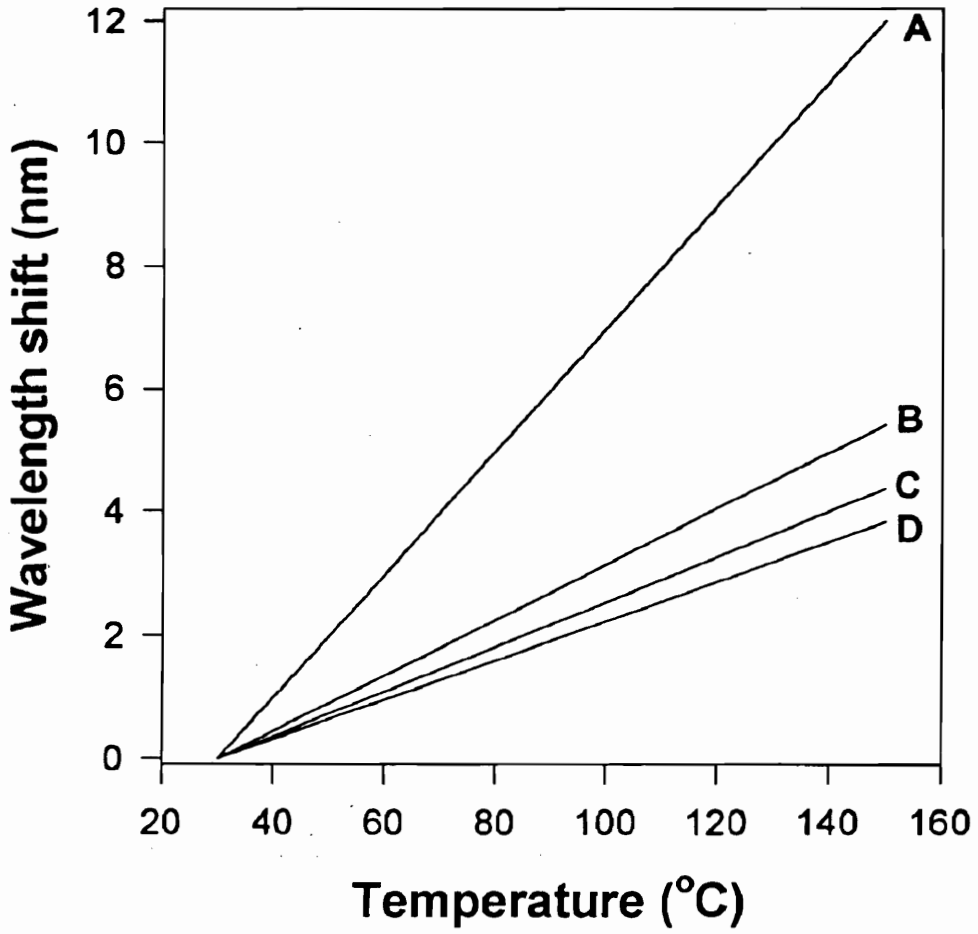

Figure 4.5. Theoretically determined temperature-induced shifts in the four resonance bands of a long-period grating written in SMF-28 fiber with Λ=280 μm. The locations of the bands A, B, C and D are 1627.8 nm, 1315.9 nm, 1197.8 nm and 1128.3 nm, respectively, for $\Delta n=4\times10^{-4}$ and temperature 30 °C.

Figure 4.5 depicts the calculated shift in the four resonance bands with temperature for a grating written in SMF-28 fiber with Λ=280 μm (n_3=1.0). For a peak index change $\Delta n=4\times10^{-4}$ the bands were found to be located at 1627.8 nm (A), 1315.9 nm (B), 1197.8 nm (C) and 1128.3 nm (D) with 30 °C as the reference temperature. The index change was determined by trial and error until the resonance bands A and B were closest to the experimental values specified in Section 4.2.2 for a grating with Λ=280 μm. The

temperature coefficients of bands A,B,C and D were determined to be 0.10 nm/°C, 0.045 nm/°C, 0.036 nm/°C and 0.032 nm/°C, respectively. This is to be expected since for the normal region of operation the higher order bands at longer wavelengths were shown to possess higher temperature sensitivity earlier in this section.

The preceding analysis was limited to gratings operating in the normal region. We now shift our attention to operation in the anomalous region and show that temperature-insensitive long-period gratings can be obtained in standard optical fibers using specific periods [35]. As discussed earlier, the gratings operating in the anomalous region have characteristic curves with negative slopes ($d\lambda/d\Lambda<0$). Thus we observe from Equation (4.6) that the waveguide contribution to the temperature sensitivity will always be negative for this region of the spectrum. Thus in order to obtain temperature-insensitive gratings we need to make the material contribution positive for the desired bands. Typically though, the thermal-induced effective index change is larger for the guided than for the cladding modes and this results in a negative material contribution in the anomalous region. As the modal order increases, it can be shown that the differential effective index reduces with rise in temperature over a spectral range that is dependent on the order of the resonance band. Hence by selecting suitable grating periods, the light from the guided mode can be coupled to the desired cladding modes, resulting in temperature-insensitive long-period gratings. The reduction in the differential effective index with temperature is due to the larger increase in the cladding mode effective indices for the higher order modes as compared to the guided mode effective index. Since the effective indices have a spectral dependence, each higher order mode has a distinct wavelength (and hence corresponding grating period) at which δn_{eff} becomes independent of temperature, resulting in zero material contribution to the temperature sensitivity (Equation (4.6)). It should be noted that it is not necessary to operate in the anomalous region to obtain the condition of temperature-insensitivity. It might be possible to design special fibers in which the temperature-induced variations in the differential effective index ($d(\delta n)/dT$) change their polarity in the normal region itself for cladding modes of certain orders. In such cases, the small waveguide contribution can be neglected or even compensated by using specific grating periods. For our analysis, we have used Corning 1060 Flexcor fiber and found that higher order modes that result in temperature-insensitivity are available in the anomalous region. The coupling to such band can be achieved for periods less than 100 μm, and hence we will limit ourselves to periods around 40 μm to obtain temperature-insensitive gratings.

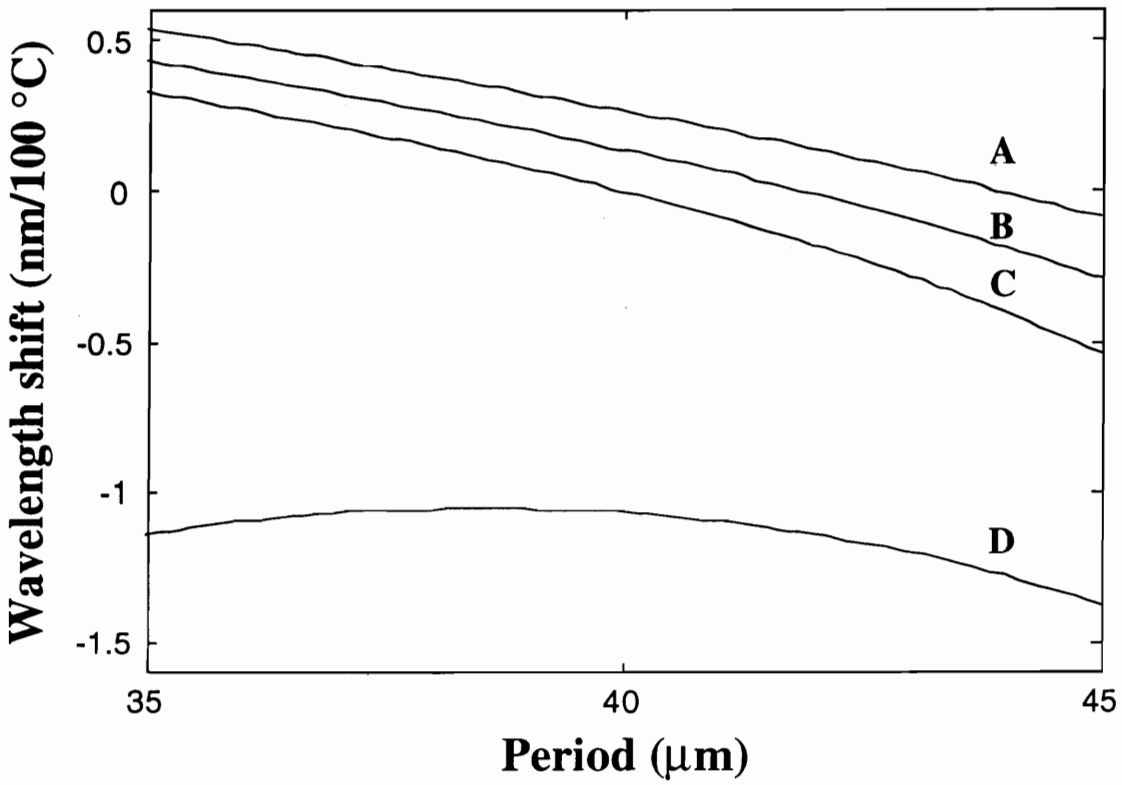

Figure 4.6. Temperature sensitivity of three bands corresponding to m=28 (A), m=29 (B) and m=30 (C) for Flexcor 1060 nm fiber with n_3=1.0 and $\Delta n=5\times10^{-4}$. Curve D is the temperature-induced shift for to m=30 with water as the ambient medium (n_3=1.33) assuming the thermo-optic coefficient of water $dn/dT=-1.34\times10^{-4}$/°C [123].

Figure 4.6 depicts the temperature sensitivity of three higher order bands as a function of period for 1060 Flexcor fiber. The peak index change assumed in the analysis is $\Delta n=5\times10^{-4}$ and it can be seen that such bands have a much smaller temperature sensitivity than conventional gratings operating in the normal region (Figure (4.2)). The three bands have shifts less than ±0.06 nm for 100 °C change in temperature for gratings with periods in the range 35 to 45 μm. Temperature-insensitivity can selectivity be obtained for the individual bands by fabricating gratings with appropriate periods. The band corresponding to m=30 is found to be almost temperature-insensitive for Λ=40 μm. The condition of temperature-insensitivity is available for other higher order modes also at specific grating periodicities. For example, for m>30, temperature-insensitive long-period gratings can be obtained for Λ<40 μm. Curve D in Figure 4.6 shows the temperature sensitivity of the gratings of different periods with water as the ambient

medium (n_3=1.33). As in the case of normal region, it was again observed that the increase in temperature sensitivity can be attributed to the finite thermo-optic coefficient of water ($dn/dT=-1.34\times10^{-4}$/°C). The temperature-induced decrease in refractive index of water reduces the effective index of the cladding mode which in turn produces a negative shift in the anomalous region. It was found that the temperature coefficient of the resonance band corresponding to m=30 increases from -0.02 nm/100 °C with n_3=1.0, to -1.1 nm/100 °C for n_3=1.33. The shifts in the bands corresponding to m=29 and m=28 were found to be 0.13 nm and 0.27 nm for 100 °C change in temperature (n_3=1.0). It should be noted that the overlap between the guided mode and these higher order cladding modes is poor and hence results in small values of coupling coefficients. The isolation can be improved by increasing the peak index change Δn in the gratings during the writing process. The enhancement in Δn can be obtained during the CW writing process by increasing the UV power and/or by reducing the scanning speed of the beam across the fiber. The higher Δn typically serves to slightly change the temperature sensitivity of the gratings due to a shift in the characteristic curve. For example, for a grating with Λ=40 μm, the band corresponding to m=30 can be shown to have a much higher (negative) wavelength shift for the same change in ambient temperature. In the present analysis we have taken the core thermo-optic coefficient of the Flexcor fiber to be the same as that for the SMF-28 fiber ($dn_1/dT=7.97\times10^{-6}$ /°C) although these fibers have slightly different amount of germania doping. For an exact model, the value of this coefficient has to be determined for the Flexcor fiber, although for periods in the region Λ=40 μm, it was observed that small changes in the thermo-optic coefficient of the core do not significantly alter the results of Figure 4.6.

In this section we discussed the temperature sensitivity of long-period gratings. It was shown that the temperature sensitivity has two distinct contributions - material and waveguide, with the former typically dominating. An analytical model was developed to explain the dependence of the temperature sensitivity on the grating period, the order of the resonance band, the index of the ambient material and the writing conditions. It was observed that for a given fiber one or more of these parameters can be manipulated to vary the temperature sensitivity. The operation of long-period gratings was evaluated in the anomalous region and it was shown that for coupling to certain higher modes, temperature-insensitive gratings can be obtained in standard fibers. The example of a grating in Flexcor fiber with Λ=40 μm was analyzed and the effect of changing the

ambient material to water was investigated. In Section 4.2.2 we discuss some experimental results to verify the temperature sensitivity of long-period gratings.

4.2.2 Experimental Results

In this section we present some experimental results to validate the operation of long-period gratings as efficient temperature sensors. The spectral shift is shown to be slightly non-linear and the magnitude of displacement is obtained for resonance bands of various orders in a grating in SMF-28 fiber. The wavelength dependence of the temperature sensitivity is compared for bands corresponding to different cladding modes.

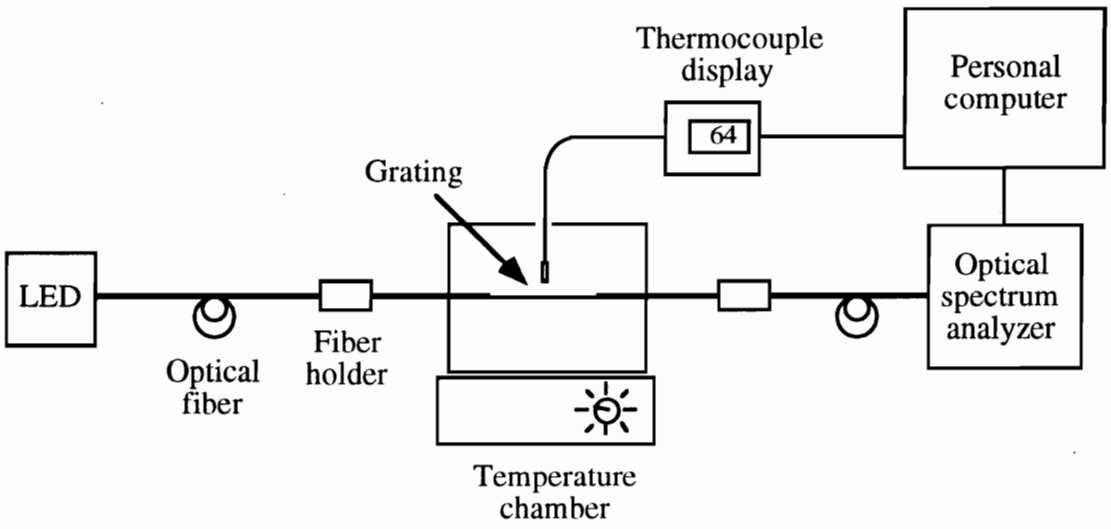

Figure 4.7. Experimental set up employed to determine the thermal-induced spectral shift in the resonance bands of a long-period grating. The thermocouple is placed adjacent to the grating in the temperature chamber.

Figure 4.7 shows the set up used to measure the spectral shift with temperature for a long-period grating. The grating under test was pre-annealed to temperatures in excess of the highest operating temperature to ensure that all unstable defect sides are removed prior to the measurement process (Section 3.3.2) [98]. If this procedure is not followed, the resonance bands are found to slowly move to shorter wavelengths (for the normal region of operation) as the grating ambient temperature approaches the annealing temperature. As a general precaution, the gratings were annealed at temperatures 50 °C higher than the maximum expected test temperature for a duration of 10 to 20 hours. The grating was

held taut between two fiber holders to prevent bends from influencing the measurement process. The section of the fiber containing the grating was enclosed in an oven whose temperature could be controlled externally. Although the temperature chamber could be heated to 600 °C, the maximum test temperature was limited to 150 °C to prevent complete burning of the acralyte coatings on both sides of the bare fiber.

The gratings were interrogated using broadband sources such as LEDs centered at 840 nm, 1275 nm or 1520 nm depending on the location of the resonance bands. For gratings that had bands spread over a wide wavelength range ($\delta\lambda$>200 nm) the spectra of two suitable LEDs were combined using a 2×2 coupler. The grating throughput was coupled into the ANDO AQ-6310C optical spectrum analyzer (OSA) using a bare-fiber adapter. The OSA was interfaced to a personal computer using a standard GPIB cable. A computer code was written to acquire data from the OSA at an interval specified by the user before the test was initiated. The grating transmission spectrum was normalized to that of the source and transferred to the computer once a single sweep was completed. Thus reference traces of the source had to be obtained in the regions where the resonance bands were located. The wavelength span used to monitor each band was typically in the range of 10 to 20 nm with the resolution depending on the magnitude of source power and the grating isolation in the operating region. Although the grating spectral width is larger than 10 nm, the smaller spans enable a more accurate determination of the grating resonant wavelengths.

The spectrum acquired by the computer was employed to determine the peak loss wavelength but it was found that noise had a significant impact on the wavelength determination. Hence another computer program was integrated into the data acquisition code to obtain a curve fit to the raw data. The polynomial least-squared algorithm was used to obtain a fit closest to the input spectrum. A modeling function was determined such that the sum of the squared errors between samples of this function and the raw data points was minimum. An alternative to the above procedure might be to reduce the high-frequency noise components by low-pass filtering the acquired spectrum. Figure 4.8 shows an example of the input spectrum and the corresponding least-squared curve fit for a resonance band. The improvement in the grating spectrum enables a more accurate determination of the grating resonance wavelength by calculating the transmission versus wavelength slope at different points in the range of interest. The resolution of a sensor using the OSA for demodulation depends on the minimum detectable wavelength shift.

Modern spectrum analyzers are available with resolutions ranging from 0.01 to 0.5 nm, depending on the cost of the system.

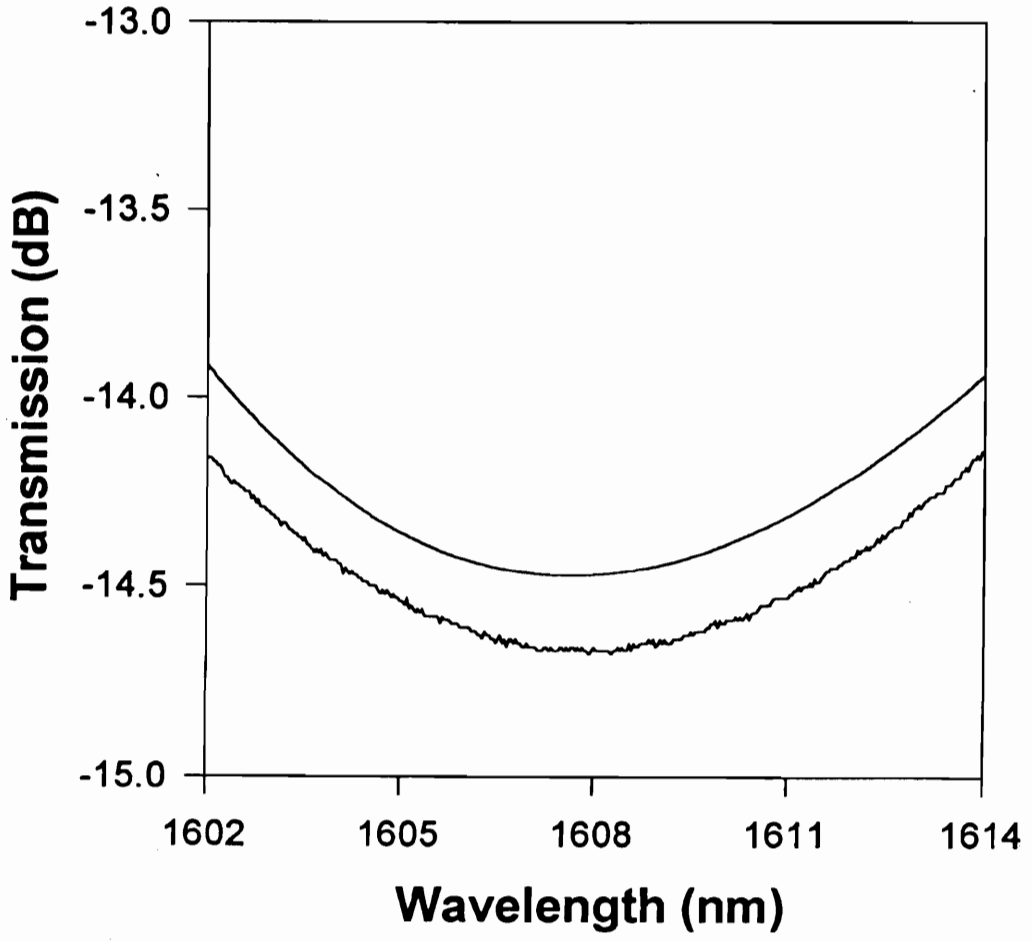

Figure 4.8. Effect of employing a least-squared curve fit on the transmission spectrum of a long-period grating. The offset between the raw data and the corresponding curve fit has been deliberately introduced to prevent overlapping.

The time taken by the OSA to complete one span varies from 5 to 25 seconds depending on various adjustable parameters. The delay introduced by the computer to acquire raw data, generate a curve fit and determine the resonant wavelength is less than 5 second per scan. Hence this method to determine perturbation is not suitable for applications where rapid fluctuations are expected. Since temperature variations are typically quasi-static, this process is adequate for such applications. In Section 4.5.1 we will introduce a simple demodulation process that can be used in high bandwidth applications.

A thermocouple was co-located with the grating in the heating chamber to measure the actual temperature with an accuracy of 0.1 °C. The analog thermocouple output was also transferred to the personal computer using an A/D card. The thermocouple temperature was recorded at the beginning and end of the OSA sweep and averaged to provide a mean value over this duration. The resonant wavelength and average temperature were displayed on the computer monitor and also saved in a file for post-processing.

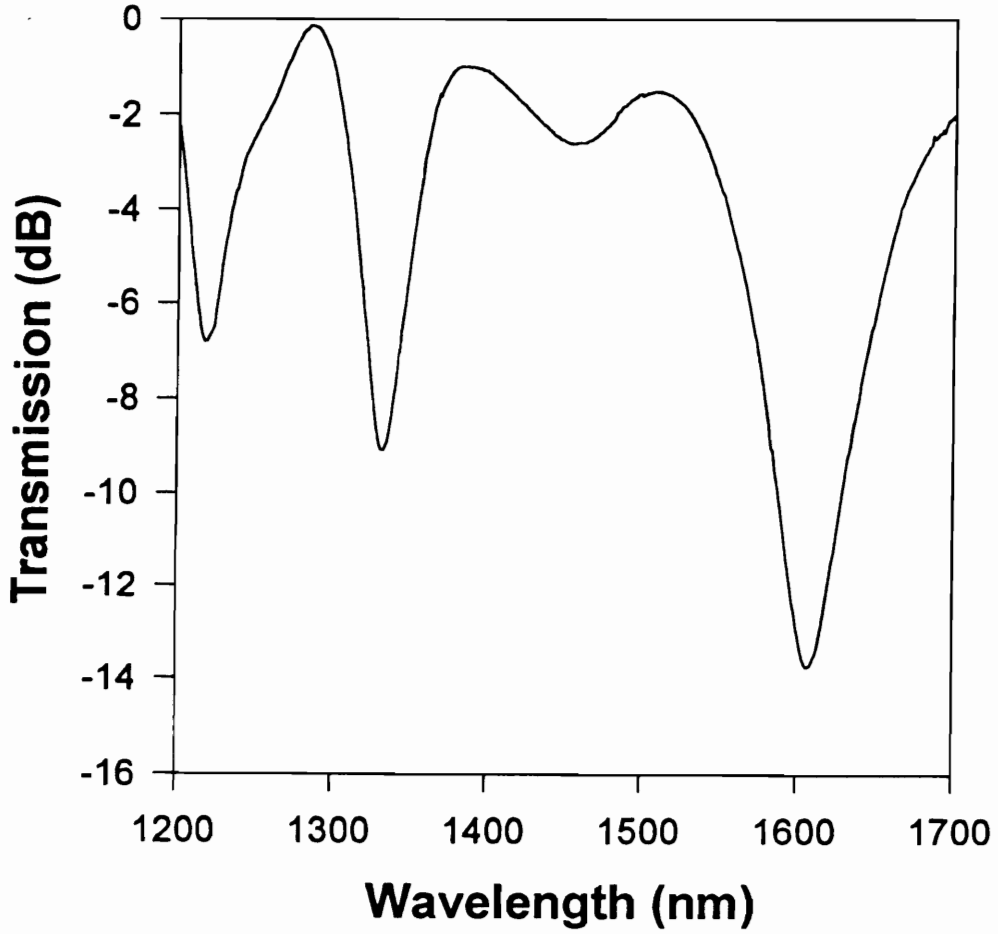

Figure 4.9. Transmission spectrum of a long-period grating used for the temperature test. The grating is fabricated in Corning SMF-28 fiber employing continuous-wave UV radiation (Λ=280 μm). The wavelength span is limited to 500 nm here but resonance bands are present at wavelengths shorter than 1200 nm also.

Figure 4.9 depicts the transmission spectrum of a long-period grating used in the temperature test. The grating was fabricated in Corning SMF-28 fiber with period Λ=280

μm and length L=1 cm using the continuous-wave method (UV power =130 mW) described in Section 3.3.1.2. The post-annealed locations of the four highest wavelength resonance bands in the optical source spectrum were found to be 1607.8 nm, 1332.4 nm, 1219.3 nm and 1159.3 nm at 22.7 °C and these are denoted by A,B,C and D, respectively. Light from two LEDs (centered at 1275 nm and 1520 nm) was combined using a 3-dB coupler and the grating was spliced to one output leg of the coupler. We observe from the characteristic curves for SMF-28 fiber (Figure 3.23) that for Λ=280 μm all the resonance bands operate in the normal region of operation. The grating was heated to 160 °C and then cooled slowly to room temperature over a period of 90 minutes. Figure 4.10 depicts the transmission spectra of resonance band A at discrete temperatures. The shift in the band with increasing temperature was towards longer wavelength as indicated by the arrow.

For a system (such as the OSA) that detects the shift in the resonance bands, a larger wavelength displacement implies increased sensitivity. Thus we would henceforth use the words wavelength shift and sensitivity in the same sense. In Figure 4.10 note the change in transmitted intensity at all the wavelengths in the range shown. The intensity variation implies that a demodulation scheme that detects the change in the intensity at one wavelength in the resonance band may be employed in conjunction with long-period gratings. Such a demodulation scheme will be proposed in Section 4.5.1.

Figure 4.11 illustrates the wavelength shift in the four resonance bands under test. All the bands were observed to have a positive temperature-induced wavelength shift, with the sensitivity reducing with the order of the band. The slopes of the linear curve fits of the bands A,B,C and D were determined to be 0.093 nm/°C, 0.049 nm/°C, 0.042 nm/°C and 0.039 nm/°C, respectively. Figure 4.11, on being compared with Figure 4.5, reveals a fair agreement between the actual and predicted results. A small non-linearity was observed in the wavelength shift of the resonance bands and this can be attributed to the temperature-dependence of the thermo-optic coefficients of the core and the cladding [77]. The non-linearity is insignificant for most practical applications as the wavelength shift versus temperature calibration curve can always be a polynomial of second or higher order. However the non-linear thermal-induced wavelength shift will be shown to limit the performance of simultaneous strain and temperature measurement systems in Chapter 5. The dashed line in Figure 4.11 is the shift due to a fiber Bragg grating at 1550 nm with temperature (Section 2.4.4.1). The temperature coefficient of a Bragg grating (0.013

nm/°C) is seven times smaller than that of resonance band A of the long-period grating considered here. Although the temperature-induced shift in a Bragg grating is also slightly non-linear [10] we have represented only the linear portion in Figure 4.11. Thus long-period gratings operating in the normal region typically have an order of magnitude larger temperature-induced wavelength shift compared to their short-period counterparts.

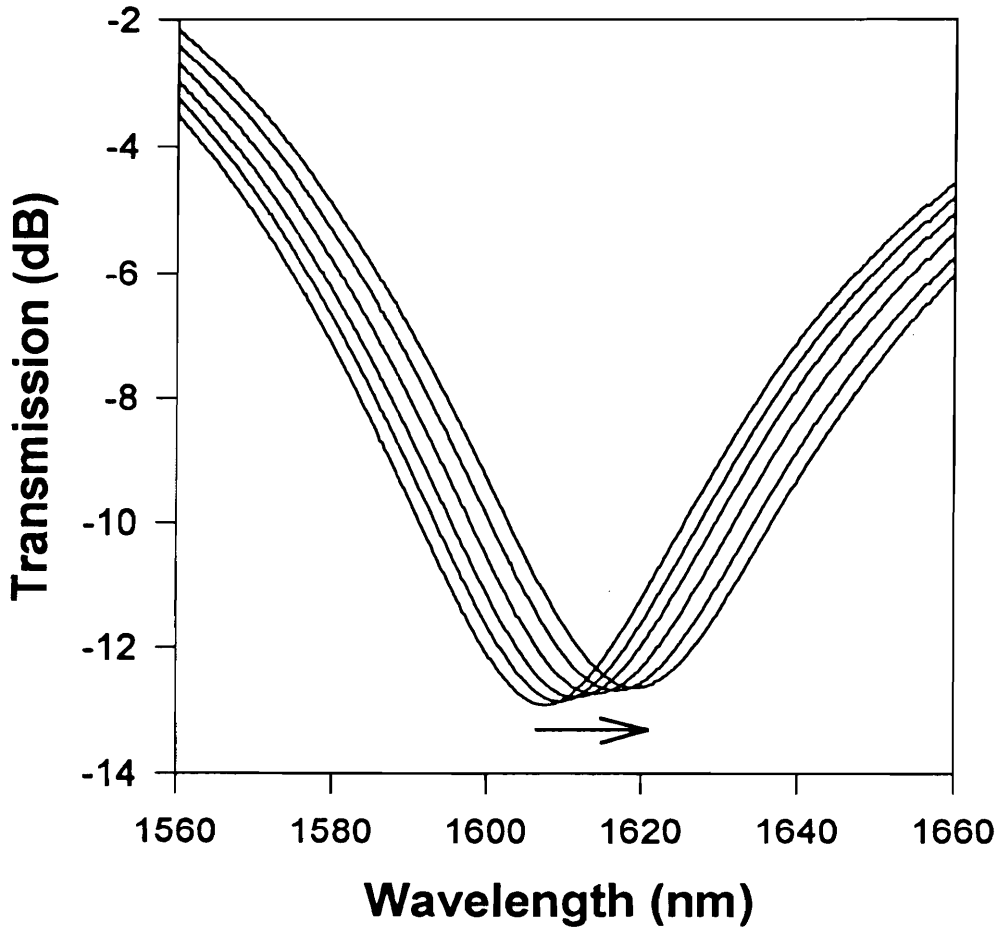

Figure 4.10. Shift in band A with temperature for the grating shown in Figure 4.9. The spectra correspond to temperatures of 22.7 °C, 49.1 °C, 74.0 °C, 100.9 °C, 127.3 °C and 149.7 °C from left to right. The resonant wavelength shifts from 1607.8 nm at 22.7 °C to 1619.6 nm at 149.7 °C.

The resolution of the temperature sensor is a function of the minimum detectable wavelength shift using the OSA. Although the resonance bands in long-period gratings are broad, resulting in uncertainty in exact determination of the peak loss wavelengths,

we have been successful in measuring wavelength shifts less than 0.05 nm using the least-squared curve fitting method described earlier. The detection of 0.05 nm wavelength shift corresponds to temperature resolutions between 0.54 °C and 1.28 °C for the different resonance bands of the test grating. The corresponding uncertainties in temperature measurements are between ±0.3 °C and ±0.8 °C. For a fixed peak index change, the uncertainty in the wavelength measurement can be reduced by fabricating gratings with longer lengths and hence smaller linewidths, as described in Section 3.4.1.

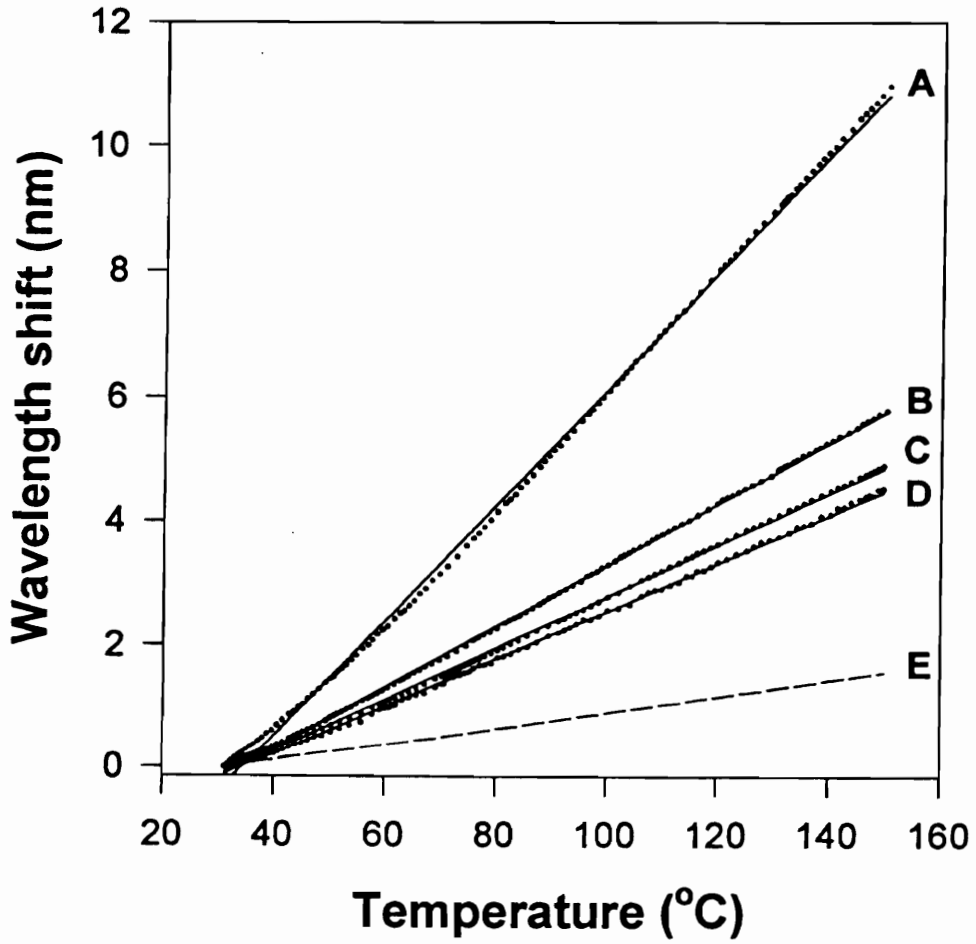

Figure 4.11. Shift in the peak loss wavelengths (with respect to that at 31.2 °C) with temperature for various resonance bands of the grating shown in Figure 4.9. The location of the bands A, B, C and D are 1608.6 nm, 1332.9 nm, 1219.7 nm and 1159.6 nm, respectively at 31.2 °C. The experimental data (symbols) are and approximated by linear curve fits. The dashed line (E) is the shift for a Bragg grating at 1550 nm with a temperature coefficient 1.3 nm/°C.

In this section we demonstrated that long-period gratings can be employed as effective temperature sensors. The large spectral shift of the resonance bands can be used to obtain highly sensitive temperature transducers. The shift with temperature was found to be slightly non-linear but this can be easily accommodated during the calibration process. The shift in the highest wavelength resonance band for a long-period grating written in Corning SMF-28 fiber was experimentally determined to be 0.093 nm/°C and is almost an order of magnitude larger than that for a conventional Bragg grating. Long-period gratings with larger temperature-induced spectral shifts have previously been demonstrated in other types of fibers [21].

4.2.3 Temperature-Insensitive Gratings

In this section we review the operation of temperature-insensitive long-period gratings fabricated in fibers with special refractive index profiles [34]. It is demonstrated that for operation in the anomalous region, gratings with reduced temperature sensitivities can be obtained in standard telecommunications grade fibers [35].

It was shown in Section 4.2.1 that the temperature-sensitivity of a long-period grating arises from the thermal-induced changes in the differential effective index and in the periodicity. For a grating written with a period that causes the resonance bands to operate in the normal region, the material and the waveguide contributions are both positive, resulting in an overall positive temperature coefficient. As demonstrated in the previous sub-section, a resonance band may shift by as much as 9.3 nm for 100 °C change in ambient temperature. The large temperature sensitivity of long-period gratings can be a major limitation in applications such as strain sensing [21,33] and gain flattening of erbium spectrum [30]. Thus it becomes important to obtain long-period gratings that have a temperature shift of 0.5 nm/100 °C or less for most practical applications.

Recently Judkins *et al.* [34] proposed a multilayer refractive index profile that could potentially result in temperature-insensitive long-period gratings. The special fiber design proposed by them counterbalanced the material and waveguide contributions for specific cladding modes, and a specific range of periods was found to produce temperature-insensitive gratings. The multi-clad structure proposed by Judkins *et al.* [34] makes the waveguide effect negative at periodicities of interest by inducing coupling to

cladding modes operating in the anomalous region. A grating (Λ=156 μm) fabricated in such fiber was found to overcompensate for the material effect and result in a shift of -0.45 nm for 100 °C change in surrounding temperature [34]. It is important to note here that the temperature sensitivity is a strong function of the grating period, the order of the resonance band and the writing conditions. Hence variations in these parameters can alter the temperature response of gratings in the special fiber.

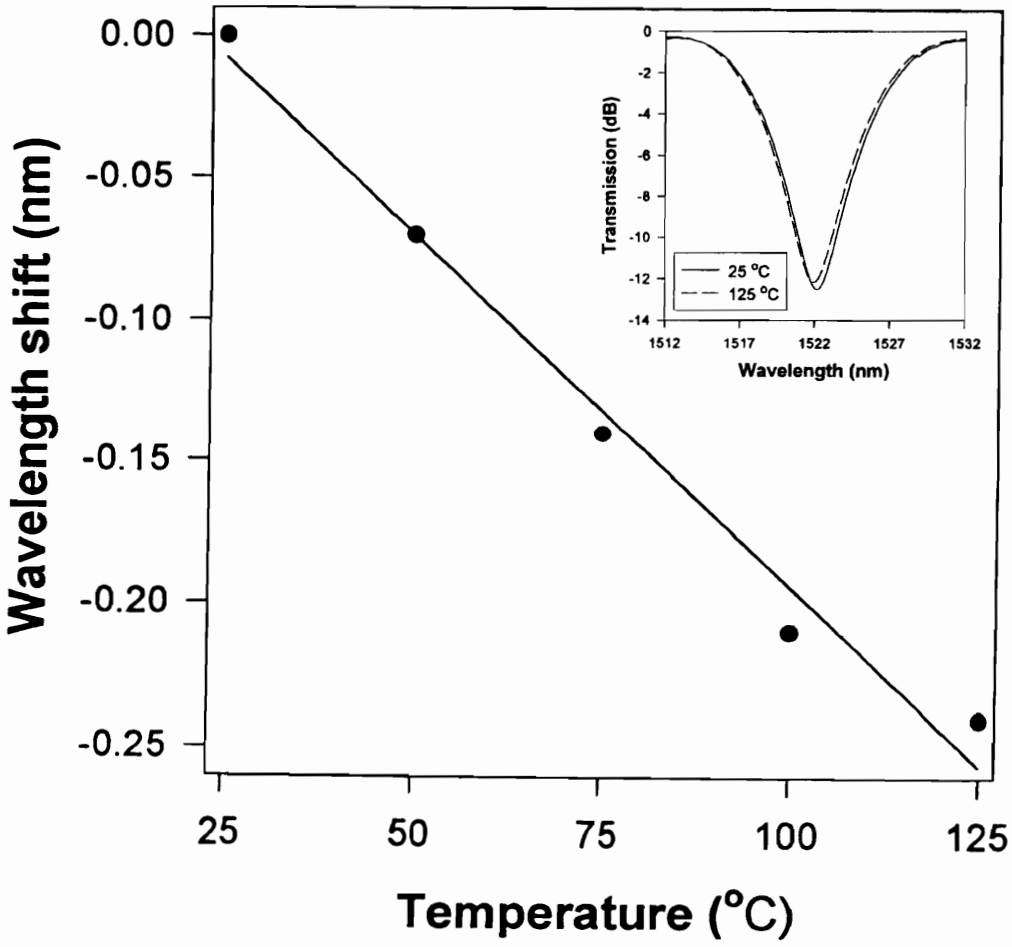

Figure 4.12. Spectral shift in the resonance band for a grating (Λ=166 μm) written in the fiber with multilayer refractive index profile [34]. The line is a curve-fit to the experimental data (circular symbols). The resonant wavelength shifts from 1522.17 nm at 25 °C (solid curve) to 1521.93 nm at 125 °C (dashed curve) as shown in the inset.

We now present experimental results obtained by using the gratings written in the fiber with special refractive index profile [34]. The gratings were provided by Bell

Laboratories and written using the excimer laser method (Section 3.3.1.1). A set up similar to the one depicted in Figure 4.7 was used to measure the temperature sensitivity of a resonance band at 1522.17 nm in a grating with period Λ=166 μm and length L=3.65 cm. The resonant wavelength for the band was measured at discrete temperatures and the results are plotted in Figure 4.12. The straight line curve fit had a slope of -0.0025 nm/°C and is more than an order of magnitude smaller than temperature coefficients of all the bands of the grating investigated in Section 4.2.2. Three other gratings with resonance bands in the range 1480 nm and 1550 nm were also tested for their temperature response. The spectral shifts were found to vary between -0.1 nm and -1.5 nm for 100 °C change in ambient temperature. The variation can be attributed to the different periods that were employed for fabricating the gratings that were tested. The response of these gratings to axial strain and refractive index changes will be discussed in Section 4.3.3 and 4.4.3, respectively.

The requirement of special fibers to obtain temperature-insensitivity may be uneconomical in system design. In Section 4.2.2 we had demonstrated theoretically that we can obtain temperature-insensitive gratings in standard fibers by using specific grating periods in the anomalous region. We now confirm those results experimentally by using gratings fabricated in Flexcor 1060 fiber.

To test the response of standard fiber gratings in the anomalous region, several gratings were fabricated in Flexcor fiber with Λ=40 μm. The period of 40 μm is smaller than the typical values used to obtain bands in the normal region of operation. Figure 3.27 reveals that Λ=40 μm clearly results in anomalous behavior for all bands of interest in the wavelength range 1100-1500 nm. The gratings were fabricated using the continuous-wave exposure with UV power ranging from 130 mW to 160 mW. The writing times varied from 20 to 30 minutes for such gratings. The requirement of larger power and longer exposure time can be attributed to the poor overlap between the guided mode and higher order cladding modes involved in coupling. After annealing gratings were found to possess a loss that increased for shorter wavelengths and its origin is currently under investigation. The out of band loss varied from 0.5 dB to 2.5 dB in the 1140 nm region and was found be a function of the writing and annealing conditions. A grating with post-annealed bands located at 1141.5 nm, 1253.1 nm and 1376.4 nm was tested for its temperature sensitivity. Figure 4.13 depicts the shift in the band at 1141.5 nm as a function of temperature [35].

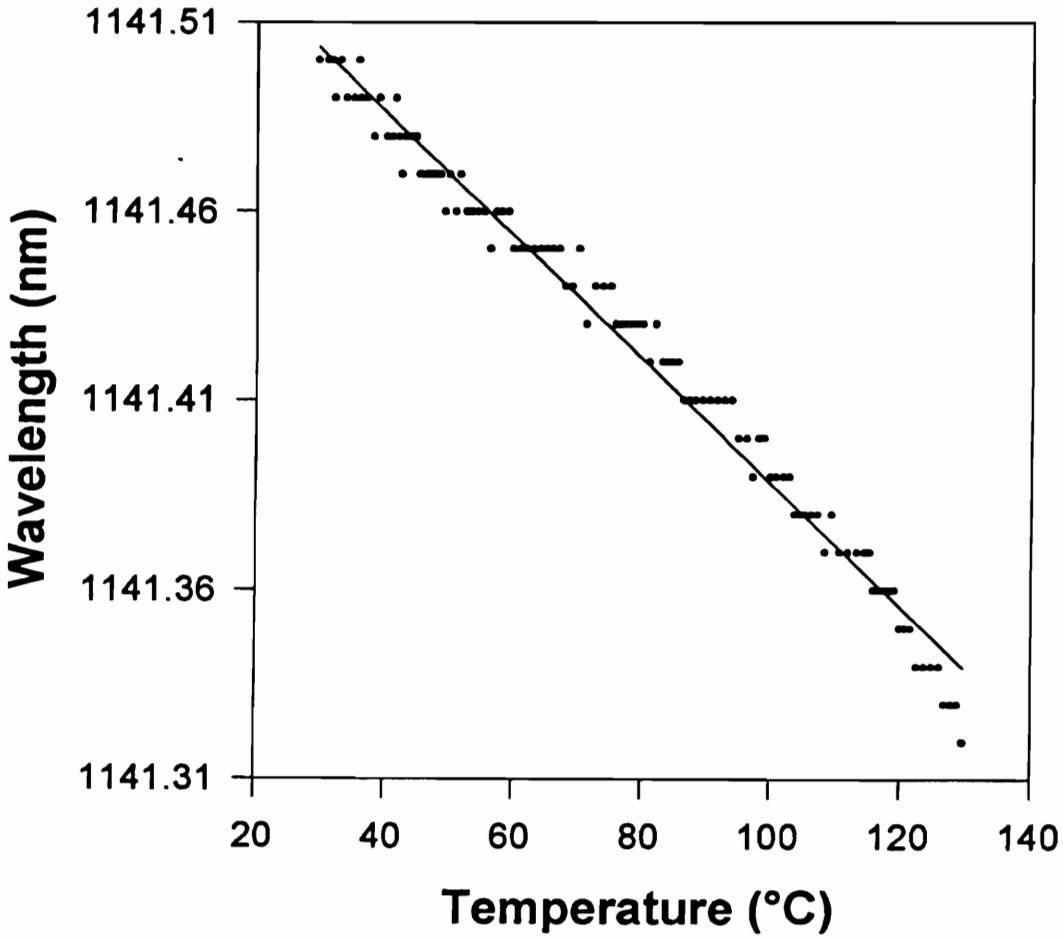

Figure 4.13. Location of a resonance band as a function of temperature for a grating with Λ=40 μm in Flexcor 1060 fiber. The straight line fit has a slope of -0.16 nm/°C.

The band was observed to shift by a mere 0.18 nm to lower wavelengths for an increase in temperature from 25 °C to 125 °C, as shown in the transmission spectra of Figure 4.14 [35]. This shift is more than an order of magnitude smaller than that for gratings operating in the normal region (Figure 4.11). The theoretically predicted shift for this band is -0.02 nm for 100 °C change in temperature. The resonance bands at wavelengths 1253.1 nm and 1376.4 nm were found to shift by 0.10 nm and 0.30 nm, respectively, to longer wavelengths. The calculated shift for these bands were 0.18 nm and 0.34 nm, respectively. The differences between the actual and calculated results can be attributed to the approximations made in the model, the use of the thermo-optic coefficients for SMF-28 fiber instead of that for Flexcor 1060 fiber, the deviations in the fiber parameters

from the values specified by the manufacturer and different peak index change compared to that used in the calculations ($\Delta n=5\times10^{-4}$). We thus see that resonance bands in gratings with certain specific periods in standard optical fibers can have temperature coefficients less than 0.005 nm/°C. These devices can be used in sensing and communication systems without employing temperature stabilization or compensation. The important thing to note in Figure 4.14 is that the transmission spectrum of the grating almost overlaps at the two temperatures which suggests that a demodulation scheme that detects the intensity change at one or more wavelengths in the band will be insensitive to temperature fluctuations. Such simple demodulation schemes will be proposed as simple alternatives to optical spectrum analyzers in Section 4.5.1.

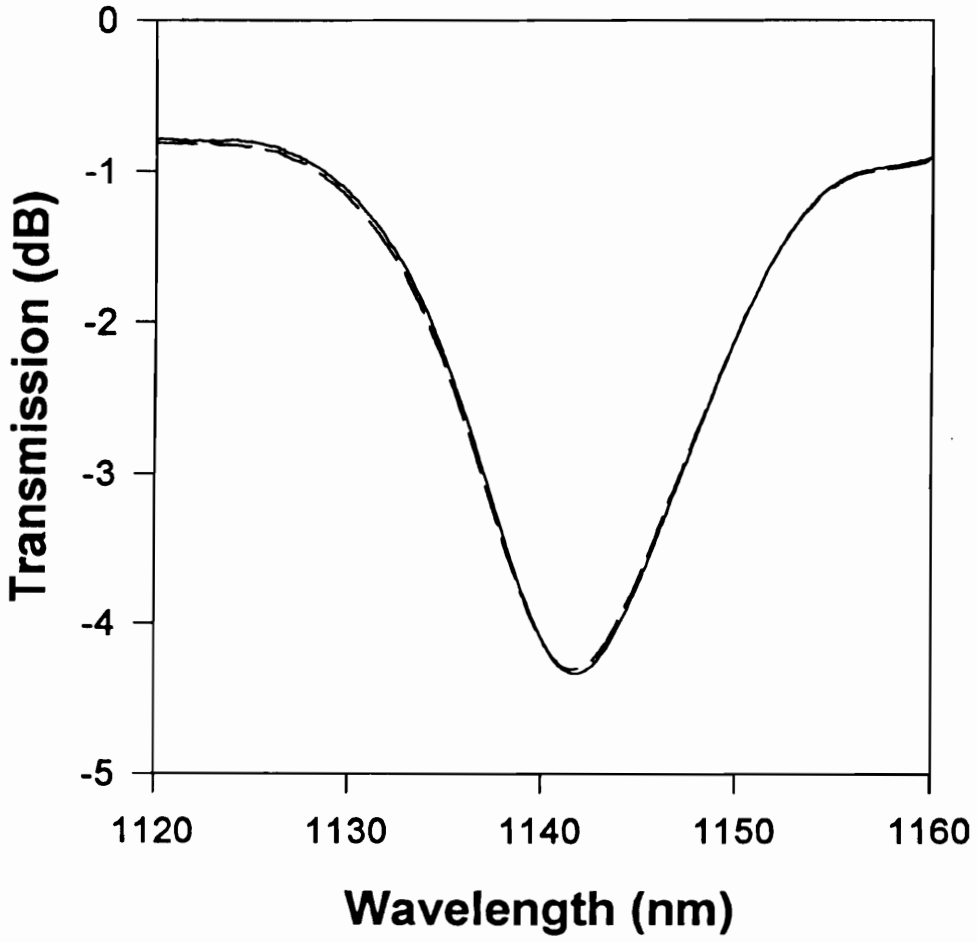

Figure 4.14. Transmission spectra of a long-period grating written in Flexcor 1060 nm fiber with Λ=40 μm at 25 °C (solid curve) and 125 °C (dashed curve). The resonance band shifts by a mere -0.18 nm for 100 °C increase in temperature.

In this sub-section we presented experimental results from the temperature sensitivity tests on long-period gratings fabricated in the profile proposed by Judkins *et al.* [34]. The counterbalancing of the material and waveguide contributions in such gratings produces wavelength shifts as small as -0.25 for 100 °C increase in temperature. We also showed that gratings with very small temperature sensitivity can be fabricated in standard optical fibers. A grating in Flexcor 1060 fiber with Λ=40 μm was demonstrated to have a shift of -0.18 nm for 100 °C rise in temperature.

Thus long-period grating-based temperature sensors are easy to fabricate and possess high sensitivity. We have discussed the principle of operation of such sensors and investigated their dependence on various parameters. Experimental results that validate the effectiveness of long-period grating temperature sensor were also presented.

4.3 Axial Strain Sensor

Fiber optic sensors that measure strain have recently gained popularity due to their small size and multiplexing capabilities [4,6]. In this section we introduce axial strain sensors using long-period gratings [21]. An analytical evaluation of the sensor is undertaken to investigate its dependence on the grating period, writing conditions and index of refraction of ambient medium. It is shown that temperature-insensitive fibers discussed in Section 4.2.3 retain their capacity to measure strain. Strain-insensitive gratings are shown to overcome the problem of the finite expansion of the host material in embedded and surface-mounted temperature sensors.

4.3.1 Theoretical Analysis

Consider a long-period grating with period Λ under the influence of axial strain $\Delta\varepsilon$, where $\Delta\varepsilon$ is a dimensionless quantity since it is the ratio of the change in length and the original length ($\Delta\varepsilon=\Delta L/L$). In the limit $\Delta\varepsilon\to 0$, Equation (4.3) can be modified with $\xi=\varepsilon$ to yield,

$$\frac{d\lambda}{d\varepsilon} = \frac{d\lambda}{d(\delta n_{eff})}\frac{d(\delta n_{eff})}{d\varepsilon} + \frac{d\lambda}{d\Lambda}\frac{d\Lambda}{d\varepsilon}. \tag{4.7}$$

We again divide the cumulative wavelength shift into material and waveguide contributions. The material contribution to the strain-induced shift is a function of the

change in the differential effective index with strain $d(\delta n_{eff})/d\varepsilon$ while the waveguide effect is dependent on the variation in the grating period with strain. Using Equation (4.2), and $\Delta\varepsilon=dL/L=d\Lambda/\Lambda$, we get,

$$\frac{d\lambda}{d\varepsilon} = \frac{d\lambda}{d(\delta n_{eff})}\left(\frac{dn_{eff}}{d\varepsilon} - \frac{dn_{cl}}{d\varepsilon}\right) + \Lambda\frac{d\lambda}{d\Lambda}. \tag{4.8}$$

Axially straining a fiber changes the core and the cladding indices of refraction and radii. The deviation in the values of these parameters from the unperturbed case serves to vary the differential effective index δn_{eff} and results in the phase-matching condition to be satisfied at a different wavelength. The waveguide effect simply depends on the period and the order of the cladding mode in a given fiber. For operation in the normal region, the waveguide contribution will be positive while its magnitude will be negative if the period is chosen such that the coupling to the corresponding cladding mode occurs in the anomalous region. It was found that unlike the temperature sensor, strain-induced changes in the core and cladding radii contribute significantly to the material effect. The variation in the core and the cladding dimensions arises from the Poisson's effect which reduces the radii based on the following expression [78],

$$\frac{dq}{d\varepsilon} = -\nu\, q\,, \tag{4.9}$$

where q=a,b for core, cladding and ν is termed the Poisson's ratio for the corresponding material. We will use ν=0.17 (fused silica) [125] for the cladding and ν=0.165 (fused silica with 3% GeO_2) [125] for the core in our calculations. We assume that the core and the cladding are homogeneous and ignore the spectral dependence of their Poisson's ratios. The strain-induced change in the material refractive index is given by [78],

$$\frac{dn}{d\varepsilon} = -\frac{n^3}{2}[p_{12} - (p_{11} + p_{12})\nu]\,, \tag{4.10}$$

where $n=n_1,n_2$ for the core, cladding and p_{11} and p_{12} are the strain-optic coefficients. For fused silica p_{11}=0.12 and p_{12}=0.27 [78] and assuming n=1.458 [78], we obtain $dn_2/d\varepsilon$=-0.316 for the cladding. The strain-optic coefficients for silica doped with germania were not available in literature and hence an approach similar to the one used for the temperature sensor model was used. A few gratings were fabricated in SMF-28 fiber and

the strain-induced shifts were determined for various resonance bands. In the model, distinct values of $dn_1/d\varepsilon$ were used and the average value giving the closest match between the actual and calculated results was found to be $dn_1/d\varepsilon$=-0.3208 for SMF-28 fiber. It was found that small changes in the values of $dn_1/d\varepsilon$ and $dn_2/d\varepsilon$ significantly altered the strain-induced shift, implying that the axial strain sensitivity is a strong function of the nature and concentration of the dopants. As for the case of the temperature sensor, we assume that the change in the material refractive indices with strain is not a function of the operating wavelength. Moreover, any non-linearities in the values of $da/d\varepsilon$, $db/d\varepsilon$, $dn_1/d\varepsilon$ and $dn_2/d\varepsilon$ are also neglected. Now that we have outlined the basic procedure to analytically model long-period grating-based strain sensors, we will shift our focus to the prediction of the functional dependence of the strain sensitivity of gratings in Corning SMF-28 fiber on various parameters such as the grating period, the writing conditions and the ambient index of refraction.

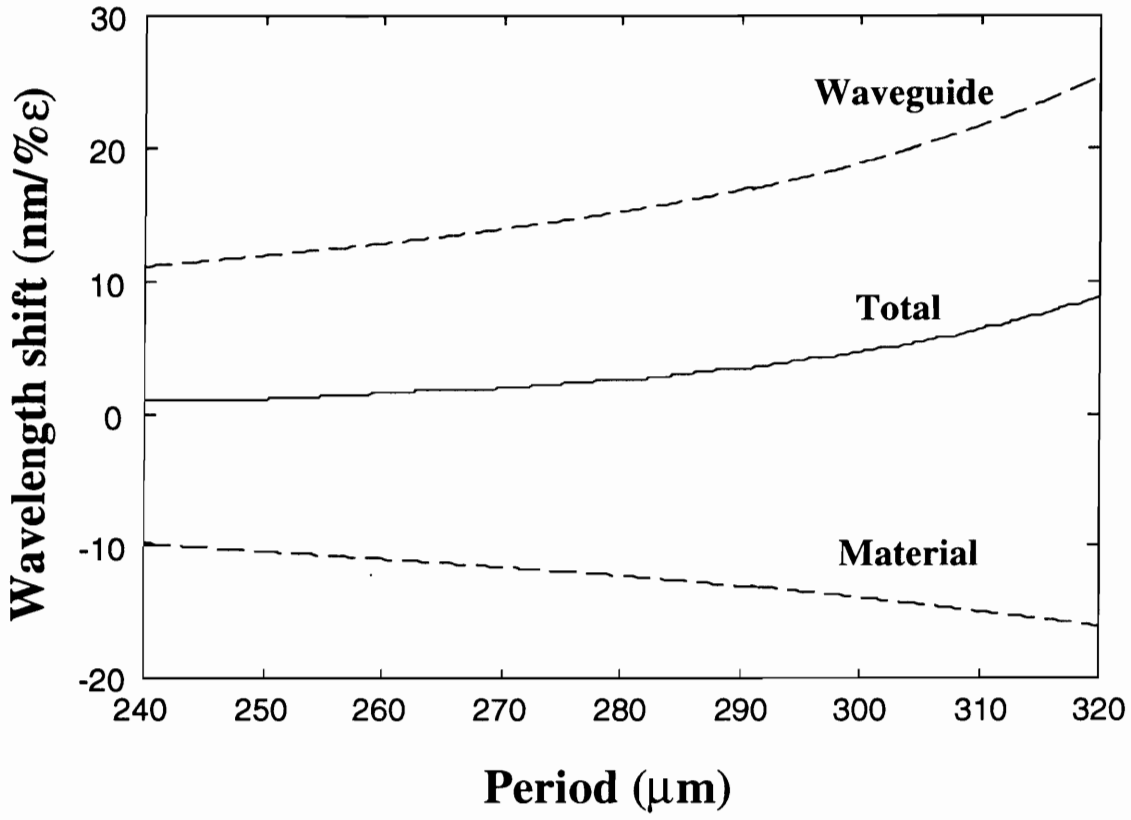

Figure 4.15. Wavelength shift (for 1%ε) as a function of period for SMF-28 fiber. The waveguide and material contributions are also shown for the mode with m=7 and peak index change $\Delta n=5\times10^{-4}$.

Figure 4.15 shows the material and waveguide contributions to the strain-induced shift for a cladding mode with m=7 as a function of the grating period ($\Delta n=5\times10^{-4}$). Also depicted is the overall shift in the resonance band for a strain magnitude of 1% ($1\%\varepsilon=10^4$ $\mu\varepsilon$). The material contribution is negative since the overall changes in the core and the cladding indices and radii produce an overall reduction in the differential effective index. The waveguide effect, unlike the case of the temperature sensor (Figure 4.1), has a significant contribution due to the strain-induced change in the grating period. The waveguide contribution increases with period since gratings with larger periods have higher slopes ($d\lambda/d\Lambda$) of the corresponding characteristic curves. The effect is more pronounced for higher order modes and introduces a non-linearity in the wavelength shift. For m=7 the overall shift is positive since the waveguide contribution dominates over the range of periods depicted here. The shift for 1% strain varies from 0.9 nm for Λ=240 μm to 8.4 nm for Λ=320 μm which reveals the versatility of using long-period gratings for strain measurement since the sensitivity can be tailored to a particular application.

The opposite polarities of the material and waveguide effects for this mode suggests that it might be possible to counter-balance the two effects to produce strain-insensitive gratings. Such gratings would be useful in temperature sensing applications where the grating is subjected to both strain and temperature changes. In fact, for a given fiber, it is possible to obtain strain-insensitive bands in long-period gratings by using specific periods. In Section 2.4.4.2, we had noted that the material and waveguide contributions to the strain sensitivity of fiber Bragg gratings were also opposite in polarity but were weak functions of the grating period and hence the coupling wavelength. This implies that in a given fiber, the wavelength shift due to axial strain is always positive for gratings with different Bragg wavelengths. Hence, strain-insensitive Bragg gratings cannot be obtained in standard fibers. We will discuss strain-insensitive long-period gratings in Section 4.3.4.

Figure 4.16 predicts the strain sensitivity of resonance bands corresponding to different cladding modes for the two different ranges of grating periods. In Figure 4.16(a) all the three lowest order bands are shown to have shifts to shorter wavelengths under axial strain. The negative shifts can be attributed to the small slope of the characteristic curves for the respective cladding modes and hence a domination of the negative waveguide contribution. In general, for operation in the normal region, the waveguide contribution

increases with the order of the cladding mode, assuming all corresponding bands are located at the same wavelength (Figure 3.23). This is obvious from Figure 4.16(b) where the bands corresponding to m=7 and m=8 are seen to have positive shifts. For m=8 the shift increases significantly for periods larger than 260 μm since the waveguide contribution grows rapidly. For higher order modes, as one approaches the equalization wavelength (Section 3.2.3.1) between the guided and cladding modes, the waveguide contribution becomes very large. Thus to get large strain sensitivities ones need to fabricate gratings with periods close to the equalization periods (Figure 3.22) of the corresponding cladding modes. For operation in the anomalous region, the waveguide contribution becomes negative and its magnitude again depends on the proximity of the resonant band location to the equalization wavelength of the corresponding cladding mode. The strain sensitivity of bands operating in the anomalous region will be discussed later in this section.

Figure 4.17 depicts the strain sensitivity of long-period gratings as a function of the peak index change (Δn) induced during the writing process. The simulation is for SMF-28 fiber and m=7. The strain sensitivity of the resonance band is found to increase with the peak index change and can be attributed to the larger waveguide contribution on increasing Δn which serves to shift the band to longer wavelengths. The enhancement in the sensitivity is larger for higher values of grating period since the shift due to the same change in Δn increases with period (Figure 3.29) and also due to the fact that the waveguide contribution is non-linear. We hence observe that the writing conditions can be varied to manipulate the strain sensitivity of long-period gratings. For example, if a band is found to have a very small strain coefficient for a particular period, another grating with the same period can potentially be made strain-insensitive by changing the value of the peak index change till the waveguide contribution balances the material contribution. Similarly, the strain sensitivity of gratings can be tuned following fabrication by annealing at particular temperatures for specific time durations. The process of annealing serves to reduce the peak index change (Δn) and hence using certain annealing temperatures and durations, the strain coefficients of long-period gratings may be selectively tuned.

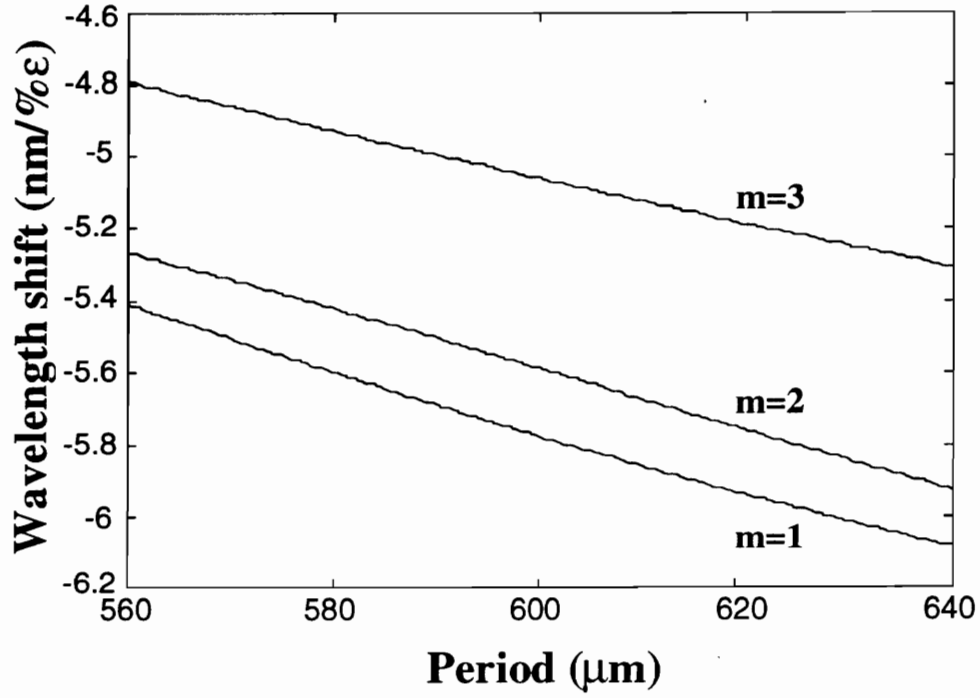

(a)

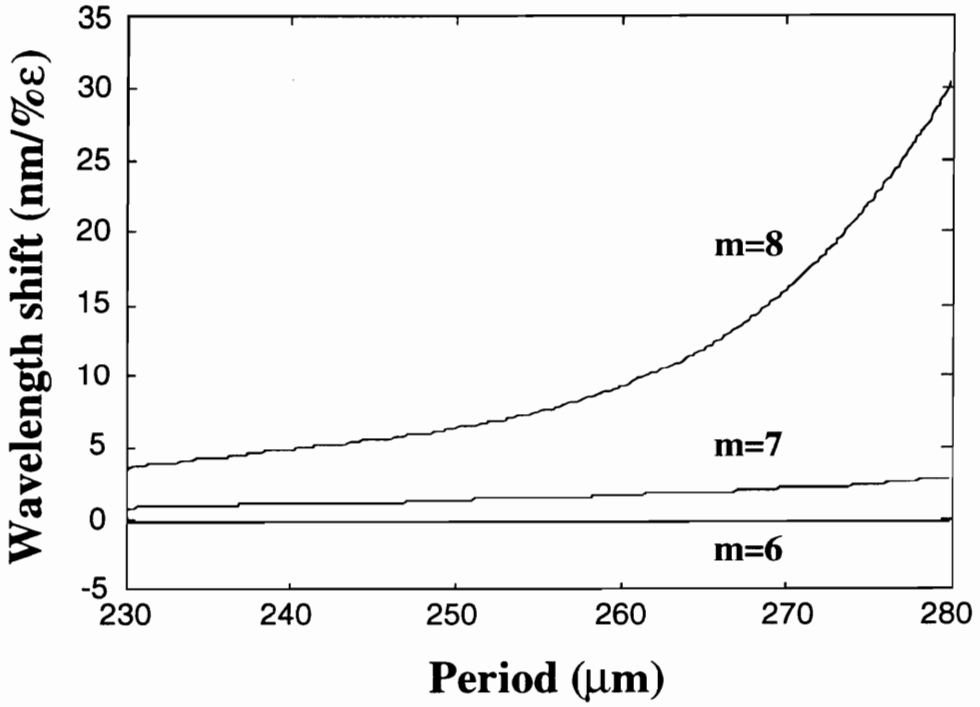

(b)

Figure 4.16. Wavelength shift (for 1%ε) as a function of period for SMF-28 fiber with (a) m=1,2 and 3, and (b) m=6,7 and 8 ($\Delta n=5\times10^{-4}$).

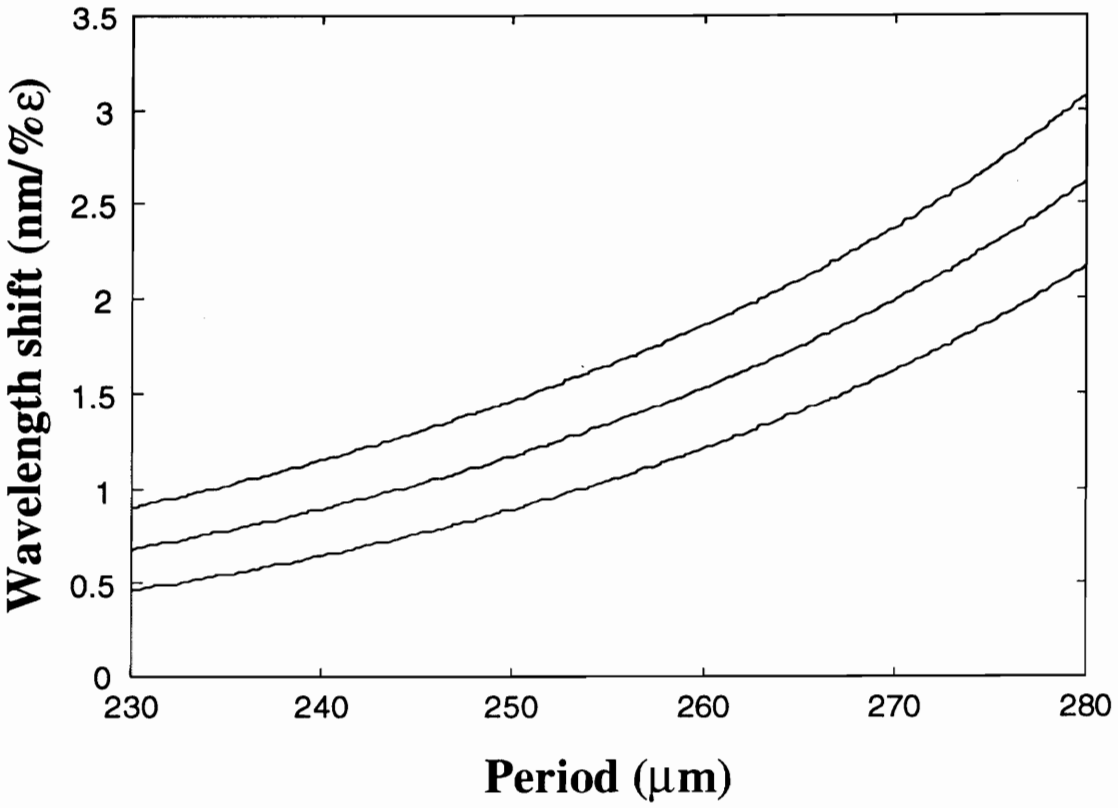

Figure 4.17. Wavelength shift (for 1%ε) as a function of grating period for SMF-28 fiber (m=7). The three curves correspond to different peak index changes in the core during the writing process - $\Delta n=3\times10^{-4}$ (bottom), $\Delta n=5\times10^{-4}$ (middle) and $\Delta n=7\times10^{-4}$ (top).

Till now we have only evaluated the strain response of gratings that have air as the ambient material ($n_3=1.0$). We now show that the strain sensitivity of a grating can be varied by changing the index of refraction of the medium surrounding the bare cladding. Figure 4.18 depicts the strain-induced shift as a function of the grating period with $n_3=1.0$, 1.33 and 1.44. The strain sensitivity for m=7 reduces from $n_3=1.0$ to $n_3=1.33$ and becomes negative for $n_3=1.44$ which may be attributed to the increase in the magnitude of the material contribution as the ambient index increases. Since the material contribution is negative for this mode (Figure 4.15), initial increase in the ambient index reduces the overall shift with strain. At $n_3=1.44$ the material effect starts dominating and hence the strain coefficient becomes negative. This discussion implies that for a certain ambient index between 1.33 and 1.44 the band under investigation would become strain-insensitive. The dependence of the strain sensitivity on ambient index thus provides a

simple method to tune the strain coefficient of gratings [99]. The change in sensitivity increases with period since the material contribution varies more rapidly at longer wavelengths for different ambient indices.

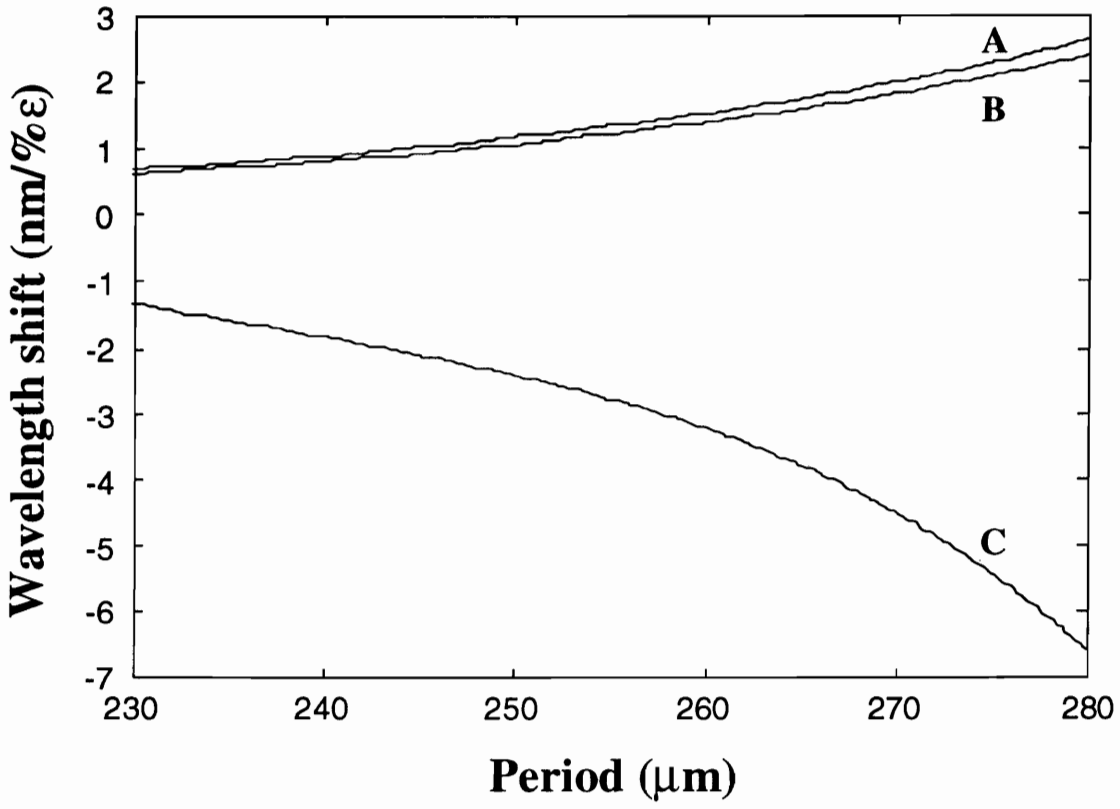

Figure 4.18. Dependence of the strain sensitivity (for 1%ε) of gratings of different periods (m=7 in SMF-28 fiber with $\Delta n=5\times10^{-4}$) as a function of ambient index. Curves A,B and C are the strain-induced shifts with n_3=1.0, 1.33 and 1.44, respectively.

Figure 4.19 shows the calculated shift in the resonance bands of a grating written in SMF-28 fiber with Λ=280 μm (n_3=1.0). For a peak index change $\Delta n=4\times10^{-4}$ the bands were found to be located at 1627.8 nm (A), 1315.9 nm (B), 1197.8 nm (C) and 1128.3 nm (D) for an unperturbed grating. The wavelength shift in band A was found to be non-linear with axial strain and this can be attributed to the non-linearity in the waveguide contribution. As expected, the higher order bands for this period were found to have larger strain coefficients. The linear curve fits to the data in Figure 4.19 were found to possess slopes 27.43 nm/%ε, 2.70 nm/%ε, -0.33 nm/%ε and -1.0 nm/%ε for bands A,B,C and D, respectively.

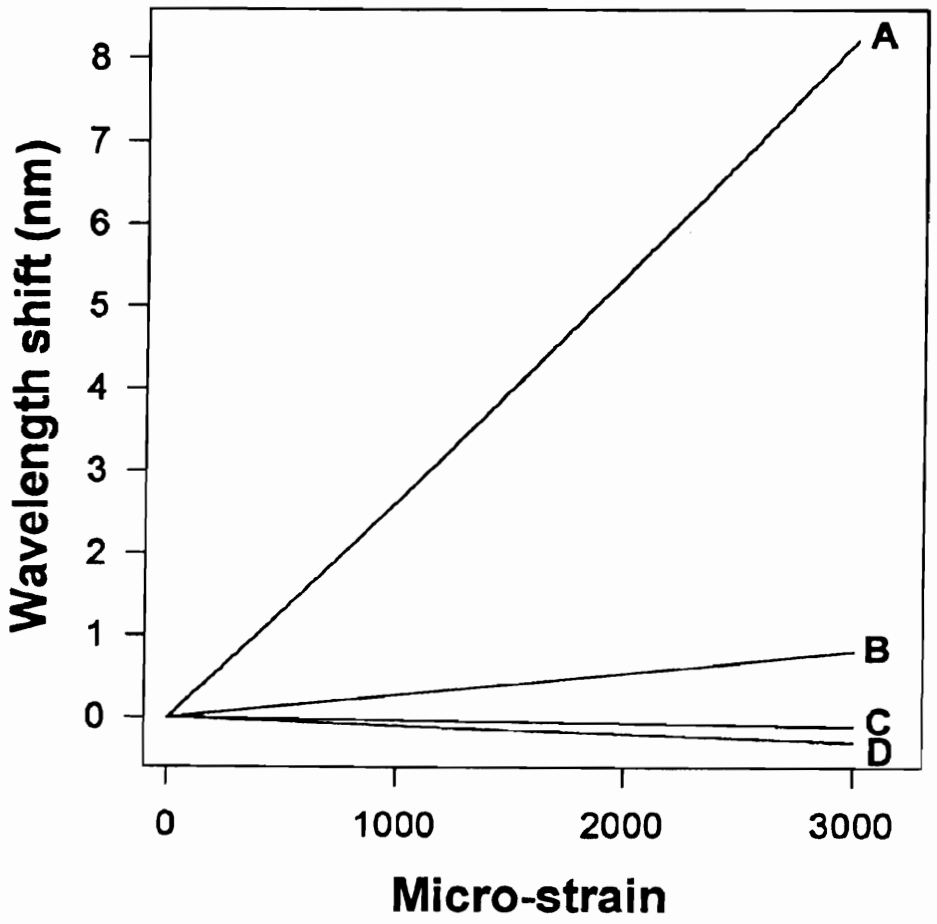

Figure 4.19. Theoretically calculated strain-induced shifts in the four resonance bands of a long-period grating written in SMF-28 fiber with Λ=280 μm. The locations of the bands A, B, C and D are 1627.8 nm, 1315.9 nm, 1197.8 nm and 1128.3 nm, respectively, for $\Delta n=4\times10^{-4}$. The shift in band A is slightly non-linear.

We now shift our attention to analysis of the strain sensitivity of gratings operating in the anomalous region. In Section 4.2.1 we had shown that gratings that involve coupling to specific modes can be made temperature-insensitive using periods in the anomalous region. The temperature-insensitivity of a grating written in Flexcor 1060 fiber was confirmed experimentally in Section 4.2.3. Figure 4.20 shows the strain sensitivity of resonance bands corresponding to m=28, 29 and 30 as functions of grating period in this fiber. The material and waveguide contributions can be shown to be negative for all three bands resulting in large magnitudes of strain-induced shift. For Λ=40 μm, the strain

coefficient of the band corresponding to m=30 was calculated to be -22.32 nm/%ε while those with m=29 and 30 were -23.18 nm/%ε and -24.17 nm/%ε, respectively. The enhancement in strain sensitivity with decreasing order of the band can be attributed to the material and waveguide contributions becoming more negative. It should be noted that for the analysis of the Flexcor fiber we have used the same strain-optic coefficients as those for SMF-28 fiber. The band corresponding to m=30 has larger strain sensitivity for periods around 45 μm due to an increased waveguide contribution for those periods. We hence observe that the temperature-insensitive gratings operating in the anomalous region retain their sensitivity to axial strain. These gratings are highly useful in strain measurement applications where the large temperature fluctuations are expected.

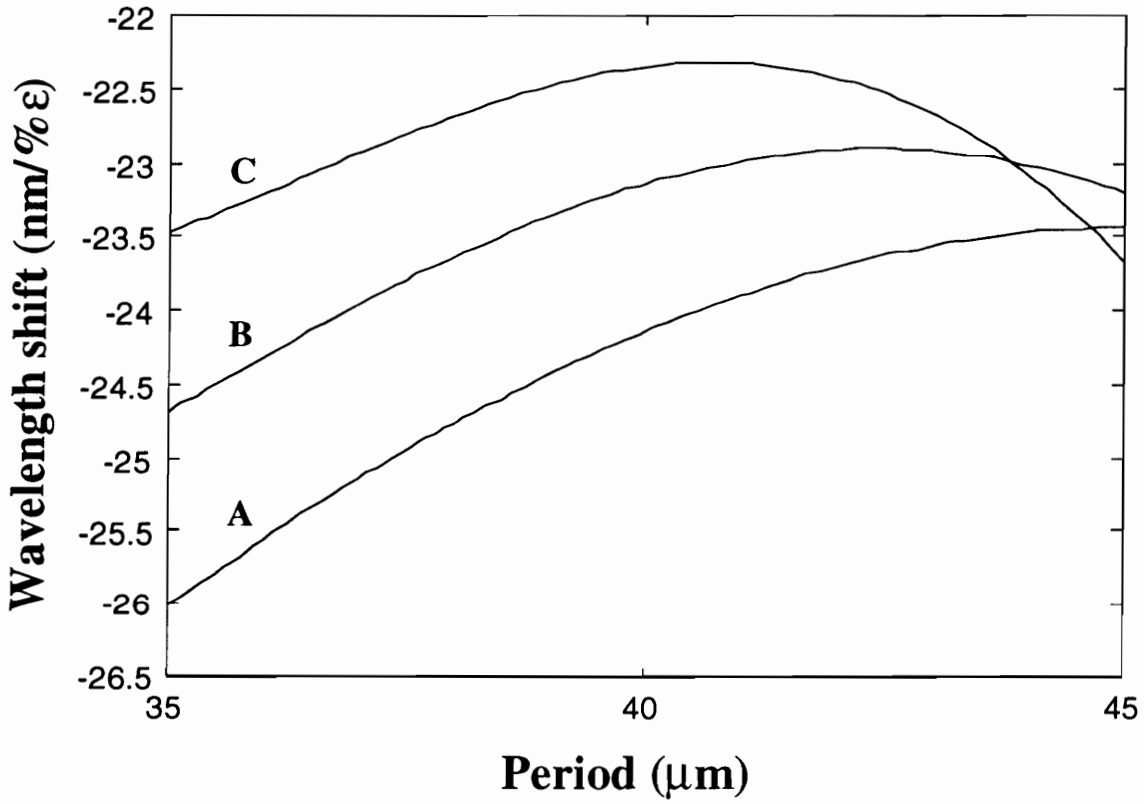

Figure 4.20. Strain sensitivity of three bands corresponding to m=28 (A), m=29 (B) and m=30 (C) for Flexcor 1060 nm fiber with n_3=1.0 and $\Delta n=5\times10^{-4}$.

In this sub-section we discussed the mechanism behind the axial strain sensitivity of long-period gratings. As in the case of the temperature sensor, the strain-induced shift was shown to have material and waveguide contributions. The strain sensitivity was shown to

be a function of the grating period, the order of the resonance band, the writing conditions and the refractive index of ambient material. Based on these parameters a number of techniques to selectively vary the strain-induced shift were proposed. The strain sensitivity was also analyzed for gratings in Flexcor fiber operating in the anomalous region and it was shown that such gratings are attractive for applications where the temperature-sensitivity of other techniques is a major limitation. We now present a few experimental results to verify the strain sensing capability of long-period gratings.

4.3.2 Experimental Results

Figure 4.21 shows the generic set up used to measure the strain sensitivity of long-period gratings. The fiber containing the grating was epoxied to two longitudinally separated translation stages after removing about 1 cm of jacket on either side of the grating region. The separation between the two epoxied regions is termed the gage-length L' of the sensor and was in the range 20 to 30 cm for our tests. Typically, only one of the translation stages was used to strain the fiber while the other was held stationary. The increase $\Delta L'$ in the length of the fiber between the epoxied region was read from the scale of the translation stage and the strain was calculated using, $\Delta\varepsilon=\Delta L'/L'$. The translation stage was moved manually, although this process can be automated by using a motorized stage. For a majority of the experiments, the strain was limited to 3000 $\mu\varepsilon$ although the fiber can survive much higher strain magnitudes. The strength of the fiber is not expected to degrade much after UV exposure and hence the grating can be strained to 15,000-20,000 $\mu\varepsilon$. The process of mechanically stripping the coating before exposure can damage the fiber by initiating propagation of small cracks in the cladding. This degradation can be avoided by using chemical stripping which also serves to completely dissolve any residual coating. For the strain test, light from a broadband source such as an LED was launched into one end of the fiber and the throughput was observed on the screen of an optical spectrum analyzer (OSA). For a grating with large spectral separations between the resonance bands it became necessary to combine the outputs of two LEDs through a coupler to determine the shifts in all the bands. The OSA was interfaced to a personal computer and the least-squared algorithm (Section 4.2.2) was used to detect the value of the resonant wavelengths in the presence of noise.

A grating fabricated in SMF-28 fiber with period Λ=280 μm and length L=1.0 cm (Figure 4.9) was used for the strain experiments. The post-annealed locations of the four highest

wavelength resonance bands were found to be 1607.8 nm, 1332.4 nm, 1219.3 nm and 1159.3 nm at 22.7 °C and these are denoted by A,B,C and D, respectively. The spectrum of two LEDs (centered at 1275 nm and 1520 nm) was combined through a coupler to measure the strain-sensitivity of all four bands. Figure 4.22 illustrates the transmission spectra of resonance band A at different values of axial strain. The test was carried out at room temperature (22.7 °C) and hence the shift is purely due to strain effects in the fiber. The shift with strain was to longer wavelengths as depicted by the direction of the arrow. The change in transmitted intensity at all the wavelengths suggests that a simple technique that detects the intensity variation at a particular wavelength may be used to demodulate the sensor.

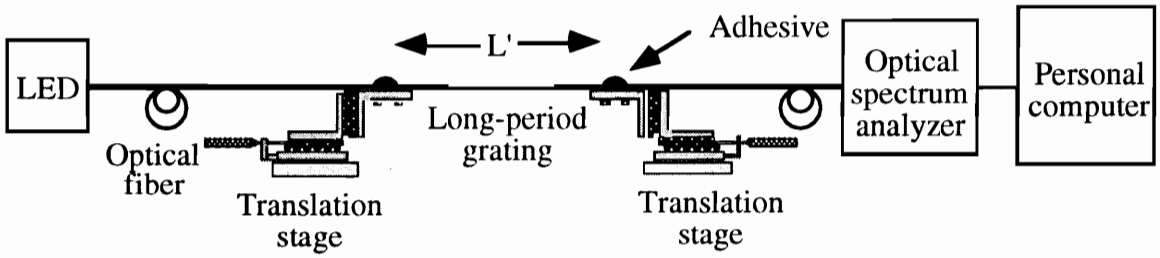

Figure 4.21. Experimental set up employed to determine the strain-induced spectral shift in the resonance bands of a grating. L' is termed the gage length of the sensor.

Figure 4.23 depicts the shift in the positions of the four resonance bands for the grating in SMF-28 fiber with axial strain at 22.7 °C. Bands A,B and C were found to shift to longer wavelengths with strain while band D had a negative strain coefficient. A small non-linearity was observed in the strain-induced shift of band A and this can be attributed to the non-linear waveguide contribution, as explained in the previous sub-section. A part of the non-linearity can also be due to the dependence of the strain-optic coefficients of the core and the cladding on the magnitude of the applied strain. The non-linearity is insignificant for most applications and can hence be neglected. The linear curve fits to the data in Figure 4.23 were found to have slopes of 19.42 nm/%ε, 2.79 nm/%ε, 0.66 nm/%ε and -0.32 nm/%ε, respectively. The data of Figure 4.23 should be compared to the theoretical results of Figure 4.19 for a grating of the same period. The differences can be ascribed to the approximations used in the analytical model and the deviations in the fiber parameters from the values used in the model. Also shown in Figure 4.23 is the shift in the band of a Bragg grating at 1500 nm with strain. Band A was found to have a

strain coefficient almost twice that of the Bragg grating (11.55 nm/%ε) which implies that long-period gratings can be used as highly sensitive strain sensors in a multitude of modern applications. Assuming that the minimum detectable wavelength shift using the least-squared curve fitting method is 0.05 nm, a strain resolution of 25 με can be achieved using band A of the long-period grating under test.

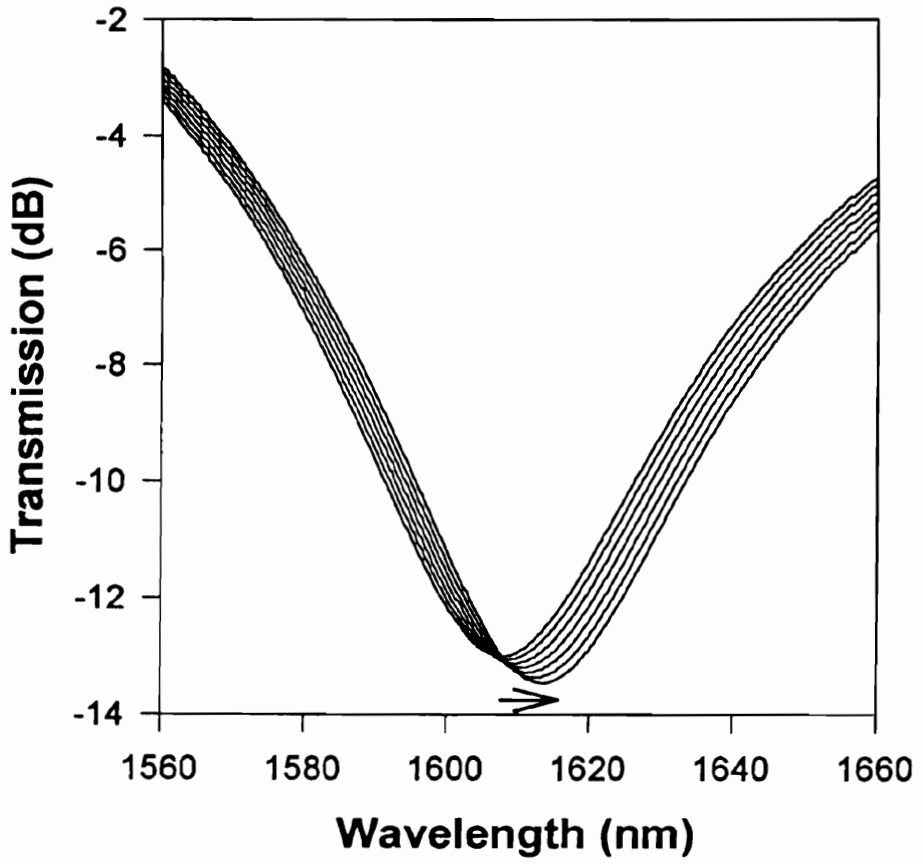

Figure 4.22. Shift in band A with strain at 22.7 °C for the grating shown in Figure 4.10. The spectra correspond to strain from 0 to 3000 με in steps of 500 με (left to right).

The effectiveness of a sensor to measure strain is a strong function of its temperature cross-sensitivity. Ideally, a strain sensor should be immune to ambient temperature fluctuations so that cross-sensitivity effects are eliminated. We observed in Section 4.4.2 that long-period gratings possess large temperature-induced spectral shifts. This suggests that thermal cross-sensitivity would limit the performance of long-period grating-based strain sensors. To test this experimentally the grating in Figure 4.9 was heated to discrete temperature and then strained axially. Figure 4.24 depicts the position of band A as a

function of strain at different temperatures. This implies that it is almost impossible to differentiate between strain- and temperature-induced shifts in this resonance band of long-period grating. For example, if an unstrained grating is heated to 55.7 °C, the use of calibration curve P would result in an erroneous strain measurement of about 1300 με. Moreover, the linear strain coefficient itself is a function of temperature, varying from 19.42 nm/%ε at 21.7 °C to 20.82 nm/%ε at 55.7 °C. For an ideal strain sensor the curves in Figure 4.24 should lie exactly on top of one another. Thus we see that the long-period grating strain sensor discussed here suffers from the effects of thermal cross-sensitivity.

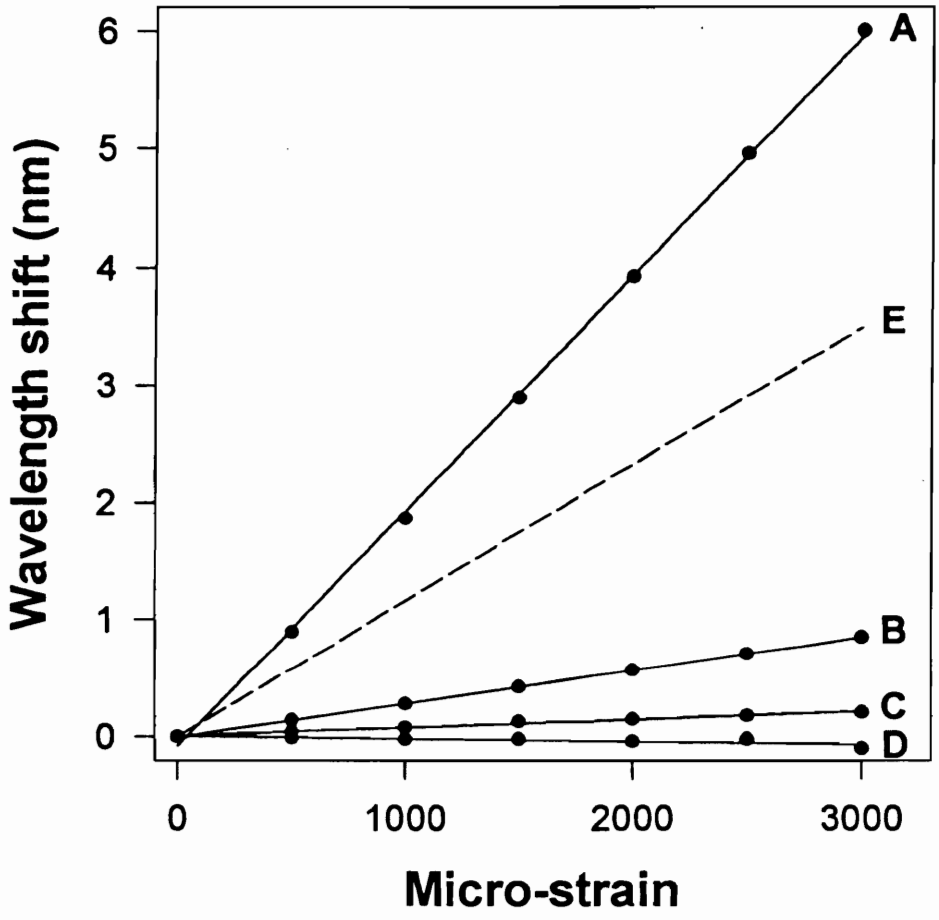

Figure 4.23. Shift in the peak loss wavelengths with strain for various resonance bands of the grating shown in Figure 4.9. The location of the bands A, B, C and D are 1607.8 nm, 1332.4 nm, 1219.3 nm and 1159.3 nm, respectively for an unstrained grating. The dashed line (E) is the shift for a Bragg grating with coefficient 11.55 nm/%ε.

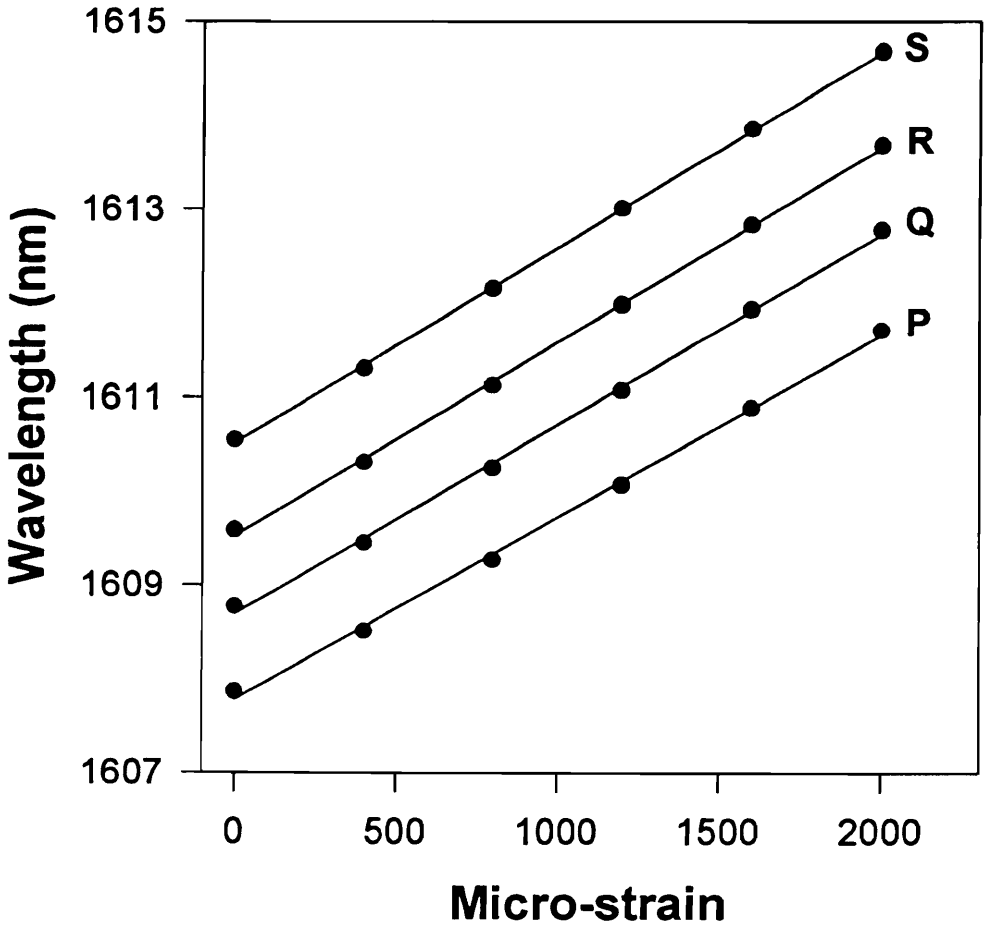

Figure 4.24. Shift in the highest wavelength band of the grating in SMF-28 fiber (Λ=280 μm) with strain at four different temperatures. Curve P,Q,R and S correspond to strain tests at temperatures 21.7 °C, 34.0 °C, 44.2 °C and 55.7 °C, respectively.

The cross-sensitivity between strain and temperature will be discussed in detail in Section 5.3 where we will also propose a scheme to separate the effects of these two perturbations. Another method to obtain strain measurements in environments with extensive temperature fluctuations is to use the temperature-insensitive gratings discussed in Section 4.2.3. The following section discusses the strain sensitivity of such gratings.

4.3.3 Temperature-Insensitive Gratings

In Section 4.2.3 we discussed experimental results from tests done on temperature-insensitive long-period gratings. It was shown that such gratings can be made to have an

order of magnitude smaller temperature sensitivity that conventional long-period gratings. In the previous sub-section we investigated the limitations imposed by the thermal cross-sensitivity of long-period gratings. We now present experimental results from strain tests done on temperature-insensitive long-period gratings.

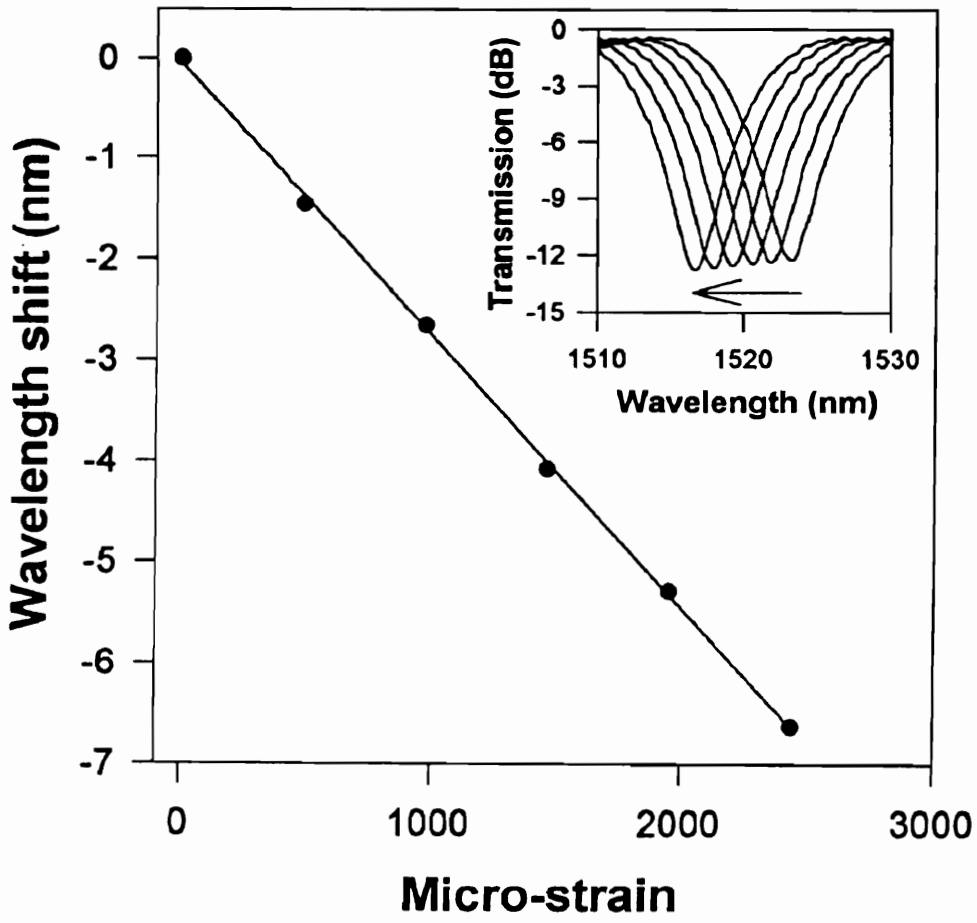

Figure 4.25. Wavelength shift as a function of axial strain for a grating with Λ=166 μm in temperature-insensitive fiber. The unperturbed band is located at 1522.17 nm at 25 °C. Inset shows the grating spectra at in steps of 488 με from right to left.

A grating written in the special refractive index profile fiber proposed by Judkins *et al.* [34] was tested for its strain sensitivity using a set up similar to that shown in Figure 4.21. The grating had a period Λ=166 μm and length L=3.65 cm and was fabricated using the excimer laser method (Section 3.3.1.1). The data from the test done at room temperature is shown in Figure 4.25. The straight line curve fit to the experimental results was found

to have a slope of -27.25 nm/%ε [126]. Thus these gratings retain their capability to measure strain despite losing their sensitivity to temperature changes.

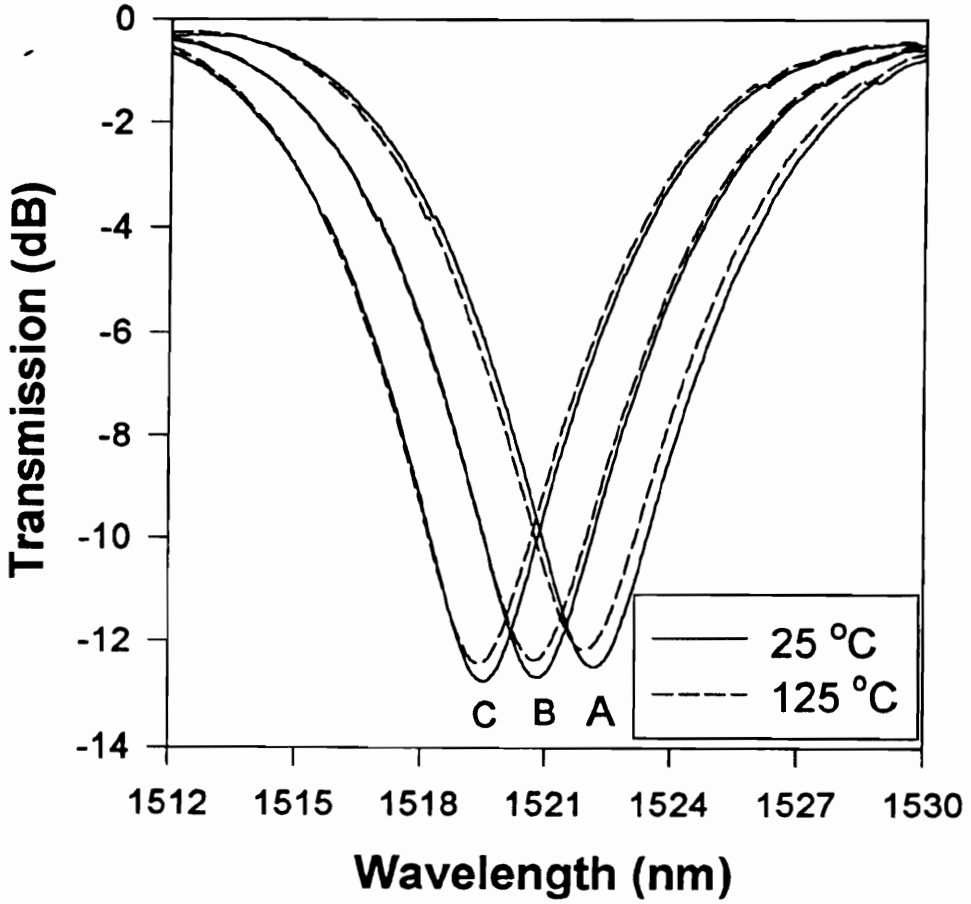

Figure 4.26. Transmission spectrum of a grating in the specially designed fiber [34] at 25 °C (solid curve) and 125 °C (dashed curve) for an unstrained grating (A), and for strain of 500 με (B) and 1000 με (C) [126].

To test the thermal cross-sensitivity of the grating at different magnitudes of strain, it was strained to discrete values and then heated from 25 °C to 125 °C. The temperature-induced shifts for an unstrained grating (A), and strain of 500 με (B) and 1000 με (C) are depicted in Figure 4.26. The temperature coefficients at 500 με and 1000 με were found -0.14 and -0.11 nm/100 °C, respectively [112]. Thus the grating has almost negligible cross-sensitivity to temperature changes at different magnitudes of axial strain.

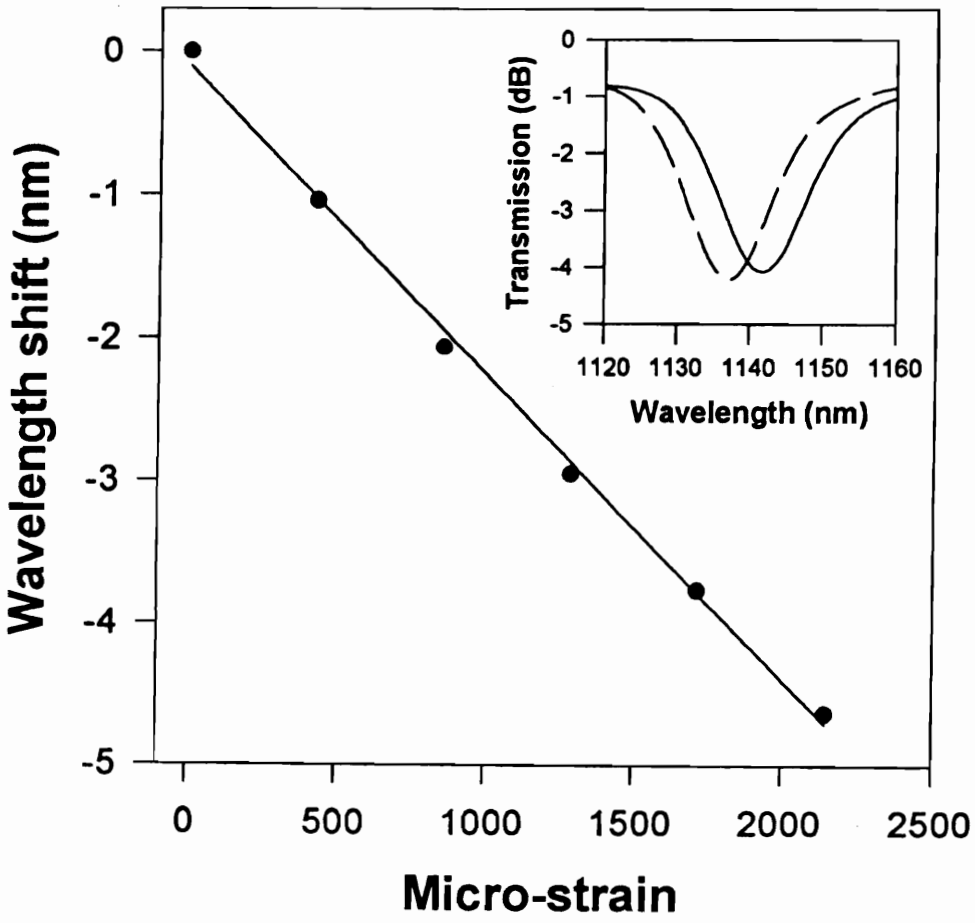

Figure 4.27. Spectral shift in the resonance band of a grating in Flexcor fiber (Λ=40 μm) with axial strain (at T=25 °C). The straight line curve fit has a slope of -21.44 nm/%ε [35]. Inset shows the transmission spectrum of the unperturbed grating (solid curve) and that at 2146 με (dashed curve).

In Section 4.3.1 we observed that the gratings with specific periods in the anomalous region are expected to have magnitudes of strain coefficients larger than 20 nm/%ε. The reduced temperature sensitivity of these gratings has already been demonstrated in Section 4.2.3. A grating written in Flexcor 1060 fiber with Λ=40 μm was tested for its response to axial strain [35]. Figure 4.27 depicts the shift in the band at 1141.5 nm as a function of strain at room temperature (25 °C). The slope of the linear curve fit was found to be -21.44 nm/%ε while the theoretically expected coefficient was -22.32 nm/%ε for the corresponding resonance band (Figure 4.19). This resonance band had a small temperature-induced shift of -0.18 nm/100 °C (Section 4.2.3) and hence possesses

minimal thermal cross-sensitivity. Two other resonance bands at wavelengths 1253.1 nm and 1376.4 nm were found to have strain coefficients of -23.47 nm/%ε and -26.96 nm/%ε, respectively. The calculated strain sensitivities for these bands were -23.18 nm/%ε and -24.17 nm/%ε, respectively. The inset in Figure 4.27 illustrates the transmission spectrum of the grating for an unstrained case and for 2146 με. The change in intensity at all wavelengths in the band again suggests the potential employment of simple demodulation schemes to obtain strain measurements.

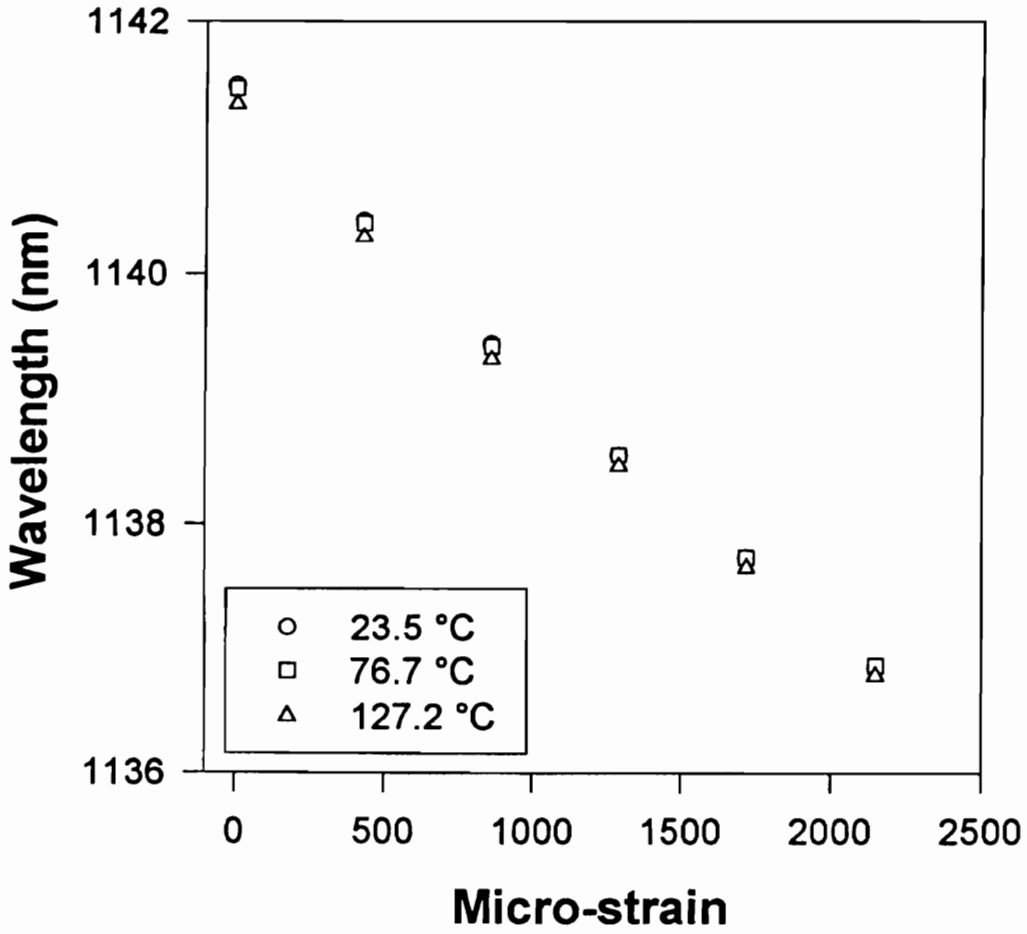

Figure 4.28. Location of the resonance band of the grating in Flexcor fiber (Λ=40 μm) as a function of strain at three distinct temperatures. The overlapping of the points predicts minimal thermal cross-sensitivity of the strain sensor.

In order for the above grating to be an effective measurement device, the strain-induced shift should be the same at all temperatures. To verify this the grating was heated to

discrete temperatures and incrementally strained to 2146 με. The results of the test done at 23.5 °C, 76.7 °C and 127.2 °C are shown in Figure 4.28. It is important to note that the y-axis in this plot represents the absolute wavelength and not the wavelength shift. The wavelength locations for a given strain magnitude at different temperatures are found to be almost identical. The small differences in the strain sensitivity can be attributed to the temperature dependence of the strain-optic coefficient and the shift in the operating point on the characteristic curve of the corresponding cladding mode. Figure 4.28 should be compared to Figure 4.24 which depicted the results from a similar test on a grating in SMF-28 fiber with period Λ=280 μm. The overlapping of the data points in Figure 4.28 reveals the reduction of cross-sensitivity for the grating with Λ=40 μm.

In this section we presented experimental results from strain tests on temperature-insensitive gratings. It was shown that such gratings are particularly attractive for strain sensing in applications where large temperature fluctuations are expected. The thermal cross-sensitivity for these gratings was found to be very small compared with the grating (operating in the normal region) discussed in the previous sub-section.

4.3.4 Strain-Insensitive Gratings

The analytical model presented in Section 4.3.1 suggested that it is possible to obtain long-period gratings that are insensitive to effects of axial strain. These gratings are obtained in a given fiber by using periods that assist in coupling light from the guided mode to specific cladding modes. The strain-insensitivity results from the equal but opposite contributions of the material and waveguide effects to the overall wavelength shift.

For a multitude of common applications it is desired that a temperature or strain sensors be embedded inside or mounted on the surface of a structure. For example, we will demonstrate in Section 4.6.1 the use of long-period gratings to determine the strain on a loaded reinforcing-bar commonly used in civil structures. The temperature sensors that are embedded or attached suffer from the problem of the expansion of the host structure due to its finite coefficient of thermal expansion. The resultant strain is typically very small but can be significant for temperature fluctuations in materials such as metals that possess large coefficients of thermal expansion. If the measurement device is sensitive to axial strain, the thermal expansion-induced strain can cause errors in the temperature

readings of the sensor. The problem can be overcome by using strain-insensitive long-period gratings.

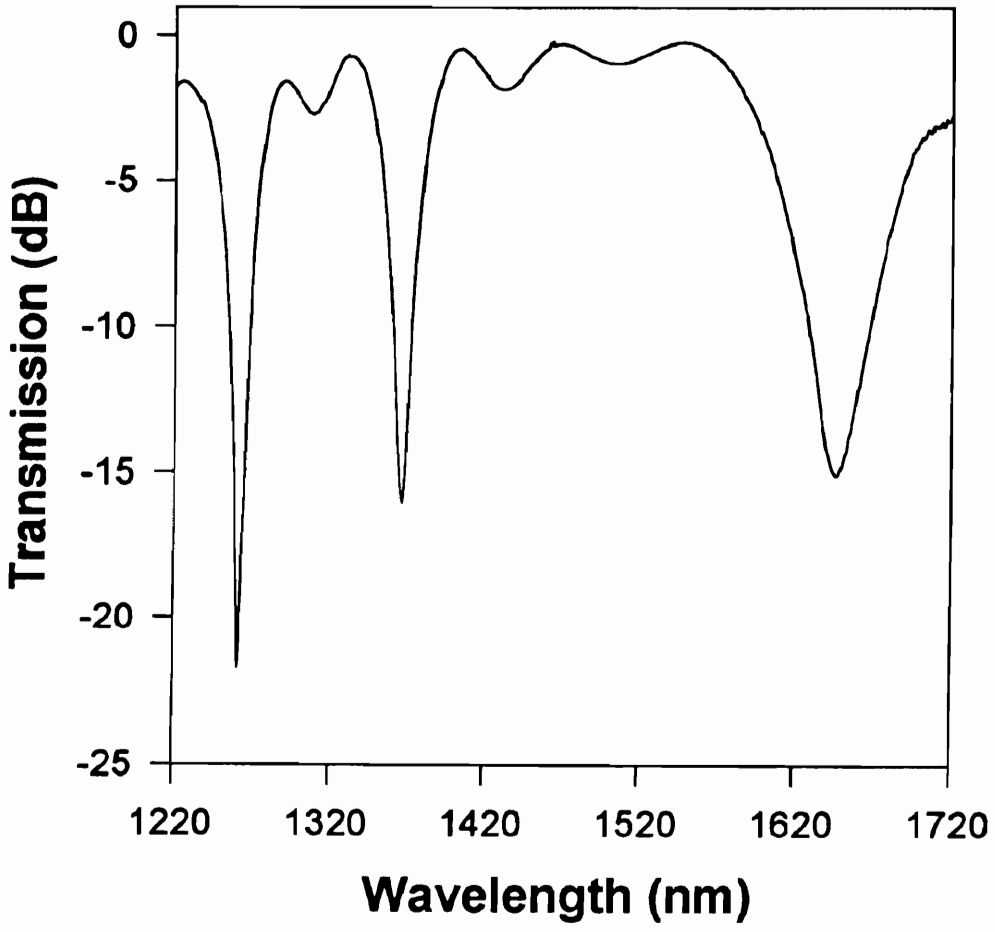

Figure 4.29. Transmission spectrum of a grating in Flexcor 1060 fiber (Λ=340 μm) with resonance bands at 1638.3 nm, 1362.3 nm and 1257.9 nm. The band at 1257.9 nm is found to have a small strain coefficient of -0.4 nm/%ε.

Figure 4.29 depicts the spectrum of a long-period grating fabricated in Flexcor 1060 fiber with period Λ=340 μm using the CW writing technique. The three highest wavelength bands for this grating were located at 1638.3 nm, 1362.3 nm and 1257.9 nm. The grating was strained to 2100 με and the shifts in the bands at 1638.3 nm and 1257.9 nm were measured as 3.13 nm and -0.08 nm, respectively. Although the band at 1257.9 nm had a finite spectral displacement, we will designate it as strain-insensitive due to the small value of the wavelength shift. Even though this band was strain-insensitive, experiments

showed that it retained its capacity to measure temperature changes. The detailed analysis of the temperature sensitivity of this band will be carried out in Chapter 5 when we discuss the use of this grating for simultaneous strain and temperature measurement. In this sub-section we will limit ourselves to demonstrating the temperature measurement capability of the strain-insensitive resonance band. The grating was first calibrated to obtain the wavelength versus temperature curve for the resonance band under investigation. The grating was then heated to 140 °C and cooled slowly. The set up depicted in Figure 5.8 was used to strain the grating while it was cooling. The objective of this experiment was to show that the grating faithfully measures temperature changes even on being perturbed by random axial strain. Figure 4.30 shows the results of this experiment. The plot on the top depicts the actual temperature variation (line) as a function of time. Also shown on the plot is the temperature calculated (symbols) using the wavelength shift in the strain-insensitive band and the pre-determined calibration curve. To test the versatility of the sensor, the temperature was increased twice during the cooling cycle and the strain was varied independently in steps of 210 $\mu\varepsilon$ from 0 to 2100 $\mu\varepsilon$ (Figure 4.30(b)). The maximum error in temperature measurement over a 106 °C range was found to be 2.2 °C. The overlapping of the actual and calculated values in Figure 4.30(a) suggests that this band is highly efficient in tracking temperature changes in presence of random axial strain. Thus strain-insensitive long-period gratings offer a novel method to overcome the problem of thermal expansion-induced strain in embedded and surface-mounted temperature sensors.

Thermal expansion-induced strain is also a problem in strain sensors commonly used in material evaluation. These strain sensors have an additional drawback of the cross-sensitivity to temperature fluctuations. We now propose a method to overcome the thermal expansion-induced strain in long-period gratings by compensating the resultant shift in the spectrum with that due to temperature cross-sensitivity. Consider a resonance band of a long-period grating with X (nm/°C) and Y (nm/$\mu\varepsilon$) as the temperature- and strain-induced shifts, respectively. Let the grating be attached to a material that has α (ppm/°C) as its coefficient of thermal expansion. For a temperature change ΔT (°C), the cumulative shift $\Delta\lambda$ in the resonance band due to the finite temperature coefficient and the thermal expansion-induced strain is given by,

$$\Delta\lambda = X\,\Delta T + \alpha\, Y\,\Delta T\,. \qquad (4.11)$$

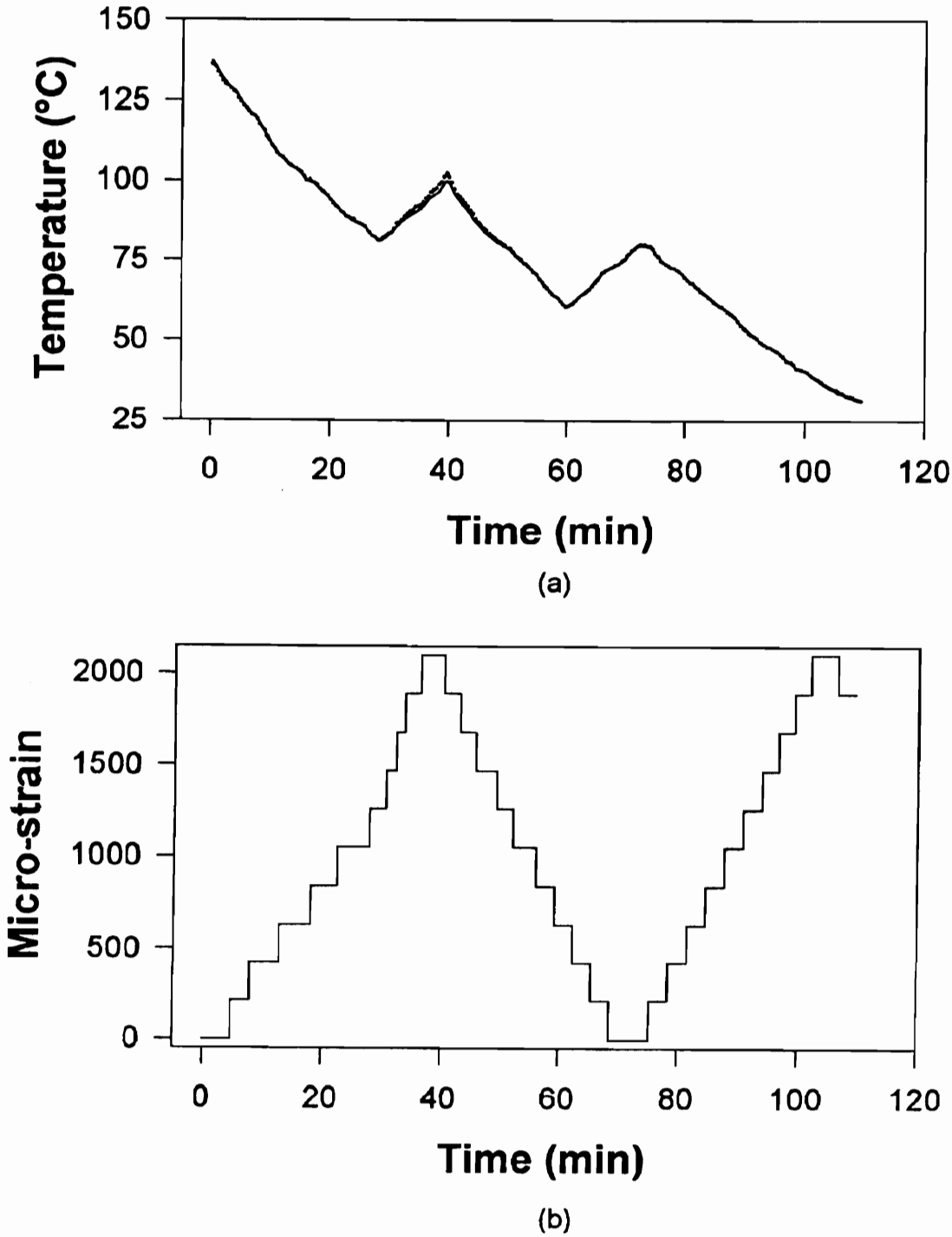

Figure 4.30. Experimental results from the temperature measurement on a grating in Flexcor 1060 fiber (Λ=340 μm) perturbed simultaneously by strain and temperature. The strain-insensitive band at 1257.9 nm is used to obtain temperature. The two plots show (a) the actual (line) and calculated (symbols) temperature and (b) applied strain.

In order to mutually cancel these two effects ($\Delta\lambda=0$), we arrive at the condition $\alpha=-X/Y$ (for $\Delta T\neq 0$). This result implies that we have to select a resonance band of a long-period grating that has opposite polarities of the temperature and strain coefficients with the magnitude of their ratio equal to the coefficient of thermal expansion of the host material. For the SMF-28 fiber grating ($\Lambda=280$ μm) that we investigated in Sections 4.2.2 and 4.3.2, it was found that the unperturbed band (D) at 1159.3 nm had positive and negative temperature- and strain-induced shifts, respectively. Thus we can use similar bands in other gratings to compensate for the effects of the temperature-induced shift and the thermal expansion-induced strain in embedded and attached gratings. Special fibers might need to be designed since the coefficient of thermal expansion is expected to be distinct for different host materials.

In this section we analyzed the implementation of strain sensors using long-period gratings. The strain sensitivity was shown to consist of the material and waveguide effect and its functional dependence on the grating period, the order of the resonance band, the writing conditions, and the refractive index of the ambient material was evaluated. The strain measuring capability of long-period grating was verified experimentally and it was shown that strain-insensitive gratings can be used for temperature measurements in the presence of axial strain perturbations. Temperature-insensitive gratings were demonstrated for strain measurements in thermally noisy environments. Such devices are useful because of their reduced temperature cross-sensitivities and large values of the axial strain coefficient. A major application of long-period grating-based strain sensors to structural monitoring will be examined in Section 4.6.1.

4.4 Index of Refraction Sensor

In this section we introduce long-period gratings as highly sensitive refractive index sensors [21]. The principle of operation of such sensors is described and experimental results are presented. We show that etching the cladding radius enhances the wavelength shift due to ambient index changes in long-period gratings. The response of temperature-insensitive gratings to changes in ambient index is also analyzed.

Conventional fiber optic refractive index sensors typically use some form of modifying the cladding to gain access to the evanescent field of the guided mode. For example,

surface plasmon sensors [15] require polishing the fiber cladding and depositing a thin layer of appropriate metal (such as aluminum) on the polished surface. Change in the overlay index is determined by detecting the variation in transmitted intensity of light. The evanescent field of the guided mode is coupled to a surface plasmon polariton and changes in the ambient index result in modulation of the coupling characteristics [127]. Limitations of this device include strong polarization sensitivity and questionable repeatability and mechanical strength. A similar approach uses a multimode waveguide overlay on a side-polished single-mode fiber to produce an ambient index-dependent coupling between the fundamental guided mode and modes of the overlay [16]. Fiber Bragg gratings have previously been proposed as refractive index sensors for chemical analysis by etching the cladding of the fiber to within a few micrometers of the core [14]. Changes in the ambient index modulate the guided mode effective index and cause the Bragg wavelength to shift (Equation 2.39). The etching of the cladding reduces the strength of the fiber and makes it susceptible to damage under harsh environmental conditions commonly encountered during chemical sensing. In the following sub-sections we will show that long-period gratings are highly sensitive refractive index sensors and can be implemented without sacrificing the integrity of the fiber [21].

4.4.1 Theoretical Analysis

In Section 3.2.2.2 we demonstrated that the effective indices of the cladding modes are strong functions of the index of refraction (n_3) of the medium surrounding the cladding (Figure 3.18). Any change in this ambient index serves to modulate the effective index n_{cl} of the cladding modes, with the higher order modes undergoing larger variations. Since the coupling wavelength λ corresponding to a particular cladding mode is dependent on n_{cl} through the phase-matching condition (Equation 4.1), a change in n_3 will effectively vary the value of λ. The shift in the coupling wavelength can be determined using an optical spectrum analyzer to produce a simple index of refraction sensor. For most applications, the index of refraction measurements need to be performed in the range 1.33 (index of water) to about 1.45. Hence we will limit our discussion to the region in which the ambient index is less than the effective index of the cladding mode. For $n_3 > n_{cl}$, propagation constant of the cladding mode becomes complex and the mode becomes leaky with exponentially increasing radial field components [128].

We will assume that the fundamental guided mode is well confined to the fiber core and is not influenced by changes in the ambient index. This approximation is well justified for the large cladding radii in the fibers under investigation (b=62.5 μm). Also since the grating period remains unchanged under the effect of the ambient index n_3 ($d\Lambda/dn_3=0$), the shift in a band is given simply by,

$$\frac{d\lambda}{dn_3} = \frac{d\lambda}{dn_{cl}} \frac{dn_{cl}}{dn_3}. \tag{4.12}$$

Since the change in the effective index of a particular cladding mode with the ambient index (dn_{cl}/dn_3) is dependent on the order of the cladding mode, each resonance band of a grating is expected to undergo a distinct shift. Moreover, the polarity of the wavelength displacement will be a function of the region of grating operation (Section 3.2.3.1). For example, for a band in the normal region, the increase in the effective index of the cladding mode serves to decrease the coupling wavelength ($d\lambda/dn_{cl}<0$) while the effect is opposite in the anomalous region ($d\lambda/dn_{cl}>0$). The increase in n_3 towards the value of effective index enhances n_{cl} ($dn_{cl}/dn_3>0$) and thus results in shifts in opposite directions for the two regions of operation. The magnitude of the shift is expected to increase as n_3 approaches n_{cl} due the non-linear change in dn_{cl}/dn_3. When the ambient index equals the effective index of the cladding mode, the outer cladding interface disappears and the coupling of the guided mode is expected to occur to a continuum of guided modes. This observation has been confirmed experimentally by Mizrahi and Sipe [86] for Bragg gratings that couple light to backward-propagating cladding modes at wavelengths on the lower side of the main resonance peak (Section 3.1). Since each cladding mode has a unique effective index, the corresponding resonance bands should disappear at different values of the ambient index. For example, higher order cladding modes will encounter the matched cladding interface at smaller values of ambient indices as compared to modes with lower m. For a grating with a given period, the index of refraction liquids used for our experiments were not available in small enough increments to detect such differences. We will now use the analytical model to predict the effect of the grating period, the order of resonance band, the writing conditions and the cladding radius on the sensitivity to surrounding refractive index changes. In the following analysis we assume that the medium outside the cladding extends to infinity so that the simplified model to evaluate cladding mode effective indices (Section 3.2.2.2) can be employed.

Figure 4.31 depicts the ambient index-induced wavelength shift in the resonance band corresponding to m=7 in SMF-28 fiber. The shifts are plotted as a function of the grating period for three distinct values of n_3 assuming a peak index change $\Delta n=5\times10^{-4}$. As can be seen, the wavelength shift is negative for these values of ambient index and increases with grating period. The enhancement in the refractive index sensitivity can be attributed to the greater increase in the cladding mode effective index at longer wavelength and hence at larger periods, for the normal region of operation. The shift with increase in ambient index is also non-linear since the sensitivity to index changes grows as the effective index of the cladding mode is approached.

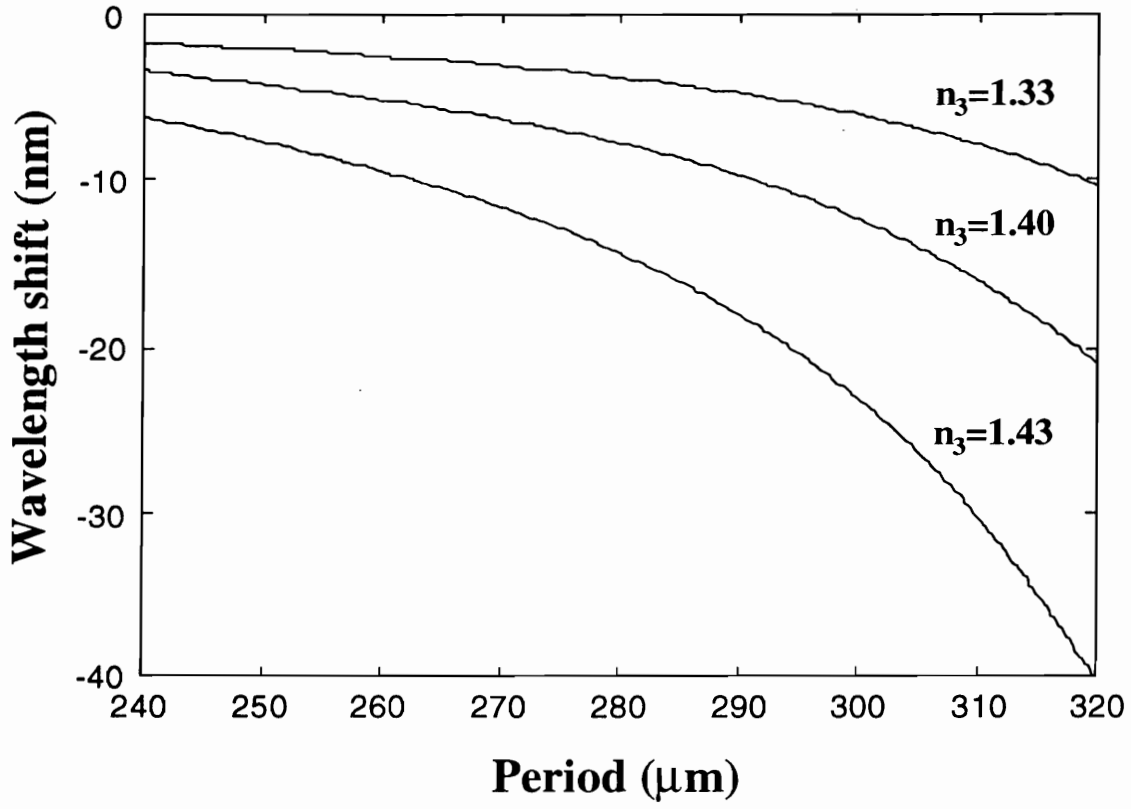

Figure 4.31. Wavelength shift as a function of period for SMF-28 fiber for three different values of ambient index n_3. The calculations are for the mode with m=7 and peak index change $\Delta n=5\times10^{-4}$. The shift for each index value is measured with respect to the wavelength location at $n_3=1.0$.

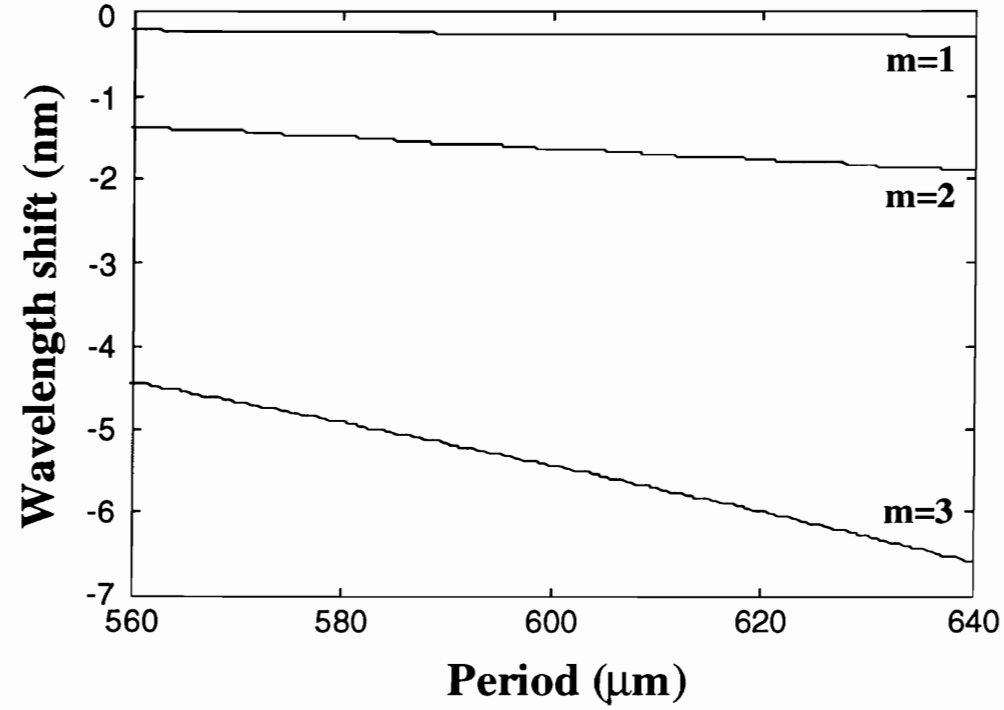

(a)

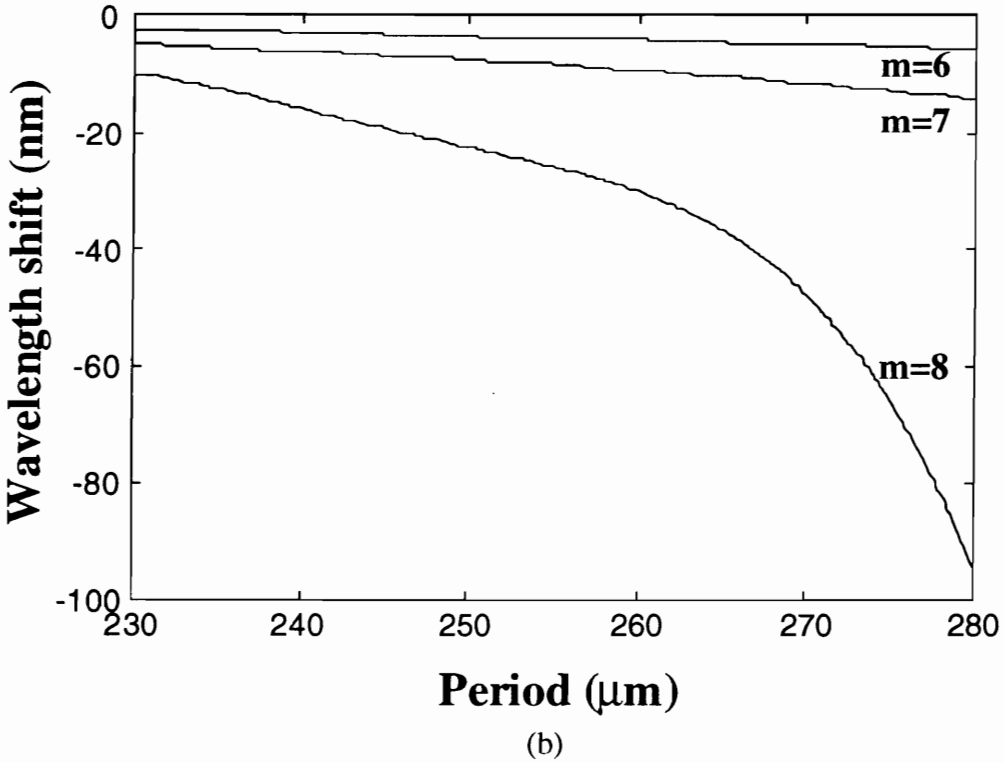

(b)

Figure 4.32. Shift in the coupling wavelength (for a change in n_3 from 1.0 to 1.43) as a function of period for SMF-28 fiber with (a) m=1,2 and 3, and (b) m=6,7 and 8.

Figure 4.32 shows the shift corresponding to n_3 changing from 1.0 to 1.43 in resonance bands of different orders for two different range of periods. The fiber is again SMF-28 with an assumed index change $\Delta n=5\times10^{-4}$ during the grating writing process. In Figure 4.32(a) the band corresponding to m=1 is found to shift by a very small amount with refractive index change for all grating periods. The small sensitivity can be attributed to the well confined modal power of the fundamental cladding mode to the fiber cladding at all wavelengths. As the order of the mode increases, a larger part of the modal field interacts with the ambient medium, resulting in enhancement in refractive index sensitivity. This implies that in order to obtain the maximum sensitivity to index of refraction changes we need to couple to the cladding mode with the largest value of m. Moreover, the factor $d\lambda/dn_{cl}$ in Equation (4.12) increases as the equalization wavelength for the band is approached. Thus to obtain maximum refractive index induced shift, the periodicity should be chosen close to the equalization period of a particular band. The polarity of the shift will then depend on the relative location of the resonance wavelength with respect to the equalization wavelength. For a given wavelength, the effective index of cladding modes reduces with increase in m (Figure 3.15) which predicts that the matching of the ambient index and the cladding mode effective index will occur at smaller and smaller values as m increases. Thus the distinct resonance bands corresponding to higher order modes will disappear for smaller values of n_3 than those for modes with smaller m. This can help the designer tailor the refractive index sensitivity of the fiber depending on the application. For example, if the maximum refractive index sensitivity occurs for $n_3=1.44$, this value can be lowered by using gratings with smaller periods. The ability to selectively tune the overall refractive index-induced shift and the index corresponding to the maximum sensitivity is an attractive feature of long-period grating-based refractive index sensors.

In Figure 4.33 we illustrate the refractive index shift as a function of the peak index change (Δn) during the writing process for m=7 in SMF-28 fiber. The enhancement in Δn results in the movement of the corresponding band to higher wavelengths where the increase in the cladding mode effective index is larger for the same change in ambient refractive index. Hence the refractive index-induced shift can simply be varied by manipulating the conditions during the fabrication process. As for temperature and strain sensors, the refractive index sensitivity can also be varied by using suitable annealing temperature and duration.

The effective index of the cladding mode is a strong function of the cladding radius (Figure 3.17). Hence the response to ambient index changes is expected to depend on the size of the cladding. For instance, reducing the cladding diameter will offer a greater access to the modal fields of the cladding modes and result in larger spectral shifts with changes in the index of the surrounding medium. This is assuming that the guided mode is itself not influenced by the etching process.

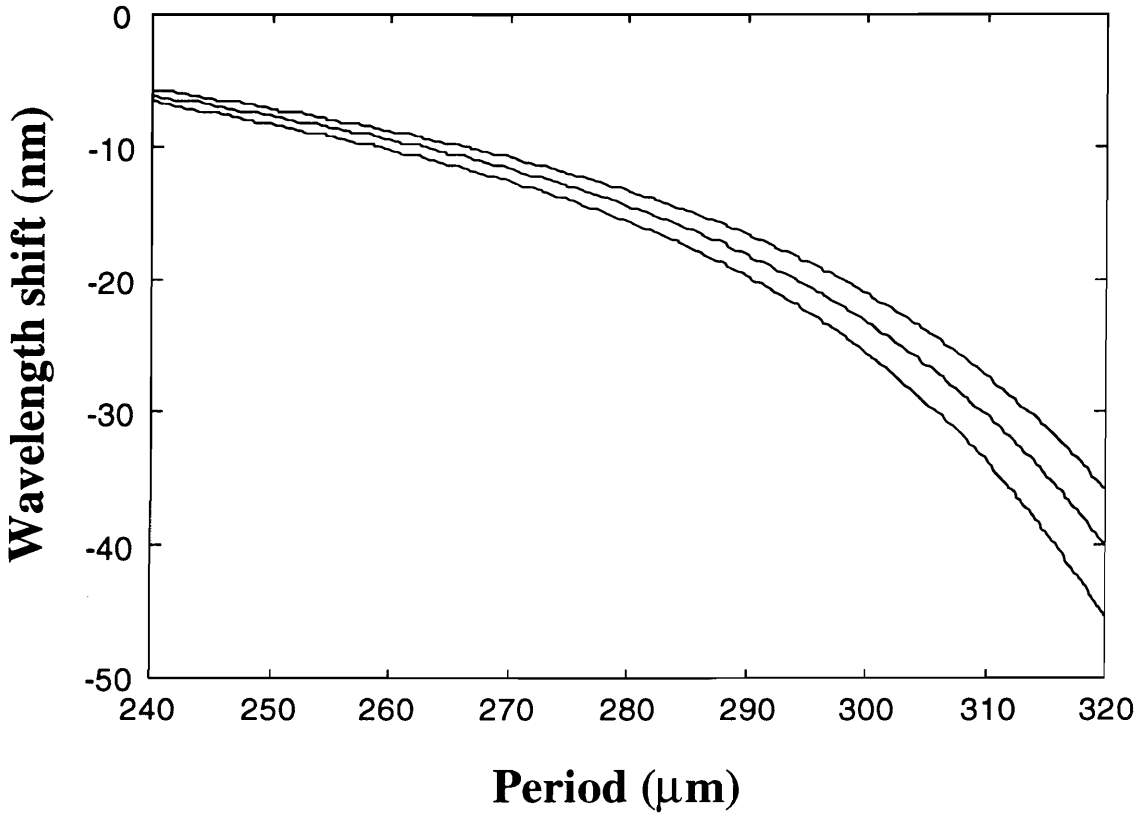

Figure 4.33. Shift in the coupling wavelength (for a change in n_3 from 1.0 to 1.43) as a function of grating period for SMF-28 fiber (m=7). The three curves correspond to different peak index changes in the core during the writing process - $\Delta n=3\times10^{-4}$ (top), $\Delta n=5\times10^{-4}$ (middle) and $\Delta n=7\times10^{-4}$ (bottom).

Figure 4.34 depicts the refractive index sensitivity of the band corresponding to m=5 for different values of the cladding diameter. As expected, the shift for the ambient index changing from 1.0 to 1.43 increases as the cladding diameter is reduced. The shift in resonance bands can be increased several times depending on the grating period, the order

of the band and the ambient index for any given fiber. Thus chemical etching of the cladding diameter is a simple method to manipulate the refractive index sensitivity of a long-period grating following the fabrication process.

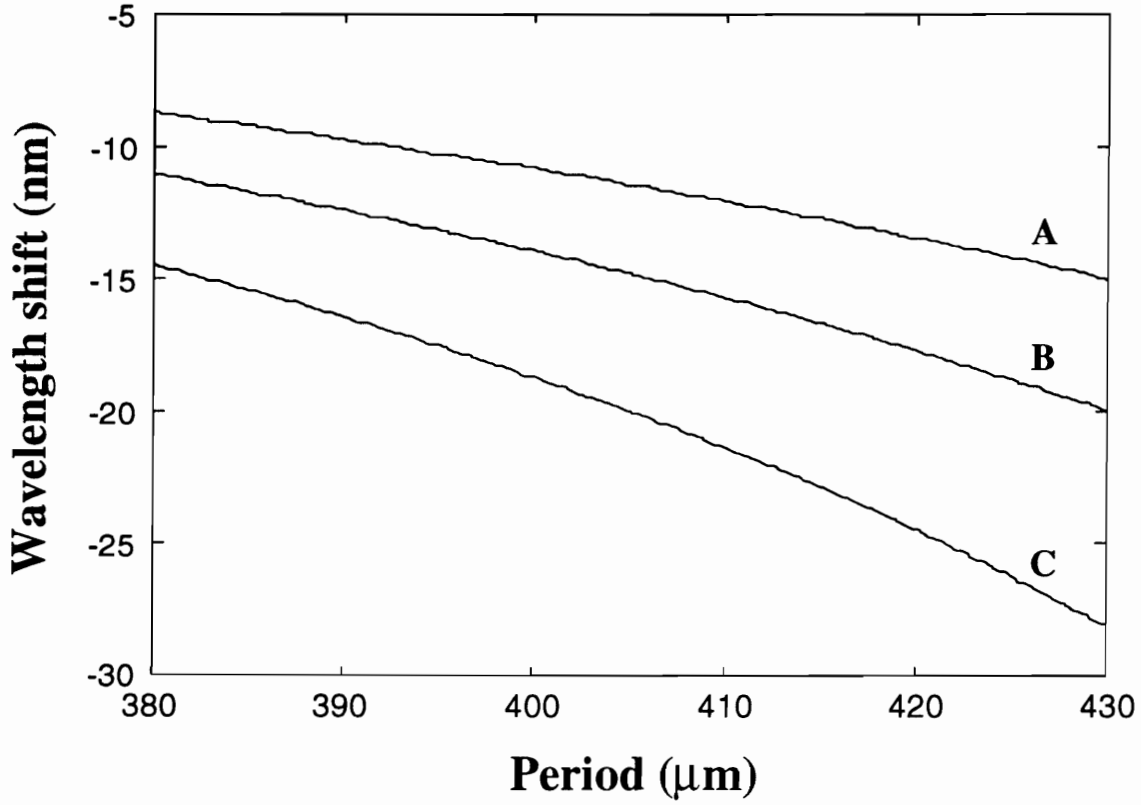

Figure 4.34. Shift in the coupling wavelength (for a change in n_3 from 1.0 to 1.43) as a function of grating period for SMF-28 fiber (m=5). The three curves correspond to cladding diameters of 125 μm (A), 120 μm (B) and 115 μm (C).

Figure 4.35 depicts the theoretically expected shift in the four resonance bands of a grating in the SMF-28 fiber with Λ=320 μm. Assuming an induced index change $\Delta n=2\times10^{-4}$ the resonant bands are located at wavelengths of 1525.5.1 nm (A), 1323.5 nm (B), 1225.1 nm (C) and 1165.4 nm (D) with air as the ambient medium (n_3=1.0). The index change was again determined by trial and error until the resonance bands A and B were closest to the experimental values specified in Section 4.4.2 for a grating with Λ=320 μm. The spectral shifts in all the four bands are towards the shorter wavelengths since a grating with the given period operates in the normal region. The wavelength displacements are measured with respect to the locations of the unperturbed bands

(n_3=1.0). As predicted, the magnitude of shift increases with the order of the resonance band (D through A). At n_3=1.441, for resonance band A, the effective index of the corresponding cladding mode is matched to the ambient index. The shifts for bands A, B, C and D for an ambient index change from n_3=1.0 to 1.441 are expected to be -64.2 nm, -16.7 nm, -6.9 nm and -3.2 nm, respectively. For indices higher than 1.441, the cladding mode becomes leaky with a complex propagation constant [128]. For reasons stated earlier, we will limit our analysis to ambient indices less than the effective indices of the cladding modes.

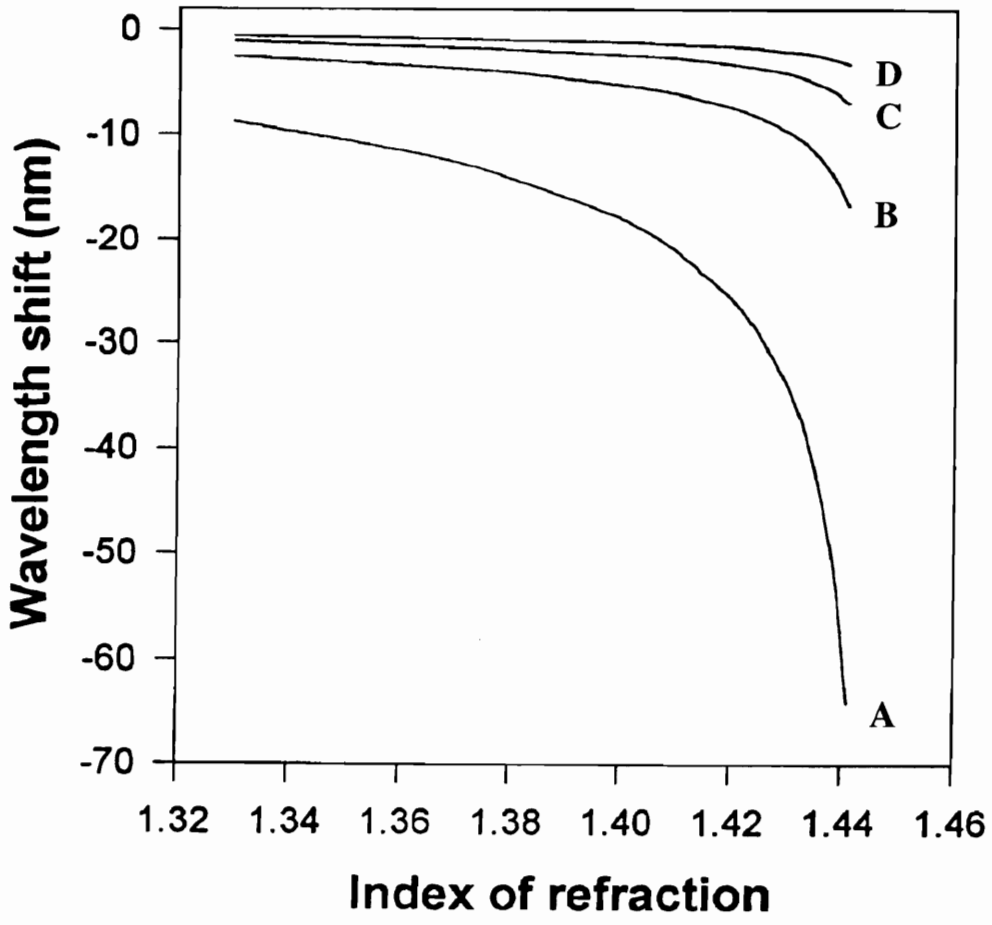

Figure 4.35. Theoretically determined shifts in the four resonance bands of a long-period grating in SMF-28 fiber (Λ=300 μm). The resonance bands A,B,C and D are located at 1525.5.1 nm, 1323.5 nm, 1225.1 nm and 1165.4 nm, respectively (n_3=1.0). The shift for each band is measured with respect to the location at n_3=1.0.

In this section we carried out a detailed investigation of the sensitivity of long-period gratings to index of refraction changes of the medium surrounding the bare fiber. It was shown that the wavelength shift is a function of the grating period, the order of the cladding mode, the writing conditions and the cladding diameter. Several techniques to enhance the refractive index sensitivity of such sensors were proposed.

4.4.2 Experimental Results

In this sub-section we present a few experimental results confirming the index of refraction measurement capability of long-period gratings. It is demonstrated that these devices offer improved performance over other fiber optic refractive index sensors. Although etching is not required to obtain spectral shifts, we show that this process serves to enhance the sensitivity of the sensor.

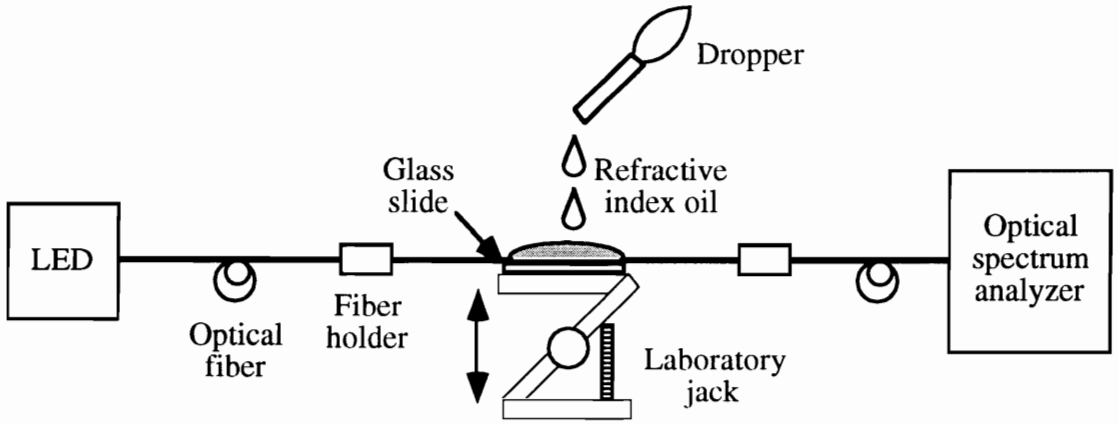

Figure 4.36. Experimental set up to determine the shift in the resonance bands of a long-period grating due to changes in the refractive index of the medium surrounding the cladding. The laboratory jack level is adjusted such that the glass slide placed on it is just below the bare fiber.

The set up used to measure the ambient index sensitivity of long-period gratings is shown in Figure 4.36. The grating was supported on two sides by fiber holders such that the fiber was parallel to the surface of the stable table. A glass slide was placed on a laboratory jack and the jack was raised until the slide was touching the fiber coating on either side of the grating. The region of the fiber containing the grating was completely immersed in refractive index oils manufactured by Cargille Laboratories, Inc. The

refractive index oils were available in steps of 0.002 or 0.004 and had an average temperature coefficient of 5×10^{-4} /°C [124]. It is important to note here that the values of refractive index specified for each oil are at 589.3 nm. Cauchy equation can be used to determine the refractive index at the operating wavelength [124]. For oils in the range 1.4 to 1.46, the refractive index values at 1550 nm are typically 0.01 smaller than those at 589.3. For the analytical results in the previous section, all the ambient indices were specified at the operating wavelength. In the experimental data presented here, all the refractive index values are specified at 589.3 nm, unless otherwise stated.

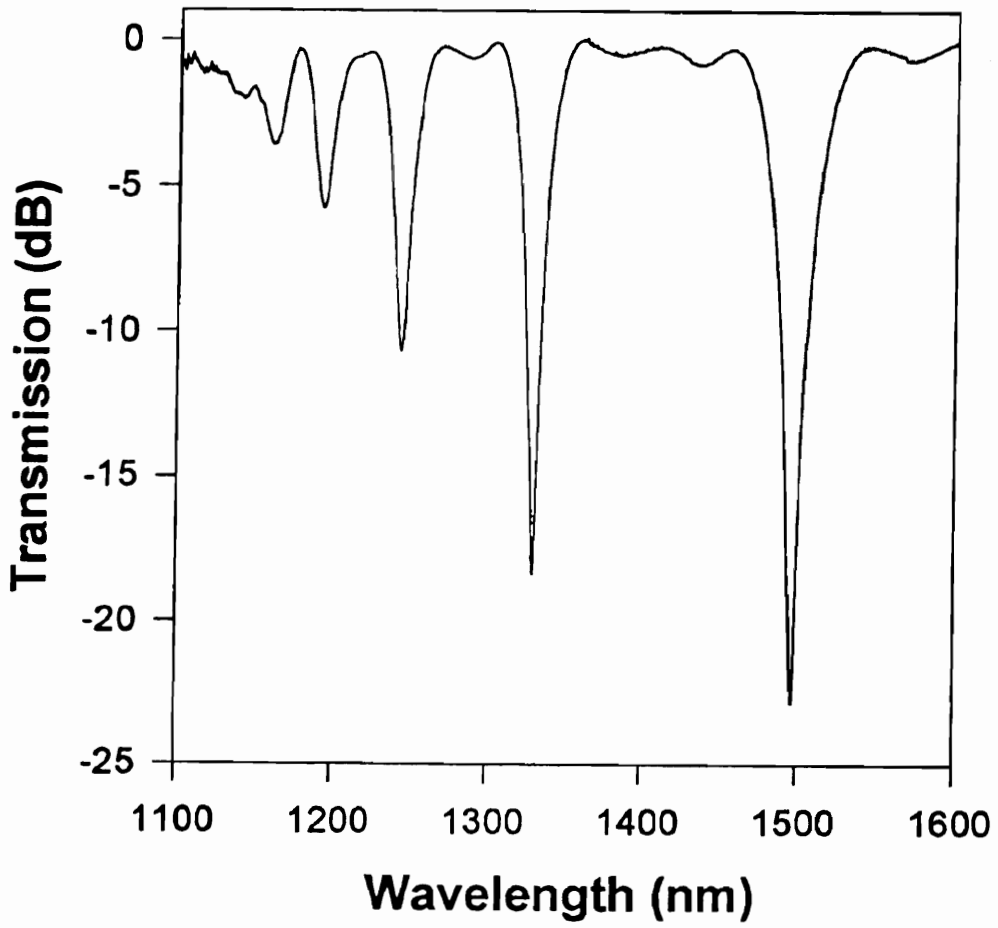

Figure 4.37. Transmission spectrum of a grating written in SMF-28 fiber with Λ=320 μm. The bands at 1496.6 nm (A), 1329.3 nm (B), 1243.8 nm (C) and 1192.1 nm (D) were used for refractive index experiments. The grating was annealed at 300 °C.

The tests were performed at room temperature with a maximum variation of ±2 °C to minimize cross-sensitivity effects. It was ensured that the fiber between the holders was taut without actually exerting strain on the grating region. The location of the resonance bands was measured in air and then for different values of ambient index. On completion of each measurement process the laboratory jack was lowered and the surface of the grating and the glass slide were cleaned carefully to remove the residual index oils. A reference scan was taken after the cleaning process to ensure that the grating spectrum returned to its unperturbed position in air.

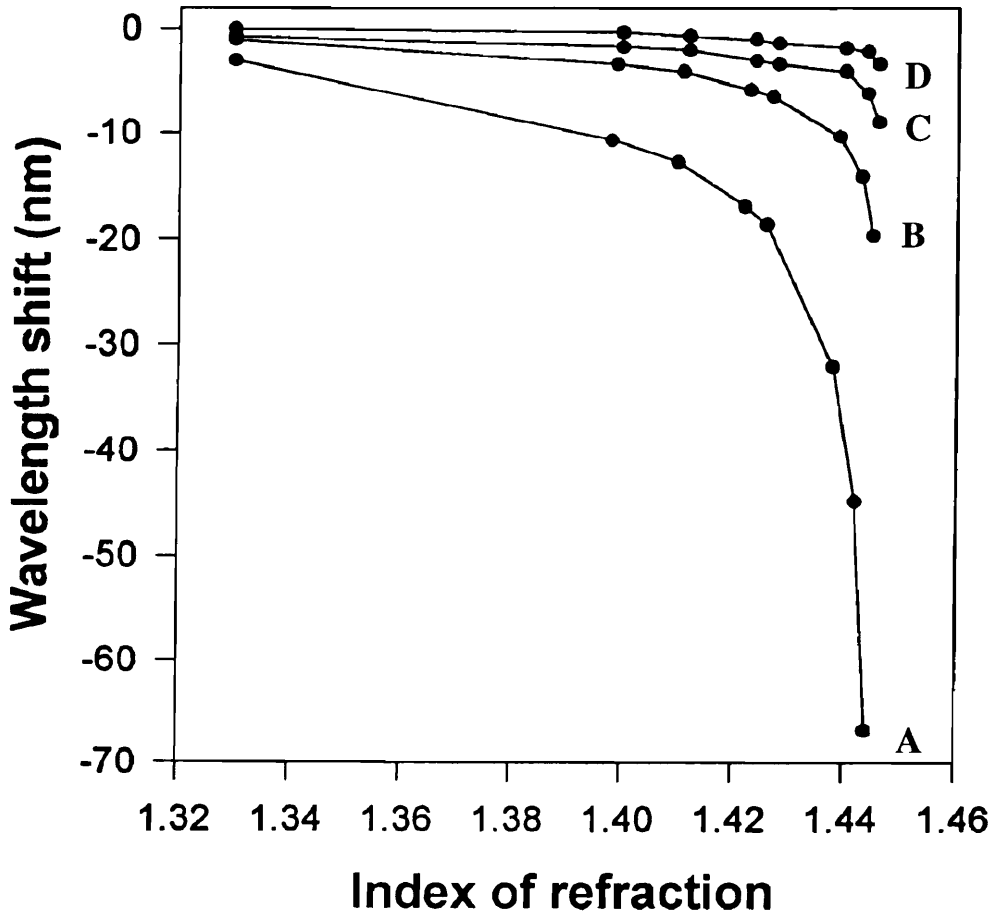

Figure 4.38. Experimental shift in the four resonance bands of the grating depicted in Figure 4.37 as a function of the index of the ambient medium. The shifts are measured with respect to the locations at n_3=1.0. The indices of the oils are calculated at the corresponding resonant wavelengths of the bands.

Figure 4.37 depicts the post-annealed transmission spectrum of the long-period grating used in experiments. The grating was fabricated in SMF-28 fiber using the CW writing technique with 120 mW of UV power (Λ=320 μm). The four highest wavelength resonance bands were located at 1496.6 nm (A), 1329.3 nm (B), 1243.8 nm (C) and 1192.1 nm (D) with air as the ambient medium (n_3=1.0). The grating was annealed at 300 °C and hence the Δn is expected to be smaller than the typical value of 5×10^{-4}. The grating was immersed in oils of different refractive indices and the measured shifts are shown in Figure 4.38. The shifts in the four resonance bands are with respect to the corresponding spectral locations with air as the ambient medium. All the refractive index values represented on the x-axis are calculated at the actual resonance wavelengths using the Cauchy equation [124]. The dispersion in the index of refraction of water was neglected for the present analysis.

The wavelength shift increases non-linearly with increasing refractive index. At a value of n_3=1.444 (λ=1500 nm) the resonance bands disappear since the effective indices of the cladding modes equal the index of the surrounding medium. Note that this value is 0.2% larger than that predicted theoretically (1.441) in the previous subsection. The difference can be attributed to the approximations made while analyzing cladding modes and the deviations in the fiber parameters from the values provided by the manufacturer. The overall shifts for bands A, B, C and D for the range n_3=1.0 to 1.444 were measured to be -66.9 nm, -19.7 nm, -9.0 nm and -3.4 nm, respectively and agree fairly well with the theoretically predicted wavelength displacements (Figure 4.35). Thus the wavelength shift is an increasing function of the order of the cladding mode for operation in the normal region. Hence if all modes operate in the normal region, the resonance bands at higher wavelengths will undergo larger shifts with change in ambient refractive index. Assuming that we can measure 0.05 nm wavelength shifts in the resonance peaks using the least-squared curve fitting method (Section 4.2.2), the average values of the minimum detectable refractive index changes are 4.49×10^{-4}, 1.77×10^{-4} and 1.86×10^{-5} in the range 1.33-1.398, 1.398-1.426 and 1.426-1.444, respectively (all indices are specified at a wavelength of 1500 nm). The increasing shift of the band ensures that the refractive index resolution is better in the range just below the effective index of the cladding modes. In Section 4.4.1, we had discussed the dependence of the refractive index sensitivity on the grating period. It was shown that this maximum sensitivity index region can be moved to lower values by using gratings with smaller periods.

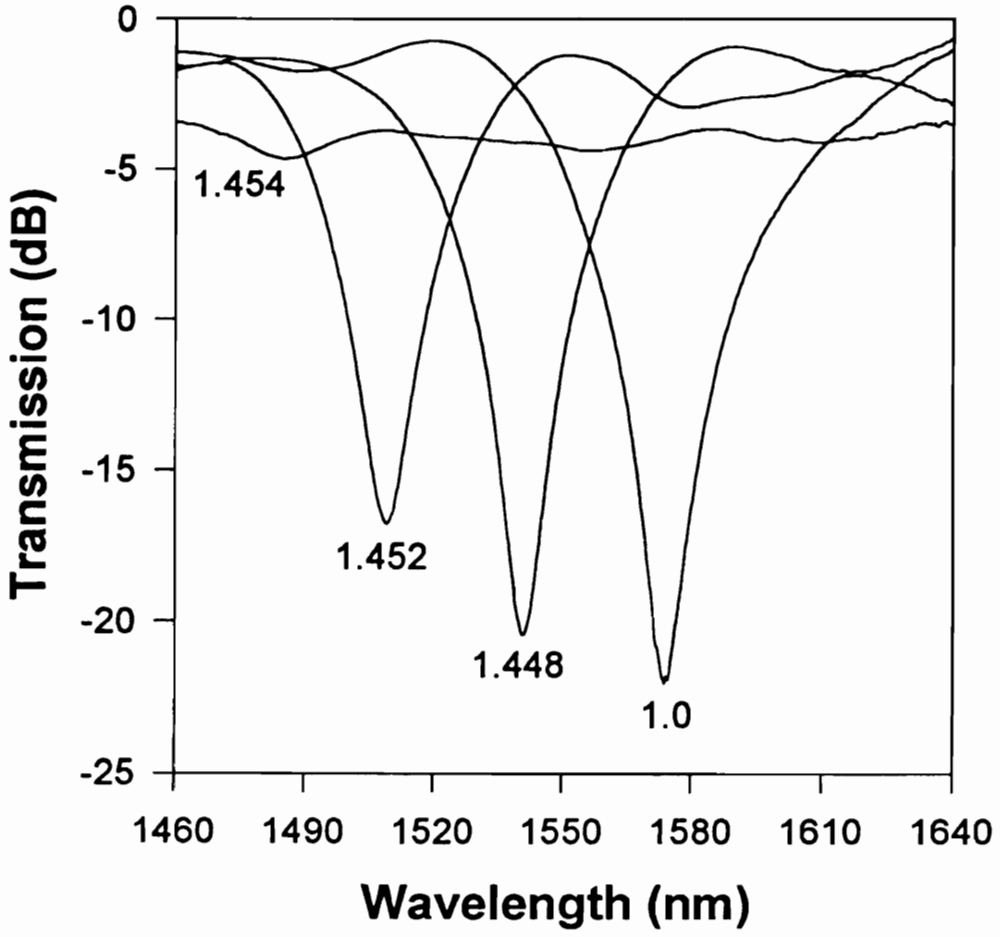

Figure 4.39. Transmission spectrum of a long-period grating written in SMF-28 fiber with Λ=320 μm at different values of ambient refractive index (n_3). The resonance band shifts to shorter wavelengths as n_3 approaches the effective index of the cladding mode. The indices of the oils are specified at 589.3 nm and should be reduced by approximately 0.01 to obtain their values at 1550 nm [124].

Figure 4.39 depicts the transmission spectrum of the longest wavelength resonance band of a grating written in SMF-28 fiber (Λ=320 μm) at four different values of ambient index [21]. The resonance band was located at 1573.1 nm with n_3=1.0 and shifted to 1506.7 nm at n_3=1.452. At an ambient index of 1.454 the isolation of the band dropped sharply and the band could scarcely be distinguished from the background loss. The reduction in the isolation with increasing n_3 can be attributed to the reduction in the coupling from the guided mode to the corresponding cladding mode. It is interesting to

note that for n_3=1.448 and higher, radiation mode losses can be observed at wavelengths longer than the main resonance loss peak. At n_3=1.454, the coupling to a continuum of radiation modes results in a constant background loss of about 4 dB at all wavelengths due to the matching of the cladding outer interface. It should be reiterated that all the refractive indices of the oils are specified at 589.3 nm. The values of indices that the light propagating in the cladding sees are less by about 0.01 due to operation in the 1550 nm region for this band.

The thermal cross-sensitivity of the refractive index sensor was measured to determine the feasibility of using the sensor at different values of the ambient temperature. The set up in Figure 4.36 was modified to include a heater between the laboratory jack and the glass slide. A grating fabricated in SMF-28 fiber with an unperturbed band at λ=1467.1 nm was used in the experiments. The grating was submerged in a water bath which was cooled from 80 °C to room temperature and the shift in the resonance band was recorded. The linear temperature coefficient for this band increased from 0.076 nm/°C for n_3=1.0 (air) to 0.085 nm/°C for n_3=1.33 (water). Using the thermo-optic coefficient of water ($dn/dT=-1.34\times10^{-4}$/°C [123]) and the extrapolated index of refraction calibration curve of the resonance band, it was determined that a large part of this change in sensitivity can be attributed to the reduction in the refractive index of water with increasing temperature. The experiment was repeated with an index oil with n_3=1.42 (λ=589.3 nm) and the temperature coefficient of wavelength shift was calculated to be 0.14 nm/°C which is almost twice the value at n_3=1.0. The increase in cross-sensitivity can be explained on the basis of the larger thermo-optic coefficient of the index oil ($dn/dT=-3.98\times10^{-4}$/°C) and the greater shift in the resonance band for the same refractive index change at n_3=1.42 compared to n_3=1.33. Hence we observe that the increase in thermal cross-sensitivity in such cases is primarily due to the temperature-induced change in the refractive index of the surrounding fluid which is in agreement with the predictions in Section 4.2.1 concerning the temperature sensitivity of a long-period grating as a function of the ambient index (Figure 4.4). One way to reduce the temperature sensitivity might be to use liquids with small thermo-optic coefficients but this might not be feasible for applications where the chemical composition of the test fluid is fixed. The second method that can be used to eliminate thermal cross-sensitivity is to design special fibers where the contribution due to the index change of the surrounding liquid is compensated by the temperature-induced wavelength shift of the grating itself. The resultant gratings are expected to have a limited dynamic range of refractive index measurement since the

above condition will be satisfied for only a small index range. It should be noted here that the cross-sensitivity tests were carried for n_3=1.33 and 1.42 only. For higher indices, the temperature-induced change in the cladding mode effective index is itself expected to have a significant contribution to the overall variation in thermal cross-sensitivity.

In Section 3.2.2.2 we had demonstrated that etching the radius of the cladding surrounding a long-period grating serves to reduce the effective index of all the cladding modes (Figure 3.17), with higher order modes undergoing larger changes. The effect on the transmission spectrum was verified experimentally in Section 3.4.2.1 where the resonance bands of a grating operating in the normal region were shown to move to longer wavelengths on reducing the cladding diameter. In Section 4.4.1 we had predicted that reducing the cladding diameter will increase the refractive index sensitivity of long-period gratings (Figure 4.34). To experimentally determine the effect of etching the cladding on the refractive index sensitivity of long-period gratings, a grating written in AT&T dispersion-shifted fiber (DSF) with period Λ=434 μm and length L=2.2 cm was etched chemically using a solution of hydrofluoric (HF) acid. For each cladding diameter, the spectral shift was monitored using an optical spectrum analyzer at three different values of ambient index - 1.33, 1.404 and 1.448. The cladding diameter was measured using a laser micrometer after each etching cycle. The resonance band was located at 1557.9 nm, 1613.4 nm and 1705.0 nm for cladding diameters 125 μm, 109.7 μm and 99.5 μm, respectively, with air as the ambient material. These values were taken as the reference wavelengths for the three diameters and the spectral shifts are plotted in Figure 4.40 as functions of ambient index. The spectral shifts for index change from n_3=1.0 to n_3=1.448 (λ=589.3 nm) were measured to be -10.69 nm, -19.31 nm, -40.52 nm for cladding diameters 125 μm, 109.7 μm and 99.5 μm, respectively. The shift in the lower order bands was also measured and a smaller increase in sensitivity was observed. The variable sensitivity to cladding diameter changes can be attributed to the distinct modulation of the effective indices of the corresponding cladding modes (Figure 3.17). The etching of the grating was observed not to significantly degrade the strength of the bare fiber since it survived the normal cleaning process during the refractive index tests. The increase in the spectral shift with change in cladding diameter is a function of the fiber parameters, the grating period, the order of the cladding mode and the writing conditions. Also, the direction of the wavelength shift on etching, and on changing the ambient index is dependent on the region of operation. For example, if a resonance band is operating in the anomalous region, reducing the cladding diameter will move the band

to lower wavelengths. It should be noted that the etching depth should be small enough so as not to perturb the evanescent filed of the guided mode significantly. For very small cladding diameters the effective index of the guided mode will itself be modified by ambient index changes.

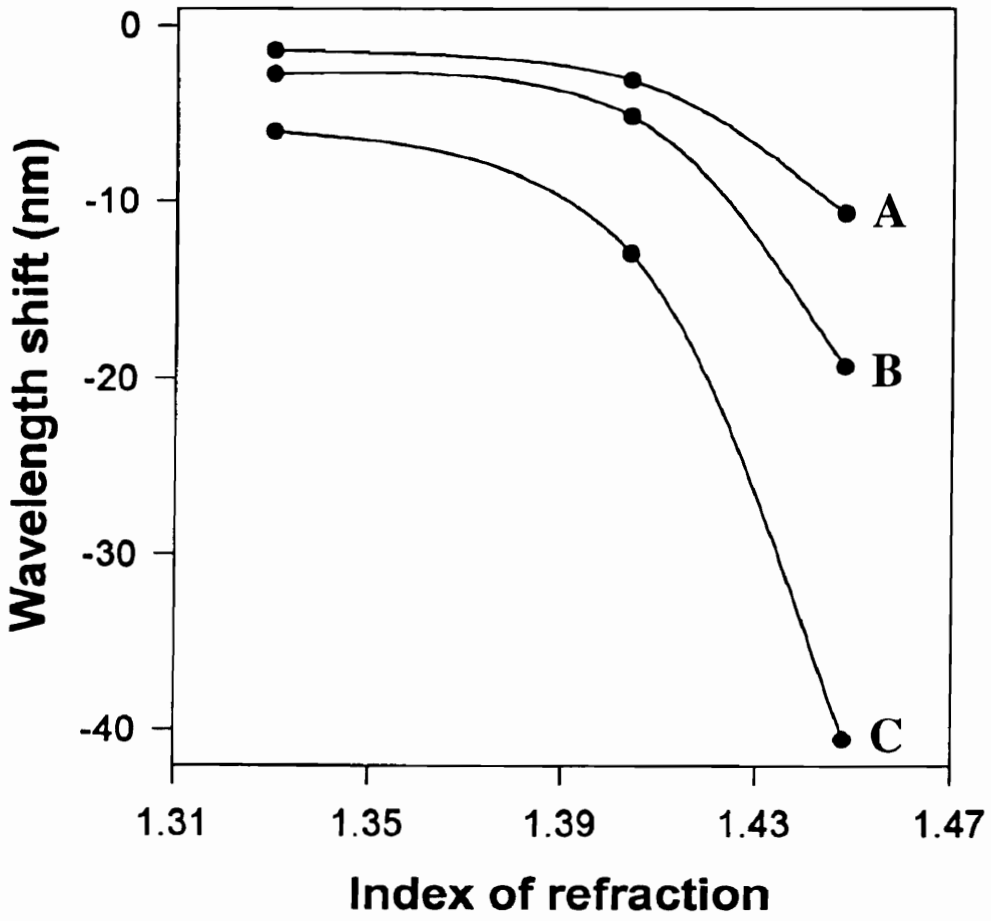

Figure 4.40. Spectral shift in a resonance band of a grating (Λ=434 μm) as a function of the ambient index for three different cladding diameters. Curves A,B and C correspond to claddings with diameters 125 μm, 109.7 μm and 99.5 μm, respectively.

In this section we showed that long-period grating can be used as highly sensitive refractive index measurement devices. The sensitivity to ambient index changes was found to be a strong function of the order of the resonance bands. It was demonstrated that index sensitivity of the order of 10^{-5} can be obtained using gratings written in standard fibers. It was experimentally determined that the cross-sensitivity to temperature is a strong function of the ambient index. Etching of a grating was proposed

as a method to increase the sensitivity to index changes with spectral shift increasing by almost a factor of four for a mere 20% reduction in the cladding diameter of a test grating. Refractive index sensors with variable sensitivities can thus be obtained by marginally reducing the cladding of long-period gratings. Additionally, the location of any desired resonance band can be selectively tuned by etching the cladding region that surrounds the grating.

4.4.3 Temperature-Insensitive Gratings

In this sub-section we present experimental results from refractive index sensitivity test carried on the temperature-insensitive long-period gratings proposed by Judkins *et al.* [34]. We also discuss the operation of gratings with reduced temperature sensitivity operating in the anomalous region in standard telecommunication fibers [35].

A grating with Λ=166 μm in the fiber with special refractive index profile [34] was subjected to oils of different indices using the setup shown in Figure 4.36 [126]. The spectral shift in the resonance band is plotted in Figure 4.41 with respect to its location in air (λ=1520.6 nm). Since this band operates in the anomalous region, the shift occurs to longer wavelengths. The overall wavelength displacement is 101.6 nm and is larger than that observed in any standard fiber to date. The higher sensitivity of this fiber results from coupling to a higher order cladding mode that undergoes a larger change in its effective index as compared to the lower order modes in standard fibers.

The resonance band was again found to reduce in isolation for higher indices and vanished completely for n_3=1.438 (λ=589.3 nm). The value of n_3 at which the ambient index matches the effective index of the cladding mode, is lower than that for standard fibers (n_3=1.452 to 1.454 at λ=589.3 nm) operating in the normal region. This can be ascribed to the fact that in the fiber with the modified profile, the coupling of the guided mode occurs to a higher order cladding mode that has a smaller value of effective index. Gratings with two different resonant wavelengths were also tested for their response to ambient index changes and shifts of 99.1 nm (λ=1522.9 nm) and 102.6 nm (λ=1500.5 nm) were measured. The small differences in the spectral shifts are due to the wavelength dependence of the effective index of the corresponding cladding mode.

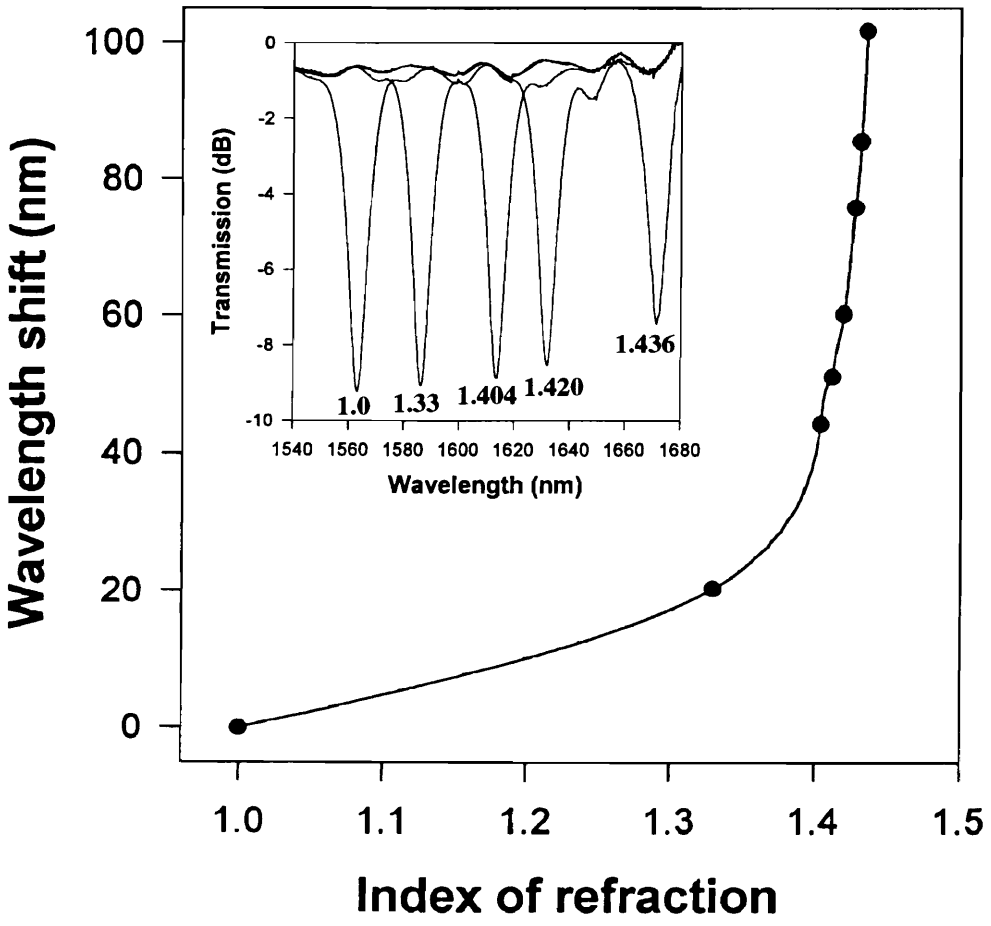

Figure 4.41. Shift in the resonance band of a long-period grating written in the fiber with special refractive index profile [126]. The unperturbed band is located at 1520.6 for the grating with period Λ=166 μm. The inset depicts the resonance spectra for different ambient indices. The indices of the oils are specified at 589.3 nm.

To measure its temperature cross-sensitivity, the grating was submerged in a water bath (n_3=1.33) and heated to 50 °C. An average spectral shift of 0.02 nm/°C was obtained as the water cooled to room temperature [126]. Although a large portion of this shift can be attributed to the heat-induced refractive index change in water (dn/dT=-1.34×10^{-4}/°C), in actual applications this modification in index of the surrounding medium is also expected to contribute to the temperature-induced shift. Hence we conclude that although these gratings have very small temperature coefficients with air is the ambient material, the shift with temperature changes can be quite significant for refractive index fluids encountered in practical applications. As proposed in Section 4.4.2, one method to obtain

temperature-insensitive long-period grating refractive index sensors is to counteract the shift due to purely temperature changes by that resulting from the finite thermo-optic coefficient (dn/dT) of the surrounding medium.

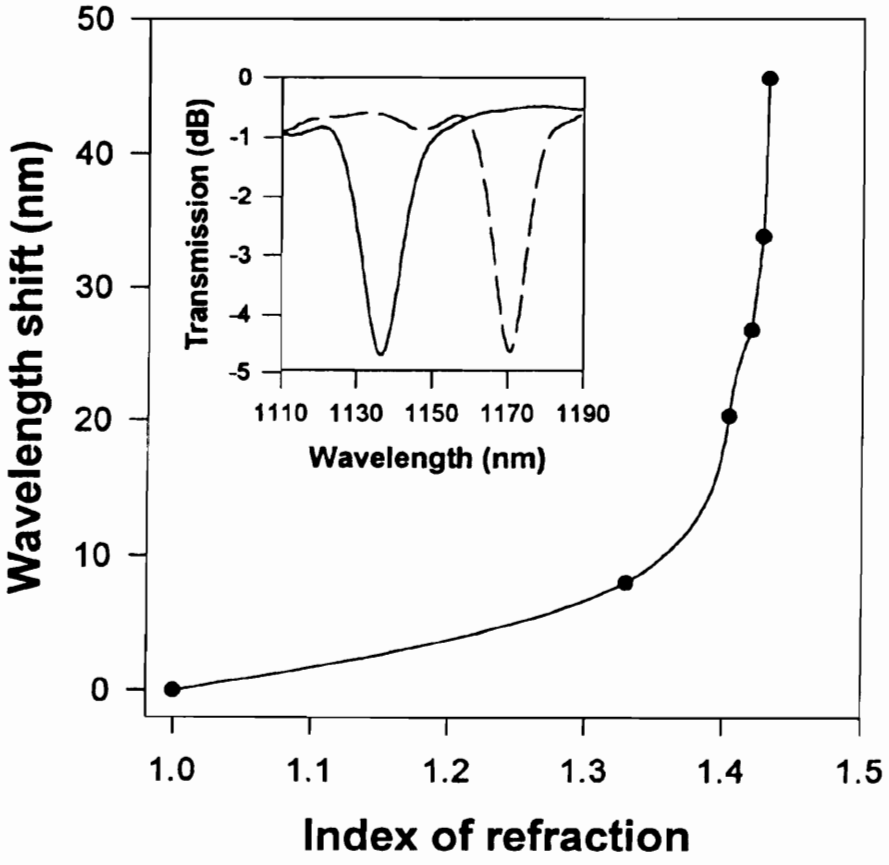

Figure 4.42. Shift in a resonance band of a grating written in Flexcor 1060 fiber with Λ=40 μm [126]. Inset depicts the transmission spectra with n_3=1.0 (solid curve) and n_3=1.428 (dashed curve). The indices of the oils are specified at 589.3 nm.

In Section 4.2.3 we had shown that gratings fabricated with appropriate periods in standard optical fibers can be made to have a very small temperature sensitivity. These gratings typically have periods less than 100 μm and hence the resulting resonance bands operate in the anomalous region. Figure 4.42 depicts the ambient refractive index-induced shift in a resonance band (located at λ=1136.3 nm for n_3=1.0) of a long-period grating written in Flexcor 1060 fiber with Λ=40 μm [35]. The resonance band shifts to longer wavelengths and disappears at n_3=1.434 nm (λ=589.3 nm) and this reduced value can again be attributed to the smaller effective index of the higher order cladding mode

involved in coupling. The inset in Figure 4.42 illustrates the transmission spectrum of the grating at n_3=1.0 and at n_3=1.428. The shifts in the three resonance bands located at 1136.3 nm, 1248.6 nm and 1369.7 nm were determined to be 45.6 nm, 49.7 nm and 50.2 nm, respectively, from n_3=1.0 to n_3=1.432.

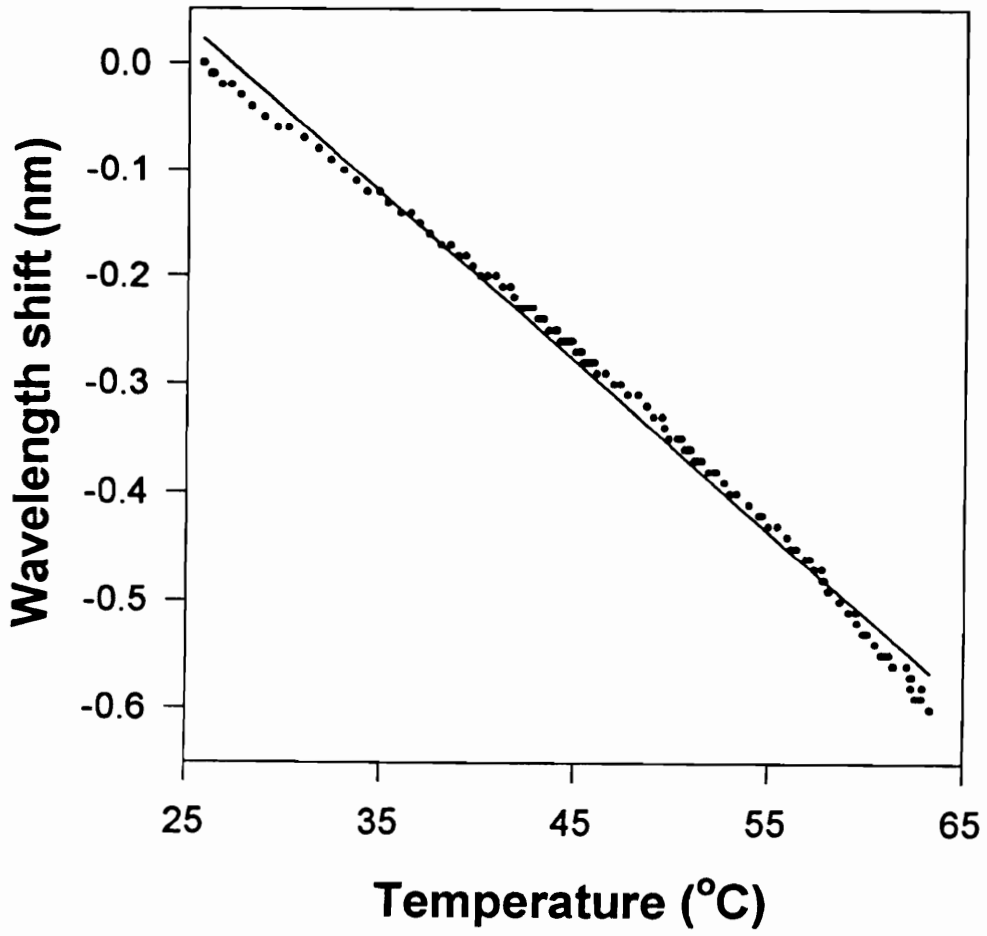

Figure 4.43. Shift in the spectral position of a grating in Flexcor 1060 nm fiber (Λ=40 μm) immersed in a water bath (n_3=1.33). The wavelength shift is measured with respect to the position of the band at 25.7 °C and n_3=1.33 (λ=1145.6 nm).

To evaluate the thermal cross-sensitivity, the same grating was immersed in a water bath that was cooled from 63 °C to room temperature (25 °C). The shift in the resonance band as a function of temperature is depicted in Figure 4.43. The spectral shift is measured with respect to the position of the band with n_3=1.33 at 25.7 °C (λ=1145.6 nm). The linear curve fit in Figure 4.43 has a slope of -0.016 nm/°C which should be compared

with the coefficient of -0.0016 nm/°C with air as the ambient material (Figure 4.13). The increase in the thermal cross-sensitivity by an order of magnitude can largely be attributed to the thermo-optic coefficient of water that results in shifts to lower wavelengths due to the decrease in index of refraction, as predicted in Section 4.2.1 (Figure 4.6). In most practical applications though, the temperature might vary by at the most ±10°C which would result in the wavelength shifts of 0.16 nm (for n_3=1.33) in either direction from the value at room temperature, for the grating used here. We hence observe that such gratings provide reduced cross-sensitivity to temperature fluctuations (for n_3=1.33) than typical gratings operating in the normal region (Section 4.4.3).

In this section we discussed the sensitivity of long-period gratings to changes in the index of the medium surrounding the cladding. The response of gratings in standard fibers was evaluated for the normal as well as the anomalous region. Temperature-insensitive long-period gratings fabricated in fibers with modified power profile were demonstrated to have large refractive index-induced shifts. Cross-sensitivity of such gratings to temperature changes were also investigated. We also determined the response of standard optical fiber gratings operating in the anomalous region to changes in the refractive index of the surrounding medium. The use of different ambient fluids also provides a method to tune the thermal response of a grating and might prove to be useful in temperature sensing applications.

In summary, long-period gratings are versatile devices that offer highly sensitive index of refraction measurement capabilities. Although the temperature cross-sensitivity of these components might be a limiting factor, we have shown that this can be overcome by using specially designed fibers or by fabricating gratings with specific periods in standard fibers. Long-period grating refractive index sensors offer suitable sensitivity without requiring the modification of the cladding surrounding the grating [21].

4.5 Demodulation and Multiplexing

Sections 4.2 through 4.4 discussed the sensitivity of long-period gratings to external perturbations such as temperature, strain and index of refraction. It was shown that these devices possess large measurand-induced spectral shifts in the unperturbed locations of the resonance bands. Also these sensors are simple and economical to mass produce and hence incorporate numerous desired characteristics of fiber optic sensors. The overall

cost of a system using long-period gratings will be a function of the signal processing required to extract the perturbation and the ease of multiplexing a number of such transducers. In this section we show that long-period grating-based sensors can be implemented with simple demodulation methods [21]. A few methods to effectively multiplex these gratings are also proposed.

4.5.1 Demodulation

In the previous sections we had restricted our discussion to the use of optical spectrum analyzers to determine the shifts in the resonance bands of long-period gratings under the influence of a perturbation. Although modern day spectrum analyzers are smaller than their traditional counterparts, the cost of these measurement systems is still a major limitation. In this sub-section we propose a few schemes that convert the wavelength shifts of the bands into intensity modulations which can be measured using a simple photodetector.

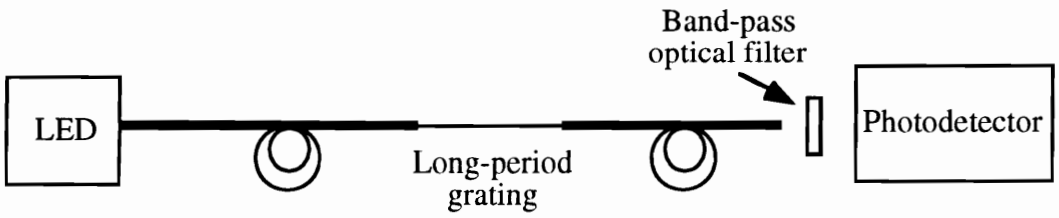

Figure 4.44. Simple demodulation scheme for long-period grating sensors.

The wide resonance bands in a long-period grating can be used advantageously to implement a number of different methods to monitor the shift. The set up for the first scheme is shown in Figure 4.44. Light from a LED is launched into the fiber with long-period grating under perturbation. Let a resonance band of the long-period grating be centered at a wavelength λ_1, as depicted in Figure 4.45. At the output of the fiber an optical band-pass filter is placed to transmit a small spectrum of the grating signal. The pass-band of the optical filter is centered at a wavelength λ_f, on one side of λ_1, such that it can extract a shift in the transmitted intensity of the LED. The exact spectral position of the filter determines the resolution and dynamic range of the sensor. If the filter is located in the region where the grating spectrum has a high slope or variation, highly sensitive measurements can be made. For the example in Figure 4.45, the decrease in the

output intensity with a shift in the band to longer wavelengths can be detected by simply employing a photodetector.

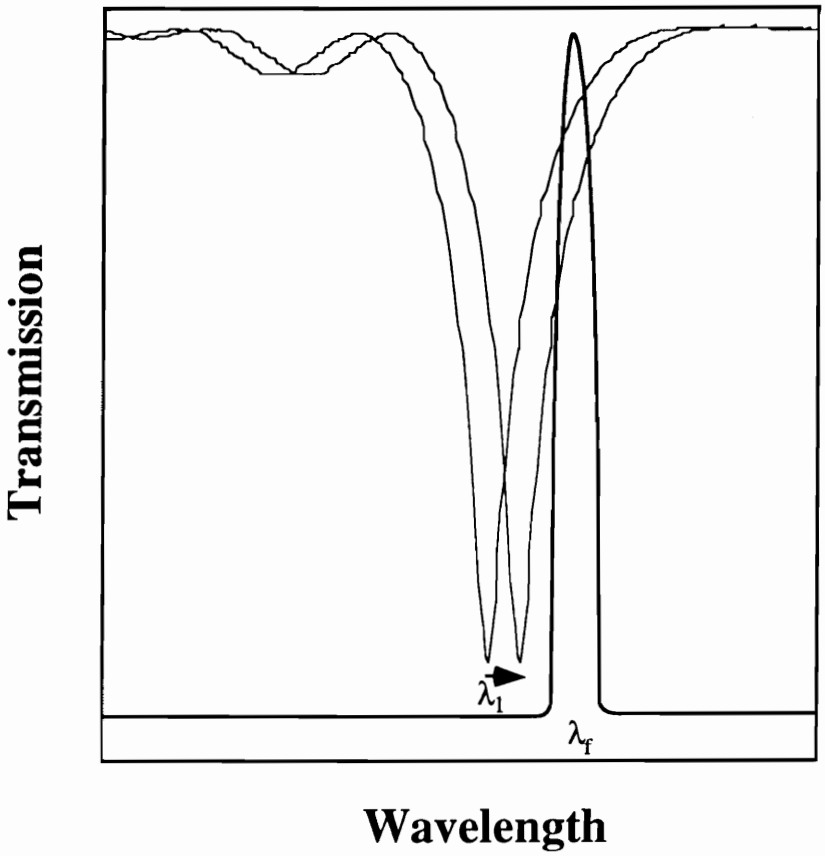

Figure 4.45. Shift in the spectral position of the resonance band (centered at λ_1) to a higher wavelength under external perturbation. The transmission spectrum of the optical filter, with pass-band centered at λ_f, is also shown.

A similar demodulation scheme uses a 3-dB coupler to interrogate a long-period grating in series with a spectrally overlapping fiber Bragg grating, as shown in Figure 4.46. The Bragg grating is shielded from the ambient perturbation and thus a shift in the long-period grating band is converted to an intensity change in the return leg of the coupler. The advantage of using a reflective configuration is that since the light makes a double pass through the long-period grating, the sensitivity of the system is effectively doubled.

Optical band-pass filters can be expensive and might be susceptible to temperature changes. Bragg gratings, on the other hand, are themselves sensitive to strain and

temperature changes, and hence need to be isolated from such perturbations. The second method to effectively detect the shift in the resonance bands involves the use of a laser diode as an optical source. The narrow linewidth laser source replaces the LED and the optical filter in the first method. The center wavelength of the laser diode is located on the region of a resonance band that undergoes a change in the transmitted intensity when a perturbation is applied [21]. Although a laser diode is typically more expensive than a standard LED, the temperature-induced shifts in its center wavelength can be detected and controlled using a number of schemes that employ feedback [81].

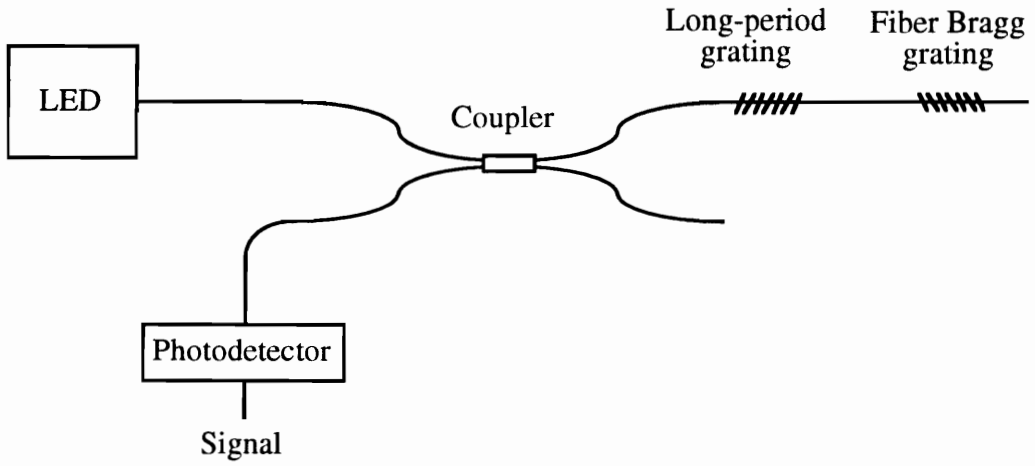

Figure 4.46. Demodulation of a long-period grating by employing a fiber Bragg grating. The reflection spectrum of the Bragg grating overlaps the resonance band in a manner similar to the optical filter in Figure 4.45.

We now present experimental results that confirm the feasibility of using the second method to implement long-period grating sensors. Figure 4.47 (inset) depicts the shift in the position of a resonance band under the effect of ambient temperature. The center wavelength of the laser diode used in the experiment was 1312 nm while the band under investigation was located at 1294 nm (50 °C). The shift in the resonance band to longer wavelengths resulted in a decreased transmission of the laser diode. The non-linearity in the diode loss characteristics in Figure 4.47 can be attributed to the shape of the resonance band and the non-linear nature of the spectral shift versus temperature curve (Section 4.2.2). The change in intensity was measured during the cooling and heating cycles and the overlapping of the curves in Figure 4.47 depicts the consistency of using

this method to demodulate the sensor output. The output of the photodetector can then be converted into the desired perturbation by using a calibration curve.

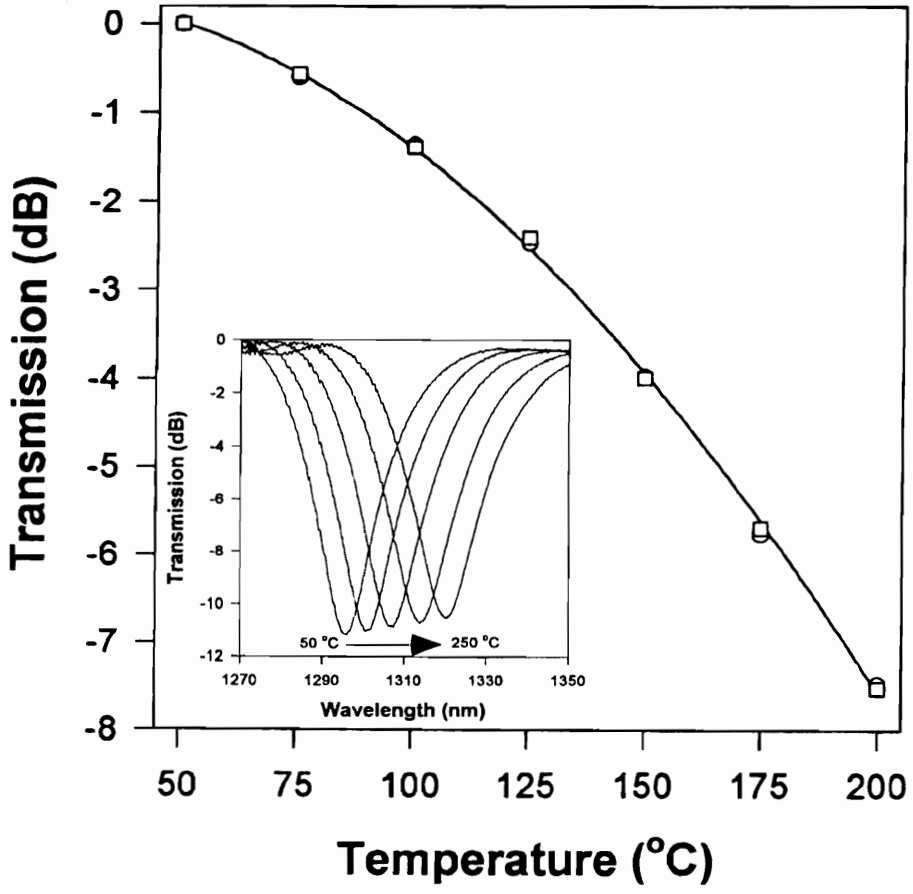

Figure 4.47. Change in transmission through a grating for increasing (circles) and decreasing (squares) temperature. The resonance band under test is centered at 1294 nm (50 °C) while the laser diode is located at 1312 nm. The transmission is normalized to 0 dB at 50 °C. Inset shows the grating transmission spectra in steps of 50 °C.

A similar test was carried out to implement a long-period grating-based strain sensor. Figure 4.48 illustrates the change in the transmitted intensity of a laser diode centered at 1317 nm [21]. The grating band with peak isolation at 1306 nm reduced in intensity by 1.6 dB at 1317 nm for 5036 με (Figure 4.48 (inset)) at room temperature. This was confirmed experimentally when the loss of the laser transmitted light increased to 1.6 dB for the same strain. The repeatability of the experiment for three independent tests confirms the feasibility of using this scheme to demodulate long-period grating sensors.

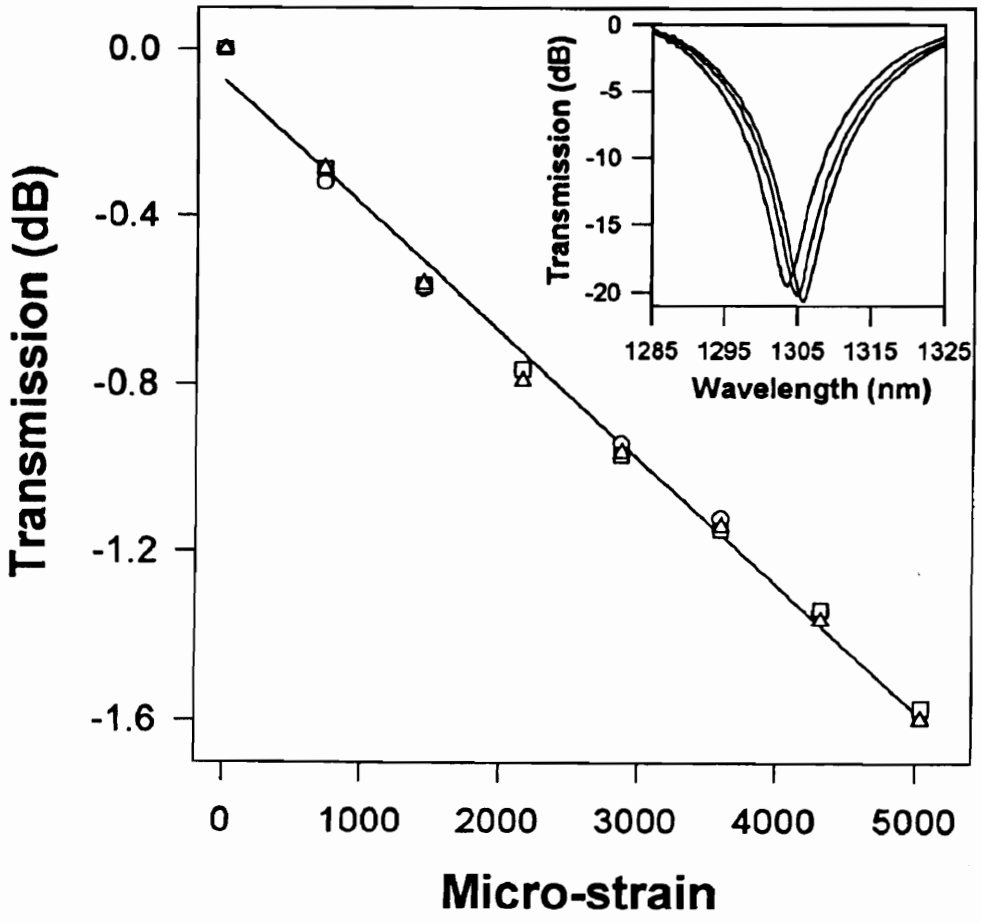

Figure 4.48. Change in transmission of a laser diode (λ=1317 nm) through a grating as a function of strain for three independent trials [21]. The transmission is normalized to 0 dB for an unperturbed grating. Inset shows the grating transmission spectra at 0, 2878 and 5036 $\mu\varepsilon$ (from left to right).

We have thus demonstrated that long-period grating sensors can be used in conjunction with simple demodulation schemes. The wide spectral width of these gratings permits the use of laser diodes at specific wavelengths as optical sources [21]. The signal processing components may simply include a photodetector with an integrated circuit that converts the intensity change into the magnitude of the applied perturbation on the basis of a calibration curve. The limitation of this scheme is that the system is now susceptible to all external factors that change the transmitted intensity. Moreover, a separate calibration curve might be required for each sensor. The first drawback can be overcome

by normalizing the sensing signal to a reference signal from another laser diode that is located at a wavelength outside the resonance band of the grating. One big advantage of these demodulation schemes is that the bandwidth of the sensing system increases a number of times over the method that employs an optical spectrum analyzer. Thus these techniques enable real-time measurements of perturbations that change rapidly with time. The temperature-insensitive gratings discussed previously can also be used with this demodulation scheme to minimize thermal cross-sensitivity. For example, Figure 4.14 depicts that the intensity variation at all the wavelengths in the resonance bands is small for a 100 °C change in temperature. Thus such gratings can be employed with simple demodulation schemes to yield inexpensive sensors.

Long-period gratings can also be employed as simple filters to demodulate the output of Bragg grating sensors. In such a case, the reflection from a perturbed Bragg grating acts as a narrowband optical source. By properly controlling the location of the bands of the long-period and Bragg gratings, a highly sensitive demodulation system can be obtained. The limitation of this system is the inherent susceptibility of the long-period grating to external perturbations such as temperature.

4.5.2 Multiplexing

To reduce the cost of sensing system it is important that a number of long-period gratings be multiplexed using the same optical source and detection scheme. In this sub-section we outline a few methods to multiplex long-period grating sensors.

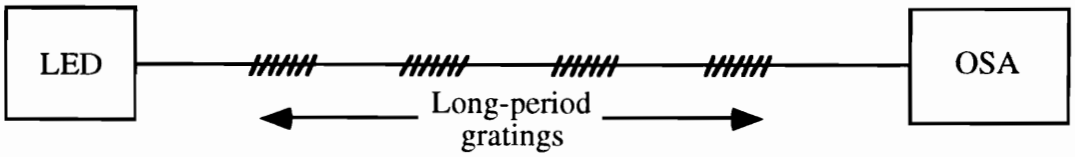

Figure 4.49. Multiplexing of spectrally offset long-period gratings using an LED and an optical spectrum analyzer (OSA).

The simplest method to multiplex long-period gratings is illustrated in Figure 4.49. The long-period gratings are written on a single fiber with the physical separation determined by the potential application. The resonance bands of the gratings within the LED spectrum are offset to prevent cross-talk between sensors. The spectral shifts in these

wavelength-multiplexed sensors is detected by the OSA. Due to the large spectral width of these gratings only a limited number of sensors may be multiplexed using a single LED. The problem can be overcome by combining the spectra of a number of LEDs with different center wavelengths using multiplexers, or by employing gratings with longer lengths and hence smaller bandwidths.

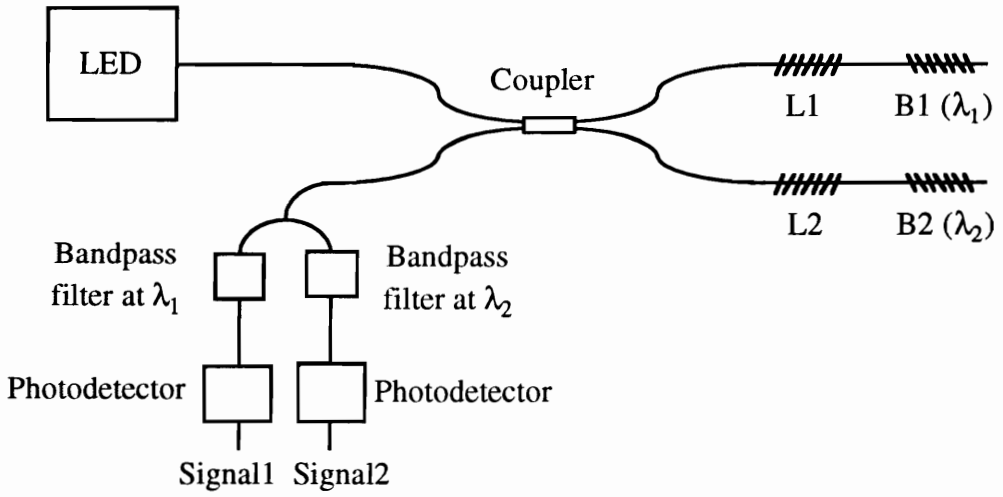

Figure 4.50. Multiplexing of two long-period gratings (denoted by L1 and L2) using a pair of Bragg gratings (B1 and B2). The center wavelengths of the two bandpass filters are matched to the resonant wavelengths of the Bragg gratings (λ_1 and λ_2).

Figure 4.50 shows a scheme to multiplex two long-period gratings located at distinct wavelengths, using fiber Bragg gratings and bandpass filters. The Bragg gratings reflect a part of the corresponding long-period grating spectrum in the return leg of the coupler (see Figure 4.46). Bandpass filters matched to the Bragg grating resonant wavelengths are used to detect the intensity change along with a pair of photodetectors. The long-period and Bragg grating pairs can also be placed serially in the same output leg of the coupler and the scheme can be modified to multiplex more than two gratings. The limitation of this system is that intensity changes due to fiber bends and source fluctuations can modify the sensor outputs and result in erroneous measurements. Moreover, temperature variations that shift the Bragg grating and the filter spectra can influence the output.

Figure 4.51 depicts a method to time-division multiplex two long-period grating sensors. A laser diode that spectrally overlaps the resonance band of both the gratings is used as a

source. Two synchronized optical switches regulate the input and output signals between the two gratings. The system uses the demodulation scheme proposed in Section 4.5.1 and eliminates the requirement of optical bandpass filters. The time-division multiplexing can easily be extended to interrogate more than two gratings. The limitation is again the sensitivity to fiber bends and intensity fluctuations of the source, and hence the sensing output has to be normalized to a reference signal that accounts for these effects.

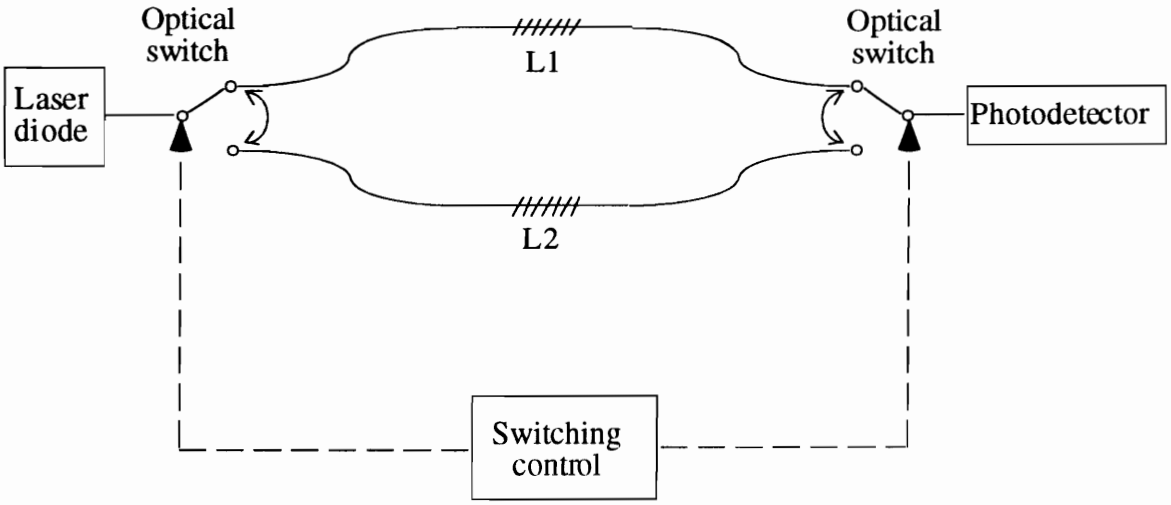

Figure 4.51. Time-division multiplexing of two long-period gratings (denoted by L1 and L2) using a single laser diode and photodetector.

In this section we proposed a few schemes for wavelength- and time-division multiplexing of long-period grating sensors. The limitation imposed by the wide bandwidth of the bands may be overcome by fabricating gratings with longer lengths. The multiplexing of gratings will enable reduction in cost per channel of the system. A number of gratings in the same or different fibers can be used for distributed sensing of the same perturbation or for simultaneous measurement of multiple parameters.

4.6 Applications of Long-Period Grating Sensors

In this section we present some practical applications of long-period grating sensors. These sensors are used to measure strain during loading of a reinforcing-bar and also to estimate the concentration of sucrose in sugar solutions.

4.6.1 Strain Sensor

The measurement of strain in high performance materials and structures has recently gained significance. The aging and deterioration of commercial and military structures such as bridges and aircraft carriers should be detected in a timely fashion to safeguard the huge investment in this field. By employing inexpensive optical fiber sensors, the real-time monitoring of such structures can yield valuable information over their lifetime.

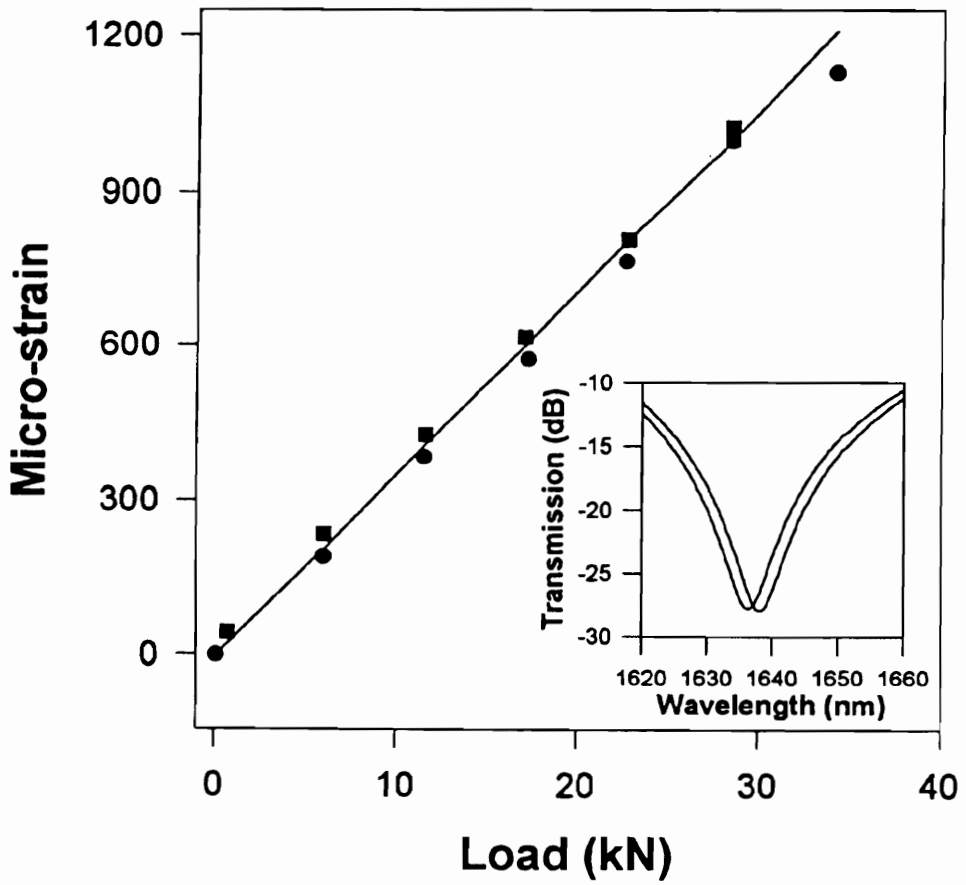

Figure 4.52. Strain measurement on a loaded reinforcing-bar using a long-period grating written in SMF-28 fiber (Λ=240 μm) [33]. Inset shows the grating transmission spectrum for an unperturbed grating (left curve) and at 1000 με.

To test the strain sensing capability of long-period gratings, a grating was fabricated in SMF-28 fiber with period Λ=240 μm [33]. The grating was attached to the surface of a

cylindrical stainless steel reinforcing-bar commonly used in civil structures. The bar was then clamped vertically on an Instron machine that could exert a maximum strain corresponding to a load of 35 kN. A mechanical extensometer was co-located to measure the strain on the reinforcing-bar during the loading process. The bar was initially loaded such that the extensometer reading was 1000 με and assuming complete transfer of strain occurred to the grating, its strain coefficient was calculated to be 16.2 nm/%ε for a resonance band located at 1636.5 nm. During the actual test, the reinforcing bar was loaded in increments of 200 με on the extensometer display. The spectral shift in the grating resonance band was measured and converted to strain using the pre-determined strain coefficient. The load versus strain curve for the grating is shown in Figure 4.52 and agrees well with that for the extensometer. A fiber Bragg grating located adjacent to the long-period grating on the reinforcing-bar also showed excellent strain measurement capability. Although an optical spectrum analyzer was used to detect the wavelength shift, the long-period grating strain sensor can easily be implemented with the demodulation schemes proposed in Section 4.5.1. Moreover, a number of such gratings can be multiplexed to provide a network of strain sensing elements over the entire length of the reinforcing-bar or to cover the surface of a larger structure.

4.6.2 Refractive Index Sensor

In Section 4.4.2 we demonstrated that long-period gratings are highly versatile index of refraction sensors that possess large spectral shifts without the requirement of etched claddings. One of the applications of such sensors could be the determination of sugar levels in water. To verify the feasibility of using long-period gratings for sugar detection, solutions of different concentration were prepared by adding varying amount of sucrose to a fixed volume of distilled water. The solutions had concentrations varying from 0% (water) to 35% and their refractive indices were measured using a standard ellipsometer. The shift in the resonance band of a grating fabricated in AT&T dispersion-shifted fiber was used to determine the change in the refractive index. The fiber was immersed in the solutions and the spectral position of the resonance band was recorded. The cladding surface was thoroughly cleaned before the fiber was immersed in a new solution. The change in the resonance wavelength with sucrose solution concentration is plotted in Figure 4.53. Since the resonance band operates in the normal region, a shift to shorter wavelengths was observed with increasing sucrose concentration. The refractive index of solutions of different concentrations is also plotted in the same figure. A shift of -2.6 nm

is obtained for change in concentration from 0 to 35%. For a minimum detectable wavelength shift of 0.1 nm this corresponds to a resolution of 1.36% in the detection of sucrose concentration. The capacity to measure sucrose level in liquids can be extended to detect sugar levels in human blood.

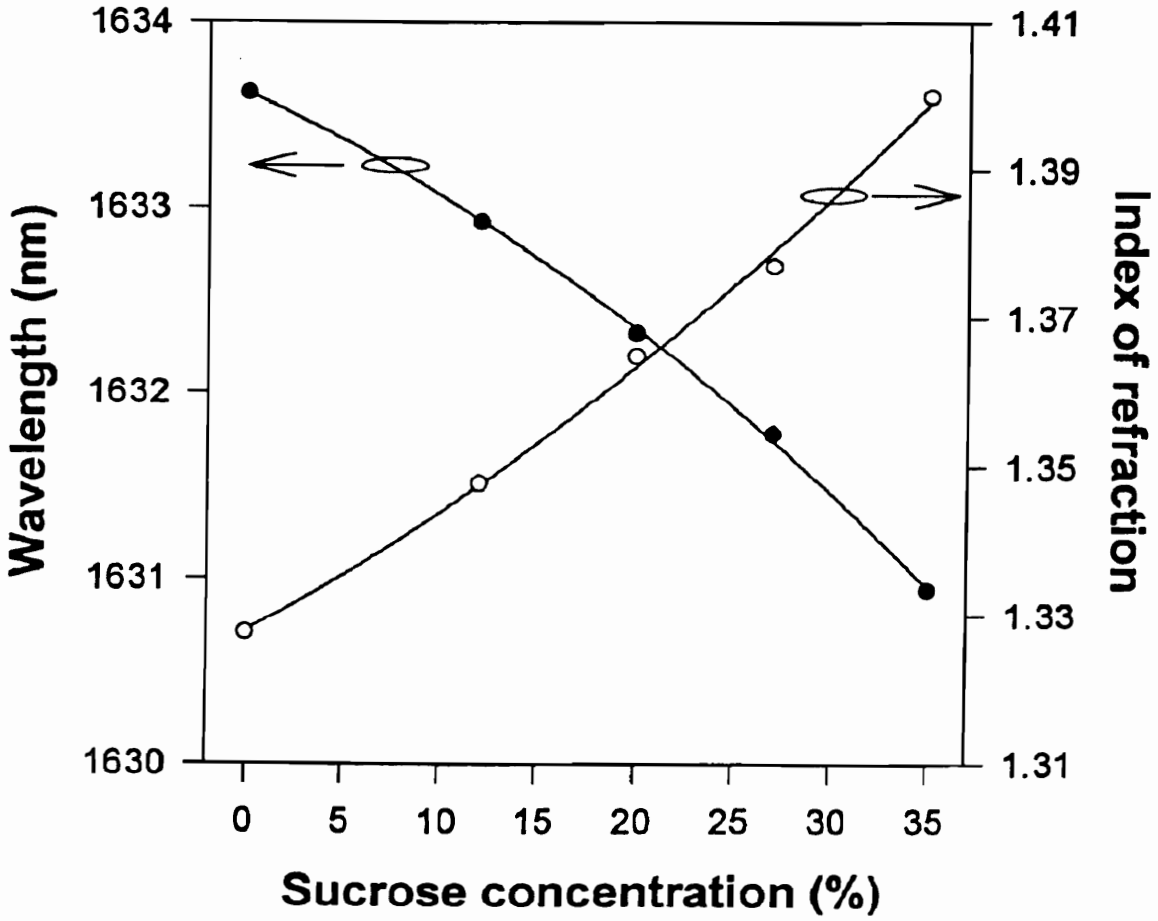

Figure 4.53. Effect of sucrose solutions on the spectral position (left axis) of a resonance band of a long-period grating in AT&T dispersion-shifted fiber. The right axis represents the index of refraction of solutions with different sucrose concentrations.

Another promising application of long-period gratings refractive index sensors is in the field of biomedical engineering [32]. Optical techniques that have been proposed to detect antibody-antigen reactions include ellipsometry [129] and surface-plasmon resonance [130]. These methods are limited by complex sensor design, limited sensitivity to index of refraction changes, or polarization sensitivity. Long-period gratings are promising alternatives as simple, rugged and highly sensitive biosensors [32].

The process of implementing a refractive index sensor for these applications includes immobilizing the antibody on the surface of the cladding and is followed by introduction of the antigen in solution form. A reaction between the antibody and the antigen results in a refractive index change that manifests itself as a shift in the resonance bands of the long-period gratings. The magnitude of the spectral shift thus provides a measure of the antibody-antigen reaction and forms the basis for a versatile sensor. The measurement scheme based on long-period gratings can reduce human involvement in this process, and result in improved performance and lower operating costs.

4.6.3 Other Applications

In this sub-section we propose a few other potential applications of long-period grating-based sensors. These devices can be employed as highly effective pressure, corrosion, and magnetic and electric field sensors.

Long-period gratings can be used as hydrostatic pressure sensors by utilizing the photoelastic effect in optical fibers. A thin layer of a material, such as silicone, with a large value of photoelastic coefficient is deposited on the cladding surface. External pressure on the fiber causes the photoelastic material to change its index of refraction by a value that is proportional to the applied pressure. The resultant change in the effective index of the cladding modes induces a shift in the resonance bands. For a calibrated grating, the magnitude of the pressure can be determined once the photoelastic coefficient is known. Electric or magnetic sensors may also be implemented by depositing thin layers of electro-optic or magneto-optic materials, respectively, on the outer surface of the cladding. These perturbations may also be converted to strain using electro- and magneto-strictive materials.

Long-period gratings have already been demonstrated for monitoring corrosion in metals [131]. The metal under consideration was deposited on the bare cladding region surrounding the grating by commonly used evaporation techniques. The grating coated with metal was then placed in a standard corrosive solution made from a combination of acids. As the metal corroded, the thickness of the outer layer reduced and a corresponding shift in the position of the grating band was observed. Once the sensor is calibrated, it can be used to monitor corrosion in embedded as well as surface-mounted configurations. The feasibility of using long-period gratings for corrosion detection

represents exciting frontiers for application of these devices to health-monitoring in materials and structures.

In this section we outlined many practical applications of long-period grating sensors. These devices possess tremendous potential as elegant optical fiber sensors and are expected to be used in many modern applications over the next few years.

4.7 Comparison of Long-Period Gratings with Other Fiber Optic Sensors

In this section we compare the performance of long-period gratings with conventional interferometric, intensity-based and Bragg grating sensors. The advantages and limitations of long-period gratings over other sensing schemes are discussed. Various parameters such as fabrication, multiplexing, signal demodulation, sensitivity, dynamic range and system cost are used in the comparison.

The operation of phase- and intensity-based sensors was outlined in Section 1.1.1. The first type of sensor is based on the modulation of the phase of light by an external perturbation. Common examples include the Mach-Zender [132], and intrinsic [133] and extrinsic [7] versions of the Fabry-Perot interferometer. These sensors are highly sensitive to even minute perturbations and are employed in applications where a high degree of resolving power is required. The basic limitation of the interferometric sensors is the requirement of a reference signal to extract the phase modulation of the sensing output. Moreover, the sensor output is differential in nature and hence loss of power causes the system to lose information. The signal processing requires fringe-counters that may be difficult to implement. These sensors are typically hard to multiplex and hence a dedicated source and demodulator is required for each sensor. For strain measurements, the cross-sensitivity to temperature can be a limiting factor in a majority of these sensors. The fabrication of some of the phase sensors, such as the intrinsic Fabry-Perot interferometer, can be cumbersome and time-consuming. The extrinsic version [7] of this sensor requires adhesives and hence mechanical issues such as slippage and strength can be limiting factors. The main advantage of the extrinsic Fabry-Perot interferometric sensor is its inherent immunity to transverse strain and temperature fluctuations [134] though problems with signal demodulation and attachment techniques have prevented its large scale commercialization. The all-fiber Mach-Zender interferometer does not require modification of the fiber properties during fabrication and hence the integrity and

strength of the fiber is maintained. On the other hand, the Fabry-Perot sensors require altering the fiber properties and hence the dynamic range of such devices might be limited. Since energy is carried by guided modes in interferometric sensors, the bend sensitivity of such devices is not a big concern.

Hence we see that long-period gratings have many advantages and limitations compared to interferometric sensors. Long-period gratings are simpler to fabricate although they require UV or CO_2 lasers. A number of gratings can be batch-produced and hence result in reducing equipment and labor use. Long-period grating strain and temperature sensors possess smaller sensitivities compared to their interferometric counterparts. Hence phase-based sensors might be a better alternative to long-period gratings in applications where resolution is the primary issue. Also the bend and transverse strain-sensitivity of long-period gratings is major limitation. The temperature cross-sensitivity can be overcome by designing special fibers [34] or by using specific grating periods in standard fibers [35]. The major advantage of long-period gratings is the absolute signal available at the output. Thus interruption of power supply to the system does not result in loss of information. Moreover, the signal processing can be simplified by using the techniques described in Section 4.5.1. The conversion of the wavelength shift to an intensity modulation causes the output to become susceptible to source fluctuations and bends in the fiber. A number of long-period gratings can be multiplexed by employing the schemes discussed in Section 4.5.2 and potentially result in inexpensive distributed systems. The strain dynamic range depends on the strength of the bare fiber in the grating region. The grating writing process is not expected to significantly degrade the fiber integrity and hence, as stated previously, improvements in dynamic range can be obtained by chemically stripping the jacket instead of using mechanical methods. Additionally, refractive index sensors can be easily implemented using long-period gratings [21]. Interferometric-based refractive index sensors require etching the cladding in order to gain access to the evanescent field of the guided mode [4] which compromises the strength of the fibers.

Intensity-based sensors are based on modulation of the propagating power by an external perturbation [4]. Intensity-based sensors require a reference signal to overcome the power variations due to fluctuations in the optical source and bends in the lead-in/lead-out fibers. Such sensors have simple demodulation and hence are economical to implement. The sensitivity of intensity-based sensors is worse than interferometric

sensors and hence the former are used in applications where system cost is the major concern. Intensity-based sensors are difficult to multiplex and hence not suitable for applications where measurements have to be made at a number of points along the length of the fiber. The complexity of fabrication of such sensors depends on the system configuration but is typically comparable to that of phase sensors. Long-period gratings used with the signal processing techniques proposed in Section 4.5.1 are similar to common intensity-based sensors. A calibration curve is required for each sensor before the system can be used for measurements. Also these two types of sensors are expected to have similar magnitudes of sensitivity. Long-period gratings used with an optical spectrum analyzer can be wavelength-division multiplexed and hence result in reduced cost per channel. The simpler batch-production of long-period gratings is another important advantage over intensity-based sensors.

Fiber Bragg grating-based sensors were discussed in detail in Section 2.4.4 [8,10]. It was shown that Bragg gratings are attractive sensors for health monitoring of high-performance structures. These sensors are simple to multiplex and are insensitive to source intensity fluctuations and bends in the fiber. The important feature of these sensors is that they can be operated in reflection or in transmission and hence are useful in applications where single-ended operation is necessary. Long-period gratings are operated in transmission and hence might be hard to install in certain areas that are not easily accessible. In this chapter we have shown that long-period grating strain and temperature sensors possess larger spectral shifts than their Bragg grating counterparts [21]. Moreover, the refractive index sensors implemented using long-period gratings do not require etching the cladding and this maintains the strength and integrity of the sensor for operation under harsh environmental conditions commonly encountered in chemical analysis. Additionally, long-period gratings can be fabricated using inexpensive amplitude masks [1]. Short-period Bragg gratings, on the other hand, require phase masks for device fabrication [13]. The spectral characteristics of long-period gratings in a given fiber may be manipulated by using different periods, ambient indices and writing conditions, and hence a greater flexibility in design is available. The larger spectral width of long-period gratings enables implementation of simple demodulation schemes without resorting to optical spectrum analyzers. On the contrary, the large bandwidth of these gratings limits the number of devices that can be multiplexed within the spectrum of a broadband source. The detection of the wavelength corresponding to maximum loss might also be much more difficult in long-period gratings although we have shown that

by using appropriate techniques, such as least-squared curve fit, small shifts in resonance bands can be measured. Additionally, it was demonstrated in Section 3.4.1 that the length of the long-period gratings can be used to manipulate the spectral width of the resonance bands. The thermal cross-sensitivity during strain measurement is much larger in long-period gratings than their short-period counterparts but suitable methods can be adopted to reduce or eliminate this effect. We have also shown that strain-insensitive long-period gratings can be used to overcome the thermal expansion-induced strain during temperature measurements. A big limitation of long-period gratings is their bend sensitivity and hence special handling and packaging is required prior to use in most measurement processes.

In summary, the use of a particular type of sensor will depend on the application under consideration. For example, in an application where the resolution is the deciding factor, interferometric sensors will be preferred over long-period gratings. On the other hand, if the cost of the system is the driving force, long-period gratings with simple demodulation schemes should be employed. For a distributed strain sensing system, multiplexed Bragg gratings might be an attractive choice.

In this chapter we have carried out an extensive analysis of long-period grating single-parameter sensors [21]. Temperature, strain and refractive index sensors were considered separately and analytical model and experimental results were presented for these three types of sensors. It was shown that for a given fiber the sensitivity to different perturbations is a function of the grating period, the order of the resonance band and the writing conditions. Based on this analysis, several methods to selectively vary the temperature, strain and refractive index sensitivity of the gratings during and after fabrication were proposed. Temperature, strain and refractive index sensors with resolutions 0.54 °C, 25 $\mu\varepsilon$ and 1.86×10^{-5}, respectively, were experimentally demonstrated and these values may be further improved by using different techniques proposed here. Temperature-insensitive gratings were shown to reduce the thermal cross-sensitivities in strain and refractive index sensors. Such gratings can be fabricated in special fibers [34] or in commonly available fibers [35] using specific periods. The demodulation and multiplexing of long-period grating sensors was investigated with an objective to design inexpensive systems. The applications of these sensors to structural health evaluation and biochemical engineering were studied. It was also shown that strain-insensitive gratings can be used to measure temperature changes in the presence of

axial strain on the fiber. The performance of these long-period gratings sensors was compared to other conventional fiber optic measurement schemes. The basic advantages of long-period grating sensors are their simple and economical fabrication and demodulation. The response of the sensors can be manipulated using different host fibers, grating periods and writing conditions. The major limitations of long-period gratings are their large temperature cross-sensitivity (for strain and index of refraction measurements), bend sensitivity and limited multiplexing capability due to the broad resonance bands. Overall, long-period grating temperature, strain and refractive sensors are highly versatile devices and are expected to find widespread use in various commercial, industrial and military applications in the future.

In this chapter we discussed temperature-insensitive gratings to obtain temperature-independent strain measurements. It is often necessary to monitor both strain and temperature in a structure. In Chapter 5 we propose novel methods to simultaneously measure strain and temperature using different configurations of long-period gratings.

Chapter 5 - Simultaneous Strain and Temperature Measurement Systems

In Chapter 4 we discussed the simplicity and versatility of using single-parameter long-period grating sensors [21]. These gratings were demonstrated as highly sensitive sensors that can be implemented with simple demodulation schemes. Experimental results and theoretical analysis were used to evaluate the feasibility of using these devices for measurement of temperature, strain and refractive index changes. Although single-parameter sensing forms a significant part of the measurement technology, the evaluation of a number of simultaneous perturbations is critical in certain applications. Chapter 5 is devoted to the analysis of long-period gratings as dual-parameter sensors for simultaneous measurement of strain and temperature.

The outline of this chapter is as follows. In Section 5.1 we discuss the importance of simultaneous measurement of perturbations in modern applications. Techniques proposed in the literature to implement multi-measurand fiber optic sensors are reviewed and their limitations are outlined. The principle of operation of the long-period grating multi-parameter sensing system is discussed in Section 5.2. The functioning mechanism of such sensors is based on the differential spectral shifts of the resonance bands of the same or different gratings under an applied perturbation [36,37]. In Section 5.3 the dynamic range of the long-period grating multi-parameter sensors is shown to be limited by the cross-sensitivity between the parameters and the non-linearities in the spectral shifts. Strain-insensitive gratings are proposed to extend the measurement range of the system [37]. Experimental results are presented to verify the feasibility of using long-period gratings for measuring concurrent perturbations in Section 5.4. It is shown that a single grating or a pair of co-located gratings can be used to obtain simultaneous strain and temperature measurements. In Section 5.5 linear system theory is employed to predict the stability of the multi-parameter sensing system. The concept of conditioning of the grating sensitivity matrix is used to mathematically predict the influence of measurement inaccuracies on the calculated values of strain and temperature [18]. The

overall system performance is evaluated in Section 5.6 and compared to previously proposed simultaneous strain and temperature measurement schemes.

5.1 Multi-Parameter Measurement

Simultaneous measurement of multi-perturbations is critical in applications where different parameters have to be monitored over the lifetime of the sensor, in situations where the output signal needs to be modified to compensate for the sensitivity to more than one external perturbation, or simply for distributed and localized sensing of a number of parameters. In this section we evaluate the significance of multi-parameter sensing and discuss the operating principle and limitations of a few conventional fiber optic techniques proposed for simultaneous measurement of strain and temperature.

An important application of multi-parameter sensors is in the detection of the curing cycle and strain in composite laminate. A sensor embedded in the composite can act as a temperature transducer during the composite cure mechanism. After the composite has cured, the same embedded sensor can be used to provide information about the mechanical changes, such as strain, that influence the performance of the material [18]. The dual-perturbation detection capability results in not only the reduction of the number of sensors required to monitor the condition of the composite during various stages of its lifetime, but also helps in conservation of manpower needed to fabricate and embed extra sensors that might otherwise be needed.

In Chapter 4 we demonstrated that conventional long-period gratings are sensitive to a number of external perturbations such as strain, temperature and index of refraction [21]. The cross-sensitivity to different parameters is undesirable in applications where only one perturbation needs to be measured. For example, while measuring strain in composite materials, fluctuations in ambient temperature can significantly alter the output of the system. In such cases it becomes difficult to separate the effects of strain and temperature changes unless the sensor possesses certain special features. The temperature sensitivity of Bragg and long-period gratings can degrade their strain sensing capability and might make them unsuitable for some applications. Thus it becomes important to develop techniques to separate the effects of different perturbations that influence the sensor performance.

In large structures it sometimes becomes important to monitor different perturbations at distinct locations. In such applications, different types of sensors can be embedded or mounted on the structure to monitor these perturbations. For example, an intensity-based sensor [6] could be employed to measure the surface temperature while an interferometric sensor [4] can be used to measure the strain in the structure. The incompatibility of such sensors in terms of optical sources and signal processing techniques results in complicated and expensive operating procedures. The use of similar sensors provides uniformity and simplifies the distributed sensing system [10]. Since intensity- and phase-based sensors are hard to multiplex, grating-based sensors are particularly attractive due to their wavelength-division multiplexing capability. A network of these sensors that monitor different perturbations at distinct locations results in an integrated and comprehensive distributed measurement system. In such cases again, suitable techniques have to be devised to separate the influence of different perturbations on each sensor. Simultaneous measurement feature of sensors is also advantageous in applications where more than one parameter has be monitored at a single point. Thus for localized measurements, a sensor that possesses multi-perturbation detection characteristics can be beneficial.

Optical fiber-based simultaneous parameter measurement has previously been reported using various configurations of fiber optic sensors. Farahi *et al.* [17] used a birefringent fiber as the cavity for a Fabry-Perot interferometer to obtain strain and temperature measurements. They also developed an technique to analyze the cross-sensitivity between strain and temperature. Huang *et al.* [78] proposed the use of the polarization and modal birefringence of a dual-mode elliptical-core fiber for concurrent measurement of strain and temperature. The simultaneous strain and temperature measurement scheme developed by Vengsarkar *et al.* [18] uses an optical fiber operated in both single and dual-mode regimes. In the single-mode region the fiber is used as a polarimetric sensor, while in the two-mode domain it acts as a modal interferometer. Two simultaneous linear equations need to be solved to obtain values of temperature change and strain. The limitation of this system is that two different optical sources are required to operate the sensor on either side of the single-mode cutoff wavelength. Moreover this, and other interferometric systems produce non-linear outputs that can be cumbersome to demodulate. Additionally, the schemes using polarization birefringence as sensing mechanism require strict control of input state of polarization [18]. It is important to note here that these methods typically involve the combination of two different interferometric

schemes to carry out simultaneous strain and temperature measurements. The incompatibility between the interferometers might prove to be a limitation in certain applications. The cross-sensitivity between the parameters and non-linearities in phase shifts typically limit the strain and temperature dynamic range [20].

The use of two or more short-period Bragg grating sensors has been demonstrated for implementing multi-parameter measurement [19]. The major limitations of this scheme are the small temperature- and strain-induced shifts of Bragg gratings, and the higher system cost due to the use of a plurality of gratings. Recently, Xu *et al.* [12] proposed a temperature-independent fiber Bragg grating strain sensor. The effective bandwidth of a chirped Bragg grating written in a tapered fiber is measured as a function of strain and is found to be insensitive to temperature fluctuations. Thus to obtain temperature-independent strain measurements, a complex fabrication procedure has to be undertaken that involves tapering the fiber and then chirping the grating. The system might be limited by the cost and repeatability of grating fabrication and is not be suitable for applications where the temperature also need to be determined.

Thus a simultaneous strain and temperature sensing scheme that does not require complex signal processing equipment, such as fringe counters, should prove to be attractive for most practical applications. The strain and temperature dynamic range of such a system should be at least a few thousand microstrain and several tens of degree Celsius, respectively. The sensor should be simple to fabricate and have a potential for implementation with economical demodulation techniques. Additionally, the sensing scheme should use only one fiber and a single optical source to keep the system cost at a minimum. Finally, the sensor should be simple to attach to or embed in materials employed in common applications. These are the desired performance characteristics of a simple and economical simultaneous strain and temperature sensing system.

The following section describes the functioning mechanism of the long-period grating simultaneous strain and temperature measurement system. It is shown that this scheme simply requires the detection of the spectral shifts in resonance bands corresponding to coupling to two different cladding modes. Moreover, this measurement system can potentially be used in conjunction with the simple demodulation schemes proposed in Section 4.5.1. Long-period gratings can be used for simultaneous measurement of parameters without chirping the grating or modifying its physical properties in any other

manner. Temperature-independent strain measurements are simple to obtain using this novel multi-parameter measurement system. Although this chapter is devoted to simultaneous sensing of strain and temperature, the analysis may be easily extended to detection of other perturbations such as changes in surrounding index of refraction.

5.2 Principle of Operation

As explained in Chapter 3, long-period gratings couple the fundamental guided mode to discrete forward-propagating cladding modes [1]. The cladding modes attenuate rapidly on propagation and give rise to distinct loss bands in the transmission spectrum of each grating (Figure 3.4) at wavelengths that satisfy the phase-matching condition (Equation (3.2)). The effective index of each cladding mode is modified in a distinct manner by an external perturbation resulting in differential shifts in the resonant positions of the corresponding bands. It was shown experimentally and analytically in Chapter 4 that these discrete resonance bands exhibit variable sensitivity to the same perturbation. The combined influence of simultaneous strain and temperature effects also produces distinct spectral shifts in the attenuation bands. By measuring these wavelength displacements and determining the contribution of each perturbation using calibration curves, two simultaneous equations can be solved for strain and temperature values [36].

Figure 5.1 depicts the shifts in three resonance bands (centered at λ_1, λ_2 and λ_3) on application of 3000 $\mu\varepsilon$ to a grating fabricated in SMF-28 fiber with Λ=280 μm (Figure 4.9). The spectral shifts of the three bands are found to be $\Delta\lambda_1$=6.0 nm, $\Delta\lambda_2$=0.86 nm and $\Delta\lambda_3$=0.66 nm. Similarly, the temperature sensitivity of the two bands is also distinct. The differential modulation of the spectral positions of the long-period grating resonance bands can be used to implement simple multi-parameter measurement systems [36,37]. It was shown in Chapter 4 that the sensitivity to different external perturbations is a function of the fiber parameters, the grating period, and the writing and annealing conditions. Hence these factors can be manipulated to vary the response of the distinct resonance bands of a grating to a given parameter. The availability of multiple resonance bands in a long-period grating thus enables the use of a single fiber to perform simultaneous strain and temperature measurements. On the other hand, two fiber Bragg gratings have to be used to implement a similar system [19]. In the following analysis, unless otherwise stated, we assume all the resonance bands of the gratings operate in the normal region.

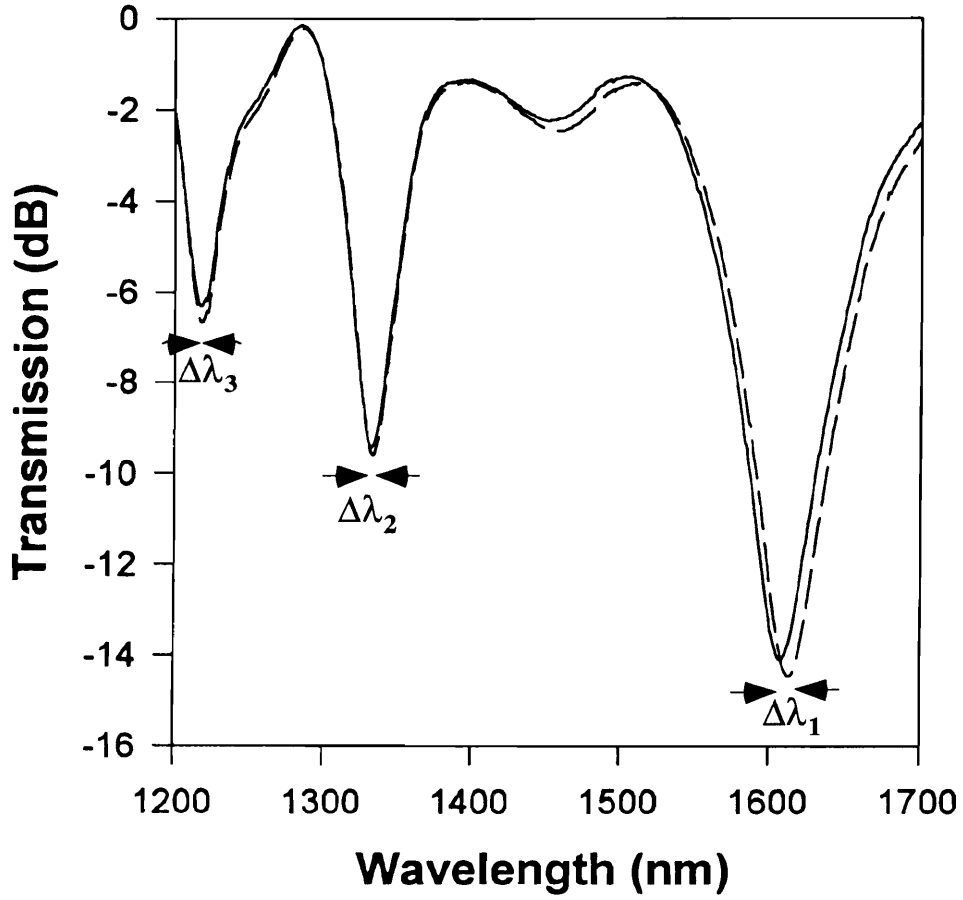

Figure 5.1. Transmission spectrum of the grating shown in Figure 4.9 for an unstrained case (solid curve) and for a strain of 3000 με (dashed curve) at 21.85 °C. The grating is fabricated in Corning SMF-28 fiber employing continuous-wave UV radiation (Λ=280 μm). The wavelength shifts $\Delta\lambda_1$, $\Delta\lambda_2$ and $\Delta\lambda_3$ correspond to the unperturbed bands located at λ_1=1607.9 nm, λ_2=1332.9 nm and λ_3=1219.4 nm, respectively.

Let us consider the influence of a temperature change ΔT, and strain $\Delta\varepsilon$, acting simultaneously on a long-period grating. It is assumed that the sensor is calibrated prior to the measurement process, that is, the temperature and strain coefficients of wavelength shift are known for any two resonance bands. For experimental analysis, the two resonance bands at the longest wavelengths (less than 1650 nm) are typically considered for this measurement system. Let $\Delta\lambda_1$ and $\Delta\lambda_2$ be the cumulative shift due to strain and temperature in the unperturbed bands located at λ_1 and λ_2 ($\lambda_1>\lambda_2$), respectively. The temperature and strain coefficients of the highest wavelength resonance band (λ_1) are

denoted by A and B while those of the next higher order band (λ_2) are represented by C and D, respectively. A and C are given in nm/°C and the units of B and D are nm/%ε or nm/με (1 %ε=10^4 με).

In this analysis, B and D are assumed to be independent of the magnitude of the temperature change, while the values A and C are assumed to be free from the influence of the applied strain. Cross-sensitivity between the perturbations would make B and D functions of the temperature, and A and C dependent on the strain magnitude. To keep the discussion simple, the cross-sensitivity between the measurands is ignored for now and will be treated in detail in Section 5.3. Moreover, A and C are assumed to be constant over the entire temperature measurement range while B and D are also assumed to be independent of the strain magnitude. Non-linearities would make A and C functions of temperature and B and D functions of strain. We had noted in Section 4.2.2 that the temperature-induced shift in a band of a long-period grating is slightly non-linear. For the ensuing analysis we will neglect non-linear response in both strain and temperature and will address that issue in Section 5.3. The spectral shifts in the two resonance bands due to strain and temperature acting simultaneously can be considered to be additive. Thus the simple linear analysis yields the following equations,

$$A\,\Delta T + B\,\Delta\varepsilon = \Delta\lambda_1\,, \tag{5.1}$$

and,

$$C\,\Delta T + D\,\Delta\varepsilon = \Delta\lambda_2\,. \tag{5.2}$$

These two simultaneous equations can be expressed in matrix form as follows,

$$\begin{bmatrix} A & B \\ C & D \end{bmatrix}\begin{bmatrix} \Delta T \\ \Delta\varepsilon \end{bmatrix} = \begin{bmatrix} \Delta\lambda_1 \\ \Delta\lambda_2 \end{bmatrix}. \tag{5.3}$$

Thus the unknown vector containing ΔT and Δε can be determined by solving the two first order simultaneous equations, such that,

$$x = S^{-1}\Delta\lambda\,, \tag{5.4}$$

where,

$$x = \begin{bmatrix} \Delta T \\ \Delta\varepsilon \end{bmatrix},\ S = \begin{bmatrix} A & B \\ C & D \end{bmatrix},\ \text{and}\ \Delta\lambda = \begin{bmatrix} \Delta\lambda_1 \\ \Delta\lambda_2 \end{bmatrix}. \tag{5.5}$$

Here x is the unknown vector that needs to be computed. S is termed the sensitivity matrix (with inverse S^{-1}) and $\Delta\lambda$ is the referred to as the wavelength shift vector [36]. S is determined from the calibration process and $\Delta\lambda$ is found through experimental measurements. Knowing S^{-1} and $\Delta\lambda$, Equation (5.4) can be solved to obtain the vector x, whose elements correspond to the temperature change ΔT and strain $\Delta\varepsilon$. It should be noted that the analysis is considerably simplified if one or more elements of the sensitivity matrix is zero. For example if D=0, the shift in the shorter wavelength resonance band is purely due to temperature. Thus, $\Delta\lambda_2$ can be used to obtain temperature, which can then be substituted in Equation (5.1) to calculate the axial strain [37]. The significance of having one term in the sensitivity matrix as zero will be much more obvious when we consider cross-sensitivities and non-linearities in the next section.

A similar analysis can be carried out for simultaneous measurement of strain and refractive index, and temperature and refractive index. By monitoring the spectral shift in three bands it is possible to monitor three perturbations, such as strain, temperature and refractive index, simultaneously. The sensitivity matrix then is modified to a 3×3 matrix owing to the inclusion of the refractive index coefficients of wavelength shift. Theoretically, if the grating has N resonance bands, it is possible to measure N distinct perturbations.

For a solution to exist for Equation (5.4), AD-BC≠0, or the ratios A/B and C/D should be unequal. If the sensitivity matrix is singular (AD-BC=0), the effects of strain and temperature can not be separated. Hence for a good detection scheme the ratios A/B and C/D should be as distant as possible [18]. The difference between the values of these ratios determines the stability of the simultaneous sensing system and this concept will be further explored in Section 5.5.

5.3 Non-Linearities and Cross-Sensitivities

In the previous section we considered a simple analysis in which the coefficients of the sensitivity matrix S were assumed to be independent of strain and temperature. Experimental analysis reveals that A,B, C and D are actually functions of the ambient temperature and strain values. In this section we modify the analysis of Section 5.2 to include non-linearities and cross-sensitivities.

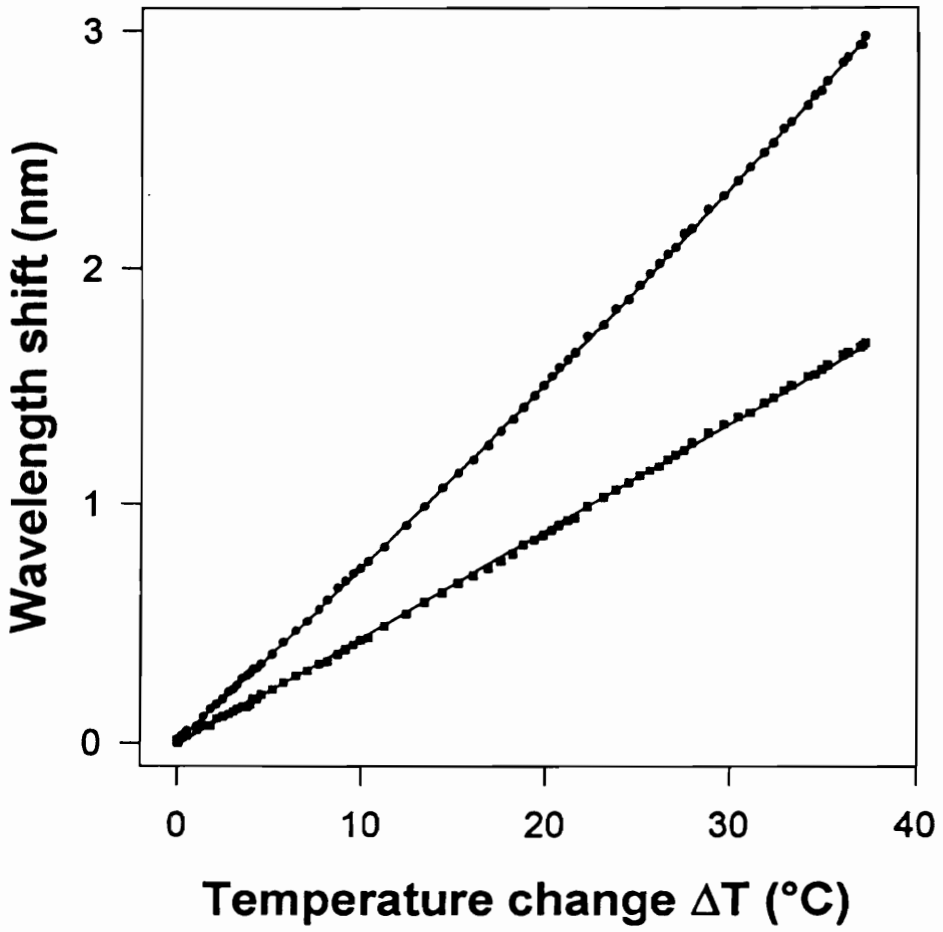

Figure 5.2. Shift in the resonance bands located at 1607.9 nm (circles) and 1332.9 nm (squares) as functions of temperature change ΔT with T_0=21.85 °C. The data for the band at the higher wavelength is fitted with a second order polynomial while that at the shorter wavelength is fitted with a straight line.

In Section 4.2.2 we demonstrated experimentally that the shift in a grating resonance band is a non-linear function of surrounding temperature. For operation in the normal region the spectral shift was found to be an increasing function of temperature. The non-linearity in the thermal-induced shift can be attributed to the temperature-dependence of the thermo-optic coefficients of the fiber core and cladding. This implies that the coefficients A and C in Equations (5.1) and (5.2) are functions of the operating temperature. Although these two elements of the sensitivity matrix can be assumed to be constant for small temperature variations, this approximation limits the dynamic range of

the simultaneous system. Usually second or third order polynomial fits are sufficient to express A and C as functions of temperature change ΔT,

$$A = A_0 + A_1 \Delta T + A_2 (\Delta T)^2 + ..., \tag{5.6}$$

and,

$$C = C_0 + C_1 \Delta T + C_2 (\Delta T)^2 + ..., \tag{5.7}$$

where A_i and C_i represent coefficients of order i, and $\Delta T = T - T_0$, T being the actual temperature and T_0 the reference or offset temperature. For a simple analysis that ignores the temperature non-linearity, $A = A_0$ and $C = C_0$, since all the higher order coefficients disappear.

Figure 5.2 depicts the second order polynomial curve fit to the temperature-induced shift of the longest wavelength resonance band of the grating shown in Figure 5.1. The next lower wavelength band can simply be approximated by a linear curve over this temperature range since the non-linearity is almost negligible. The values for an unstrained fiber were found to be $A_0 = 0.0706$ nm/°C, $A_1 = 0.000244$ nm/(°C)^2, and $C_0 = 0.0452$ nm/°C. We hence we observe that the required order of the polynomial curve fit is a function of the non-linearity in the temperature response of a particular resonance band.

A precise analysis of the grating strain sensitivity reveals that the wavelength shift with strain is also slightly non-linear in certain cases. Such effects can be ascribed to the non-linearities in the characteristic curves and the strain-optic coefficients of the fiber. As for the case of temperature, the assumption of a constant strain coefficient limits the operating range of the simultaneous sensing system. Hence for an exact analysis B and D should be expressed as,

$$B = B_{0\varepsilon} + B_{1\varepsilon} \Delta\varepsilon + B_{2\varepsilon} (\Delta\varepsilon)^2 + ..., \tag{5.8}$$

and,

$$D = D_{0\varepsilon} + D_{1\varepsilon} \Delta\varepsilon + D_{2\varepsilon} (\Delta\varepsilon)^2 + ..., \tag{5.9}$$

where $\Delta\varepsilon$ is the applied strain and $B_{i\varepsilon}$ and $D_{i\varepsilon}$ represent coefficients of order i. Figure 5.3 shows the second order curve fit to the strain data from the longest wavelength band of the grating in Figure 5.1. Owing to its negligible non-linearity, the strain-induced shift in

the next lower order band can be approximated by a straight line and hence $D_0=D_{0\varepsilon}$. The curves in Figure 5.3 are for room temperature (21.85 °C) and the corresponding coefficients are $B_{0\varepsilon}=16.77$ nm/%ε, $B_{1\varepsilon}=13.28$ nm/(%ε)^2, and $D_{0\varepsilon}=2.81$ nm/%ε. The reason for using the subscript ε in the coefficients of Equations (5.8) and (5.9) will be obvious when we consider the cross-sensitivity effects.

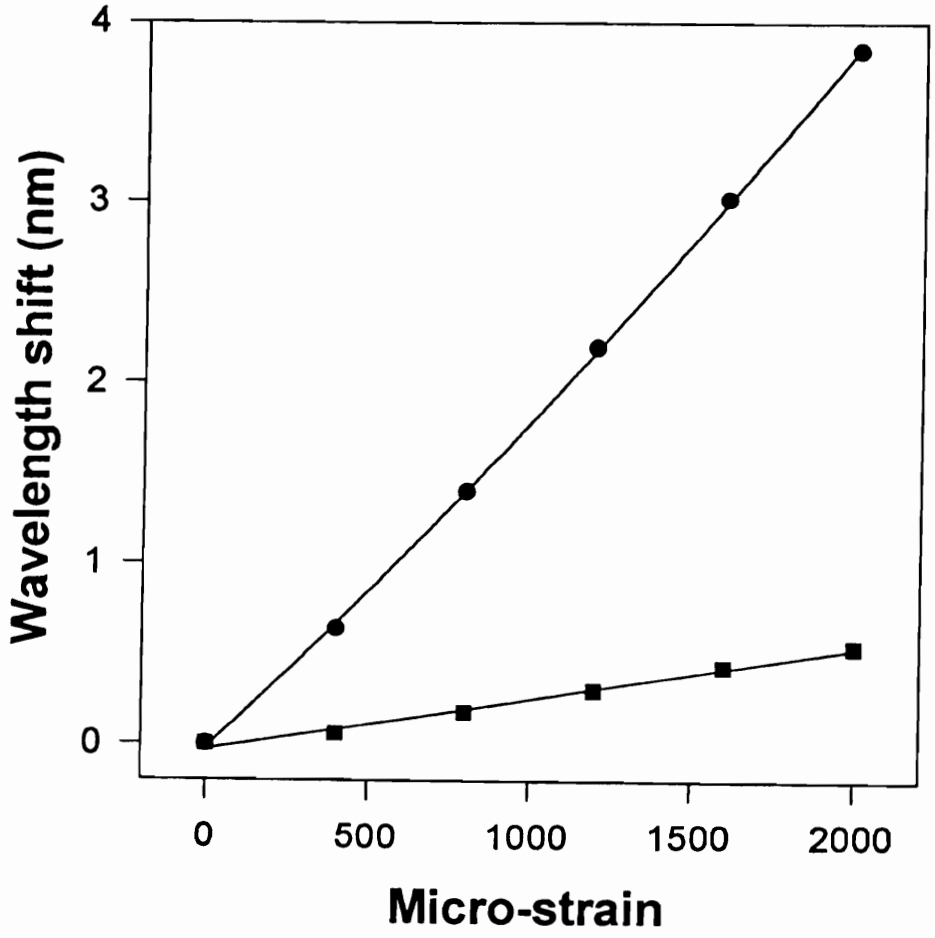

Figure 5.3. Shift in the resonance bands located at 1607.9 nm (circles) and 1332.9 nm (squares) as functions of axial strain at 21.85 °C. Polynomials of order two and one are used to obtain curve fits for the data of the higher and lower wavelength bands, respectively.

In Section 4.2.2 we observed that the strain coefficient of a particular band is a function of the ambient temperature. This phenomenon is termed as cross-sensitivity between strain and temperature. As an example, Figure 5.4 depicts the variation of the linear

strain coefficient as a function of temperature for the longer wavelength band of the grating in Figure 5.1. The data points are simply the slopes of the straight line curve fits to the strain-induced shifts in Figure 4.24. It is seen that the strain coefficient is an increasing function of temperature in the range of interest. The cross-sensitivity arises from the temperature-dependence of the strain-optic coefficients of the fiber core and cladding, and from the change in the operating point on the characteristic curve.

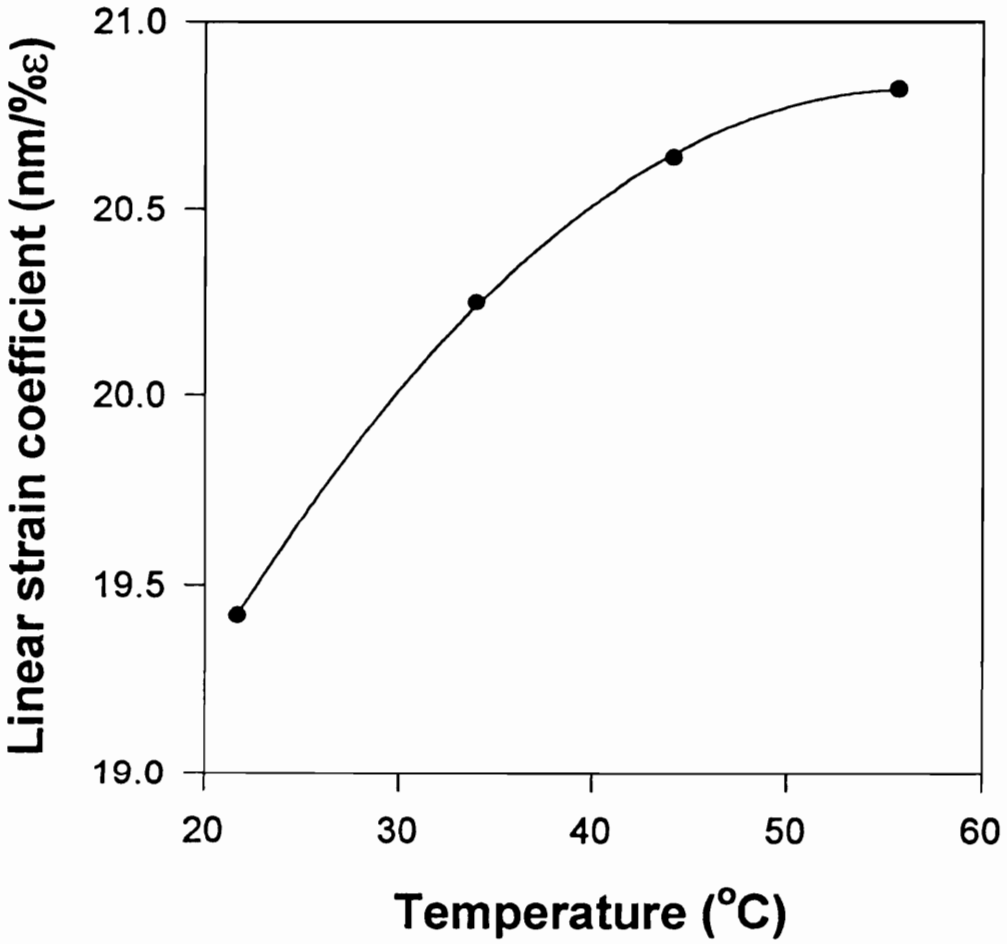

Figure 5.4. Variation of the linear strain coefficient of the higher order peak as a function of temperature. The cross-sensitivity between strain and temperature makes the coefficient B (Equation 5.1) a function of temperature.

To elucidate the cross-sensitivity between strain and temperature further we express the coefficients in Equation (5.8) as functions of the temperature change ΔT,

$$B_{0\varepsilon} = B_0 + B_2 \Delta T + B_4 (\Delta T)^2 + ..., \quad (5.10)$$

and,

$$B_{1\varepsilon} = B_1 + B_3 \Delta T + B_5 (\Delta T)^2 + ..., \quad (5.11)$$

where we have assumed that $B_{2\varepsilon}$ and other higher order terms can be neglected in the expansion of B. The coefficients $D_{i\varepsilon}$ in Equation (5.9) can similarly be expanded as functions of ΔT. For the grating under investigation, it was found that the cross-sensitivity of the lower order band was small and was ignored for the analysis. Moreover for a small temperature range, higher order terms such as B_4 and B_5 can be neglected in Equations (5.10) and (5.11).

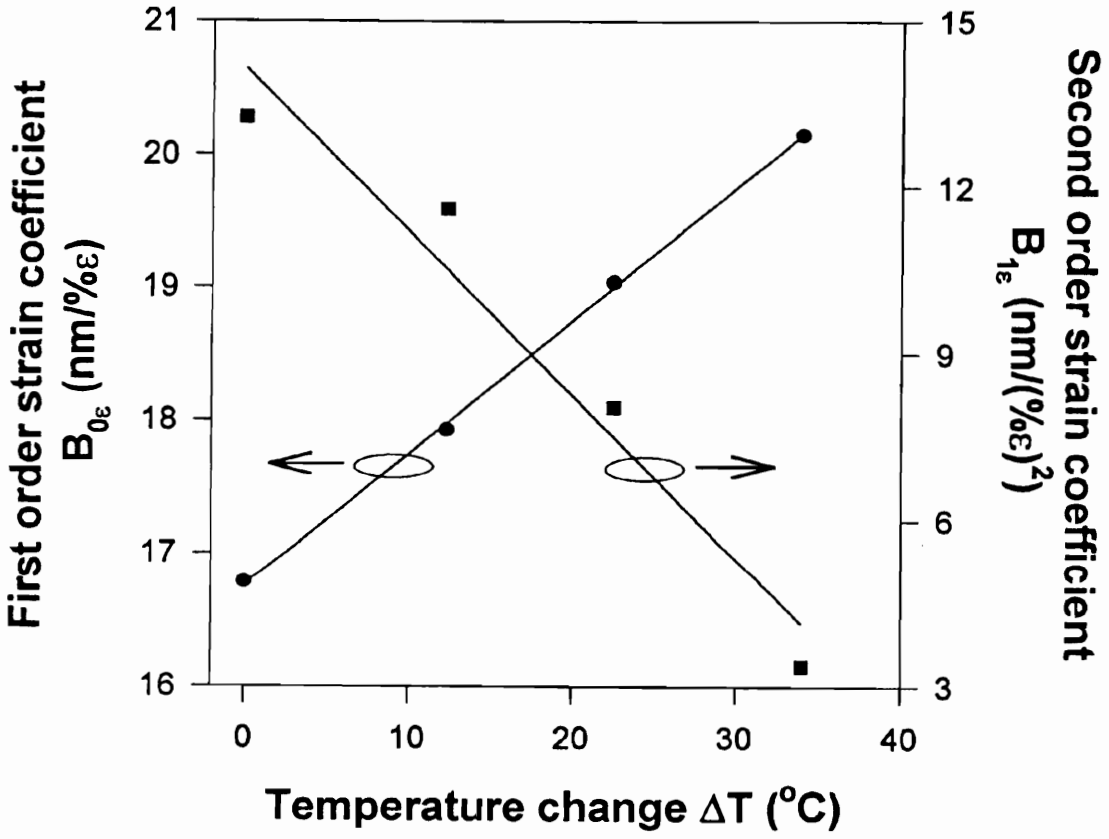

Figure 5.5. Variation of the first ($B_{0\varepsilon}$) and second ($B_{1\varepsilon}$) order cross-sensitivity coefficients of the higher wavelength band as functions of ΔT (T_0=21.85 °C). The linear curve fits to the data points yield values of the coefficients B_0, B_1, B_2 and B_3.

B_0 and B_2 in Equation (5.10) are determined by plotting $B_{0\varepsilon}$ as functions of ΔT and getting a straight line curve fit. B_2 represents the slope of this linear curve fit while B_0 is the intercept on the $B_{0\varepsilon}$ axis. Figure 5.5 (left axis) shows the variation of $B_{0\varepsilon}$ at as a function of ΔT for the grating in Figure 5.1. The calculated values of the coefficients in Equation (5.1) are B_0=16.74 nm/%ε and B_2=0.1003 nm/(%ε.°C) for an offset temperature of T_0=21.85 °C. It should be stressed here that the values of the coefficients in Equation (5.10) are strong functions of the order of the polynomial curve fit used in Equation (5.8). For example, B_0 and B_2 would have different values than those specified here if $B_{2\varepsilon}$ term were included in the expansion of B. In a similar manner, B_1 and B_3 in Equation (5.11) are determined by plotting $B_{1\varepsilon}$ at as a function of ΔT and obtaining a linear curve fit. B_3 represents the slope of this straight line and B_1 is the offset on the $B_{1\varepsilon}$ axis. Figure 5.5 (right axis) also shows $B_{1\varepsilon}$ versus ΔT for the grating under test and the calculated values at T_0=21.85 °C are B_1=14.16 nm/(%ε)^2 and B_3= 0.2959 nm/((%ε)^2.°C).

Hence we observe that including the non-linearity and cross-sensitivity introduces complexity in the analysis of the simultaneous strain and temperature measurement system. To operate the system over a wide dynamic range all the four elements of the sensitivity matrix have to be expanded as functions of strain and temperature change. On the other hand, operation over a sizable measurement range can be obtained by simply using lower order polynomial curve fits to these coefficients. Although this might also lead to errors in the measured strain and temperature, this is necessary to maintain the simplicity in mathematical analysis and reduce computation time. We thus observe that non-linearities and cross-sensitivities introduce a tradeoff between the dynamic range and system complexity.

Neglecting the non-linearities and cross-sensitivities in the lower wavelength band, Equations (5.1) and (5.2) can be modified using Equation (5.6), (5.8), (5.10) and (5.11) as follows,

$$\left(A_0 + A_1 \Delta T\right)\Delta T + \left(B_0 + B_1 \Delta\varepsilon + B_2 \Delta T + B_3 \Delta\varepsilon \Delta T\right)\Delta\varepsilon = \Delta\lambda_1 , \qquad (5.12)$$

and,

$$C_0 \Delta T + D_0 \Delta\varepsilon = \Delta\lambda_2 , \qquad (5.13)$$

where A_1 and B_1 represent the non-linearity in temperature and strain, respectively, while B_2 and B_3 arise from the cross-sensitivity between strain and temperature. Ignoring these

terms yield Equations (5.1) and (5.2) with $A=A_0$, $B=B_0$, $C=C_0$ and $D=D_0$. Equations (5.12) and (5.13) yield two simultaneous equations that can be combined to yield,

$$B_3C_0^2(\Delta T)^3 + [A_1D_0^2 + B_1C_0^2 - B_2C_0D_0 - 2B_3C_0(\Delta\lambda_2)](\Delta T)^2 + [A_0D_0^2 - B_0C_0D_0 + (B_2D_0 - 2B_1C_0)(\Delta\lambda_2) + B_3(\Delta\lambda_2)^2](\Delta T) - D_0^2(\Delta\lambda_1) + B_0D_0(\Delta\lambda_2) + B_1(\Delta\lambda_2)^2 = 0, \quad (5.14)$$

and,

$$\Delta\varepsilon = \frac{(\Delta\lambda_2) - C_0(\Delta T)}{D_0}. \quad (5.15)$$

For a calibrated system, the values of all the coefficients are known. The grating is first heated to determine the temperature coefficients. The strain coefficients are evaluated at discrete temperatures and polynomial curve fits (Equations (5.10) and (5.11)) are employed to estimate the values at intermediate temperatures. During the actual test $\Delta\lambda_1$ and $\Delta\lambda_2$ are determined and the cubic Equation (5.14) is solved for the temperature difference ΔT, which is further substituted in Equation (5.15) to obtain the axial strain $\Delta\varepsilon$. The actual temperature T is obtained from $T=T_0+\Delta T$, where T_0 is the reference temperature. This is the principle of operation behind simultaneous measurement of strain and temperature in the presence of non-linearities and cross-sensitivities. It is to be noted that this analysis is for the measurement of these parameters in the range 0 to 2000 $\mu\varepsilon$ and 22 to 55 °C for the grating under test. In order to increase the temperature range it is necessary to include the non-linearity in the temperature response of the lower order mode. For example, if the coefficient C_1 is introduced in Equation (5.13) it would make Equation (5.14) a fifth order equation in ΔT which increases the computation time and hence makes the system more complex. Putting $A_1=B_1=B_2=B_3=0$, Equations (5.14) and (5.15) reduce to solutions of Equation (5.1) and (5.2) with $A=A_0$, $B=B_0$, $C=C_0$ and $D=D_0$.

We had noted in Section 5.2 that the analysis of the simultaneous measurement system is expected to simplify considerably if one of the four basic elements of the sensitivity matrix S is identically zero. Let us for example, consider the system of Equations (5.12) and (5.13) and put $D_0=0$. The assumption implies that the lower order band is independent of axial strain and is modulated by temperature only. The strain-insensitivity of this band enables the calculation of temperature using the spectral shift $\Delta\lambda_2$ which further suggests that the shift in the two bands is now coupled only through the temperature change ΔT. The non-linearity in temperature response of the lower order

band can now easily be included in the analysis since Equation (5.13) no longer involves the strain $\Delta\varepsilon$. This results in increasing the dynamic range of temperature measurement over the case where all the four elements of the sensitivity matrix are finite. Once the temperature change ΔT has been calculated, it can be substituted in Equation (5.12) to obtain the strain $\Delta\varepsilon$. Again, higher order non-linearity and cross-sensitivity terms can be included since the analysis is considerably simplified. This also helps to increase the dynamic range of strain measurement for the simultaneous system. In this analysis, the strain-insensitivity of the band should extend over the desired temperature and strain range. Thus we observe that by employing long-period gratings with a strain-insensitive band, the measurement range for both temperature and strain can be enhanced, even in the presence of non-linearities and cross-sensitivities. The same effect can be achieved by making any other term of the sensitivity matrix zero. For the ideal case, one band should be strain-insensitive while the other should be temperature-insensitive throughout the measurement range. This would completely decouple the strain and temperature effects and result in increasing the system dynamic range considerably.

We now outline the mathematical analysis behind the simultaneous measurement system using strain-insensitive long-period gratings. Again, unperturbed bands at longer and shorter wavelengths are assumed to be located at wavelengths λ_1 and λ_2, respectively. Consider the grating in Figure 4.29 in which the band at 1257.9 nm is almost immune to axial strain. Figure 5.6 depicts the temperature versus wavelength curve for this particular band. It should be noted that the temperature is represented on the y-axis since this would yield a polynomial curve fit that can be used to calculate the temperature T from the wavelength location λ_2,

$$T = c_0 + c_1 \lambda_2 + c_2 \lambda_2^2 + c_3 \lambda_2^3 \ldots, \tag{5.16}$$

where c_0=-48792317.47 °C, c_1=115004.4746 °C/nm, c_2=-90.364752 °C/nm^2 and c_3=-0.02367047 °C/nm^3 for a third order curve fit to the data in Figure 5.6. We thus observe that temperature can be directly calculated from the position of the strain-insensitive resonance band without using any information from other bands of the grating. Moreover, to increase the dynamic temperature range of the system, a curve fit of order higher than three may be employed in Equation (5.16).

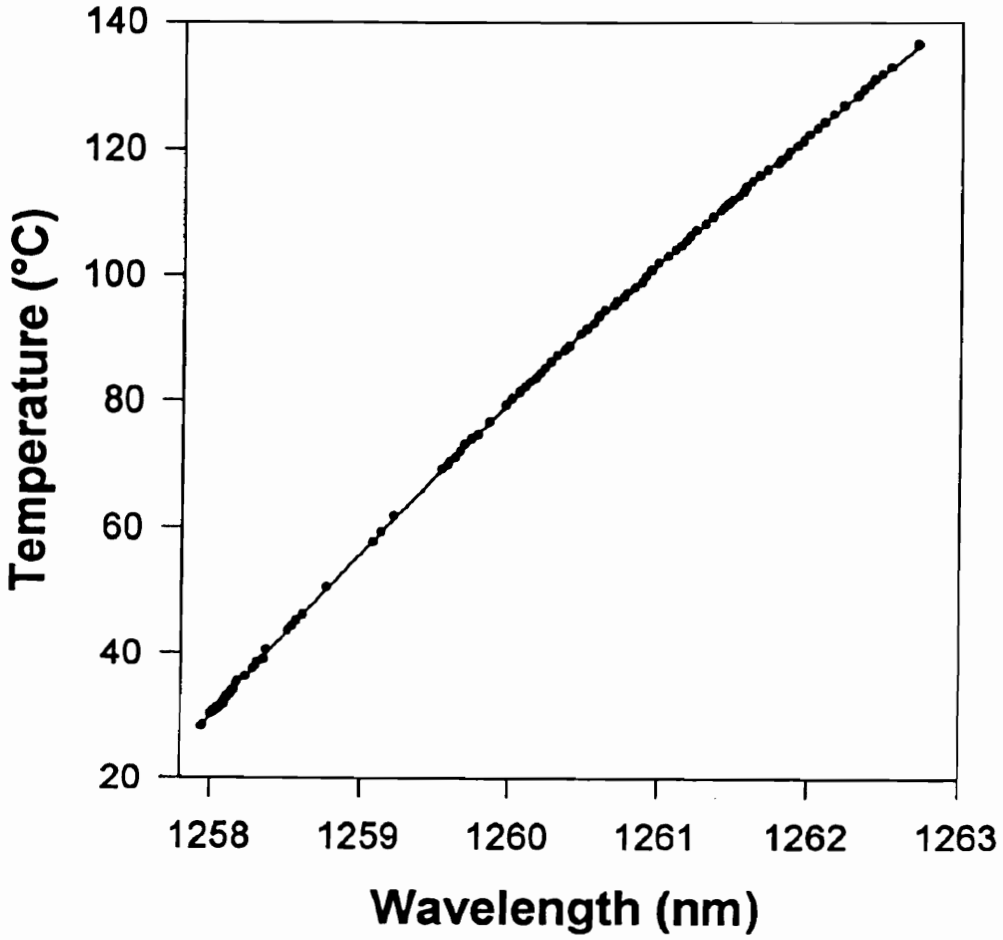

Figure 5.6. Variation in wavelength of the strain-insensitive band (Figure 4.29) with ambient temperature. The wavelength is represented on the x-axis to obtain values of the coefficients c_0, c_1, c_2 and c_3 (Equation (5.16)) using a third order curve fit.

Once the temperature has been determined, we use that value to calculate the corresponding position of the higher order band λ_{10} at zero strain. The resonance band at 1638.3 nm (Figure 4.29) was used for this experiment. This involves expressing the location of this band as a function of the temperature T,

$$\lambda_{10} = a_0 + a_1 T + a_2 T^2 + a_3 T^3 + ..., \qquad (5.17)$$

and for the grating in Figure 4.29 such a curve fit is shown in Figure 5.7. For a third order polynomial fit the values of the coefficients are a_0=1637.01 nm, a_1=0.0425 nm/°C, a_2=2.11×10^{-4} nm/(°C)^2 and a_3=4.88×10^{-7} nm/(°C)^3. The remainder of the shift in this

band, $\Delta\lambda_1=\lambda_1-\lambda_{10}$, can be attributed to axial strain, where λ_1 is the position of the band at temperature T and strain $\Delta\varepsilon$. Thus the strain can then be calculated from,

$$\Delta\varepsilon = \frac{\Delta\lambda_1}{B}, \tag{5.18}$$

where B is the strain coefficient of the higher wavelength band. Thermal cross-sensitivity and non-linearity in strain response make B a function of T and strain $\Delta\varepsilon$, respectively. Expanding B as,

$$B = B_0 + B_1\,\Delta\varepsilon + B_2\,(\Delta\varepsilon)^2 + ..., \tag{5.19}$$

we account for the non-linear response in strain. Cross-sensitivity effects are included by assuming B_0, B_1 and B_2 as functions of ambient temperature. For example, for a linear curve fit to B , the coefficients are B_0=10.92 nm/%ε and B_1=15.68 nm/(%ε)^2 at 30.6 °C, and B_0=17.68 nm/%ε and B_1=16.39 nm/(%ε)^2 at 134.7 °C. The grating is thus heated to discrete temperatures and then strained to calculate the values of B_0 and B_1. Polynomial curve fits are then employed to approximate these values at intermediate temperatures. Equations (5.18) and (5.19) are then combined to yield a higher order equation in $\Delta\varepsilon$ that be easily solved. Although the procedure outlined here for simultaneous measurements appears to be more demanding than the case when all the four elements of the sensitivity matrix are finite, in reality, the former is much more simpler in that it requires reduced pre-test calibration and also provides larger dynamic range for the system.

In this section we analyzed the influence of non-linearities and cross-sensitivities on the operation of the simultaneous strain and temperature measurement system. It was found that such effects result in reduction of the dynamic range of the system. The measurement range can be improved by including higher order terms in the expansion of the strain and temperature coefficients but doing so increases the system complexity. Hence an optimum combination of the dynamic range and simplicity is desired in such applications. We also introduced strain-insensitive long-period gratings for simultaneous measurement of strain and temperature. It was shown that such gratings extend the measurement range of the system by providing methods to incorporate non-linearities and cross-sensitivities. The next section is devoted to experimental results obtained for different long-period grating-based simultaneous strain and temperature sensing schemes.

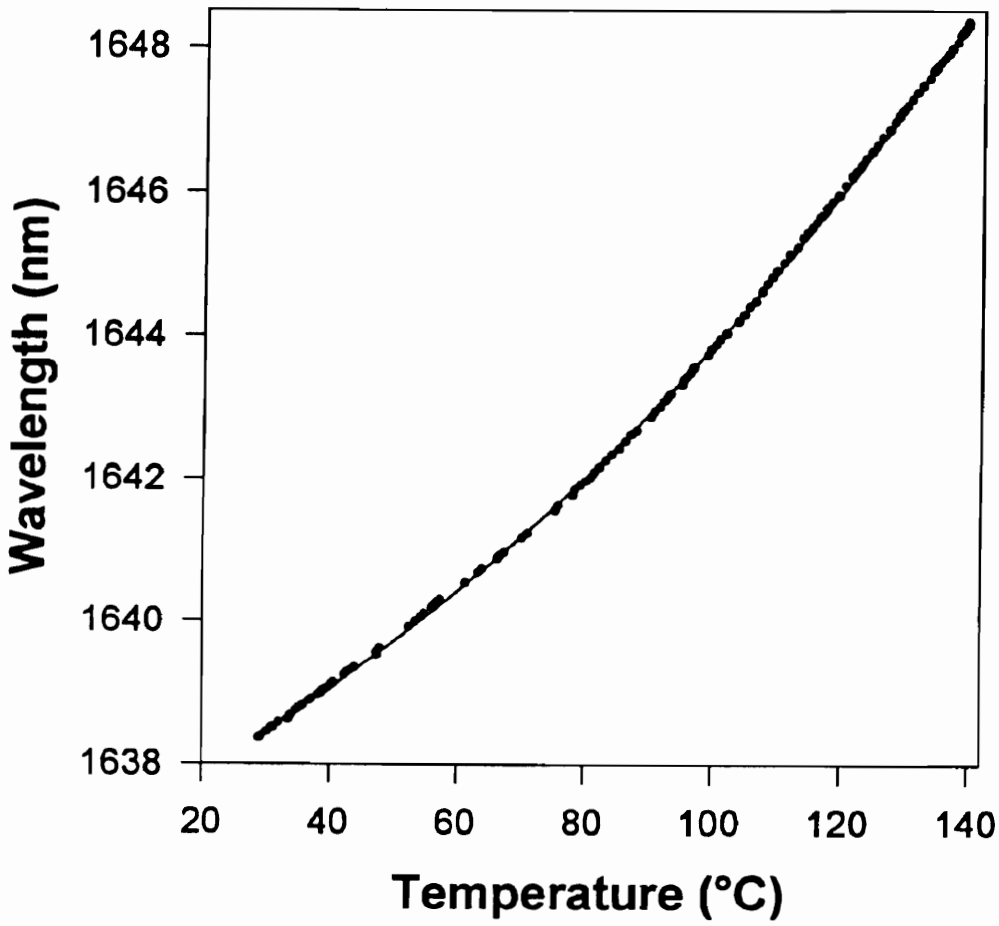

Figure 5.7. Variation in wavelength of the higher order band (Figure 4.29) with ambient temperature. The third order curve fit yields values of the coefficients a_0, a_1, a_2 and a_3 in Equation (5.17).

5.4 Experimental Results

In Section 5.2 we outlined the operating principle of multi-parameter measurements using long-period gratings while Section 5.3 included the modifications that need to be made for a system that has non-linearities and cross-sensitivities. In this section we present data from experiments that were carried out to determine the validity of using long-period gratings for simultaneous strain and temperature sensing. Results from three different system configurations are presented. The first set of experiments uses the grating shown in Figure 5.1. Since this grating is like most others with finite strain- and temperature-

induced shifts for both resonance bands under investigation, we will term this the "conventional" grating. Data is also presented from the simultaneous strain and temperature tests on the strain-insensitive grating shown in Figure 4.29. Finally, results from an experiment that combines two different gratings for measurement, are discussed.

5.4.1 Conventional Grating System

The generic set up for measuring strain and temperature concurrently using a single long-period grating is illustrated in Figure 5.8. Owing to the large separation between the two resonance bands of the grating in Figure 5.1 (λ_1=1607.8 nm and λ_2=1332.4 nm), two LED sources were used for experiments. LED1 is centered at 1275 nm while LED2 has maximum power at 1520 nm. The spectra of these two LEDs was combined using a 2×2 coupler to provide greater than -60 dBm power in the wavelength range 1100 nm to 1650 nm. A splice tube was used to couple the concatenated spectra of the LEDs into the fiber containing the long-period grating. About 1 cm length of coating was removed from the fiber at distances of approximately 10 cm on either side of the grating. A small temperature chamber was placed between two translation stages separated by about 30 cm. The bare fiber regions on both sides of the grating were then epoxied to the translation stages such that the grating was suspended in air inside the temperature chamber and this enabled the grating to be axially strained and heated at the same time. The gage-length was measured for each sensor and was typically between 20 and 30 cm. The output of the grating was coupled into the ANDO AQ-6310C optical spectrum analyzer (OSA) using a bare-fiber adapter. The OSA was interfaced to a personal computer to transfer the transmission spectra of the grating for post-processing. The temperature measured by a thermocouple co-located with the grating inside the temperature chamber was also read into the computer.

The computer code for data acquisition (Section 4.2.2) was modified such that the OSA scanned over two wavelength ranges specified by the user. Although one scan can be used to cover both the resonance bands, this results in loss of accuracy in the exact wavelength determination. Each scan was limited to a wavelength range of 10 to 20 nm to enable the use of the least-squared curve fitting method described in Section 4.2.2. This process provided highly accurate wavelength measurements in presence of noise in the transmission spectrum (Figure 4.8). In Section 5.5 we will show that even small measurement errors in wavelength can result in large differences between the calculated

and actual values of strain and temperature. Hence the curve fitting method helps in reducing the measurement errors in strain and temperature. At each value of discrete strain and temperature, two scans were read from the OSA and the wavelength locations were determined. The scans that are output by the OSA were normalized with respect to the source spectrum to eliminate the effect of spectral non-uniformity in the LED spectra. The temperature measurements from the thermocouple were taken three times during each cycle and averaged. The initial reading was taken before the OSA scanned the first wavelength range, the second between the two scans and the third after the second wavelength range had been scanned. This process averaged out the temperature fluctuations during the time taken by the OSA to complete the two sweeps (approximately 30 seconds). The small sweep speed also implies that the system is bandlimited to strain and temperature changes that are slower than the time taken to complete the two scans. Thus the system is presently suitable for only static and quasi-static measurements but its bandwidth can be improved by using OSAs with higher scanning speeds. The main advantage of this system is the simplified signal processing compared to other simultaneous measurement techniques that typically require fringe counting [17,18].

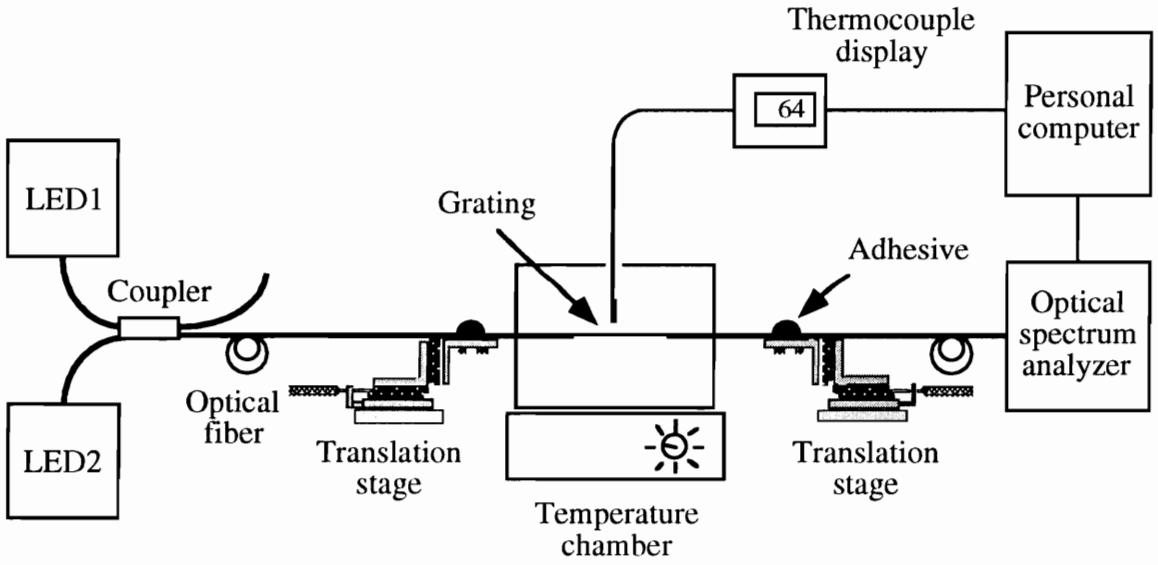

Figure 5.8. Experimental set up for simultaneous measurement of strain and temperature using a single long-period grating. The coupler combines the spectrum of the two LEDs centered at distinct wavelengths.

The grating was first calibrated by heating to 55 °C and determining A_0, A_1 and C_0 in Equations (5.12) and (5.13) using curve fits of appropriate orders. The grating was then heated to discrete temperatures and strained to find out the first and higher order strain coefficients as functions of temperature. The band at 1332.4 nm was found to have a negligible dependence of the strain coefficient on the ambient temperature and hence the term D_0 was considered sufficient to represent its strain characteristics. Once all the coefficients in Equations (5.12) and (5.13) had been calculated during the calibration process, two different tests were carried out to determine the feasibility of the simultaneous measurement system.

The first experiment involved heating the grating to 54.8 °C and then straining it at that temperature. The wavelength shifts $\Delta\lambda_1$ and $\Delta\lambda_2$ were determined and a computer code that solved the simultaneous Equations (5.14) and (5.15) was used to determine the temperature change ΔT and strain $\Delta\varepsilon$. The time taken by the computer to acquire the two scans, implement the least-squared curve fits and calculate ΔT and $\Delta\varepsilon$ was about 2 seconds and is small compared with the time taken by the OSA to complete two sweeps (30 seconds). The grating was held steady at 54.8 °C during the strain cycle in which the strain was increased in steps of 400 $\mu\varepsilon$ from 0 to 2000 $\mu\varepsilon$. The temperature was then reduced to 46 °C and the same process for repeated. The static temperature test was carried out at 33.7 °C and 23.2 °C also, and the results of the test are depicted in Figure 5.9. The comparison between the actual and measured strain and temperature values reveals that the system faithfully tracked the two perturbations. The maximum error in temperature for the 24 test points was found to be 0.83 °C for a 31.6 °C dynamic range. For strain, the largest error was 38 $\mu\varepsilon$ for a 2000 $\mu\varepsilon$ measurement range. The average strain and temperature resolutions for this system were found to be 30 $\mu\varepsilon$ and 0.6 °C, respectively. At each value of discrete temperature, the strain was also decreased from 2000 to 0 $\mu\varepsilon$ and the maximum errors in temperature and strain were calculated to be 0.83 °C and 35 $\mu\varepsilon$, respectively. This preliminary experiment demonstrates the feasibility of using a single long-period grating for simultaneous sensing of strain and temperature.

The second test involved measuring the strain and temperature simultaneously as the grating cooled from 56.2 °C to 25.8 °C. Thus this experiment predicts the system performance for the case when the temperature is varying dynamically during the measurement cycle. The test was done over a period of 47 minutes and hence the average rate of temperature change was -0.64 °C/min. The strain was limited to three values - 0,

1000 and 2000 με, and was static in the sense that it was varied only after the two scans corresponding to each data point were completed by the OSA. The results of the test are shown in Figure 5.10 where temperature and strain are plotted separately as functions of time. It is again seen that measured temperature and strain are in close agreement with the actual values. The maximum error in temperature over a 30.4 °C range was measured to be 0.7 °C while the largest error in strain was 42 με for a 2000 με range. The minimum detectable strain and temperature changes were again found to be around 30 με and 0.6 °C, respectively. A test to evaluate the system performance under a finite strain rate would have been useful but was not performed due to lack of appropriate equipment.

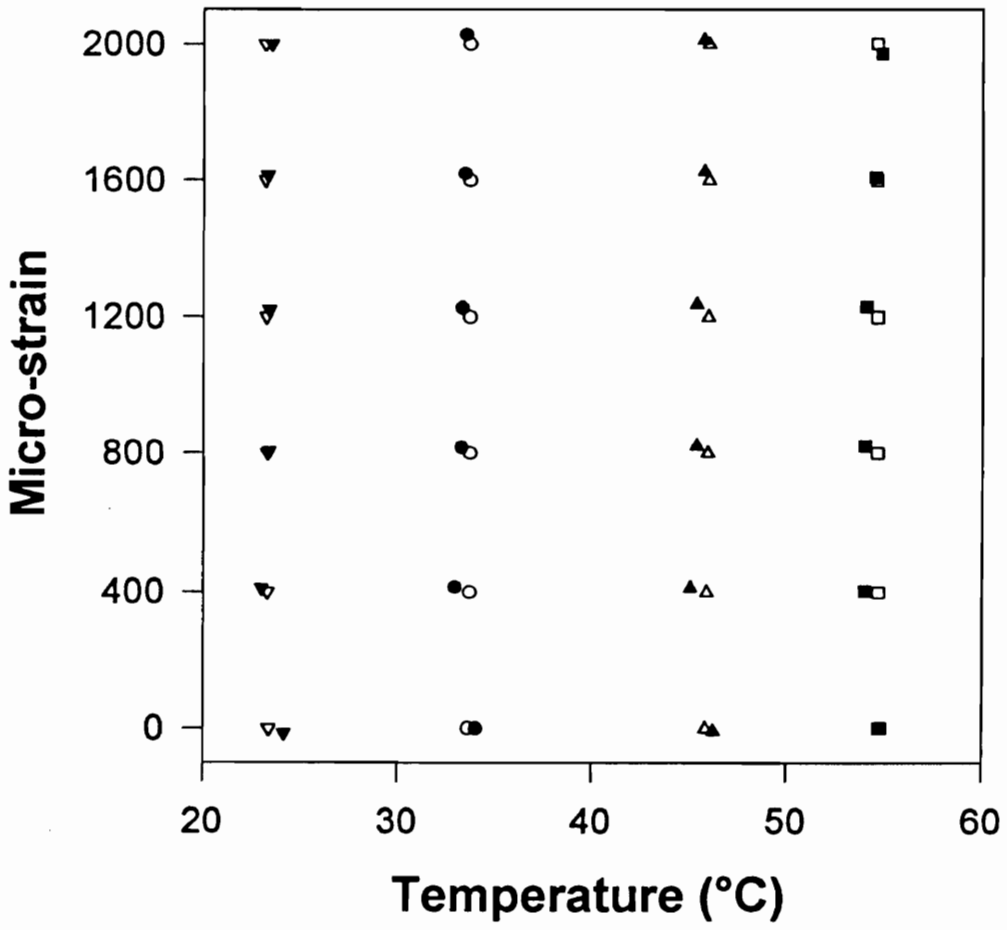

Figure 5.9. Comparison between actual (unfilled symbols) and calculated (filled symbols) values for simultaneous measurement of strain and temperature using a long-period grating written in SMF-28 fiber with Λ=280 μm. Results are from a static test where the grating was stabilized at different temperatures and then strained.

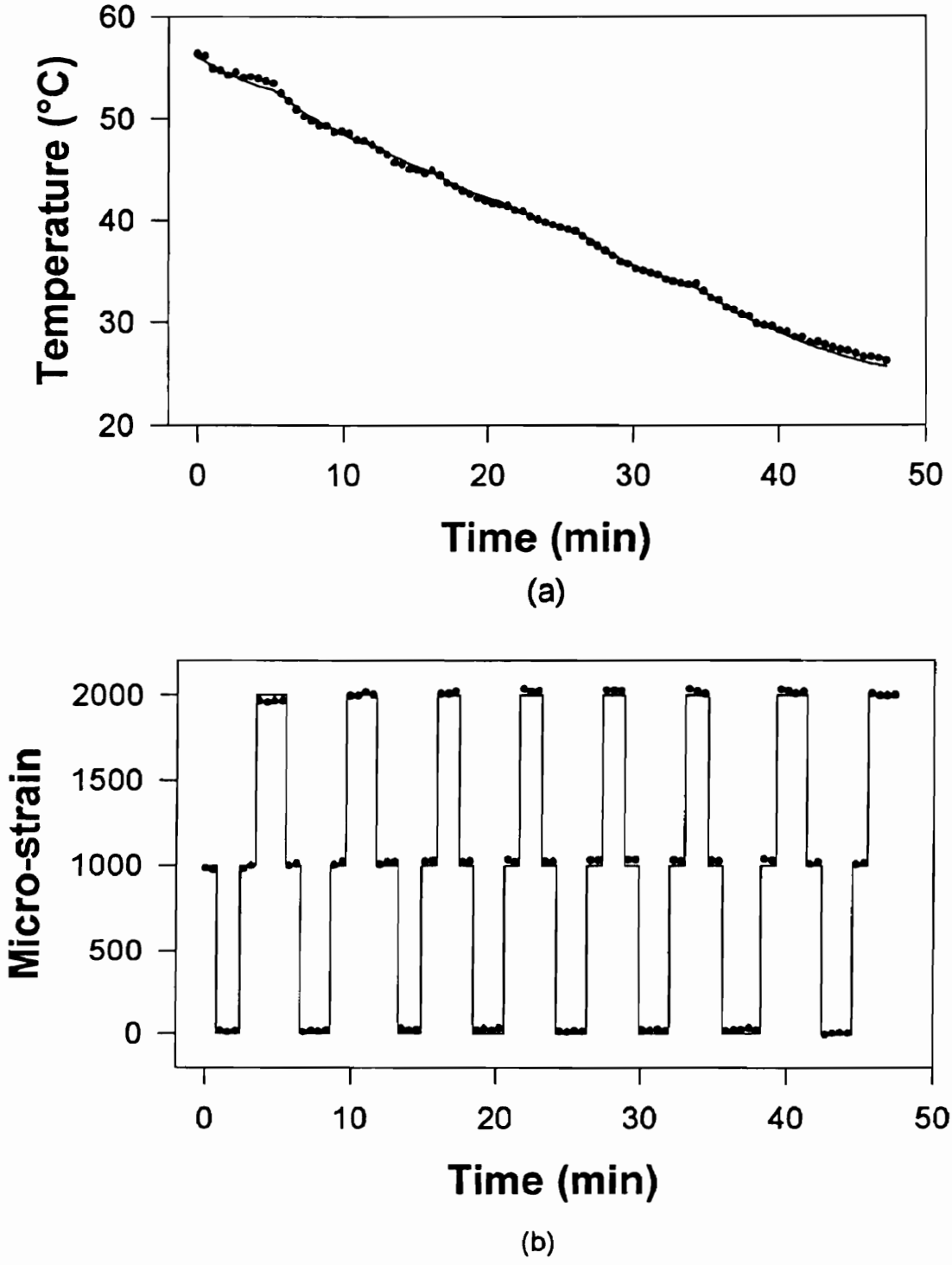

Figure 5.10. Comparison between measured (symbols) and actual (lines) values of (a) temperature (b) strain using the long-period grating shown in Figure 5.1. The average rate of temperature change was -0.64 °C/min.

The differences between the actual and calculated strain and temperature values can be attributed to many different causes. The first of these could be the error introduced due to miscalibration of the strain and temperature characteristics of the grating. For example, one can see in Figure 5.10(b) that the measured strain values are consistently higher than the actual values when the ambient temperature was between 30 and 45 °C. This implies that the strain or temperature coefficients in Equations (5.12) and (5.13) might be different form those actually calculated during the calibration process. The second reason for the errors could be the inaccuracy in the measurement of wavelength shifts $\Delta\lambda_1$ and $\Delta\lambda_2$ during the experiment. Although this is minimized by employing the least-squared curve fit, small errors are still expected to influence the system. The stability of the system to inaccuracies in the wavelength measurement process will be investigated in Section 5.5. Errors could also arise from the variations in the spectra of the LEDs during the actual test. Although the grating transmission spectrum is normalized to that of the source after every scan, the reference scan is acquired during the calibration process and hence any fluctuations following that are expected to alter the experimental results. This effect can be minimized by updating the reference scans for both the bands periodically or by simply cooling the LEDs to prevent spectral variations. Another reason for the errors could be that the curve fits used in Figure 5.5 did not accurately represent the data at intermediate temperature values. This can be overcome by using higher order polynomial curve fits which also increases the system complexity. Thus the tradeoff between the accuracy and simplicity of the sensing scheme is evident.

In this section we experimentally demonstrated simultaneous measurement of strain and temperature using a standard grating written in SMF-28 fiber. Results from tests involving static and dynamic temperature changes were presented and it was shown that the calculated strain and temperature correlate well with the actual values.

5.4.2 Strain-Insensitive Grating System

In Section 5.3 we had shown that the simultaneous measurement system using long-period gratings is considerably simplified if one of the elements of the sensitivity matrix is zero. In this sub-section we present experimental results from tests carried out using a grating in which one of the resonance bands is strain-insensitive.

For these experiments, the grating with the transmission spectrum depicted in Figure 4.29 was employed. The grating was first calibrated to determine various coefficients required in Equations (5.16), (5.17) and (5.19). This was done by first independently heating the grating to 140 °C and then measuring the strain coefficients of the resonance band at 1638.3 nm at discrete temperatures by using the set up shown in Figure 5.8. The principle of operation for this configuration is very straightforward. In the presence of both strain and temperature, the strain insensitive band is first used to determine the temperature. The information about temperature is then employed to obtain strain measurements from the higher order band, which shifts with both the perturbations [37].

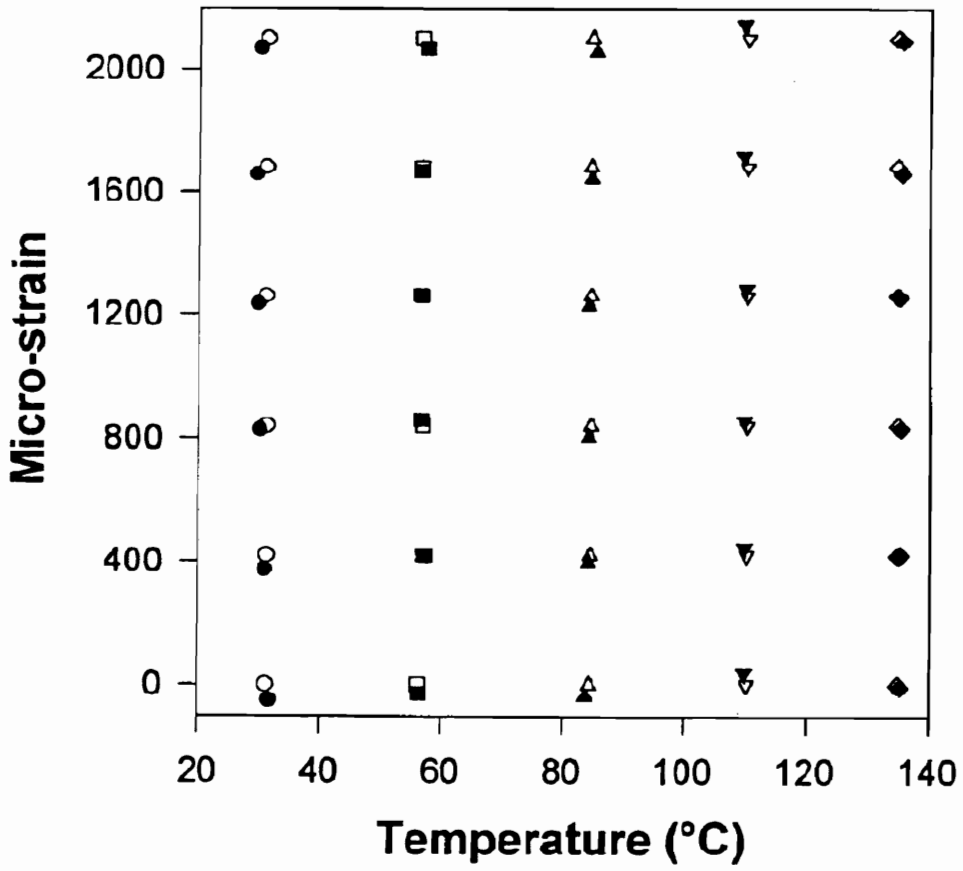

Figure 5.11. Comparison between actual (unfilled symbols) and calculated (filled symbols) values for simultaneous measurement of strain and temperature using a long-period grating written in SMF-28 fiber with Λ=340 μm (Figure 4.29). Results are from a static test where the grating was stabilized at different temperatures and then strained.

Figure 5.11 depicts the results from the simultaneous strain and temperature measurement test using the strain-insensitive long-period grating. The grating was heated to 140 °C and during the cooling cycle was stabilized to distinct temperatures and strained to 2100 με in steps of 210 με. The temperature and strain were hence static during a measurement cycle which consisted of the completion and acquisition of two OSA scans and related calculations. The maximum errors in the measured values of strain and temperature were 51 με and 1.7 °C, respectively. We observe that although the errors are slightly larger than the configuration in Section 5.4.1, the temperature dynamic range obtained here (104 °C) is three times larger. The increase in measurement range results from the strain-insensitivity of the shorter wavelength band that assists in incorporating the effects of higher order non-linearities and cross-sensitivities. The average strain and temperature resolutions for this system were measured to be 40 με and 0.8 °C, respectively.

To evaluate the performance of the measurement system under varying temperature, the grating was heated to 97 °C and cooled. The axial strain on the grating was varied independently and the results from the experiments are plotted in Figure 5.12. Once again, there is a close agreement between the actual and measured values of temperature and strain. The largest differences between the actual and calculated values of strain and temperature were 53 με and 1.8 °C, respectively. The temperature dynamic range was 67 °C with an average rate of change of -1.08 °C/min. Other than the ones discussed in the previous section, an additional source of inaccuracy for this configuration could arise from the fact that we have neglected the strain coefficient of the lower order peak. Although small (-0.4 nm/%ε), the strain sensitivity of this peak is temperature-dependent and hence would potentially introduce errors as functions of the operating temperature.

In this section we demonstrated the use of strain-insensitive long-period gratings for simultaneous sensing of strain and temperature. It was shown that the dynamic range of temperature measurements can be extended to over 100 °C by employing the special features available from these gratings.

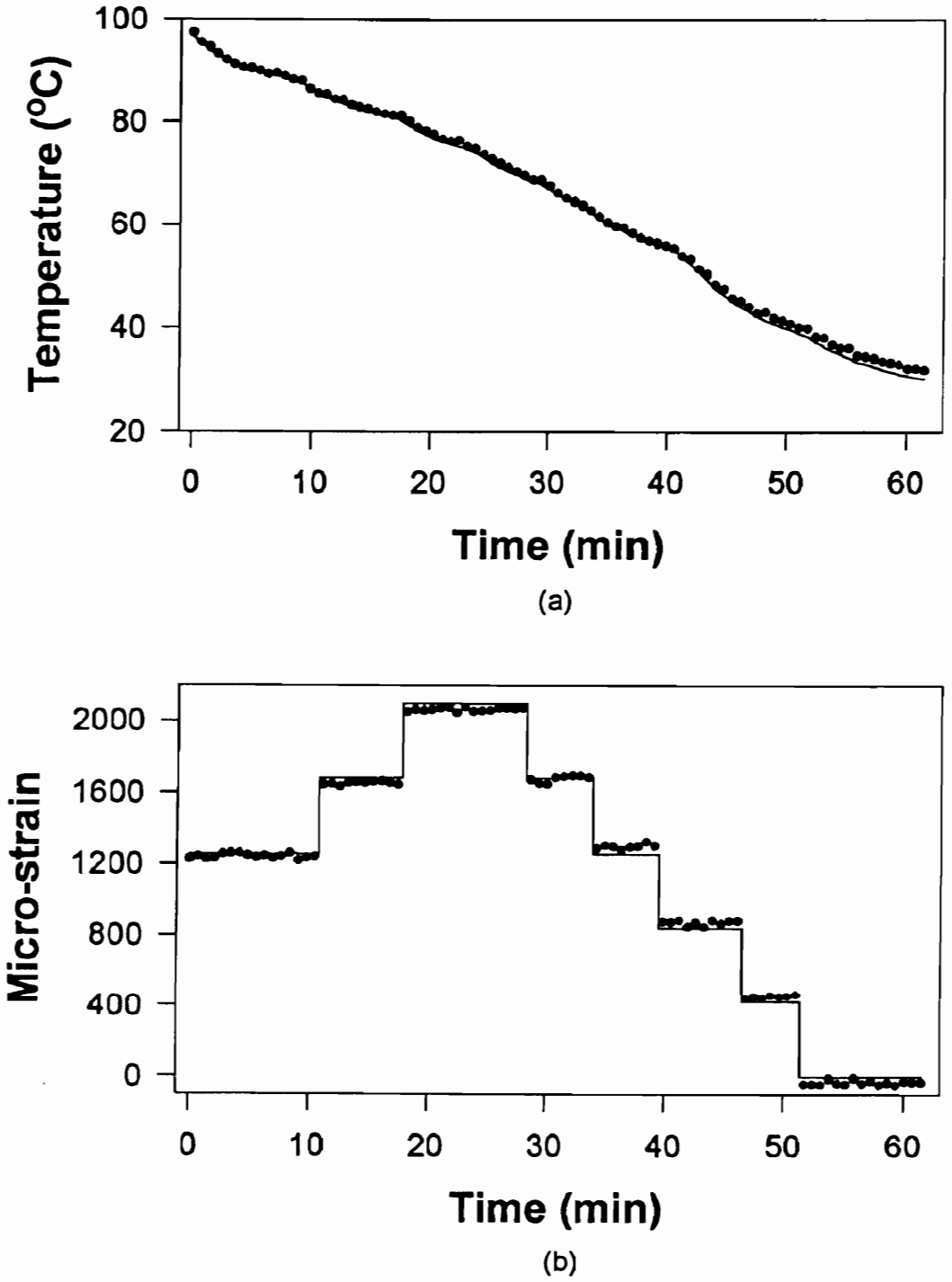

Figure 5.12. Comparison between measured (symbols) and actual (lines) values of (a) temperature (b) strain using the long-period grating shown in Figure 4.29. The average rate of temperature change was -1.08 °C/min.

5.4.3 Dual-Grating System

In the previous two sub-sections we presented results from systems that use a single grating for simultaneous strain and temperature measurement. This sub-section is devoted to demonstration of multi-parameter sensing using resonance bands from gratings written in two distinct fibers. Although an ideal system would use a single grating for simultaneous measurement, the following experiments are intended to depict the versatility of using long-period gratings in different configurations.

The first grating was fabricated in SMF-28 fiber with Λ=320 μm while the second was written in the fiber with special refractive index profile [34] with Λ=166 μm (Section 4.2.3). The resonance band of the former that was used in the experiment was located at 1316.6 nm while that of the latter was at 1501.9 nm. The set up employing these two long-period gratings was similar to the one in Figure 5.9 except that the gratings were interrogated by different LEDs. The SMF-28 fiber was spliced to the LED centered at 1275 nm while the special fiber was spliced to the LED at 1520 nm. The coupler was then used at the output to combine the transmission spectra of the two gratings. This configuration ensured that there was no cross-talk between the different bands of the two gratings. The gratings had the same gage-length and hence underwent equal strain for the same extension on the translation stages. Also the gratings were located close to each other in the temperature chamber to reduce the effects of thermal gradient. The temperature sensitivity of the grating in the special fiber was small (<0.001 nm/°C) and hence was ignored for this analysis. Thus the axial strain was directly determined from the cumulative shift in this band and using a strain coefficient of -26.6 nm/%ε. The resonance band in the SMF-28 fiber had a non-linear temperature-induced spectral shift and a second order curve fit was used to fit the experimental data. A linear fit to the strain and temperature data yielded slopes -1.3 nm/%ε and 0.038 nm/°C, respectively. The strain coefficient was found to be a function of temperature and hence a cross-sensitivity term was included in the analysis. The strain was first determined from the temperature-insensitive grating and this value was then used to calculate the position of the band in SMF-28 fiber grating under that strain and at room temperature. The temperature was then calculated using the non-linear temperature coefficient of the SMF-28 fiber grating. The use of a system in which one element of the sensitivity matrix was again zero, enabled the extension of the temperature dynamic range.

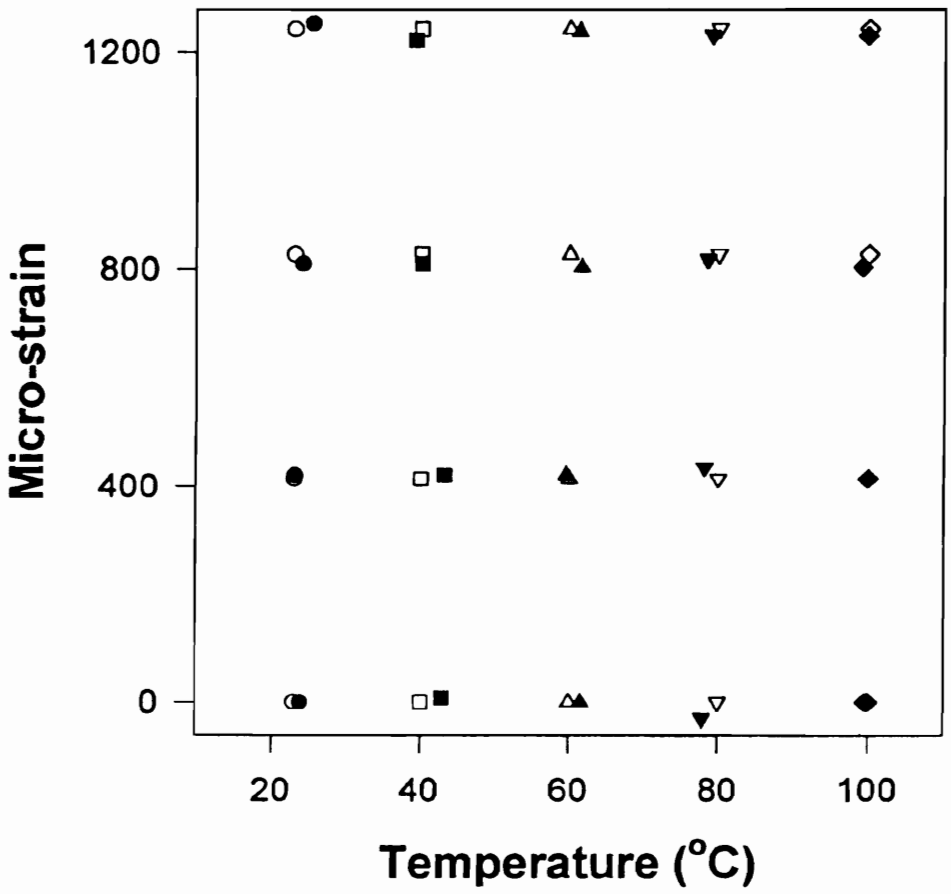

Figure 5.13. Comparison between actual (unfilled symbols) and calculated (filled symbols) values for simultaneous measurement of strain and temperature using two long-period gratings. Results are from a static test where the gratings were stabilized at different temperatures and then strained.

The experiments were again carried out in two different ways. In the first set of tests the temperature was maintained constant while the gratings were being strained. Figure 5.13 depicts the comparison between the actual and calculated values for this static strain and temperature test. The maximum errors were 3.2 °C and 31 με for a temperature range of 22 to 100 °C and strain range of 0 to 1243 με, respectively The temperature and strain resolutions were determined to be 2.5 °C and 40 με. It is important to note here that the experiments using two gratings did not involve the use of the least-squared curve fits to reduce noise components in the transmission spectra. Moreover, by neglecting the small temperature sensitivity of the grating written in the special fiber we introduce additional

errors in the strain and temperature measurements. Thus the system performance may be improved by taking care of these two factors.

The second set of experiments involved taking measurements while the temperature was dynamically varied. In this case a three hour uninterrupted test was performed to determine the feasibility of using this system in practical applications. Figure 5.14 depicts the comparison between the actual and calculated values of strain and temperature as functions of time. The temperature was varied cyclically between 25 and 128 °C and the measured values were observed to follow the actual temperature variation closely. The strain was also varied randomly between 0 and 2070 με with the transition between two strain magnitudes taking place after both the bands were scanned completely. The largest errors in temperature and strain were found to be 4 °C and 73 με, respectively. Another similar experiment was done over a four hour period and the maximum errors in strain and temperature were found to be 4 °C and 84 με, respectively. The current supply to both the LEDs was deliberately varied by almost 10% at certain periods during the test and no noticeable degradation in the system performance was observed. This shows that the measurement configuration is immune to small changes in the source spectrum for tests carried out over extended duration.

In this section we presented experimental results from three different configurations of long-period grating-based simultaneous strain and temperature measurement systems. The first set up used a conventional SMF-28 fiber grating with finite values for all the four elements of the sensitivity matrix. Following this, it was shown that the dynamic range of such systems can be extended by using strain-insensitive long-period gratings. Finally two gratings written in different types of fibers were used to demonstrate the versatility of the simultaneous measurement scheme. For all the three systems, tests were carried out for both static and dynamic temperature variations while the strain was always static. Although two LEDs were required for all the experiments, proper choice of fiber parameters, grating periods and writing conditions can reduce the wavelength separation between the bands under investigation and enable the use of a single broadband source. Also the analysis can be simplified by combining strain- and temperature-insensitive bands on standard fibers. This can be done by fabricating two gratings with different periods in the same fiber - one that satisfies the strain-insensitivity condition, and the other that produces a temperature-insensitive resonance band.

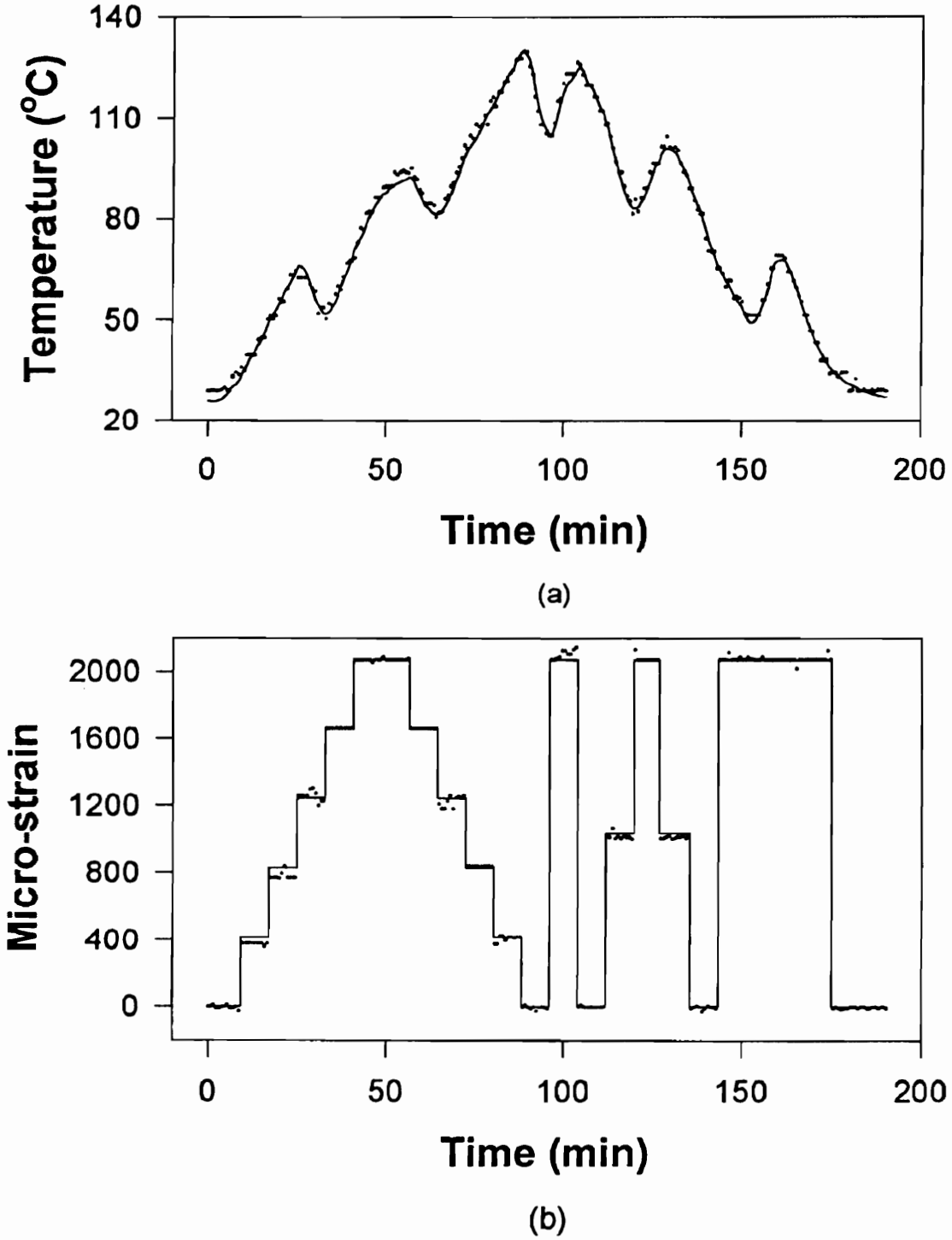

Figure 5.14. Comparison between measured (symbols) and actual (lines) values of (a) temperature (b) strain using two long-period gratings. The temperature rate of change was as large as 2 °C/min.

These experiments reveal the feasibility of using long-period gratings for simultaneous strain and temperature measurements. Such systems would reduce the cost of installation and maintenance of sensors and could potentially result in a network of multi-parameter transducers for distributed measurements on advanced materials and structures.

5.5 Sensor Stability Analysis

To determine the sensitivity of the simultaneous sensing system on measurement errors we proceed parallel to the approach used by Vengsarkar *et al.* [18]. To simplify the analysis we use the linear system of equations in Section 5.2 (Equations (5.1) and (5.2)) and ignore cross-sensitivity between perturbations. Linear system theory is then employed to determine the accuracy of the calculated results assuming there are errors in the wavelength shift vector of Equation (5.4). A graphical analysis of the sensing system is also used to enable easier visualization of the concept of stability.

5.5.1 Analytical Approach

It was observed during the experimental analysis of Sections 5.4 that small inaccuracies in the measurement of the wavelength shifts, $\Delta\lambda_1$ and $\Delta\lambda_2$, of the two resonance bands resulted in significant differences between the calculated and actual values of perturbations. These errors can be explained by writing Equation (5.3) as follows,

$$\begin{bmatrix} \Delta T \\ \Delta\varepsilon \end{bmatrix} = \begin{bmatrix} A & B \\ C & D \end{bmatrix}^{-1} \begin{bmatrix} \Delta\lambda_1 \\ \Delta\lambda_2 \end{bmatrix}. \tag{5.20}$$

Thus the difference between the actual and calculated values of temperature ΔT and strain $\Delta\varepsilon$ can be due to the errors in the sensitivity matrix S or result from inaccuracies in the measurements of $\Delta\lambda_1$ and $\Delta\lambda_2$. The first type of error arises from an inaccurate calibration process and from the presence of cross-sensitivity and non-linearity terms. For our analysis we will assume that cross-sensitivities and non-linearities are negligible and that the sensitivity matrix can be accurately determined during the calibration process. Thus the errors in the temperature ΔT, and strain $\Delta\varepsilon$, can be attributed to the measurement inaccuracies in $\Delta\lambda_1$ and $\Delta\lambda_2$. The sensitivity of the system to measurement errors then depends on the properties of the sensitivity matrix S that is used in Equation

(5.20) to transform the wavelength shift vector to the unknown vector x ([ΔT Δε]). From linear system theory we find that the parameter that determines the stability of a system of simultaneous equations is called the condition number of the sensitivity matrix [135]. To explain the concept of condition number we let x_t and x_a be the true and approximate solutions when the wavelength measurements are precise and inaccurate, respectively. The relative normalized error is bound on both sides and is given by the inequality [135],

$$\frac{1}{||S||\,||S^{-1}||}\frac{||Sx_a - \lambda||}{||\lambda||} \le \frac{||x_a - x_t||}{||x_t||} \le ||S||\,||S^{-1}||\frac{||Sx_a - \lambda||}{||\lambda||}, \qquad (5.21)$$

where $||S||$ and $||S^{-1}||$ are matrix norms, and $||Sx_a - \lambda||$ and $||\lambda||$ are vector norms. Thus the normalized relative error is in Equation (5.21) is bound on both sides by the common term $||S||\,||S^{-1}||$ that is defined as the condition number, κ(S) of the sensitivity matrix S. Equation (5.21) can then be written as [135],

$$\frac{\delta}{\kappa(S)} \le \frac{||x_a - x_t||}{||x_t||} \le \kappa(S)\,\delta, \qquad (5.22)$$

where,

$$\kappa(S) = ||S||\,||S^{-1}||, \qquad (5.23)$$

and,

$$\delta = \frac{||Sx_a - \lambda||}{||\lambda||}. \qquad (5.24)$$

Equation (5.22) reveals that closer κ(S) is to unity, the more precise δ becomes as a measurement of the relative error. Also since the condition number $\kappa(S) \ge 1$, its reciprocal rcond(S) lies between zero and one. Thus for a well-conditioned matrix, rcond(S) is close to unity while for an ill-conditioned matrix rcond(S) is near zero [135]. The parameter rcond(S) hence determines the stability of the system of simultaneous Equations (5.1) and (5.2) [18]. We used value of rcond(S) to compare the different configurations of long-period grating simultaneous strain and temperature sensing systems. Experimental observations in the previous section reveal that cross-sensitivity and non-linearity influence the performance of each configuration. For each system we obtained a linear curve fit to the wavelength shift versus perturbation experimental data and neglected cross-sensitivity between strain and temperature. Thus all strain coefficients used in the calculations correspond to room temperature values.

To determine the reciprocal of the condition number rcond(S) of the sensitivity matrix S in 1-norm, we use the LINPACK [136] condition estimator in MATLAB. We express the elements A and C in nm/°C while B and D are converted to nm/με. Table III depicts these four elements of the sensitivity matrix for the three experimental cases analyzed in Section 5.4. Also calculated in the last column are the values of rcond(S) for the corresponding configurations.

Table III. Linear temperature and strain coefficients for the two bands in each of the three configurations proposed in Section 5.4. Also shown is the corresponding reciprocal of the sensitivity matrix condition number, rcond (S).

System Configuration	A (nm/°C)	B (nm/με)	C (nm/°C)	D (nm/με)	rcond(S)
Conventional grating	0.0792	0.00194	0.0452	0.00028	0.0077
Strain-insensitive grating	0.0890	0.00142	0.0433	0	0.0062
Dual-grating	0	-0.00266	0.0384	-0.00013	0.0735

Table III reveals all the configurations using long-period gratings as multi-parameter sensors have a poor matrix conditioning due to the small value of rcond(S). We have ignored the small temperature coefficient of the grating in the special fiber used in the dual-grating configuration (third row). The strain coefficient of the lower order band in the second row of table III has also been neglected. It can be shown that the final rcond(S) values for the respective systems do not change significantly if the finite coefficients are included in the analysis. A comparison of the experimental results for each system reveals that although the dual grating system has the highest rcond(S), it has the largest errors between the actual and calculated values of strain and temperature. The discrepancy can be attributed to the fact that the while the least-squared curve fitting method was used for the experiments with conventional and strain-insensitive gratings, the wavelength determination capability of the optical spectrum analyzer was relied upon for the system employing two gratings. This implies that the processing of the transmission spectrum to reduce noise improves the overall performance of the simultaneous measurement systems.

As stated earlier, the higher the value of rcond(S), the greater is the stability of the simultaneous strain and temperature sensing system. The small values of rcond(S) for the long-period grating measurement schemes makes them highly susceptible to errors in the wavelength detection. But we have shown that employing techniques such as least-squared curve fitting, the system stability can be improved considerably.

5.5.2 Graphical Approach

In this section we use a simple graphical method to evaluate the stability of the long-period grating multi-parameter sensing scheme [18]. Apart from giving an estimate of the conditioning of the sensitivity matrix, this graphical representation enables visualization of the non-linearities and cross-sensitivities present in the system.

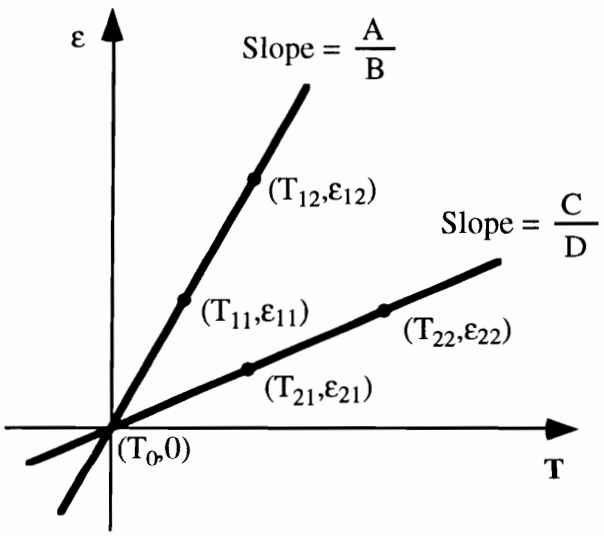

Figure 5.15. Equiwave plots for the two resonance bands in the T-ε plane. The degree of linearity of the curves predicts the non-linearity and cross-sensitivity while the difference in their slopes gives a measure of the stability of the dual-parameter measurement system.

In Section 5.2 we observed that the singularity of the sensitivity matrix results in the inability to separate concurrent perturbations. In fact, the concept of condition number discussed in Section 5.5.1 gives us an estimate of the proximity of the sensitivity matrix (S) to the ultimate ill-conditioned matrix - the singular matrix, such that [135],

$$\frac{1}{\kappa(S)} = \min\left\{\frac{||S - W||}{||S||}\right\}, \tag{5.25}$$

where W is a singular matrix. Thus for the sensitivity matrix to be well-conditioned, the value of its determinant should be as far away from zero as possible. But the determinant of the sensitivity matrix, given by Equation (5.5) is expressed as,

$$\Delta = (AD - BC) = BD\left(\frac{A}{B} - \frac{C}{D}\right). \tag{5.26}$$

Hence for the system to be stable to inaccuracies in the measurement process, the ratios A/B and C/D should be algebraically well separated, as predicted in Section 5.2. The difference in ratio of the temperature and strain sensitivities of the two resonance bands can also be represented in graphical form using what we will term as the constant wavelength shift plots or simply, equiwave plots [18]. For these plots, the grating bands are assumed to be unperturbed with strain $\varepsilon=0$ (strain in this section is represented by ε and not $\Delta\varepsilon$) and temperature $T=T_0$, the room temperature. For resonance band at the higher wavelength, the temperature (T_{11}) and the strain (ε_{11}) that result in equal wavelength shift, say $\Delta\lambda$, are determined. The point (T_{11},ε_{11}) is then plotted in the T-ε plane as shown in Figure 5.15 which is then joined to the origin (T_0,0) such that the slope of the resulting straight line is given by the ratio A/B, provided $\Delta\lambda$ is infinitesimally small. The same wavelength shift $\Delta\lambda$, is then used to find the point (T_{21},ε_{21}) in the T-ε plane for the second resonance band. The slope of the second straight line is given by C/D. Thus for the dual-parameter measurement system to be stable, these two lines in the T-ε plane should be as distant as possible, or as stated earlier, their slopes (A/B and C/D) should be well separated. The difference in the slopes of the two lines can hence be used to visualize the stability of the sensing system. The next step assumes that we are operating at the point (T_{11},ε_{11}) for the higher wavelength resonance band and at the point (T_{21},ε_{21}) for the adjacent band. A new point denoted by (T_{12},ε_{12}) is determined such that the temperature change T_{12}-T_{11} and strain ε_{12}-ε_{11} gives the same wavelength shift $\Delta\lambda$. The point is then joined to the first point (T_{11},ε_{11}) in the T-ε plane as shown in Figure 5.14. The same procedure is followed for the lower wavelength resonance band and the new point (T_{22},ε_{22}) is joined to the point (T_{12},ε_{12}). The process is continued till the desired measurement range in the T-ε plane is covered.

For a linear response to temperature and strain, the two lines in the T-ε plane are straight with constant slopes throughout [18]. Non-linearities and cross-sensitivities in the strain and temperature response make the elements of the sensitivity matrix functions of T and ε and transform the two straight lines to curves in the T-ε plane. Hence the degree of linearity of the two curves gives us a measure of the cross-sensitivities and non-linearities present in the simultaneous system. To observe the smallest influence of non-linearities and cross-sensitivities, the value of $\Delta\lambda$ should be as close as possible to zero.

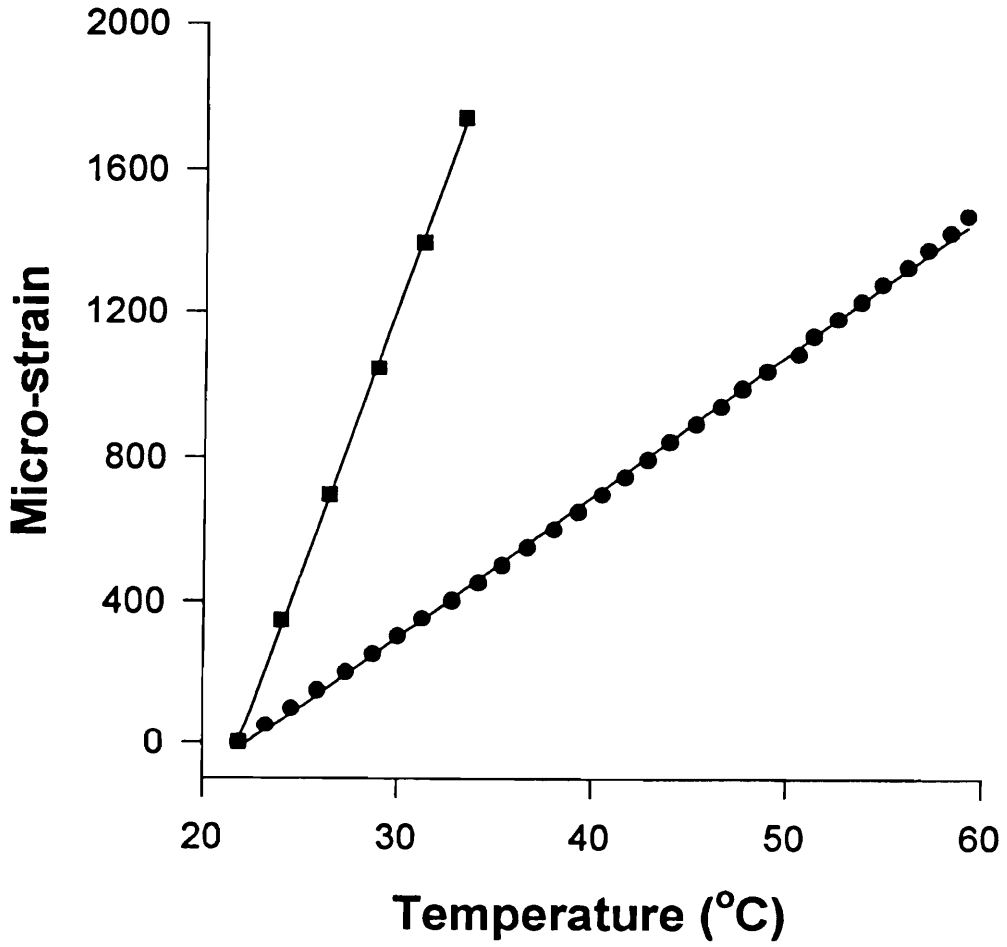

Figure 5.16. Equiwave plots for the simultaneous temperature and strain sensing scheme using the long-period grating shown in Figure 5.1 ($\Delta\lambda$=0.1 nm, T_0=21.85 °C). The calculated data for the higher (circles) and lower (squares) wavelength resonance bands are fitted to straight lines.

The equiwave curves were plotted for the simultaneous temperature and strain system that employs the conventional grating in Figure 5.1. The coefficients A and B (Equation (5.1)) were determined as functions of temperature from the calibration data. The non-linearity in B and D was ignored to simplify the calculations. The procedure described above was then used to determine the equiwave plots for $\Delta\lambda$=0.1 nm, as shown in Figure 5.16. The difference in the number of calculated points for the plots can be ascribed to the distinct strain and temperature coefficients of the two corresponding bands. The higher order band deviates from the linear curve fit and this reflects the non-linearity and cross-sensitivity in its response. The non-linearity at the lower temperatures (22 to 40 °C) is dominated by cross-sensitivity (Figure 5.4) while at higher temperatures (>50 °C) the departure from linearity can be attributed to the non-linearity in temperature. The difference in the slopes of the two plots gives a measure of the susceptibility of the calculated strain and temperature values to the wavelength measurement inaccuracies. To increase the system stability in this case, we need to move the plots for the lower and higher order bands towards the ε- and T-axis, respectively. This can be done by reducing the strain coefficient for the band at lower wavelength (D) and increasing that for the longer wavelength band (B) which effectively increases the separation between the slopes (A/B and C/D) of the two curves. Thus equiwave plots are convenient for analyzing the stability of the simultaneous measurement scheme based on the elements of the sensitivity matrix.

The equiwave plots provide a graphical illustration of the system stability and influence of non-linearities and cross-sensitivities. For an ideal system, the two curves in the T-ε plane should be straight lines for the operating regime and be orthogonal to one another. The simplest system would be one in which the first resonance band is sensitive to only temperature while the other is affected only by strain. Assuming negligible non-linearity we would get two perpendicular lines along the T and ε axes (Figure 5.17 (a)). If the equiwave curve for the higher order resonance band lies in the first and third quadrant, the curve for the adjacent band (or any other lower order band) should lie in the second or fourth quadrant to improve the system stability (Figure 5.17 (b)). This simply implies that one of the four elements A, B, C or D of the sensitivity matrix should have a polarity different than that of the other three. For example, if the higher order resonance band has a positive spectral shift with both temperature and strain (A>0 and B>0), the other resonance band being monitored should have one and only one negative coefficient (either C<0 or D<0). This analysis implies that the ratios A/B and C/D should be

opposite in polarity to improve the stability of the simultaneous measurement system. For such a system, the determinant of the sensitivity matrix (Equation (5.26)) can never be zero and hence singularity of the matrix is not a concern. The actual conditioning of the system is then determined by the relative values of A/B and C/D that influence the separation between the sensitivity and singular matrices, as discussed earlier in the section. For the grating in Figure 5.1 such a system can be obtained by using the combination of the resonance band at 1159.3 nm with any other higher wavelength band. This is because this band has a negative strain coefficient (-0.32 nm/%ε) while the higher order bands have positive strain-induced shifts (Figure 4.23). This band was not used for actual experiments since the relatively small magnitudes of its strain and temperature coefficients yield resolutions that might not be acceptable in practical applications.

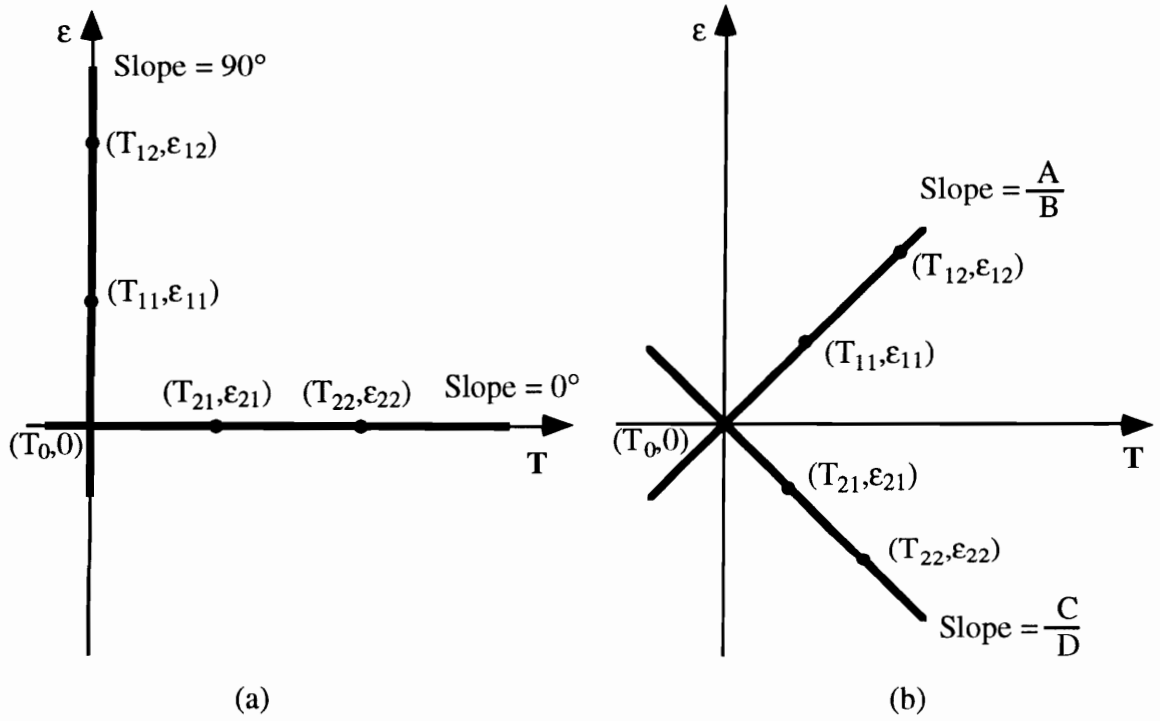

Figure 5.17. Depiction of equiwave plots for well-conditioned sensitivity matrices in the T-ε plane. (a) Equiwave plots along the T and ε axes since the higher order resonance band is affected only by strain and the other resonance band is influenced only by temperature. (b) Equiwave plots in different quadrants. The temperature and strain coefficients of the higher order resonance bands are positive. For the second resonance band the temperature coefficient is positive while the strain coefficient is negative.

For simultaneous measurement of three perturbations, the equiwave plot can be extended to three axes. The three resultant curves should again be straight lines in three-dimensional space if cross-sensitivity is ignored, and large differences should exist between the slopes of these lines for good system stability.

The magnitude and polarity of the sensitivity matrix coefficients are functions of the parameters of the fiber in which the grating is fabricated. By manipulating the fiber properties, the grating period and the writing conditions it may be possible to obtain highly stable simultaneous strain and temperature measurement systems. Also for our experimental analysis, we have typically considered only the two highest wavelength bands of a grating in the range 1100 nm to 1650 nm. By employing a proper combination of resonance bands, a larger value of rcond(S) than those for the higher wavelength bands might be available.

In this section we discussed the stability of the long-period grating-based simultaneous strain and temperature measurement systems. It was assumed that the elements of the sensitivity matrix can be accurately determined and hence the errors in strain and temperature can be attributed to the imprecise measurement of the peak isolation wavelengths of the resonance bands. An analytical method was first used to evaluate the stability of the linear system and it was shown that the robustness of the scheme to measurement inaccuracies is a function of the conditioning of the sensitivity matrix. Analysis employing linear system theory revealed that the system is stable if the reciprocal of the condition number rcond(S) is close to unity [135] which implies that the value of the corresponding determinant (Δ=AD-BC) should be as far away as possible from zero. This observation was confirmed by employing a graphical method to investigate system stability. It was found that the slopes (A/B and C/D) of the two curves in the equiwave plots should be well separated for the scheme to have small sensitivity to wavelength measurement errors. The equiwave plots provide a simple pictorial representation of the system stability and of the degree of non-linearity and cross-sensitivity in the strain and temperature response of the resonance bands. Such a plot was obtained for the conventional grating configuration from actual experimental data and the system stability was analyzed for this case.

5.6 System Performance

In this section we will evaluate the performance of the long-period grating-based simultaneous strain and temperature measurement system and compare it with other fiber optic techniques discussed in Section 5.1.

Long-period grating dual-parameter systems involve the detection of the differential shifts in two or more bands. The shifts are typically detected using an optical spectrum analyzer and are absolute in nature. Thus unlike interferometric systems, a reference measurement is not required to obtain information about the perturbations. Moreover, phase-based sensors produce non-linear outputs in terms of fringes and hence can be difficult to demodulate. Although conventional optical spectrum analyzers are expensive, the economical versions available these days have smaller dynamic ranges but can be easily interfaced with computers and provide comparable resolving power. Additionally, the absolute grating-based system does not lose information if the power is turned off, and turned back on again. The simultaneous interferometric systems, on the other hand, are susceptible to losing strain and temperature measurements since the output of such sensors is differential in nature.

Long-period gratings multi-parameter sensors can be implemented by using the simple demodulation schemes proposed in Section 4.5.1. Such systems would involve using one or more broadband sources that span the bandwidth of the resonance bands under investigation. At the output, the signals are divided into two parts using a coupler and bandpass filtered to obtain a narrow spectral slices of the two bands. The differential wavelength shifts in the bands yield distinct changes in the intensity throughput of the filters which can be monitored and processed using photodetectors and associated electronics. The second system configuration would be to use two stable laser diodes centered on the transmission versus wavelength slopes of the two bands. Hence each diode converts the wavelength shift of the corresponding band to an intensity variation. In such a system it might be necessary to employ some type of optical switching, in conjunction with time-division multiplexing, to alternately access the output of the each laser source. A photodetector, and electronics synchronized to the switching signal are required at the output end of the fiber. These two techniques would enable the use of the multi-parameter sensing capability of long-period gratings without employing optical spectrum analyzers.

All the experiments described in Section 5.4 used two LEDs for implementing simultaneous strain and temperature sensing systems which might be a limitation in applications that require the least number of components for inexpensive sensing. Such a drawback can be overcome by using resonance bands that have very small wavelength separations. Although this would yield a system with smaller rcond(S), the use of a single broadband source would result in a simple and economical system. Special fiber designs that produce larger differential modulation in spectral bands with small separation would assist in improving the system stability. The interferometric-based technique proposed by Vengsarkar *et al.* [18] also uses two optical sources for implementing the simultaneous measurement system. In such a configuration, the operation on both sides of the single-mode cutoff wavelength necessitates the employment of two laser sources. Moreover since that system is polarization-based, a strict control of the input state of polarization is required [18].

A simultaneous strain and temperature measurement system has also been proposed using a pair of overlapping Bragg gratings [19]. The drawbacks of such a scheme are the poor conditioning of the sensitivity matrix and the limited temperature resolution due to the small spectral shift. Although interferometric demodulation improves the system sensitivity, the resultant signal processing increases the implementation cost manifold. Bragg grating-based simultaneous measurement systems also suffer from non-linearities and cross-sensitivities which reduce the dynamic range if a linear analysis is employed [20]. We have demonstrated that long-period gratings typically have an order of magnitude larger temperature-induced spectral shifts than fiber Bragg gratings. Hence temperature resolutions that satisfy the requirements of most applications can be easily attained by using optical spectrum analyzer-based demodulation. Additionally, strain-insensitive long-period gratings can be employed to extend the dynamic range in the presence of non-linearities and cross-sensitivities.

Another attractive feature of long-period gratings is the availability of attenuation bands other than the two utilized for simultaneous strain and temperature measurements. A third band, for example, could be used to verify the strain and temperature data obtained from the first two bands. The third band will also have to be pre-calibrated for strain- and temperature-induced shifts and if the cumulative wavelength shift in this band is not consistent with the measured values, the calculated strain and temperature can be ignored

and a fresh measurement can be taken. This scheme might be useful in applications where even small errors in strain and temperature are not acceptable. It might also be possible to use shifts in several bands to overcome the cross-sensitivities and non-linearities. This might increase the system dynamic range at the expense of introducing complexity in signal processing.

Owing to coupling to cladding modes, long-period gratings are susceptible to bends in the fiber. This inherent drawback of these gratings might limit their use to applications where the sensing region is maintained taut during operation. Moreover, such a system is not suitable for applications where the refractive index of the ambient material changes with time. Although a third resonance band can be used to separate the influence of variations in the surrounding index, this would require increased signal processing and higher system cost. The attachment or embedding process of long-period gratings is expected to be similar to that for Bragg gratings. Another limitation of the present system is the inability to actively monitor rapidly varying strain and temperature changes. This problem arises due to the slow scanning speed of the optical spectrum analyzer. Faster spectrum analyzers can be used to upgrade the static and quasi-static measurement system. The use of simpler demodulation schemes discussed earlier is also expected to solve this problem since the requirement of optical spectrum analyzer can be precluded.

In summary, long-period gratings offer novel methods to simultaneously detect strain and temperature in various applications. Although these systems have their limitations, they offer many advantages over traditional dual-parameter sensors. Long-period grating sensors are economical to batch-produce [1] and simple to demodulate [21]. The versatility of such sensors provides methods to overcome the limitations imposed by non-linearities and cross-sensitivities.

In this chapter we have demonstrated simultaneous strain and temperature measurements with resolutions of 30 $\mu\varepsilon$ and 0.6 °C, respectively, using a conventional long-period grating. Experimental verification of the dual-parameter sensing capability of these devices was carried out for static and dynamic temperature variations. The errors between the actual and measured values were found to be a few percent of the system dynamic range. The temperature measurement range was extended to over 100 °C by employing strain-insensitive long-period gratings. Experimental results from a configuration using a pair of long-period gratings were used to demonstrate the versatility

of the long-period grating sensing system. The system stability was investigated using linear system theory and the conditioning of the sensitivity matrix was found to influence the susceptibility to wavelength measurement inaccuracies. A graphical method was used to represent the system stability and the degree of non-linearity and cross-sensitivity. Finally, the long-period grating measurement scheme was compared to other fiber optic systems and its advantages and limitations were listed. Overall, long-period grating-based multi-parameter systems show promise as important tools for health monitoring in advanced materials and structures.

Chapter 6 - Conclusions

In this chapter we present an overview of the study on long-period grating sensors and discuss future directions in this field. The advantages and limitations of long-period grating single- and dual-parameter sensors are reviewed and it is demonstrated that the versatility of these systems offers unparalleled features that can be employed in a number of applications. Long-period gratings are shown to overcome a multitude of drawbacks that plague conventional fiber optic systems. Finally, an investigation into the major drawbacks of long-period grating-based sensors is undertaken and research directions to surmount these problems are briefly outlined.

The objective of this dissertation was to provide the reader with an in-depth analysis of the properties of photoinduced long-period gratings and their applications as fiber optic sensing systems. Chapter 1 presented the state-of-the-art optical fiber sensor technology and related problems. It was observed that existing sensors suffer from complexity of fabrication and signal processing. For example, interferometric sensors [7] are difficult to multiplex and require a reference signal to extract information from the sensing output. Fiber Bragg gratings [8,10] require complex demodulation techniques to overcome the limited strain and temperature-induced shifts. Additionally, the implementation of a majority of the existing optical fiber index of refraction sensors necessitates some form of cladding modification to gain access to the evanescent field of the guided mode [14,16]. It was also shown that the thermal cross-sensitivity is a major limiting factor in applications where the sensors are employed for strain and refractive index measurements. Interferometric-based simultaneous strain and temperature sensing systems are limited by the requirement of complex signal processing at the receiver to demodulate the outputs [17,18]. The requirement of two Bragg gratings to perform dual-parameter measurements increases the cost of the system [19]. Hence the goal of this work was to develop a novel sensing system that would overcome a majority of these drawbacks.

Long-period gratings were recently proposed by Vengsarkar *et al.* [1] as simple in-fiber devices that couple light from the guided to cladding modes. The use of inexpensive amplitude masks for grating fabrication and the negligible back-reflection and polarization-sensitivity are major advantages of these devices. Long-period gratings were the focus of this study since preliminary results [21] indicated that these devices offer a number of advantages over conventional fiber optic sensors.

Chapter 2 reviewed the phenomena of photosensitivity and mode coupling in optical fibers. It was shown that a number of useful components may be fabricated by inducing refractive index changes in the fiber core. The periodicity of the refractive index modulation characterizes the spectral properties of the device through the phase-matching condition. Coupled mode theory was employed to investigate the coupling between co- and counter-propagating modes in a perturbed system. Fiber Bragg gratings were demonstrated as elegant devices that can be employed in a number of communication and sensing systems.

Once the basic understanding of the concepts of mode coupling and photosensitivity had been developed, it was extended to the investigation of the fundamental characteristics of long-period gratings (Chapter 3). We presented an analytical model to explain the spectral modulation offered by these devices. It was shown that the multiple loss bands in a grating result from coupling to discrete forward-propagating cladding modes. Characteristic curves that predict the resonant wavelengths for different grating periods were obtained for the three fibers used in this study. It was demonstrated that the location of the bands are strong functions of the properties of the host fiber, the grating period and the writing and annealing conditions. The notation of normal and anomalous regions was introduced to differentiate the operation at wavelengths with positive and negative slopes of the characteristic curves, respectively. The sensitivity of the characteristic curves to small deviations in the fiber parameters specified by the manufacturer, was also investigated. The spectral width of the resonance bands was found to depend on the grating length and the peak index change induced during the fabrication process [1].

The optical and physical properties of long-period gratings were studied and these devices were shown to have small insertion loss, and negligible polarization sensitivity and back-reflection [1]. The limitations include a large sensitivity to bends and to the materials used for recoating the bare cladding. We analyzed three different methods to

fabricate long-period gratings in hydrogen-loaded germanosilicate fibers. This included a novel technique that uses low power CO_2 laser to induce periodic index changes in the fiber core. We finally reviewed the applications of long-period gratings to communication systems. These devices were found to have excellent spectral-shaping [30] and filtering [1,2] characteristics, and possible applications as polarizers and modulators were proposed.

Chapter 4 discussed the use of long-period gratings as temperature, strain and index of refraction sensors [21]. An analytical model was presented for each sensor and it was shown that the sensitivity to different perturbations is a complex function of many different parameters such as the grating period, the order of the cladding mode and the writing and annealing conditions. A temperature and strain sensitivities were observed to be an algebraic sum of material and waveguide contributions. The temperature sensor operating in the normal region was found to possess an order of magnitude larger spectral shift than Bragg grating sensors. It was shown that the temperature sensitivity can be selectively tuned by changing the ambient index, or the writing and annealing conditions. The large temperature sensitivity of long-period gratings is a limitation during their implementation as strain and index of refraction measurement devices. It was shown that this drawback may be overcome by fabricating gratings in fibers with special refractive index profiles [34]. Experimental results revealed that such gratings have an order of magnitude smaller temperature-induced wavelength shifts than gratings with resonance bands in the normal region. It was also proposed that temperature-insensitive long-period gratings can be obtained in conventional fibers by using specific periods [35]. These gratings couple light to higher order cladding modes which can be shown to have negligible material contribution to the cumulative spectral shift.

The long-period grating-based axial strain sensor was analyzed for its dependence on the grating period, the order of the cladding mode, the writing and annealing conditions and the index of the ambient medium. It was demonstrated that resonance bands with positive and negative strain-induced shifts can be obtained in the same grating. The strain-insensitivity of a particular band was used to implement a temperature sensor in the presence of actively varying axial strain. The temperature-insensitive gratings in special and standard fibers were investigated for their response to strain. It was observed that such gratings offer large strain-induced shifts that have negligible dependence on ambient temperature fluctuations.

Long-period gratings were demonstrated as highly sensitive index of refraction sensors. It was shown that for a given fiber, the spectral shift due to index changes in the medium surrounding the bare cladding is a strong function of the grating period and the order of the resonance band. Although these sensors can be implemented without violating the integrity of the fiber, it was shown that their sensitivity may be tuned by selectively etching the cladding diameter. A number of techniques to vary the maximum sensitivity region and the cumulative shift in these devices were proposed. Refractive index sensors in temperature-insensitive gratings were shown to possess smaller thermal cross-sensitivity than those in conventional gratings.

It was shown that long-period grating sensors can be implemented with simple demodulation techniques [21]. Strain and temperature sensors using a laser diode as a source and a detector at the output, were demonstrated as inexpensive systems. Techniques to wavelength- and time-division multiplex these devices were also proposed. Finally, it was shown that long-period gratings can be used in a number of practical applications. The strain sensor was demonstrated as an effective measurement device on a reinforcing-bar commonly used in civil structures [33]. The concentration of different sucrose solutions was detected using a long-period grating refractive index sensor.

Chapter 5 proposed the use of long-period gratings for simultaneous measurement of temperature and strain. The principle of operation is based on the differential modulation of the distinct resonance bands of a grating [36,37]. It was shown that conventional gratings, where the two bands under investigation have finite temperature- and strain-induced shifts, are limited by the sensor dynamic range. Although this can be improved by including the non-linearities and cross-sensitivities, this process introduces complexity in the signal processing. Strain-insensitive gratings were demonstrated to increase the temperature dynamic range. It was shown that for cases where one of the elements of the sensitivity matrix is zero, higher order non-linearities and cross-sensitivities can be included in the analysis without sacrificing the simplicity of the system. Experimental results from three different configurations of long-period grating dual-parameter sensing system were presented. It was demonstrated that signal processing the grating transmission spectrum can assist in reducing the measurement inaccuracies. The stability of the sensing scheme was analyzed using linear system theory and was found to be a function of the conditioning of the sensitivity matrix [18]. A graphical technique was

employed to illustrate the system stability, and its cross-sensitivity and non-linearity characteristics [18].

We hence conclude that long-period gratings are versatile devices that can be employed for a multitude of sensing applications. Their optical properties such as small insertion loss and negligible polarization-sensitivity are advantages over conventional bulk-optic and optical fiber devices. Long-period gratings undergo large spectral shifts on being perturbed by ambient strain, temperature and index of refraction changes. These sensors can be multiplexed to provide a network of sensors to monitor variations over large regions. One of the biggest advantages of long-period grating sensors is their potential for implementation with simple demodulation schemes. Since these devices are economical to batch produce, an inexpensive system with low cost sensors and signal processing will help bring optical fiber sensors to the forefront of the commercial market. Moreover, the versatility of these gratings can be utilized in many different applications. For example, strain- and temperature-insensitive gratings have been shown to possess a number of attractive features. The refractive index sensor may be implemented without etching the fiber cladding. Long-period gratings can also be modified for multi-parameter measurements. The multiple bands in a single grating can be used to separate the effects of two or more perturbations acting on the system. The limiting effects of non-linearities and cross-sensitivities can be overcome by designing special fibers or by using specific grating periods in standard fibers.

Although long-period gratings have a number of advantages over conventional sensors, they also possess certain drawbacks which need to be addressed before a successful sensing system can be commercialized. For example, the bend sensitivity of long-period gratings might be a big concern in certain applications. During strain sensing, the device is expected to be taut due to the fixed gage-length of the sensor. For applications such as refractive index sensing where constant access to the fiber cladding is required, the bend sensitivity may be a major limitation. Also long-period grating sensors can be operated only in transmission which can make the installation of such devices cumbersome. The wide spectral width of the resonance bands introduces an uncertainty in the measurement of the exact peak isolation wavelength, thus limiting the sensor resolution. Moreover, the large bandwidth also limits the number of gratings that can be multiplexed using a single broadband source.

Future work in this field can focus on overcoming the above problems and also improving the analytical model proposed here. The inclusion of the core during the analysis of the cladding modes would help in improving the accuracy of the calculated results. The resonant wavelengths and corresponding loss magnitudes can be predicted more reliably if an exact analysis is used. The sensor model can also include non-linearities and spectral dependence of the temperature and strain-optic coefficients. The results obtained would still be limited by the accuracy of the specified fiber parameters. Hence fibers with strict tolerance on various parameters need to be used to obtain precise results. The bend sensitivity problem may be addressed by modifying the properties of the host fiber or by using grating periods that couple to lower order cladding modes [1]. The uncertainty in wavelength measurement can be reduced by manipulating the writing and annealing conditions which control the peak index change in the core. Moreover by increasing the length of the gratings, narrower bands can be obtained for multiplexing purposes. Chirped or blazed long-period gratings can be fabricated for different applications. Gratings in few-mode or multi-mode fibers could also yield interesting features. One of the future directions could be to investigate the recovery of light lost to the cladding modes. This may possibly be implemented by writing gratings in couplers and could ultimately result in low-cost demodulators for wavelength-division multiplexed systems.

This study has focused on investigating the properties and sensing applications of long-period gratings. The characteristics of these devices were studied, and an analytical model was proposed to predict the spectral modulation. Long-period gratings were demonstrated as simple sensors that can be implemented with inexpensive demodulation techniques. Temperature, strain and index of refraction sensors were shown to possess large spectral shifts and dynamic range [21]. The versatility of these sensors provides methods to separate a number of simultaneous perturbations acting on the fiber. Although improvements have to be made in the system performance, long-period grating-based sensors promise to find a niche in the fiber optic sensing community over the next few years.

References

1. A. M. Vengsarkar, P. J. Lemaire, J. B. Judkins, V. Bhatia, J. E. Sipe, and T. E. Ergodan, "Long-period fiber gratings as band-rejection filters," *Journal of Lightwave Technology*, vol. 14, 58, 1996.

2. A. M. Vengsarkar, P. J. Lemaire, J. B. Judkins, V. Bhatia, J. E. Sipe, and T. E. Ergodan, "Long-period fiber gratings as band-rejection filters," *Proc. Conference on Optical Fiber Communications*, post-deadline paper PD4, 1995.

3. A. M. Vengsarkar, P. J. Lemaire, G. Jacobovitz-Veselka, V. Bhatia, and J. B. Judkins, "Long-period fiber gratings as gain flattening and laser stabilizing devices," *Proc. Conference on Integrated Optics and Optical Fiber Communication*, post-deadline paper PD1, 1995.

4. J. Dakin and B. Culshaw, *Optical Fiber Sensors: Principles and Components*, Artech House, Boston, 1988.

5. V. Bhatia, K. A. Murphy, M. J. de Vries, and M. B. Sen, "A comparative evaluation of the types and applications of various sensors," *The Photonics Design and Applications Handbook*, H-164, 1995.

6. D. A. Krohn, *Fiber Optic Sensors*, Second Edition, Instrument Society of America, North Carolina, 1992.

7. K. A. Murphy, M. F. Gunther, A. M. Vengsarkar, and R. O. Claus, "Quadrature phase-shifted, extrinsic Fabry-Perot optical fiber sensors," *Optics Letters*, vol. 16, 273, 1991.

8. G. Meltz, J. R. Dunphy, W. H. Glenn, J. D. Farina, and F. J. Leonberger, "Fiber optic temperature and strain sensors," in *Proc. SPIE Conference on Fiber Optic Sensors II*, vol. 798, 104, 1987.

9. G. Meltz, W. W. Morey and W. H. Glenn, "Formation of Bragg gratings in optical fibers by transverse holographic method," *Optics Letters*, vol. 14, 823, 1989.

10. W. W. Morey, J. R. Dunphy, and G. Meltz, "Multiplexing fiber Bragg grating sensors," *Proc. SPIE on Distributed and Multiplexed Fiber Optic Sensors*, vol. 1586, 216, 1991.

11. M. G. Xu, L. Dong, L. Reekie, J. A. Tucknott and J. L. Cruz, "Chirped fiber gratings for temperature-independent strain sensing," *Proc. OSA Topical Meeting on Photosensitivity and Quadratic Nonlinearity in Glass Waveguides*, paper PMB2, 217, 1995.

12. A. D. Kersey and T. A. Berkoff, "Fiber-optic Bragg-grating differential-temperature sensor," *IEEE Photonics Technology Letters*, vol. 4, 1183, 1992.

13. D. Z. Anderson, V. Mizrahi, T. Ergodan, and A. E. White, "Phase-mask method for volume manufacturing of fiber phase gratings," *Proc. Conference on Optical Fiber Communication*, post-deadline paper PD16, 68, 1993.

14. G. Meltz, W. W. Morey, S. J. Hewlett, and J. D. Love, "Wavelength shifts in fiber Bragg gratings due to changes in the cladding properties," *Proc. OSA Topical Meeting on Photosensitivity and Quadratic Nonlinearity in Glass Waveguides*, paper PMB4, 225, 1995.

15. W. Johnstone, G. Stewart, T. Hart, and B. Culshaw, "Surface plasmon polaritons in thin metal films and their role in fiber optic polarizing devices," *IEEE Journal of Lightwave Technology*, vol. 8, 538, 1990.

16. W. Johnstone, G. Thursby, B. Culshaw, S. Murray, M. Gill, A. McDonach, D. Moodie, G Fawcett, G. Stewart, and K. McCallion, "A multimode approach to optical fiber components and sensors, " *Proc. SPIE Conference on Micro-Optics II*, vol. 1506, 145, 1991.

17. F. Farahi, D. J. Webb, J. D. C. Jones, and D. A. Jackson, "Simultaneous measurement of temperature and strain: Cross-sensitivity considerations," *Journal of Lightwave Technology*, vol. 8, 138, 1990.

18. A. M. Vengsarkar, W. C. Michie, L. Jankovic, B. Culshaw, and R. O. Claus, "Fiber-optic dual-technique sensor for simultaneous measurement of strain and temperature," *Journal of Lightwave Technology*, vol. 12, 170, 1994.

19. M. G. Xu, J. L. Archambault, L. Reekie, and J. P. Dakin, "Discrimination between temperature and strain effects using dual wavelength fiber grating sensors," *Electronics Letters*, vol. 30, 1085, 1994.

20. W. Jin, W. C. Michie, G. Thursby, M. Konstantaki, and B. Culshaw, "Simultaneous strain and temperature recovery: Error analysis," *Proc. Conference on Optical Fiber Sensors,* paper Tu5-3, 116, 1996.

21. V. Bhatia and A. M. Vengsarkar, "Optical fiber long-period grating sensors," *Optics Letters*, vol. 21, 692, 1996.

22. B. E. A. Saleh and M. C. Teich, *Fundamentals of Photonics*, John Wiley, New York, 1991.

23. H. F. Taylor and A. Yariv, "Guided wave optics," *Proceedings of the IEEE*, vol. 62, 1044, 1974.

24. A. Yariv, "Coupled-mode theory for guided-wave optics," *IEEE Journal of Quantum Electronics*, vol. 9, 919, 1973.

25. K. O. Hill, Y. Fujii, D. C. Johnson, and B. S. Kawasaki, "Photosensitivity in optical fiber waveguides: Applications to reflection filter fabrication," *Applied Physics Letters* , vol. 32, 647, 1978.

26. K. O. Hill, B. Malo, K. Vineberg, F. Bilodeau, D. Johnson, and I. Skinner, "Efficient mode-conversion in telecommunication fibre using externally written gratings," *Electronics Letters*, vol. 26, 1270, 1990.

27. F. Bilodeau, K. O. Hill, B. Malo, D. Johnson, and I. Skinner, "Efficient narrowband LP_{01}<->LP_{02} mode convertors fabricated in photosensitive fiber: Spectral response," *Electronics Letters*, vol. 27, 682, 1991.

28. P. J. Lemaire, R. M. Atkins, V. Mizrahi, and W. A. Reed, "High-pressure H_2 loading as a technique for achieving ultrahigh UV photosensitivity and thermal sensitivity in GeO_2 doped optical fibres," *Electronics Letters*, vol. 29, 1191, 1993.

29. P. J. Lemaire, A. M. Vengsarkar, W. A. Reed, V. Mizrahi, and K. S. Kranz, "Refractive index changes in optical fibers sensitised with molecular hydrogen," *Proc. Conference on Optical Fiber Communication*, paper TuL1, 47, 1994.

30. A. M. Vengsarkar, J. R. Pedrazzani, J. B. Judkins, P. J. Lemaire, N. S. Bergano, and C. R. Davidson, "Long-period fiber-grating based gain equalizers," *Optics Letters*, vol. 21, 336, 1996.

31. A. M. Vengsarkar, P. J. Lemaire, G. Jacobovitz-Veselka, J. B. Judkins, V. Bhatia, J. E. Sipe, and T. E. Ergodan, "Long-period cladding-mode-coupled fiber gratings: properties and applications," *Proc. OSA Topical Meeting on Photosensitivity and Quadratic Nonlinearity in Glass Waveguides*, paper SaB2, 10, 1995.

32. T. A. Tran, J. A. Greene, K. A. Murphy, V. Bhatia, T. D'Alberto, R. O. Claus, B. Carman, D. M. Lyerly and T. D. Wilkins, "Real-time immunoassays using fiber optic long-period grating sensors," *Proc. SPIE Conference on Biomedical Sensing, Imaging, and Tracking Technologies*, vol. 2676, paper 27, 1996.

33. V. Bhatia, D. Campbell, T. D'Alberto, D. Sherr, G. Ten Eyck, M. De Vries, N. Zabaronick, K. A. Murphy and R. O. Claus, "Structural health-monitoring using long-period gratings," *Smart Materials and Structures*, 1997.

34. J. B. Judkins, J. R. Pedrazzani, D. J. DiGiovanni, and A. M. Vengsarkar, "Temperature-insensitive long-period fiber gratings," *Proc. Conference on Optical Fiber Communication*, postdeadline paper PD1, 1996.

35. V. Bhatia, D. Campbell, T. D'Alberto, G. Ten Eyck, D. Sherr, K. A. Murphy and R. O. Claus, "Standard optical fiber long-period gratings with reduced temperature-sensitivity for strain and refractive index sensing," *Proc. Conference on Optical Fiber Communication*, FB1, 1997.

36. V. Bhatia, M. K. Burford, K. A. Murphy, and A. M. Vengsarkar, "Long-period fiber grating sensors," *Proc. Conference on Optical Fiber Communication*, paper ThP1, 265, 1996.

37. V. Bhatia, K. A. Murphy, R. O. Claus, and A. M. Vengsarkar, "Simultaneous measurement systems employing long-period grating sensors," *Proc. Conference on Optical Fiber Sensors*, paper Fr2-5, 702, 1996.

38. D. G. Hall: Editor, *Selected Papers on Coupled-Mode Theory in Guided Wave Optics*, SPIE Optical Engineering Press, Bellingham, 1993.

39. A. M. Vengsarkar, P. J. Lemaire, W. A. Reed, and K. W. Quoi, "Adiabatic mode-field transformers based on photo-induced refractive-index changes in hydrogen-loaded germanosilicate fibers," *Proc. Conference on Optical Fiber Communication*, paper TuL3, 48, 1994.

40. D. P. Hand and P. St. J. Russell, "Photoinduced refractive index changes in germanosilicate fibers," *Optics Letters*, vol. 15, 102, 1990.

41. D. L. Williams, S. T. Davey, R. Kahyap, J. R. Armitage, and B. J. Ainslie, "Direct observation of UV induced bleaching of 240 nm absorption band in photosensitive germanosilicate glass fibres," *Electronics Letters*, vol. 28, 369, 1992.

42. M. M. Boer, R. L. Cone, and J. R. Simpson, "Ultraviolet-induced distributed-feedback gratings in Ce^{3+} doped silica optical fibers," *Optics Letters*, vol. 16, 1381, 1991.

43. K. O. Hill, B. Malo, F. Bilodeau, D. C. Johnson, T. F. Morse, A. Kilian, L. Reinhart, and O. Kyuinghwan, "Photosensitivity in Eu^{2+}:Al_2O_3-doped-core fiber: Preliminary results and application to mode converters," *Proc. Conference on Optical Fiber Communication*, post-deadline paper PD3, 14, 1991.

44. D. L. Williams, B. J. Ainslie, J. R. Armitage, and R. Kahyap, "Enhanced photosensitivity in germania doped silica fibers for future optical networks," *Proc. European Conference on Optical Communication*, 425, 1991.

45. A. Tomita and P. J. Lemaire, "Hydrogen-loaded loss increase in germanium-doped single-mode optical fibers: Long-term predictions," *Electronics Letters*, vol. 21, 71, 1985.

46. F. Ouellette, K. O. Hill, and D. C. Johnson, "Enhancement of second-harmonic generation in optical fibers by hydrogen heat treatment," *Applied Physics Letters,* vol. 54, 1086, 1989.

47. G. D. Maxwell, R. Kashyap, and B. J. Ainslie, "UV written 1.5 μm reflection filters in single mode planar silica guides," *Electronics Letters*, vol. 28, 2016, 1992.

48. G. P. Agarwal, *Fiber-Optic Communication Systems*, John Wiley and Sons, New York, 1992.

49. P. J. Lemaire and T. Ergodan, "Hydrogen-enhanced UV photosensitivity of optical fibers: mechanisms and reliability", *Proc. OSA Topical Meeting on Photosensitivity and Quadratic Nonlinearity in Glass Waveguides*, paper SuA4, 78, 1995.

50. P. J. Lemaire, V. Mizrahi, R. M. Atkins, and K. S. Kranz, "High-temperature stability of phase gratings in GeO_2-doped optical fibers," *Proc. Conference on Optical Fiber Communication*, 242, 1993.

51. B. I. Greene, D. M. Krol, S. G. Kosinski, P. J. Lemaire, and P. N. Saeta, "Thermal and photo-initiated reactions of H_2 with germanosilicate fibers," *Proc. Conference on Optical Fiber Communication*, paper TuL2, 48, 1994.

52. R. Syms and J. Cozens, *Optical guided waves and devices*, McGraw-Hill, England, 1992.

53. G. Keiser, *Optical Fiber Communications*, second edition, McGraw-Hill, New York, 1991.

54. D. Gloge, "Weakly guiding fibers," *Applied Optics*, vol. 10, 2252, 1971.

55. D. Marcuse, *Theory of Dielectric Optical Waveguides*, Academic Press, New York, 1974.

56. J. R. Pierce, "Coupling of modes of propagation," *Journal of Applied Physics*, vol. 25, 1954.

57. D. Marcuse, "Microdeformation losses single-mode fibers," *Applied Optics*, vol. 23, 1082, 1984.

58. C. B. Probst, A. Bjarklev, and S. B. Andreasen, "Experimental verification of microbending theory using mode coupling to discrete cladding modes," *Journal of Lightwave Technology*, vol. 7, 55, 1989.

59. D. G. Hall, "Theory of Waveguides and Devices," in *Integrated Optical Circuits and Components*, L. D. Huctheson: Editor, Marcel-Dekker, New York, 1987.

60. R. Kashyap, "Photosensitive Optical Fibers: Devices and Applications," *Optical Fiber Technology*, vol. 1, 17, 1994.

61. Corning product information sheet , *Flexcor Specialized Single-Mode Optical Fiber*, Corning Incorporated, New York, 1996.

62. J. W. Fleming, "Material dispersion in lightguide glasses," *Electronics Letters*, vol. 14, 326, 1978.

63. R. Kashyap, R. Wyatt, and R. J. Campbell, "Wideband gain flattened erbium fibre amplifier using a photosensitive fiber blazed grating," *Electronics Letters*, vol. 29, 154, 1993.

64. A. W. Snyder and J. W. Love, *Optical Waveguide Theory*, Chapman and Hall, New York, 1983.

65. Corning product information sheet, *SMF-28 CPC6 Single-Mode Optical Fiber*, Corning Incorporated, New York, 1996.

66. S. Huang, M. LeBlanc, M. M. Ohn, and R. M. Measures, "Bragg intragrating structural sensing," *Applied Optics*, vol. 34, 5003, 1995.

67. R. Kashyap, J. R. Armitage, R. Wyatt, S. T. Davey, and D. L. Williams, "All-fibre narrowband reflection gratings at 1500 nm," *Electronics Letters*, vol. 26, 730, 1990.

68. V. Mizrahi, T. Erdogan, D. J. DiGiovanni, P. J. Lemaire, S. G. Kosinski, T. A. Strasser and A. E. White, "Fiber-grating transmission filters for use in all-fiber demultiplexer," *Proc. Conference on Optical Fiber Communication*, paper TuL6, 52, 1994.

69. G. A. Ball, W. W. Morey, and J. P. Waters, "Nd^{3+} fibre laser utilizing intra-core Bragg reflectors," *Electronics Letters*, vol. 26, 1829, 1990.

70. J. L. Zyskind, J. W. Sulhoff, P. D. Magill, K. C. Reichmann, V. Mizrahi and D. J. DiGiovanni, "Transmission at 2.5 Gbit/s over 654 km using an erbium-doped fiber grating laser source," *Electronics Letters*, vol. 29, 1105, 1993.

71. G. Meltz and W. W. Morey, "Bragg grating formation and germanosilicate fiber photosensitivity," *Proc. International Workshop of Photoinduced Self-Organization Effects in Optical Fibers*, SPIE, vol. 1516, 185, 1991.

72. H. Tsuchiya and N. Imoto, "Dispersion-free single-mode fiber in 1.5 mm wavelength region," *Electronics Letters*, vol. 15, 396, 1979.

73. A. M. Vengsarkar, W. A. Reed, and C. D. Poole, "Effect of refractive-index profiles on two-mode optical fiber dispersion compensators," *Optics Letters*, vol. 17, 1503, 1992.

74. F. Ouellette, "All-fiber filter for efficient dispersion compensation," *Optics Letters*, vol. 16, 303, 1991.

75. R. Kashyap, R. Wyatt, and P. F. McKee, "Wavelength flattened saturated erbium amplifier using multiple side-tap Bragg gratings," *Electronics Letters*, vol. 29, 1025, 1993.

76. C. G. Askins, M. A. Putnam, G. M. Williams, and E. J. Friebele, "Stepped-wavelength optical-fiber Bragg gratings arrays fabricated in line on a draw tower," *Optics Letters*, vol. 19, 147, 1994.

77. N. P. Bansal and R. H. Doremus, *Handbook of Glass Properties*, Academic Press, Florida, 1986.

78. S. Y. Huang, J. N. Blake, and B. Y. Kim, "Perturbation effects on mode propagation in highly elliptical core two-mode fiber," *Journal of Lightwave Technology*, vol. 8, 23, 1990.

79. A. M. Vengsarkar, J. A. Greene, and K. A. Murphy, "Photoinduced refractive-index changes in two-mode, elliptical-core fibers: sensing applications," *Optics Letters*, vol. 16, 1541, 1991.

80. D. C. Johnson, F. Bilodeau, B. Malo, K. O. Hill, P. G. J. Wigley, and G. I. Stegeman, "Long-length, long-period rocking filters fabricated from conventional monomode telecommunications optical fibers," *Optics Letters*, vol. 17, 1635, 1992.

81. V. Bhatia, K. A. Murphy, A. Wang, R. O. Claus, and J. A. Greene, "Attometer resolution of wavelength shifts by use of fiber modal interferometers," *Optics Letters*, vol. 20, 97, 1995.

82. J. L. McMillan and S. C. Robertson, "Cutoff wavelength determination in single-mode optical fibers by measurement of equalisation wavelength," *Electronics Letters*, vol. 20, 698, 1984.

83. C. D. Poole, J. M. Wiesenfeld, A. R. McCormick, and K. T. Nelson, "Broadband dispersion compensation by using the higher-order spatial mode in a two-mode fiber," *Optics Letters*, vol. 17, 985, 1992.

84. A. M. Vengsarkar, J. A. Greene, B. R. Fogg, and K. A. Murphy, "Spatially weighted, grating-based, two-mode, elliptical-core optical fiber vibration sensors," *Optics Letters*, vol. 16, 1707, 1991.

85. A. M. Vengsarkar, B. R. Fogg, W. V. Miller, K. A. Murphy and R. O. Claus, "Elliptical-core, two-mode optical fiber sensors as vibration-mode filters," *Electronics Letters*, vol. 27, 931, 1991.

86. V. Mizrahi and J. E. Sipe, "Optical properties of photosensitive fiber phase gratings," *IEEE Journal of Lightwave Technology*, vol. 11, 1513, 1993.

87. William B. Jones, *Introduction to Optical Fiber Communication Systems*, Holt, Rhinehart and Winston, Inc., New York, 1988.

88. J. W. Fleming, "Material and mode dispersion in GeO_2-B_2O_3-SiO_2 glasses," *Journal of American Ceramic Society*, vol. 59, 503, 1976.

89. D. N. Payne and W. A. Gambling, "Zero material dispersion in optical fibers," *Electronics Letters*, vol. 11, 176, 1975.

90. M. J. Adams, *An Introduction to Optical Waveguides*, Wiley-Interscience, New York, 1981.

91. B. Edlén, "The refractive index of air," *Meterologia*, vol. 2, 71, 1965.

92. E. W. Swokowski, *Calculus with Analytic Geometry*, PWS-KENT Publishing Company, Boston, 1988.

93. H. Taub and D. L. Schilling, *Principles of Communication Systems*, McGraw-Hill Book Company, New York, 1986.

94. F. Bilodeau, D. C. Johnson, B. Malo, K. A. Vineberg, K. O. Hill, T. F. Morse, A. Kilian, and L. Reinhart, "Ultraviolet-light photosensitivity in Er^{3+}-Ge-doped optical fiber," *Optics Letters*, vol. 15 1138, 1990.

95. M. R. Spiegel, *Mathematical Handbook of Formulas and Tables*, McGraw-Hill, New York, 1994.

96. E. M. Dianov, A. S. Kurkov, O. I. Medvedkov, and S. A. Vasil'ev, "New sensitive method for measuring induced refractive index change in optical fiber core", *Proc. OSA Topical Meeting on Photosensitivity and Quadratic Nonlinearity in Glass Waveguides*, paper SuB4, 104, 1995.

97. C. Narayanan, H. M. Presby, and A. M. Vengsarkar, "Band-rejection filter using periodic core deformation," *Proc. Conference on Optical Fiber Communication*, paper ThP3, 267, 1996.

98. T. Ergodan, V. Mizrahi, P. J. Lemaire, and D. Monroe, "Decay of ultra-violet-induced fiber Bragg gratings," *Journal of Applied Physics*, vol. 76, 73, 1994.

99. V. Bhatia, T. D'Alberto, K. A. Murphy, R. O. Claus, and A. M. Vengsarkar, "Optical fiber long-period grating sensors," *Proc. Conference on Optical Fiber Sensors*, paper We4-3, 360, 1996.

100. E. Desurvire, *Erbium-Doped Fiber Amplifiers*, John Wiley and Sons, New York, 1994.

101. C. R. Giles and E. Desurvire, "Modeling erbium-doped fiber amplifiers," *IEEE Journal of Lightwave Technology*, vol. 9, 271, 1991.

102. C. Y. Kuo and E. E. Bergmann, "Erbium-doped fiber amplifier second order distortion in analog links and electronic compensation," *IEEE Photonics Technology Letters*, vol. 3, 829, 1991.

103. K. Kikushima and Y. Yoshinaga, "Distortion due to gain tilt of erbium-doped fiber amplifiers," *IEEE Photonics Technology Letters*, vol. 3, 945, 1991.

104. K. Simon, *Technical Handbook for CATV Systems*, General Instruments, 1986.

105. I. M. Habab and L. J. Cimini, "Optimized performance of erbium-doped fiber amplifiers in subcarrier multiplexed lightwave AM-VSB CATV systems," *IEEE Journal of Lightwave Technology*, vol. 9, 1321, 1991.

106. V. L. da Silva, Y. Silberberg, J. S. Wang, E. L. Goldstein, and M. J. Andrejco, "Automatic gain flattening in Er-doped-fiber amplifiers," *Proc. Conference on Optical Fiber Communication*, paper ThD2, 174, 1993.

107. L. Eskildsen, E. Goldstein, V. da Silva, M. Andrejco, and Y. Silberberg, "Optical power equalization for multiwavelength fiber-amplifier cascades using periodic inhomogeneous broadening", *IEEE Photonics Technology Letters*, vol. 5, 1188, 1993.

108. R. I. Laming, J. D. Minelli, L. Long, and M. N. Zevras, "Erbium-doped-fiber amplifier with passive spectral-gain equalization," *Proc. Conference on Optical Fiber Communication*, paper ThD3, 175, 1993.

109. C. R. Giles and D. DiGiovanni, "Dynamic gain equalization in two-stage fiber amplifiers," *IEEE Photonics Technology Letters*, vol. 2, 866, 1990.

110. C. R. Giles and D. DiGiovanni, "Spectral dependence of gain and noise in erbium-doped fiber amplifiers," *IEEE Photonics Technology Letters*, vol. 2, 797, 1990.

111. T. Kashiwada, M. Shigematsu, M. Kakui, M. Onishi, and M. Nishimura, "Gain-flattened optical-fiber amplifiers with a hybrid Er-doped-fiber configuration for WDM transmission," *Proc. Conference on Optical Fiber Communication*, paper TuP1, 77, 1995.

112. M. Wilkinson, A. Bebbington, S. A. Cassidy, and P. McKee, "D-fibre filter for erbium gain spectrum flattening," *Electronics Letters*, vol. 28, 131, 1992.

113. M. Tachibana, R. I. Laming, P. R. Morkel, and D. N. Payne, "Erbium-doped fiber amplifier with flattened gain spectrum," *IEEE Photonics Technology Letters*, vol. 3, 118, 1991.

114. G. Grasso, F. Fontana, A. Righetti, P. Scrivener, P. Turner, and P. Maton, "980 nm diode-pumped Er-doped fiber optical amplifiers with high gain-bandwidth product," *Proc. Conference on Optical Fiber Communication*, paper FA3, 195, 1991.

115. S. F. Su, R. Olshansky, G. Joyce, D. A. Smith, and J. E. Baran, "Gain equalization in multiwavelength lightwave systems using acousto-optic tunable filters," *IEEE Photonics Technology Letters*, vol. 4, 269, 1992.

116. K. Inoue, T. Kominato, and H. Toba, "Tunable gain equalization using a Mach-Zender optical filter in multistage fiber amplifiers," *IEEE Photonics Technology Letters*, vol. 3, 718, 1991.

117. R. A. Betts, S. J. Frisken, and D. Wong, "Split-beam Fourier filter and its application in a gain-flattened EDFA," *Proc. Conference on Optical Fiber Communication*, paper TuP4, 80, 1995.

118. G. Jacobovitz-Veselka, P. F. Wysocki, A. M. Vengsarkar, J. M. Borick, T. Ergodan, V. Mizrahi, and S. W. Granlund, "Single-stage booster amplifier with two 980 nm pumps stabilized by fiber gratings," *Proc. Optical Amplifiers Meeting*, paper FC4, 1995.

119. C. R. Giles, T. Erdogan and V. Mizrahi, "Reflection-induced changes in the optical spectra of 980-nm QW lasers," *IEEE Photonics Technology Letters*, vol. 6, 903, 1994.

120. S. G. Grubb, T. Ergodan, V. Mizrahi, T. Strasser, W. Y. Cheung, W. A. Reed, P. J. Lemaire, A. E. Miller, S. G. Kosinski, G. Nykolak, and P. C. Becker, "1.3 μm cascaded Raman amplifier in germanosilicate fiber," *Proc. Optical Amplifiers Meeting*, postdeadline paper PD3, 1994.

121. A. Wang, V. Arya, M. H. Nasta, K. A. Murphy, and R. O. Claus, "Optical fiber polarizer based on highly birefringent single-mode fiber," *Optics Letters*, vol. 20, 279, 1995.

122. T. H. Wood, "Multiple quantum well (MQW) waveguide modulators," *IEEE Journal of Lightwave Technology*, vol. 6, 743, 1988.

123. D. R. Lide: Editor, *CRC Handbook of Chemistry and Physics*, 74th edition, CRC Press, 1993.

124. Technical bulletin, *Specialty Optical Liquids*, R. P. Cargille Laboratories, New Jersey, 1994.

125. N. Lagakos, J. A. Bucaro, and R. Hughes, "Acoustic sensitivity predictions of single-mode optical fibers using Brillouin scattering," *Applied Optics*, vol. 19, 3668, 1980.

126. V. Bhatia, M. K. Burford, N. Zabaronick, K. A. Murphy, and R. O. Claus, "Strain and refractive index sensors using temperature-insensitive long-period gratings," *Proc. Conference on Optical Fiber Sensors*, post-deadline paper Fr3-1, 1996.

127. M. N. Zervas and I. P. Giles, "Optical-fiber surface-plasmon-wave polarisers with enhanced performance," *Electronics Letters*, vol. 25, 321, 1989.

128. M. H. Kuhn, "Optimum attenuation of cladding modes in homogeneous single mode fibers," *Archiv fur Electronik and Ubertragungstechnik*, vol. 29, 201, 1975.

129. H. Nygren and M. Stenburg, "Calibration by ellipsometry of the enzyme-linked immunosorbent assay," *Journal of Immunological Methods*, vol. 80, 15, 1985.

130. D. C. Cullen, R. G. W. Brown, and C. R. Brown, "Detection of immuno-complex formation via surface plasmon resonance on gold-coated diffraction gratings," *Biosensors*, vol. 3, 211, 1988.

131. J. A. Greene, K. A. Murphy, T. A. Tran, V. Bhatia, and R. O. Claus, "Grating-based optical fiber corrosion sensors," *Proc. SPIE Conference on Smart Sensing, Processing, and Instrumentation*, vol. 2718, paper A-19, 1996.

132. T. G. Giallorenzi, J. A. Bucaro, A. Dandridge, G. H. Sigel, Jr., J. H. Cole, S. C. Rashleigh, and R. G. Priest, "Optical fiber sensor technology," *IEEE Journal of Quantum Electronics*, vol. 18, 626, 1982.

133. C. E. Lee and H. F. Taylor, "Fiber-optic Fabry-Perot temperature sensor using a low-coherence light source," *Journal of Lightwave Technology*, vol. 9, pp. 129-134, 1991.

134. J. Sirkis, "Phase-strain-temperature model for structurally embedded interferometric optical fiber strain sensors with applications," *Proc. SPIE Conference on Fiber Optic Smart Structures and Skins IV*, vol. 1588, 26, 1991.

135. L. W. Johnson and R. D. Reiss, *Numerical Analysis*, Addison-Wesley, Reading, 1982.

136. J. J. Dongarra, C. B. Moler, J. R. Bunch, and G. W. Stewart, *LINPACK User's Guide*, SIAM, Philadelphia, 1979.

Vita

Vikram Bhatia was born in Srinagar, the capital city of the northern Indian state of Jammu and Kashmir on August 9, 1970. His family moved to New Delhi a year later where Vikram completed his schooling at the Delhi Public School. He received his Bachelor of Engineering degree from the Birla Institute of Technology, Ranchi in Electronics and Communications in May 1992.

Vikram came to the United States in August 1992 to pursue graduate studies at Virginia Tech in Blacksburg, VA. He joined the Fiber & Electro-Optics Research Center as a Graduate Research Assistant and was involved with the research and development of optical fiber interferometric sensors, fiber components and modal interferometers. Vikram completed his Master of Science degree in Electrical Engineering in December 1993. His thesis, under the supervision of Dr. Kent A. Murphy, focused on overcoming the limitations of the extrinsic Fabry-Perot interferometer using white light interferometry.

In the Fall of 1994, Vikram had the opportunity to work at Bell Laboratories, Murray Hill, NJ with Dr. Ashish M. Vengsarkar. Vikram was responsible for the fabrication, packaging and testing of long-period gratings. He also assisted in developing these devices for applications such as gain equalization and ASE suppression in erbium-doped fiber amplifiers.

During the next two years, Vikram was a part of the team at the Fiber & Electro-Optics Research Center that investigated long-period grating sensors. He was involved with the development of long-period gratings as temperature, strain and index of refraction sensors. His Ph.D. research comprises of the analysis of the properties and sensing applications of long-period gratings. His other technical interests include Bragg gratings, dispersion compensating techniques and erbium-doped fiber amplifiers. Vikram is a member of the Optical Society of America.

Vikram Bhatia